Composite materials for structural performance: towards higher limits

Risø National Laboratory for Sustainable Energy
Technical University of Denmark
Post box 49
4000 Roskilde, Denmark
www.risoe.dtu.dk

ISBN 978-87-550-3925-4

ISSN 0907-0079

Composite materials for structural performance: towards higher limits

Proceedings of the 32nd Risø International Symposium
on Materials Science

5-9 September
2011

Editors

S. Fæster, D. Juul Jensen,

B. Ralph, B.F. Sørensen

RISØ NATIONAL LABORATORY FOR SUSTAINABLE ENERGY
TECHNICAL UNIVERSITY OF DENMARK
ROSKILDE, DENMARK

Risø International Symposium on

Composite materials for structural performance: towards higher limits

INTERNATIONAL ADVISORY COMMITTEE

Martin Bendsøe, Denmark

Robin Olsson, Sweden

Karl Schulte, Germany

Ramesh Talreja, USA

Michael D. Thouless, USA

LOCAL ORGANIZING COMMITTEE

T.L. Andersen

C. Berggreen

K. Branner

P. Brøndsted

L. Danielsen

S. Fæster

D. Juul Jensen

H. Lilholt

B. Madsen

L.P. Mikkelsen

L. Mishnaevsky

R.T.D. Prabhakaran

B.F. Sørensen

H.L. Toftegaard

PREFACE

A major trend in today's society is the development of new, more efficient and/or larger structures. Composite materials based on long aligned fibres are increasingly used in large structures such as wind turbine blades, aeroplanes and ships. This striving for larger and more efficient structures creates a constant push for materials science to develop new materials with enhanced properties (moving the limits of the materials) and to develop better, more precise and reliable design methods and criteria (moving the design limits).

The limits of materials properties can be increased by materials development, by understanding how composite materials work at various length scales, e.g. understanding the interplay between properties of fibres, matrix and the fibre/matrix interface through micromechanical modelling and microscale experiments.

Design limits, e.g., criteria for material failure and lifetime predictions, can be expanded by developing and validating improved models for the critical limit states, e.g. the onset of fatigue failure under multiaxial stress state, the use of damage tolerant design approach and the use of more advanced modelling tools such as cohesive zone modelling.

The limits of composite materials and structures were the theme of the Symposium. The presentations covered the challenges of identifying and moving the experimental and modelling limits. A central issue was the multi-scale approach to composites: Composites were addressed at various length scales, from material scale (nano-/micrometre) to structural scale (decametre scale), potentially leading to optimisation of properties (moving the limits of the composite material), the development of new test methods for the characterisation of composite materials, processing of optimised composite materials as well as the characterisation of all required material properties for structural design and the development of new design criteria and design methods (moving the design limits).

The proceedings contain 12 key-note presentations and 36 contributing presentations. We hope that the symposium and the proceedings will inspire the future development in the composite materials and structures.

The 32nd International Risø Symposium on Materials Science was organised by the Materials Research Division, Risø National Laboratory for Sustainable Energy, The Technical University of Denmark (DTU) and the Danish Centre for Composite Structures and Materials for Wind Turbines (DCCSM) supported by grant no. 09-067212, from the Danish Strategic Research Council. We are also very grateful for financial support from the following foundations: Civilingeniør Frederik Leth Christiansens Almennyttige Fond, Fabrikant Mads Clausens Fond, Knud Højgaards Fond, Kraks Fond, Otto Mønsteds Fond and Oticon Fonden.

T.L. Andersen C. Berggreen K. Branner P. Brøndsted
L. Danielsen S. Fæster D. Juul Jensen H. Lilholt B. Madsen
L.P. Mikkelsen L. Mishnaevsky R.T.D. Prabhakaran
B. Ralph B.F. Sørensen H.L. Toftegaard

Contents

INVITED PAPERS

CONTRIBUTED PAPERS

Proceedings of the 32nd
Risø International Symposium on Materials Science:
Composite materials for structural performance:
Towards higher limits
Editors: S. Fæster, D. Juul Jensen,
B. Ralph, B.F. Sørensen
Risø National Laboratory for Sustainable Energy,
Technical University of Denmark, 2011

MULTI-SCALE APPROACHES TO FRACTURE AND FATIGUE OF FIBER COMPOSITES – WHERE ARE THE EXPERIMENTAL AND COMPUTATIONAL LIMITS AND CHALLENGES?

B.N. Cox*, M.R. Begley**, P. Kroll***, D.B. Marshall*,
R.O. Ritchie**** and Q.D. Yang*****

*Teledyne Scientific Co LLC, Thousand Oaks, California
**University of California, Santa Barbara
***University of California, Berkeley
****University of Texas, Arlington
*****University of Miami, Coral Gables, Florida

ABSTRACT

Building on the recent success of simulations that homogenize fiber plies ("ply-scale models"), experimenters and theorists are now seeking to predict the details of failure events within a single ply in a laminate, where the discreteness of fibers must enter the problem. This new frontier of research demands a multi-scale representation of failure, bridging the ply and infra-ply scales. Such a multi-scale model promises to revolutionize the optimization of composite materials and the prediction of their safe life. However, the infra-ply scale is much more difficult than the ply-scale problem and will not be easily conquered. The key experimental challenges is acquiring 3D data that reveal the random microstructure and damage events in the interior of the composite with very high resolution (~ 1 μm). Key theoretical challenges include understanding how to represent the essential stochastic characteristics of the 3D microstructure, how to model the failure events that evolve within it, and resolving the fundamental question of what is predictable and what cannot be predicted because of the extreme sensitivity of the failure sequence in a random material to initial conditions.

1. INTRODUCTION

Numerous efforts are under way to establish Virtual Tests as engineering tools to aid materials design and reduce the number of actual tests required to certify a given material for service. In the particular application of continuous fiber composites, significant successes have been realized by representing individual plies as homogeneous, anisotropic materials, thus ignoring

the discrete nature of the fibers within a ply. The use of ply homogenization can be called modeling at the ply scale. A number of research groups have contributed to ply-scale model development based on discrete representation of multiple cracking events. Some recent papers (Iarve, Mollenhauer and Kim 2005; Hallett and Wisnom 2006; Van de Meer, Oliver and Sluys 2010; Van de Meer and Sluys 2010; Fang, Zhou, Cox and Yang 2011b) have demonstrated encouraging fidelity in discrete damage models in reproducing experimental observations for polymer composites. The global stress-strain curve, the shape and rate of growth of delamination cracks, the rate of growth of dominant shear (e.g., splitting) cracks, and the density of transverse ply cracks can all be predicted by models that are calibrated by independent data. This level of success has demanded not only computational power, but more importantly, the development of new computational elements, especially those that allow arbitrary cracking (the X-FEM and A-FEM methods (Moës, Dolbow and Belytschko 1999; Strouboulis, Copps and Babuška 2001; Moës and Belytschko 2002; de Borst 2003; Zi and Belytschko 2003; Andersson and Stigh 2004; Ling, Yang and Cox 2009)) and deal correctly with crack bifurcation and coalescence in the presence of nonlinear fracture zones (Fang, Yang, Cox and Zhou 2011a). A further key ingredient is the use of nonlinear cohesive zone models of fracture, which unify the processes of crack initiation and growth within a single physical model, avoiding the non-physical nature of linear elastic fracture mechanics in the limit of very small crack length (Needleman 1990; Corigliano 1993; Wisnom and Chang 2000; Elices, Guinea, Gomez and Planas 2002; Moës and Belytschko 2002; de Borst 2003; Remmers, de Borst and Needleman 2003; Yang and Cox 2005; Cox and Yang 2006).

While the number of loading cases studied using ply-scale models is still small, mainly focusing on monotonic tensile loading for a few ply lay-ups and simple specimen types, generalizing to other cases is expected to be relatively straightforward. Critical comparisons with experimental data must be carried out for each new case before global validation can be claimed, a laborious and essential process, but the principles needed for success can be reasonably believed to be mainly in place. No further new physics or basic computational technique needs to be developed. The task appears to lie in the realm of engineering, rather than science. As a scientific problem, the community can claim victory for ply-level simulations of polymer composites; we know how to do it.

The next challenge in a top-down strategy of model development lies at the infra-ply level, or the fiber level, where fibers are represented as discrete entities. Accomplishments to date at the fiber level are sparse; we are a long way from fidelity equivalent to that achieved at the ply level. Neither, in the opinion of the authors, will progress occur easily. Adding the fiber level to a Virtual Test formulation poses serious challenges and difficulties, ranging from a clear vision of what is expected to be gained in engineering applications to fundamental questions of what is predictable and what is not, due to the potential for chaotic behavior in predicted failure patterns in the random microstructure of a typical fiber bundle.

This paper discusses some (but by no means all) of the key challenges in adding the infra-ply scale. Questions are posed in the context of the top-down strategy for constructing high-fidelity simulations.

2. WHY TAKE THE TROUBLE TO DO FIBER-LEVEL SIMULATIONS?

To motivate the exploration of fiber-level phenomena, consider first the structure of a successful ply-level simulation or “Virtual Test” and all the things that a ply-level simulation can already do. Only then can one speak of what additional engineering tool can be sought via fiber-level modeling.

Recent ply-level formulations incorporate two types of damage: systems of discrete cracks of

different type, including delaminations, splitting cracks, and transverse intra-ply cracks; and continuous plasticity. The last represents irreversible damage that occurs in small volumes of the polymer matrix and involves damage (crazing, etc.) at the μm scale, which is not included in the larger-scale (ply-scale) cracking systems (Wisnom and Chang 2000; Hallett and Wisnom 2006; Fang et al. 2011b). The ply-level simulations successfully replicate macroscopic engineering test data by using failure parameters for each of these failure mechanisms that have been calibrated by independent engineering tests.

For the discrete cracks, calibration is needed for the parameters that appear in non-linear fracture cohesive laws. These laws consist of relationships between the crack opening vector across a crack (or localized damage band) and the tractions that persist across the crack due to the fact that the cracking material fails not instantaneously but progressively. Experience to date indicates that faithful replication of macroscopic engineering tests can be achieved by using just two parameters for mode I cracking and two more parameters for modes II and III combined. The two parameters for each mode can be chosen to be the maximum stress supported by the material before it begins to fail, $\sigma_c^{(I)}$ or $\sigma_c^{(II)}$, and the work of fracture, $G_c^{(I)}$ or $G_c^{(II)}$ (the area under the traction-separation law). With this choice, some combination of $\sigma_c^{(I)}$ and $\sigma_c^{(II)}$, say $\eta_c = \mathrm{fn}\left(\sigma_c^{(I)}, \sigma_c^{(II)}\right)$, also provides a criterion for local crack initiation in previously pristine material, with cracking beginning when some gauge-averaged combination of the components of the computed local stress (or strain) attains the value η_c. (Gauge averaging is appropriate because the fracture is nonlinear (Clarke and McGregor 1993; Rossmanith 1995; Sheppard, Kelly and Tong 1998; Feih and Shercliffe 2004; Yang and Cox 2010a; Yang and Cox 2010b). Thus the cohesive law unifies crack initiation and propagation.

For continuous plasticity, constitutive laws relate local shear stress to shear strain, $\tau_p(\gamma_p)$, and can be deduced from macroscopic tests on cross-plied laminates (Jelf and Fleck 1994; Dadkhah, Morris and Cox 1995; Fang et al. 2011b).

When multiple failure mechanisms act (the usual case), including fiber failures and matrix cracks of different types, separate sets of calibration parameters are expected for each mechanism, although sometimes for physical reasons the same parameter values $\{\sigma_c^{(I)}, \sigma_c^{(II)}, G_c^{(I)}, G_c^{(II)}, \eta_c\}$ can represent two or more crack types (Fang et al. 2011b). Other material parameters that may need calibration include the composite elastic modulus, but at least for polymer composites, the composite elasticity can be predicted accurately from fiber and matrix properties, which in turn can be regarded as known *a priori* (this is not true for ceramic matrix composites (Flores, Evans, Zok, Genet, Cox, Marshall, Sudre and Yang 2010)).

The calibration procedure treats the parameters $\sigma_c^{(I)}$, $\sigma_c^{(II)}$, $G_c^{(I)}$, $G_c^{(II)}$, η_c, and $\tau_p(\gamma_p)$ as material constants determined by tests on well chosen composite specimens. (The question of how to choose and analyze calibration tests for mixed-mode cracks is one of the more difficult remaining in the development of ply-level virtual tests – see below.) The calibrated values depend implicitly on myriad, poorly known details of events occurring at the infra-ply or fiber level (or the nano-scale), but no explicit knowledge of these dependences is needed to execute a successful prediction of most engineering performance. This the beauty and power of the top-down approach to prediction; the influence of details at finer scales is necessarily captured in the calibration of the failure parameters describing the coarser scales, provided the parameters and their calibration methods have been properly chosen (Hutchinson and Evans 2000; Cox and Yang 2006).

The strategy of feeding calibrated parameters into a simulation engine to generate engineering predictions succeeds not only for average engineering properties, but also for predicting

variance, as demonstrated recently for tensile test simulations (Fang et al. 2011b). The natural variance in calibration parameters can be deduced from the scatter found in the calibrating experiments. The probability distribution for any engineering metric can then be computed by feeding deviant calibration values through the simulator.

Design engineers concerned with assuring the life of structures could well be content with such virtual tests, used in conjunction with real test data. For a given fiber and resin choice, one set of calibration tests would be enough to enable predictions of engineering performance for any ply lay-up, set of ply thicknesses, or component shape and loading condition. Why then push on into the complexity of the infra-ply level?

First, one must emphasize that the above positive report is based on success with the case of monotonic tension. Two other loading cases in particular might require at least some account of infra-ply details to achieve similar fidelity in simulations: monotonic compression and cyclic loading, whether in tension or compression. For both of these cases, damage tends to be confined within single plies until a critical degree of local softening is reached, whereupon global failure ensues. The passage from local damage to global failure involves cracking of the type already simulated accurately for tensile failure, but the crack growth often occurs unstably in compression or fatigue loading, without significant additional load increase or load cycles. Therefore, the local damage accumulation is the key to life; a useful engineering prediction must deal with how this infra-ply or fiber-level phenomenon depends on material and extrinsic conditions (load and geometry).

Second, the ply-level strategy allows optimization of a composite only at the ply level, e.g., it can predict whether one ply lay-up is better than another. It cannot support optimization based on the manipulation of material components (e.g., the twisting of fiber bundles, or changing the matrix or interface coatings), other than by the empirical method of re-calibrating the model for each material candidate. Fiber-level modeling can reveal the influence of details of the material composition and microstructure, opening a pathway to material optimization by design.

Third, while one study to date of the predicted scatter in engineering properties has shown reasonable agreement with experiment (Fang et al. 2011b), whether this success will hold up in other cases is unknown. Rather than using empiricism to treat variance, a more useful approach may be to account for variance by probabilistic models of the effects of stochastic microstructure on failure mechanisms (see below). Since real tests of engineering properties show significant scatter, one can only claim to have created a fully functional virtual test when it also predicts scatter, in agreement with experiment.

A fourth reason to study the infra-ply scale, and one might say the most important, is pure scientific curiosity! To go to the infra-ply scale, new types of experiment must be developed and new theories formulated. As well as the traditional disciplines of materials experimentation and modeling, opportunities arise in image analysis, probability theory, statistical physics, molecular dynamics, and quantum chemistry. The infra-ply scale presents a huge opportunity to do novel engineering science, provides new territory for young researchers to occupy, and will surely yield many unpredictable discoveries and potential benefits. It is the natural continuation of the top-down approach to creating virtual tests, with the ultimate goal of reaching all the way down to the atomic scale.

3. DESCRIBING THE GEOMETRY OF INFRA-PLY MICROSTRUCTURE

Irregularities in the spatial positioning of fibers within tows are involved in several failure mechanisms. Local patches of fiber misalignment trigger kink band formation in compressive loading (Rosen 1965; Argon 1972; Budiansky 1983; Fleck and Shu 1995) and matrix and fiber

attrition in cyclic loading (Lam and Piggott 1990; Piggott and Lam 1991). Transverse intra-ply matrix cracking is promoted by the high stress concentration that arises between two fibers that are unusually close to one another (Marshall, Morris, Cox, Graves, Porter, Kouris and Everett 1994). The meandering of fibers leads to oblique fiber bridging across splitting cracks running along the nominal fiber direction (Kaute, Shercliff and Ashby 1993) and across delamination cracks when the fracture surface wanders from the ply interface (Spearing and Evans 1992). In all these cases, the key microstructural characteristic is a stochastic deviation of the fiber deployment from the ideal of uniformly spaced, parallel fibers. Fiber deviations are a likely source of scatter in engineering properties. The deviations are typically defined by the positions of ~1000 fibers, which occupy a width ~ 1 – 10 mm in a ply of typical thickness. The saturation spacing of transverse intraply cracks and the width of a kink-triggering wavy fiber patch, for example, are typically ~ 1 – 10 mm.

To include fiber deviations in a virtual test simulation, we need to find a way of generating instances of random fiber positioning, for incorporation in virtual specimens, which recreate the statistics of fiber positioning measured in a real specimen. The first challenge is therefore to measure fiber positions in a real specimen. Early attempts have used serial sectioning of composites to track individual fibers through the interior volume, a tedious effort with imperfect results (Yurgatis 1987; Hillig 1994). A much better approach is now available using micron-resolution x-ray computed tomography (μCT), either on laboratory systems or at high intensity synchrotron sources. While detailed geometrical information on large populations of individual fibers has yet to be extracted by the analysis of μCT images, sufficient resolution of individual fibers has clearly been demonstrated (Moffat, Wright, Buffiere, Sinclair and Spearing 2008; Wright, Fu, Sinclair and Spearing 2008). Progress awaits automation of image analysis, to make practicable the extraction of positional data for ~1000 fibers.

With data for a few real specimens in hand, the next challenge is to characterize the statistics of fiber population, and then find an algorithm that can generate a set of virtual populations, each with a distinct instantiation of the fiber positions but adhering to the measured statistics on average.

For a single section of a fiber bundle, the required algorithm solves a random-packing problem, but in distinction to the very popular problem of sphere and circle packing in statistical physics (e.g., http://www.math.cornell.edu/~connelly/PackingsIII.IV.pdf, (Kausch, Fesko and Tschoegl 1971; Powell 1979; Torquato, Truskett and Debenedetti 2005)), one seeks to generate a particular, often relatively low average fiber volume fraction, rather than the maximum achievable. An example of an algorithm for generating random fiber positions for a population of N fibers occupying a square space is as follows. First, fibers are positioned with uniform random spatial position (a Poisson process). Next, each fiber's neighbors are determined using the Voronoi polygon construction (Voronoi 1907). Next, if the distance between the centers of any two neighboring fibers is less than $2R$, with R the fiber radius, then the two fibers are moved apart to a distance $\geq 2R$. Finally, because neighbor sets may have changed when fibers that were too close were separated, the neighbor map is re-computed and the distance check and correction iterated. The fiber separation process tends to dilute the average fiber density and therefore a target volume fraction is achieved by beginning with a higher volume fraction in the initial fiber positioning; the required target is easily hit by iteration, for typical composite values. Sample spatial distributions generated by this algorithm appear qualitatively similar to those seen on sections of composites (Fig. 1.). It remains to verify that the distribution of fiber separations (Fig. 1b) in this "corrected Poisson distribution" is the same as that in real specimens.

Much more difficult than the problem of generating fibers sections on a single plane is the generation of 3D fiber positions, including variations along the nominal fiber direction.

Importantly, fibers wander and exchange neighbors as one progresses along the fiber direction, due to deliberately imposed twist on the fiber bundle, as in a textile composite, or accidental deviations caused by fiber handling during any of the steps between fiber fabrication and final composite consolidation. The exchange of neighbors is a topological variation in the connectivity of the population and is potentially critical to cracking: fibers that change neighbors can make it impossible for a crack to run along the nominal fiber direction without being crossed by oblique bridging fibers. Methods of characterizing and generating the variations of fiber position along the fiber direction are yet to be devised. Some early progress has been based on the use of Markov Chain algorithms (Dennis Coon, unpublished work; (Blacklock, Bale, Begley and Cox 2011; Rinaldi, Blacklock, Bale, Begley and Cox 2011)).

Other defects at the fiber scale can also matter. Any porosity or microcracking left by imperfect processing, variance in the fiber/matrix interfacial strength, or defect in the fibers can trigger premature failure.

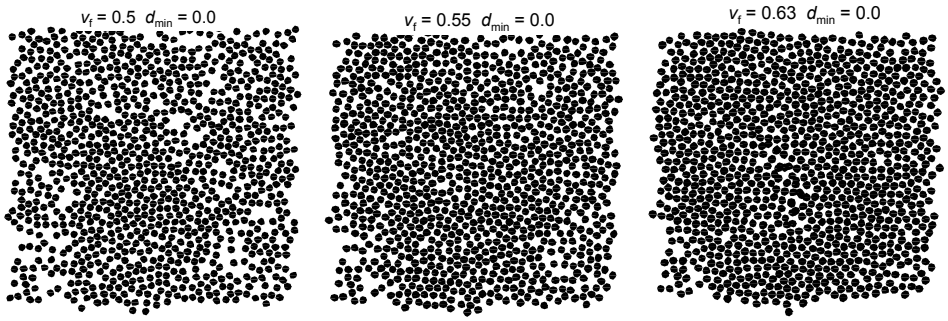

(a)

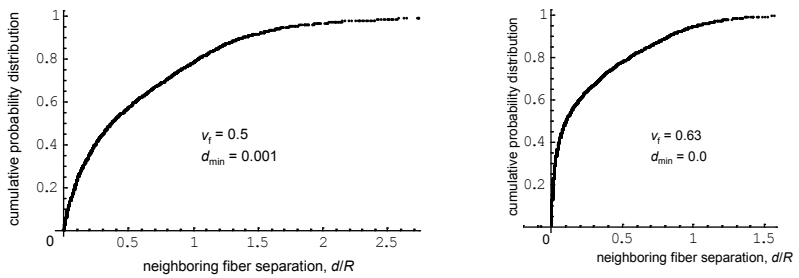

(b)

Fig. 1. (a) Populations of 999 randomly positioned fibers with fiber volume fractions v_f = 0.5, 0.55, and 0.63, generated by the algorithm described in the text. (b) The cumulative probability distribution for the separation of fibers for v_f = 0.5 and 0.63.

4. CALIBRATING MIXED-MODE COHESIVE FRACTURE LAWS

The calibrations of ply-level fracture parameters used in (Fang et al. 2011b) were taken from old single-mode fracture tests, which provided strength and toughness for each mode, the toughness taken under LEFM conditions. The fracture parameters were assumed to be the same for different ply-level crack types, in the absence of more complete calibration data. While this *ad hoc* calibration procedure worked out well, the challenge remains: what new experiments could be used to calibrate cohesive laws for each fracture mode? Critically, to calibrate a law that can

accurately predict crack initiation, the experiment must yield data when the crack is small compared to the nonlinear fracture zone, i.e., not in LEFM conditions. Thus all current standard toughness tests are ruled out.

Furthermore, one expects different cohesive laws to be operative at the different scales of a multi-scale model: crack bridging mechanisms for ply-level and fiber-level cracks originate in distinct aspects of the composite. For example, fiber-level cracking in the matrix originates as polymer crazing, which is the re-arrangement of entangled molecules, quite distinct from the fiber-bridging mechanism that operates, among others, on a ply-level crack.

The most attractive prospects for calibrating small cracks appear to lie with x-ray μCT. Detailed 3D images of cracks initiating in miniature composite specimens have been made in the last few years. Even more encouraging, maps of the crack displacement vector have been prepared for cracks ~ 1 mm long and wide, dimensions comparable to the size of the fracture process zone (Moffat et al. 2008; Wright et al. 2008). Such data in principle contain the best possible information for calibrating the fracture law.

Other recent work exploiting μCT data has revealed details of the spatial distribution and progressive increase in density of fiber breaks in a miniature specimen (Scott *et al.*, University of Southampton, unpublished work). Such data have exciting potential for calibrating and validating fiber-scale models.

5. LINKS BETWEEN PLY AND FIBER LEVEL MODELS

In simulations based on discrete damage representations, the principal link between the ply and infra-ply scales is the cohesive fracture law (Kulkarni, Geubelle and Matous 2009; Cid Alfaro, Suiker, Verhoosel and De Borst 2010; Fang et al. 2011a). A challenge for infra-ply scale modeling is to predict the law in terms of fiber and matrix properties, taking into account the randomness of fiber positioning. One illustration of such predictions exploits the A-FEM method of treating nonlinear fracture on arbitrary fracture surfaces (Fang et al. 2011a). Simulations of the failure of a composite sample containing 25 randomly positioned fibers under transverse loading incorporate separate mixed-mode cohesive laws governing the failure of fiber/matrix interfaces and the matrix. The fracture laws used correspond to a model material with interfaces somewhat weaker than those in a polymer composite and a matrix somewhat tougher than that in a ceramic composite (a choice made to test the computational technique, rather than explore a particular material). The random positions of matrix crack initiation events are determined by the local stress state computed during the simulation, which depends on the separation of the nearby fibers (Fig. 2a). The fatal fracture surface is eventually formed by the coalescence of matrix and interface crack segments (Fig. 2b). The global stress-displacement curve is equivalent to the cohesive traction-displacement law that would appear in a ply-level model to govern transverse intra-ply cracking. Its dependence on the separate fracture properties of the interfaces, the matrix and the fibers can be predicted by repeating the fiber-level model for different parameter choices (Fig. 3). Thus such a calculation forms a physical link in a multi-scale model.

The simulations of Fig. 2 are appealing in their qualitative appearance, but serious challenges remain to be taken up. First, while the patterns of multiple incipient microcracks is plausible, verification by high resolution imaging showing similar damage patterns in real specimens is needed. Such imaging is not as easy as the clearly demarked damage loci in Fig. 2 might suggest. Most of the damage events in Fig. 2 contain material in the earliest stages of failure: the material still bears stress close to the critical stress marking the end of linear elasticity and the material is still continuously connected across the band (the damage band is far from a

stress-free crack). Only the highest resolution imaging (SEM rather than optical imaging) would reveal such damage in detail, e.g., incipient polymer crazing. Second, to understand the effects of fiber wandering on cracking, especially on cracks that follow the nominal fiber direction, 3D simulations must be carried out, rather than 2D simulations. Third, virtual specimens containing only 25 fibers are insufficient to study the effects of random fiber positioning satisfactorily; for the reasons stated above, ~1000 fibers would be preferable. Unfortunately, the nonlinear fracture calculations of Fig. 2 take several hours each and the calculation time scales roughly as the square of the problem size. Thus 1000-fiber calculations, even under plane conditions, are far off in the future. To make full use of future geometrical models that generate 3D fiber patterns, e.g., to deduce statistical effects in predictions such as those of Fig. 3, new computational approaches will be needed to solve fracture problems in even larger models. A possible fast-computation formulation based on weight function methods will be described elsewhere.

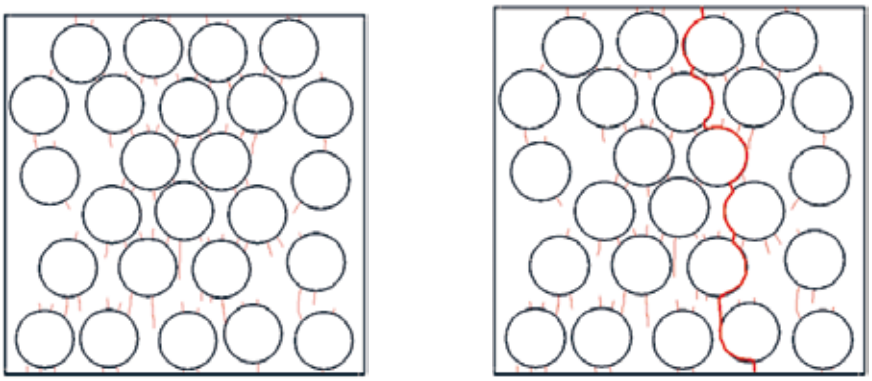

(a) (b)

Fig. 2. Simulation of progressive damage evolution in a composite volume containing 25 randomly located fibers. At strain $\varepsilon_{applied} = 0.10\%$, matrix microcracks have begun to connect different fiber/matrix interface segments (a), leading at strain $\varepsilon_{applied} = 2.96\%$ to the formation of the final fracture path (b). For a composite with relatively brittle matrix (from (Fang et al. 2011a).

6. MESH EFFECTS AND INHERENTLY UNPREDICTABLE CHARACTERISTICS OF FAILURE

Tests of mesh independence for the simulations of Fig. 2 reveal some unusual results (Fang et al. 2011a). While the global stress-strain curves can be made mesh-independent by choosing computational element sizes that are not large compared to either the fiber diameter or the lengths of nonlinear fracture zones, the locus of the fatal fracture event proves remarkably inconstant. As the mesh size is reduced, the locus continues to jump from position to position, indicating high sensitivity to the details of local stress computation.

The locations of microcracks are especially sensitive to the exact positions and separations of fibers, which determine local stress concentrations. Furthermore, when one microcrack initiates, the balance of the failure conditions at other locations can tip, causing a tendency for extension of the existing crack rather than new cracking elsewhere. A consequence is that the pattern of microcracking is chaotic: slight changes in the initial physical conditions lead to wholesale

changes in the evolving crack pattern. Changes in mesh play into this extreme sensitivity. Therefore, for this particular problem, mesh independence is sought and found only in spatially averaged quantities, such as the far-field load and displacement, or the average density of microcracks.

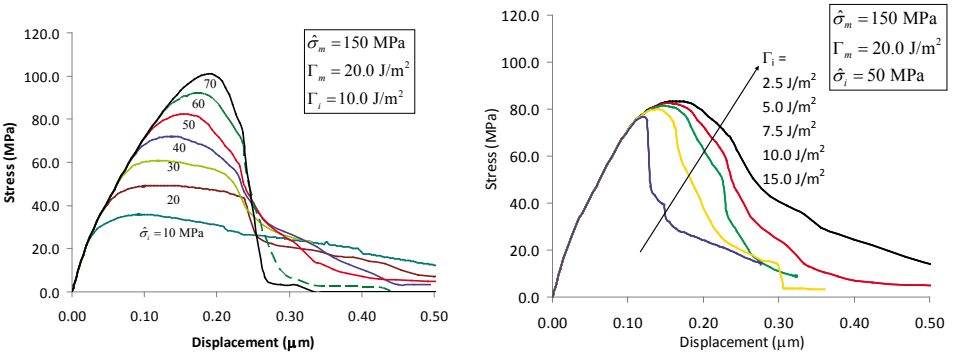

(a) (b)

Fig. 3. The influence of (a) the interface strength ($\hat{\sigma}_i$) and (b) the interface toughness (Γ_i) on predicted traction-separation curves.

The sensitivity of the failure locus to the spatial distribution of fibers can be roughly quantified as follows. One contributing factor determining the locus of first damage initiation is the separation between pairs of fibers, the first microcrack tending to initiate between the two fibers with the smallest separation. Let P(s) denote the probability density function for the separation s of pairs of neighboring fibers in a fiber population. Suppose that the smallest value of s is s_0. Suppose all fiber positions are perturbed slightly in such a way that the separation of the two closest fibers increases from s_0 to $s_0 + \delta s_0$, while the overall density function remains P. Then the probability that $s_0 + \delta s_0$ remains the smallest spacing, i.e., that the same two fibers are still the closest pair, can be found as follows. Consider the conditional probability that expresses the likelihood that a separation value s_j in the unperturbed set of separations remains greater than $s_0 + \delta s_0$, given that it was greater than s_0:

$$\mathrm{P}_{0j} = \mathrm{Prob}\{\, s_0 + \delta s_0 < s_j \mid s_j < s_0 \,\} = \frac{\int_{s_0+\delta s_0}^{\infty} \mathrm{P}\, ds}{\int_{s_0}^{\infty} \mathrm{P}\, ds} \approx 1 - \mathrm{P}(s_0)\delta s_0 \qquad (1)$$

From this result

$$\mathrm{Prob}\{\, s_0 + \delta s_0 \text{ remains the smallest spacing} \,\} = \prod\nolimits_j P_{0j} \approx \frac{1 - \mathrm{cpd}(s_0) - \mathrm{P}(s_0)\delta s_0}{1 - \mathrm{cpd}(s_0)} \qquad (2)$$

where cpd denotes the cumulative probability distribution associated with the density P. This function falls to 0.5 when the size of the population N is approximately the reciprocal of $\delta s/R$,

where R is the fiber radius (Fig. 4). Thus, for example, for $N = 10{,}000$, the position of each fiber needs only shift by $\sim 10^{-4}R$ in the perturbation step for the location of the closest pair of fibers to change. For $R = 7$ μm, the required shift of fibers is ~ 1 nm: the location of the nearest pair and therefore the likely site of the first matrix cracking is extremely sensitive to details of the fiber configuration. When the location of the closest fiber pair changes, it does so with equal probability to any pair of neighboring fibers in the population. Furthermore, for a perfectly brittle material, a change in the location of the first crack initiation indicates a change in the final failure path; and thus the final failure path will generally shift wholesale. While nonlinear fracture processes can diminish the likelihood of a change in the final fracture path when the closest fiber pair relocates, the sensitivity may still remain very high.

The hypersensitivity of some aspects of fracture to initial conditions is reminiscent of the butterfly effect in the theory of chaos (Lorenz 1963). A fundamental challenge of modeling at the infra-ply scale (or modeling any material at the scale of random heterogeneity in its structure) is to categorize characteristics that are predictable and those that are not.

7. REACHING FOR THE ATOMIC SCALE

Attempts to use classical or even quantum atomistic computations within top-down modeling strategies for composite materials have been very limited. The main reason for this is that, within a top-down strategy, the molecular scale can only be meaningfully introduced when the fiber-scale model is already in place. The top-down paradigm systematically adds phenomena from smaller scales only when their influence at larger scales, especially the macroscopic engineering scale, demands their inclusion. If the link to the engineering scale is incomplete, the process cannot flow. Thus while previous research may have demonstrated correlations between atomistic results and engineering properties, this is essentially empirical progress and not the same as exploiting atomistic results within validated high-fidelity simulations.

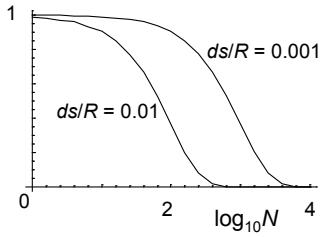

Fig. 4. Probability that the smallest gap between fibers will remain between the same pair when the fibers are randomly perturbed falls as the number of fibers in the population increases.

Opportunities and demand for atomistic calculations might arise in the need for more detailed knowledge of the strength and toughness of fiber/matrix interfaces or the matrix itself. Neither of these constitutive properties, summarized for example in the constitutive laws of interfacial or matrix fracture, is readily accessible to direct experimental measurement. Neither has any experiment addressed the question of how much variance might be present in the interface and matrix fracture properties due to material variance. Yet both the properties and their deviations will govern the spatial distribution of damage events in a failing material, with potentially important consequences for infra-ply fracture and thence macroscopic performance. Atomistic

simulations can predict the dependence of interfacial fracture on the local orientation of the graphitic layers within a carbon fiber, for example, or the thickness of coatings applied to the fiber, results that could lead to useful predictions of the distribution of interfacial strengths.

Given the development of computational resources and methods, the potential of atomistic simulations within high-fidelity simulations will increase significantly. But the challenges of formulating and calibrating atomistic models for real engineering materials, with all their typical, messy heterogeneity, and validating the influence of the atomistic results, as it percolates up through the model hierarchy to the macroscopic scale where comparison against test data must be made, remain formidable. Formalizing these processes is obligatory for a top-down strategy.

8. SUMMARY REMARKS

The above assessment of status has been confined to models of damage in which damage bands or cracks are represented discretely. A contrasting approach is continuum damage mechanics, in which the effects of discrete cracks are averaged spatially into nonlinear continuum constitutive laws. Major accomplishments have also been achieved in this other modeling world: the question of whether to prefer discrete or continuum representations is therefore a central one for engineers.

Part of the answer to the question is the fact that discrete damage models are not be feasible for large components or structures. While the maximum material volume that can be modeled depends on formulation details and computational power, both of which change with time, it is not likely ever to exceed several tens of mm in linear dimension. Therefore, at some stage, any discrete damage model will need to be coupled into a continuum damage model that deals with larger components. The question of what is the critical size for this modeling transition will be permanently with us. Furthermore, the challenge of demonstrating that the superior fidelity of discrete damage representations yields tangible improvements over the simpler formulation of continuum damage mechanics should always be in the minds of those developing discrete damage models. In the engineering world, they must know how to pay their way.

ACKNOWLEDGEMENTS

This work was supported by the US AFOSR and NASA under the National Hypersonics Science Center for Materials and Structures (AFOSR Contract No. FA9550-09-1-0477). Previously reported work related to the A-FEM was supported by NASA Langley (NASA Contract No. NNL08AA19C). The authors are grateful to Drs. C. Davila, C. Rose, and S. M. Spearing for critical comment.

REFERENCES

Andersson, T. and U. Stigh (2004). "The stress–elongation relation for an adhesive layer loaded in peel using equilibrium of energetic forces." *International Journal of Solids and Structures* **41**(2): 413-434.

Argon, A.S. (1972). *Fracture of composites*. New York, Academic Press.

Blacklock, M., H. Bale, M.R. Begley and B.N. Cox (2011). "Generating virtual textile composite specimens using statistical data from micro-computed tomography." *Journal of the Mechanics and Physics of Solids* submitted.

Budiansky, B. (1983). "Micromechanics." *Composite Structures* **16**(1): 3-12.

Cid Alfaro, M.V., A.S.J. Suiker, C.V. Verhoosel and R. de Borst (2010). "Numerical homogenization of cracking processes in thin fibre-epoxy layers." *European Journal of Mechanics, A Solids* **29**: 119-131.

Clarke, J.D. and I.J. McGregor (1993). "Ultimate Tensile Criterion Over a Zone: A New Failure Criterion for Adhesive Joints." *Journal of Adhesion* **42**: 227-245.

Corigliano, A. (1993). "Formulation, identification and use of interface models in the numerical analysis of composite delamination." *International Journal of Solids and Structures* **30**: 2779-2811.

Cox, B.N. and Q.D. Yang (2006). "In quest of virtual tests for structural composites." *Science* **314**: 1102-1107.

Dadkhah, M.S., W.L. Morris and B.N. Cox (1995). "Compression-compression fatigue in 3D woven composites." *Acta Metallurgica et Materialia* **43**(12): 4235-4245.

de Borst, R. (2003). "Numerical aspects of cohesive-zone models." *Engineering Fracture Mechanics* **70**: 1743-1757.

Elices, M., G.V. Guinea, J. Gomez and J. Planas (2002). "The cohesive zone model: Advantages, limitations and challenges." *Engineering Fracture Mechanics* **69**: 137-163.

Fang, X.J., Q. Yang, B.N. Cox and Z.Q. Zhou (2011a). "An augmented cohesive zone element for arbitrary crack coalescence and bifurcation in heterogeneous materials." *International Journal of Numerical Methods in Engineering* **in press**.

Fang, X.J., Z.Q. Zhou, B.N. Cox and Q. Yang (2011b). "High-fidelity simulations of multiple fracture processes in laminated composites in tension." *Journal of the Mechanics and Physics of Solids* **59**: 1355-1373.

Feih, S. and H.R. Shercliffe (2004). "Adhesive and composite failure prediction of single-L joint structures under tensile loading." *International Journal of Adhesion and Adhesives* **25**: 47-59.

Fleck, N.A. and J.Y. Shu (1995). "Microbuckle initiation in fibre composites: a finite element study." *Journal of the Mechanics and Physics of Solids* **43**(12): 1887-1918.

Flores, S., A.G. Evans, F.W. Zok, M. Genet, B.N. Cox, D.B. Marshall, O. Sudre and Q. Yang (2010). "Treating Matrix Nonlinearity in the Binary Model Formulation for 3D Ceramic Composite Structures." *Composites, Part A* **41**: 222-229.

Hallett, S. and M.R. Wisnom (2006). "Numerical investigation of progressive damage and the effect of layup in notched tensile tests." *Journal of Composites Materials* **40**: 1229-1245.

Hillig, W.B. (1994). "Effect of fibre misalignment on the fracture behaviour of fibre-reinforced composites. Part I. Experimental." *Journal of Materials Science* **29**: 419-423.

Hutchinson, J.W. and A.G. Evans (2000). "Mechanics of Materials: Top-Down Approaches to Fracture." *Acta Materialia* **48**: 125-135.

Iarve, E.V., D. Mollenhauer and R. Kim (2005). "Theoretical and experimental investigation of stress redistribution in open-hole composite laminates due to damage accumulation." *Composites A* **36**: 163-171.

Jelf, P.M. and N.A. Fleck (1994). "The failure of composite tubes due to combined compression and torsion." *Journal of Materials Science* **29**: 3080.

Kausch, H.H., D.G. Fesko and N.W. Tschoegl (1971). "The random packing of circles in a plane." *Journal of Colloid and Interface Science* **37**(3): 603-611.

Kaute, D.A.W., H.R. Shercliff and M.F. Ashby (1993). "Delamination, fibre bridging and toughness of ceramic matrix composites." *Acta Metallurgica et Materialia* **41**(7): 1959-1970.

Kulkarni, M.G., P.H. Geubelle and K. Matous (2009). "Multi-scale modeling of heterogeneous adhesives: effect of particel decohesion." *Mechanics of Materials* **41**: 573-583.

Lam, P.W.K. and M.R. Piggott (1990). "The durability of controlled matrix shrinkage composites. Part 3 Measurement of damage during fatigue." *Journal of Materials Science* **25**: 1197-1202.

Ling, D., Q. Yang and B.N. Cox (2009). "An augmented finite element method for modeling arbitrary discontinuities in composite materials." *International Journal of Fracture* **156**: 53-73.

Lorenz, E.N. (1963). "Deterministic nonperiodic flow." *Journal of the Atmospheric Sciences* **20**(2): 130-141.

Marshall, D.B., W.L. Morris, B.N. Cox, J. Graves, J.R. Porter, D. Kouris and R. Everett (1994). "Transverse strengths and failure mechanisms in Ti3Al matrix composites." *Acta Metallurgica et Materialia* **42**: 2657-2673.

Moës, N. and T. Belytschko (2002). "Extended finite element method for cohesive crack growth." *Engineering Fracture Mechanics* **69**: 813-833.

Moës, N., J. Dolbow and T. Belytschko (1999). "A finite element method for crack growth without remeshing." *International Journal for Numerical Methods in Engineering* **46**: 131-150.

Moffat, A. J., P. Wright, J.Y. Buffiere, I. Sinclair and S.M. Spearing (2008). "Micromechanisms of damage in 0° splits in a [90/0]s composite material using synchrotron radiation computed tomography." *Scripta Materialia* **59**(10): 1043-1046.

Needleman, A. (1990). "An Analysis of Decohesion along an Imperfect Interface." *International Journal of Fracture* **42**: 21-40.

Piggott, M.R. and P.W.K. Lam (1991). *Fatigue failure processes in aligned carbon-epoxies*. Third symposium on Composite Materials: Fatigue and Fracture, Lake Buena Vista, Florida, American Society for Testing and Materials.

Powell, M. J. (1979). "Site percolation in randomly packed spheres." *Physical Review B* **20**(10): 4194-4198.

Remmers, J. J. C., R. de Borst and A. Needleman (2003). "A cohesive segments method for the simulation of crack growth." *Computational Mechanics* **31**(1-2): 69-77.

Rinaldi, R., M. Blacklock, H. Bale, M.R. Begley and B.N. Cox (2011). "Constructing 3D models of textile composites using statistical data from micro-computed tomography." *Journal of the Mechanics and Physics of Solids* **to be submitted**.

Rosen, B. W. (1965). Mechanics of composite strengthening. *Fiber Composite Materials*. Metals Park, Ohio, American Society of Metals**:** 35-75.

Rossmanith, H. P. (1995). "An introduction to K Weighardt's historical paper on splitting and fracture of elastic bodies." *Fatigue and Fracture of Engineering Materials and Structures* **12**: 1367-1369.

Sheppard, A., D. Kelly and L. Tong (1998). "A Damage Zone Model for the Failure Analysis of Adhesively Bonded Joints." *International Journal of Adhesion and Adhesives* **18**: 385-400.

Spearing, S.M. and A.G. Evans (1992). "The role of fiber bridging in the delamination resistance of fiber-reinforced composites." *Acta Metallurgica et Materialia* **40**(9): 2191-2199.

Strouboulis, T., K. Copps and I. Babuška (2001). "The generalized finite element method." *Computational Mechanics Advances* **190**: 4801-4193.

Torquato, S., T. M. Truskett and P.G. Debenedetti (2005). "Is random close packing of spheres well defined?" *Physical Review Letters* **84**(10): 2064-2067.

Van de Meer, F.P., C. Oliver and L.J. Sluys (2010). "Computational analysis of progressive failure in a notched laminate including shear nonlinearity and fiber failure." *Composite Science and Technology* **70**: 692-700.

Van de Meer, F.P. and L.J. Sluys (2010). "Mesh-independent modeling of both discrete and distributed matrix cracking in interaction with delamination in composites." *Engineering Fracture Mechanics* **77**(4): 719-735.

Voronoi, G. (1907). "Nouvelles applications des paramètres continus à la théorie des formes quadratiques." *Journal für die Reine und Angewandte Mathematik* **133**: 97-178.

Wisnom, M. R. and F.-K. Chang (2000). "Modelling of splitting and delamination in notched cross-ply laminates." *Composites Science and Technology* **60**: 2849-2856.

Wright, P., X. Fu, I. Sinclair and S. M. Spearing (2008). "Ultra high resolution computed tomography of damage in notched carbon fiber-epoxy composites." *Journal of Composite Materials* **42**(19): 1993-2002,.

Yang, Q. and B.N. Cox (2010a). "Predicting failure in textile composites using the Binary Model with gauge averaging." *Engineering Fracture Mechanics* **77**: 3174-3189.

Yang, Q.D. and B.N. Cox (2005). "Cohesive models for damage evolution in laminated composites." *International Journal of Fracture* **133**(2): 107-137.

Yang, Q. D. and B.N. Cox (2010b). "Predicting failure in textile composites using the Binary Model with gauge averaging." *Engineering Fracture Mechanics* **77**: 3174-3189.

Yurgatis, S. W. (1987). "Measurement of small angle fiber misalignments in continuous fiber composites." *Composites Science and Technology* **30**: 279-293.

Zi, G. and T. Belytschko (2003). "New crack-tip elements for XFEM and applications to cohesive cracks." *International Journal for Numerical Methods in Engineering* **57**: 2221-2240.

Proceedings of the 32nd
Risø International Symposium on Materials Science:
Composite materials for structural performance:
Towards higher limits
Editors: S. Fæster, D. Juul Jensen,
B. Ralph, B.F. Sørensen
Risø National Laboratory for Sustainable Energy,
Technical University of Denmark, 2011

STRATEGIES FOR IMPROVING THE DAMAGE TOLERANCE OF FUTURE COMPOSITE MATERIALS

P.J. Hogg and P. Potluri

Northwest Composites Centre, School of Materials, University of Manchester, Sackville Street Manchester M13 9PL, UK

ABSTRACT

Improving the damage tolerance of a composite is identified as a key goal for future development. A change in emphasis is suggested with a move away from the philosophy of improving performance by increasing the resistance of the laminate to damage formation, which should be accompanied by attempts to control the nature of damage such that energy can be absorbed through cracking in a way that is not deleterious to the final properties of the structure.

Different strategies are proposed to achieve this, consisting of specific attempts to maximise the resistance of the laminate to damage growth by improving interlaminar toughness, G_I (prop) or by introducing new architecture into the composite such that the nature of damage is modified. Examples are provided of the use of interlaminar veils, 3D textile forms and the use of specific fiber hybridisation to facilitate the improved resistance to crack propagation.

1.INTRODUCTION

There is a continuing need to develop composites that are damage-tolerant in service. Damage tolerance in this context means that a composite part can suffer some form of service abuse that results in damage without the service performance of that part falling below an acceptable level. The need for damage tolerant composites transcends all parts of our industry and is common to structures made from glass fiber and carbon fiber, for aerospace to marine and wind turbine applications. Perhaps the most high profile and historically most critical applications have been carbon fiber composites in primary aerospace structures. Here the problem of damage is compounded by the fact that damage is commonly sub-surface, undetectable by eye, but can have a considerable detrimental effect on key laminate properties such as compression after impact (Bibo, Hogg, Backhouse and Mills, 1998).

The importance of damage tolerance in the aerospace sector is increasing given the trend to manufacture more primary civil aircraft structures from CFRP, including the fuselage which is susceptible to significant airfield abuse (baggage handling, vehicles etc) and from large hail

stones. However damage tolerance in general is also of prime concern to the wind turbine industry and automotive sector. It is simply not economic to replace damaged wind turbine blades in service, especially if the turbines are deployed off-shore (Det Norske Veritas, 2008)). The automotive sector is used to operating with metallic materials and there is no culture of (or infrastructure for) in-service non-destructive inspection of structures that would be required if the predicted widespread usage of composites for automotive structures becomes a reality but based on the use of composites with poor damage tolerance.

The industry has made considerable progress for a thirty year time period in improving the damage tolerance of all classes of composites. This is exemplified by the improvements in carbon fiber composites intended for service as primary structure in aerospace where the damage tolerance of the composite laminate is usually quantified by measuring the compression after impact strength according to some recognised standard (ASTM). Low energy impact is a significant in-service problem which results in difficult to detect damage, primarily consisting of delaminations, Fig.1, which can seriously reduce the compression strength of a composite laminate (Saito and Kimpara,2006, Prichard and Hogg,1990).

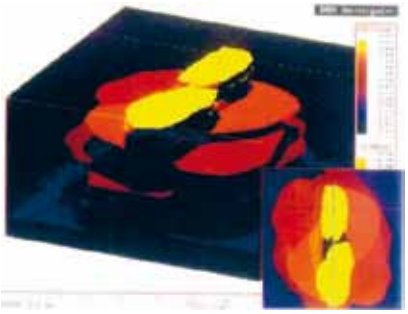

Fig. 1. Time of flight ultrasonic C-scan image of impact damage in a quasi-isotropic carbon fiber-epoxy laminate

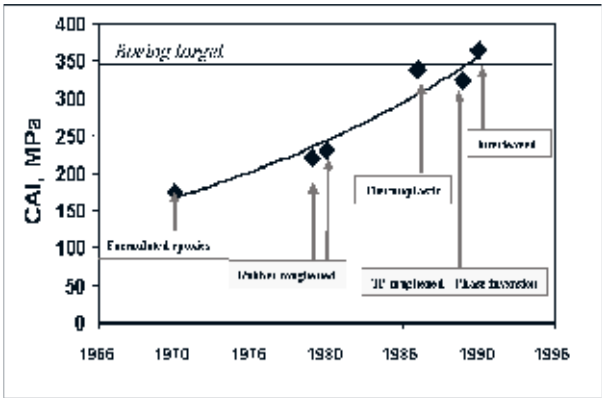

Fig. 2a Typical compression after impact test results for various categories of toughened composites (data selected from multiple literature sources).

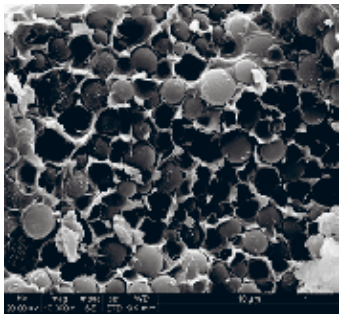

Fig. 2b Fracture surface of an epoxy resin toughened with a thermoplastic additive, showing phase inversion. Islands of thermoset polymer are surrounded by a tough contiguous thermoplastic phase (Wong, Lin, McGrail, Peijs and Hogg,2010)

The compression after impact properties have increased when measured using the Boeing standard test method from a level of about 170 MPa to almost 400 MPa in this period. The improvements have been largely the result of increases in resin toughness, with associated increases in interlaminar strength (Bascom, Bitner, Moulton and Siebert, 1980). The developments, Fig.2, have included the introduction of formulated epoxies, followed by rubber-toughened systems (Davy, Hashemi, and Kinloch 1989), thermoplastic toughened systems (Di Pasquale, Motto, Rocca, Carter, McGrail, and Acierno, 1997), through to thermoplastic, phase inverted thermoplastic-epoxies, monolithic thermoplastics and interleaf toughened epoxies (Wong, Lin, McGrail, Peijs, and Hogg, 2010).

It is noticeable however that no significant improvements in damage tolerance have been developed over the last ten years, possibly as no specific new targets have been set by the industry. Boeing had stipulated a challenging CAI value of 350 MPa for selection of prepreg systems for use on the Boeing 777 empennage which was achieved by Toray with their 3900 resin prepregged with T800 fibers (Boeing). Most work undertaken recently by industry has focused on developing composite systems (materials and preforms) that can be used in alternative out-of-autoclave processes to deliver equivalent damage tolerance to conventional autoclave processed materials. It might be concluded that the process of achieving increased toughness via improvements in resin toughening have reached the end of its life and that there is little room for further development. If this is indeed the case then alternative strategies for developing an enhanced damage tolerance must be considered. In aerospace the desirability of developing a carbon fiber fuselage for medium size single aisle commercial aircraft, when the fuselage thickness is very low, means that composites systems with a damage tolerance substantially above the level achieved to date are required. While the composite fuselage of a large twin aisle aircraft is tough enough to withstand damage from hail stones, service abuse etc, a thinner single aisle aircraft would not be capable of safe operation. Whereas this is a particular issue for the aerospace sector, any alternative approach to increasing damage tolerance will be welcomed by all sectors of the composite industry. Sectors such as the wind and marine industries that rely largely on infusion processing are restricted from using epoxies toughened with large quantities of thermoplastics as the resins are too viscous to be infused. Variants of infusion processing are now also being adopted by the aerospace sector, emphasising the need for alternative solutions to generating damage tolerant composites.

2. DAMAGE TOLERANCE: MECHANISMS

The compression after impact test used to measure the damage tolerance of composites consists of two separate events- a low energy out of plane impact test, and a subsequent in-plane compression test. A traditional method of presenting the data obtained from such testing is plotting the compression strength versus the kinetic energy of the striker, sometimes normalised to account for variations in the target laminate thickness. This presentation obscures the relative performance of the composite under each part of the test protocol. Observation by many research groups over the years has shown that variations in materials constituents can influence the extent and nature of damage formed in the initial impact test (e.g Hull and Shi, 1993, Shyr and Pan, 2003 and Naik and Logan 1999). The damage is primarily delaminations that form between different layers of the composite. In a quasi-isotropic laminate the individual delaminations take a peanut shape in each layer and combine overall to provide a roughly circular damage zone when detected using NDE techniques such as ultrasonic C-scan, figure 1. The magnitude of this damage has been characterised by different groups according to either the area of the damage zone or the width of the damage zone (Saito and Kimpara, 2006, Prichard and Hogg, 1990).

In the second part of the test the delaminations will propagate towards the extremity of the plate loaded in compression, at which point the laminate may buckle in the center with major failure taking place usually via an in-plane shear fracture. While it has not proved very easy to observe the propagation of the delamination during compression failure of carbon fiber composites due to their opacity, it has proved feasible to study the growth in glass fiber systems which show that the delaminations only propagate perpendicular to the loading direction. This has prompted the use of damage width as being the key damage parameter (Prichard and Hogg, 1990). It is therefore possible to deconstruct the compressing after impact test and observe the effects of materials variables such as resin toughness on a) the initial width of the delaminations after the initial impact as a function of kinetic energy of the striker and b) the compression after impact strength of the laminate as a function of the width of the delaminations.

What is noticeable is that when the data has been examined in this way, the prime influence of increasing resin toughness is to reduce the extent of the initial delaminations in the laminate. When laminates are then compared on the basis of the damage width, irrespective of what level of impact blow was required to create that damage, then laminates with a different toughening system, result in almost identical compression strengths, Fig.3. This is an important observation in the light of the apparent roadblock on improvements in damage tolerance that result from increases in resin toughness.

The philosophy adopted by the industry over the years has in effect been to improve damage tolerance by restricting the tendency of the composite to suffer damage in the first instance. If this philosophy cannot provide any room for improvement, then an alternative strategy needs to be considered, namely to allow damage to form (or at least recognise the inevitably of damage at a sufficient impact blow) but to focus on reducing the consequences of that damage under subsequent loading. This could be approached by changing the nature of the damage itself such that it does not reduce the compression strength, and by increasing the resistance to growth of that damage provided by the laminate.

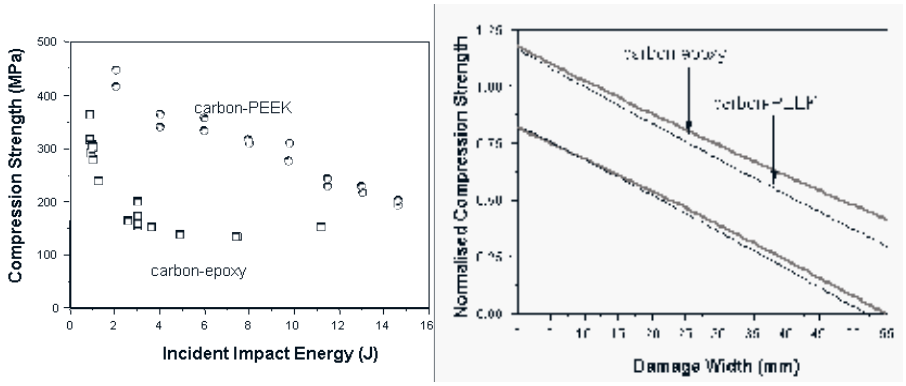

Fig.3. A set of data for the compression after impact strength of a conventional, quasi-isotropic carbon fiber epoxy laminate and an equivalent carbon fiber PEEK laminate. The first plot shows the data plotted as a function of impact energy and the PEEK laminates are clearly superior. The second plot shows 95% prediction internals for the same data normalised and plotted as a function of damage width showing that both data sets are now almost identical (from Prichard and Hogg 1990).

3. STRATEGIES FOR IMPROVING THE RESISTANCE TO DAMAGE PROPAGATION

There are two independent strategies that can be considered in order to increase the resistance of a laminate to damage growth. The first of these is to incorporate into the laminate features and modifications that provide additional toughness in the propagation phase, whilst accepting that damage will be formed in essentially the same manner as in traditional composites. This implies that the laminate must achieve a higher value of interlaminar toughness $G1_{(prop)}$, a property that is not linked closely to the resistance of the laminate to the initial creation of that damage under impact conditions.

The second strategy is to deliberately modify the architecture of the composites such that when damage forms it does so in a different geometric pattern and that the nature of this new form of damage is that it is either harder to propagate and/or is less deleterious on the compression strength of the laminate.

3.1 Improving resistance to crack growth. Strategies for increasing the resistance to crack growth could concentrate on increasing interlaminar mode-I toughness. A simplistic interpretation of the various parameters influencing the compression after impact performance suggests that the Mode-II toughness is primarily responsible for the extent of the initial damage formed during the impact event, while mode-I interlaminar toughness controls the susceptibility to crack propagation in the final compression phase (Prichard and Hogg, 1990). Techniques such as through-thickness stitching or tufting can be considered in some situations as routes to improving Mode-I toughness, although these approaches have little effect on mode-II toughness, Fig. 4. The use of stitching/tufting implies an additional operation in the manufacturing process and as such is expensive and these methods also have the drawback of disturbing the underlying fibers, creating possibly defect sites and reducing the overall volume fraction of the reinforcement (Potluri, Sharif, Jetavat, Hogg and Foreman, 2009). The technique has been shown to have merit in certain situations, especially for the local reinforcement of key interlayer

connections (for example at T-sections) but it may not be suitable for application over a large area such as a wing skin or fuselage, and may be too intrusive in a thin laminate.

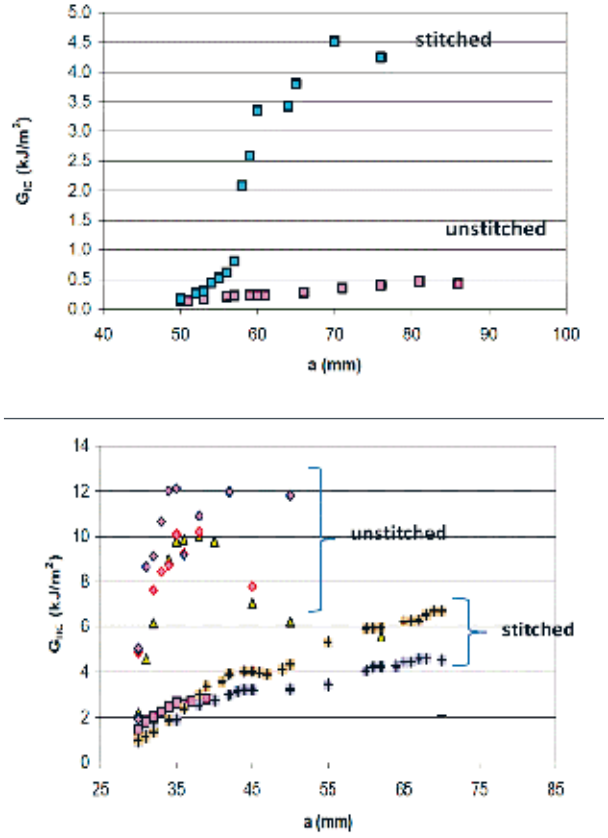

Fig.4. Two sets of data from similar resin/glass fiber laminates showing the effect of stitching on R-curves for G_{IC} (UD laminates) and G_{IIC} (multiaxial), from Cauchi Savona, 2005

In some cases stitching has such a deleterious effect on the underlying composite structure that the susceptibility of the laminate to the formation of damage in the initial impact phase is increase. This is illustrated by the following data on infused carbon fiber epoxy cross-ply laminates where a variety of stitch pitches (separation) were used, Fig. 5 (Ahmadnia, Daniel and Hogg, 1999) . The basic compression after impact strengths were reduced as a result of the stitching in all cases due to an increase in the initial impact damage size, but the resistance of the laminate to subsequent crack propagation was improved.

An alternative approach is to selectively reinforce the interlaminar region with a fibrous veil, Fig. 6. In some respects this mimics the use of interleaved tough resin layers that are very effective in improving damage tolerance by minimising the initial damage area due to impact. A tough resin interlayer can yield in shear during impact.

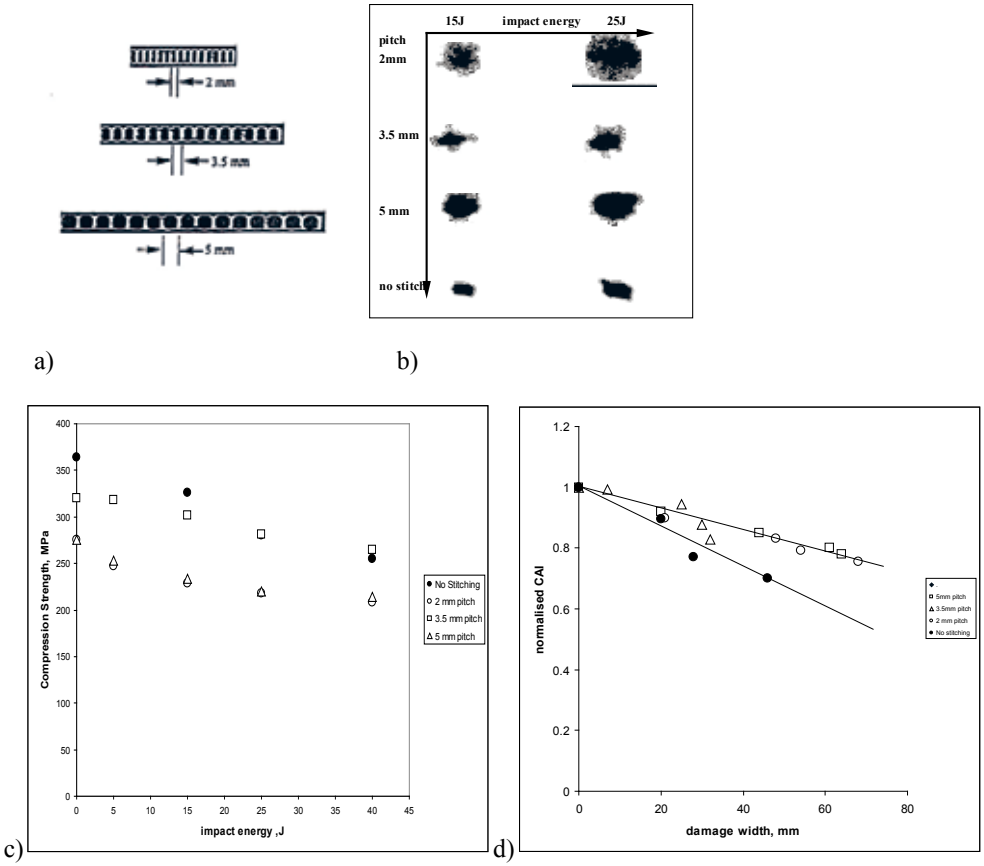

Fig.5. A set of data illustrating the effect of stitching on CAI properties. a) The pitch of the stitching is varied from 2 to 3.5 to 5 mm. b) The damage at a given impact blow is increased in the stitched laminates. c) The absolute compression after impact strength is reduced in the stitched laminates (open symbols) but d) the resistance to crack propagation (delamination growth) is increased (Ahmadnia et al., 1999).

However during the crack propagation phase such an interlayer is thought to be less effective as mode-I crack growth could occur at the interface between a tough zone and the underlying composite. If a thin fibrous layer such as a low areal weight veil, is used, especially where the fibers are thermoplastic fibers, then the ability to resist initial crack growth during impact is maintained. However in addition, due to the fibrous nature of a veil it is likely to interact with the underlying structural layers facilitating a degree of crack bridging which will enhance mode-I toughness (Kuwata, 2010). Data on the performance of veils in the interlaminar region is sparse but encouraging (Hogg, Kuwata, Jamshidi, Hjadaei and Teztzis, 2010). Some thermoplastic veils have demonstrated an ability to improve both the resistance to damage formation (impact) and propagation (compression) resulting in a significant improvement in compression after impact strength (Hogg et al), Fig. 6. The effectiveness of an interlaminar veil seems to depend on how and where a delamination propagates in the laminate.

Stiff veils based on fibers such as carbon, seems to force the crack to propagate at the boundary between the structural layers and the resin rich zone adjacent to the veil. This only results in a

marginal increase in toughness and minimal fiber bridging. A soft veil based on thermoplastic fibers in contrast induces crack propagation to occur at the interface between the veil and resin rich layer and within the veil itself. This maximises pull out and fiber bridging, results in a significant increase in mode I and mode II toughness and is responsible for the improvement in compression after impact properties. The various possibilities are shown schematically in figure 7. This form of toughening also has the advantage of being compatible with out of autoclave vacuum infusion processing.

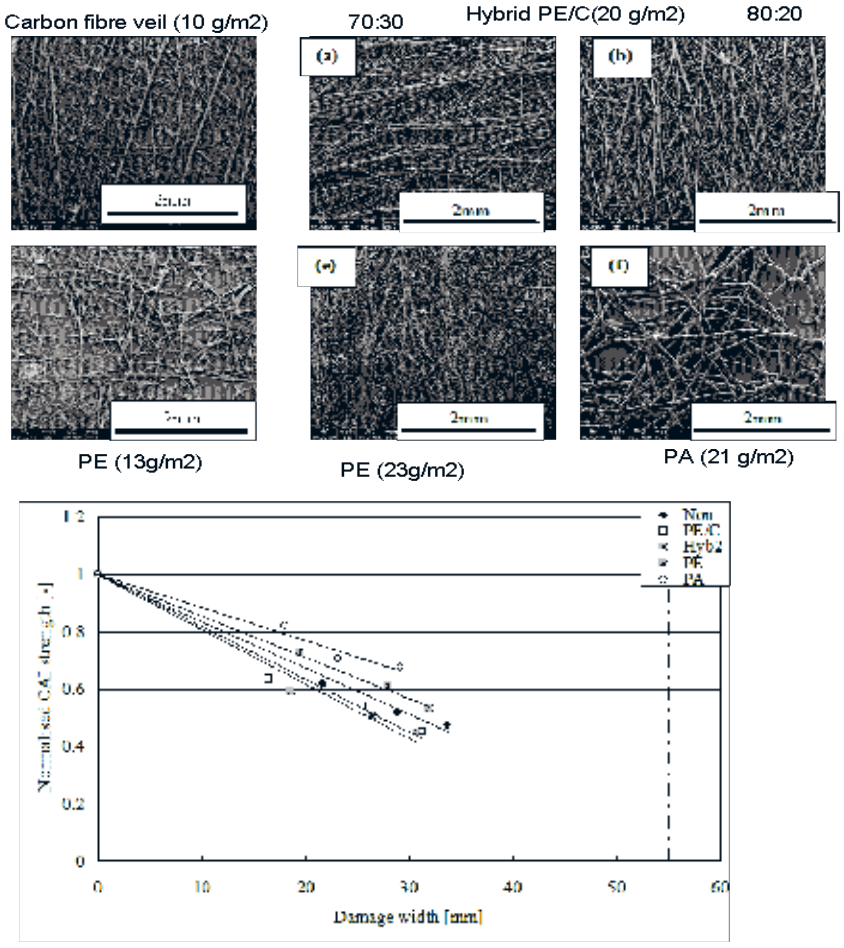

Figure 6.a) Light weight veils based on thermoplastic fibers (polyester and polyamide) and carbon fibers, used to provide improved resistance to delamination growth in infused, woven carbon fiber epoxy laminates and b) Normalised compression after impact data, plotted versus damage width (from Hogg et al., 2010)

a) Crack initiates and grows at interface between resin rich region bordering structural carbon fibre layers and the interleaf veil. Little improvement in toughness is likely over that exhibited by laminates without an interleaf veil. Favoured by stiff interleaf (.eg. Carbon)

b) Crack initiates and grows within the interleaf veil or at interface between veil and resin rich region. This is likely to encourage additional bridging and increase toughness. Favoured by softer interleaf veils (e.g. PE, PA)

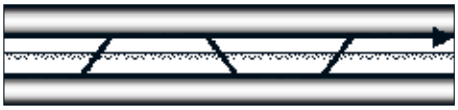

c) Crack oscillates between interfaces, Favoured by hybrids and woven substrates. Intermediate case.

Fig.7. Possible crack paths in laminates with interlaminar veils

3.2 Mitigating the consequences of damage: Mesoscopic control The second strategy proposed is based on the concept that cracking is inevitable eventually. Instead of seeking to always improve the resistance to initial cracking, it may be more productive to allow or tolerate cracking but to ensure that this takes place in positions that are not likely to cause a significant reduction in compression strength. To facilitate energy absorption by cracking, without serious consequences, the damage must be diffused into the laminate, with sufficient undamaged material remaining in critical positions. The basic concept is illustrated simply in Fig. 8. For an equivalent damage area, a concentration of cracks as long delaminations leads the structure susceptible to buckling failure, whilst a distribution or diffusion of damage would result in shear failure at higher loads.

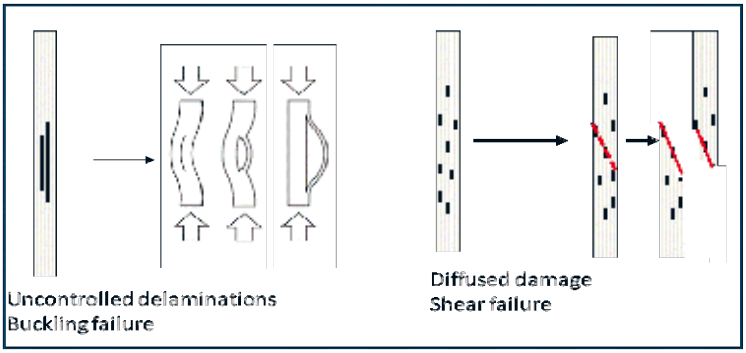

Fig.8. Schematic illustration of the diffused damage concept

A number of different concepts have been proposed to achieve this with one of the first practical attempts to introduce a controlled damage state being that of Sun and Norman in 1990. Their approach involved introducing adhesive strips into a cross ply laminate that would form a grid that inhibited crack growth on impact. This method reduced damage area significantly and resulted in a modest improvement in residual post impact compression strength, albeit at the expense of a lower initial undamaged compression strength, Fig. 9.

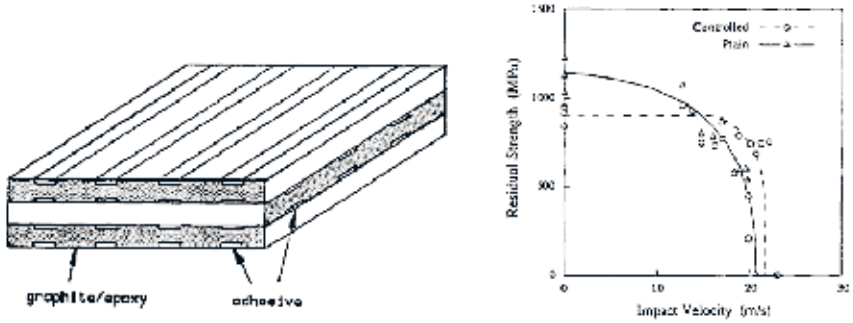

Fig.9. Controlled damage concept of Sun and Norman, 1990

Some other early observations were based on the performance of non-crimp fabrics. Early examples of non-crimp fabrics (NCF's) prepared for the marine industry and consisting of glass fibers assembled using a polyester knitted mesh, show that cracking occurred in impact by growing around isolated bundles. The apparent effect was very similar to laminates made from similar lay-up orientations using unidirectional prepregs. The overall area of damage was not greatly changed. However the compression strengths of the laminates, as a function of the original strength were higher. The cracks around bundles gave the appearance of a macroscopic delamination but the individual bundles cracks had not coalesced and as such did not reduce the in-plane stiffness to the same degree as a major delamination, Fig. 10. Compression after impact strength was therefore increased (Hogg, Ahmadnia and Guild, 1993).

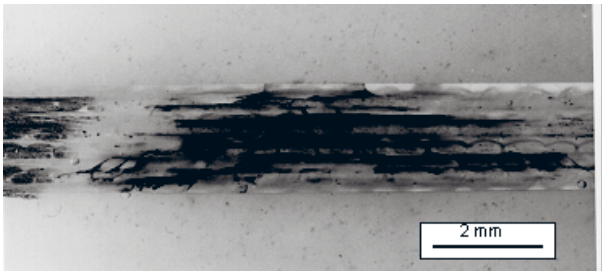

Fig.10. Cross section through an impacted glass fiber polyester resin composite (2mm thick) produced using an early non crimp fabric. The apparent delaminations are comprised of assemblies of cracks that form around individual fiber bundles

This effect was emphasised when comparing composites manufactured from nominally identical non crimp fabrics via different process routes including prepreg/autoclave, resin transfer moulding and vacuum infusion. The RTM and Vacuum infusion laminates retained more of the discrete bundle structure after processing than prepregged NCFs and as a consequence exhibited superior compression after impact properties as a function of impact energy. Part of this was due to a reduction in damage area.

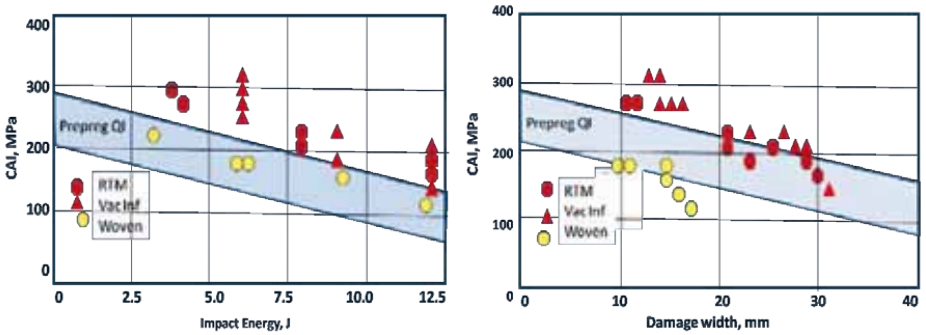

Fig.11. A comparison of CAI data for carbon fiber (quasi-isotropic) NCF laminates prepared via a prepregging route (scatter band only is shown) , RTM, and Vacuum Infusion. Also shown for comparison is prepregged plain weave fabrics.

However, as is shown in Fig. 11, when the same results are plotted as a function of damage width, it is apparent that the relative performance changes but there is still an improvement with the RTM and Vacuum infusion laminates suggesting that at least in part they are better at resisting crack growth than their prepregged analogues. It is interesting to note that woven fabric laminates, also feature in Fig. 11, exhibit similar overall damage tolerance to the NCF prepregged laminates, but when the data is compared on the basis of damage width, the woven materials appear inferior. This suggest that the damage in the woven fabric is smaller for a given impact but the consequences are more significant and more likely to propagate. The retention of fibers in a discrete bundle format in non-crimp fabrics is encouraged by many factors including the presence of the fine knitting yarn that assembles the fibers and keeps them in place within the fabric. The knitting yarn may have a high tension which will ensure that the bundle integrity is retained. The recent industrial attempts to improve NCF fabric properties have focused on providing a uniform distribution of fibers within a layer thereby eliminating the discreet bundle geometry of these early fabrics. Another mechanism for controlling crack morphology could be the use of more complex textile architectures including the use of 3D woven fabrics with angle-interlocking formats, orthogonal weaves or layer to layer 3D structures, Fig. 12.

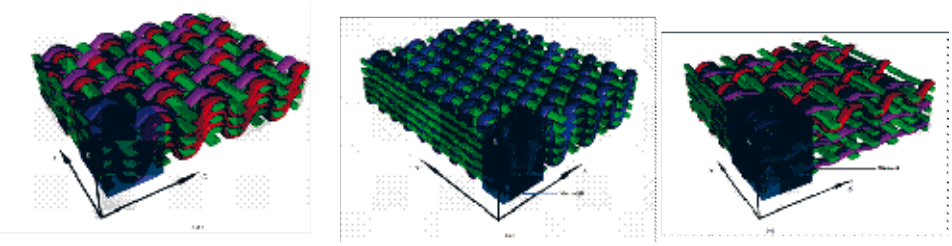

Fig.12. A variety of different 3D woven constructions with differing degrees of interlayer linkages.

In all such cases the yarns in the various directions are kept in position by the presence of other yarns in differing orientations and there is little or no possibility of bundles merging and spreading. The consequence is that, in addition to 3D fabrics possessing no obvious weak interlaminar plane, the nature of damage that forms in their composites has a very different format to that created in simpler 2D materials. In all such cases the yarns in the various directions are kept in position by the presence of other yarns in differing orientations and there

is little or no possibility of bundles merging and spreading. The consequence is that, in addition to 3D fabrics possessing no obvious weak interlaminar plane, the nature of damage that forms in their composites has a very different format to that created in simpler 2D materials. This can be illustrated by the x-ray tomographic images that reveal the cracking patterns and cracking densities in different 2D and 3D versions of otherwise similar materials (S-2 glass/epoxy) and subjected to similar impact blows, Figs. 13 and 14. The 2D fabrics themselves in this case are unusual. The bundles are very discrete and tightly woven. The impact event results in a number of discrete debonds from woven fiber yarns where the debond extends to the area of one tow that is crossed by an adjacent tow. This in effect creates small pockets of debonded bundles but does not result in an extensive single delamination as would be expected in as laminate based on unidirectional prepregs, figure 14c. When the laminates shown in Fig.13 were subjected to compression after impact (Potluri, Hogg, Arshad, Jetavat and Jamshidi, 2011) it was determined that the 3D fabrics provided much greater resistance to damage formation in the impact event than both UD cross ply materials and 2D woven fabrics as shown in Fig. 15.

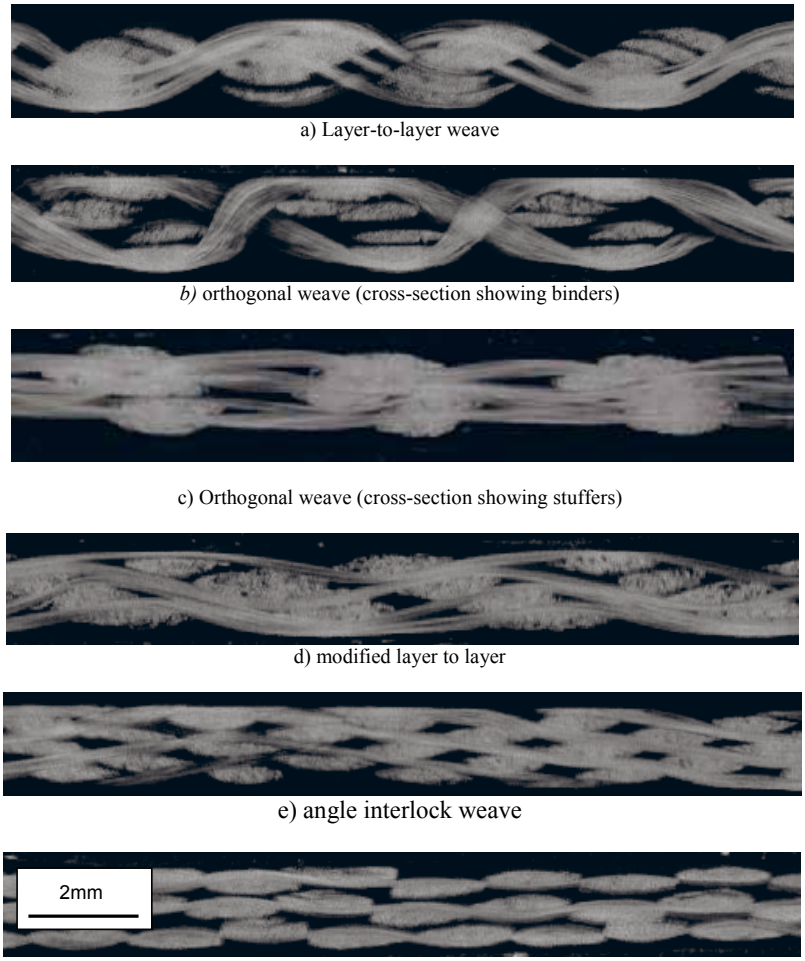

a) Layer-to-layer weave

b) orthogonal weave (cross-section showing binders)

c) Orthogonal weave (cross-section showing stuffers)

d) modified layer to layer

e) angle interlock weave

f) 3 layers of 2D plain wea*ve*

Fig.13. X-ray tomograms of a series of 2D and 3D weaves

However when tested in compression, Fig. 16, the actual residual properties were inferior to the cross ply laminates, which seems to be a result of the lower undamaged compression strength in these materials, which can itself be linked to the presence of crimped and wavy fibers in the 3D architectures. The 3D fabric laminates tested are a little unrepresentative of commercial materials as their fiber volume fraction is low (a function of the yarn text used). It is apparent that judicious control of the fiber architecture within a composite can influence the nature and subsequent growth of damage.

At this stage the nature and location of damage has not been deliberately controlled and fracture events are allowed to occur naturally. It can be envisaged that a next stage in this process would be the deliberate introduction of selective interfacial control at bundle level to trigger fracture at sites and positions that are considered benign within the overall composite architecture. This could allow the dissipation of energy within the structure without creating defects that are liable to propagate and lead of a significant reduction in properties.

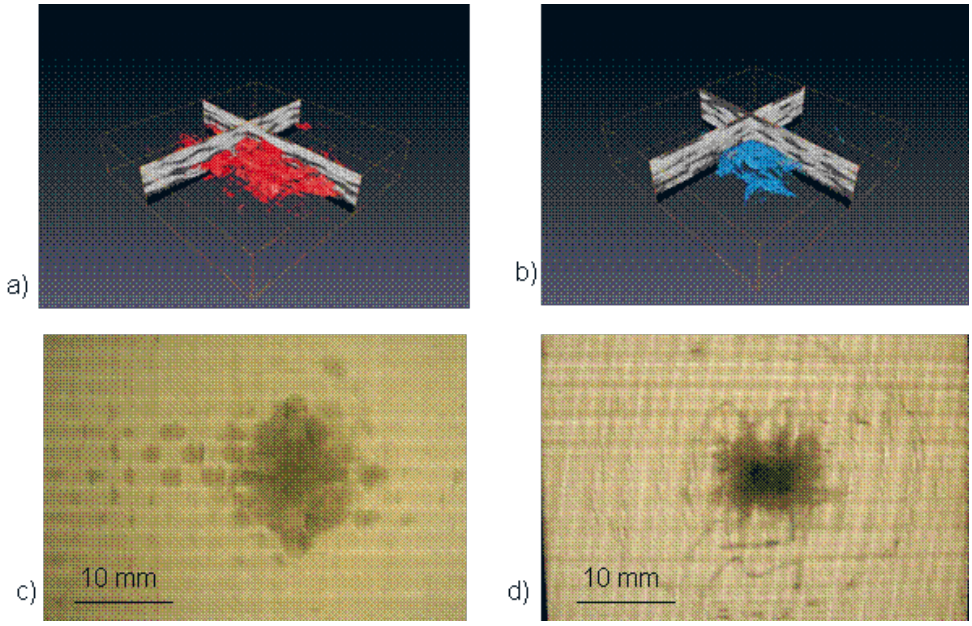

Fig.14. X-ray tomographic images showing cracking in a) 2D and b) a 3D woven S-2Glass fiber/epoxy composite subjected to equivalent impacts. The damage is more extensive and of a different format in the 2D laminate compared to the 3D sample. The optical transmission photographs, of the c) 2D and d) 3D damage areas are seen from above the impact site.

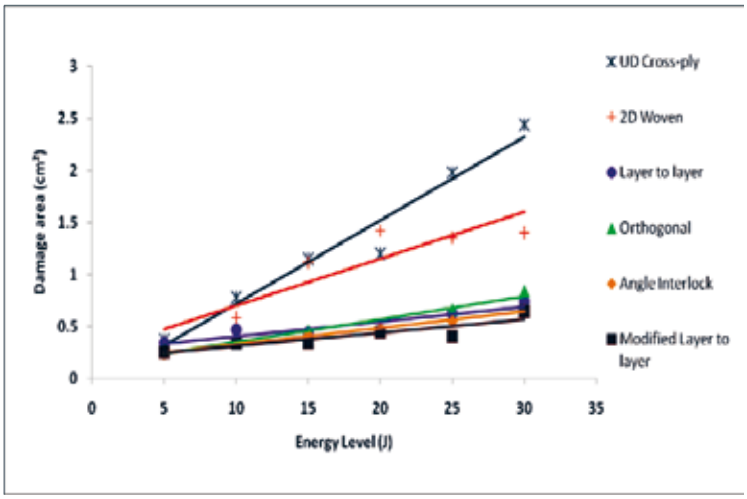

Fig.15. The damage area after impact of the 2D and 3D fabric laminates shown in Fig. 13

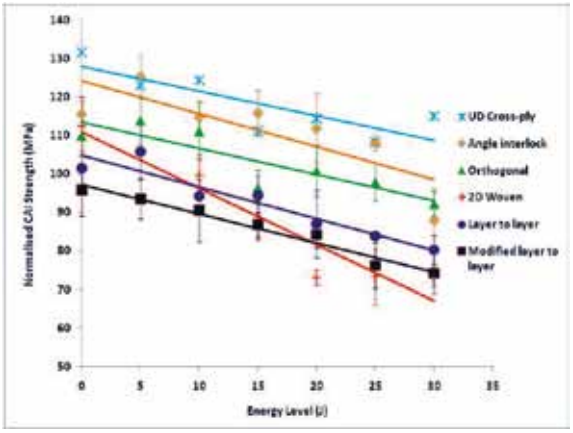

Fig.16. Residual compression strength after impact of 3D woven laminates compared to 2D woven and cross ply laminates (materials as per figure15).

3.3 Mitigating the consequences of damage: Microscopic control. The dissipation of energy within a structure via controlled cracking could also be pursued by control of deformation processes at the micro (fiber) level. An interesting hybrid composite system has been explored over a number of years (Hogg, 2005), conceived as a route to providing through penetration impact and ballistic resistance. This has involved the use of hybrid yarns systems whereby a structural fiber is combined with a non-structural low cost but ductile fiber in a commingled yarn that is used to produce an otherwise conventional fabric, Fig. 17a.

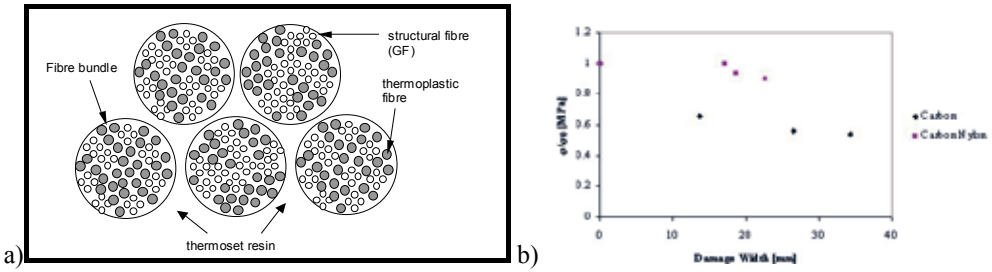

Fig.17. a) A schematic showing the concept of a hybrid yarn toughened composite and b) normalised compression after impact results for a hybrid yarn-epoxy laminate compared to a conventional carbon fiber laminate

These materials when impregnated with a thermosetting resin provide significant improvements in the energy necessary to rupture a composite plate, in some cases by a factor of 2 to 3. Typical combinations of materials include glass fibers with polypropylene fibers and carbon fibers with polyamide fibers. An unexpected benefit may also result from the use of such hybrid systems in compression after impact. The data shown in Fig. 17b illustrates this point for a carbon fiber/nylon commingled laminate infused with a low temperature epoxy. The compression after impact strength as a percentage of the original compression strength is much higher than that of the equivalent composite produced from a plain carbon fiber woven fabric. The result should be considered in context however. It demonstrates the greater resistance to damage propagation in this system, which may be due in part to some thermoplastic fiber bridging or possibly crack blunting and damage delocalisation as a result of multiple debonds between thermoplastic fibers and the thermosetting matrix. The absolute compression after impact strength of the hybrid composite is poor as the introduction of the thermoplastic fibers reduces the volume fraction of structural carbon fibers that can be contained in the final laminate, thereby reducing compression stiffness and compression strength. Hybridisation of tows may in principle however provide an additional mechanism for damage dissipation by cracking between dissimilar materials without reducing the strength of the material itself under the critical loading conditions imposed.

4. A FUTURE STRATEGY

The control of damage and an improvement in the resistance to crack propagation can evidently be expected if composites are designed with new fabric additions and architectures. At present a systematic assessment of architectural effects on damage diffusion into laminate has not been adequately explored.

There are numerous concepts that have been proposed and which show some promise as a route to improving these critical properties. However most of the results have been generated in an ad-hoc fashion. What is needed now is a modelling-led drive to examine the consequences of deliberate architectural modifications, the role of weak interfaces at bundle and fiber level, and the combination of different features with a view to providing a step improvement in properties.

Examination of an SEM micrograph, Fig. 18, of a region from an impacted woven carbon fiber laminate shows extensive cracking within a fiber bundle. If the accompanying fractures in the orthogonal woven fiber bundles had been avoided, perhaps this composite would have absorbed more energy without suffering from significant reduction in compression strength. Selective

local control of bond strength, between fibers and/or bundles could facilitate easy/early cracking in some locations to absorb energy and avoid damage in others.

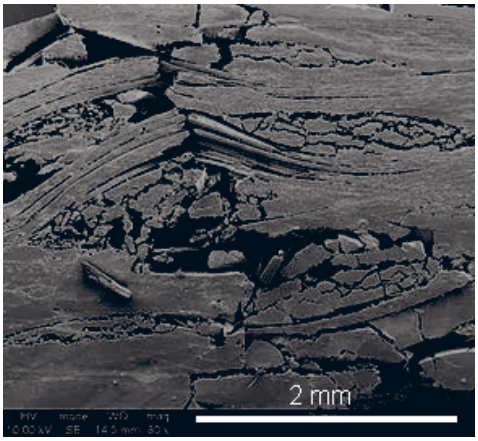

Fig.18. SEM image showing extensive cracking within a bundle of fibers in a woven fabric laminate, accompanied by cracking in the fibers in adjacent bundles.

The following image, Fig. 19, of a hybrid carbon-nylon bundle also illustrates some possible routes to achieving selective and controlled cracking. The hybrid bundle of carbon and nylon fibers is wrapped with a thin layer of nylon fibers which would act as a weak interface allowing primary bundle cracking to occur. Such bindles could be introduced randomly throughout a laminate or spaced at critical locations. The ability to deploy relatively straight forward textile processes to organise fibers and bundles with specific properties suggest that a new toughening technology is waiting to be developed. What is missing at present however is the ability to predict the effects of local architectural control to introduce selective areas of weakness. All results to date have been based on empirical observations which, while proving insights, are not sufficient to produce an optimised new generation of materials.

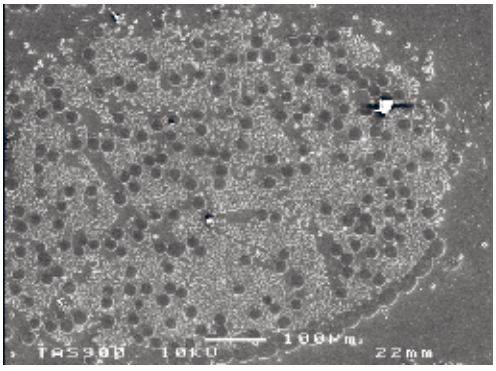

Fig.19. SEM image showing a single bundle in a hybrid carbon fiber/nylon fiber laminate where the bundle is surrounded by nylon fibers that act to retain bundle integrity, but could also act as a controlled weak interface

This discussion has not as yet mentioned the possible use of nano-materials as an added route to toughening a resin and improving damage tolerance. This is not to say that such a route does not have some value. However while the addition of most nano-particulates and even carbon nanotubes, does indeed increase resin toughness, it does not seem to translate into a significant improvement in composite damage tolerance (Iqbala, Khana, Munirb and Kim, 2009). This is likely to be because the ultimate benefit in resin toughness has already been achieved. However the addition of nano-materials in low quantities does not greatly influence the viscosity of the resin and as such, a nano-composite route is probably of greatest benefit in restoring the toughness of laminates made via an infusion process where resins are produced without conventional toughening additives because of viscosity based restrictions on the processing route. Hence nano-materials could be an important complement to complex 3D preforms allowing a base line resin toughness to be retained whilst the composite uses an infusion processes to consolidate a complex architecture. Nano-additives may also have a specific role to play as coatings on fibers to yarns to assist in interfacial control.

What is most likely is that the step change in composite damage tolerance, as defined by a compression after impact measurement, will need an integrated approach harnessing many different individual toughening mechanisms to result in the improvements required by the industry. The problem is made more complex by the need to ensure that any solution is cost effective and compatible with manufacturing processes, and that additional service requirements such as lightning strike protection can be integrated within a commercial system. The indications however are that progress can be made as long as the industry is prepared to accept new material forms and to move away from conventional unidirectional prepreg-based construction methods.

The idea of accepting that damage will happen and seeking to nullify the consequences of damage, as opposed to continually seeking to stop damage forming has been applied in other fields of materials and by nature. A classic example lies in the use and role of rubber particles in high impact modified polystyrene (HIPS). Polystyrene is a brittle polymer at room temperature that readily forms crazes that grow into cracks.

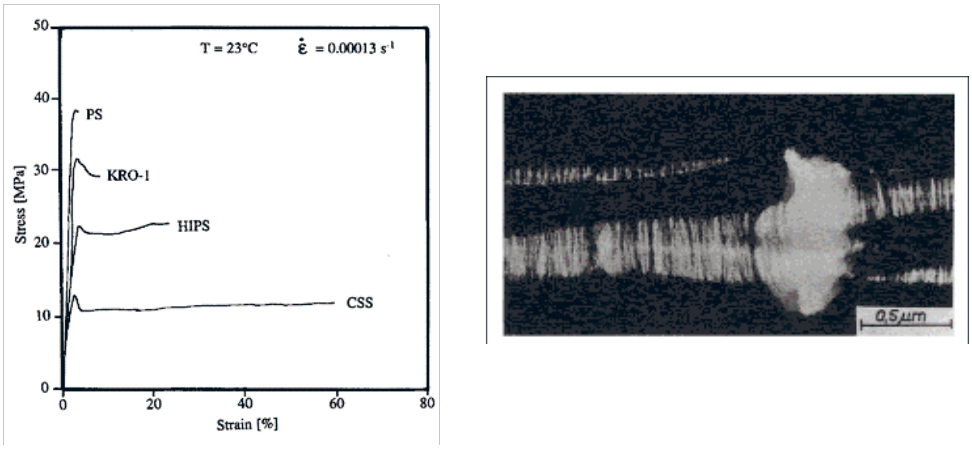

Fig.20. (left) Stress strain curves for polystyrene and derivatives toughened with rubber particles showing an increase in toughness (from Michler 1986) and (right) an electron micrograph showing crazing induced by a rubber particle in ABS (from Argon and Cohen, 1990).

Rubber particles in HIPS promote craze formation but ensure that crazes grow between the rubber particles and are stabilised and do not readily propagate as cracks, converting a brittle polymer into a tough system, Fig. 20. A similar process occurs in ABS, Fig. 20. In nature, wood and bone have micro and ultra-structures that allow cracks to form but do not provide a path for subsequent propagation.

The challenge for composite engineers is to create systems based on similar concepts that work in structural fiber composites, without incurring any weight or other performance penalties.

REFERENCES

Ahmadnia A, Daniel, L and Hogg, P J, (1990), The effect of secondary through-thickness stitching on damage and energy absorption in glass and carbon fiber laminates, Fracture and Damage Mechanics, ed M H Aliabadi, Queen Mary and Westfield College (ISBN 0 904188 54X), p489-503.

Argon A S , Cohen R E, in Kausch H H (ed), (1990) Crazing in polymers, p 301, Springer

ASTM, D 7136 - Test method measuring the damage resistance of a fiber-reinforced polymer matrix composite to a drop-weight impact event, American Society for Testing and Materials, West Conshohocken, Pennsylvania

Bascom, W D, Bitner, J L, Moulton R J and Siebert A R (1980) , The interlaminar fracture of organic-matrix, woven reinforcement composites , Composites, Volume 11, Issue 1, Pages 9-18

Bibo G A, Hogg, P J , Backhouse R and Mills A (1998), "Carbon fiber non-crimp fabric laminates for cost effective damage tolerant structures", Composites Science and Technology, vol 58, pp129-143

Boeing, Materials specification BMS 8-276

Cauchi Savona S, (2005) PhD thesis, Queen Mary, University of London, Energy absorbing composites for crash energy management.

Davy G, Hashemi, S and Kinloch A J, (1989), The fracture of a rubber-modified epoxy polymer containing through-thickness and surface cracks, International Journal of Adhesion and Adhesives, Volume 9, Issue 2, Pages 69-76

Det Norske Veritas AS, (2008), Future perspectives for design and testing of wind turbine blades, A white paper on a rational approach to defects and damage tolerance, Det Norske Veritas AS, Report no WTDK-6022. (http://www.dnv.us/binaries/damage_tolerance-white_paper_2008_tcm153-295072.pdf)

Di Pasquale G, Motto,O Rocca A, Carter J T, McGrail and P T, Acierno D (1997), New high-performance thermoplastic toughened epoxy thermosets, Polymer, Volume 38, Issue 17, Pages 4345-4348

Hogg P J, Ahmadnia A and Guild F J (1993),The mechanical properties of non-crimped fabric-based composites, Composites, vol 24, pp 423-432

Hogg, P J, (2005), Toughening of thermosetting composites with thermoplastic fibers , Materials Science and Engineering: A, Volume 412, Issues 1-2, Pages 97-103

Hogg P J, Kuwata M, Jamshidi,M, Hjadaei, A Teztzis, D, (2010) The potential for improved durability in vacuum infused composites by the use of interlayer veils, Compo2010, Harbin China,

Hull D, and Shi Y B, (1993) Damage mechanism characterization in composite damage tolerance investigations, Composite Structures, 23, pp 99-120

Iqbal, K , Khan S U, Munir A and Kim J K, (2009), Impact damage resistance of CFRP with nanoclay-filled epoxy matrix, Composites Science and Technology Volume 69, Issues 11-12, Pages 1949-1957

Kuwata, M, (2010) PhD thesis, Mechanisms of interlaminar fracture toughness using non-woven veils as interleaf materials, Queen Mary, University of London,

Naik, R A and Logan C P, (1999), Damage resistant materials for aeroengine applications, AIAA Paper 99-1370, 40th AIAA/ASME/ASCE/AHS/ASC Structures, Structural Dynamics and Materials (SDM) Conference, St. Louis, MO.

Michler GH (1986), Determination of the morphology and mechanical microprocesses in polymer combinations by electron microscopy, Polymer 27, p 323-328

Prichard J C and Hogg, P J,(1990) The role of impact damage in post-impact compression testing", Composites, Vol 21, pp 503-511

Potluri P Sharif T, Jetavat D, Hogg P J, and Foreman A, (2009), Benchmarking of 3D preforming strategies, International Conference on Composite Materials ICCM17, Edinburgh: 27-31 Jul 2009, IOM3.

Potluri P, Hogg P J, Arshad M, Jetavat D, Jamshidi P, (2011) Influence of fiber architecture on damage tolerance in 3D Woven Composites, Deformation and Fracture of Composites (DFC-11), Cambridge, 12-15 April 2011 .

Saito, H and Kimpara,I, (2006) Evaluation of impact damage mechanism of multi-axial stitched CFRP laminate, Compos Part A 37, pp. 2226–2235.

Shyr T W and Pan Y H, (2003) Impact resistance and damage characteristics of composite laminates, Composite Structures, 62, pp 193-203

Sun C T and Norman T L, (1990), Design of a laminated composite with controlled-damage concept, Composites Science and Technology, Volume: 39 no 4, Pages: 327-340

Wong W Y, Lin L , McGrail P T , Peijs, T and Hogg P J (2010), Improved fracture toughness of carbon fiber/epoxy composite laminates using, dissolvable thermoplastic fibers, Composites: Part A 41,759–767

Proceedings of the 32nd
Risø International Symposium on Materials Science:
Composite materials for structural performance:
Towards higher limits
Editors: S. Fæster, D. Juul Jensen,
B. Ralph, B.F. Sørensen
Risø National Laboratory for Sustainable Energy,
Technical University of Denmark, 2011

MATERIALS TECHNOLOGY FOR LARGE WIND TURBINE ROTOR BLADES - LIMITS AND CHALLENGES

T.K. Jacobsen

LM Windpower A/S, Product Development
Østre Allé 1, 6640 Lunderskov, Denmark

ABSTRACT

Wind energy is more than ever competing with other sources of energy and as subsidies reduce the development of materials technology becomes driven by reducing the cost of energy. Therefore, the choice of materials technology for rotor blades is not only driven by the direct cost of materials, but also the processing cost and product reliability.

Materials development is focused on decreasing the cost of specific stiffness and expanding the strength limits of the composite materials. Moreover, enhanced durability and functionality of the surface protection is becoming a key challenge to solve.

The over-arching theme of the paper is to put forward the industrial challenges to the research communities and discuss which research directions in composite materials could add value in reducing the cost of energy of future wind turbine power plants.

1. INTRODUCTION

For the last 30 years the use of composite materials has been the only viable option for developing longer and more effective rotor blades for wind turbines. Over the years the length of commercial rotor blades has increased from 6 m to 60 m. Recently, LM Windpower announced that we will launch a 73.5 m long blade for a 6 MW offshore wind turbine developed by the industrial energy and transportation giant, Alstom.

The wind industry has so far undergone the usual transformation from the pioneering to the industrialized stage. Now the industry is moving into the last stage of the transformation journey, namely the matured stage. The characteristics of these three different stages are that for each stage the margins become lower, competition stronger and industrial giants consolidate the business through mergers, acquisitions and by out-competing smaller companies. The single

most important driver for the business will become the Cost of Energy (*CoE*), which is the cost to produce kWhs over the lifetime of the wind-turbine. *CoE* is defined by:

$$CoE = \frac{CoT+CoI+CoM}{PP}, \quad (1)$$

where

CoT : Cost of the Turbine

CoI : Cost of the Installation and transportation.

CoM : Cost of the Operation and Maintenance during the lifetime of the turbine.

PP: Power produced (kWh)

Each of the three major cost elements of the *CoE* set the scene for the objectives for the materials and process technology and the underlying design philosophy on how to utilize the material properties. In this paper we take a specific look at the rotor blades and where the limits and challenges are for significantly lowering the *CoE* in the future. The key objective is thus different from e.g. the transportation industry, where a reduction in fuel consumption is the key objective. One can say that research in wind-power reduces the cost of fuel and transportation research reduces the need for fuel. Both industries are relying more and more on composite materials to deliver cost-efficient light weight structures.

The challenges are divided into:

a) Increasing materials and process performance in a cost-effective manner.

b) Using strength allowable closer to the strength limits based on an increased understanding of failure mechanisms and damage tolerance. Furthermore, the methods to design against certain failure modes (product reliability) need understanding.

2. CURRENT STATE OF ART

Rotor blades are to a large extent made out of composite materials. The most common wind-turbine technology is a horizontal axis 3-bladed rotor. The critical structural design drivers for a blade are divided into extreme load cases and fatigue load cases. Extreme load case design drivers are the tip-to-tower clearance, buckling and root moment. Fatigue design drivers are related to the edge- and flap-wise fatigue of the laminate and root section. For the edgewise fatigue the weight of the blade is critical. No metallic parts except for the bolted attachment to the rotor bearing are used as load carrying elements.

Irrespective of the manufacturer and manufacturing concept a rotor blade can be said to have 7 major parts:

1. Root section (circular area that is used to attach the blade to hub)

2. Main spar (provides the flap-wise stiffness of the blade and is made of unidirectional laminate and shear webs made as a sandwich construction with bi-axially reinforced laminate).

3. Root to main spar transition (the laminate that connects the circular root to the main spar).

4. Edge main laminate (reinforcement of leading and trailing edges)

5. Sandwich panels in shells (connect the edges with the main spar and secure the structural stability)

6. Tip section.

7. Surface protection.

Many different routes to process and manufacture these parts are available. The most common is to manufacture two shells and bond them together after a quality inspection. The methods to arrive at the main spar are numerous within the industry:

a. Integrate unidirectional fabrics in shells and infuse the whole shell in one go. Then bond the shear webs to the two shells during closure of the blade.

b. Manufacture the main spar separately on e.g. a mandrel and then bond the main spar to the shells during closure of the blade.

c. Manufacture the unidirectional laminate separately and then integrate into shells by either bonding or some kind of lamination.

The materials technology is based on:

Reinforcement: E-glass or PAN derived carbon fibers and hybrid combinations thereof.

Matrix: Thermo-set resins like polyester, vinylester or epoxy.

Core: PVC, balsa, PET, SAN, PUR and PS.

Adhesive: Epoxy, Vinylester or MMA.

Surface protection: Gelcoats and PUR paints combined with either thermoplastic foils or special paints on leading edges.

The main focus for most manufacturers has been to learn to master a specific materials and process technology for building the blades. LM Windpower has chosen to master a technology based on glass/polyester processed by vacuum assisted resin transfer molding. This choice of technology has been successful in the sense that LM Windpower over many years have been the leading rotor blade manufacturer by providing a high performance at a low cost.

The materials technologies applied have been around for a long time and the choices are in fact limited and very conventional.

3. STRUCTURAL REINFORCEMENT

The most efficient way of increasing *PP* is by increasing the length of the blade, but that obviously increases the need for structural reinforcement to secure tip-to-tower clearance. The Cost of specific Modulus (*CsM*) is therefore a key driver for the blade component of *CoT*. The

two main fiber types used today are E-glass, carbon or hybrid combinations of the two. Today, LM Windpower reduces material consumption by pre-bending the blades and in principle utilizing the full strain limits of glass fibers. There is a large variety of carbon fibers available and Fig. 1 shows the cost of the specific modulus relative to conventional E-glass fibers (Normalized cost of specific modulus = 1).

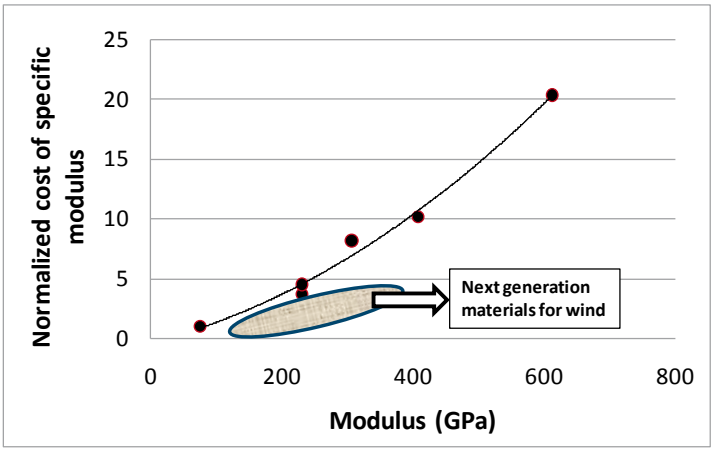

Fig. 1. Normalized cost of specific modulus using E-glass as normalizing reference.

The two most common choices are E-glass and standard modulus carbon fiber. The performance of these two fibers is significantly different as shown in Table 2.

Table 1: A comparison between the two most used fibers in the industry.

Variable	Modulus	Density	Specific modulus	Normalized Cost of specific modulus
Unit	MPa	Kg/m3	MPa/kg/m3	-
E-Glass	75000	2600	29	1
Carbon	230000	1800	128	4

As Table 1 shows the cost of the specific modulus (*CsM*) is 4 times higher for carbon. In our opinion there is a large gap between going from glass to carbon and we need to search for an intermediate fiber solution in-between E-glass and carbon. In general the range from E-glass to standard carbon should exhibit a much lower *CsM*. Some proposed solutions to this fiber type could be:

- Carbon fiber with lower modulus (130-190 MPa) derived from new types of pre-cursors.
- Carbon fiber derived from cheaper pre-cursor materials like lignin.
- A radically changed processing technology for glass and carbon.

The future challenge is to develop materials that enable a reduction in CsM of 50 % as shown in Fig. 2. Natural fibers are often mentioned as alternatives, but the variation in properties needs to be reduced considerably to be applied efficiently. The main trend will most likely be synthesis of "natural fibers" based on cheap renewable resources.

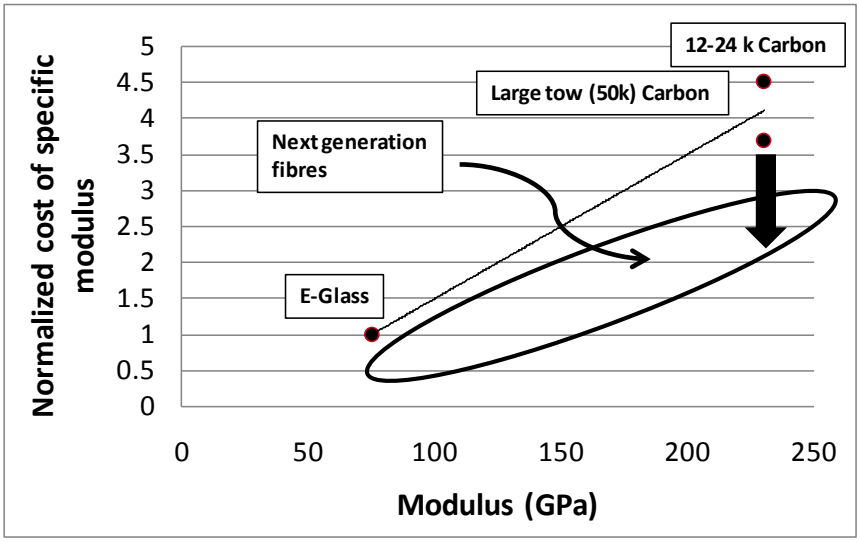

Fig. 2. Target for next generation of fibers for rotor blades.

4. RESIN TECHNOLOGY

The resin is crucial for the laminate performance as it connects the fibers into a load-sharing system. The two most popular systems today are polyester and epoxy. LM Windpower uses the polyester system as it gives some highly advantageous processing properties over epoxy, when using the vacuum assisted resin transfer molding process for molding the blade.

Irrespective of the resin system the major challenge for large blades will be to manufacture as many blades as possible in a mould per week. The cost of moulds for large blades will be a significant contributor to *CoT*. To increase productivity the future challenge will be to develop resins and master the processing technology around speeding up the curing time for the resin. Today we are talking hours, but in the future we need to talk minutes. The huge masses that have to be heated and cooled afterwards lead to an intrinsic limit in the production cycle time. The development of UV or electron beam curing resin systems could be one answer to the next generation material systems. Another very important characteristic will be use of liquid materials with near-to-zero emission to give a good working environment. Low variation processing characteristics of the liquid materials is needed to yield robust and predictable processes. Such systems will enable introduction of reliable automated process control.

Nano-reinforced resins have been a hot topic for a long time, but it still remains to be proven that the property enhancements in fiber composites are real.

Liquids derived from renewable resources with recycling potential are also a trend that represents a major challenge for the research communities.

5. SANDWICH PARTS

Fig. 3 shows the commercially-available cores offered today plotted by shear modulus and density. Main choices have so far been balsa wood or one of the many foam materials. Over the recent years engineered foams have gained ground. The principle is to wind structural fibers around a low density foam core and assemble these wound foam blocks into a sheet. The core thus acts as carrier of the fibers. The engineered foams are mainly applicable for resin transfer molding processes, where the fibers are filled with resin and after curing form a truss-like structure. High strength and stiffness can be achieved. However, engineered foams have process and design limitations that still need to be overcome to end up with the same flexibility as foams or balsa wood. The main problem in the core business is that almost all available solutions end up costing the same for a specific shear modulus as an example – even though they are quite different from a materials standpoint. The key challenges will be to reduce the cost of the foam core solutions provided – mainly by drastically reducing the process transformation cost from liquid phase into foam that can be placed in the blade mould.

The use of "engineered" foams based on nano-sized fibers or nano-clays have not really proven to be effective in reinforcing the cellular walls of foams, but the potential is still large if an efficient materials discovery can be made.

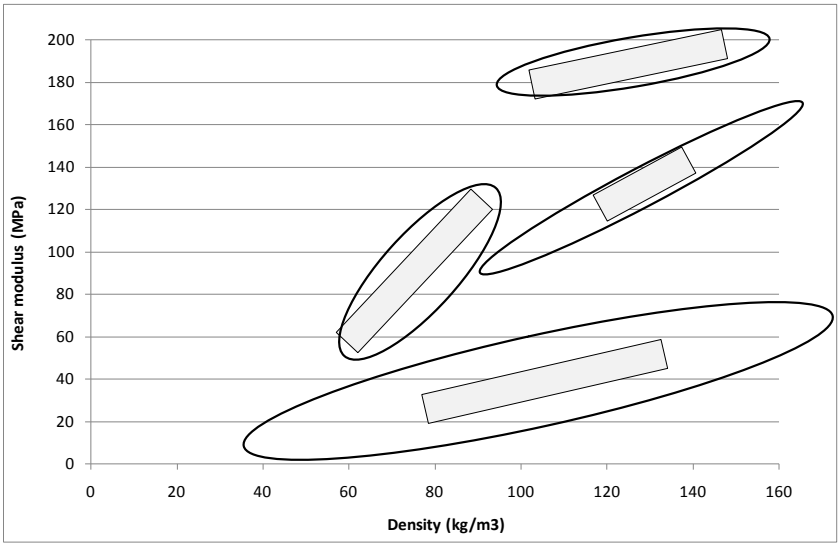

Fig. 3. Relevant shear modulus and density ranges of core materials for sandwich panels in rotor blades.

6. SURFACE PROTECTION

Surface protection has not undergone a radical development within the blade business. Gelcoats and paints have worked fine. The surface protection is affecting the *CoM* and *PP* significantly as it prevents degradation of the structural reinforcement and secures an undisturbed air-flow with a certain surface roughness to it. The upcoming trend is to increase tip speed such that the centrifugal force helps stiffening the blade and thus reduces the need for structural reinforcement. The increase in tip speed will put tougher requirements to the leading edge protection. Erosion caused by rain drops and harder particles is the main concern. Fig. 4 shows

erosion damage on a painted surface and a foil protected surface caused by rain drops in a highly accelerated test environment. The phenomena is well known in the aerospace industry, where foils are usually applied.

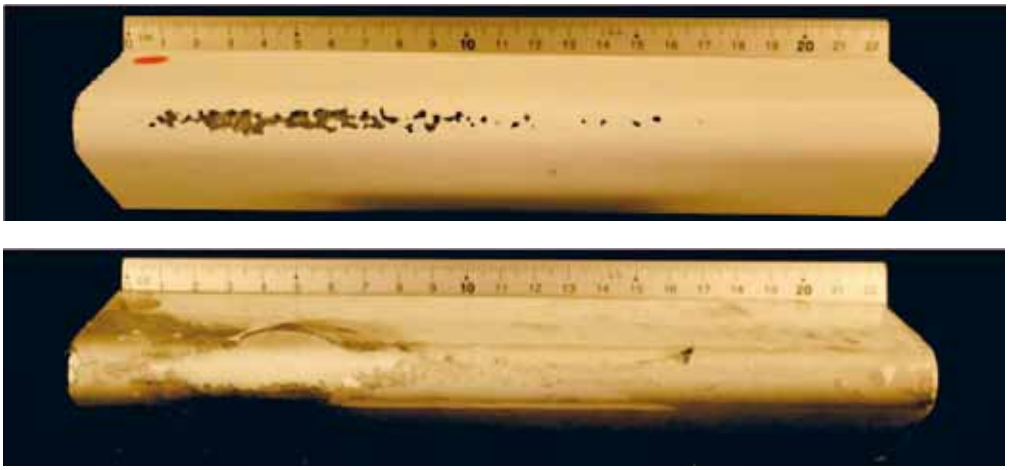

Fig. 4. Accelerated rain drop erosion test of a painted surface (top) and a foil protected surface (bottom).

Most wind turbines available for sale today are operated with tip speeds between 60 and 95 m/s, Fig. 5. A number of new announcements have been made, where the tip speed is significantly increased and now up to 111 m/s. Further tip speed increases can be expected once break-throughs in aerodynamics and noise reduction appear.

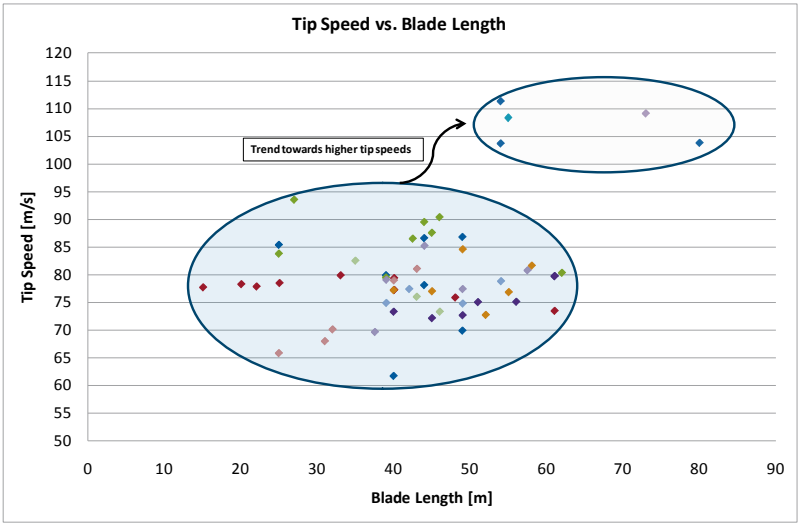

Fig. 5. Tip speeds versus blade length on commercially available wind turbines.

The main challenge of increasing tip speed is how to predict the durability of the leading edge as function of the different site conditions and develop accelerated test methods that capture the same failure modes as in real life. There are many contributing factors like rain, hail, sand

particles, temperature variation, corrosive elements in the air and UV exposure. There is thus a large need for more deep research into the mechanisms of degradation on existing materials to understand what can be done to prevent and predict onset of the various failure modes. As shown in Fig. 4 the failure modes of a foil and a painted surface are completely different. Today the leading edge of a wind turbine is to be considered as a wear part and it adds to *CoM* – especially off-shore.

In general, there is a need for developing more functional surfaces that can prevent loss of *PP* by avoiding turbine stops due to icing of the blades in cold regions (de-icing), and dirt and insects in warmer regions (anti-fouling). Both of these challenges probably need to be solved by application of nano-technology.

7. STRENGTH LIMITATIONS

Many strength calculations are done using a set of partial coefficients that knocks down the characteristic strength due to a variety of degrading reasons like temperature, moisture, creep etc. These are all based on some industrial experience and the use of partial coefficients is strongly linked to the accuracy of the design method. It is clear that a simple design method normally would require quite some knock down in strength allowable to account for that stress concentrations are not considered.

Probabilistic design methods open up for rewarding more advanced calculations and better production process control. There is thus a need for verifying and validating more advanced fracture mechanics calculation methods for assessing the severity of processing tolerance settings.

LM Windpower is currently engaged in developing more advanced test and calculation methods for predicting cyclic fatigue crack growth in interfaces. The method is based on being able to measure changes in cohesive strength parameters during fatigue. The final aim of the project is to be able to simulate interfacial crack growth in blades and predict the reliability as function of the processing tolerances.

Another development is to be able to link the microstructure of uni-directional laminates to the fatigue strength. A characterisation method of the microstructure has been developed and correlations to fatigue strength are promising. The final aim of the project is to avoid the need for mechanical testing to verify that the right fatigue strength has been met for a certain composite laminate system being processed and as part of the incoming inspection of materials.

Another limiting aspect in the design process are the multi-axial static and fatigue strength criteria. Currently, the design methods and partial coefficients applied are fairly simple and high, respectively. Therefore, significant reduction in *CoT* can be expected if the current test and design methods for multi-axial strength of laminates can be better understood – potentially a probabilistic approach.

8. SUMMARY

In this paper we have tried to outline some of the challenges that are so generic in nature that they apply to any wind turbine blade concept. The challenges are:

Reinforcement:

- 50 % cost reduction of glass and carbon fiber by raw materials processing methods and new synthesis methods. Are there any other fiber solutions?

Resins:

- Curing times have to be reduced from hours to minutes by new resin chemistry and curing methods

Cores:

- 50 % cost reduction achieved by reducing the transformation cost from liquid to foam.
- Discover new ways of making engineered foams with the flexibility of the current foam and balsa.

Surfaces:

- Leading edge protection that can sustain 20 years of harsh site conditions at tip speeds above 110 m/s.
- Develop functional surfaces that prevent icing and repel dirt on the blade surface.

Strength

- Change from a partial coefficient system approach to probabilistic design methods.
- New design and testing methods for multi-axial static and fatigue laminate strength
- New design and testing methods for interfacial fatigue strength.

In LM Windpower we are constantly searching for solutions to the above and invites anyone to join us in achieving our targeted mission of "….. making our customers more successful and wind energy more compelling".

REFERENCES

The values shown in this paper are all retrieved from public available websites and market research reports (e.g. Chemical Economics Handbook, SRI Consulting).

Proceedings of the 32nd
Risø International Symposium on Materials Science:
Composite materials for structural performance:
Towards higher limits
Editors: S. Fæster, D. Juul Jensen,
B. Ralph, B.F. Sørensen
Risø National Laboratory for Sustainable Energy,
Technical University of Denmark, 2011

ADVANCES AND CHALLENGES IN THE COMPUTATIONAL SIMULATION OF COMPOSITES

J. LLorca*†

* Madrid Institute for Advanced Studies of Materials
(IMDEA Materials Institute)
C/ Profesor Aranguren s/n, 28040 - Madrid, Spain
† Department of Materials Science
Polytechnic University of Madrid
E. T. S. de Ingenieros de Caminos, 28040 - Madrid, Spain.

ABSTRACT

State-of-the-art simulation techniques to predict the mechanical behavior of composites are reviewed. They are encompassed within a bottom-up, multiscale modeling strategy based on finite element simulations performed at different length scales (ply, laminate and component). The main features of each simulation strategy, current limitations as well as the information transferred between length scales are briefly described. Future lines of development are finally indicated.

1. INTRODUCTION

Fiber-reinforced polymers (FRP) are widely used in structural applications due to their outstanding stiffness and strength combined with low density. Nevertheless, optimization of composite structures remains a challenge because of the differences in the mechanical behavior of metallic alloys (the standard structural materials) and composites. In particular, damage tolerance (and, thus, reliability) of metallic alloys comes from their large ductility and fracture toughness. FRP are also tough but fracture normally occurs at low strains as the fibers (which carry most of the load) are brittle. In addition, metallic alloys are isotropic and failure takes place by one dominant failure process involving the nucleation, growth and coalescence of voids under extensive plastic deformation. FRP are anisotropic and fracture involves several different failure mechanisms (Fig. 1) and the dominant one depends on the loading conditions. Fracture due to tensile stresses parallel to the fibers is controlled by the tensile fracture of the fibers, while compressive stresses along the fibers lead to fracture by fiber kinking, a mechanism which mainly depends on the fiber misorientation and the matrix shear strength. Tensile fracture perpendicular to the fibers is brittle and is controlled by the fracture of the epoxy resin and of the fiber-matrix interface, while fracture caused

by compressive stresses perpendicular to the fibers or by shear is accompanied by large deformations as a result of the non-linear response of the epoxy matrix when subjected to compression and/or shear. Finally, composite laminates are made up by stacking lamina (or plies) with different fiber orientations and interply delamination is another typical failure mechanisms in FRP due to the elastic mismatch between adjacent plies. Thus, accurate models of fracture of FRP have to include all these micromechanisms and the complex interaction among them. For instance, intraply matrix cracks (which propagate parallel to the fibers) are very often the origin of interply delaminations, while it is well known that the compressive strength parallel to the fibers is severely reduced in the presence of shear stresses.

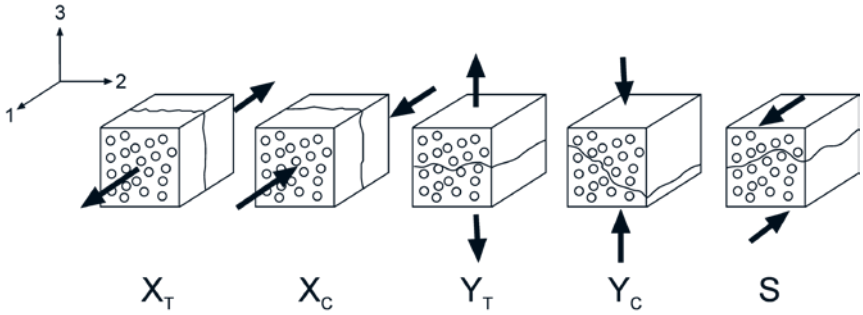

Fig. 1: Schematic of failure micromechanisms in fiber-reinforced polymers.

Obviously, the concurrent simulation of all these micromechanisms is a daunting task. The standard strategy to tackle this problem started from a numerical analysis of the whole structure (normally using the finite element method) in a global-to-local approach. This initial evaluation identified "hot spots" in which damage was likely to occur, and these regions were subjected to refined analyses. Non-linear constitutive models (as well as damage) were included in these cases using phenomenological models for the material behavior. These models contained a number of parameters whose values were chosen to reproduce the actual material behavior as a result of experience and costly testing campaigns (Cox and Yang, 2006). Although this strategy has been in place for many years, its ability to predict accurately the failure load of composite structures is limited due to the phenomenological nature of the failure models, which cannot capture faithfully the interaction among failure mechanisms or assess the effect of defects for all loading scenarios. As a result, design of composite structures is very conservative and engineers do not take full advantage of the material properties.

Recent developments in multiscale simulations, increased computational power and improvements in modeling tools are rapidly changing this scenario. Nowadays it is starting to be possible to accurately predict the behavior until failure of composite coupon specimens and simple components through the application of bottom-up approaches. The main features of this novel approach to carrying out high-fidelity simulations of the mechanical behavior of composite materials and structures are briefly presented, together with their current limitations.

2. MULTISCALE MODELING STRATEGY

Most advances in the simulation of the mechanical behavior of composite materials and structures can be summarized in the multiscale simulation strategy depicted in Fig. 2. This scheme takes advantage of the fact that composite structures are made up of laminates which in turn are obtained by stacking individual plies with different fiber orientations. This leads to three different entities (ply, laminate and component) whose mechanical behavior is characterized by three different length scales, namely fiber diameter, ply and laminate thickness, respectively. Fiber diameters are of the order of 5-10 μm, while lamina thicknesses are in the range 100-300 μm and standard laminates are several mm in thickness and above. This clear separation of length scales is very useful to carry out multiscale modeling by computing the properties of one entity (e.g. ply) at the relevant length scale, homogenizing the results into a constitutive model, and passing this information to the simulations at the next length scale to determine the mechanical behavior of the larger entity (e.g. laminate). Thus, multiscale modeling is carried out through the transfer of information between different length scales rather than by coupling different simulation techniques.

High fidelity simulations up to the component level can thus be carried out in three successive steps within the framework of finite element (FE) method (LLorca and González, 2011a; LLorca, González, Molina-Aldareguía *et al.*, 2011b). In the first one, *computational micromechanics* is used to predict the ply properties from the thermo-mechanical properties of the constituents (fiber, matrix and interfaces), together with the volume fraction and spatial distribution of the fibers within an individual ply. Starting from the homogenized ply properties and information about the interply behavior, *computational mesomechanics* is then used to determine the homogenized behavior of laminates. These results are finally used within the framework of *computational mechanics* to obtain the response until fracture of structural components. The main features of the simulation techniques at each step of the simulation ladder as well as the current limitations and challenges are detailed in the following sections.

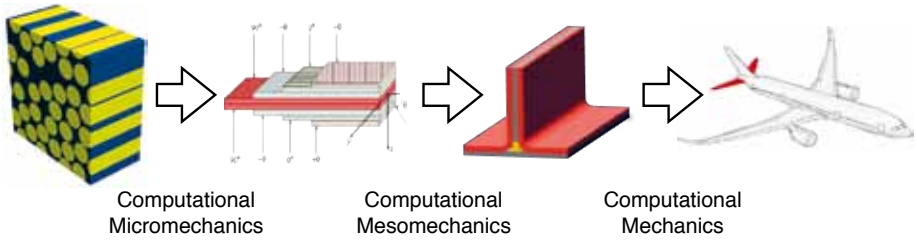

Fig. 2: Multiscale modeling strategy for high fidelity simulation of composites.

3. COMPUTATIONAL MICROMECHANICS

Homogenization theory is a well-established, efficient and accurate methodology to compute the elastic properties of a ply from the properties and spatial distribution of the different phases in the composite. Nevertheless, extension to the non-linear regime, and particularly to situations involving strain localization and fracture, is more complex and the accuracy of the results is not always guaranteed. This is critical to obtain the failure surface of FRP plies, which indicates the maximum load-bearing capability of the ply under any stress state. The failure surface is made up of the intersection of the various smooth surfaces,

which correspond to the different physical failure modes depicted in Fig. 1. So far, the failure surface —basic element to predict the onset of intraply damage— was obtained by means of phenomenological models (Puck and Schürmann, 2002; Dávila, Camanho and Rose, 2005; Pinho, Iannucci and Robinson, 2006) whose predictions could not be extrapolated to materials with a different fiber volume fraction or matrix or interfacial properties.

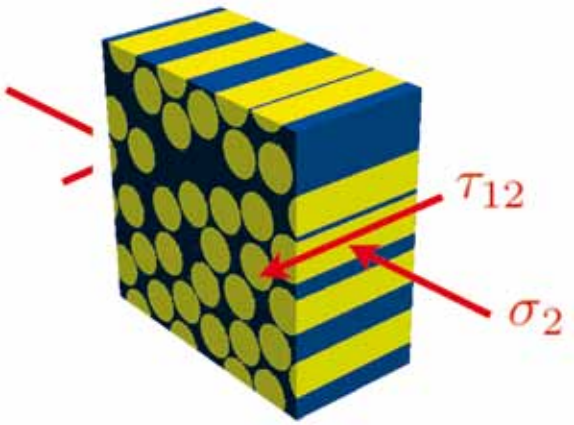

Fig. 3: 3D RVE of composite ply containing 60 vol. % of C fibers.

These limitations have been overcome with the rapid development of computational micromechanics in the last decade. The strategy to determine the failure locus begins with the creation of a Representative Volume Element (RVE) of the ply. In the typical case of unidirectional reinforcement, fiber centers are generated randomly and sequentially to reach the desired volume fraction in a square domain. The fiber distribution within the domain is periodic, and the 3D RVE is obtained by extruding the 2D periodic microstructure along the fiber direction (Fig. 3). Fibers behave as linear elastic solids and their properties (strength and stiffness) are normally well characterized by the fiber manufacturer. Polymeric matrices are modeled as isotropic, elasto-plastic solids following the Mohr-Coulomb criteria. Matrix properties can be obtained from tests on matrix coupons or by means of in situ nanomechanical tests (LLorca *et al.*, 2011b). Finally, fiber-matrix decohesion is included in the model by means of interface elements whose behavior is controlled by a cohesive crack model (González and LLorca, 2007; Totry *et al.*, 2008). The strength and toughness of the interface can be obtained from push-in tests in which a single fiber is pushed by means of a nanoindentor on a cross-section of a bulk specimen until interface debonding occurs (Molina-Aldareguía, Rodríguez, González and LLorca, 2011).

Once the lamina model is built, the failure locus is obtained by solving the boundary value problem for different loading conditions by means of the FE method. Periodic boundary conditions are normally used because they eliminate border effects and provide the best approximation to the homogenized properties of the material. For instance, the RVE depicted in Fig. 3 was subjected to compression perpendicular to the fibers (σ_2) and in-plane shear (τ_{12}) and the corresponding failure locus in the stress space is plotted in Fig. 4a, together with the experimental results for a PEEK matrix reinforced with 60 vol. % of AS4 C fibers (Totry *et al.*, 2008). The agreement is excellent for the whole shape of the failure locus and it is worth noting that the experimental points in Fig. 4a should be interpreted as lower bounds of the actual strength under shear-dominated fracture because of the end plate effects. In addition, the numerical model captured the transition from shear failure by

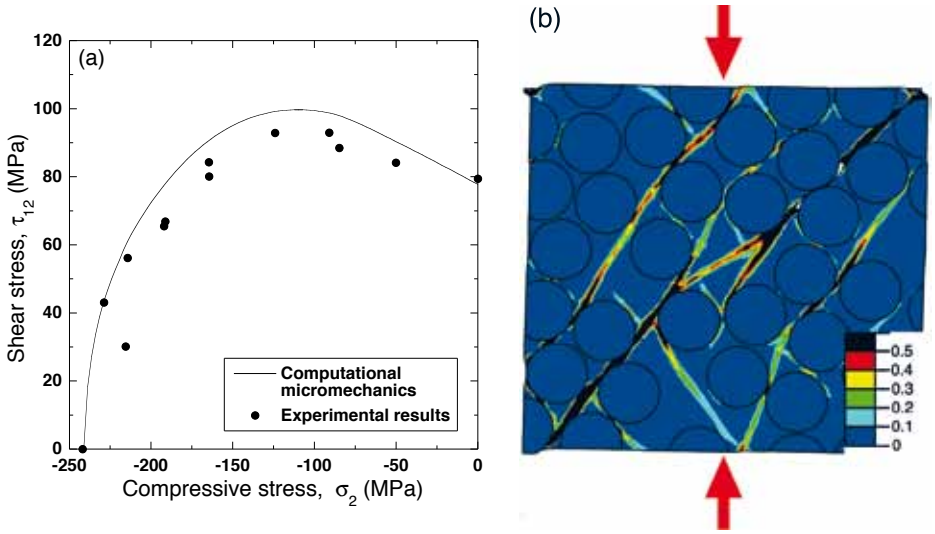

Fig. 4: (a) Failure locus of ply made up of a PEEK matrix uniaxially reinforced with AS4 C fibers subjected to compression perpendicular to the fibers, (σ_2), and shear parallel to the fibers (τ12) (Totry *et al.*, 2008) (b) Contour plot of the accumulated plastic strain in the matrix showing the localization of failure in a shear band during transverse compression (González and LLorca, 2007).

splitting along the fibers for low compressive stresses ($<$ 100 MPa) to compressive failure along an inclined surface parallel to the fibers ($>$ 100 MPa). The former was characterized by a linear increase of the shear strength with the applied compressive stress as a result of the pressure-sensitivity of the polymeric matrix. The end of this regime was accompanied by a change in the failure mode to compressive failure, leading to a gentle reduction in the maximum shear strength at failure. In addition, the model was able to accurately capture the physical failure mechanisms. For instance, failure during compression perpendicular to the fibers took place by the development of a macroscopic shear band at an angle of 56° with the direction perpendicular to the compression axis. The microscopic failure mechanisms within the shear band were strain localization in the matrix and decohesion at the fiber-matrix interface. Both microscopic mechanisms were found in the numerical simulations (Fig. 4b) and, in addition, the average orientation of the shear band in the RVE was very close to the one found in the experimental samples.

Computational micromechanics presents several significant advantages as compared to standard homogenization. For instance, complex non-linear behaviors (geometrical and material) can be accounted for as well as multiaxial stress states, which are very difficult to obtain experimentally. In addition, the details of the stress and strain microfields are resolved and thus it is possible to track the nucleation and growth of damage during the simulation, a key aspect to model the localization of damage and fracture. Finally, the experimental scatter (associated with processing defects, free-edge effects, stress concentrations at loading points, etc.) is eliminated, leading to the true material behavior. Of course, the main limitation of this approach comes from the computational cost (particularly in 3D simulations) but this problem was overcome by the ever increasing power of digital computers.

A further challenge of composite micromechanics is its extension to compute the failure locus

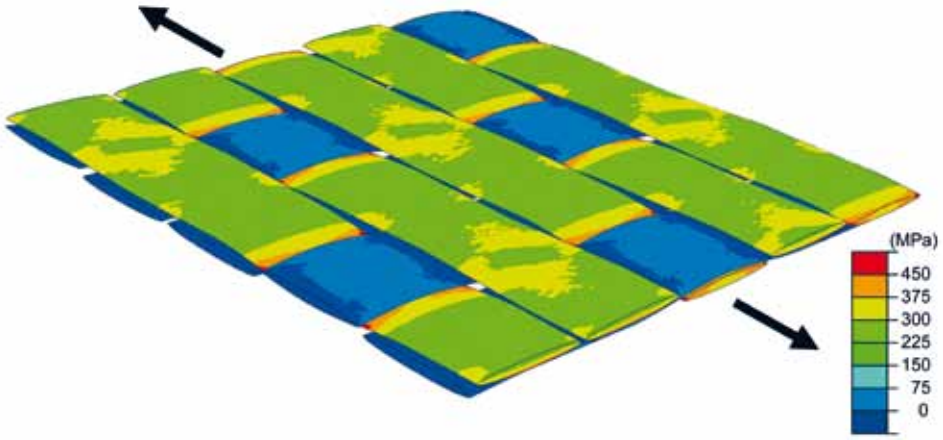

Fig. 5: Finite element simulation of a representative unit cell of 5-harness satin fabric composites subjected to tensile deformation. The contour plot shows the stresses in the fiber yarns along the loading direction.

of textile fiber preforms. Textile plies are formed by impregnated fiber yarns (containing several thousands of fibers) arranged in a given pattern defined by the type of fabric (woven, knitted, braided) and the free space between the yarns is filled with matrix. Besides the constituent properties, the stiffness and the failure locus of the textile ply depend on fabric architecture (yarn waviness, crimps, spatial disposition and density) and it should be noted that the geometry of textile preforms is complex and the choice of possible architectures unlimited. Models are based on a representative unit cell of the textile preform that allows for the simulation of the mechanical behavior of the whole fabric by the application of adequate boundary conditions (Fig. 5). Fiber yarns are considered as transversally-isotropic solids and the elastic constants are obtained from the fiber and matrix properties using standard homogenization techniques.

The extension of this approach to obtain the corresponding failure locus is more complex. Damage mechanisms in fabrics differ from those found in uniaxially reinforced lamina. Upon deformation, damage starts in textile composites by the formation of matrix cracks, which occur within the fiber yarns (parallel to the fibers), delamination cracks (which propagate between yarns and are arrested when they reach yarns of a different orientation), and microcracks in matrix pockets between yarns. Further loading may lead to either matrix- or yarn-dominated failure. The former occurs by coalescence of matrix cracks into a shear band transverse to the yarns or into an interplay delamination crack, while the second takes place by yarn fracture in tension or kink failure and/or buckling in compression. Several of these failure micromechanisms can be incorporated easily into the numerical model, e.g. by means of interface elements or cohesive surfaces to simulate decohesion at the matrix/yarn interface. However, the damage mechanisms associated with the yarns (matrix microcracking within the yarns and yarn failure) have to be incorporated into the constitutive equation of the yarn, which is considered a homogeneous solid in this approach. The standard treatment of damage within the yarns involves a failure criterion (which is analogous to the failure locus obtained by computational micromechanics for unidirectional plies) and a damage evolution law. These features are normally implemented in a Continuum Damage Mechanics (CDM) framework, similar to the one used to model damage in unidirectional

plies and which will be presented in the following section.

4. COMPUTATIONAL MESOMECHANICS

The main elements of the computational mesomechanics simulations are the individual plies. The virtual laminate is built by stacking plies with different fiber (or fabric) orientations (θ) and the FE model explicitly includes each ply as well as the interfaces between plies (Fig. 6a). Meshing of the laminate is carried out with solid elements for the plies while cohesive interface elements (or cohesive surfaces) are used to take into account the ply interfaces. This modeling strategy presents two main advantages. Firstly, full three-dimensional stress states can be considered, as opposed to simulations based on shell elements for the composite plies, which are limited to two-dimensional stress states. Secondly, intraply and interply damage can be introduced separately together with the complex interaction between them. The main limitation of this approach lies in the computational power required to carry out these simulations, which limit their application to coupons or structural details.

Interply decohesion is induced by the elastic mismatch of adjacent plies with different fiber orientation. The crack path is defined a priori and progressive interply decohesion under mixed-mode loading can be analyzed by means of a cohesive crack model coupled with interface elements between the ply surfaces (Camanho and Dávila, 2002). A similar approach was used to model decohesion at the fiber-matrix interface within the framework of computational micromechanics (González and LLorca, 2007; Totry *et al.*, 2008) and to simulate intraply damage in the case of matrix cracking under tensile and shear stresses (Jiang, Hallet and Wisnom, 2007; Hallet, Jiang, Khan and Wisnom, 2008).

In the case of intraply damage mechanisms, the onset of damage is predicted by the failure surface, which can be obtained from numerical simulations based on computational micromechanics (as described in the previous section) or from experimentally-validated phenomenological models (Puck and Schürmann, 2002; Dávila *et al.*, 2005; Pinho *et al.*, 2006). In this way, the combination of stresses which leads to the initiation of damage and the particular damage mode activated (matrix cracking, fiber kinking, etc.) is known. Nevertheless, laminate failure is not always associated with the initiation of damage and the accurate prediction of the maximum load-bearing capacity requires computing the evolution of damage, including the interaction among the different physical failure modes. This is a very complex problem and successful, accurate results were only obtained recently through the application of two different approaches based on cohesive surfaces and CDM. They are described below, together with their advantages and limitations.

Application of cohesive crack models is very useful to model intraply damage in the case of matrix cracking under tensile and shear stresses. In this situation, the crack propagates through the matrix in the fiber direction and interface elements are inserted a priori along the fiber direction. The combination of interply delamination and matrix cracking using interface elements has been successfully used to model the behavior of composite laminates with a notch or a central hole under tension (Jiang *et al.*, 2007; Hallet *et al.*, 2008), including the influence of stacking sequence, ply thickness and specimen size on the maximum load and the sequence of deformation and failure mechanisms. One significant advantage of modeling interply and intraply damage within the same framework is that coupling between both damage processes is easily captured by the simulations. However, the use of interface elements to model intraply damage presents two important limitations. Firstly, interface elements have to be inserted in each ply following the fiber direction. This requires costly re-meshing if the stacking sequence or the fiber orientation is changed and there is a penalty

stiffness associated with the initial stiffness of the cohesive crack which limits the number of parallel interface elements that can be inserted in the mesh. Secondly, this methodology cannot not be used if the crack plane is not known a priori. This is the case of failure under compression parallel or perpendicular to the fibers.

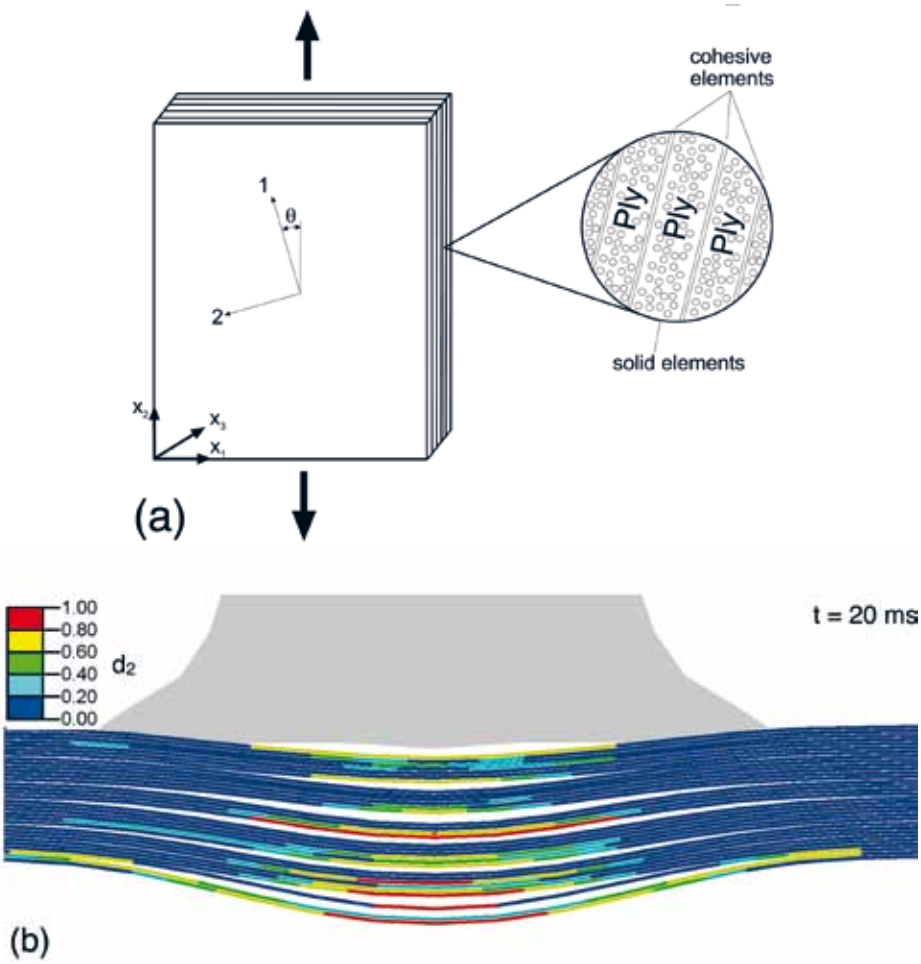

Fig. 6: (a) Schematic of computational mesomechanics approach. (b) Simulation of high-velocity impact on a C/ epoxy laminate. Interply damage was modelled using CDM and interply decohesion was included by means of interface elements. Damage by decohesion between plies is clearly visible. In addition, contour plot indicates the level of damage by matrix cracking — from intact (0) to fully damaged (1) — within the individual plies.

An alternative to capturing all the intraply failure mechanisms within a single framework is provided by the formalism of CDM. The ply behaves as a homogeneous, linear orthotropic solid, and the relationship between strains ($\boldsymbol{\epsilon}$) and stresses ($\boldsymbol{\sigma}$) is given by the compliance tensor $\boldsymbol{\epsilon} = \mathbf{H}(\mathbf{d})\,\boldsymbol{\sigma}$, where $\mathbf{d}$ is the damage tensor, whose components provide the influence of each damage mode on the ply compliance. The onset of damage is dictated by the failure surface of the ply, which can be obtained using computational micromechanics (as

described in section 3) within a multiscale approach. In the event that this information is not available, it is also possible to use experimentally-verified phenomenological models for the failure locus (Puck and Schürmann, 2002; Dávila *et al.*, 2005; Pinho *et al.*, 2006).

Continuum damage models have been implemented in either implicit or explicit finite element codes in combination with a crack band model (Bazant and Oh, 1983) to ensure that the results are independent of the numerical discretization. In combination with interface elements to simulate interply decohesion, they have been successfully used to simulate size effects in notched laminates loaded in tension (Camanho, P. Maimí, C. G. Dávila, 2007) and the mechanical behavior of laminates under impact (Arávalo, González, Gálvez and LLorca, 2007; Lopes, Camanho, Gürdal, Maimí, González, 2009) (Fig. 6b). In particular, damage initiation and energy dissipation during fracture are captured very accurately. Nevertheless, current limitations should also be indicated. In order to deal with all the intraply damage mechanisms within one single framework, CDM treats the lamina as a homogeneous, although anisotropic, material, neglecting the actual presence of matrix and fibers with very different stiffnesses. This simplification leads to erroneous predictions in particular cases. For instance, damage is computed from strain components calculated from the symmetric part of the deformation gradient and, therefore, shear deformation parallel or perpendicular to the fibers leads to the same response. However, this is not the case in uniaxial composite plies subjected to large shear deformation. Shear parallel to the fibers leads to failure by the localization of shear deformation in the matrix (and the shear strength is similar to the matrix shear strength) while shear perpendicular to the fibers induces fiber rotation and a marked strain hardening due to the load taken up by the fibers (Totry, Molina-Aldareguía, González, LLorca, 2010).

CDM also presents problems to predict the correct path for splitting matrix cracks. In the real material, they run in the weaker matrix parallel to the fibers but this distinction is lost during homogenization and the crack path sometimes follows the direction perpendicular to the maximum principal stress in continuum damage models. The more the principal stress differs from the fiber direction, the more the crack path deviates from the experimental pattern (van der Meer and Sluys, 2009a). In order to overcome these limitations, formulations based on the extended finite element method are being developed to simulate splitting cracks in combination with CDM for all the other intraply damage mechanisms (Iarve, Gurvich, Mollenhauer, Rose and Dávila, 2011; van der Meer and Sluys, 2009b; Fang, Yang, Cox and Zhou, 2011). Potential crack paths (along the fiber direction) are introduced a priori in the finite elements and the cracks remain close until the corresponding failure criterion is met. The discontinuity in the element displacement field is then introduced by enrichment of the element shape functions with the Heaviside step function.

5. COMPUTATIONAL MECHANICS

As indicated above, computational mesomechanics is limited to composite coupons or small panels but it cannot be extended to structural components due to the associated computational cost. This problem is the last step in the multiscale simulation strategy (Fig. 2) and the one that still needs the development of a robust methodology to bridge the length scales. Computational simulation of the composite structures is currently carried out using shell elements within the framework of the FE method (Fig. 7a). This approach is limited to bidimensional stress states but it is very efficient from the numerical viewpoint and ideal for analyzing large structures. The shell elements contain as many integration points through the thickness as the number of plies in the laminate in each region of the component but

different plies are not modeled independently.

Damage is included within the framework through the application of CDM at the ply level (Heimbs, Cichosz, Klaus, Kilchert and Johnson, 2010; Smojver and Ivancevic, 2010). Damage is initiated at each ply when the corresponding failure criterion is fulfilled, leading to a progressive reduction of the laminate stiffness. Obviously, interply decohesion cannot be included explicitly and this hinders the accuracy of the simulations as the actual interaction between intraply and interply damage is not accounted for. This problem may be overcome in particular situations, in which the most likely decohesion surfaces are known a priori (e.g. stiffener-skin surfaces). If there is only one interply crack, two shell elements, each representing a sublaminate, are connected by a delamination contact interface in which a penalty force method is used to compute contact forces between adjacent shells and eventually simulate decohesion (Greve and Pickett, 2006).

An example of this metholodogy to simulate bird impact at 170 m/s on the leading edge of a horizontal tail plane is shown in Fig. 7b (LLorca *et al.*, 2011b). The bird (a water sphere 20 cm in diameter) was discretized using an Eulerian mesh with 25000 8-node solid elements with reduced integration. The leading edge and the reinforcing ribs were discretized using a Lagragian mesh with 50000 shell elements with one integration point per ply. The onset of damage in each ply was dictated by the Hashin failure criteria (Hashin, 1980) and damage evolution was dictated by CDM. The ribs and the leading edge were joined by means of beam elements, which could be broken according to a maximum stress criterion, leading to the possibility of decohesion. The contour plot of damage by fiber fracture in the leading edge and in the ribs is shown in Fig. 7b at the instant of maximum deformation. The simulations were in good agreement with the experimental results and the information provided in terms of damage accumulation was very useful to assess the localization of damage during impact and design the laminate lay-up as well as the geometry in order to optimize the structural behavior. It should be noted, however, that the parameters which control the onset and evolution of damage simultaneously represent intraply and interply fracture mechanisms and their complex interaction in a given laminate. Thus, they could not be obtained from independent tests or simulations at the coupon level and a certain degree of parameter fitting -based on previous experience or on the analysis of experimental data- was always required to obtain good results.

6. CONCLUDING REMARKS

The results presented in the previous sections demonstrate that virtual testing of the mechanical behavior of composite materials and structures is a real possibility in the near future. There are still gaps in the multiscale modeling ladder but the overall framework is robust and has already shown its ability to carry out high-fidelity tests of composite coupons and small components subjected to very different loading conditions. The whole strategy is based on finite element simulations performed at different length scales to take into account the relevant microstructural and structural features relevant to the mechanical behavior. Instead of directly coupling simulations at different length scales, multiscale modeling is introduced by successive homogenization of the mechanical behavior, so information about the deformation and damage is introduced in a constitutive model and passed on to the simulations at the next scale.

Future developments will proceed in different directions. Besides refining the current strategy, it should be noted that it is built up from the experimental values of fiber, matrix and interfaces. While this is feasible from the industrial viewpoint, a more academic approach

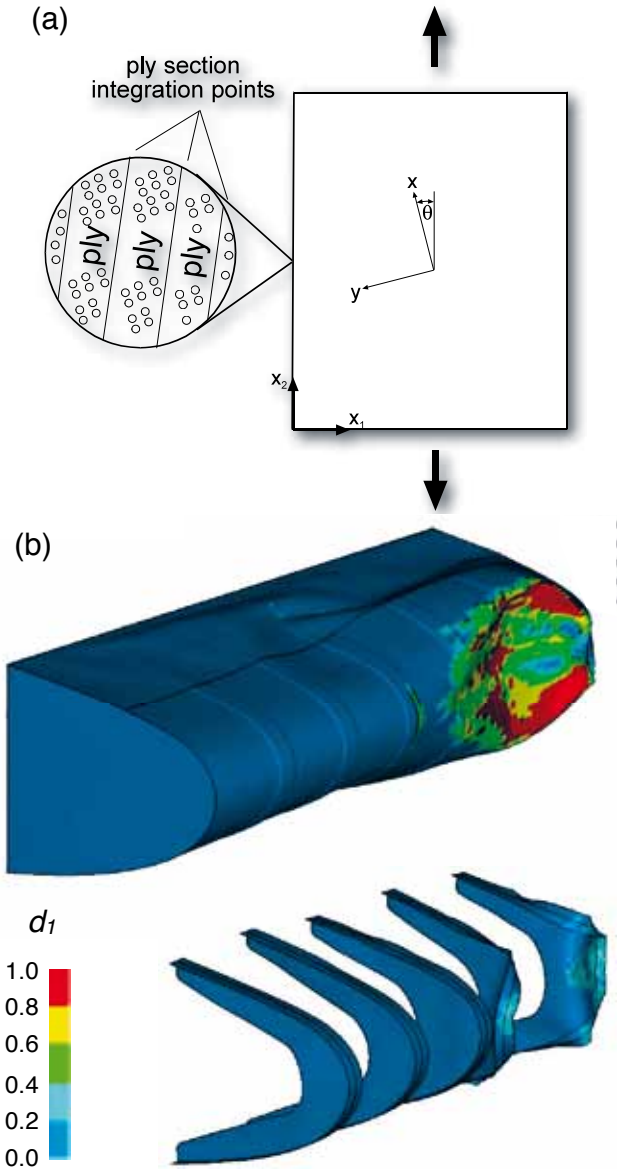

Fig. 7: (a) Schematic of computational mechanics approach. (b) Simulation of high-velocity bird impact on a composite leading edge. Contour plot of damage by fiber fracture is shown in the figure.

would aim to compute these properties from first principles, so new composite materials can be designed and validated *in silico*, well before they are actually manufactured and tested. In addition, incorporation of other physical properties to the simulation ladder (thermal and electrical conductivity, permeability, moisture absorption, etc.) will pave the way to designing and characterizing multifunctional composites. Finally, integrated computational materials engineering of composites will require coupling this virtual testing strategy with similar models devoted to virtual processing.

ACKNOWLEDGEMENTS

The author is indebted to the contributions of Drs. C. González J. Segurado and J. M. Molina-Aldareguía. This investigation was supported by the Ministerio de Ciencia e Innovación de España through the grant MAT 2009-14396, by the Comunidad de Madrid through the program ESTRUMAT (S2009/MAT-1585), by the research project DEFCOM (Era-Net MATERA, EU, 6th FP) and by the European Communitys Seventh Framework Programme FP7/2007-2013 under grant agreement 213371 (MAAXIMUS, www.maaximus.eu). In addition, the author wants to acknowledge the support of Airbus, Gamesa, Astrium España and Airbus Military through various industrial projects.

REFERENCES

Arévalo, E., González C., Gálvez, F., and LLorca J. (2007) Modelling low velocity impact in C/epoxy laminates. In 23rd International Symposium on Ballistics, (Eds: F. Gálvez and V. Sánchez-Gálvez), Tarragona, Spain, pp. 1123-1132.

Bazant, Z. P., and Oh, B. H. (1983) Crack band theory for fracture of concrete, Mater. Struct. 16, 155-177.

Camanho, P. P., Dávila C. G. (2002) Mixed-mode decohesion finite elements for the simulation of delamination in composite materials, NASA/TM-2002-211737.

Camanho, P. P., Maimí; P., and Dávila C. G. (2007) Prediction of size effects in notched laminates using continuum damage mechanics, Compos. Sci. Technol. 67, 2715-2727.

Cox, B., and Yang, Q. (2006) In quest of virtual tests for structural composites. Science 314, 1102-1107.

Dávila, C. G., Camanho, P. P., and Rose, C. A. (2005) Failure criteria for FRP laminates. J. Compos. Mater. 39, 323-345.

Fang, X. J., Yang, Q. D., Cox, B. N., Zhou, Z. Q. (2011) An augmented cohesive zone element for arbitrary crack coalescence and bifurcation in heterogeneous materials. Int. J. Numer. Meth. Engng, in press.

Greve, L., and Pickett, A. K. (2006) Delamination testing and modelling for composite crash simulation, Compos. Sci. Technol. 66, 816-826.

González, C., and LLorca, J. (2007) Mechanical behavior of unidirectional fiber-reinforced polymers under transverse compression: microscopic mechanisms and modeling. Compos. Sci. Tech. 67, 2795-2806.

Hallett, S. R., Jiang, W. G., Khan, B., and Wisnom M. R. (2008) Modelling the interaction between matrix cracks and delamination damage in scaled quasi-isotropic specimens, Compos. Sci. Technol. 68 80-89.

Hashin, Z. (1980) Failure criteria for unidirectional fiber composites, J. Appl. Mech. 47, 329-334.

Heimbs, S., Cichosz, J., Klaus, M., Kilchert, S., and Johnson A. F. (2010) Sandwich structures with textile-reinforced composite foldcores under impact loads, Comp. Struct. 92,

1485-1497.

Iarve, E. V., Gurvich, M. R., Mollenhauer, D. H., Rose, C. A., Dávila, C. G. (2011) Mesh independent matrix cracking and delamination modeling in laminated composites. Int. J. Numer. Meth. Engng, 2011, in press.

Jiang, W. G., Hallett, S. R., Wisnom, M. R., and Green, B. (2007) A concise interface constitutive law for analysis of delamination and splitting in composite materials and its application to scaled notched tensile specimens, Int. J. Numer. Meth. Eng. 69, 1982-1995.

LLorca, J., and González, C. (2011a). Virtual mechanical testing of composites: from materials to components. In: 1st World Congress on Integrated Computational Materials Engineering (The Minerals, Metals and Materials Society, Warrendale, PA).

LLorca, J., González, C., Molina-Aldareguía, J. M., Segurado, J., Seltzer, R., Sket, F., Rodrguez, M., Sádaba, S., Muñoz, R., and Canal, L. P. (2011b). Multiscale modeling of composite materials: a roadmap towards virtual testing. Adv. Mater. 23, in press.

Lopes C. S., Camanho, P. P., Gürdal, Z., Maimí P., and González, E. V. (2009) Low-velocity impact damage on dispersed stacking sequence laminates. Part II: Numerical simulations. Compos. Sci. Techno. 69, 937-947.

Molina-Aldareguía, J. M., Rodríguez, M., González, C., and LLorca, J. (2011). An experimental and numerical study of the influence of local effects on the application of the fibre push-in test. Phil. Mag. 91, 1293-1307.

Pinho, S. T., Iannucci, L., and Robinson, P. (2006) Physically-based failure models and criteria for laminated fibre-reinforced composites with emphasis on fibre kinking. Part I: Development., Composites Part A, 37, 63-73.

Puck, A., Schürmann, H. (2002) Failure analysis of FRP laminates by means of physically based phenomenological models, Compos. Sci. Technol.62, 1633-1662.

Smojver, I., and Ivancevic, D. (2010) Numerical simulation of bird strike damage prediction in airplane flap structure, Comp. Struct. 92, 2016-2026.

Totry, E., González, C., and LLorca, J. (2008) Prediction of the failure locus of C/PEEK composites under transverse compression and longitudinal shear through computational micromechanics. Compos. Sci. Technol. 68, 3128-3136.

Totry, E., Molina-Aldareguía, J. M., González, C., and LLorca, J. (2010) Effect of fiber, matrix and interface properties on the in-plane shear deformation of carbon-fiber reinforced composites. Compos. Sci. Technol. 70, 970-980.

Van der Meer, F. P., and Sluys, L. J. (2009a) Continuum models for the analysis of progressive failure in composite laminates. J. Comp. Mater. 43, 2131-2156.

Van der Meer, F. P., and Sluys, L. J. (2009b) A phantom node formulation with mixed mode cohesive law for splitting in laminates. Int. J. Fract. 158, 107-124.

Proceedings of the 32nd
Risø International Symposium on Materials Science:
Composite materials for structural performance:
Towards higher limits
Editors: S. Fæster, D. Juul Jensen,
B. Ralph, B.F. Sørensen
Risø National Laboratory for Sustainable Energy,
Technical University of Denmark, 2011

NUMERICAL SIMULATIONS OF LARGE SCALE WIND TURBINE BLADES - LIMITATIONS AND CHALLENGES

E. Lund* and A.L. Hansen**

* Department of Mechanical and Manufacturing Engineering,
Aalborg University, 9220 Aalborg East, Denmark
** LM Wind Power, Jupitervej 6, 6000 Kolding, Denmark

ABSTRACT

The development of cost effective wind turbines is to a large extent dependent on efficient use of numerical simulation methods for predicting the structural performance, and in this paper some of the issues related to simulations of large scale wind turbine blades are described. Typical designs of wind turbine blades, the loading scenarios and structural design criteria are outlined, before the typical use of finite element methods for the structural analysis is described. Some of the limitations and challenges when predicting the performance of large scale wind turbine blades from a strength point of view are described, and it is suggested to use a multi-scale based understanding of the mechanical behavior of composite materials and structures for wind turbine blades. A hierarchical analysis method that in a consistent way supports the multi-scale analysis approach is described and outlined by a simple example, before the hierarchical analysis approach is demonstrated by an example of predicting the structural collapse of a wind turbine blade where the numerical predictions are compared with results from full scale collapse tests.

1. INTRODUCTION

The major trends in the wind turbine industry are towards wind turbines that can operate for a long time, towards increased blade length (and consequently increased weight), and towards offshore placement. Wind turbines have continued to increase dramatically in size because a lot of the infrastructure and some components of wind turbines are size independent. This is even more pronounced for off-shore wind turbines. Furthermore, larger wind turbines have larger energy output per unit rotor area, and large wind turbines are thus usually able to produce more cost-effective electricity than small wind turbines.

For several years the world's largest wind turbine has been the Enercon E-126, which has a rotor diameter of 126 meters. In comparison, this is much larger than the wingspan of the Boeing 787 "Dreamliner" (60 meters) and Airbus A380 (79.8 meters). This wind turbine is

rated at 6 MW, however, it will most likely produce more than 7 MW (or 20 million kilowatt hours per year), which is equivalent to powering about 5,000 households of four people in Europe. Another wind turbine of equivalent size is the REpower 6 MW wind turbine with blades from LM Wind Power, each having a length of 61.5 meters.

However, several larger wind turbines have recently been announced. This year LM Wind Power has built the world's largest wind turbine blade, having a length of 73.5 meters, which will be used on a 6MW offshore wind turbine from Alstom. Other wind turbines with rotor diameters exceeding 160 meters have recently been announced by manufacturers, for example the Vestas V164 7 MW with blades having a length of 80 meters and a weight of 35 tonnes, and even larger wind turbines are being planned.

Due to the high competition on the wind energy market, a key issue is to be able to design new, reliable products faster than the competitors, and as wind turbines grow in size and their blades become longer and more flexible, it becomes more difficult to test the blades for endurance. Full scale fatigue testing is an inherent part of the test program when verifying the final structural design of new prototype blades, and due to the lower eigenfrequencies of larger blades, such test programs take a longer time than for smaller blades. This makes it even more important to have consistent, reliable methods for efficient structural design of wind turbine blades, and numerical simulations of the structural performance play a key role in the strive for reliable new wind turbine designs. This paper will describe some of the limitations and challenges when predicting the performance of large scale wind turbine blades from a strength point of view, and it will describe a hierarchical analysis approach that in a consistent way can be used for a multi-scale based understanding of the mechanical behavior of composite materials and structures for wind turbine blades.

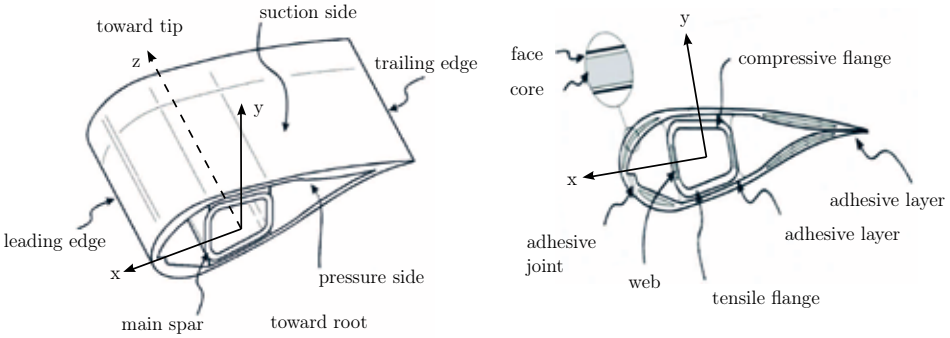

Fig. 1: Illustration of the structural definitions of typical wind turbine blade. The aerodynamic lift generates the dominant flap-wise bending moment $M_x(z)$ and shear force $V_y(z)$ in the local xyz-coordinate system, which basically dictates the amount of composite laminates and core material in the flange and web, respectively, which again make up the primary load-carrying main spar (Overgaard, Lund and Thomsen 2010).

Modern wind turbine blades are high performance and hybrid material structures that are being manufactured using polymer matrix composite materials in a combination of monolithic (single skin) and sandwich composites. Present designs are mainly based on glass fiber-reinforced polymers (GFRP), but for very large blades carbon fiber-reinforced polymers (CFRP) are being used increasingly by several manufacturers, in addition to GFRP, to

satisfy all structural requirements and reduce the weight. Parts of a typical wind turbine blade can be seen on Fig. 1.

In Fig. 1 the blade is composed of a main spar and outer shell parts. These are typically manufactured separately and then joined in a separate bonding process. Alternative designs may involve that the two wing shells are joined with one, two or more internal webs (stiffeners) as shown schematically in Fig. 2. In this conceptual design, the wing shells are manufactured with relatively thick so-called spar caps, which usually are monolithic composite laminates. Other wind turbine manufacturers have adopted a manufacturing technique, where the entire blade structure including internal webs/stiffeners is manufactured in one single process.

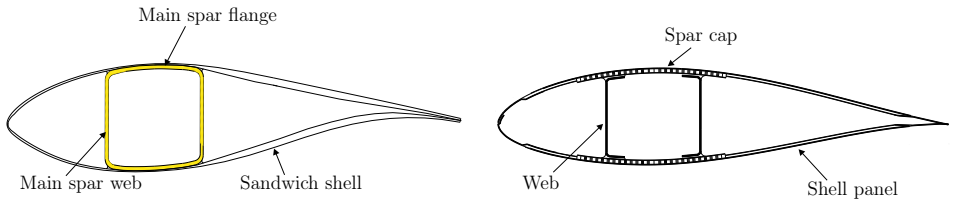

Fig. 2: Different blade design concepts. Left: Design with internal main spar. Right: Design with internal shear webs (Kühlmeier 2007 and Thomsen 2009).

Wind turbine blades include numerous joints (at leading and trailing edges of the wing shells, between wing shells and main spar, between spar cap and internal stiffeners/shear webs), and furthermore, there are many material transitions (from monolithic laminates to sandwich structures, ply drops, etc.). In the vicinity of geometric and material discontinuities, localized effects cause the inducement of stress concentrations that may significantly affect the static and fatigue strengths.

The loading on a wind turbine blade consists of the following (Risø/DNV 2002):

- Flapwise and edgewise bending due to the pressure load on the blade (skew bending).
- Gravitational loads, which change direction during the rotation of the blade, and which mainly generate edgewise bending loading.
- Torsional loading because the shear resultants of the flap- and edgewise loads do not go through the shear centre of the blade section.
- Normal loading due to the rotation of the blade (inertia forces).
- Relative small loads due to pitch de-accelerations and accelerations.

The flapwise and edgewise loads case are very important for the overall structural design and the blade cross sections. The spar carries most of the flapwise bending, while the edgewise bending primarily is carried by the leading and trailing edges of the aerodynamic profile, which are strengthened due to this. The maximum flapwise bending load normally corresponds to the situation when the turbine has been brought to a standstill due to high wind, and the blade is hit by the 50-year extreme gust wind. The maximum edgewise bending load used in the design is derived from a combination of different loading situations taken from dynamic simulations (Thomsen 2009). Adhesive joints bonding the blade shells

and webs carry longitudinal shear forces and are furthermore loaded by in-plane deformation of the blade cross section caused by torsional loading.

Wind turbine blades are subjected also to severe fatigue loads. A number of criteria must be considered in the design of wind turbine blades including (Risø/DNS 2002; Wacker 2003):

- global stiffness (blade tip deflection - tower clearance),
- buckling resistance (main flange or spar cap and trailing edge panel on suction side of airfoil),
- blade eigenfrequencies,
- material failure under static and fatigue loading,
- local face instability of sandwich parts.

The amount of loading situations and design criteria to consider, together with the increasing size of the blades, makes it a challenging task to develop reliable predictions of structural strength. Furthermore, many of the failure mechanisms that occur in composites are so localized that it is not possible to capture them at a global model scale, but they are often the result of nonlinear effects that must be included at the global scale.

Since different types of damage and subsequent failure can develop at different length scales in wind turbine blades, it is necessary to develop a coherent, multi-scale based understanding of the mechanical behavior of composite materials and structures for wind turbine blades. The length scale goes from nano- and microscale (materials) to global scale (the whole blade). Thus, the numerical simulations should support such a multi-scale analysis approach in order to obtain reliable and accurate predictions of structural strength.

It is important to note that the numerical simulations of wind turbine blades will always be an approximation to reality. Composite structures can have significant variability in the actual layup and quality of the laminate due to variations in manufacturing processes, imperfections in materials, a range of assembly tolerances, etc. This may yield variability in stiffness and in particular in strength. Thus, uncertainty and variability should be considered, but in this paper focus is mainly on a deterministic analysis from an engineering point-of-view.

2. FINITE ELEMENT ANALYSIS OF WIND TURBINE BLADES

The current tradition in industry when making finite element models of wind turbine blades is to use standard layered shell elements based on first-order shear deformation theory. Typically, these elements are used with nodes offset to the outer surface of the blade, as this geometry is the well-defined smooth reference geometry given by aerodynamic considerations. The laminates used are easily assigned to the model by modern pre-processing tools capable of constructing complex lay-ups with different thicknesses, materials and orientations of each ply. Ply drops together with other material thickness step changes are conveniently handled by the Equivalent Single Layer (ESL) theory applied because discontinuous thickness changes are allowed between adjacent elements. These shell elements yield accurate predictions of structural stiffnesses and overall stress/strain levels. However, the node offset

option for shells should be used with care in case of modeling structures with high curvature like closed cross sections with large shell thicknesses (i.e. low radius/thickness ratio), see Laird, Montoya and Malcolm (2005), where the implications on erroneous stiffnesses of wind turbine blade models are described. An example of a global FE model of a blade is seen in Fig. 3.

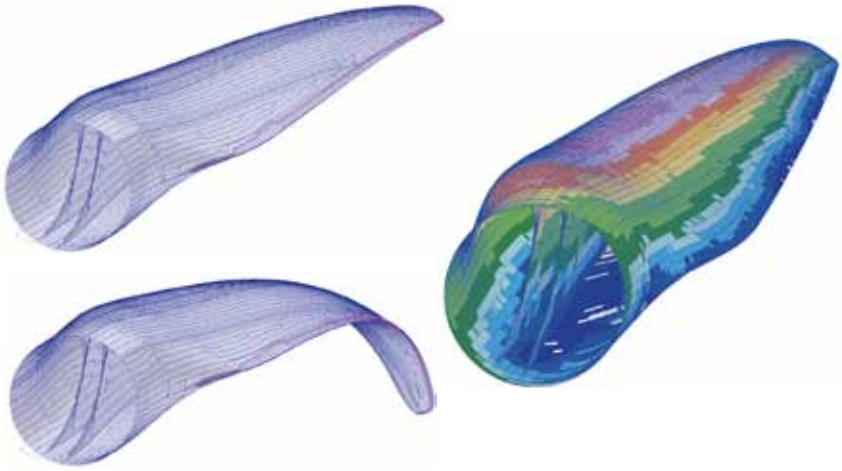

Fig. 3: Global FE models of wind turbine blades (courtesy of LM Wind Power).

Thus, standard layered shell elements have many advantages from a modeling point of view, but when the objective is to predict structural strength of a wind turbine blade accurately, more detailed analyses are needed. Local effects due to geometric and material discontinuities are critical issues that must be examined carefully at a much more detailed level. One of the disadvantages of using layered shell elements is, that these models do not give accurate predictions of transverse strains and stresses needed to evaluate interlaminar failure modes which is one of the important failure modes to consider for laminated composite structures. These quantities can be provided by solid shell finite elements, which are based on a complete solid isoparametric trilinear kinematic representation with additional internal degrees of freedom (DOF) to stabilize the shell-like solid element, see e.g. Klinkel, Gruttmann and Wagner (1999). These solid shell elements can have very large aspect ratios and still perform well.

However, modeling the whole wind turbine blade with solid shell elements represents a significant change with respect to model generation. Now the three-dimensional finite element geometry must match the physical geometry of the blade, i.e., be continuous also at the inner surface. Thus, ply drops and other material thickness step changes must be modeled by tapering the layer thicknesses. As another example, the modeling of webs also becomes very different as the foot of the webs is included as part of the main laminate in the spar cap in standard shell models. Thus, existing automated preprocessing tools using ESL shell elements need many changes when changing the modeling to layered solid shell elements in order to have a consistent description of the structural parts that might be subjected to more detailed analyses.

The resulting finite element models when using solid shell elements will have approximately the same number of global DOF as standard shell models, as the incompatible, internal DOF typically are eliminated by static condensation on the element level. Standard shell

elements have 6 DOF per node, 3 translational and 3 rotational, whereas the solid shell element used in the examples in this paper has 8 nodes, each with 3 translational global DOF, and 7 internal DOF, see Johansen and Lund (2009) and Johansen, Lund and Kleist (2009). However, for the same number of DOF the storage requirements for solid shell models are normally higher due to a larger bandwidth of the resulting system of equations.

The main advantage of using layered solid shell elements for the global model is a better description of the three-dimensional stress and strain state in the model, and furthermore it is easier to create detailed submodels or make hierarchical models in a consistent way as described in Section 4.

Many finite element programs offer efficient tools for shell-to-solid or solid-to-solid submodeling where displacements at the cut boundary of the global model are used as boundary conditions for refined solid submodels. Alternatively, section forces and moments can be extracted from the global shell model and be applied for subsequent detailed analysis of substructures. In most cases, the global model should be nonlinear, such that the extracted boundary conditions for the local model are as accurate as possible, but it is important to realize the limitations of such approaches. At increasing loads, the nonlinear areas of the model may expand and provoke redistribution of stresses in the structure, and such effects may not be captured by one-way linearized submodeling techniques. Hence, submodeling requires an engineering judgement on how large the submodel needs to be in order to avoid strong nonlinearities on the boundary conditions of the submodel.

3. MULTI-SCALE ANALYSIS

In order to predict the structural strength of wind turbine blades, it is necessary to have accurate models for characterizing deformation and fracture which is an on-going challenging research area. The initiation and evolution of material damage in laminated composites is highly complex as it depends not only on the behavior of the individual constituents but also on the interfaces between them. Many different failure mechanisms are important to consider, and in general the strive for accurate predictions of structural strength naturally leads to the need for multi-scale analysis approaches.

When analyzing a large scale structure like a wind turbine blade, the current practice normally is to perform a sequence of uncoupled analyses corresponding to the different length scales modeled, see examples of analysis models at different length scales in Fig. 4. However, this practice might be time consuming, and furthermore, as structures are being optimized closer to the design limit, it becomes important to consider phenomena simultaneously at different scales. An example is the possible interaction between loss of stiffness due to delamination and its interaction with structural stability as illustrated by a wind turbine blade example in Section 6.

There is an obvious need for performing nonlinear analysis of industrial problems like wind turbine blades at a fine scale, and much on-going research in the computational mechanics community is devoted to non-linear multi-scale analysis approaches. However, it is out of the scope of this paper to cover this area in detail. Let us just note that most research is related to the use of Domain Decomposition Methods (DDM) because of the flexibility they offer to solve both linear and non-linear large systems of equations by dividing the structure into many subdomains that can be solved simultaneously using parallel computing. Examples of non-overlapping DDM include the Finite Element Tearing and Interconnecting (FETI) and Balanced Domain Decomposition (BDD) algorithms, that have proved to be very efficient

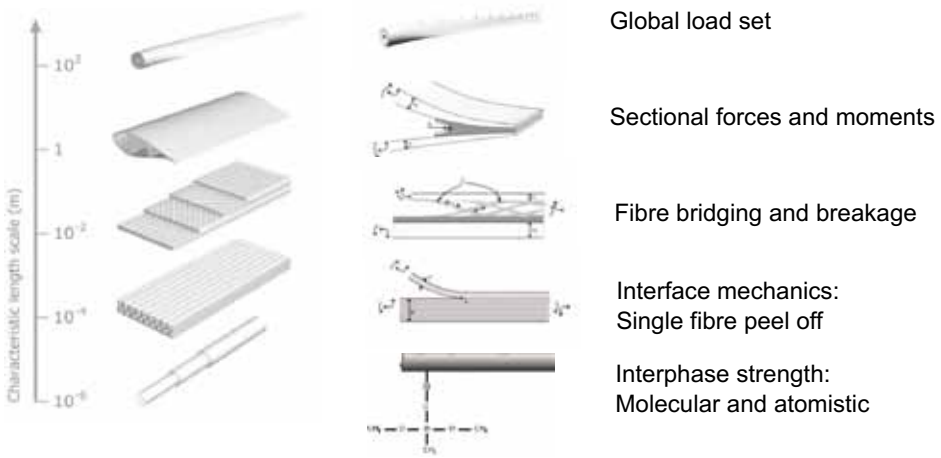

Fig. 4: Examples of analysis models at different length scales (courtesy of LM Wind Power)

for the parallelization of the global problem, and the local problems can then be solved with the preferred solver, see, e.g., Farhat and Roux (1991), Le Tallec, De Roeck and Vidrascu (1991), Farhat, Pierson and Lesoinne (2000), Gosselet and Rey (2006), Cresta (2010), and Guèye, El Arem, Feyel, Roux and Cailletaud (2011). In the following we will focus on the multi-scale analysis from the modeling point of view and not from the algorithmic point of view as in these papers.

An example of a major research project designed to make progress in solving large scale industrial nonlinear problems related to laminated composite structures is the EU FP7 research project MAAXIMUS (More Affordable Aircraft structure through eXtended, Integrated, & Mature nUmerical Sizing), which has both Airbus and Dassault Systèmes SIMULIA as partners, see FP7 MAAXIMUS (2011) and Ostergaard, Ibbotson, Le Roux and Prior (2011). It is expected that within the time frame of this project, the size of the models that can be handled in a nonlinear finite element approach can be increased by between 1 and 2 orders of magnitude. The Giga-DOF model (10^9 DOF) is the figure being used as a target for the developers in the project.

In Denmark many of the wind turbine blade manufacturers and universities collaborate in a research project entitled "Danish Centre for Composite Structures and Materials for Wind Turbines - DCCSM" funded by the Danish Council for Strategic Research. The project runs from 2010 to 2017, and a key vision is to develop a coherent, multi-scale based understanding of the mechanical behavior of composite materials and structures for wind turbine blades, such that lighter and stronger wind turbine blades can be developed.

A central hypothesis in this research project is that successful coupling between models at various length scales can be achieved by stress-strain laws (representing distributed deformation phenomena) and cohesive laws (stress-separation laws, representing localized fracture behavior). Specifically, models at a small length scale give stress-strain and cohesive laws as output for the next, coarser length scale model.

The need for both strain and stress prediction tools together with fracture mechanics based

tools originate from the nature of damage evolution in composite materials. A strain or stress prediction does not reveal anything about what happens after a local failure or fracture, and a failure point does not necessarily give rise to a global failure of the structure. In most cases, a single failure will not have any impact on the load carrying capacity, since the loads will be redistributed around the fracture. However, at some point the accumulation of fractures and damage will either directly cause global failure or lead to the limit point that will produce the fracture necessary to bring down the structure. Consequently, strain and stress models can be insufficient to determine the load carrying capacity of a structure, and it is essential to include progressive damage mechanisms.

One of the challenges is to set up continuum mechanics models that predict the non-linear behavior of composite materials and the damage evolution related to different failure mechanisms. For the first part, non-linear stress-strain laws can be measured for the matrix materials. Also, plasticity laws and visco-elastic material behavior can be considered. For the second part, simulation of fracture can be modeled using fracture mechanics based procedures. A more direct approach is to use cohesive laws to characterize different types of fracture in composites. Such cohesive laws can be used to smear different energy dissipating failure mechanisms into a single model that is described by the energy uptake of the traction-separation laws. The methodology is to use coupon-sized test specimens to characterize the traction-separation laws, e.g. under mixed mode loading as described by Sørensen, Jørgensen, Jacobsen and Østergaard (2006). However, validation of constitutive models that rely on a smeared approach is a key issue. One of the advantages of using cohesive laws to represent different types of failure mechanisms is that the number of coupon tests can be reduced compared to other more sophisticated models that distinguish between the different material non-linearities.

In order to predict, measure, and validate the constitutive damage models, it is important to understand the physics governing the mechanical behavior from all different length scales. On a nano-scale, the chemical properties of the materials can be related to the mechanical properties. On a micro- and macro-scale, the mechanical behavior such as yielding of matrix material and bridging of fibres across cracks can be established. On the basis of this, the strength of composite materials can be predicted on the macro-scale, sub-structural, and structural scale. By understanding the mechanisms on each of these length scales, it is possible to optimize/control the stress-strain and stress-separation response and thereby achieve better and more reliable structures.

4. A HIERARCHICAL ANALYSIS METHODOLOGY FOR LAYERED SHELL STRUCTURES

Layered composite materials may fail/fracture due to different types of failure mechanisms. Typically, the fracture is categorized as inter-laminar and/or intra-laminar failure. Inter-laminar failure is related to fracture in the interface between two laminae, also referred to as delamination. Delamination can be caused by transverse normal and shear loading (caused by load inserts, geometric and material discontinuities, impact, etc.), defects from the manufacturing process, or be initiated due to an intra-laminar failure. In the case of fiber reinforced polymers, intra-laminar failure is related to fiber and/or matrix failure inside the lamina. Under longitudinal tensile loading, intra-fiber failure may occur forming transverse cracks through the lamina. Compressive fiber failure is seen as the formation of kink bands in which the matrix material fails to support the fiber causing a stability-induced fiber failure. Under shear loading and tensile transverse loading, the matrix material may

fail causing inter-fiber fracture. For layered fiber reinforced polymer materials, the different fracture mechanisms may interact, e.g. a delamination may kink into a lamina causing an intra-fiber failure and then continue propagating as a delamination between other plies.

Due to the anisotropy (directionality) of the stiffness and strength of fiber reinforced laminates, an evaluation of failure in layered composite structures requires a detailed through-the-thickness modeling. Furthermore, physically-based failure models are needed to predict failure caused by different failure mechanisms. As an example, the Puck failure criterion can be used to predict inter-fiber failure based on the stress state at a fracture plane. As part of the World Wide Failure Exercise, different types of failure criteria have been proposed, some of which also include different types of non-linear material behavior. Advances within this area of research have resulted in methods where stress/strain based failure criteria are combined with fracture mechanics and material softening laws. One example is the development of interface finite elements, see e.g. Camanho, Dávila and Ambur (2001), Camanho and Dávila (2002), Camanho, Dávila and de Moura (2003), and Turon, Dávila, Camanho and Costa (2005), in which traction-separation laws (or cohesive laws) are used to model initiation and propagation of delamination under mixed mode loading. This furthermore allows one to model non-linear material behavior within the damage/fracture process zone and contact between cracked surfaces. In parallel, inter-fiber failure criteria such as the criterion by Puck, are used together with material softening laws to model damage evolution related to the fracture process zone of different types of failure mechanisms. Hereby, redistribution of stresses due to the formation of a fracture can be taken into account. This allows one to model in-situ effects on the strength of a laminate such as the thickness and stacking sequence of the laminae, see e.g. Pinho, Dávila, Camanho, Iannucci and Robinson (2005). Such failure models involve rather advanced constitutive models that are part of the generalized framework within damage mechanics, see e.g. work by Ladevéze and Lubineau (2003), and Allix and Blanchard (2006).

One of the disadvantages of the (complex) physical based failure models is that a larger number of material tests need to be done in order to characterize the material models needed for failure analysis. From a modeling point of view, the complex failure models require that the layered composite is modeled in detail such that stresses and material degradation can be modeled for each layer. In the case of prediction of inter-lamina failure, fully 3D constitutive models are needed to calculate the transverse normal shear stresses accurately. In a finite element analysis, the composite structures need to be modeled by solid (shell) finite elements rather than standard shell elements. Because of this, attention should be drawn on ways of doing efficient modeling of layered shell structures using solid elements. For this purpose, a hierarchical modeling approach can be used, see also Hansen, Lund, Pinho and Branner (2009). The methodology is described in the following, and it has been implemented in the in-house finite element system MUST (the MUltidisciplinary Synthesis Tool), developed at Aalborg University.

The basic idea is to start out with a finite element model with only one element through-the-thickness and use an automated procedure for through-the-thickness mesh refinement of a selected region of the model. The refinement region is identified based on a user defined criterion for failure, stress, strain, or element selection set. Thus, the global model is used for predicting zones of interest that need more detailed modeling. The present formulation utilizes a user specified spherical filter with a statically user specified filter radius, see Figure 5.

On element boundaries between refined and non-refined zones, compatibility of displacements is enforced by setting up linear constraint equations using the Lagrange multipliers

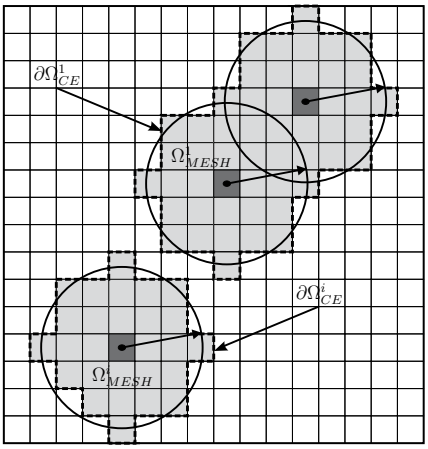

Fig. 5: Plane illustration of how elements are filtered for re-meshing. Black elements represent hot spot elements either based on a failure criterion or a user-defined set. Black and grey elements illustrate the identified re-meshing zones. The filtering radius is illustrated by a black arrow and circle (Johansen and Lund 2009).

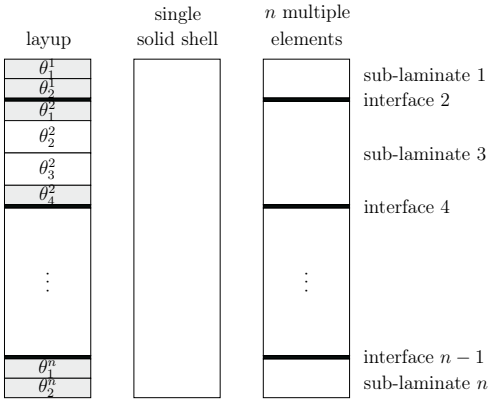

Fig. 6: A through-the-thickness adaptive re-meshing routine has been implemented to convert single solid shell elements to multiple solid shell elements with sub-laminates and interfaces with mixed-mode cohesive elements for interlaminar crack propagation. It re-calculates a new layup sequence data for each solid shell sub-laminate and adds cohesive interface elements based on the original layup sequence and writes a new nodal and element topology (Overgaard and Lund 2010).

method, see Johansen and Lund (2009) and Johansen et al. (2009). These linear constraints enforce restrictions that may result in spurious stresses in the elements at boundaries between coarse and fine meshed regions. Thus, these interfaces between refined and non-refined zones should be positioned sufficiently far away from the zone of interest.

An equivalent single layer (ESL) solid shell element with eight-nodes is used to calculate the element stiffness, strains, and stresses based on the formulation by Klinkel et al. (1999),

see implementation details in Johansen and Lund (2009) and Johansen et al. (2009). Incompatible internal degrees of freedom are added to enhance the in-plane membrane and out-of-plane bending behavior while locking effects are diminished by enhanced assumed strain and assumed natural strain methods. This makes the ESL solid shell element suitable for calculation of all six stress components with a rather good approximation on the transverse normal and shear stresses.

A through-the-thickness adaptive re-meshing procedure is used to convert the single layer of solid shell elements to multiple layers of solid shell elements. The re-meshing procedure is based on an automatic partition of the original laminate layup into a sequences of sub-laminates. For that reason, all elements filtered for re-meshing in the ith domain Ω^i_{MESH} must have the same partitioning of new sub-laminates, i.e. the same total number of sub-laminates n as schematically illustrated in Figure 6. If specified by the user, cohesive interface elements can be embedded between the solid shell element layers such that delamination initiation and propagation can be analyzed in the re-meshed model.

A re-meshed model may be further refined by repeating the procedure as will be illustrated in the following example. However, in the present implementation, element boundaries of the refinement regions cannot intersect due to the formulation of the linear constraint equations used. The hierarchical modeling approach can be used on full scale problems or on submodels of the full scale problem.

5. EXAMPLE OF HIERARCHICAL ANALYSIS OF LAYERED SHELL STRUCTURES

In order to illustrate the methodology of the hierarchical modeling approach to composite shell structures, a rather simple curved beam model is presented. The curved beam is loaded in bending and only a half-symmetric (could be further reduced to a double-symmetric) model is analyzed. The model has been generated from a solid model meshed with only one layer of solid elements with the stacking direction normal to the laminate surface, see model (1) in Figure 7. This model is referred to as the base line model.

The curved beam is loaded in bending with a tensile normal strain in the inner (bottom) layer and a compressive normal strain in the outer (top) layer of the composite laminate. Such a loading generates tensile transverse normal strains in the curved region that may develop an inter-laminar type of failure followed by delamination propagation. The hierarchical modeling approach is in the following used to carry out a progressive failure analysis with delamination propagation initiated from an embedded delamination, i.e. from a manufacturing defect. The hierarchical approach is used consecutively to generate two refined models with increased element layers through-the-thickness within the critical region. The two refined models (2) and (3) are shown in Figure 7.

In the following, the steps involved in the hierarchical model generation are described in detail with supporting illustrations for each step in Figure 8.

1) The base line model of the curved composite beam consists of solid-shell elements with only one element through-the-thickness. The solid elements are assigned to laminate sections consisting of a number of plies of different material, thickness, and orientation. In this case, the composite beam consists of 8 layers of an orthotropic material with orientation $[0, 0, 45, -45]_{Sym}$ and thickness $[0.15t, 0.15t, 0.1t, 0.1t]_{Sym}$ with a total thickness of $t = 5mm$. Regions of special interest can be assigned different laminate sections such that different hi-

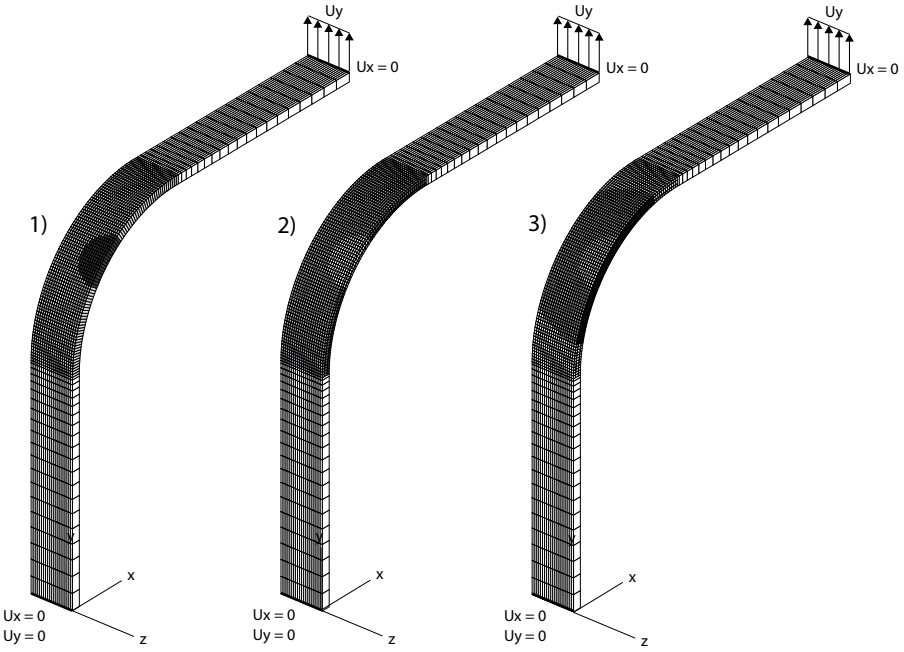

Fig. 7: Adaptive through-the-thickness mesh refinement used to analyze the influence of a circular delamination between two plies in a curved composite beam.

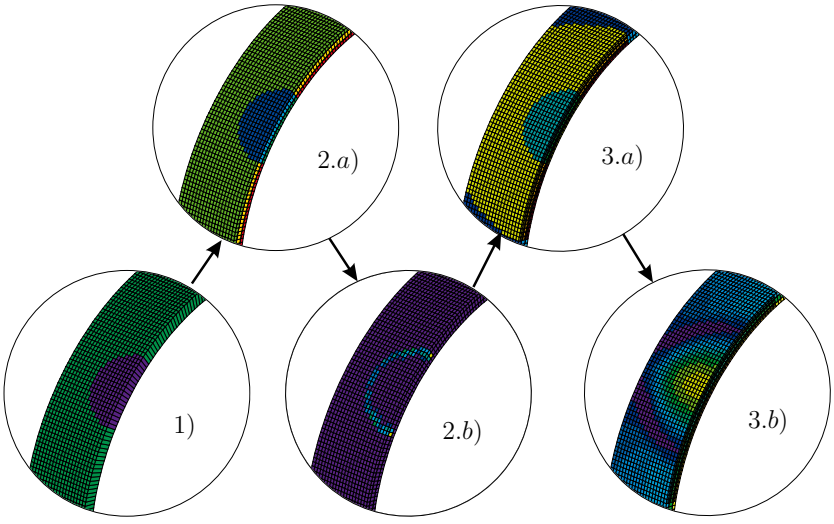

Fig. 8: Illustration of each step in the hierarchical modeling approach used in the example.

erarchical refinement procedures can be applied to different sections of the model. Laminate sections can be specified with a number of zero-thickness interfacial layers such that cohesive elements can be embedded between plies. Such interfacial layers are assigned to material properties characterized by cohesive laws. This enables one to embed delaminations and other material flaws or manufacturing imperfections into the model without much modeling effort. In this particular case, a selection of elements within a circular region is used to embed a delamination between plies of that region. Between plies 2-3 and 6-7, cohesive interfacial layers are defined in the laminate section of the curved part of the composite beam. The delamination is specified by assigning a cohesive layer to a material that is fully damaged corresponding to a zero-thickness layer of contact elements without friction.

2.a) In this example, the first step in the hierarchical refinement procedure is to embed cohesive elements between plies of the laminate sections of the curved part of the composite beam. This is specified by the user by a selection of laminate sections. The hereby obtained model consists of 3 layers of solid elements and two layers of cohesive (zero thickness) interfacial elements. Each layer of solid elements is automatically assigned to a new set of laminate sections, in this case three sections consisting of ply numbers 1-2, 3-6, and 7-8, respectively. On element boundaries with prescribed displacements, the added nodes (on the boundary) are automatically prescribed by linear interpolation of the prescribed displacements of the top and bottom nodes. In this case, the added nodes on the symmetry plane are automatically prescribed by the symmetry boundary condition as well. Furthermore, constraint equations are automatically set up for non-conforming element boundaries where the number of elements through-the-thickness do not correlate.

2.b) After the embedment of cohesive interfacial elements, the updated model is ready to be analyzed. In this example, a linear stress analysis is carried out such that failure criteria can be evaluated. In the case of evaluation of both linear and non-linear failure criteria, one should be careful choosing an appropriate load level. Damage very often occurs under mixed mode loading. For that reason, a quadratic nominal stress (QNS) criterion has been used to predict initiation of delamination, see Ye (1988) and Brewer and Lagace (1988). As can be seen in Figure 2.b, the QNS failure index highlights the crack front of the embedded delamination.

3.a) Based on a user input, the result obtained in (2.b) is used to generate a second refinement model with a layer of solid elements for each ply in the composite. However, this is only done for a selection of elements within a user specified distance of the most critical elements in the model. This selection can be further controlled by the user by specifying that e.g. elements with 90% of the maximum failure index should be included.

3.b) The fully-refined model (in the region next to the embedded delamination) is finally used for a progressive damage analysis in which the initiation of delamination growth is simulated and the load response under delamination propagation can be determined under quasi-static equilibrium conditions. The delamination growth is simulated using a mixed mode cohesive law that is based on a fracture criterion proposed by Benzeggagh and Kenane (1996). Furthermore, intra-laminar failure is in this case evaluated based on a Puck like fiber/matrix failure criterion together with a tensile and compressive fiber failure criterion.

The example illustrates how the structural response of a composite sub-component can be predicted using constitutive damage models for the simulation of inter-laminar fracture. Intra-laminar failure is predicted in the locally mesh refined region with automatic through-the-thickness re-meshing of layered solid-shell elements and cohesive elements. Hence, a rather detailed analysis can be achieved in a modeling efficient way using the hierarchical

analysis methodology described in Section 4.

6. PROGRESSIVE FAILURE ANALYSIS OF A WIND TURBINE BLADE

An example of using submodeling techniques and hierarchical refinement for failure analysis of a wind turbine blade has been presented in Overgaard (2008), Overgaard and Lund (2010), and Overgaard, Lund and Camanho (2010). As part of a Danish research project, a full-scale static flap-wise bending test to collapse of a 25 meters wind turbine blade was performed, see Thomsen, Jørgensen, Borum, McGugan, Debel, Sørensen and Jensen (2003) and Sørensen, Jørgensen, Debel, Jensen, Jensen, Jacobsen and Halling (2004). The idea was to map the apparent sequence of events both during loading and the aftermath of the collapse, thereby gaining some understanding and insight to the chain of events leading to the collapse of this layered composite blade structure.

The overall ultimate strength of such laminated composite blade structures is typically governed by instability phenomena in the form of material and geometric nonlinearities, like delamination and buckling. Interaction between both the material and the geometric nonlinearities may occur, and for the blade considered this caused a progressive damage of the structure resulting in a sudden collapse. This was derived from global finite element models of the blade, combined with an advanced submodel using geometrical nonlinear analysis and cohesive zone modeling. The results obtained using the submodel are described in the following.

The pre-processing of the finite element model was done with an in-house blade builder program based on Patran Command Language (PCL) and spreadsheets with interpolated lay-up data for a predefined element size, such that blade models consisting of either standard shell elements or solid shell elements with one element in the thickness direction could be made. The solid shell model used for this study could then be expanded into a user-defined submodel using an adaptive through-the-thickness routine that generated solid shell elements for each laminate layer or subsection of laminate layers combined with cohesive elements at the interfaces as described in the previous section. It was assumed that initiation of delamination could be predicted using the QNS criterion, and the Benzeggagh-Kenane criterion was used to predict mixed mode delamination growth.

The cross section of the wind turbine blade considered is illustrated in Fig. 9 (left). In the finite element model the aerodynamic shells were disregarded in the model, however, the shells were included at the flanges of the main spar in the defined lay-up. This simplification might have lead to some missing stiffnesses of the main spar, but based on numerical experiments this simplification was seen to be of minor importance in the flap-wise bending situation.

The flange consisted of a monolithic lay-up and the web was made up of a sandwich structure. The corner had a multiple ply-insert and -drop configuration and a transition from a monolithic laminated composite material to the sandwich structure. Additionally, the material groups changed along the length of the blade in order to have a constant longitudinal strain distribution and thereby utilizing the material optimally w.r.t. aerodynamic loads. This resulted in many thousand lay-up sequences. In order to have a finite element model of a reasonable structural size in the geometrically non-linear fracture mechanical analysis and still having a relative fine element mesh, an assumed double symmetric corner of the main load-carrying spar was simulated, and a section that contained the buckling

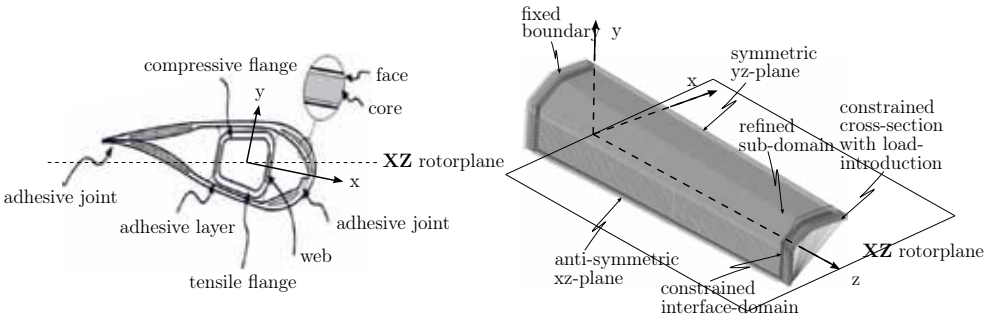

Fig. 9: The model consisted of 196.894 nodes, 156.516 elements, 2.253 real constant sets (lay-up sequences) and 5 linear elastic base materials for core material and glass fibre reinforced epoxy. The models used fracture energies taken from Benzeggagh and Kenane (1996), see details in Overgaard (2008) and Overgaard and Lund (2010).

and collapse region of the complete main spar was used, see Fig. 9 (right). The model was restricted by a symmetrical boundary condition in the yz-plane at the compression flange and an antisymmetrical boundary condition in the xz-plane at the webs. The model had a rigid diaphragm for all x and y nodal displacements at the load-introduction, i.e. the u_x and u_y displacements at the constrained cross-section were set to be equal. Additionally the nodal displacements u_z were equal for nodal sets through-the-thickness, i.e. not allowing any rotation of the constrained cross-section. This constrained cross section with load introduction resembled the experimental test setup.

Delaminations were found to be at the interface of angle plies and to propagate into very large portions of the structure, see Overgaard and Lund (2010). Crushed laminae were found to be very localized compared to the delaminations, and thus no progressive intralaminar damage models were used. The main fracture energy uptake in the structure was at four cohesive zones through the length of the model. The finite element model did not allow for any cracks to kink into the core material of the sandwich structure due to the use of standard cohesive elements. All delamination paths were located between the angle plies and core material similarly to what one would see in a static flap-wise test of this type of structure. The solution was done in a geometrically non-linear setting as previously described, so interaction between geometric and material non-linearities could be accounted for. The blade was fixed at the end toward the root and loaded with transverse and normal nodal loads corresponding to the applied section moment and shear force at the tip end of the complete blade as in the full-scale experiment. This corresponds to a cantilever beam subjected to a bending moment and a shear force in the flap-wise direction. At the ends of the spar a row of elements acted as load introduction regions, where no damage could be initiated and propagate.

The load response as a function of the global compressive displacement u_z at the flange center of the load introduction area is shown on Fig. 10(a). The model showed a progressive collapse of the structure as seen in full scale tests of wind turbine blades, since no stable equilibrium was reached in the analysis, see Fig. 10(a). The limit load was dependent on the constrained cross section, which had an influence on the critical buckling load. Furthermore, the missing shell would improve the elastic response and elevate the limit load, since it would contribute to the buckling resistance. The limit load was 6% below the first failure event measured in the full scale experiment.

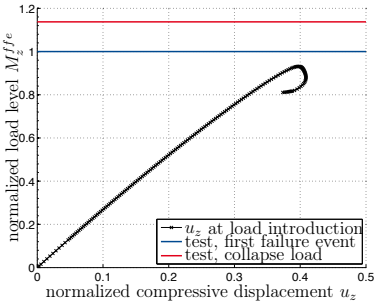

(a) Load level as a function of the global compressive displacement at the flange, which is compared with experimental values.

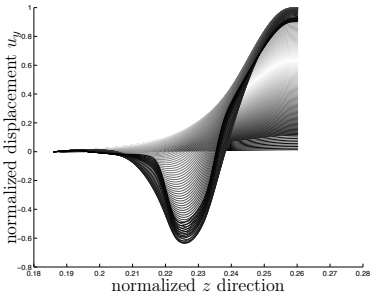

(b) The y displacement along the flange center, which shows the gradual development of the buckling pattern.

Fig. 10: The finite element model response is shown in subfigures (a) and (b) (Overgaard et al. 2010).

Fig. 10(b) displays the development of the buckling pattern at the flange center. The gray scale color of the curves relates to the equilibrium points on the equilibrium path on Fig. 10(a). At low load levels the curves are black and gradually converted into white colors (mid-range load levels). Then the curve colors are gradually converted back to black at high load levels. Initially the displacement response is linear, eventually, at the mid range load levels the displacement field has a significant non-linear displacement response, and it becomes highly non-linear at the limit load of the structure. The results showed that the delamination is triggered by geometric instability and that the material and geometric nonlinearities interact.

Fig. 11 shows the correlation between the results of an acoustic emission system used in the full scale test to triangulate high energy bursts and the finite element model. The acoustic emission system had only a detectable range corresponding to the damaged area. The two damage areas shown by the finite element model and the full scale test were just before the blade collapsed, i.e. the damage state prior to the limit point. The red elements were fully damaged and blue elements were undamaged. Only elements with a nodal damage larger than zero were selected in the element entity plot in order to be able to display the delaminated zones inside the structure.

The damage in the model was located precisely at the same normalized blade length as in the full scale test. The delamination front from the model is displayed by a dotted line on the acoustic emission picture. The results of the acoustic emission system compared with the model indisputably suggested that the model captured the correct interlaminar fracture processes. The delamination at $z = 0.196$ was through all four cohesive zones, where it initiated at the inner most cohesive zone and gradually developed in the four zones through-the-thickness, i.e. it was a multiple layered delamination zone. This correlation dictated that the structural collapse of the generic wind turbine blade was governed by interdisciplinary local buckling and delamination, for further information see Overgaard and Lund (2010).

Furthermore, in the finite element model some large delaminations were found at the load introduction, which were caused by the constrained sub-domain interfaces. The constrained

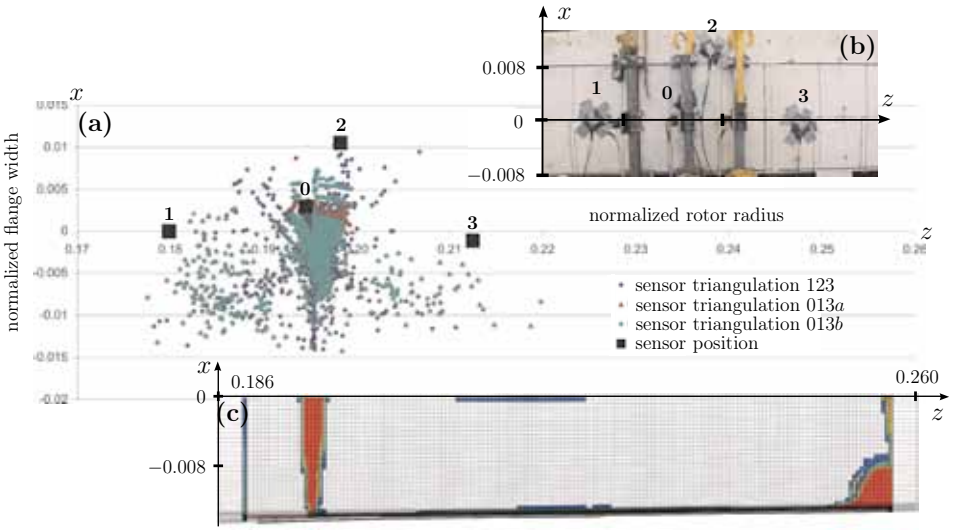

Fig. 11: (a) Results of three sensor triangulation setups, which were used in the full-scale test to locate the damage prior to the complete structural collapse of the blade. (b) shows the actual blade setup with courtesy of Risoe DTU, National laboratory for Sustainable Energy (Thomsen et al. 2003) and (c) shows the FE model results.

interfaces resulted in oscillating stresses, which then initiated delamination. However, this was located separately and far from the area of interest. Thus, the example demonstrates how submodeling techniques and hierarchical refinement can be used for efficient failure analysis of a wind turbine blade.

7. CONCLUDING REMARKS

The paper has described some of the limitations and challenges when predicting the performance of large scale wind turbine blades from a strength point of view. Since different types of damage and subsequent failure can develop at different length scales in wind turbine blades, it is necessary to develop a coherent, multi-scale based understanding of the mechanical behavior of composite materials and structures for wind turbine blades. Thus, the numerical simulations should support such a multi-scale analysis approach in order to obtain reliable and accurate predictions of structural strength, and it has been suggested to use a hierarchical analysis approach, such that the global model is either hierarchically refined in zones of interest or hierarchically refined submodels are used. In both cases the hierarchical through-the-thickness re-meshing procedure allows for an automatic conversion of single solid shell elements to multiple solid shell elements with an automatic re-calculation of the layup sequences for each solid shell sub-laminate and interfaces with mixed-mode cohesive elements for interlaminar crack onset and propagation capabilities. The finite element model may have layered cohesive elements in regions with laminae inserts and ply drops such that interlaminar cracks can propagate across these material transitions. These refined models can also embed other types of damage models or criteria for failure predictions, for example of intra-laminar failure.

The hierarchical analysis procedure combined with a submodeling technique has been illustrated for a progressive collapse analysis of a generic wind turbine blade. It has been found that the interlaminar progressive failure finite element analysis of the generic blade corresponded excellently with the available findings and observations in a full-scale experiment. The ultimate strength of the generic wind turbine blade was documented to be governed by a coupled delamination and buckling phenomenon where the interaction between both instability phenomena caused a progressive collapse of the structure. The material and geometric-induced instability interacted in such a way that local delamination was initiated at the boundary of the adjoining structural elements and in the center of the compressive flange due to local buckling. This interaction resulted in an enforcing chain of events, which produced a sudden structural collapse and subsequently compressive fiber failure in the delaminated flange material. Consequently, it has been deduced that in order to determine the ultimate strength of the generic wind turbine blade, structural instability phenomena in the form of interlaminar material and geometric induced instability must be accounted for in the analysis.

In order to support such a hierarchical analysis approach, it is necessary to have experimentally validated models for coupling the various length scales by stress-strain laws (representing distributed deformation phenomena) and fracture mechanics based models such as cohesive laws (stress-separation laws, representing localized fracture behavior). The need for both strain and stress prediction tools together with fracture mechanics based tools originate from the nature of damage evolution in composite materials. Many different failure mechanisms are important to consider, but there are many challenges related to accurate predictions of the initiation and evolution of material damage in laminated composites. As stated by Ostergaard et al. (2011) in relation to virtual testing of Airbus aircraft structures made of composites: "The maturity of reliable composite failure modes for all modeling scales and, in particular, for detailed failure predictions, is still to be demonstrated."

Thus, in order to create reliable predictions of the structural performance of large scale wind turbine blades, it is of the greatest importance to have a close collaboration between structural analysis specialists and material science specialists, such that experimentally validated models for coupling the various length scales can be combined with state-of-the-art numerical modeling techniques. The hierarchical modeling approach demonstrated in this paper supports in a consistent way such a multi-scale analysis approach from an engineering point of view.

ACKNOWLEDGEMENT

The work has been partly supported by the Danish Energy Authority through the 2005 Energy Research Programme (EFP 2005). The EFP-project is entitled Improved design of large wind turbine blades of fibre composites - phase 3 with journal no. 33031-0078. The support is gratefully acknowledged. Also, the authors would like to acknowledge Ph.D. Leon S. Johansen, now at Vestas Wind Systems, and Ph.D. Lars C.T. Overgaard, now at Siemens Wind Power, for their contributions to the hierarchical methodology, and Lars C.T. Overgaard for the wind turbine blade example presented in this paper.

REFERENCES

Allix, O., and Blanchard, L. (2006). Mesomodeling of delamination: towards industrial applications. Compos. Sci. Technol. 66, 731-744.

Benzeggagh, M.L., and Kenane, M. (1996). Measurement of mixed-mode delamination fracture toughness of unidirectional glass/epoxy composites with mixed-mode bending apparatus. Compos. Sci. Technol. 56, 439-449.

Brewer, J.C., and Lagace, P.A. (1988). Quadratic stress criterion for initiation of delamination. J. Compos. Mater. 22, 1141-1155.

Camanho, P. P., and Dávila, C.G. (2002). Mixed-mode decohesion finite elements for the simulation of delamination in composite materials. Technical report, NASA/Techical Memorandum, TM-2002-211737, NASA Langley Research Center, Hampton, VA 23681.

Camanho, P.P., Dávila, C.G., and Ambur, D.R. (2001). Numerical simulation of delamination growth in composite materials. Technical report, NASA/Technical Publication, TP-2001-211041, NASA Langley Research Center, Hampton, VA 23681.

Camanho, P.P. , Dávila, C.G., and de Moura, M.F. (2003). Numerical simulation of mixed-mode progressive delamination in composite materials. J. Compos. Mater. 37, 1415-1438.

Cresta, P. (2010). Implementation of a multi-level nonlinear substructuring scheme for the analysis of large structures with local nonlinearities. Abstract book, IV European Conference on Computational Mechanics Palais des Congrès, Paris, France, May 16-21, 2010.

Farhat, C., and Roux, F.-X. (1991). A method of finite element tearing and interconnecting and its parallel solution algorithm. Int. J. Numer. Methods Engrg. 32, 1205-1227.

Farhat, C., Pierson, K., and Lesoinne, M. (2000). The second generation FETI methods and their application to the parallel solution of large-scale linear and geometrically non-linear structural analysis problems. Comput. Method. Appl. M. 184, 333-374.

FP7 MAAXIMUS - More Affordable Aircraft through eXtended, Integrated and Mature nUmerical Sizing (2011). http://www.maaximus.eu/

Gosselet, P., and Rey, C. (2006). Non-overlapping domain decomposition methods in structural mechanics. Arch. Comput. Method. E. 13, 515-572.

Guèye, I., El Arem, S., Feyel, F., Roux, F.-X., and Cailletaud, G. (2011). A new parallel sparse direct solver: Presentation and numerical experiments in large-scale structural mechanics parallel computing. Int. J. Numer. Methods Engrg., available online, DOI: 10.1002/nme.3179

Hansen, A.L., E. Lund, S.T. Pinho, and K. Branner (2009). A hierarchical FE approach for simulation of geometrical and material induced instability of composite structures. Proc. Composites 2009, 2nd ECCOMAS Thematic Conference on the Mechanical Response of Composites, April 1-3, 2009, Imperial College, London, 6 pp.

Johansen, L.S. and Lund, E. (2009). Optimization of laminated composite structures using delamination criteria and hierarchical models. Struct. Multidiscip. O. 38, 357-375.

Johansen, L.S., Lund, E., and Kleist, J. (2009). Failure optimization of geometrically linear/nonlinear laminated composite structures using a two-step hierarchical model adaptivity. Comput. Method. Appl. M. 198, 2421-2438.

Kenane, M., and Benzeggagh M. L. (1997). Mixed-mode delamination fracture toughness of unidirectional glass/epoxy composites under fatigue loading. Compos. Sci. Technol. 57, 597-605.

Klinkel, S., Gruttmann, F., and Wagner, W. (1999). A continuum based three-dimensional shell element for laminated structures. Comput. Struct. 71, 43-62.

Kühlmeyer, L. (2007). Buckling of wind turbine rotor blades. Ph.D. thesis, Department of Mechanical Engineering, Aalborg University, Denmark.

Ladevéze, P., and Lubineau, G. (2003). On a damage mesomodel for laminates: microme-

chanics basis and improvement. Mech. Mater. 35, 763-775.
Laird, D.L., Montoya, F.C., and Malcolm, D.J. (2005). Finite element modeling of wind turbine blades. Proc. AIAA/ASME Wind Energy Symposium, Reno, Nevada, USA, AIAA-2005-0195, 9-17.
Le Tallec, P., De Roeck, Y.-H., and Vidrascu, M. (1991). Domain-decomposition methods for large linearly elliptic three dimensional problems. J. Comp. Appl. Math. 34, 93-117.
Ostergaard, M.G., Ibbotson, A.R., Le Roux, O., and Prior, A.M. (2011). Virtual testing of aircraft structures. CEAS Aeronautical J., accepted.
Overgaard, L.C.T. (2008). Structural instability phenomena in wind turbine blades. Ph.D. thesis, Department of Mechanical Engineering, Aalborg University, Denmark.
Overgaard, L.C.T., Lund, E., and Thomsen, O.T. (2010). Structural collapse of a wind turbine blade. Part A: Static test and equivalent single layered models. Compos. Part A-Appl. S. 41, 257-270.
Overgaard, L.C.T., and Lund, E. (2010). Structural collapse of a wind turbine blade. Part B: Progressive interlaminar failure models. Compos. Part A-Appl. S. 41, 271-283.
Overgaard, L.C.T., Lund, E., and Camanho, P.P. (2010). A methodology for the structural analysis of composite wind turbine blades under geometric and material induced instabilities. Comp. Struct. 88, 1092-1109.
Pinho, S.T., Dávila, C.G., Camanho, P.P., Iannucci, L., and Robinson, P. (2005). Failure models and criteria for FRP under in-plane or three-dimensional stress states including shear non-linearity. Technical report, NASA/Techical Memorandum, NASA/TM-2005-213530, NASA Langley Research Center, Hampton, VA 23681.
Risø/DNV (2002). Guidelines for design of wind turbines, 2nd edn, Jydsk Centraltrykkeri, Denmark.
Sørensen, B.F., Jørgensen, E., Debel, C.P., Jensen, F.M., Jensen, H.M., Jacobsen, T.K. and Halling, K.M. (2004). Improved Design of Large Wind Turbine Blade of Fibre Composites based on Studies of Scale Effects (Phase 1) - Summary Report. Risø-R-1390(EN), Risø National Laboratory, Roskilde, Denmark.
Sørensen, B.F., Jørgensen, K., Jacobsen, T.K., and Østergaard, R.C. (2006). DCB-specimen loaded with uneven bending moments. Int. J. Fracture 141, 163-176.
Thomsen, O.T. (2009). Sandwich materials for wind turbine blades - present and future. J. Sandw. Struct. Mater. 11, 7-26.
Thomsen, C.L., Jørgensen, E.R., Borum, K.K., McGugan, M., Debel, C.P., Sørensen, B., and Jensen, F.M. (2003). V52 statisk styrke. Internal test report: Risø-i-1908(da), Risø National Laboratory, Danmark, 65 pp.
Turon, A., Dávila, C.G., Camanho, P.P., and Costa, J. (2005). An engineering solution for using coarse meshes in the simulation of delamination with cohesive zone models. Technical report, NASA/Techical Memorandum, TM-2005-213547.
Wacker, G. (2003). Requirements for the certification of rotor blades. Germanisher Lloyd WindEnergie GmbH, Hamburg, Germany.
Ye, L. (1988). Role of matrix resin in delamination onset and growth in composite laminates. Compos. Sci. Technol. 33, 257-277.

Proceedings of the 32nd
Risø International Symposium on Materials Science:
Composite materials for structural performance:
Towards higher limits
Editors: S. Fæster, D. Juul Jensen,
B. Ralph, B.F. Sørensen
Risø National Laboratory for Sustainable Energy,
Technical University of Denmark, 2011

CELLULOSE FIBERS AND THEIR POTENTIAL FOR REINFORCEMENT IN COMPOSITES

B. Madsen* and E.K. Gamstedt**

*Materials Research Division, Risø National Laboratory for Sustainable Energy, Technical University of Denmark, DK-4000 Roskilde, Denmark
**Department of Engineering Sciences, Uppsala University, SE-75121 Uppsala, Sweden

ABSTRACT

An introduction is given to cellulose fibers and their potential for reinforcement in composite materials. This includes an overview of the chemical composition and microstructure of the fibers, the fiber preforms, the mechanical properties of the composites, and their applications. Moreover, some of the special issues of cellulose fiber composites are presented: modeling of fiber microstructure and mechanical properties, composite porosity, micromechanical modeling and hygromechanical properties, in addition to considerations on the perspectives of cellulose nanofiber composites. The general work on cellulose fiber composites is typically strictly divided in two separated research fields depending on the fiber origin, i.e. fibers from wood and from annual plants representing the two different industries of forest and agriculture, respectively. The present paper evaluates in parallel wood fibers and plant fibers to highlight their similarities and differences regarding their use as reinforcement in composites, and to enable mutual transfer of knowledge and technology between the two independent research fields. The performance of cellulose fiber composites is also compared to the synthetic glass and carbon fibers conventionally used for composites, and advantages and drawbacks of the different fibers are discussed.

1. INTRODUCTION

Cellulose fiber composites are promising new types of composite materials. They have a green profile, and they offer good technical performance. During the last decade, there has been a considerable increase in research on composites made from natural cellulose fibers, predominantly originating from wood or plants (Eichhorn et al. 2001; Pandey et al. 2010). For several load-carrying applications, where glass or carbon fiber composites are conventionally used, cellulose fiber composites can be a worthwhile alternative. This is particularly the case for

applications where the green advantages (renewability, biodegradability) play an important role, and top-end mechanical properties are not the primary motivation. A vast amount of scientific literature on cellulose fibers for composite applications has been compiled during the last decade, although the publications tend to be divided into two separate fields depending on the origin of the fibers, i.e. from wood or plants (annual crops). The reason for this division is perhaps that the raw material producers are looking for new markets for their fibers (technology pull), and that the end-users (market pull) have yet to exploit the potential of cellulose fibers, independent of the origin of the fibers. The raw material producers in this case, i.e. forestry for wood fibers and agriculture for plant fibers, have developed their specific technologies along the value chain to produce fibers depending on the traditional usage of the fibers. For wood fibers, pulp mills have been built to produce raw material for making paper and board. For plant fibers, textile technologies are honed to produce yarns and fabrics. In view of the maturing research field of cellulose fibers shifting towards achieving the technical performance demands of the end-users, and the rather independent existence of research communities of wood and plant fibers, respectively, this paper has been written to shed some further light on the similarities and difference of these two types of cellulose fibers (wood and plant origin), with regard to industrial usage to produce cellulose fiber composites for structural applications. The performance of cellulose fibers will also be compared to the main current competitors, i.e. composites made from glass or carbon fibers. Advantages and drawbacks of the different fibers are then discussed, in light of future potentials in engineering applications. By bringing the disciplines of wood and plant fiber science closer together, one could hope for a mutual transfer of knowledge, as the two research fields have evolved rather independently and have thus reached different levels of understanding with regard to various aspects, such as fibrillation, characterization techniques, fiber treatment, fiber preform processing, and composite manufacturing.

Work is on-going to further develop cellulose fiber composites, and from a solid mechanics point of view, the results from this work could be reduced to a number of fiber properties that are of key importance for the mechanical performance of composites. One of the primary properties concerns the geometry of the fibers, i.e. the fiber aspect ratio, which is its length to diameter ratio. The longer the fibers, aligned in the primary load direction, the more efficient will be the use of the load carrying constituent. This is due to the ineffective lengths close to the fiber ends, which do not carry full load (see e.g. Cox, 1952). In the present paper, we focus on the cellulose fibers based on separate cells, which have a high aspect ratio and therefore also high reinforcing potential. The cells typically have similarly sized cross-sections with diameters in the range 15 – 30 μm. It is therefore more convenient to characterize the geometry by the length of the cell or fiber. Thus, in the perspective of composite reinforcement, cellulose fibers can be grouped into two groups:

- Short fibers (1 – 5 mm), originating typically from wood species (e.g. spruce, pine, birch, eucalyptus), typically used for making composites with in-plane isotropic properties, i.e. composites with non-specific (random) fiber orientation. In the present paper, these fibers will be denoted *wood fibers*.
- Long fibers (5 – 50 mm), originating typically from plant species (e.g. flax, hemp, jute), typically used for making composites with anisotropic properties, i.e. composites with a specific fiber orientation. In the present paper, these fibers will be denoted *plant fibers*.

Here follows first an introduction to cellulose fibers and their composites. This will include (i) an overview of the chemical composition and microstructure of the fibers, (ii) the fiber preforms available for manufacturing of composites, (iii) the typically obtainable mechanical properties of the composites, and (iv) the current industrial applications of the composites, in addition to some examples of recently made demonstrators. Then, presentations will be given of some of

the special issues of cellulose fiber composites: (i) modeling of microstructure and mechanical properties of the fibers, (ii) porosity in composites, (iii) micromechanical modeling of the mechanical properties of the composites, (iv) hygromechanical properties of the composites, and (v) the future perspectives and challenges of cellulose nanofiber composites. Finally, the differences and resulting advantages of the two types of cellulose fibers, viz. wood and plant fibers, will be summarized, as well as the differences and resulting advantages of cellulose fibers vs. synthetic fibers.

2. CHEMICAL COMPOSITION AND MICROSTRUCTURE OF FIBERS

Cellulose fibers have a highly complex chemistry and microstructure. This is not surprising, since the fibers originate from living organisms with a long evolutionary history, and as such, they have been optimized to meet a number of specific mechanical requirements, in addition to other functional requirements. In contrast, the synthetic fibers that traditionally are used for reinforcement in composites, such as glass and carbon fibers, are monolithic and with a much more simple microstructure (Bunsell and Renard 2005). Glass fibers are primarily composed of silicon oxide molecules organized in an amorphous configuration. Carbon fibers are composed of carbon atoms in graphite layers that are organized in a stack wise configuration. Thus, the study of cellulose fibers as alternative to traditional synthetic fibers is not just an assessment of their reinforcement potential in composite materials, but it will as well provide insight into the form and function of sophisticated types of fibers.

Cellulose fibers originate from green plants such as wood and annual plants. The cells of these living organisms are surrounded by a rigid *cell wall* (which is the main feature distinguishing plants from animals). In some types of cells, the cell walls are enlarged and this makes these cells responsible for the good structural performance of plants. The physical dimensions of these so-called fibers vary between different plants but their overall shape is most often elongated with lengths in the range 1-50 mm, and diameters in the range 10-30 μm (Fig. 1a), which give them a high aspect ratio (length/diameter ratio). In living plants, when the cellulose fibers are fully developed, their intracellular organelles start to degenerate resulting in fibers having an empty central cavity, the so-called lumen. The actual size of the lumen varies considerably both within and between fiber types. In wood fibers, the luminal area is in the range 20 - 70 % of the fiber cross-sectional area (Siau 1995). In contrast, plant fibers, such as hemp and flax, have a relatively smaller luminal area in the range 0 - 5 % (Perry 1985; Aslan et al. 2011).

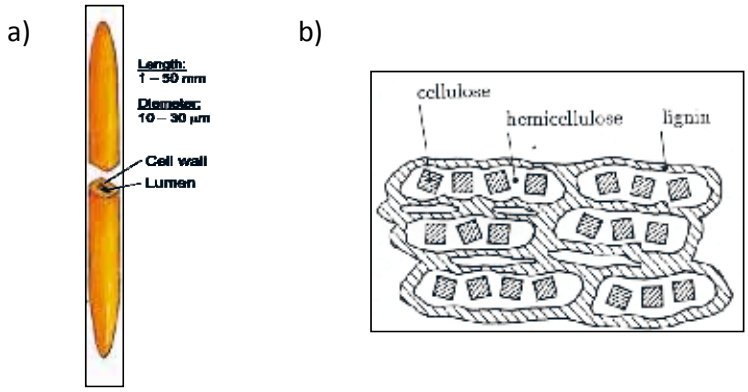

Fig. 1. Schematic drawings: a) a cellulose fiber, and b) a cross-section of the cell wall showing the organization of the three types of constituent polymers. Wadsö 1993.

2.1. Cell wall constituents. The cell wall of cellulose fibers is mainly composed of three types of polymers: cellulose, hemicellulose and lignin. *Cellulose* is a non-branched polysaccharide made up of the cellobiose monomer, which consists of two glucose units covalently bound to each other by a glycosidic carbon (1-4)-linkage. This allows cellulose to form a flat and ribbon like long straight chain, which for wood fibers is having an average length of 5 μm corresponding to a degree of polymerization (i.e. glucose units) of 10,000 (Siau 1995). This molecular linearity makes cellulose highly anisotropic with a theoretical stiffness and strength of about 130 and 15 GPa, respectively in the chain direction (Lilholt and Lawther 2000). The cellulose chains are arranged in parallel to form bundles, which are denoted *microfibrils*. In some regions of the microfibrils, the molecules are arranged in a highly ordered crystalline structure. *Hemicellulose* is a heterogeneous group of polysaccharides composed of monosaccharides, such as glucose, galactose, mannose, xylose and arabinose. Compared to cellulose, the hemicellulose polymers are generally characterized by being short (a maximum of 150 units), non-linear and more branched. *Lignin* is a highly branched polymer composed of phenylpropane units organized in a very complex three-dimensional structure. In the cell wall, the exact structural organization of the three polymers (cellulose, hemicellulose and lignin) is a much-debated subject; however it is generally believed that the hemicellulose polymers are bound to the cellulose microfibrils by hydrogen bonds forming a layer around the microfibrils, and these cellulose microfibril/hemicellulose units are then encapsulated by lignin (Fig. 1b). Thus, the cell wall is essentially organized like a composite material with the stiff and strong cellulose microfibrils embedded in a matrix of hemicellulose and lignin.

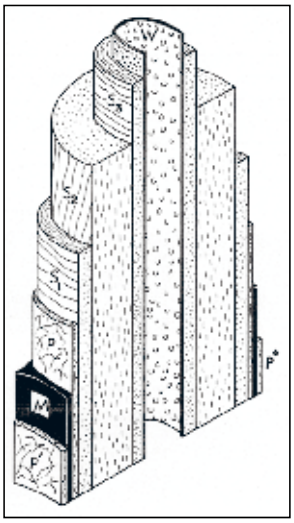

Fig. 2. Schematic drawing of the layered structure of the cell wall, and the orientation of the cellulose microfibrils. M is the middle lamella, which connects the fibers in the plants; P is the primary layer, which is formed during growth of the fiber; S1, S2 and S3 are the three secondary layers, which are formed when fiber growth has stopped; W is the cell membrane. Siau 1995.

2.2. Cell wall structure. In addition to the organization of the chemical constituents, the structural complexity of the cell wall is increased by being organized into a number of layers differing by the angle of the cellulose microfibrils to the longitudinal fiber axis (Fig. 2). In the three secondary layers, S1, S2 and S3, the cellulose microfibrils are arranged in helices coiling around the longitudinal axis of the fiber with a constant angle within each layer but with large angular shifts between the layers. The microfibril angle in the S1 and S3 layers is large, meaning that the fibrils are oriented nearly transverse to the fiber axis. The microfibril angle in the S2 layer is small, and these fibrils are therefore oriented more parallel to the fiber axis. Since the S2 layer is by far the thickest layer, including about 60-80% of the cell wall in wood fibers (Siau 1995), the angle of the microfibrils in this layer dictates the overall mechanical performance of the fibers.

Table 1. Chemical composition and microstructure of cellulose fibers.

	Chemical composition			Microstructure		Reference
	Cellulose (% w/w)	Hemi-cellulose (% w/w)	Lignin (% w/w)	Microfibril angle (degrees)	Cellulose crystallinity (% w/w)	
Wood fibers						
Spruce	49	20	29		67	Thygesen et al. 2005
Pine	42	29	28		57	Sjöström 1993
Pine (kraft pulp)	76				68	Liitiä et al. 2003
Cedar	44	21	30		57	Rowell 1984
Balsa	48	28	22		56	Sjöström 1993
Birch	41	32	22		54	Sjöström 1993
Poplar	39	28	30		54	Rowell 1984
Soft wood				3-50		Anagnost et al. 2002
Plant fibers						
Hemp	63	10	6		96	Thygesen et al. 2005
Hemp	64	14	3		94	Thygesen et al. 2011
Hemp (retted)	74	12	5		92	Thygesen et al. 2007
Hemp (scutched)	66	15	5		98	Thygesen et al. 2011
Flax (cottonized)	76	14	2		88	Thygesen et al. 2011
Hemp (textile)	91	7	2			Madsen et al. 2007b
Hemp and flax				6-10		Gassan et al. 2001

2.3. Chemical composition and microstructure of fibers. Table 1 shows key numbers of chemical composition and microstructure of cellulose fibers. The cellulose content of raw and unprocessed fibers is in the range of 40 - 50 % w/w for wood fibers, and in the range of 60 - 70 % w/w for plant fibers. Accordingly, the content of hemicellulose and lignin is higher in wood fibers, and this is particularly true for lignin which shows a content of about 30 % w/w in wood fibers, in comparison to only about 5 % w/w in plant fibers. Thus, the chemical composition of wood and plant fibers is clearly different from each other. In addition, wood fibers show lower cellulose crystallinity than plant fibers, with typical values of about 70 and 95 % w/w, respectively. The microfibril angle in wood fibers vary in the range 3 - 50 ° depending on the type and location of the fibers in the wood (e.g. late and early wood), whereas the microfibril angle in plant fibers is more constant in the range 6-10 °.

The effect of processing treatments on the chemical composition of the fibers is also shown in Table 1. In general, for both wood and plant fibers, the cellulose content is increased after

processing treatments, due to removal of non-cellulose residues of the fibers (e.g. pectins and waxes). The effect of processing treatment is most clearly seen for the highly processed textile hemp fibers in the study by Madsen et al. (2007b) where the cellulose content was measured to be as high as 91 % w/w.

It is a well-recognized that the chemical composition and microstructure of cellulose fibers are directly correlated with their mechanical properties (as well as other technical properties, such as thermal and moisture sorption properties). In a study by Thygesen et al. (2007), an increase in the cellulose content of the fibers was found to be well correlated with an increase of their stiffness and strength. In the case of the microfibril angle, a study of wood fibers by Page et al. (1971) showed that an increase of the microfibril angle of the fibers was correlated with a clear decrease of their stiffness. Qualitatively speaking, both changes can be expected from the microstructure of the fibers as shown in Figs. 1 and 2. In addition, it can be expected that the stiffness and strength of the fibers is positively correlated with the cellulose crystallinity. Thus, based on these correlations, and by observation of the values in Table 1, it is indicated that the potential for reinforcement in composites is better for plant fibers than wood fibers, due to their higher cellulose content, lower microfibril angle, and higher cellulose crystallinity. On the other hand, the low microfibril angle of plant fibers makes them highly anisotropic which leads to relatively low transverse mechanical properties which will influence the overall mechanical performance of the composites. In terms of more complex mechanical properties, like fracture toughness and fatigue, it can moreover be speculated that the higher microfibril angle and the lower crystallinity of the wood fibers will benefit these fibers in comparison to plant fibers.

The complex chemistry and structure of cellulose fibers, and the influence of growth conditions and processing treatments, lead typically to fibers with more variable properties than it is the case for synthetic fibers. This is frequently considered to be one of the major disadvantages of using cellulose fiber composites for structural applications, since this is conflicting with the normal industrial demand of constant product quality. It is however believed that this concern is caused by a general uncertainty about the cause for the variability in properties, and the lack of a system for categorizing the quality of cellulose fibers (e.g. by their chemistry and structure), similar to the system that exist for solid wood. It should also be mentioned that a variability of mechanical properties of fibers can have a positive effect on the notch sensitivity and the fracture toughness of composites (Lindhagen and Berglund 1998; Ridruejo et al. 2010). The variability would make the crack divert and damage to accumulate in various places simultaneously, in contrast to brittle fracture along one plane indicative of homogenous materials. The cellulose fibers show a hierarchical structure with heterogeneous, yet organized, structures on several length scales which imparts very high damage tolerance adapted to specific load conditions (see e.g. Fratzl and Weinkamer 2007).

3. PREFORMS OF FIBERS

The processing route of cellulose fibers for making preforms for composites is generally more complex and contains a larger number of steps than for synthetic fibers, where in the simple case, glass fibers are melt extruded from a formulation of silicon and metal oxides, and in the more complicated case, carbon fibers are made by oxidation and carbonization of constantly tensed polyacrylonitrile fibers (Bunsell and Renard 2005). The one-dimensional and continuous glass and carbon fiber rovings can then be converted into two-dimensional preforms (fabrics and mats) by textile techniques such as weaving and stitching. The types of preforms that can be fabricated from cellulose fibers are in principle identical to the ones for synthetic fibers, although concerns must be addressed to some particular characteristics. Here follows details of the processing route of wood and plant fibers starting from the green plants and ending at the composite preforms.

3.1. Wood fiber preforms. Separated wood fibers are available at a low cost as pulp fibers (Fig. 3a). These are used to make paper sheets or board materials for packaging. One way to make composites based on wood fibers is thus to use fiber mats (Fig. 3b), which could be impregnated by using e.g. resin-transfer molding (e.g. Almgren et al. 2009a). A viscous thermoset resin is then impregnating the fiber mat by the aid of a pressure vessel attached to the mould inlet and sometimes also assisted by vacuum suction at the outlet. The fiber mat is placed in the mould. After impregnation, the thermoset resin is cured and solidified to form at solid composite component. This manufacturing technique is only adequate for low-viscosity resins, typically thermosets. Thermoplastics usually have a high viscosity in the molten state, and resin-transfer molding is not suitable since the impregnation times would be too high, or the required high pressure would induce severe deformation of the preform. Instead, a commingling technology can be advocated. By using papermaking machines, e.g. so-called French or Finnish sheet formers in the laboratory scale, one can produce sheets composed of commingled wood pulp fibers and thermoplastic fibers (e.g. Almgren et al. 2009b). The thermoplastic fibers should preferably have similar dimensions as the pulp fibers, in order to have approximately the same hydrodynamic properties during the formation process. Thermoplastic fibers could be spun to have diameters around 30 μm and be chopped to roughly 3 mm length (similar to the dimensions of wood cell tracheids). When the commingled fiber mat has been dried, it can be placed in a hot press and composite components can be molded. This method is not only limited to flat plates for materials testing, but complex parts with double curvatures can also be made (Lindström et al. 2008). Shaped preforms can then be made using shaped suction wires that are dipped into a high-consistency fiber suspension, as e.g. in manufacture of egg cartons.

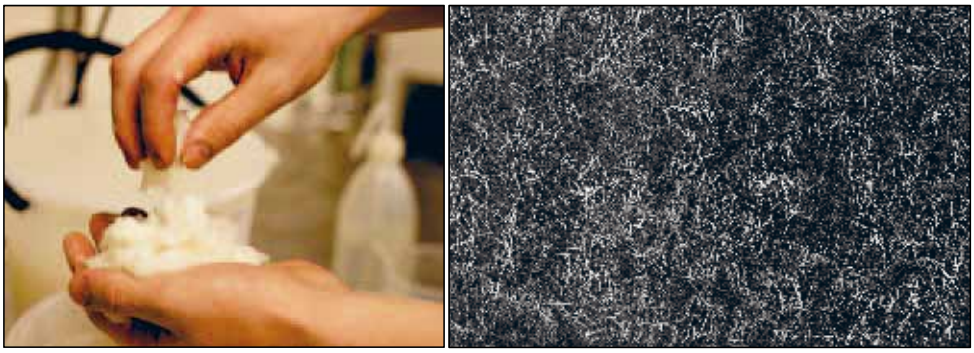

Fig. 3. (a) Pulp made from bleach softwood fibers (courtesy of Innventia, Sweden), and (b) fiber distribution in wood fiber mat (image height ~ 1 cm).

The papermaking industry encompasses a huge infrastructure to produce wood fiber sheets. Anticipated volumes of fiber preforms for composite applications are extremely small compared with produced volumes of conventional paper and board. Nevertheless, there is an opportunity to build upon the experiences and use small-scale paper mills to produce composite preforms. In the laboratory scale, two main techniques are used to mimic the paper manufacturing process. The most common are sheets produced by dynamic sheet forming and regular in-plane isotropic handsheets, commonly termed as French and Finnish sheets, respectively. In dynamic sheet forming, a fiber suspension jet is directed towards a rotating wire drum (Neagu et al. 2005). The fibers will deposit onto the wire whereas the water goes through the wire. Depending on the jet to wire speed difference, the fibers will orient along the machine direction (circumferential direction of the rotating drum). An anisotropic sheet can then be obtained, with similar features

as those manufactured in paper mills, where the fibers are preferably oriented in the machine direction compared with the cross direction. In the Finnish type handsheets, the fibers randomly are mixed with water in a large container. The water is abruptly let out at the bottom of the container, and the fibers are deposited on a flat wire at the bottom. The fibers are then predominantly randomly oriented in the plane. Thus, the main difference between sheets that are formed using a dynamic sheet former and handsheets is that the former are generally in-plane anisotropic, whereas the latter are in-plane isotropic.

3.2. Processing of plant fibers. Plant fibers are extracted from annual plants, such as flax and hemp. After *harvesting* of the plants, the raw fibers are separated from the plant stems by retting, followed by mechanical extraction processes. The primary goal of *retting* is to degrade the stem tissue that interconnects the single fibers, i.e. the middle lamella (see Fig. 2). Traditionally, plant stems are left in the field to be decomposed by microbial organisms. This is denoted field retting, and is a strictly natural process strongly influenced by the actual weather conditions. Alternatively, to make the retting process more controllable, the plant stems can be retted in water tanks, which is then denoted water retting. After retting, the fibers are extracted from the stems by a *mechanical process*, in which the core of the stems is broken into small extractable lengths, the so-called shives. This is typically performed by progressing the stems through pairs of profiled rotating rolls (Hobson et al. 2001). For hemp fibers, the yield of plant fibers after retting and mechanical extraction is in the range 15-30 w/w % (expressed as a percentage of stem dry matter) (Sankari 2000).

To be able to spin the raw plant fibers into a yarn (Fig. 4), the separation of fiber bundles into single fibers, as was taken place during the retting process, needs to be further enhanced. This can be achieved by a *carding* process, where the fiber bundles are drawn apart by toothed surfaces working against each other (Klein 1998). After carding, the fibers are situated in a robe-like assembly which is denoted a *sliver*. Before spinning the yarn, order must be imparted to the fibers in the sliver, and this is accomplished by (i) combing (or hackling), which aligns the fibers and removes a portion of the shortest fibers, and (ii) drafting, which straightens out the fibers and ascertains that the number of fibers in a sliver cross-section is within specified limits (Klein 1998). In *combing*, the sliver is progressed through a series of pinned rollers that comb out the short and tangled fibers, and align the long fibers. In *drafting*, the filament is as well progressed through a series of rollers, but the rotational speed of the roller pairs is increased in the forward direction, and subsequently the sliver is drawn apart.

A range of different techniques exists for spinning the discontinuous and (almost) parallel fibers of a sliver into a twisted yarn structure: e.g. ring spinning, rotor spinning, wrap spinning and air-jet spinning (Grosberg and Iype 1999). Ring spinning is however the most widely used method. During spinning, the sliver is twisted so that the fibers take up a helical configuration (see image of a yarn in Fig. 4). Because of the inherent friction between the fibers, the twisting action will slightly stretch the fibers and this will lead to the generation of a compressive force exerted towards the yarn interior. This compressive force will increase the frictional forces between the fibers, which will furthermore impart axial strength to the yarn (Klein 1998). Therefore, the number of twists per yarn length (which is correlated to the twisting angle of the fibers), is a main factor determining the strength of a yarn. When a plant fiber *yarn* is used as reinforcement in composites, the effect of the fiber twisting angle on the mechanical properties of the composites has previously been addressed in a few studies (Goutianos et al. 2006; Rask and Madsen 2011), but the exact numerical correlation, and the underlying mechanical mechanisms, need still to be established. In addition, the cross-sectional area of the yarn (which is specified indirectly by its linear density given in units of g/1000 m), and the degree of yarn compactness (Madsen et al. 2007b) are other important yarn characteristics in the perspective of composite

reinforcement. It can be speculated that the degree of yarn compactness will be correlated with the permeability of the yarn for matrix impregnation during manufacturing of composites, and this will influence the resulting content of impregnation porosity (see section 7 below on porosity in composites). Altogether, more studies are needed to improve the understanding of the correlation between the various structural characteristics of plant fiber yarns, and the mechanical performance of the yarns in composites.

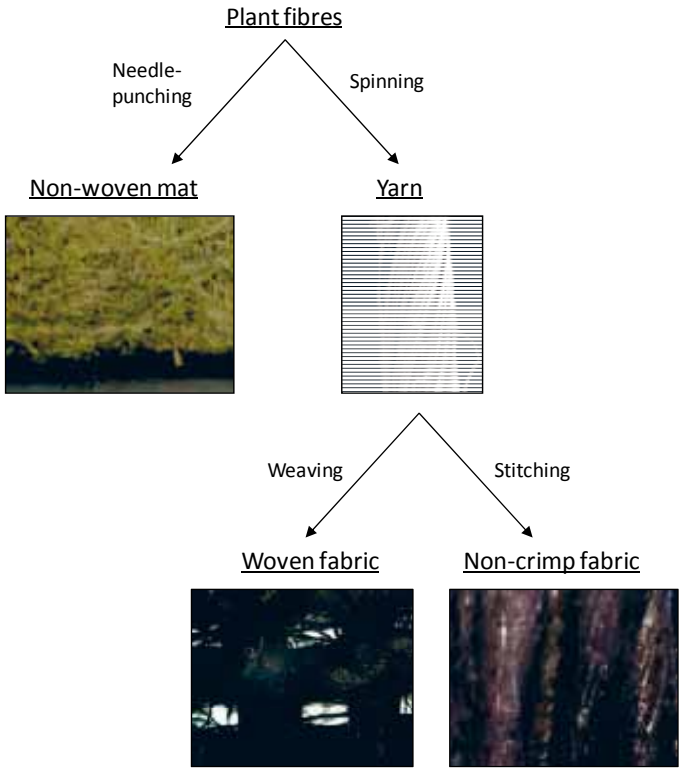

Fig. 4. Overview of typical plant fiber preforms for composites.

3.3. Plant fiber preforms. After the raw plant fibers have been extracted from the plants, they can then be converted into non-woven mats (Fig. 4) by air-laid and needle-punching techniques (Eriksen and Pallesen 2002). The planar fiber orientation in non-woven mats is nominally 2-D random, but they can show a preferred fiber orientation in the machine direction of the mats (Kim et al. 2000) (see numerical examples in Figs. 13b and 14b). The area weight of the mats is usually in the range 200 - 800 g/m^2.

The plant fiber yarns can be used to make the two composite preforms: woven fabrics and non-crimp fabrics (Fig. 4). *Woven fabrics* are fabricated by using a range of weaving patterns, such as plain, twill and sateen weave, in which the yarns are differently interlaced in the two main, orthogonal, planar directions. The yarns in the two directions can have different linear densities, and they can be placed with different distances to each other. Altogether, woven fabrics offer the possibility of having composite preforms where the planar yarn configuration in two dimensions can be exactly designed to meet the loading profile of a given composite application. Woven

fabrics of flax, jute and cotton fibers are widely available, but they are most often tailored for textile applications, and not for composite applications. *Non-crimp fabrics* consist of yarns that are not held together by being woven into each other, but instead they are stitched together. This means that the yarns are fully stretched, i.e. they have no crimp, since they do not have to go over and under each other. Single layers of parallel yarns held together by transversely directed stitching threads are denoted *uniaxial* non-crimp fabrics. Such uniaxial layers can then be stacked and stitched together to form *biaxial* or *multiaxial* non-crimp fabrics with specific planar yarn orientations, e.g. ± 45°, 0°/90°, and 0°/+45°/-45°/90°. In comparison to woven fabrics, the composite reinforcement efficiency of the fibers in non-crimp fabrics are (expected to be) better since the fibers are straight, and not crimped. However, the twisted configuration of fibers in plant fiber yarns needs yet to be taken into account in the analysis of the expected negative effect of crimp. Recently, a number of European companies have started production of non-crimp fabrics of flax fibers; for the first time, commercially available fabrics of plant fibers that are specifically tailored for composites have been produced.

4. MECHANICAL PROPERTIES OF COMPOSITES

The mechanical behavior of cellulose fiber composites have been extensively characterized and analyzed. The work has mainly been addressing tensile properties, as well as bending and impact properties. However, other more complex mechanical properties, such as fatigue (Gassan and Bledzki 1999a) and creep (Gassan and Bledzki 1999b), have been studied as well. In addition, fiber/matrix interface properties have been investigated by microbond tests and fragmentation tests (Khalil et al. 2001; Zafeiropoulos et al. 2002). Table 2 presents typical reported tensile properties of wood and plant fiber composites.

In Table 2, the stiffness and strength of a set of wood and plant fiber composites can be compared to corresponding values for some typical glass fiber and carbon fiber composites. It should be noted that the high stiffness and strength of kraft paper impregnated phenol formaldehyde (Cox and Pepper 1944) have hitherto not been reached for wood fiber composites. These materials were developed during World War II for use in skins of aircraft wings. The results by Cox and Pepper (1944) can hence be regarded as outliers. Furthermore, in Table 2, it can be observed that cellulose fiber composites (both wood and plant fibers) with a nominal random fiber orientation, made by using the preforms of loose fibers, paper, and non-woven mats, possess moderate tensile properties with a stiffness in the range 4-9 GPa and a strength in the range 30-60 MPa. In comparison to glass fiber composites with a similar random fiber orientation, cellulose fiber composites show in general comparable stiffnesses, and slightly lower strengths. In the studies by Thomason (2005), and Oksman (2000), the strength of glass fiber/polypropylene composites were measured to be 100 and 77 MPa, respectively, and this is slightly higher than the maximum strengths of 60 MPa in Table 2 measured in the study by Marcovich et al. (1996) on eucalyptus saw dust/polyester composites. It is however well known that various chemical approaches can be used to improve the interface bonding, and thereby increase the mechanical properties of the composites. Acetylation is one type of surface treatment that can be used to reduce the polarity of the fibers making them more compatible with the (typically) non-polar matrix (Khalil et al. 2001). Also, coupling agents, such as maleic anhydride, can be used to form covalent bonds between the fibers and the matrix (Myers et al. 1991). In the study by Clemons (2000) (see Table 2), the strength of wood fiber composites were shown to be increased from 28 to 52 MPa by using maleic anhydride as a coupling agent, whereas the stiffness did not show any changes. A similar large increase in strength has been found by Andersen and Plackett (2002), whereas other studies have only showed smaller increases in strength (Mishra et al. 2000; Hornsby et al. 1997).

Table 2. Typical reported tensile properties of cellulose fiber composites. The type of fiber preforms used for the composites is indicated, in addition to the nominal fiber orientation; random (RD) and unidirectional (UD). For means of comparison, also mechanical properties of glass and carbon fiber composites are shown.

	Fiber content (% v/v)	Tensile properties		Reference
		Stiffness (GPa)	Strength (MPa)	
Wood fiber composites				
Wood/PP – Pulp[1]; RD	27	4.2	28	Clemons 2000
Eucalyptus saw dust/UP[1]; RD	46	6.2	60	Marcovich et al. 1996
Kraft + TMP/PP; RD	40	4.5	43	Woodhams et al. 1984
Sulphite pulp/PP[1]; RD	50	3.9	51	Bengtsson et al. 2007
Kraft/PF – Paper; RD	72	[a] 26.2	247	Cox and Pepper 1944
Kraft/PF – Paper; RD	72	[b] 11.7	156	Cox and Pepper 1944
Plant fiber composites				
Flax/starch – Loose fibers[1]; RD	37	8.3	51	Nättinen et al. 2009
Jute/PP – Non-woven mat; RD	32	8.4	39	Toftegaard 2002
Jute/PP – Non-woven mat; RD	30	5.2	40	Andersen and Plackett 2002
Flax/epoxy – Yarn[2]; UD	40	28.0	133	Van de Weyenberg et al. 2003
Flax/PP – Yarn[2]; UD	55	28.2	321	Madsen et al. 2003
Flax/PLA – Non-crimp fabric; UD	39	19.5	150	Madsen et al. 2009a
Flax/epoxy – Non-crimp fabric; UD	35	19.8	234	Bottoli and Pignatti 2011
Glass fiber composites				
Glass/PP – Loose fibers[1]; RD	30	7.3	100	Thomason 2005
Glass/PP – chopped strand mat; RD	20	5.4	77	Oksman 2000
Glass/PP – Roving[2]; UD	60	45.0	1020	Gamstedt et al. 1999
Glass/epoxy – Roving; UD	55	39.0	1080	Bunsell and Renard 2005
Carbon fiber composites				
Carbon [c]/epoxy – Roving; UD	60	313.0	1140	Calculated
Carbon [d]/epoxy – Roving; UD	60	142.0	2140	Calculated

[1] Injection molding; [2] Filament-winding

[a] Machine direction; [b] Cross direction; [c] High modulus fibers; [d] High strength fibers

As expected, when preforms with nominally unidirectional fibers, such as yarns and non-crimp fabrics are used (Table 2), the tensile properties of cellulose fiber composites are markedly increased with stiffnesses in the range 20-28 GPa and strengths in the range 130-320 MPa. It can also be observed in the table that in comparison to the composites with a random fiber orientation, the fiber volume content of the unidirectional composites is in general higher (up to 55 %). This is related to the packing ability of fibers, which is much better for aligned fibers than for randomly oriented fibers, and this leads to a higher maximum fiber volume content in unidirectional composites (Madsen et al. 2007c). However, in comparison to synthetic fibers, such as glass and carbon, the packing ability of cellulose fibers is generally lower (Madsen and Lilholt 2002), which means that the maximum fiber volume content is typically lower in cellulose fibers composites, which also is shown in Table 2. The effective stiffness of cellulose fibers has been estimated to be in range of 30-50 GPa (Madsen et al. 2009b), whereas the stiffnesses of glass and carbon fibers are in the ranges of 70-80 and 200-800 GPa, respectively. Moreover, the discontinuous cellulose fibers are situated in a twisted yarn configuration, in comparison to the continuous and straight glass and carbon fibers situated in rovings. Thus, altogether, it is expected that unidirectional glass and carbon fiber composites in general have

larger stiffnesses than cellulose fiber composites, as shown in Table 2 (even though that the stiffness of cellulose and glass fiber composites are comparable with maximum values of 28 and 45 GPa, respectively). In terms of strength, cellulose fiber composites show however radically lower values than glass and carbon fiber composites. The explanation for the relatively low strength of cellulose fiber composites is currently not known, however, it might be speculated that fiber defects, which are introduced to the fibers during their processing, might play a role. In a recent study by Rask et al. (2011), the damage mechanisms of unidirectional flax fiber composites have been studied by X-ray tomography.

In conclusion, the values in Table 2 well illustrate the current status of cellulose fiber composites where stiffness is acceptable, and comparable to synthetic fiber composites, but the strength of the composites needs to be improved.

5. APPLICATIONS OF COMPOSITES

In Europe, cellulose fiber composites are mainly used by the automotive industry (Broge 2000; Ellison and McNaught 2000; Karus et al. 2002; Parikh et al. 2002). The applied fiber preforms are loose fibers used for injection molding techniques, and non-woven mats used for compression molding techniques. Due to the nominal random fiber orientation in these composites, they possess only moderate mechanical properties (see Table 2), but this makes them nevertheless well qualified to be used in non-structural components such as door liners, boot liners and parcel shelves. The low prices of loose fibers and non-woven mats of cellulose fibers, compared to their synthetic counterparts, form a strong motivation for the use of these two preforms in the automotive industry (Bledzki et al. 2002). However, because of concerns about the sensitivity towards water exposure, mostly interior components are made with cellulose fiber composites. Outside Europe, the use of non-structural components based on cellulose fibers is considerable more widespread, and wood fibers are by far the preferred fiber type. In the USA, the main applications are building components, such as deckings, windows profiles and floorings, in addition to pallets, flowerpots and office accessories. In India, houses, grain silos and fishing boats have been fabricated with the use of jute fiber composites (Mohanty and Misra 1995).

Recently, in the context of research and development projects, a number of demonstrators have been made to reveal the good potential of cellulose fiber composites:

- Sculpture shown at the Louisiana Museum of Modern Arts, Denmark, special exhibition ‘Green architecture for the future’, winner of the JEC innovation award 2010; composites of plant fibers in a bioresin; Joint venture of 20 companies coordinated by 3XN architects, Denmark. Fig. 5.
- Exhibition stands at the Swedish Nautical Historical Museum in Stockholm, Sweden; composites of non-crimp plant fiber fabrics in a bioresin matrix; EU 7th Framework Programme Project, WOODY (2009-2012). Fig. 5.
- Chair, designed by Michael Strøm and Lasse Svensson, exhibited at “Copenhagen Furniture Fair” in Bella Centre, Denmark; composites of woven plant fiber fabrics in a biopolymer matrix; EU 7th Framework Programme Project, BIOCOMP (2005-2008), national funding via Musicon Valley and internal Risø DTU funding.
- Chair for children (“Parupu”) developed by Innventia AB, Sweden, in collaboration with the pulp company Södra and the architect firm Claesson Koivisto Rune; exhibited at the Milan furniture fair 2009; composites of wood pulp fibers in a biopolymer matrix. Fig. 5.

- Double-curvature panels, designed by Martin Larsen and Karina Rios Nielsen, exhibited at "Klimaforum09/Ideas at work" in connection with COP15, Copenhagen 2009, and at the JEC exhibition in Paris, France, 2010; composites of plant fibers in a biopolymer matrix; Danish national project, BIO/BIO (2008-2009).

Fig. 5. Examples of demonstrators of cellulose fiber composites: (left) sculpture shown at the Louisiana Museum of Modern Arts (joint venture of 20 partners coordinated by 3XN architects, Denmark), (middle) exhibition stands at the Swedish Nautical Historical Museum in Stockholm, Sweden (EU 7th Framework Programme Project, WOODY), and (right) chair for children developed by Innventia AB, Sweden, in collaboration with the pulp company Södra and the architect firm Claesson Koivisto Rune.

6. SPECIAL ISSUE: MODELING OF MICTROSTRUCTURE AND MECHANICAL PROPERTIES OF FIBERS

From a geometrical point of view, the cell wall in cellulose fibers can be approximated by layers of concentric cylindrical shells. Fig. 6 shows such an idealized fiber geometry used in micromechanical modeling of the mechanical properties of cellulose fibers. Summaries of how the microstructural features of the cell wall affect the mechanical properties of the fibers have been compiled by Neagu et al. (2006b), Salmén and Burgert (2009) and Salmén (2004).

In principle, the most important mechanical properties of fibers used in composites are the stiffness and strength in the axial direction, i.e. along the fiber length direction. It is in this direction that the fibers are supposed to carry load when embedded in a composite material. In the case of cellulose fibers, the key microstructural features of the cell wall that affect the axial mechanical properties are:

- Fiber density, or relative lumen size: Only the cell-wall carries load, i.e. the fiber stiffness is proportional to the relative cell-wall area for a normal cross-section. The lower the fiber density, the larger the relative lumen size, and the lower the axial fiber stiffness and strength.
- Microfibril angle: The effective elastic properties in the axial direction scales with the local stiffness in the microfibril direction multiplied with $\cos^4 \theta$, where θ is the microfibril angle, according to a coordinate transformation of the stiffness matrix. The fiber stiffness (and strength) is thus very sensitive to the microfibril angle, even if the mechanical properties in the microfibril direction are constant.

– Cellulose content: Particularly crystalline cellulose and crystallite aspect ratio is known to affect the stiffness of the cell-wall in the microfibril direction (e.g. Hofstetter et al. 2005).

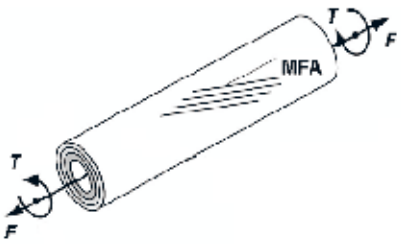

Fig. 6. Idealized fiber geometry used in micromechanical modeling. MFA is microfibril angle.

Of the three above-mentioned microstructural features, the strongest effect on the mechanical properties of the fibers can probably be attributed to the microfibril angle, since fiber lumens can be collapsed (as for earlywood in chemically pulped fibers) and filled with resin in a composite, and the cellulose content is an intrinsic property, which is roughly constant for plant fibers and constant, albeit lower, for wood fibers (cf. Table 1). The dependence of the fiber stiffness on the microfibril angle is a well known effect (e.g. Page et al. 1971), and can be described by classic laminate theory (Salmén and de Ruvo, 1985). These trends are displayed in Fig. 7, based on work in a study by Neagu and Gamstedt (2007), where a more accurate model has been used to predict axial fiber stiffness as a function of the microfibril angle for free unconstrained fibers, and for fibers that are not allowed to rotate. Note, that for angles above 10°, there is a larger dependency on the angle for constrained fibers, which would be the situation of end-clamped tensile testing of single fibers. The additional deformation mode of twist has a large effect on stiffness up to an angle of about 40°, where after the constrained and unconstrained fibers show almost the same dependency on the microfibril angle.

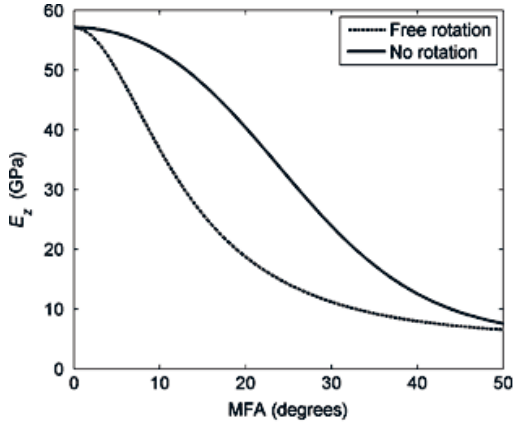

Fig. 7. Effect of microfibril angle on the axial fiber stiffness for constrained fibers and for fibers that are free to twist. Neagu and Gamstedt 2007.

7. SPECIAL ISSUE: POROSITY IN COMPOSITES

Porosity cannot be avoided in composite materials and is caused by the mixing and consolidation of two different materials, the fibers and the matrix. Several studies have shown that porosity is an important factor influencing the mechanical performance of composites (Judd and Wright 1978; Varna et al. 1995). In the case of traditional composites, such as glass and carbon fiber composites, considerable knowledge has been accumulated to diminish the porosity part to contents below 1 % (Månson et al. 2000). In the case of cellulose fiber composites, the porosity part typically makes a noteworthy contribution to the overall composite volume with porosity contents above 5 % (Madsen et al. 2007a). The relatively large porosity content in these composites is caused by a number of factors: (i) the existence of luminal cavities in cellulose fibers, (ii) the complex surface chemistry of cellulose fibers which complicates fiber/matrix bonding, (iii) the irregular form and dimensions of cellulose fibers which restrict matrix impregnation, (iv) the low packing ability of cellulose fibers which limits the maximum obtainable fiber volume content, and (v) the applied processing techniques which normally are directly adopted from synthetic fiber composites and need yet to be tailored for cellulose fiber composites. Altogether, porosity can typically not be neglected in cellulose fiber composites, and *porosity must therefore routinely be integrated in the evaluation of composite performance*.

The porosity content is defined as the ratio of volume of air-filled cavities in relation to the total volume of the composite, and it is given in values of fractions or percentages. Depending on the chosen classification criteria (e.g. size, location or origin), different types of porosity in the composites can be identified; see examples in the studies of synthetic fiber composites by Wisnom et al. (1996) and Hamidi et al. (2005). In a study of cellulose fiber composites by Madsen et al. (2007c), three main types of porosity are identified:

- Fiber correlated porosity, which is assumed to be correlated with the fiber volume content. These types of porosities are located (i) inside the fibers (i.e. in the fiber lumen), (ii) at the fiber/matrix interface, and (iii) in the interior of fiber sub-assemblies (e.g. fiber bundles). The interface porosity is created both during processing of the composites (e.g. due to poor fiber/matrix compatibility), and during service of the composites (e.g. due to external mechanical influences). The impregnation porosity is caused by incomplete matrix impregnation of the fibers.
- Matrix correlated porosity, which is assumed to be correlated with the matrix volume content. This type of porosity is located in the matrix rich regions (i.e. between fiber sub-assemblies), and it is typically caused by improper processing conditions (i.e. time, temperature and pressure) with respect to removal of air.
- Structural porosity, which is related to the situation where the available matrix volume is insufficient to fill the free space in the fully compacted fiber assembly. This type of porosity exists only when the fiber weight content is higher than a given transition value, which is controlled by the maximum packing ability of the fiber assembly.

Fig. 8 shows examples of the three types of fiber correlated porosity that typically are found in cellulose fiber composites: fiber porosity, interface porosity and impregnation porosity. The microscope images shown of unidirectional hemp fiber composites illustrate well the characteristic location of the three types of porosities. In these composites (for a fiber volume content of 50 %), the total porosity content was determined to be 4.5%, of which the contents of fiber porosity, interface porosity and impregnation porosity was determined to be 1.3, 0.6 and 2.6 %, respectively. Thus, in these composites, the impregnation porosity takes up the largest part of the total porosity.

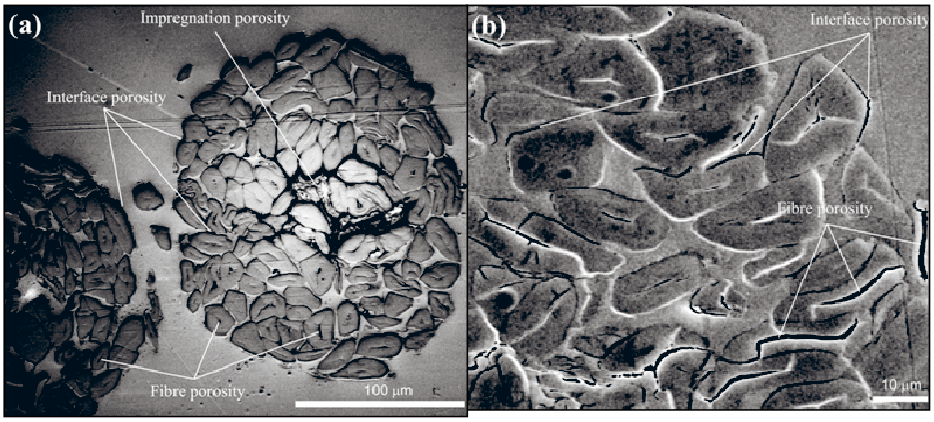

Fig. 8. Types of porosity in cellulose fiber composites. Shown are cross-sectional images of unidirectional hemp/polyethylene terephthalate composites. The optical microscope image in (a) shows a hemp fiber yarn, and the scanning electron microscope image in (b) shows a close-up of the fibers in the yarn. Madsen et al. 2007c.

As indicated by the above description of porosity types, the porosity content in cellulose fiber composites (and in composites in general) can be correlated with the fiber and matrix contents. Fig. 9 shows an example of typical experimental data for volume fractions of fibers and porosity for increasing fiber weight fractions measured for a series of composite laminates. The data shows that (i) at the region of low fiber weight fraction, the fiber volume fraction is monotonically increasing, and the porosity is low, and (ii) at the region of high fiber weight fraction, the fiber volume fraction tends to be constant, and the porosity starts to increase. The transition between the two regions of fiber weight fractions is marked in the diagram by a vertical line. As will be shown below, *the transition fiber weight fraction determines the best possible combination of high fiber content, and low porosity content*, which typically results in composites with maximum obtainable mechanical properties.

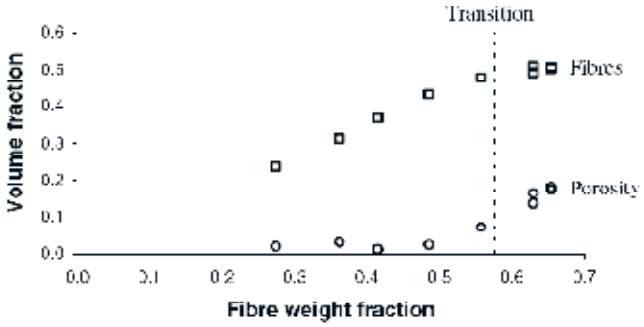

Fig. 9. Volume fractions of fibers and porosity as a function of fiber weight fraction of a series of composite plates of hemp yarn fibers in polyethylene terephthalate matrix. Madsen et al. 2007c.

A model for the numerical correlation between the fiber, matrix and porosity contents in composites is presented in the study by Madsen et al. (2007c). In the present paper, the equations of the model will not be presented, but only examples of predicted volumetric compositions of composites will be shown. Input parameters are the density of fibers and matrix, which can be measured by pycnometry and buoyancy methods (Pratten 1981), and porosity constants, which can be measured from images of composite microstructures, or alternatively they can be back-calculated by fitting the model to experimental data of porosity. The model predicts the volume fractions of fibers, matrix and porosity as a function of the *fiber weight fraction*. The model applies to composites in general, but is particular relevant to composites with relatively high porosity contents, which is typically the case for cellulose fiber composites.

Fig. 10 shows experimental data and model predictions of the volumetric composition of a series of hemp fiber/thermoplastic matrix composites with variable fiber weight fractions. It can be observed that the model predictions (solid lines in the diagram) are well predicting the experimental data. The volume fractions of fibers and porosity are increased as a function of the fiber weight fraction, until a certain value where after the fiber volume fraction is constant, and the porosity starts to increase more dramatically. The transition fiber weight fraction is determined to be 0.58. Thus, the model predicts that composites should be manufactured with a fiber weight fraction of 0.58 to have the best possible combination of high fiber volume fraction, and low porosity. Fig. 10 shows also the predictions made using a conventional model (dotted lines in the diagram), which originally are developed for synthetic fiber composites. This conventional model is based on the assumptions of no porosity in the composites, and unlimited packing ability of the fibers. With these (unrealistic) assumptions, the predicted values of fiber and matrix volume fraction are overestimating the experimental values (especially for composites with a fiber weight fraction above the transition value), and in addition, no transition value can be determined. Altogether, it is believed that the new model offers an improved tool for calculating the volumetric composition in composites.

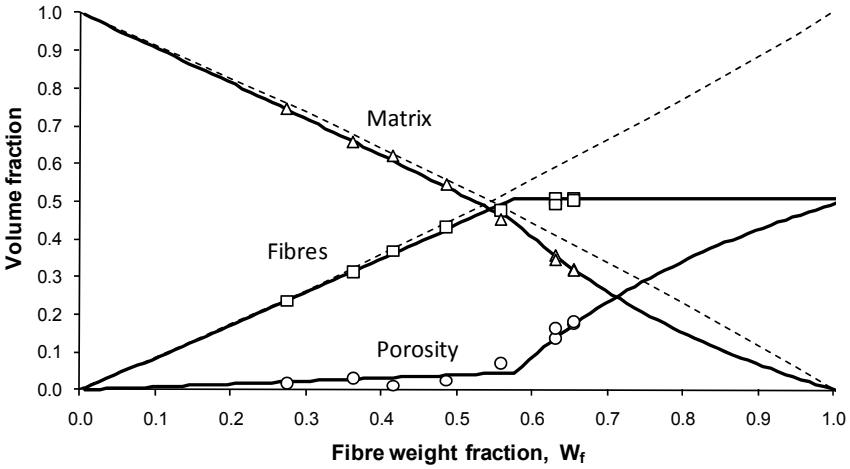

Fig. 10. Experimental data and model predictions of the volumetric composition of hemp fiber/polyethylene terephthalate composites. Dotted lines are model predictions assuming no porosity and unlimited packing ability of the fibers. Madsen et al. 2007c.

8. SPECIAL ISSUE: MICROMECHANICAL MODELING OF MECHANICAL PROPERTIES OF COMPOSITES

For composite materials, the quantitative relation between microstructure and mechanical properties is generally termed micromechanics, and it has been the scope of extensive research for high-performance composites, such as glass and carbon fiber composite. Micromechanical models developed for these materials are generally applicable also for cellulose fiber composites, with some modifications to account for the specificities of cellulose fibers. By far, the relation between microstructure and elastic properties is the one that has attracted most attention. Stiffness is one of the foremost design parameters, and is also amenable to modeling efforts since stiffness represents an average property, unlike strength which is controlled by the largest defect for relatively brittle materials.

Just as for glass and carbon fiber composites, the fibers are the main load carrying constituent in cellulose fiber composites, and the more compliant polymer matrix has the role of distributing the load between the fibers and protecting the fiber assembly. Since cellulose fibers are generally much stiffer than the polymer matrix, with a Young's modulus in the longitudinal direction of 20 - 80 GPa (e.g. Lilholt and Lawther 2000; Neagu et al., 2006a) vs. 1 - 5 GPa for typical polymer matrix materials, efforts should be made to align the fibers in the main load direction. Furthermore, the fibers should be as long and slender as possible, since this assures that the ineffective lengths close to the fiber ends are relatively short. Shear stresses are transferred over the fiber-matrix interface along the ineffective lengths, and the tensile load is built up. These can be modeled by shear-lag theories (Cox 1952; Nairn 1997), and it can be shown that a higher aspect ratio leads to a higher stiffness. If oriented transversely to the load direction, the fibers merely act as stress raisers, and do not contribute as much to the composite stiffness as they would if they were oriented along the load direction.

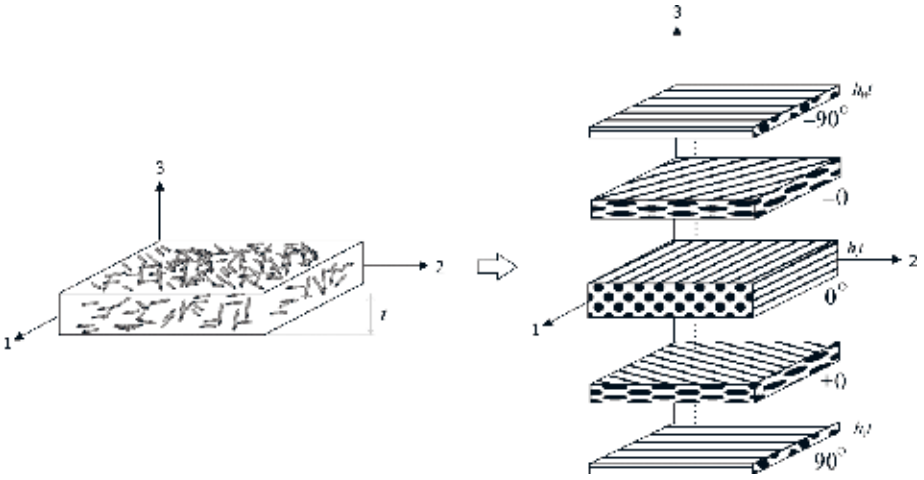

Fig. 11. Schematic illustration of a laminate analogy for randomly oriented cellulose fiber composites. The relatively slender fibers have an in-plane random distribution given by the fiber orientation distribution $p(\theta)$.

8.1. Composites with randomly oriented fibers. For composites with a random fiber orientation distribution, which is usually the case for wood fiber composites, the composite can be regarded as stack of unidirectional plies, where the relative thickness of each ply is determined from the

density function d$p(\theta)$. This is known as a laminate analogy, where classical laminate mechanics can be used to relate the elastic properties of a hypothetical unidirectional ply to those of a composite plate. The laminate analogy is schematically illustrated in Fig. 11. The stiffness symbols of the layered structure follow the conventions in classic laminate mechanics. For a given fiber orientation distribution for a short fiber composite or mat, the global stiffness matrix [$\overline{Q}$] can be described as:

$$\left[\overline{Q}\right] = \frac{1}{\pi}\int_{-\frac{\pi}{2}}^{\frac{\pi}{2}} \left[T(\theta)\right]^{-1}\left[Q\right]\left[T(\theta)\right] p(\theta)\,\mathrm{d}\theta \tag{1}$$

where $T(\theta)$ is the transformation matrix for a rotation angle of θ radians, and $[Q]$ is the local stiffness matrix, whose elements are as usual defined as $Q_{11} = E_L/(1 - \nu_{LT}\nu_{TL})$, $Q_{22} = E_T/(1 - \nu_{LT}\nu_{TL})$, $Q_{12} = \nu_{LT}E_T/(1 - \nu_{LT}\nu_{TL})$, $Q_{66} = G_{LT}$, and $Q_{16} = Q_{61} = Q_{26} = Q_{62} = 0$ for orthotropic materials. The generalized Hooke's law of the unidirectional laminate is:

$$\begin{bmatrix}\sigma_{LL}\\ \sigma_{TT}\\ \tau_{LT}\end{bmatrix} = \begin{Bmatrix}Q_{11} & Q_{12} & Q_{16}\\ Q_{21} & Q_{22} & Q_{26}\\ Q_{61} & Q_{62} & Q_{66}\end{Bmatrix}\begin{bmatrix}\varepsilon_{LL}\\ \varepsilon_{TT}\\ \gamma_{LT}\end{bmatrix} \tag{2}$$

It is assumed that $p(\theta)$ is symmetric, which is typically the case for wood fiber mats produced with conventional wet-forming techniques (Erkkilä et al. 1998). This means that the material is also globally orthotropic, and the stiffness matrix is described by five elastic constants, namely the longitudinal and transverse Young's moduli, the major and minor Poisson ratios and the shear modulus. The components in the global stiffness matrix can be determined from standardized macroscopic testing, and the orientation distribution can readily be found by image analysis of scanned sections of the fiber mat (Gadala-Maria and Parsi 1993). Measurement of the Young's moduli and Poisson's ratios along the main material axes does generally not pose any technical problems.

Softwood pulp fibers have an aspect ratio of about 100 (Duanmu et al. 2007). From a mechanical point of view, these slender fibers can be regarded as continuous, i.e. of infinite length, since the ineffective lengths close to the fiber ends are relatively small. The stiffness contribution of wood fibers to the unidirectional ply can then be described by simple mechanical models, such as the rule-of-mixtures for longitudinal elastic properties, and the Halpin-Tsai equation for shear and transverse elastic properties (e.g. Gamstedt et al. 2002). For the off-axis properties, Hashin's concentric cylinder model is more accurate (Hashin 1979). This model has been used by Neagu et al. (2006a) to back-calculate the contributing stiffness of wood fibers to the stiffness of composites, and thereby ranking different chemical treatments of wood fibers with respect to composite stiffness. An example is shown in Fig. 12, where the effect of bleaching and retained lignin (characterized by the kappa number) on the fiber stiffness contribution is plotted. This serves as an illustration on how a micromechanical approach can be used to find the optimal bleaching level and hydrolization level irrespective of the fiber content and fiber orientation in the composite. These last two parameters may be hard to control in a reproducible manner in the manufacturing of composites.

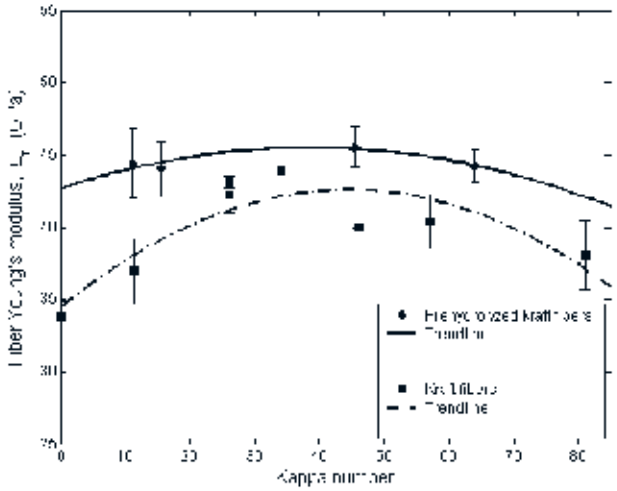

Fig. 12. The effect of kappa number on the longitudinal Young's modulus of laboratory softwood kraft and prehydrolyzed kraft fibers. Neagu et al. 2006a.

8.2. Effect of porosity. The predictions of the volumetric composition of composites, as presented in a previous section, can be integrated with micromechanical models. Typically, in these models, the fiber volume fraction (V_f) is used as the sole parameter to characterize the volumetric composition of the composites. This is however not optimal in the case of composites containing a significant amount of porosity, such as cellulose fiber composites, since the sum of V_f and V_m is then not equal to 1, and V_m can therefore not be calculated as ($1-V_f$). Moreover, in terms of composite manufacturing, V_f is not an easily controllable parameter, but it depends on the amount of porosity created in the composites during manufacturing. By contrast, the fiber weight fraction (W_f) is not affected by the porosity created, and W_f can therefore be precisely controlled prior to fabrication. In addition, W_f can in principle be varied in the whole range from 0 (no fibers) to 1 (only fibers), and this cannot be done for V_f since this parameter has a limiting maximum value, which is below 1 (see Fig. 10). Thus, altogether, it is more appropriate to use W_f as an indirect parameter for the volumetric composition in the composites, and this can be accomplished by implementing the already-presented volumetric composition model (see section 7) into a micromechanical model. This has been done in the study by Madsen et al. (2009b) by applying the widely used rule of mixtures model for predicting stiffness of composites. A modified version of the rule of mixtures model was used in which the effect of porosity giving stress concentrations in the composites was included. In the present paper, the equations of the model will not be presented, but only examples of predicted volumetric compositions and stiffnesses of composites will be shown.

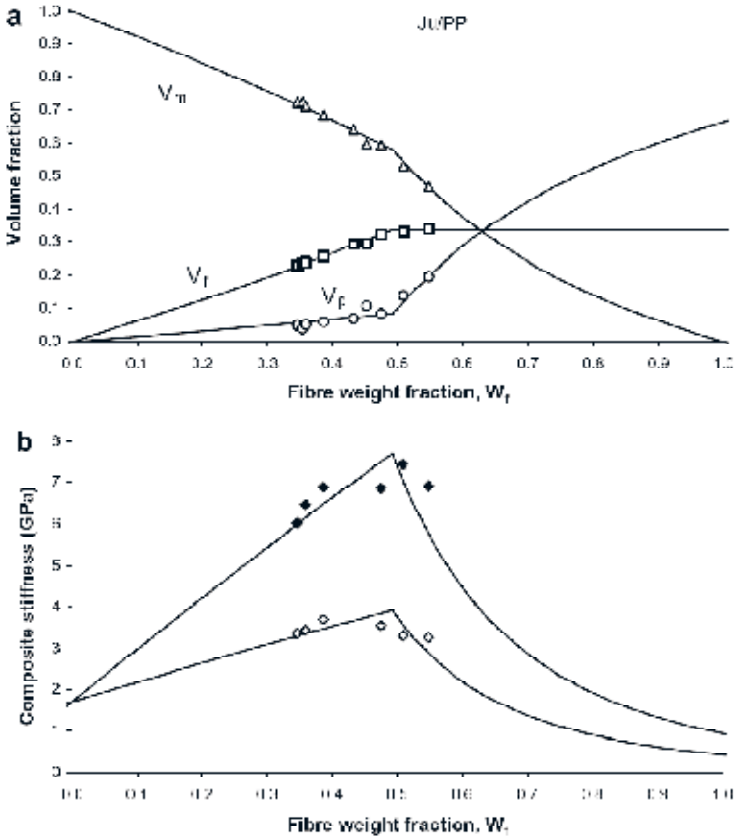

Fig. 13. Experimental data and model predictions of (a) volumetric composition and (b) stiffness as a function of the fiber weight fraction of jute fiber/polypropylene composites. Stiffness is measured along (upper data points) and transverse (lower data points) to the preferred fiber direction of the composites. Madsen et al. 2009b.

Figs. 13 and 14 show examples of experimental data, in addition to integrated model predictions of the volumetric compositions and stiffnesses of two types of plant fiber composites: jute fiber/polypropylene and flax fiber/polypropylene. The fiber preforms used for both composites were non-woven mats which had a preferred fiber orientation in one of the two main planar directions, which resulted in a difference in stiffness in the two directions. It can be observed in both Figs. 13a and 14a that the volumetric composition of the composites is well predicted by the model lines. The transition W_f is determined to be 0.49 and 0.52 for the jute and flax fiber composites, respectively. The modeling of stiffness properties was done by using the predicted volumetric composition as input to the modified rule of mixtures model. The difference in stiffness along and transverse to the preferred direction of the non-woven mats was included by using different values of the fiber orientation efficiency factor (Madsen et al. 2009b).The rule of mixtures model was fitted to the experimental data by using the fiber stiffness as the only fitting parameter. The determined values of the fiber stiffness were 47 and 53 GPa for the two types of cellulose fiber composites. This is within the range of 20-70 GPa typically reported for stiffness

of the bast type of cellulose fibers, such as jute and flax fibers (Lilholt and Lawther 2000). It can be observed that the experimental values of stiffness in both of the two main planar directions are well supporting the trend of the model lines showing a maximum stiffness at the transition fiber weight fraction. Thus, it is demonstrated that *the transition fiber weight fraction is a valuable design parameter since it determines the best possible combination of a high fiber volume fraction and a low porosity leading to the maximum obtainable stiffness.*

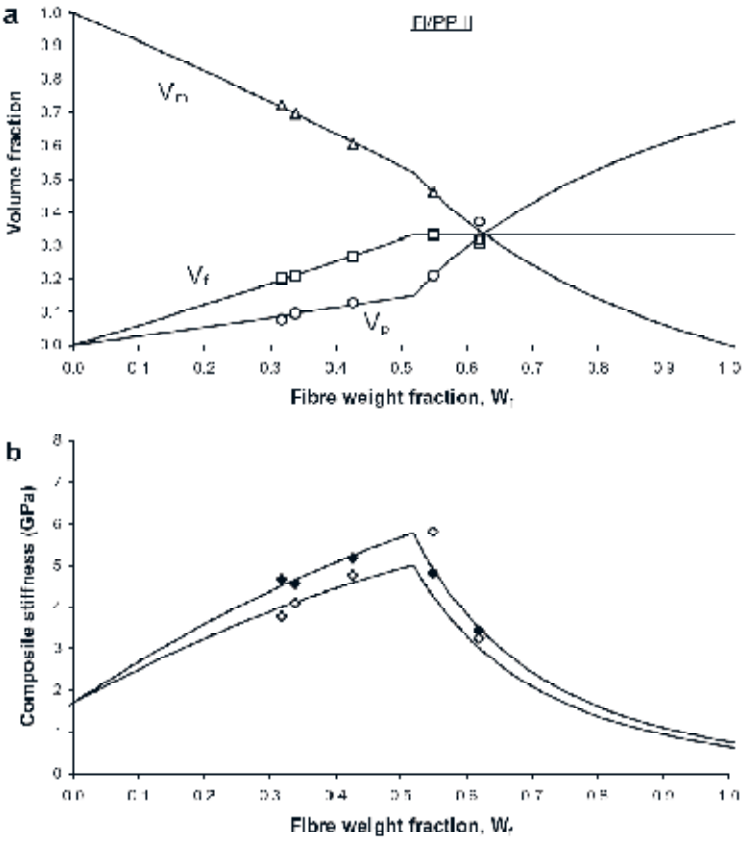

Fig. 14. Experimental data and model predictions of (a) volumetric composition and (b) stiffness as a function of the fiber weight fraction of flax fiber/polypropylene composites. Stiffness is measured along (upper data points) and transverse (lower data points) to the preferred fiber direction of the composites. Madsen et al. 2009b.

8.3. Concluding remarks. The above-outlined two micromechanical approaches to predict the stiffness of composites may be used both to back-calculate the effective fiber stiffness from tensile tests of composites, and to predict the stiffness of composites with an arbitrary lay-up. Once validated, the developed micromechanical models for stiffness and to some extent also strength for cellulose fiber composites, can be used to provide better guidelines in the microstructural design of materials, aiming for improved mechanical performance. For instance, classical laminate theory is an example of a modeling approach that has proven to be very efficient in the design of carbon fiber composite laminates for aeronautical applications.

However, further research needs still to be done to develop micromechanical design tools for composites based on cellulose fibers. The main reason is that these composites have a more irregular microstructure, with a rather large variation of fiber properties and geometries.

9. SPECIAL ISSUE: HYGROMECHANICAL PROPERTIES OF COMPOSITES

Compared with composites with conventional fibers, the Achilles' heel of cellulose fiber composites is their propensity to take up water, swelling, dimensional instability, and the subsequent degradation in mechanical properties due to softening or even microbial degradation. This hydrophilicity is due to the abundance of available hydroxyl groups in hemicellulose, amorphous cellulose and surface of cellulose crystallites. For certain specific applications, the moisture sensitivity could even be considered an advantage, e.g. sanitary tissues, moisture actuators, etc. For structural materials, the moisture sensitivity is generally considered to be a disadvantage, and should be reduced, if possible. This could be done by cross-linking of the cell wall polymers, use of a stiff and hydrophobic matrix, and encapsulation of the composite materials with an impermeable cover. Prevention of moisture ingress leads to retained stiffness and strength, since moisture usually act as a softener, breaking the hydrogen bonds and facilitating molecular movements.

How the swelling of the fibers affects the dimensional stability of the composite is more complicated due to the fibrillar and in some cases random structure of the fiber assembly. One way to isolate the hygroexpansion of the fibers, and quantify its contribution to the hygroexpansion of the composite, is to use a micromechanical model. These are similar to models primarily developed for thermal expansion and residual stresses in ceramic-matrix composites. Thermal expansion and hygroexpansion is governed by the same physical equations, where the hygrothermal strains are proportional to the temperature and moisture content, respectively. Since hygroexpansion is intimately linked with the elastic properties of the constituents, the latter need to be characterized before any conclusions can be made on how the hygroexpansion coefficients of the constituents affect expansion of the composite material.

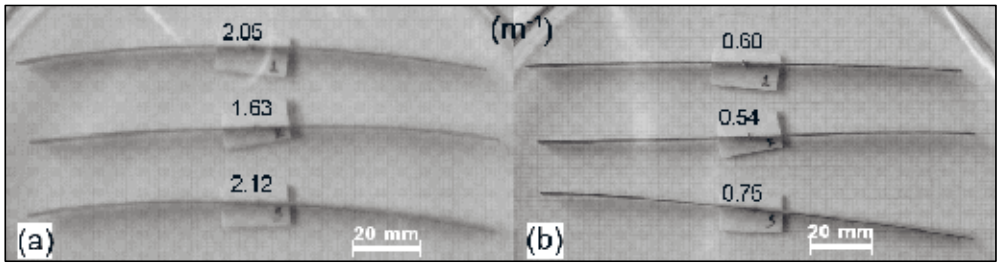

Fig. 16. Measured curvature for three non-symmetric specimens of cellulose composites at (a) 0% RH and (b) 50% RH. The specimens are curled around the longitudinal axis, i.e. the machine direction of the fiber mat. The curvature values are given in m^{-1}. Neagu et al. 2005.

A particular problem in composite applications is when the structure curls as the relative humidity changes after manufacturing or in use. A micromechanical approach would be useful to quantify the curl, and suggests ways to suppress this kind of buckling. It could also be used to

back-calculate the contribution of the fibers to the curl, and thereby provide a method to select fibers that prevents this deformation mechanism. Analogous to the laminate stiffness, the hygroexpansion properties of fibers may be determined from curl measurements. Hygroscopic strains in the laminate result from changes in the moisture content of the laminate. These strains are assumed to depend linearly on the moisture content over the humidity range under investigation. This proportionality is given by the coefficients of moisture expansion. If the laminate is completely free to expand, bend and twist when subjected to a change in moisture content ΔC, from a given moisture content C_1 to another C_2, the relationship between the changes in fictitious hygroscopic forces and moments $\{\Delta N^{\mathrm{H}}\}$ and $\{\Delta M^{\mathrm{H}}\}$ that produce the changes in the midplane strains $\{\Delta\varepsilon^0\}$ and plate curvatures $\{\Delta\kappa\}$ can be expressed as:

$$\begin{Bmatrix} \Delta N^{\mathrm{H}} \\ \Delta M^{\mathrm{H}} \end{Bmatrix} = \begin{bmatrix} A & B \\ B & D \end{bmatrix} \begin{Bmatrix} \Delta\varepsilon^0 \\ \Delta\kappa \end{Bmatrix} \tag{3}$$

The $[A]$, $[B]$ and $[D]$ matrices are conventionally defined as the extensional stiffness matrix, the extension-bending coupling stiffness matrix and the bending stiffness matrix, respectively. The hygroscopic forces and moments can be evaluated from the hygroscopic strains induced in the laminate by a uniform change in moisture content ΔC of the laminate. By integration of the lamina stresses induced by the constraints placed on its deformation by adjacent layers, the hygroscopic force and moment vectors can be calculated as:

$$\{\Delta N^{\mathrm{H}}\} = \Delta C \sum_{i=1}^{n} [\bar{Q}]_i \{\bar{\beta}\}_i (z_i - z_{i-1}) \tag{4}$$

and

$$\{\Delta M^{\mathrm{H}}\} = \frac{\Delta C}{2} \sum_{i=1}^{n} [\bar{Q}]_i \{\bar{\beta}\}_i (z_i^2 - z_{i-1}^2) \tag{5}$$

where $[\bar{Q}]_i$ is the effective global stiffness matrix of layer i, $\{\bar{\beta}\}_i$ is a vector with the coefficients of moisture expansion for layer i, and z_i are layer coordinates with the origin of the z-coordinate chosen in the midplane. From manipulation of equations (3) to (5), the hygroexpansion coefficients of the cellulose fibers can be estimated.

Using this methodology, curl measurements of composite or fiber-mat strips (cf. Fig. 16) can be used to determine the transverse hygroexpansion coefficient of cellulose fibers which turns out to be approximately 0.10 strain per relative moisture content (Neagu et al. 2005). This is in accordance with a few scarce data found in the literature on the hygroexpansion properties of cellulose fibers (refs. in Almgren et al. 2010). More work along this line would be useful to assess physicochemical treatments of fibers to suppress moisture swelling, such as hornification and cell-wall cross-linking by e.g. butyl tetracarboxylic acid.

Glass and carbon fibers do not take up any moisture, although glass fibers are sensitive to environmental stress corrosion in the presence of moisture and tensile stress (Rodriguez 1987). However, the degradation processes in glass fibers is insignificant in comparison with those for cellulose fibers in a moist environment. The deleterious process due to moisture is larger for wood fibers than for plant fibers, since the former contains a larger relative amount of hemicellulose which is the most hydrophilic polymer in the cell wall.

10. SPECIAL ISSUE: CELLULOSE NANOFIBER COMPOSITES

In recent years, considerable attention has been directed towards composites made from cellulose nanofibers (e.g. Eichhorn et al. 2010). The cell wall is structured like composites with cellulose microfibrils with lateral dimensions in the 10-100 nm range and axial dimensions in the micrometre range, and with a matrix of hemicellulose and lignin. The cellulose microfibrils can be used as reinforcement to produce cellulose nanofiber composites. The idea is to achieve considerable improvements in engineering properties with the addition of nanofibers, way beyond those obtained with conventional composites based on fibers in the micrometre range. This can be attributed to the high specific surface area of the nanoscale fibers, which will affect the properties of the surrounding matrix. The success of nanocomposites is particularly obvious if only a minute addition of fibers is considered, and the dispersion of nanofibers is preserved.

Carbon nanotubes have shown great promise for a relatively long time, but have yet to deliver in large volume applications (Dzenis 2004). A difference between cellulose nanofibers and carbon nanotubes is the ability of the cellulose nanofibers to bond to each other, by hydrogen bonding, whereas the carbon nanotube surfaces are very inert. The cellulose nanofibers can therefore form a very strong network, and furthermore also bond well to polymer matrix materials with polar groups. This also leads to processing difficulties, since the cellulose nanofibers tend to aggregate and take a long time to dry after wet processing. Processability and performance are thus complementary and mutually opposing behaviors. The functional hydroxyl end-groups of the fibers can however be modified to improve dispersion and processability, although this is accompanied with increased costs. The main challenges for cellulose nanofiber composites are probably to learn how to manufacture bulk composite components with retained fiber slenderness. The raw material is the cellulose fibers themselves, from wood pulp or plant fibers, making the raw material costs negligible compared with processing costs.

11. SUMMARISED COMPARISON BETWEEN FIBERS

As shown in the sections above, wood and plant fibers differ in some respects and are similar in others. Thus, depending on the intended application, one particular fiber type is more suitable than the other. In the following, a summarized comparison is given to highlight some advantages of wood versus plant fibers, and vice versa. Similarly, cellulose fibers will be compared to their synthetic counterparts, glass and carbon fibers.

Advantages of wood fibers, as compared with plant fibers:

- Low cost, readily available from pulp mills.
- Relatively short fibers mean better processability.
- Mature infrastructure available in pulp and paper mills to produce large quantities at low cost.
- Preforms can be made using paper-making technologies.
- Rather uniform batches of pulp qualities can be achieved.
- Does not compete with cultivation of food crops.

Advantages of plant fibers compared with wood fibers:

- High cellulose content, high degree of cellulose crystallinity, low microfibril angle, small lumen means excellent mechanical properties.
- Textile technologies can be used to produce yarns, weaves, non-crimp fabrics etc.
- It is possible to control fiber orientation and lay-up.

- High productivity and yield.

Despite the aforementioned differences, wood and plant fibers have more in common than in what differ them from one another. Some advantages of cellulose fibers as compared with glass and carbon fibers can be mentioned:

- Renewable.
- Biodegradable.
- Light, i.e. the composites have improved specific properties which are important in vehicles and packaging.
- Low cost raw materials.

The main disadvantages of cellulose fibers compared with glass and carbon fibers are:

- Moderate mechanical properties.
- Sensitivity to moisture, leading to water uptake, softening and susceptibility to fungal attack.
- The composite manufacturing techniques are not yet as developed and tuned as for the more well-established glass and carbon fiber composites.

The above lists are by no means comprehensive, but only serve to show some of the traits of wood and plant fibers in an applied composite context. In further development of cellulose fiber composites, both advantages and drawbacks play an important role. The specific advantages guide which application areas that are relevant. For instance, the combination of low cost, renewability and biodegradability make cellulose composites a suitable material for packaging applications. The drawbacks limit their application. Research on how to alleviate these shortcomings can expand the proliferation of cellulose fibers. If we could modify cellulose fibers to become less hydrophilic, and process the fibers to retain better their innate high strength and stiffness, they would also be potential reinforcement fibers in advanced structural outdoor applications, e.g. in rotor blades for wind turbines.

REFERENCES

Almgren, K.M., Gamstedt, E.K., Berthold, F. and Lindström, M. (2009b). Moisture uptake and hygroexpansion of wood fiber composite materials with polylactide and polypropylene matrix materials. Polym. Compos. 20, 1809-1816.

Almgren, K.M., Gamstedt, E.K., Nygård, P., Malmberg, F., Lindblad, J., Lindström, M. (2009a). Comparison of stress-transfer mechanisms in paper sheets and composites made from resin-impregnated sheets. Int. J. Adhes. Adhes. 29, 551-557.

Almgren, K.M., Gamstedt, E.K., Varna, J. (2010). Contribution of wood fibers to the moisture-induced dimensional instability of composite plates. Polym. Compos. 31, 762-771.

Anagnost S.E., Mark R.E. and Hanna R.B. (2002). Variation of microfibril angle within individual tracheids. Wood and Fiber Science. 34, 337-349.

Andersen T.L. and Plackett D. (2002). Polymer composite product, a process for the manufacture thereof and use of the product. International Application Number: PCT/DK02/00085. International Publication Number: WO 02/064670 A1. International Publication Date: 22 August 2002.

Aslan M., Chinga-Carrasco G., Sørensen B.F., Madsen B. (2011). Strength variability of single flax fibers. Journal of Materials Science, DOI 10.1007/s10853-011-5581-x.

Bengtsson, M., Le Baillif, M., Oksman, K. (2007). Extrusion and mechanical properties of highly filled cellulose fiber–polypropylene composites. Compos. Part A 38, 1922-1931.

Bledzki A.K., Sperber V.E. and Faruk O. (2002). Natural and wood fiber reinforcement in polymers. Rapra Review Reports. Vol. 13; No. 8.

Bottoli F., Pignatti L. (2011). Design and processing of structural components in biocomposite materials – Case study: Rotor blade for wind turbine cars. Master student project, Feb-Aug 2011. Materials Research Division, Risø National Laboratory for Sustainable Energy, Technical University of Denmark. On-going work.

Broge J.L. (2000). Natural fibers in automotive components. Automotive Engineering International. 108, 120-.

Bunsell A.R. and Renard J. (2005). Fundamentals of fiber reinforced composite materials. Institute of Physics Publishing Ltd, London, United Kingdom.

Clemons C.M. (2000). Woodfiber-plastic composites in the United States – History and current and future markets. In the Proceedings of the 3rd International Wood and Natural Fiber Composites Symposium. Kassel, Germany. September, 2000. p. 1-7.

Cox, H.L. (1952). The elasticity and strength of paper and other fibrous material. British Journal of Applied Physics. 3,72-79.

Cox H.L. and Pepper K.W. (1944). J. Soc. Chem. Ind., 63, 150.

Duanmu, J., Gamstedt, E.K., Rosling, A. 2007. Synthesis and preparation of composites of crosslinked allylglycidyl-ether modified starch reinforced by wood fibers. Starch Stärke, 59, 523-532.

Dzenis, Y. (2004). Spinning Continuous Fibers for Nanotechnology. Science. 304: 1917-1919.

Eichhorn, S., Dufresne, A., Aranguren, M., Marcovich, N., Capadona, J., Rowan, S., Weder, C., Thielemans, W., Roman, M., Renneckar, S., Gindl, W., Veigel, S., Keckes, J., Yano, H., Abe, K., Nogi, M., Nakagaito, A., Mangalam, A., Simonsen, J., Benight, A., Bismarck, A., Berglund, L., Peijs, T. (2010). Review: Current international research into cellulose nanofibers and nanocomposites. J. Mater. Sci. 45: 1-33.

Eichhorn, S.J., Baillie, C.A., Zafeiropoulos, N., Mwaikambo, L.Y., Ansell, M.P., Dufresne, A., Entwistle, K.M., Herrera-Franco, P.J., Escamilla, G.C., Groom, L., Hughes, M., Hill, C., Rials, T.G., Wild, P.M. (2001). Review: Current international research into cellulosic fibers and composites. Journal of Materials Science. 36: 2107-2131.

Ellison G.C. and McNaught R. (2000). The use of natural fibers in nonwoven structures for applications as automotive component substrates. Research and Development Report. Ministry of Agriculture Fisheries and Food Agri – Industrial Materials. Reference NF0309. London, United Kingdom.

Eriksen M. and Pallesen B.E. (2002). New generation airforming for flax and hemp. Nonwovens World. June-July. p. 80-84.

Erkkilä, A.-L., Pakarinen, P., Odell, M. 1998. Sheet forming studies using layered orientation analysis. Pulp Paper Canada. 99: 81-85.

Fratzl, P, Weinkamer, R. 2007. Nature's hierarchical materials. Progress Mater. Sci. 52: 1263-1334.

Gadala-Maria, F., Parsi, F. 1993. Measurement of fiber orientation in short-fiber composites using digital image processing. Polym. Compos. 14: 126-131.

Gamstedt E.K, Berglund L.A. and Peijs T. (1999). Fatigue mechanisms in unidirectional glass-fiber-reinforced polypropylene. Composites Science and Technology. 59: 759-768.

Gamstedt, E.K., Sjöholm, E., Neagu, C., Berthold, F., Lindström, M. (2002). Effects of fiber bleaching and earlywood-latewood fraction on tensile properties of wood-fiber reinforced vinyl ester" in Proceedings of the 23rd Risø International Symposium on Materials Science: Sustainable Natural and Polymeric Composites - Science and Technology, Lilholt, H. et al. (Eds.), Risø National Laboratory, Roskilde,, pp. 185-196.

Gassan J. and Bledzki A.K. (1999a). Effect of cyclic moisture absorption desorption on the mechanical properties of silanized jute-epoxy composites. Polymer Composites. 20: 604-611.

Gassan J. and Bledzki A.K. (1999b). Influence of fiber surface treatment on the creep behavior of jute fiber-reinforced polypropylene. Journal of Thermoplastic Composite Materials. 12: 388-398.

Gassan J., Chate A. and Bledzki A.K. (2001). Calculation of elastic properties of natural fibers. Journal of Materials Science. 36: 3715-3720.

Goutianos S., Peijs T., Nyström B., Skrifvars M. (2006). Development of flax fiber based textile reinforcements for composite applications. Applied Composite Materials; 13: 199-215.

Grosberg P. and Iype C. (1999). Yarn production. Theoretical aspects. The Textile Institute, Manchester, United Kingdom.

Hamidi YK, Aktas L, Altan MC. Three-dimensional features of void morphology in resin transfer molded composites. Comp Sci Tech 2005; 65: 1306-1320.

Hashin, Z. (1979). Analysis of properties of fiber composites with anisotropic constituents. J. Appl. Mech. 46: 543-550.

Hobson R.N., Hepworth D.G. and Bruce D.M. (2001). Quality of fiber separated from unretted hemp stems by decortification. Journal of Acricultural Engineering Research. 78: 153-158.

Hofstetter, K., Hellmich, C., Eberhardsteiner, J. (2005). Development and experimental validation of a continuum micromechanics model for the elasticity of wood. Eur. J. Mech. A Solids. 24: 1030-1053.

Hornsby P.R., Hinrichsen E. and Tarverdi K. (1997). Preparation and properties of polypropylene composites reinforced with wheat and flax straw fibers. Part II. Analysis of composite microstructure and mechanical properties. Journal of Materials Science. 32: 1009-1015.

Judd NCW, Wright WW. Voids and their effect on the mechanical properties of composites – an appraisal. SAMPE journal 1978; January/February: 10-14.

Karus M., Kaup M. and Ortmann S. (2002). Use of natural fibers in the German and Austrian automotive industry. Market survey 2002: Status, analysis and trends. Nova-Institute GmbH, Hürth, Germany.

Khalil H.P.S.A., Ismail H., Rozman H.D. and Ahmad M.N. (2001). The effect of acetylation on interfacial shear strength between plant fibers and various matrices. European Polymer Journal. 37: 1037-1045.

Kim HS, Pourdeyhimi B, Abhiraman A, Desai P. (2000). Characterization of structural changes in non-woven fabrics during load–deformation experiments. J Text Apparel Tech Manage. 1:1–6.

Klein W. (1998). The technology of short-staple spinning. 2nd ed. The Textile Institute, Manchester, United Kingdom.

Liitiä T., Maunu S.L., Hortling B., Tamminen T., Pekkala O.and Varhimo A. (2003). Cellulose crystallinity and ordering of hemicelluloses in pine and birch pulps as revealed by solid state NMR spectroscopic methods. Cellulose 10: 307–316. *Cited in Thygesen et al. 2005.*

Lilholt H. and Lawther J.M. (2000). Natural organic fibers. In Comprehensive Composite Materials (6 vols). Eds. A. Kelly and C. Zweben. Elsevier Science. Vol. 1, chap. 10, p. 303-325.

Lindhagen, J., Berglund, L. (1998). Microscopical damage mechanisms in glass fiber reinforced polypropylene. J. Appl. Polym. Sci. 69: 1319-1327.

Lindström, M., Berthold, F., Gamstedt, K., Varna, J. and Wickholm, K. (2008). Hierarchical design as a tool in materials development. In: Proceedings of the 10th International Conference on Progress in Biofiber Plastic Composites, Toronto, 7 p.

Madsen B, Lilholt H. (2002). Compaction of plant fiber assemblies in relation to composite fabrication. In: Proceedings of the 23rd Risø International Symposium on Materials Science. Sustainable natural and polymeric composites – Science and technology. Risø National Laboratory, Roskilde, Denmark, p. 239-250.

Madsen B. and Lilholt H. (2003). Physical and mechanical properties of unidirectional plant fiber composites – an evaluation of the influence of porosity. Composites Science and Technology. 63: 1265-1272.

Madsen B., Hoffmeyer P. and Lilholt H. (2007a). Hemp yarn reinforced composites – II. Tensile properties. Composites Part A. 38: 2204-2215.

Madsen B., Hoffmeyer P., Thomsen A.B. and Lilholt H. (2007b). Hemp yarn reinforced composites – I. Yarn characteristics. Composites Part A. 38: 2194-2203.

Madsen B., Lilholt H., Thygesen A., Arnold E., Weager B., Joffe R. (2009a). Aligned flax fiber/polylactate composites – A materials model system to show the potential of biocomposites in engineering applications. Journal of Nanostructured Polymers and Nanocomposites. 4: 139-145.

Madsen B., Thygesen A., Lilholt H. (2007c). Plant fiber composites – porosity and volumetric interaction. Composites Science and Technology. 67: 1584-1600.

Madsen B., Thygesen A., Lilholt H. (2009b). Plant fiber composites – porosity and stiffness. Composites Science and Technology. 69: 1057-1069.

Marcovich, N.E., Reboredo, M.M., Aranguren, M.I. (1996). Composites from sawdust and unsaturated polyester . J. Appl. Polym. Sci. 61: 119-124.

Mishra S., Naik J.B. and Patil Y.P. (2000). The compatibilising effect of maleic anhydride on swelling and mechanical properties of plant-fiber reinforced novolac composites. Composites Science and Technology. 60: 1729-1735.

Mohanty A.K. and Misra M. (1995). Studies on jute composites – A literature review. Polymer Plastics Technology and Engineering. 34: 729-792.

Myers G.E., Chahyadi I.S., Coberly C.A. and Ermer D.S. (1991). Wood flour/polypropylene composites: Influence of maleated polypropylene and process and composition variables on mechanical properties. International Journal of Polymeric Materials. 15: 21-44.

Månson JAE, Wakeman MD, Bernet N. (2000). Composite processing and manufacturing – An overview. In: Kelly A, Zweben C, editors. Comprehensive Composite Materials, vol. 2, chap. 2, p. 577-607, Elsevier Science.

Nairn, J.A. (1997). On the use of shear-lag methods for analysis of stress transfer in unidirectional composites. Mech. Mater. 26: 63-80.

Neagu, C., Gamstedt, E.K., Berthold, F. (2006a). Stiffness contribution of various wood fibers to composite materials. Journal of Composite Materials. 40: 663-699.

Neagu, R.C. and Gamstedt, E.K, (2007). Modeling of effects of ultrastructural morphology on the hygroelastic properties of wood fibers. Journal of Materials Science. 42: 10254-10274.

Neagu, R.C., Gamstedt, E.K., Bardage, S.L. and Lindström, M. (2006b). Ultrastructural features affecting mechanical properties of wood fibers. Wood Material Science & Engineering, 1: 146-170.

Neagu, R.C., Gamstedt, E.K., Lindström, M. (2005). Influence of wood-fiber hygroexpansion on the dimensional instability of fiber mats and composites", Compos. Part A, 36: 772-788.

Nättinen K., Hyvärinen S., Joffe R., Wallström L., Madsen B. (2010). Naturally compatible: Starch acetate/cellulosic fiber composites. I. Processing and properties. Polymer Composites. 31: 524-535.

Oksman K. (2000). Mechanical properties of natural fiber mat reinforced thermoplastic. Applied Composite Materials. 7: 403-414.

Page, D.H., El-Hosseiny, F., Winkler, K. (1971). Behaviour of single wood fibers under axial tensile strain. Nature. 229: 252-253.

Pandey, J.K., Ahn, S.H., Lee, C.S., Mohanty, A.K., Misra, M. (2010). Recent advances in the application of natural fiber based composites. Macromol. Mater. Eng. *295*: 975-989.

Parikh D.V., Calamari T.A., Sawhney A.P.S., Blanchard E.J., Screen F.J., Myatt J.C., Muller D.H. and Stryjewski D.D. (2002). Thermoformable automotive composites containing kenaf and other cellulosic fibers. Textile Research Journal. 72: 668-672.

Perry D.R. (1985). Identification of textile materials. 7th ed. The Textile Institute, Manchester, United Kingdom.

Pratten NA. (1981). Review. The precise measurement of the density of small samples. J Mater Sci. 16: 1737-1747.

Rask M. and Madsen B. (2011). Twisting of fibers in yarns for natural fiber composites. In Proceedings of the 18th International Conference on Composite Materials, Korea, August 2011.

Rask M., Madsen B., Sørensen B.F., Julie F., Martyniuk K. and Lauridsen E.M. (2011). In situ observations of microscale damage evolution in natural fiber composites. Submitted to Composites Part A.

Ridruejo, A., Gonzalez, C., LLorca, J. (2010). Damage micromechanisms and notch sensitivity of glass-fiber non-woven felts: An experimental and numerical study. J. Mech. Phys. Solids. 58: 1628-1645.

Rodriguez, E.L. (1987). Corrosion of glass fibers. J. Mater. Sci. Lett. 718-720.

Rowell, R. (1984). The Chemistry of Solid Wood, American Chemical Society, Washington, USA.

Salmén, L. (2004). Micromechanical understanding of the cell-wall structure, Comptes Rendus Biologies. 327: 873-880.

Salmén, L., Burgert, I. (2009). Cell wall features with regard to mechanical performance. A review. Holzforschung 63: 121-129.

Salmén, L., de Ruvo, A. (1985). A model for the prediction of fiber elasticity. Wood Fiber Sci. 17: 336-350.

Sankari H.S. (2000). Comparison of bast fiber yield and mechanical fiber properties of hemp (Cannabis sativa L.) cultivars. Industrial Crops and Products. 11: 73-84.

Siau J.F. (1995). Wood: Influence of moisture on physical properties. Department of Wood Science and Forest Products, Virginia Polytechnic Institute and State University, USA.

Sjöström, E. (1993). Wood Chemistry, Fundamentals and Applications (2nd Ed.), Academic Press, San Diego, USA.

Thomason J.L.(2005). The influence of fiber length and concentration on the properties of glass fiber reinforced polypropylene: 6. The properties of injection moulded long fiber PP at high fiber content. Comp A; 36: 995-1003.

Thygesen A,., Madsen B., Bjerre A.B., Lilholt H. (2011). Cellulosic fibers: effect of processing on fiber bundle strength. Journal of Natural Fibers. In press.

Thygesen, A., Oddershede, J., Lilholt, H., Thomsen, A.B., Ståhl, K. (2005). On the determination of crystallinity and cellulose content in plant fibers. Cellulose 12, 563–576.

Thygesen, A., Thomsen, A.B., Daniel, G., Lilholt, H. (2007). Comparison of composites made from fungal defibrated hemp with composites of traditional hemp yarn. Ind. Crops Prod. 25: 147-159.

Toftegaard H. (2002). Tensile testing of jute/PP laminates. Risø Report: Risø-I-1824(EN), Risø National Laboratory, Materials Research Department, Denmark; 2002. 52 p.

Van de Weyenberg I., Ivens J., De Coster A., Kino B., Baetens E. and Verpoest I. (2003). Influence of processing and chemical treatment of flax fibers on their composites. Composites Science and Technology. 63: 1241-1246.

Varna J, Joffe R, Berglund LA. (1995). Effects of void on failure mechanisms in RTM laminates. Comp Sci Tech. 53: 241-249.

Wadsö L. (1993). Studies of water vapor transport and sorption in wood. Ph.d.-thesis. Building Materials, Lund University, Sweden.

Wisnom RW, Reynolds T, Gwilliam N. (1996). Reduction in interlaminar shear strength by discrete and distributed voids. Comp Sci Tech. 56: 93-101.

Woodhams, R.T., Thomas, G., Rodgers, D.K. (1984). Wood fibers as reinforcing fillers for polyolefins. Polym. Eng. Sci. 24: 1166-1171.

Zafeiropoulos N.E., Baillie C.A. and Hodgkinson J.M. (2002). Engineering and characterisation of the interface in flax fiber/polypropylene composite materials. Part II. The effect of surface treatments on the interface. Composites: Part A. 33: 1185-1190.

Proceedings of the 32nd
Risø International Symposium on Materials Science:
Composite materials for structural performance:
Towards higher limits
Editors: S. Fæster, D. Juul Jensen,
B. Ralph, B.F. Sørensen
Risø National Laboratory for Sustainable Energy,
Technical University of Denmark, 2011

MECHANICAL PROPERTIES OF CARBON-CARBON COMPOSITES-EXPERIMENTS AND SIMULATIONS

P. Mahajan and R. Sharma

Department of Applied Mechanics, Indian Institute of Technology
Delhi, India

ABSTRACT

The procedure for determining a homogenized Young's modulus of a 3-D orthogonal carbon-composite composite is laid out. X-ray tomography is performed to determine the dimensions of bundles and defects in the composite after manufacturing. Voids, intra-bundles, inter-bundles and interfacial cracks are visible in the scanned images. Push-out and pull-out tests are performed on composite specimens and a shear lag model is used to determine the interfacial fracture energy. These tests are then simulated by a finite element model with cohesive elements used to represent the interface. An iterative approach is used to determine the fracture energy, shear strength and coefficient of friction of a cohesive zone model. These properties are next used in the analysis of a unit cell with periodic boundary conditions for determining the Young's modulus. The unit cell of the 3-D composite is obtained from tomography images, although a number of features have been neglected during the analysis to keep computations manageable.

1. INTRODUCTION

Multidirectional composites are attractive for making parts and structures that need to withstand multidirectional mechanical stresses and thermal stresses. 3-D reinforcements are commonly used in carbon–carbon (C/C) composites employed in aerospace applications, such as rocket engines and re-entry noses cone, etc. In these applications ablation of the material occurs and experiments show that multidirectional carbon composites have a lower ablation rate as compared to other types. The performance of multidirectional composites is a function of such variables as choice of fiber, fiber architecture, type of matrix material, and the temperature and pressure history experienced during the fabrication process. In the liquid impregnation route for manufacturing these composites a woven preform is passed through a series of high pressure impregnation, carbonization, and graphitization cycles to get the desired density of the product. Shrinkage in the matrix during carbonization results in cracks in the matrix. Also, different coefficients of thermal expansion of the fiber and matrix lead to debonding at the interface. Damage in the form of matrix cracking, debonding of fibers and fiber bundle interfaces occurring during manufacturing affects the properties adversely.

The elastic moduli for different architectures (2-directional, 3-direction orthogonal and plain woven) of C/C composites were experimentally determined by Mohamed, Hatta, Wakayama, Watanabe and Miyagawa (2003), Tensile and Iosipescu shear tests were performed by Siron and Lamon (1998), to determine mechanical properties of a 3-directional needle layered 8-harness satin weave C/C composite. The authors observed inter-fiber, inter-bundle and matrix cracks in the composite. Hatta, Goto, Ikegaki, Kawahara, Mohamed, and Hamada (2005[a]), observed that the Young's modulus increased with an increase in the composite density, and decreased with an increase in the heat treatment temperature. A comparison of tensile and compressive Young's moduli by Hatta, Goto and Aoki, (2005[b]) and Hatta, Taniguchi and Kogo, (2005[c]), showed that the ratio of the tensile modulus to the compressive modulus is about two. The homogenization theory, along with unit cell approach, has been used to predict the effective mechanical properties of C/C composites (2000, Piat and Schnack (2003)). Aubard, Cluzel, Guitard and Ladeveze, (2000) performed meso-mechanical modeling of 4-D C/C composites and also gave a damage mechanics based macro-mechanical model. Rao (2008) used asymptotic homogenization and periodic boundary conditions on a unit cell to study and compare three different architectures of C/C composites. The surface separation at the fiber bundle/matrix interface due to residual stresses was investigated using the cohesive zone model.

It is generally accepted that the fiber-matrix interfacial properties, such as, coefficient of friction, interfacial shear strength and interfacial fracture energy release rate have a significant influence on the fracture behavior of fiber-reinforced materials. Sakai, Matsuyama and Miyajima, (2000) have designed a novel geometry of tensile test to examine the interfacial fracture behavior of unidirectionally reinforced C/C composite materials. Domnanovich, Peterlik and Kromp, (1996), and Brandstetter, Peterlik, Kromp and Weiss (2003) studied the interfacial behavior of bidirectional, layered satin weave C/C composites and a 4D inplane C/C composite has been characterized by Valette, Rouby, and Tallaron, (2002). The interfacial properties were obtained by fitting a shear lag model (Gao, Mai, and Cotterell (1988)) to the experimentally observed load-displacement curves of pull-out and push-out tests Aoki, Yamane, Ogasawara, Ogawa, Sugimoto and Ishikawa, (2007) developed fiber bundle push-out and pullout test setups for interfacial characterization of a 3D C/C orthogonal composite at room as well as elevated temperatures. Rollin, Jouannigot, Lamon and Pailler, (2009) have conducted push-out and transverse tensile tests to confirm the pure shear and opening mode of the failure of a C/C composite. The specimens were examined under optical microscopy (OM) for the confirmation of the crack before loading and after ultimate failure. The contribution of the surface roughness to the interfacial shear stress was observed in push-out test.

X-ray computed tomography (CT) is a non destructive way to observe material artifacts and structure with a sufficient resolution and has been used to observe bundles in C/C composites (Aoki and 2007). Finite Element models of the pull-out test and push-out tests, reconstructed using the CT data, are analysed to determine the interfacial properties of the composite. These interfacial properties are used in the finite element analysis of a unit cell, to determine the mechanical properties of the composite using asymptotic homogenization. The unit cells, reconstructed from the CT data, are taken from different regions of C/C composite samples.

2. MATERIAL

C/C composites come in various architectures and arrangement of bundles in 3-D orthogonal C/C and 3-D satin weave as shown in figure 1. The 3D Orthogonal Hybrid C/C composite which is studied here was prepared using pitch (liquid impregnation) and consists of bundles of rectangular cross-section in the x and y directions and circular rods in the z-direction. The rods are made of 24,000 fibers and rectangular bundles contain 15,000 fibers. The fiber bundle

volume fraction is nearly 47% in the composite.

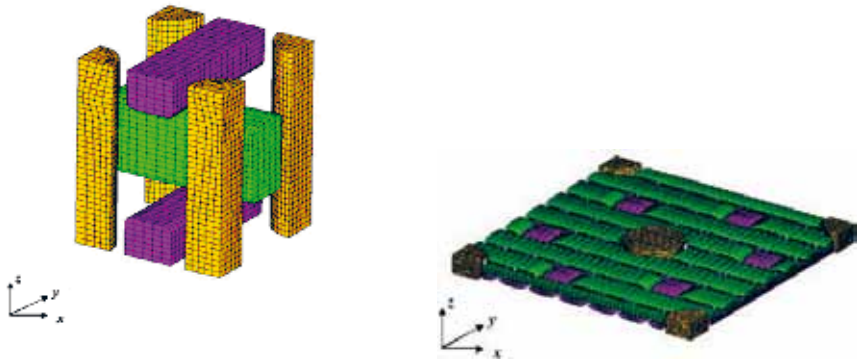

Fig.1. Stack of the bundles for 3D orthogonal and C/C composites.

3. X-RAY TOMOGRAPHY OF COMPOSITE SPECIMENS

The X-ray computed tomography (CT) is a non destructive way to observe the material artifacts and structure with a sufficient resolution. The CT scan facility available at the Snow and Avalanche Study Establishment (SASE), Manali, India was utilized for the X-ray tomography experiments. It consists of fan type X-ray source and can scan up to 1µm resolution. The details of the scan are given in Table 1. During the CT scan process the specimen rotates with a fixed rotation step up to 180 degrees and at each angular position shadow or projection images are captured by the detector.

Table 1: CT parameters used for 3D composite

X-raytube: energy/intensity		Radiograph acquisition		Reconstruction area		
Voltage (kV)	Current (mA)	Angular displacement (°)	Exposure time (ms)	Pixel size (µm)	Width (pixel)	Height (pixel)
80	100	0.30	1178	6.936	1028	1028

The projection images are saved as 16 bit TIFF files on disk. The cross-sectional images (slices) are reconstructed by utilizing 16 bit TIFF images through a reconstruction algorithm (SkyScan, 1172). The cross-sectional images, containing all the information about the actual material structure are stacked in three orthogonal directions. The 2D reconstructed images of the cross-section in z, x, and y directions for one of the pullout specimens are shown in Fig.2 a, b and c, respectively. Almost all the details of the internal material structure of composite can be seen in these images. The accuracy of the internal material structure depends on the resolution of image. The reconstructed images are imported to the Scan IP software (Simpleware, 2010) and the image processing is done to enhance the contrast between the phases. The imperfections are broadly divided into two categories; local and global imperfections. Local imperfections contain

defects like voids and cracks, where as global imperfections are referred to as cross-sectional distortions and misalignments.

The cracks are categorised in three different categories: 1) Interfacial cracks 2) Intra-bundle cracks, and 3) Matrix cracks. Some intra-bundle cracks are generated during the stacking or during the manufacturing of bundles. Interfacial cracks are generated by the thermal stress produced due to the mismatch in expansion coefficients of the fiber bundle and matrix. Matrix cracking is caused by a shrinkage stress. The network of cracks that develop in the composite is shown in Fig. 2, which is a scan of a pull-out specimen. In Fig. 2b the interfacial cracks present at the bundle and matrix interface, cover almost half the length of the bundle. In Fig.2c the interfacial crack propagates through the matrix and is likely to join the void. It is also observed that interfacial cracks in rectangular bundles generally enter and propagate through the matrix whereas in the rods in the z-direction the cracks remain on the interface. The propagation of the interfacial cracks, in the case of rectangular bundles, through the matrix makes the debonded surface highly rough. Transverse cracking is observed in the matrix and at some locations; interfacial cracks join the network of transverse cracks. The interfacial cracks of the bundle running in the transverse direction also join the interfacial crack network of the z-bundle.

Along with the cracks, the microstructure of the C/C composite also contains voids of different sizes. The porosity of the composite can be characterized into two types; bubble and micro-pores. The bubbles are present in pockets of the matrix, covering nearly half of its volume. On the other hand, the micro-pores are voids with a size less than 100 μm and are present inside the fiber bundles, at the bundle-matrix interface and in the rest of the matrix. Some micro-voids are also visible near the bundle-matrix interface with small gaps between them.

From the above study of the cracking network of C/C composite it is clear that the interface is partially damaged during the manufacturing process and interfacial cracks partially propagate through the matrix in x and y bundles. These cracks have highly rough surfaces which provide a high friction during the sliding process. Also the porosity near the interface accelerates the fracture process due to a stress concentration.

It can be concluded that there are mainly three forces contributing against the fiber movement during pull-out or push-out processes,

1) An adhesive force at the interface

2) A frictional force between debonded surfaces.

3) An anchorage force between cracked matrix blocks.

The fracture phenomenon is very complex and the experiments have been performed to get average interfacial shear stress and average fracture energy release rate. These tests were performed on z-bundles which are circular in cross-section.

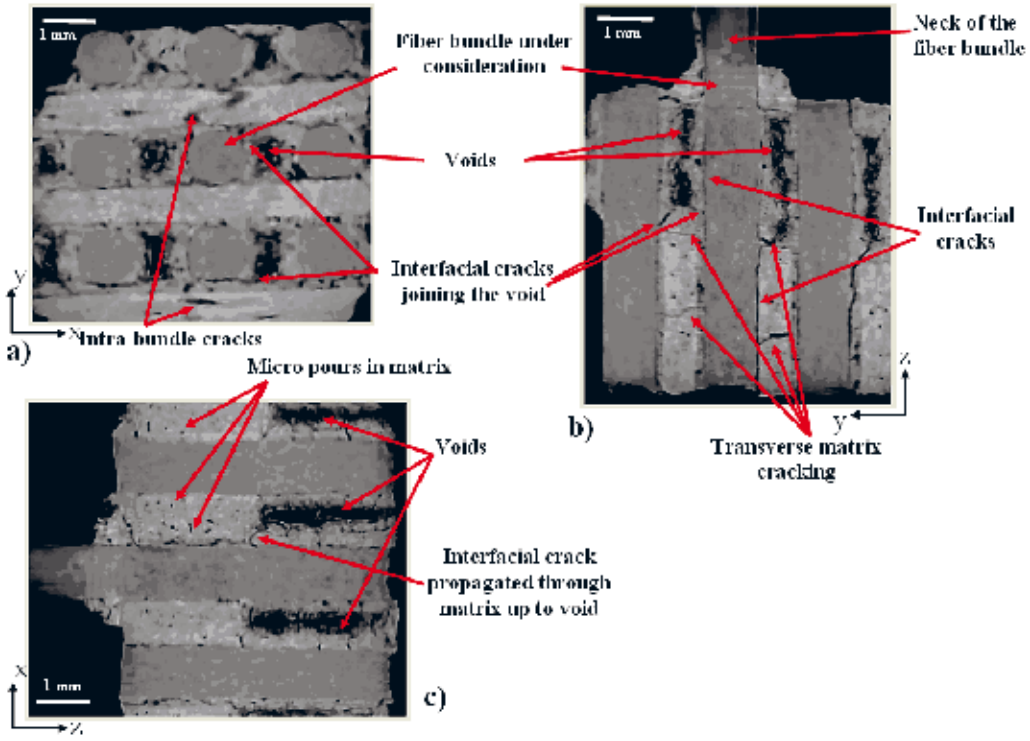

Fig.2. Reconstructed 2D stacked images of the pull-out test specimen.

4. INTERFACIAL PROPERTIES

4.1 Pull-out and push-out tests. The interfacial properties were determined for fiber bundles in the z-direction using pull-out and push-out tests. The specimens for these tests were prepared by removing the surrounding material of the composite from a central bundle of the z-direction, as discussed by Aoki et al. (2007) and shown in Fig.3(a) and (b). Specimen dimensions, B and D are selected such that there are at least three fiber bundles in each direction. L_1 is the debond length that is kept to 5-6 mm to cover at least one unit cell in the z-direction. L_2 is the anchorage length and is approximately 5 to 7 times L_1. A slot of nearly 4mm is made across the periphery of the z-direction bundle of pull-out specimens. This way the prismatic specimen is made in two parts, head and anchor. The head is made small so that fiber bundle will experience pull out stresses, whereas the anchor part is made larger so that it can hold the bundle without any damage. The width of the cut made at the periphery of the fiber bundle is 1 *mm* in order to avoid the effect of buckling or bulging of the fiber bundle under compressive loading.

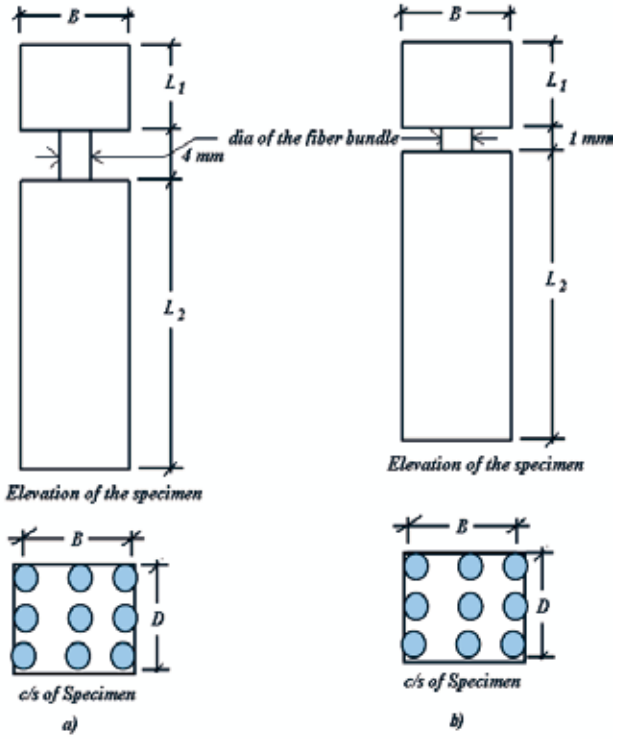

Fig.3. Details of the test specimens.

4.2 Interpretation of the parameters. Sakai et al. (2000) have calculated the fracture energy release rate using uniaxial load data whereas Domanowich et al. (1996) used the shear lag model of Gao et al. (1988). Sakai et al. calculated the critical debond stress σ_d and G_{II}.

$$\sigma_d = \frac{P_d}{\pi r^2} \tag{1}$$

$$G_{II} = \frac{\left(\frac{P_d^2}{2}\right)}{\left(\frac{\partial C_d}{\partial A_d}\right)}, \qquad G_{II} = \frac{\sigma^2 D}{8E} = \frac{2P_d{}^2}{\pi^2 D^3 E} \tag{2}$$

Here C_d is the compliance of the debonded bundle, l_d is the debond length, D is the diameter of the fiber bundle, A_d is the debond area and E is the Young's modulus of the fiber bundle in the longitudinal direction. The average shear stress is calculated from the maximum load under the assumption that the shear stress is uniformly distributed along the interface.

Domanowich et al. (1996) provide the following simplified equation for the critical energy in the absence of the friction and residual stresses:

$$G_c = \frac{\left(1-2k\nu_f\right)\left[P\right]^2}{4\pi^2 r^3 E_f\left(1+\beta\right)}, \tag{3}$$

where;

$$\beta = \frac{\gamma\left(1-2k\nu_m\right)}{\alpha\left(1-2k\nu_f\right)} \tag{4}$$

$\alpha = E_m/E_f$, γ = volume fraction of the fiber bundle, r_f = fiber bundle radius

l = location of the crack front, μ = coefficient of the friction, T_m = tensile force in matrix.

E_m, E_f and μ_m, μ_f are the Young's moduli and Poisson's ratios for matrix and fiber bundle, respectively.

E_m = 18000 N/mm^2, $E_f^{\,T}$= 190,000 N/mm^2 , $E_f^{\,c}$= 95,000 N/mm^2, ν_m = 0.2, ν_f = 0.2, r_f =0.49 mm, $\gamma = 0.01931$ $\alpha = 0.0947$, $K = 0.01735$, $\beta = 0.201$.

4.3 Finite element modeling of pullout test. The pullout tests were also simulated using finite element model made using the X-ray tomography images. A number of simplifications had to me made in the mesh, obtained from these images, to keep the computations feasible. In 2-D images the fiber bundles and matrix are distinguishable visually and features described above are seen. However, the gray levels of the matrix and fiber bundles are nearly the same and it is hard to differentiate these using grey scale values. A manual segmentation process was carried out for the reconstruction of the fiber bundles. The cracks and voids in the matrix can be segmented from the composite by using gray scale values but including cracks and voids at the interface resulted in a finite element mesh which was too fine and for now these features have been neglected. 3-D reconstruction of bonded and debonded regions by manual intervention was far too tedious and the interface was assumed initially bonded everywhere. Commercial software "Simpleware" **(**2010**)** is used for the 3D reconstruction of the composite and the mesh was modeled with tetrahedral elements. The fiber bundle-matrix interface was modeled using cohesive surfaces characterized by traction-separation behavior (abaqus.6.10).
For pure Mode-I and Mode-II loading, the exponential softening constitutive behavior represented in Fig. 4 (a, b) were used. In the Figures, N is the interfacial normal tensile strength and S is the interfacial shear strength.

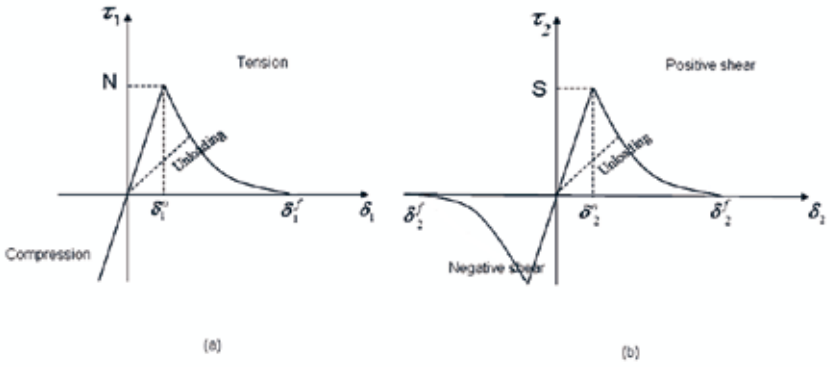

Fig. 4. Constitutive relations at the interface: (a) Normal traction for pure Mode-I and (b) Shear traction for pure Mode II.

Once the cohesive stiffness starts degrading, the friction between the contacting surface becomes active and begins contributing to the shear stresses. If ω_{int}, K_N and K_T are the interfacial damage parameter, and stiffness in the normal and tangential directions respectively, the unilateral contact and adhesion conditions in the normal directions is:

$$t^N(x) - (1 - \omega_{\text{int}}(x))K_N \delta^N(x) \leq 0; \tag{5}$$

$$\delta^N(x) \geq 0; \tag{6}$$

$$\left\{ t^N(x) - (1 - \omega_{\text{int}}(x))K_N \delta^N(x) \right\} \delta^N(x) = 0; \tag{7}$$

The friction and adhesion conditions in the tangential direction are:

$$t^T(x) = t^{Ta}(x) + t^{Tf}(x), \tag{8}$$

$$t^{Ta}(x) = (1 - \omega_{\text{int}}(x))K_T \delta^T(x) \tag{9}$$

$$t^{Tf}(x) = \omega_{\text{int}}(\mu t^N) \tag{10}$$

Using the values obtained above in section (4.2) as an initial guess an iterative procedure was adopted to obtain values of interfacial parameters such that load displacement curves from experiments and simulations matched. The matrix properties were degraded once the matrix strength was exceeded. The completely degraded elements were eliminated from the mesh. In ABAQUS this was achieved by using the explicit scheme as implementation of a cohesive contact algorithm was easier as compared to an implicit scheme. Mass scaling was used to keep the time step in the explicit scheme reasonable and it was ensured that the kinetic energy of the system was less than 5% of the strain energy. Once, debonding was completed the time step was reduced considerably to capture the friction phenomenon.

Debonding initiated at the end being pulled and grew slowly till one third of the fiber bundle had debonded. Subsequently, complete debonding of the bundle took a very short time. The stress in the matrix, particularly at rough locations, reached its maximum value, close to the time debonding was completed at those locations. This phenomenon corresponds to failure and subsequent abrasion of the matrix reported/conjectured by Aoki et al. (2007). It was also observed that friction alone without cohesive surfaces could not have produced the load displacement slopes in simulations similar to those observed experimentally. Although initial debonded regions exist in these composites, bonded regions are quite significant.

5. ASYMPTOTIC HOMOGENIZATION AND UNIT CELL MODELING

Analyzing huge composite structures by considering fibers and matrix on a microstructural level, is a complex problem. Analysis methods, therefore, approximate composite structures by an equivalent homogeneous material (EHM) the properties of which are derived using a small periodic repetitive block, called a unit cell. The unit cell, fully represents the behavior of the composite and the composite can be synthesized by replication and translation of the unit cell in the three coordinate directions. The properties of the EHM can be determined by applying the asymptotic homogenisation method to a single unit cell. In this, it is assumed that the structure has two distinct length scales, a global length scale of the order of the size of the structure, and a

local length scale which is proportional to the wavelength of the variation of the microstructure. Since the structure is periodic, it can be completely generated by translation of the unit cell. The size of the unit cell is further assumed to be much smaller than the size of the structure. The relation between the global length coordinate x_i for the structure and the local system y_i for the unit cell are related as:

$$y_i = \frac{x_i}{\varepsilon}, \tag{11}$$

where ε is the scaling factor between the two length scales.

The displacements $u_i(x)$ are assumed as asymptotic expansions with respect to parameter ε i.e.:

$$u_i(x) = u_i^0(\boldsymbol{x},\boldsymbol{y}) + \varepsilon u_i^1(\boldsymbol{x},\boldsymbol{y}) + \varepsilon^2 u_i^2(\boldsymbol{x},\boldsymbol{y}) + \cdots, \tag{12}$$

The functions $u_i^0, u_i^1, u_i^2, \ldots\ldots,$ are periodic functions in y_i, and are governed by the periodicity of microstructure. Following the steps given in (Rao, 2008) it can be shown that the volume averaged stress-strain relations for the homogenized elastic body are given as

$$\left\langle \sigma_{ij} \right\rangle = C_{ijkl}^H(e^{(0)}) \left\langle e_{kl}^{(0)} \right\rangle \tag{13}$$

Where

$$\begin{aligned} \left\langle e_{ij}^0 \right\rangle &= \frac{1}{|V_e|}\int_{V_e} e_{ij}^{(0)}(\boldsymbol{x},\boldsymbol{y})dv_e \\ &= \frac{1}{|V_e|}\left[\int_{V_{\bar{f}}} e_{ij}^{(0)}(\boldsymbol{x},\boldsymbol{y})dv_e + \int_{V_{\bar{m}}} e_{ij}^{(0)}(\boldsymbol{x},\boldsymbol{y})dv_e + \int_{V_{\text{int}erface}} e_{ij}^{(0)}(\boldsymbol{x},\boldsymbol{y})dv_e\right] \end{aligned} \tag{14}$$

$V_{\bar{m}}$, $V_{\bar{f}}$ and $V_{interface}$ in the above equation correspond to the fiber, matrix and interface domains in the unit cell, respectively. By applying a divergence theorem to the last term in equation (14), the average strain may be derived as:

$$\left\langle e_{ij}^0 \right\rangle = \frac{1}{|V_e|}\left[\int_{V_{\bar{f}}+V_{\bar{m}}} e_{ij}^{(0)}(\boldsymbol{x},\boldsymbol{y})dv_e + \frac{1}{2}\int_{S_c^m/S_c^f}\left(\left[u_i\right]n_j + \left[u_j\right]n_i\right)dS_e\right] \tag{15}$$

If the composite is perfectly bonded, the C^H_{ijkl} matrix is a constant and can be evaluated by subjecting the unit cell to periodic boundary conditions and six independent load cases:

$$\begin{Bmatrix} e_{11}^{(0)} \\ e_{22}^{(0)} \\ e_{33}^{(0)} \\ e_{23}^{(0)} \\ e_{13}^{(0)} \\ e_{12}^{(0)} \end{Bmatrix} = \begin{Bmatrix} 1 \\ 0 \\ 0 \\ 0 \\ 0 \\ 0 \end{Bmatrix}, \begin{Bmatrix} e_{11}^{(0)} \\ e_{22}^{(0)} \\ e_{33}^{(0)} \\ e_{23}^{(0)} \\ e_{13}^{(0)} \\ e_{12}^{(0)} \end{Bmatrix} = \begin{Bmatrix} 0 \\ 1 \\ 0 \\ 0 \\ 0 \\ 0 \end{Bmatrix}, \begin{Bmatrix} e_{11}^{(0)} \\ e_{22}^{(0)} \\ e_{33}^{(0)} \\ e_{23}^{(0)} \\ e_{13}^{(0)} \\ e_{12}^{(0)} \end{Bmatrix} = \begin{Bmatrix} 0 \\ 0 \\ 1 \\ 0 \\ 0 \\ 0 \end{Bmatrix}, \begin{Bmatrix} e_{11}^{(0)} \\ e_{22}^{(0)} \\ e_{33}^{(0)} \\ e_{23}^{(0)} \\ e_{13}^{(0)} \\ e_{12}^{(0)} \end{Bmatrix} = \begin{Bmatrix} 0 \\ 0 \\ 0 \\ 1 \\ 0 \\ 0 \end{Bmatrix}, \begin{Bmatrix} e_{11}^{(0)} \\ e_{22}^{(0)} \\ e_{33}^{(0)} \\ e_{23}^{(0)} \\ e_{13}^{(0)} \\ e_{12}^{(0)} \end{Bmatrix} = \begin{Bmatrix} 0 \\ 0 \\ 0 \\ 0 \\ 1 \\ 0 \end{Bmatrix} \text{ and } \begin{Bmatrix} e_{11}^{(0)} \\ e_{22}^{(0)} \\ e_{33}^{(0)} \\ e_{23}^{(0)} \\ e_{13}^{(0)} \\ e_{12}^{(0)} \end{Bmatrix} = \begin{Bmatrix} 0 \\ 0 \\ 0 \\ 0 \\ 0 \\ 1 \end{Bmatrix} \tag{16}$$

Alternatively, one can follow the procedure given by Pinho et al. (2009) and determine C. If however, debonding occurs the C^{H}_{ijkl} is path dependent and no longer constant. Here for the perfectly bonded case all the properties are calculated whereas for the debonded composite the only load history applied is $e_{11} \neq 0$ to study the change in E_1 with loading.

To take into account the periodicity of the structure, periodic boundary conditions are imposed on the unit cell. In a real composite, the effective properties change with location due to the damage mechanisms such as interfacial debonding, matrix cracking, fiber or fiber-bundle breakage, etc. Here, we assume that defects too are periodic.

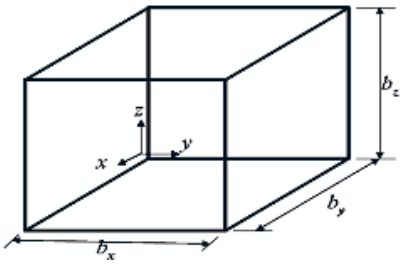

Figure: 5 unit cell for boundary conditions

The boundary conditions of a reflective type as given by Li (2008) are used. For this consider a cuboid of dimensions $b_x \times b_y \times b_z$ as shown in Fig.5. The boundary conditions for two opposite faces of a unit cell are given in equation (17-20), when normal loadings given in equation 17(a), (b) and (c) are applied, one by one. The directions *1*, *2* and *3* are analogous to *x*, *y* and *z* directions respectively.

$$\left.\begin{aligned} u|_{x=0} &= 0 \;\; \& \;\; u|_{x=b_x} = b_x \varepsilon_{11} \\ v|_{y=0} &= 0 \;\; \& \;\; v|_{y=b_y} = b_y \varepsilon_{22} \\ w|_{z=0} &= 0 \;\; \& \;\; w|_{z=b_z} = b_z \varepsilon_{33} \end{aligned}\right\} \tag{17}$$

where u, v and w are there degrees of freedom at each node of the face, in *x*, *y* and *z* directions, respectively. The boundary conditions for the unit cell under τ_{23}, τ_{13} and τ_{12} when considered one by one are given as below by equations (18), (19) and (20) respectively.

$$\left.\begin{aligned} u|_{x=0} &= 0 \qquad\qquad u|_{x=b_x} = 0 \\ u|_{y=0} &= \; w|_{y=0} = 0 \qquad u|_{y=b_y} = \; w|_{y=b_y} = 0 \\ u|_{z=0} &= \; v|_{z=0} = 0 \qquad u|_{z=b_z} = 0 \;\; \& \;\; v|_{z=b_z} = b_z \gamma_{23} \end{aligned}\right\} \tag{18}$$

$$\left.\begin{array}{ll} v|_{x=0} = w|_{x=0} = 0 & v|_{x=b_x} = w|_{x=b_x} = 0 \\ v|_{y=0} = 0 & v|_{y=b_y} = 0 \\ u|_{z=0} = v|_{z=0} = 0 & u|_{z=b_z} = b_z\gamma_{13} \;\&\; v|_{z=b_z} = 0 \end{array}\right\} \tag{19}$$

$$\left.\begin{array}{ll} v|_{x=0} = w|_{x=0} = 0 & v|_{x=b_x} = w|_{x=b_x} = 0 \\ u|_{y=0} = w|_{y=0} = 0 & u|_{y=b_y} = b_y\gamma_{12} \;\&\; w|_{y=b_y} = 0 \\ w|_{z=0} = 0 & w|_{z=b_z} = 0 \end{array}\right\} \tag{20}$$

The 3D reconstructed images of the composite unit cells (UC) with imperfections, from three different locations in a sample are shown in Fig.6. The locations in the samples from where these unit cells were taken are randomly chosen.

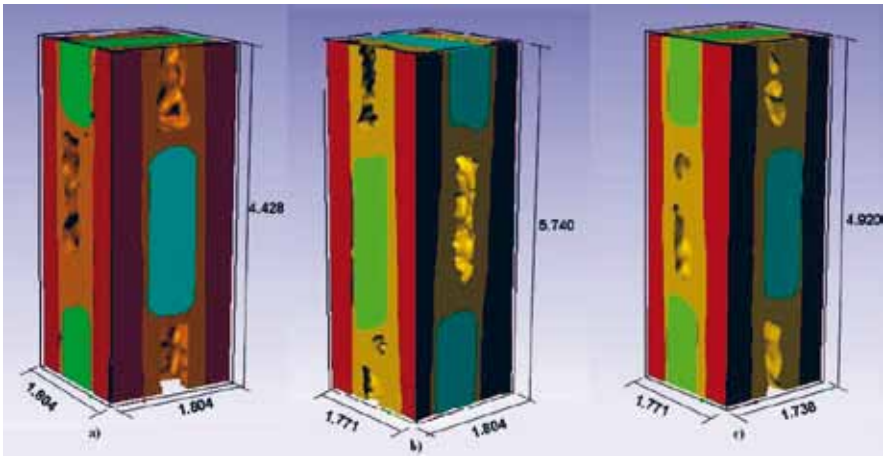

Figure: 6. 3D reconstructed image of composite unit cells including imperfections.

6. RESULTS AND DISCUSSION

6.1 Pull-out and push-out tests. The fiber bundle in the head of the pullout specimen of the composite is subjected to shear stresses at the interface. Since the interfaces in z-bundles were smooth, the failure is considered to be in mode-II. Typical load versus bundle displacement curves are shown in Fig.7 for pullout test specimens. The slope of the curve depends upon the progress of the debonding and frictional shear stress between the debonded surfaces. A sudden drop in the load after the peak load indicates total debonding at the interface. This is followed by a region of abrasion of the debonded surfaces during the sliding of the fiber bundle and the load reaches a value of 40-50 % of the maximum load. The load displacement curves for push-out tests are shown in Fig.8.

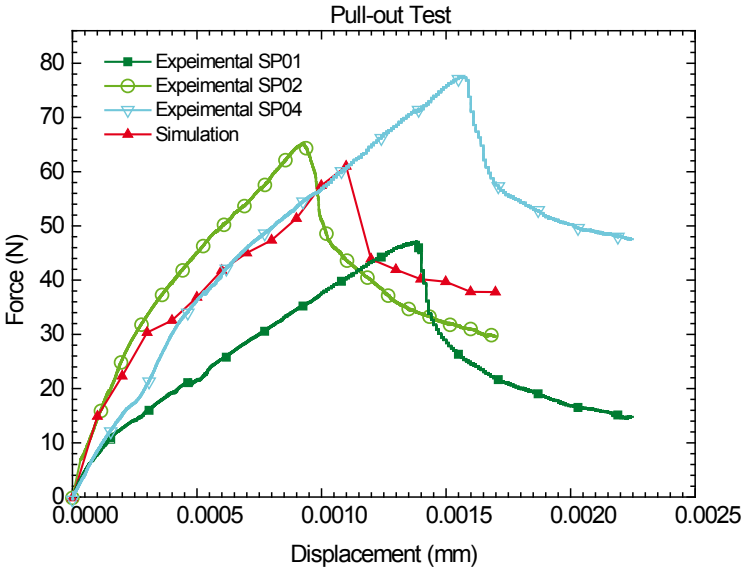

Fig.7: Force vs displacement curves for pull-out tests

In push-out tests the load initially increased nonlinearly, followed by a linear region up to a peak. After the peak load a flat post peak region is observed. One curve showed the stick-slip behavior with two conjugative load drops in the load-displacement curve.

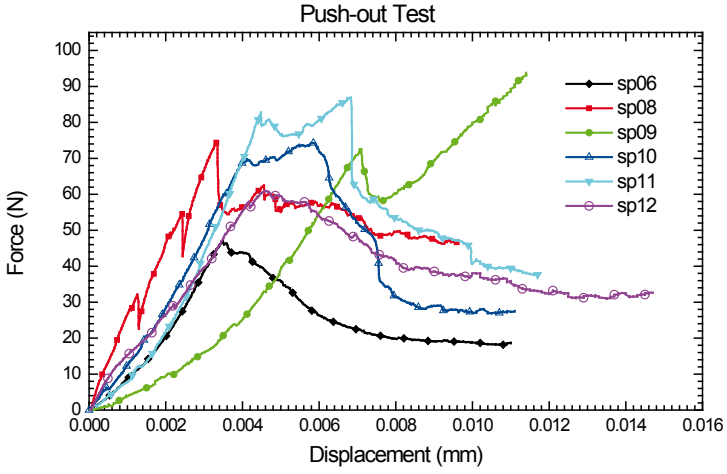

Fig.8: Force vs displacement curves for push-out tests

This phenomenon is probably due to the failure of the matrix blocks near the interface. The phenomenon of the push-out test is dominated by fiction and the matrix failure. The last portion of the load displacement curve shows the contribution of the abrasion.

The fracture release rate, average interfacial shear stress and the normal stress in the bundle using the two approaches for pull-out and push-out tests mentioned in 4.2 are presented in Table.2.

Table 2: Interfacial parameters of the composite from pull-out test and push-out test respectively

Test	Average shear stress (τ_a) N/mm^2	Normal debond stress(σ_d) N/mm^2	Fracture energy release rate using G_{IIC} N/m (Sakai et al, 2000)	Fracture energy release rate using MM G_{IIC} N/m (Domnanovich et al, 1996)
Pull out	4.15 ± 0.68	83.12 ± 11.2	4.73 ± 1.24	3.83 ± 1.01
Push out	4.22 ± 0.55	91.98 ± 9.02	5.80 ± 1.10	5.10 ± 0.98

The FE simulation for one of the specimens (sp02) is also presented in Fig.7. The values of the debond initiation shear stress (S in figure 4b) and fracture energy in Mode II were taken as 26 MPa and 2.5 N/m respectively. The coefficient of friction was considered as 0.25. The mode III values were the same as mode II where as for Mode I the values were doubled.

6.2 Material properties of the phases. Each bundle is a unidirectional composite made of matrix and fiber. Due to the infiltration of the matrix in the bundle during the processing of the composite the orientation, size and shape of the bundles change. This is indicated by larger cross-sectional areas of the bundles in the scanned images, as compared to the cross-section area before processing. From these images the volume of the matrix that has infiltrated into the bundle can be calculated. This volume is taken into account while calculating the Young's modulus of the bundles in the scanned images using the rule of mixture. The properties of the fiber bundles of unit cells used in the simulation are given in Table 3 and subscripts *x, y* and *z* represent the directions of the fiber bundle (Rao, 2008).

Table 3: Effective properties of fiber bundles and matrix

Engineering constants	A	B	C	Matrix
E_{11x} (GPa)	229.55	227.56	226.21	19
E_{11y} (GPa)	229.45	227.84	231.25	-
E_{11z} (GPa)	235.09	238.84	232.85	-
E_{22}=E_{33} (GPa)	19	19	19	19
$\nu_{12}=\nu_{13}$	0.2	0.2	0.2	0.2
ν_{23}	0.35	0.35	0.35	-
G_{12}=G_{13} (GPa)	23	23	23	
G_{23} (GPa)	7.92	7.92	7.92	-

6.3 Perfectly bonded composite. In the case when the fiber bundle and matrix interface is assumed perfectly bonded, the engineering constants obtained for unit cells are presented in Table 4. The effective homogenized properties of the composite are given as the volume average of unit cells. The material shows orthotropic behavior and the deviation from transverse isotropy is due to different volume fraction and orientation of the bundles in the x and y directions. The effect of the voids is not predominant in the elastic properties of the composite.

Table 4: Effective properties of a composite for a perfectly bonded condition GPa

Engineering constants	A	B	C	Volume Average
E_{11}(GPa)	55.17	57.24	59.42	57.31
E_{22}(GPa)	53.20	52.37	55.23	53.53
E_{33}(GPa)	57.06	53.98	58.82	56.44
ν_{12}	0.08	0.09	0.09	0.08
ν_{13}	0.08	0.09	0.08	0.08
ν_{23}	0.08	0.09	0.08	0.08
G_{12}(GPa)	7.40	7.72	8.62	7.90
G_{13}(GPa)	7.86	8.24	8.59	8.23
G_{23}(GPa)	7.78	8.11	8.75	8.21

6.4 Composite with debonding and friction. Simulations were also performed for the composite in Fig.6b with an interface (section 6.2) modeled using cohesive elements with properties determined from pull-out simulations. Only E_{11} was calculated and that too without using periodic boundary conditions. It was also assumed that the interfacial properties for all the bundles were the same as determined in section 6.1.The value of E_{11} was 53.5 GPa initially and remained so till the strain reached 0.12%. Around this strain the bundle in direction 1 underwent debonding in mode II and the bundle in direction 2 underwent debonding in mode 1 on one surface & in mode III on another causing E_{11} to drop to 46 GPa.

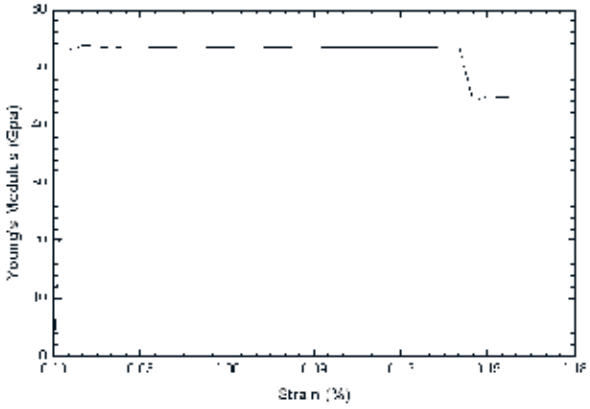

Figure: 7. Variation of the Young,s Modulus (E_{11}) with axial strain.

7. CONCLUSIONS

A procedure for determining the mechanical properties of C/C composites is set up. X-ray tomography was used for reconstruction of these composites. As densities of bundles and matrix were similar it was difficult to do segmentation of phases by computer algorithm. Manual segmentation was therefore used. However, features such as debonding although visible in 2-D images could not be reconstructed in 3-D. Some features such as cracks and micropores which could be reconstructed could not be included in the FE analysis. A voxel based mesh which would have allowed this leads to a large number of elements particularly at cracks and micropores. It was therefore decided to neglect micropores and cracks and assume the interface to be perfectly bonded during the simulations. Pull out tests were performed and simulation of one of these using the mesh from tomography images was used to obtain the cohesive and frictional properties of the interface. Due to limitations in the resolution of images, difficulties in the 3-D reconstruction and computational limitations the geometry of the interface cannot be completely modeled and therefore interfacial properties are approximate. These have been used in unit cell, reconstructed from 2-D tomography images, to obtain E_{11} of the composite. For a perfectly bonded composite the modulus values are approximately 55GPa. For a composite with provision for debonding the initial value of E_{11} is similar but around 0.12 % strain the value drops to 46 GPa due to debonding. A similar procedure can be used to obtain properties in other directions.

REFERENCES

Aubard X., C. Cluzel, L. Guitard, P. Ladeveze, (2000), Damage modeling at two scales for 4D carbon/carbon composites, Computers & Structures, Volume 78, Issues 1-3, Pages 83-91.

Aoki Takuya, Yuhsuke Yamane, Toshio Ogasawara, Takeshi Ogawa, Sunao Sugimoto, Takashi Ishikawa, (2007), Measurements of fiber bundle interfacial properties of three-dimensionally reinforced carbon/carbon composites up to 2273 K, Carbon, Volume 45, Issue 2, Pages 459-467.

Brandstetter J., Peterlik H., Kromp K., Weiss R. (2003), A new fiber-bundle pull-out test to determine interface properties of a 2D-woven carbon/carbon composite." Composites Science and Technology, Volume 63, Issue 5, Pages 653-660.

Domnanovich Andreas, Herwig Peterlik, Karl Kromp, (1996), Determination of interface parameters for carbon/carbon composites by the fiber-bundle pull-out test, Composites Science and Technology, Volume 56, Issue 9, Pages 1017-1029.

Gao Y.C., Mai Y.W., Cotterell B., (1988) Fracture of fiber-reinforced materials, ZAMP, 39 (4), pp. 550-572.

Hatta Hiroshi, Ken Goto, Shinya Ikegaki, Itaru Kawahara, Mohamed S. Aly-Hassan, Hiroyuki Hamada, (2005), Tensile strength and fiber/matrix interfacial properties of 2D and 3D carbon/carbon composites, Journal of the European Ceramic Society, Volume 25, Issue 4, Pages 535-542.

Hatta Hiroshi, Ken Goto, Takuya Aoki, (2005), Strengths of C/C composites under tensile, shear, and compressive loading: Role of interfacial shear strength, Composites Science and Technology, Volume 65, Issues 15-16, 20th Anniversary Special Issue, Pages 2550-2562.

Hatta Hiroshi, Keisuke Taniguchi, Yasuo Kogo, (2005), Compressive strength of three-dimensionally reinforced carbon/carbon composite, Carbon, Volume 43, Issue 2, Pages 351-358.

Li S., (2008), Boundary conditions for unit cells from periodic microstructures and their implications. Composites Science and Technology, Volume 68, Pages 1962-1974.

Mohamed S. Aly-Hassan, Hiroshi Hatta, Shuichi Wakayama, Mitsuhiro Watanabe, Kiyoshi

Miyagawa, (2003), Comparison of 2D and 3D carbon/carbon composites with respect to damage and fracture resistance, Carbon, Volume 41, Issue 5, Pages 1069-1078

Piat R., E. Schnack, (2003), Hierarchical material modeling of carbon/carbon composites, Carbon, Volume 41, Issue 11, Pages 2121-2129.

Pinho Cruz J., J.A. Oliveira, F. Teixeira-Dias, (2009), Asymptotic homogenisation in linear elasticity. Part I: Mathematical formulation and finite element modelling, Computational Materials Science, Volume 45, Issue 4 , Pages 1073-1080

Rao M. V., (2008), Mechanical properties of multidirectional carbon -carbon composites, PhD thesis, Applied mechanics department, Indian Institute of Technology Delhi, New delhi-16 India, 2008

Rollin Magali, Stephane Jouannigot, Jacques Lamon, Rene Pailler, (2009), Characterization of fiber/matrix interfaces in carbon/carbon composites, Composites Science and Technology, Volume 69, Issue 9, Special Issue on the 12th European Conference on Composite Materials (ECCM12), organized by the European Society for Composite Materials (ESCM), Pages 1442-1446.

Sakai M., R. Matsuyama, T. Miyajima, (2000), The pull-out and failure of a fiber bundle in a carbon fiber reinforced carbon matrix composite, Carbon, Volume 38, Issue 15, Pages 2123-2131.

Simpleware Ltd., Innovation Centre, Rennes Drive, Exeter, EX4 4RN, UK.

Siron O., J. Lamon, (1998), Damage and failure mechanisms of a3-directional carbon/carbon composite under uniaxial tensile and shear loads, Acta Materialia, Volume 46, Issue 18, Pages 6631-6643,

SkyScan 1172, DRDO facility at SASE, Manali, India.

Valette Ludovic, Dominique Rouby, Christophe Tallaron, (2002), Analysis of pull-out and failure of unidirectional bundles in a laminated carbon/carbon composite, Composites Science and Technology, Volume 62, Issue 4, Pages 513-518.

Abaqus 6.10., http://www.simulia.com

Proceedings of the 32nd
Risø International Symposium on Materials Science:
Composite materials for structural performance:
Towards higher limits
Editors: S. Fæster, D. Juul Jensen,
B. Ralph, B.F. Sørensen
Risø National Laboratory for Sustainable Energy,
Technical University of Denmark, 2011

FATIGUE PERFORMANCE OF COMPOSITES USED IN WIND TURBINE BLADES

R.P.L. Nijssen* and P. Brøndsted**

*Knowledge Centre Wind turbine Materials and Constructions (WMC), Kluisgat 5, 1771MV, Wieringerwerf, the Netherlands
**Risø DTU, Frederiksborgvej 399, 4000 Roskilde, Denmark

ABSTRACT

Wind turbines are fatigue machines, and their blades are the most heavily loaded-structures in composite engineering. Taking into account stiffness, fatigue performance and weight, composite materials offer tough competition to other materials in terms of cost. In the present paper focus is on the fatigue performance of composite materials. In this paper, composite fatigue behavior and themes of previous and ongoing research are discussed, including the demands for accurate tests and qualification methods.

1. INTRODUCTION

Globally, the sustainable energy sources have been in focus for the last four decades, and the amount of energy generated from wind has exponentially grown in the last 30 years. Windmills with a capacity of 55 kW and rotor diameters of 25 meters in the beginning of the 80s are now replaced by modern high-performance wind turbines with a capacity of 7 MW and rotor diameters of 164 m have recently been announced (Vestas, 2011).

Wind turbines are fatigue machines, and their blades are the most heavily loaded structures in composite engineering, see Fig. 1 (Nijssen 2006). This has been a challenge for the blade designers, the manufacturers and the material producers. Polymer reinforced glass fiber composite material (or Glass Fiber Reinforced Polymer, GFRP) was very early found to be the material having the main potential for blades.

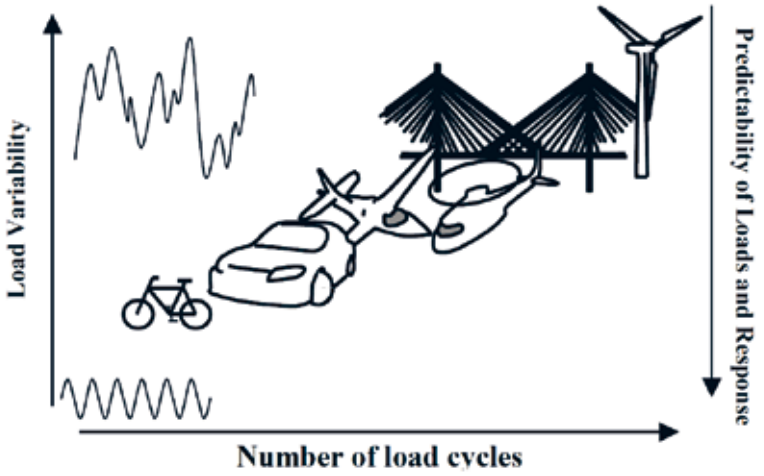

Fig. 1. Wind turbines are fatigue machines (Nijssen 2006)

Taking into account stiffness, fatigue performance and weight, composite materials offer tough competition to other materials in terms of cost. Through the years, high performance fibers have been developed and hybrid combinations of standard E-glass fibers, high performance glass fibers and carbon fibers are the future solutions for materials for the continuously growing blades.

While the exponential growth of blade diameter is losing speed, resin systems have been introduced that enable 24 hour maximum mould times to meet the demand for large amounts of relatively short (40-50 m) blades to be deployed onshore in emerging markets such as China and India. Today the research and focus is also directed toward sustainable materials from fibers made from biomass and resins based on recyclable materials.

In the present paper the focus is on the fatigue performance of composite materials. Fatigue behavior and the significance of damage mechanisms are emphasized; themes of previous and ongoing research are discussed, including the demands for accurate tests and qualification methods.

2. LOADING ON THE BLADES

The blades are subjected to load from wind forces, gravity forces and centrifugal forces. These load combinations result in combined axial and torsional loads with a complex spectrum that results in multi-axial stress fields in the different sections of the blades. Hence, the blade dimensioning and resulting strength must be designed against these stresses.

In particular, the variations in loads resulting in stochastic load patterns are challenging to design for. The stochastic behavior is a result of the variability in wind loads and is site dependent. Wind force measurements map the loads and by aero-elastic modeling, the transformation functions from load into stress fields in the blade sections can be estimated. The resulting stress fields are the challenge for the blades designer to account for in dimensioning the blades and demonstrating the resulting strength against e.g. fatigue.

3. BLADE DESIGN AND MATERIALS

A historical overview of structural solutions for the rotor blade is given by Joncas (2010), from which Fig. 2 was constructed. The top right cross-section shows a solution from topological optimization, which was explored in this work.

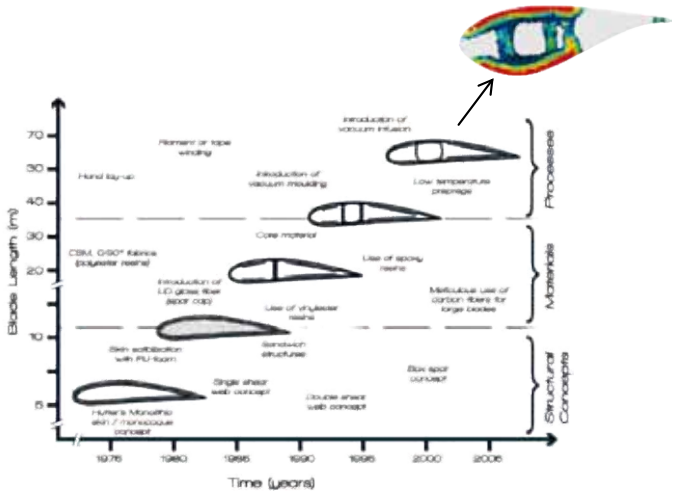

Fig. 2.Typical cross sections of a wind turbine blade (combination of figures from Joncas 2010)

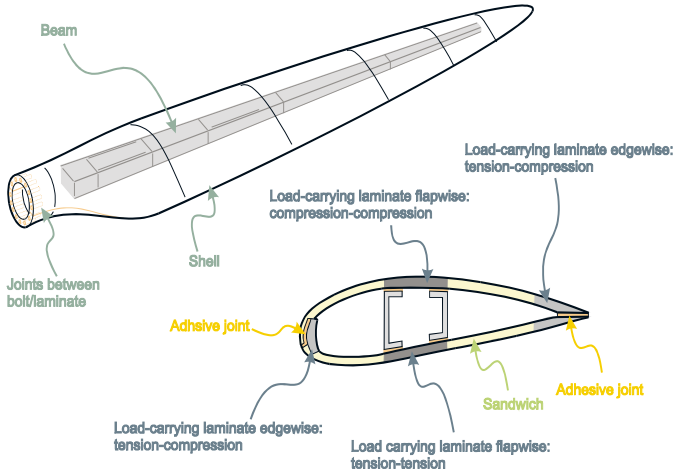

Fig. 3. Rotor structure and wind turbine blade cross-section (Courtesy B.F. Sørensen)

Typical blade construction of a wind turbine blade is shown in Fig. 3. Two longitudinal laminates are carrying the flapwise load. They are separated by one or more shear webs, primarily to take up the shear and the edgewise loads. Around this central structure, aerodynamic shells are mounted giving the aerodynamic geometry and stabilizing the blade in torsion, bending and against buckling.

The materials used for the various parts of the blade are typically selected to be glass fiber

reinforced polymers (Brøndsted, Lilholt, and Lystrup 2005). The different substructures are built using laminates and sandwich components. The main load-carrying parts in the beam, in the leading edge and in the trailing edge are made from solid thick laminates tapered off in thickness from the root end to the blade tip. The webs and the shells are primarily made from a sandwich consisting of composite skin layer laminates moulded on a core made from balsa wood, PVC foams or PET foams. In Fig. 4, a typical wind turbine PVC sandwich specimen after a 3-point bending (reversed loading) fatigue test is shown, using a fixture designed and manufactured at WMC.

Fig. 4. Typical wind turbine PVC sandwich specimen after a reversed loading fatigue test

As rotor blades are subject to 'leaner' design, to achieve more optimal and reliable usage of the materials, more knowledge on the materials' performance is required for suitable blade design. Ongoing research attempts to gather and render this knowledge into suitable design tools.

4. WIND TURBINE ROTOR BLADE FATIGUE RESEARCH

Fatigue research into wind turbine composites has been ongoing for approximately 2 decades, (e.g.: Bach (1992); Kensche and Seifert (1990); Joosse and van Delft (1993); van Delft, Hagg, and Joosse (1990); Mandell, Reed, and Samborsky (1992)). Through various research programmes, it has become clear, that established fatigue models that were used for metallic materials require considerable modification in order to be applicable to composites in general, and to wind turbine rotor blade composites in particular. The difficulty in modeling fatigue behavior of wind turbine composites lies in:

- the large amount of significant load cycles
- their strongly stochastic nature
- the influence of environmental conditions
- the influence of fabric and laminate architecture and chemical composition

Up to a certain point, the OPTIMAT BLADES research programme was the first EU-funded research effort that aimed to investigate various aspects of fatigue modeling in an integrated

manner (OPTIMAT 2006). In the UPWIND programme (UPWIND 2011), working group 'Rotor Structure and Materials', this experience was used to further investigate wind turbine rotor blade composite fatigue behavior in a consistent manner.

This paper builds both on the general literature and on the experience of the authors within these research programmes.

5. FATIGUE MODELING

First, the general lay-out of every current fatigue life prediction model for variable amplitude loading is presented, to place into perspective the remainder of the paper.

It is hereby assumed, that at any location in the blade, for any part of the rotor blade's operational life, the loads are known as a time series of stress or strain. Such data are the outcome of a wind turbine dynamic simulation.

Three main steps exist in the fatigue model:

1. cycle counting, resulting in a classification per cycle type;

2. estimating allowable number of cycles for each cycle type;

3. damage calculation, combining the results from step 2 with a damage criterion.

The above steps are, often, strongly interdependent. For instance, the type of damage calculation method (step 3) requires a certain input from step 1. For instance, the order of the loading cycles may or may not be discarded, putting constraints on the counting method followed.

The most commonly used methods for the above steps are: Rainflow counting in step 1 (discarding the order of the cycles), a constant life diagram in step 2, and Miner's sum in step 3. For an explanation of Rainflow counting, various sources are available in the literature, e.g. (de Jonge, 1969; Matsuishi and Endo, 1968), and this step is therefore not further explained. This is in keeping with the common use of frequency domain dynamic simulations, where the structural loads are presented as histograms rather than time series, effectively skipping the first step.

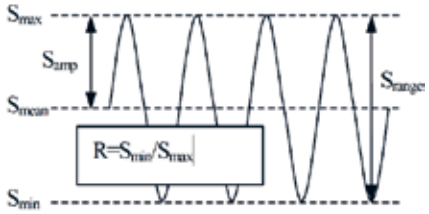

Fig. 5. Fatigue cycle - picture of fatigue cycle with S_{amp}, S_{mean}, R, etc.

Before going into an estimation of the allowable number of cycles for each cycle type, a few definitions are given. For each cycle type in the loading sequence or –histogram, it is necessary to quantify the number of cycles that would lead to the fulfillment of the failure criterion. Before elaborating on this, it is necessary to specify 'cycle type' and 'failure criterion'. Most commonly, breakage (loss of ability to carry the applied load) is used as a failure criterion. For the description of a fatigue cycle, one could choose any combination of two of the parameters

shown in Fig. 5. Since fatigue behavior in composites is thought to depend both on the cyclic mean and amplitude, cycle type is usually formulated as R-value, S_{min}/S_{max}. This has the advantage of keeping the ratio of tensile and compressive components in the cycle constant.

5.1 Constant Life Diagram (CLD). The designer uses a constant life diagram (CLD) to estimate the number of cycles to failure. Essentially, this is a diagram spanning all possible combinations of cyclic mean and amplitude, showing lines that connect points with equal (expected) fatigue life. All straight lines from the origin represent constant R-values, and there are sections where the loading is pure compression, tension, or a mix, see Fig. 6.

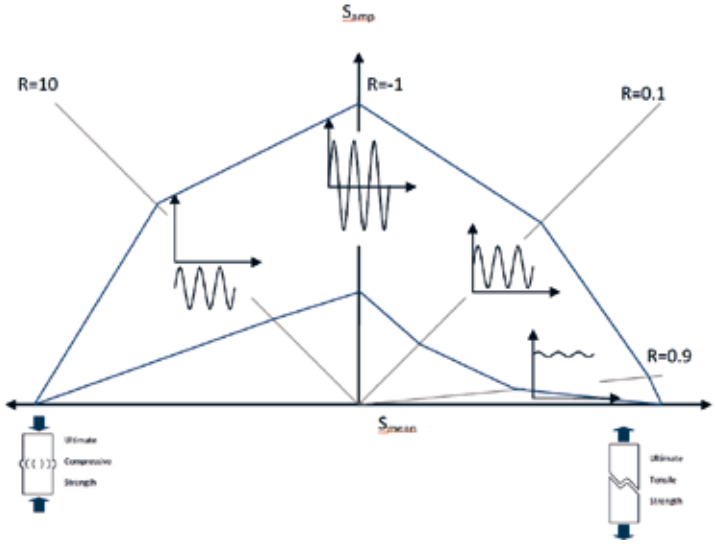

Fig. 6. Schematic of a constant life diagram (CLD)

On the abscissa (which represents static loading of the material), the constant life lines typically converge to the Ultimate Tensile/Compressive Strength, but this is an artifact forced by the designer. Recent results by DOE/MSU and UPWIND suggest, that constant life lines run parallel for R-values close to 1 (Nijssen, Westphal, Stammes, Lekou, and Brøndsted 2008).

Since it is impossible to determine the complete constant amplitude fatigue behavior experimentally, the CLD is usually an interpolation of experimental S-N curves, which are typically obtained by doing constant amplitude fatigue tests on (rectangular) specimens, to failure, and grouping experimental results by R-value.

5.2 Fatigue Damage in GFRP laminates. Although considerable effort should be expended to improve the descriptive quality of S-N curves and CLDs, the key to better fatigue modeling is the incorporation of fatigue damage mechanisms.
A famous description of fatigue damage in composite materials was demonstrated by Talreja (1986), Fig. 7. In this Figure, the Characteristic Damage State (CDS), or the saturation distance for matrix cracks is plotted.

The matrix material, the interfacial bonds, and the fibers contribute to the laminate strength, as well as determine the failure mechanisms through their interaction. Fatigue damage initiated from matrix cracking leads to interface debonding and delamination, ending up with fiber breakage leading to final fracture.

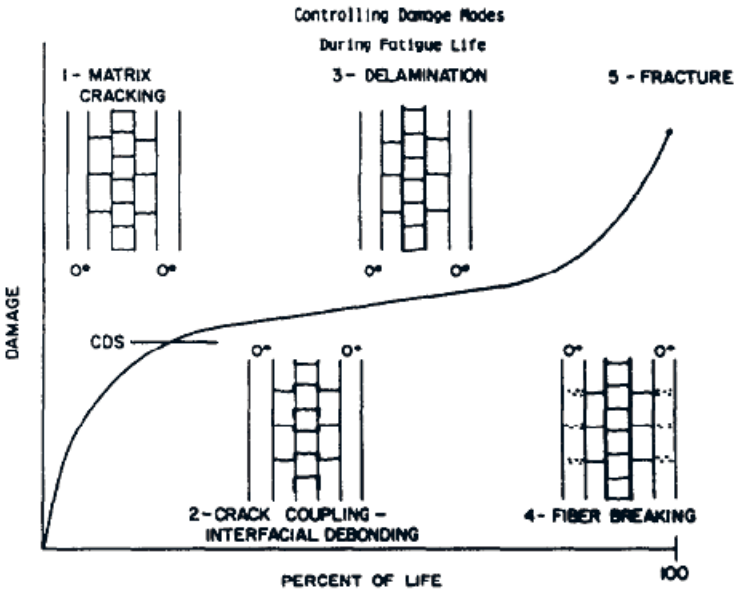

Fig. 7. Development of damage (Talreja, 1986)

5.3 S-N curve. An S-N curve (load level S versus number of cycles N) is shown in Fig. 8. To illustrate the possible relation with the damage mechanisms of Fig. 7, it is divided into 3 stages. The low-cycle stage (A) is a nearly horizontal line where the number of cycles to failure depends more on the statistical strength distribution of the fibers than on the stress level. Stage B is the classical fatigue behavior where the behavior is described by a modified wear-out model and the S-N correlation can be described as a power law function, e.g. the Basquin equation. The long-life stage C suggests a fatigue limit where an infinite lifetime is found below a given stress or strain level.

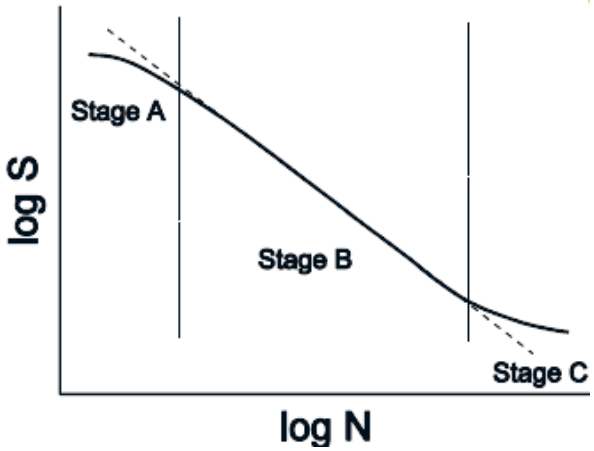

Fig. 8. Schematic S-N curve (16)

The deterministic model describing stage B is a power law presenting the S-N curve analytically

expressed as the Basquin equation:

$$N_f S^m = C \tag{1}$$

where C is a constant, N_f is the number of cycles to failure, and m is a shape parameter (Wöhler exponent) reflecting the slope of the log-log line in the Wöhler diagram (S-N curve).

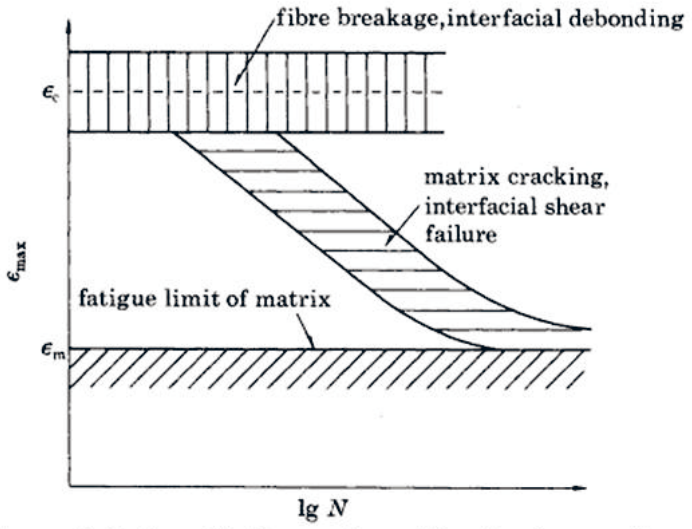

Fig. 9. Damage modes in fatigue (Talreja 1981)

The damage mechanisms during fatigue (Fig. 7) are made active by the local stress levels and can be illustrated in a three level fatigue damage mechanism map originally suggested by Talreja, 1981 as illustrated in Fig. 9. Low stress levels lead to initiation of matrix cracking progressing into interfacial crack formation and growth and the final fracture will mainly be observed as delamination and cracks along the fibers. The intermediate stress levels show a similar behavior, but can lead to localization by fiber fracture due to the stochastic distribution (Weibull) of individual fiber strengths. At the highest stress levels, matrix and interfacial cracks immediately lead to fiber fracture and overall global damage.

Thus, the damage mechanisms are different for the different regimes of the S-N curve, which must be taken into account in life prediction models, used for e.g. accelerated fatigue tests.

In typical fatigue testing for the wind industry, the cycle range is typically taken between one thousand and one million cycles. In this region, the S-N curve can be described by a log-log S-N curve, a fatigue formulation which has proven to have particular descriptive value when using it to describe high-cycle fatigue. When plotting a fatigue curve in this manner (a straight line in graph with both axes logarithmic), no fatigue limit has to date been found for UD rotor blade composites, or for the fibers or matrix separately (see Fig. 10) (van Delft, Rink, Joosse, and Bach (1994); Mandell, Samborsky, Wahl, and Sutherland 2003).

This is in apparent contradiction with the work by Talreja. Whether the fatigue limit in that work (Fig. 9) is partly due to the boundaries of experimental efforts (testing at low strains and high cycles can be very time consuming, leading to pre-failure stops, i.e. “run-outs”), or to the

plotting method (in a graph with a linear ordinate, many S-N formulations seem to 'flatten' near the high cycle region), or a reality, remains to be seen.

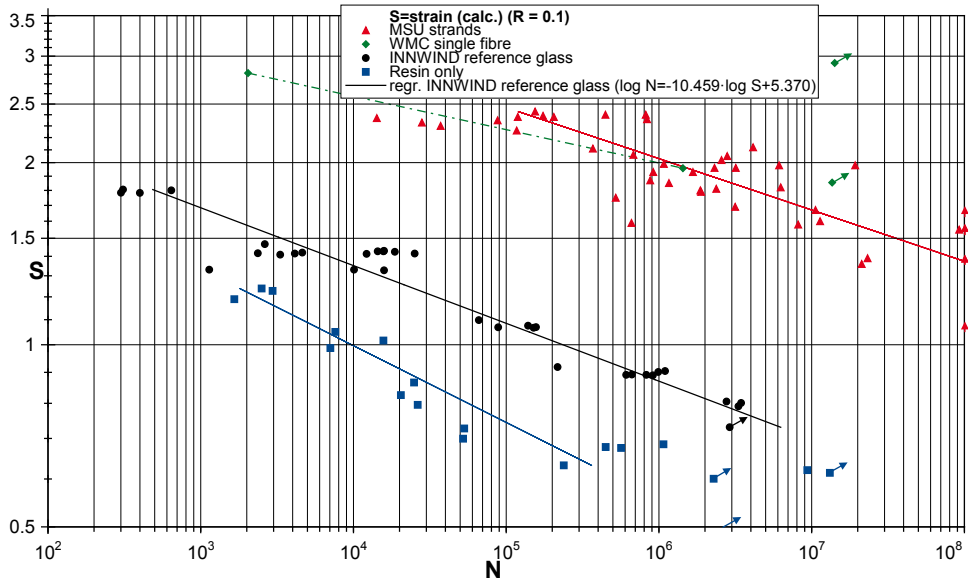

Fig. 10. Double logarithmic S-N lines for fiber bundles, neat resin, and composite (Nijssen, Westphal, Stammes, and Sari (2010)

5.4 Influence of damage on hysteresis. Apart from noting only the fatigue load and resulting life in a fatigue test, the damage in some polymer matrix composites can be measured by analyzing the individual hysteresis loops in the stress-strain cycle. The damage progression under the influence of fatigue loads has an effect on the stiffness and the toughness properties of the materials and can be measured and verified through changes in stiffness and damping properties. The methodology was described by Andersen, Brøndsted, Jørgensen, and Lilholt (1996) following the stress-strain history where the composites are studied under constant amplitude fatigue loading. This leads to hysteresis loops and thus to the modulus determined by the hysteresis loop slope and the damping determined by the hysteresis loop area and combined in the loss factor as an experimental parameter (see Fig. 11).

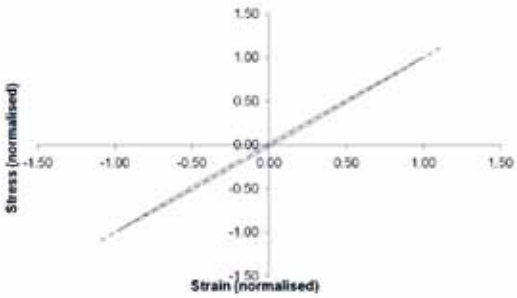

Fig. 11. Example of a normalised stress-strain hysteresis loop sampled during fatigue

The modulus in the individual stress-strain cycle is defined as the slope of the stress-strain loop by a maximum-minimum calculation or better as the best fit linear regression line of the hysteresis loop, i.e:

$$E_i = (\sigma_{i,max} - \sigma_{i,min})/(\varepsilon_{i,max} - \epsilon_{i,min}) \quad (2)$$

Based on calculation of the area ΔW of the stress-strain hysteresis loop in the fatigue cycle normalized by the elastic energy W:

$$\Delta W = \int \sigma d\varepsilon \quad (3)$$

$$W = \frac{1}{2}\sigma_a \varepsilon_a \quad (4)$$

Where σ_a and ε_a are respectively the stress and strain amplitudes.

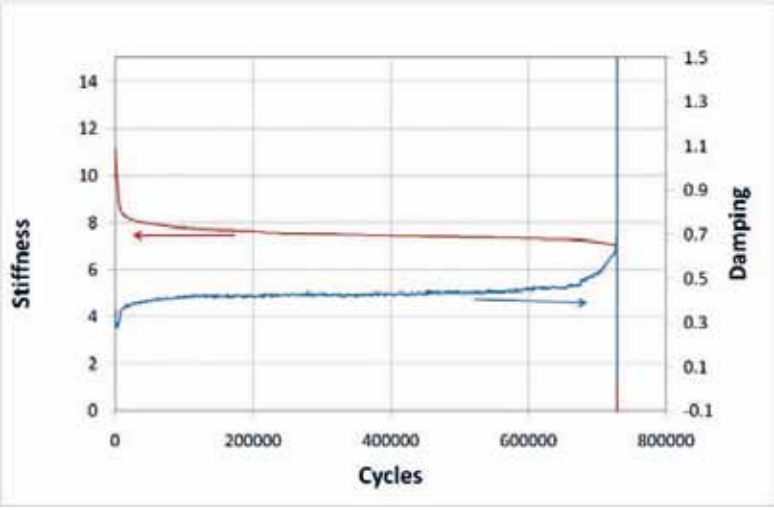

Fig. 12. Example showing stiffness degradation and increase in loss factor during fatigue

The damage can then be described in a two parameter presentation following the full life time and the composite material (Fig. 12).

5.5 Influence of resin on fatigue damage. The significance of knowing fatigue mechanisms is also evident when attempting to draw conclusions from e.g. Fig. 13. Here, an identical glass fabric had been impregnated with various resins, using, as much as possible, the same manufacturing methods. In tensile fatigue (where one would expect the fatigue mechanisms to be fiber dominated), a relatively small, but clear distinction can be seen in terms of longevity between the different materials.
Although the plot seems to lead to the conclusion, that epoxy is the preferred material for tensile fatigue, detailed observations of the failure mechanisms would be required to draw a better conclusion. It is very well possible, that the compatibility with the sizing, different degrees of shrinkage, etc., lead to the observed difference in life. Hence, it might be possible, that when each interface was separately optimized for the combination of glass and resin, the performance ranking would have been very different.

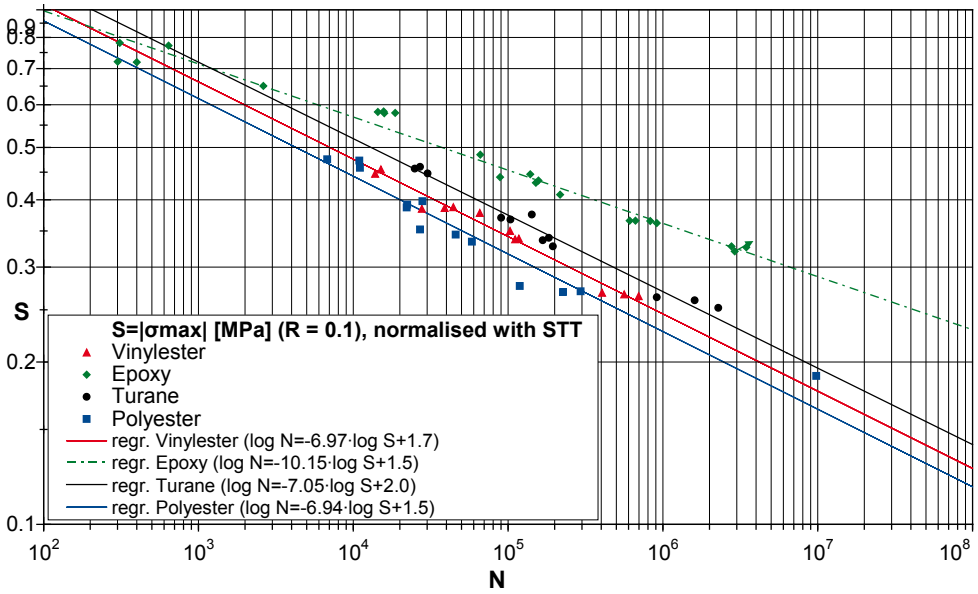

Fig. 13: Life time curves from different resins in tension

6. MICROMECHANICAL MODELING

That the internal structure of a composite is of paramount importance to the fatigue behavior is well-known, and efforts to quantify these effects are numerous, e.g. (Hedgepeth (1961); Gamstedt (1997); Qian, Nijssen, Samborsky, Kassapoglou, Gürdal, and Zhang (2010); Mishnaevsky and Brøndsted (2009a&b). This includes the effects of fiber packing and content, misalignment with respect to load, local damage, clustering of fibers and bundles, etc.

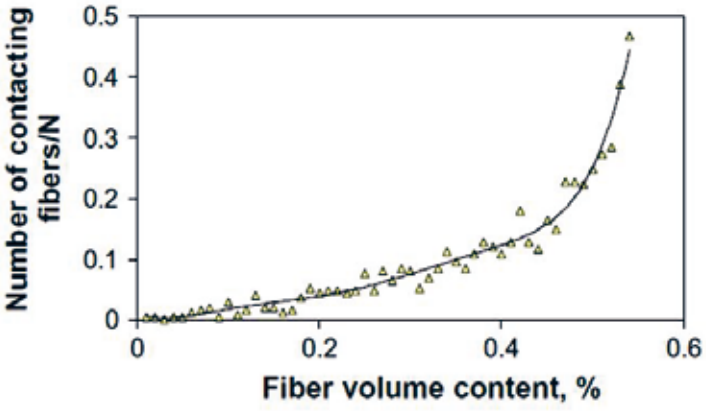

Fig. 14. Relation between fibre content and amount of touching fibers Mishnaevsky and Brøndsted (2009a)

Mishnaevsky and Brøndsted have performed various case studies, where parameters relating to the lamina architecture were studied (2009). For instance, using meso-mechanical modeling it was found that the packing of fibers can be very important. Packing leads to many fibers in contact, and because the fiber contacts initiate the matrix cracks, packing is an important parameter. They also addressed the effect of fiber distribution, from uniformly distributed fibers to bundle and bundle in bundle effects. A good correlation between the fibers in contact and the two-dimensional experimental characterization was found from the work by Zangenberg and Hansen (in press).

7. SIGNIFICANCE OF MATERIAL MODELS FOR BLADE TESTS

New blade designs are subjected to static and fatigue tests. While static tests are used to validate the ability of the design to withstand extreme loads, the ability of the blade to withstand the design fatigue load histogram is verified in accelerated fatigue tests. Accelerated means that the test loads are scaled up from the design loads, such that a damage state equivalent to the (variable amplitude) design life of ca. 20 years is achieved within a practical test duration, i.e. 1-5 million (constant amplitude) fatigue cycles.

These fatigue tests have proven valuable in identifying the critical areas in a blade design, as well as in finding the cause of unexpected damaged encountered in the field.

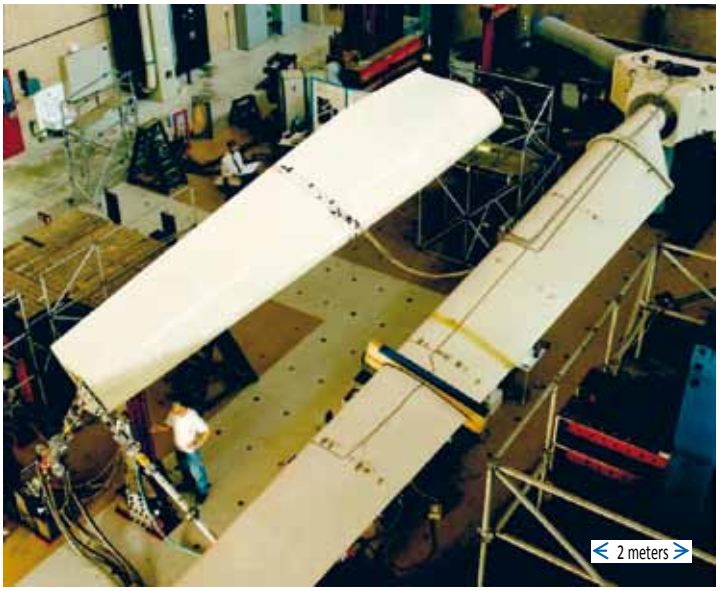

Fig. 15: Bi-axial forced displacement tests on steel (right) and laminated wood blade (WMC, 1984)

Accurate fatigue characterization of the materials is not only vital for a sound blade design, but also key to the derivation of test loads. Generally the design load spectrum is translated to a constant amplitude test load. Therefore both the shape of the CLD as well as the slope of the S-N-curves have an impact on the test loads, which highlights the importance of a good material characterization. As a blade is a hybrid structure, different material characteristics (different S-N

slopes) inevitably mean that not all parts are tested equally and some parts are overloaded or underloaded.

An interesting aspect is that if an incorrect slope parameter for a material is derived in the material test program for a blade, that this is not tested for in the blade fatigue test. For instance, a too flat slope for the S-N curve will result in too high allowable stress assumptions for the blade design, when extrapolating to high cycle counts. In the blade fatigue test however, the same slope parameter will cause the tests loads to be scaled up correspondingly (in this case lower than for the correct S-N slope). Therefore the blade is only tested against the assumed fatigue characteristics, and the accuracy of the blade test is determined by the accuracy of the material model.

Blade fatigue tests are limited by the test method chosen. Various methods exist, such as single-axis (near) resonance, bi-axial forced displacement (e.g. Fig. 15), and bi-axial (near) resonance. Each method has its particular advantages and disadvantages related to energy consumption, speed, and realism. Every simplification in the test loading (e.g. testing at R=-1 in resonance tests) will increase the dependence on the accuracy of the material models to design a suitable test. Furthermore validation of a part and construction details of the blade not only requires a suitable test method, but also requires that representative material data for all materials in these components is available.

8. CONCLUDING REMARKS

Reaching higher limits in durability of wind turbine composites must be preceded by gaining insight in failure initiation and growth. The currently used fatigue models are predominantly based on description of time to failure. This complicates the integration of various durability aspects into a limited amount of design models, such as temperature, frequency, variable amplitude, repair, complex stress states, and more.

The key of focusing research efforts and enabling characterization of a plethora of possible material combinations may be to delve deeper into description of fatigue damage mechanisms rather than quantification of merely the result of these damage mechanisms.

In line with that, it is noted that most of the above was related to fatigue of composite materials, treated as bulk material. However, ‘the devil is in the detail’, and a blade is not likely to break in the bulk material only, but in a design detail combining various materials in a complex geometry.

Experimental validation of subcomponents –structural specimens that represent generic or specific design details in a blade, while being cost-effective and testable using fairly standard equipment– is a relatively cost-effective way of identifying issues that cannot be derived from material models that are limited in their description of possible failure modes and –progressions.

Well-designed material and structural testing helps identifying the material limits and guides the material and structural design towards new horizons.

REFERENCES

Andersen, S.I., Brøndsted, P., Jørgensen, O., Lilholt, H. (1996), Damping properties of polymers and polymeric composites for wingblades, proc. European Union wind energy conference, Göteborg (SE), 20-24 May 1996. Zervos, A., Ehmann, H., Helm, P. (eds.), (H.S. Stephens & Associates, Bedford, 1996) pp. 954-959.

Bach, P.W. (1992), Fatigue properties of glass- and glass/carbon-polyester composites for wind turbines, Energy research Centre of the Netherlands report: ECN-C-92-072, Petten, the Netherlands, 1992.

Brøndsted, P., Lilholt, H., Lystrup, A. (2005), in the Ann. Rev. Mater. Res. 35, 505. 2005.

Brøndsted, P.; Andersen, S.I.; Lilholt, H. (1996), Fatigue performance of glass/polyester laminates and the monitoring of material degradation, Mech. Compos. Mater. (1996) 32 (no.1) , 32-41.

de Jonge, J.B. (1969), Fatigue load monitoring of tactical aircraft, National Aerospace Laboratory of the Netherlands report: NLR TR 69063 LI, prepared for presentation at the 29th meeting of the AGARD Structures and Materials Panel, Istanbul, Turkey, 28 September to 8 October 1969.

Gamstedt E.K. (1997), Fatigue Damage Mechanisms in Polymer Matrix Composites, dissertation, Luleå University of Technology, 1997.

Hedgepeth J.M. (1961), Stress Concentrations in Filamentary Structures, NASA TN D-882, May, 1961.

Joncas, S. (2010), Thermoplastic Composite Wind turbine blades, dissertation, Delft University of Technology, 2010, ISBN978-2-921145-73-2.

Joosse, P.A., van Delft, D.R.V. (1993), Fatigue design curves of fiberglass blade material compared to test data, proc. Wind Energy Conversion, 1993, pp. 275-280.

Kensche, C.W., Seifert, H. (1990), Wind Turbine Rotor Blades Under Fatigue Loads, proc. 4th European Conference on Composite Materials, 1990, pp. 173-180.

Mandell, J. F., Reed, R.M., Samborsky, D.D. (1992), Fatigue of Fiberglass Wind Turbine Blade Materials, Sandia National Laboratory contractor report: SAND92-7005, Montana State University, August 1992.

Mandell, J.F., Samborsky, D.D., Wahl, N.K., and Sutherland, H.J. (2003), Testing and Analysis of Low Cost Composite Materials Under Spectrum Loading and High Cycle Fatigue Conditions, proc. The 14th International Conference on Composite Materials (ICCM-14), Society of Manufacturing Engineers, San Diego, California, July 14 - 18, 2003. Paper 1811. (2003).

Matsuishi, M., Endo, T. (1968), Fatigue of Metals Subjected to Varying Stress – Fatigue Lives under Random Loading, preliminary proceedings of the Kyushu District Meeting, Japan Society of Mechanical Engineers, March 1968, pp. 37-40.

Mishnaevsky, L. Jr., Brøndsted, P. (2009a), Micromechanisms of damage in unidirectional fiber reinforced composites: 3D computational analysis, Composites Science and Technology, 2009, Vol. 69, pp. 1036-1044.

Mishnaevsky, L. Jr., Brøndsted, P. (2009b), Micromechanical modellingmodeling of damage and fracture of unidirectional fiber reinforced composites : A review.,Computational Materials Science, Vol: 44(4), p. 1351-1359 (2009). Elsevier Science BV 2009.

Nijssen, R. (2006), Fatigue life prediction and strength degradation of wind turbine rotor blade composites, dissertation, Delft University of Technology, 2006, ISBN: 978-90-9021221-0

Nijssen, R., Westphal, T, Stammes, E., Lekou, D., Brøndsted, P. (2008), Rotor structures and materials – strength and fatigue experiments and phenomenological modeling, proc. European Wind Energy Conference, 2008.

Nijssen, R.P.L., Westphal, T., Stammes, E., Sari, J. (2010), Strength and fatigue of wind turbine rotor laminates and subcomponents, proc. AIAA Wind Energy Symposium, paper 1189, January 2010.

OPTIMAT (2006), http://www.wmc.eu/optimatblades.php.

Qian, C., Nijssen, R.P.L., Samborsky, D.D., Kassapoglou, C. Gürdal, Z., Zhang, G.Q. (2010), Tensile fatigue behavior of single fibers and fiber bundles, proc. 14th European Conference on Composite Materials, Budapest, 2010.

Talreja, R. (1981), Fatigue of Composite Materials: Damage Mechanisms and Fatigue-Life Diagrams, Proceedings of the Royal Society of London, A378, 461-475. 1981.

Talreja, R. (1986), Stiffness Properties Of Composite Laminates With Matrix Cracking And Interior Delamination, Engineering Fracture Mechanics Vol. 25. NOS 5/6. pp. 751-762. 1986

UPWIND (2011), http://www.UPWIND.eu.

van Delft, D.R.V., Hagg, F., Joosse, P.A. (1990), The influence of fatigue design line criteria on the rotor blade design, proc. European Wind Energy Conference, September 1990, pp. 395-399.

van Delft, D.R.V., Rink, H.D., Joosse, P.A., Bach, P.W. (1994), Fatigue Behavior of Fiberglass Wind Turbine Blade Material at the Very High Cycle Range, proc. EWEA Conference and Exhibition, 1994, pp. 379-384.

Vestas (2011), http://worldofwind.vestas.com/presentations/generic.

Zangenberg, J. Larsen, J.B., Østergaard, R.C., Brøndsted, P., A methodology for characterisation of Glass Fiber Composite Architecture, in press.

Proceedings of the 32nd
Risø International Symposium on Materials Science:
Composite materials for structural performance:
Towards higher limits
Editors: S. Fæster, D. Juul Jensen,
B. Ralph, B.F. Sørensen
Risø National Laboratory for Sustainable Energy,
Technical University of Denmark, 2011

HIGH RESOLUTION TOMOGRAPHY STUDIES OF COMPOSITES: THE DATA RICH MECHANICS OPPORTUNITY

S.M. Spearing and I. Sinclair

University of Southampton
Southampton, UK, SO17 1BJ, UK

ABSTRACT

High resolution X-ray tomography has been used to observe and quantify damage mechanisms in composite materials under load. Using synchrotron and micro-focus X-ray sources resolutions of less than 2 μm have been routinely achieved. This enables individual broken fibres to be observed and crack opening and shear displacements for delaminations and intra-laminar cracks to be measured. Examples of the application of these techniques to transverse ply cracking, notch-tip splitting and fibre fracture accumulation are presented. Quantitative data are compared to model predictions. The overall implications for using such high resolution 3-D measurements to inform a "data-rich mechanics" approach to materials evaluation and modeling is discussed.

1. INTRODUCTION

Over the past four decades a plethora of mechanics models have been developed with the aim of predicting the failure of composite materials. Over the last fifteen years a series of "World wide failure exercises" (Hinton et al. 2004) have been conducted in order to assess the predictive capability for the failure of composite materials. The results have indicated that the overall modeling capability is relatively poor, at least compared to that for the metallic materials which composites are often used to replace. The difficulty in predicting failure is that composites typically fail by multiple interacting damage mechanisms, which occur in three dimensions. Furthermore it is usually difficult to infer the underlying damage mechanisms solely by inspection of the surface of the structure or test coupon. The response of the modeling and design communities has been to rely on extensive testing for any safety-critical parts in order to supplement, or in some case, completely replace any reliance on modeling. These issues are further compounded when issues of durability are to be addressed, and where comprehensive test programmes are particularly time consuming and expensive.

We have been conducting research over the past six years into the use of high-resolution computed tomography (HRCT) to elucidate damage mechanisms in composite materials

(Wright et al. 2008, Moffat et al. 2008, Moffat et al. 2010, Wright et al. 2010, Scott et al. 2011, Renault et al. 2011). In particular we have found the ability to identify features in composites under load and to measure their relative displacements in order to infer strains or to calculate crack opening and shear displacements is a very powerful tool by which to interrogate and validate mechanics models for composite failure processes. This approach has the potential to change radically the approach to composite modeling and mechanical testing. This paper provides an overview of our initial work in this area and an assessment of the potential for HRCT to contribute to the understanding and modeling of composite failure.

2. TESTING METHOD

The details of the testing and imaging procedures are described more fully elsewhere (Wright et al. 2010). High-resolution tomographic imaging was conducted on beam line ID19 at the European Synchrotron Radiation Facility (ESRF) in Grenoble. In this facility resolutions down to 0.3 μm can be achieved, although for most of the work described herein a voxel dimension of 1.4 μm was found to represent the best compromise between the resolution and field of view. The synchrotron produces a highly coherent, monochromatic X-ray source, which allows for both absorbtion and phase contrast imaging, which is particularly important for allowing crack surfaces to be identified. Lower resolution imaging was conducted using the three microfocus beamlines available at the μVis facility at Southampton. Although lower resolution, and not permitting phase contrast imaging, resolutions of lower than 3 μm can be routinely achieved, as well as allowing larger specimens to be imaged and larger fields of view obtained.

For in situ tensile loading a small loading rig was designed and built, shown schematically in Fig. 1. This has a load capacity of 1kN and is designed to allow 360° X-ray access with isotropic absorbtion. The fixture is particularly suited to use in the synchrotron, with its high resolution capabilities, but can be used in conjunction with micro-focus sources. The load frame allows damage development to be tracked as a function of load, as well as allowing damage to be imaged in the loaded and unloaded states, which allows for the separation of the effect of residual stresses and applied loads on crack opening and shear displacements. The majority of *in situ* loading tests conducted to date have used a double edge notched specimen with a total width of 4 mm, with two semi-circular notches of nominally 1mm radius/depth. This leaves a net section between the notches of 2 mm. In other work, particularly for the imaging of transverse ply cracking, straight-sided specimens with a cross-section of 1 mm x 1 mm were employed. All of the in situ loading conducted to date has focused on aerospace grade graphite epoxy, Hexel, Hexply® M21 in a (90/0)s lay-up.

An example of the utility of *in situ* loading is shown in Fig. 2, in which the effect of shear loading on a notch tip split is shown. The microscopic structure of the split; consisting of a series of microcracks, is clearly visible. Fig. 2a shows the unloaded damage and Fig. 2b the image of the damage under load. The mode I opening of the microcracks is evident from the images and measurements can be made. High resolution computed tomography in general is extremely valuable for allowing the initiation of damage to be understood, as it allows examination of the full specimen under load, rather than just the surfaces, thereby eliminating concerns that surface damage may be the result of un-representative stresses or machining damages. Fig. 3 shows the initial stages of delamination, near the cross-over of a transverse ply crack and a 0° split, clearly indicating the role of fibre-matrix debonds in initiating damage.

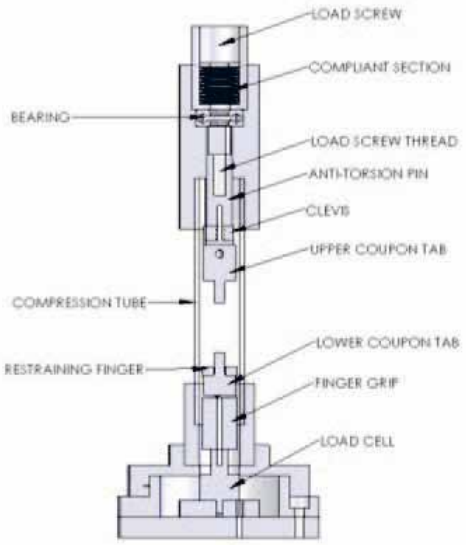

Fig. 1. Schematic of *in situ* loading fixture. Tensile specimens fit between the upper and lower coupon tabs.

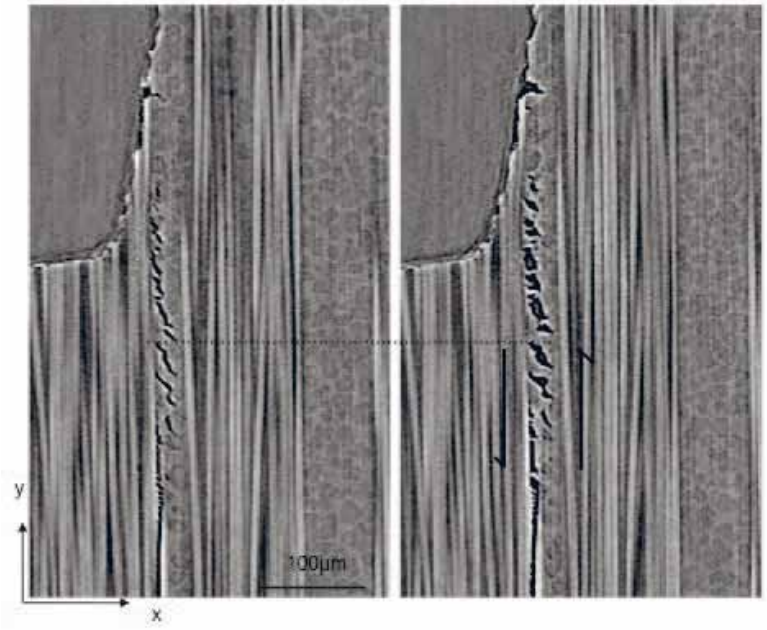

Fig. 2. An example of imaging with *in situ* loading of a split emanating from a notch tip (top left). The left hand image is unloaded and the right hand loaded.

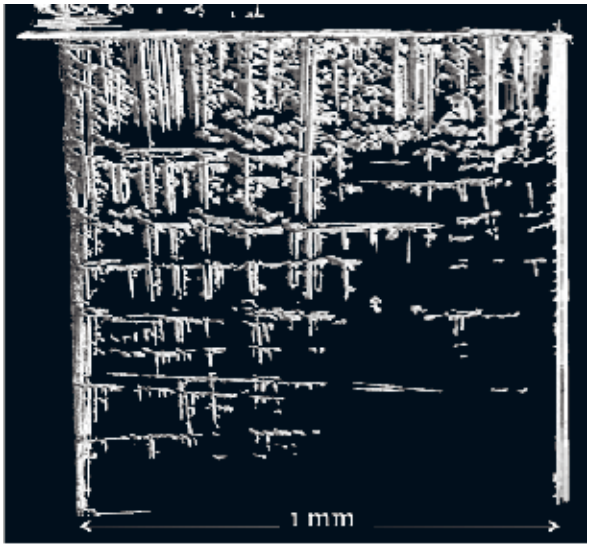

Fig. 3. A three-dimensional rendering of a early stage delamination, showing initial damage consisting of fibre-matrix debonds which subsequently links together.

3. TRANSVERSE PLY CRACKING

Unnotched graphite-epoxy (90/0)s laminates were loaded incrementally to failure (Renault et al. 2011). Fig. 4 shows a low-resolution microfocus CT scan of the gauge length of a specimen showing the resulting array of cracks. It is noteworthy that there is a strong correlation of the crack locations with the surface texture of the laminate left by the peel ply.

The data presented here consists of crack opening displacements measured from the same individual transverse ply crack at two load levels. Images were obtained by SRCT. A cross-section of a crack is shown in Fig. 5. The resin rich regions at the ply interface and intra-ply interface within the 90° ply are clearly visible. The particle toughening of this material is also visible. It is also noteworthy that the crack arrests within the interfacial region rather than at the uppermost 0° ply.

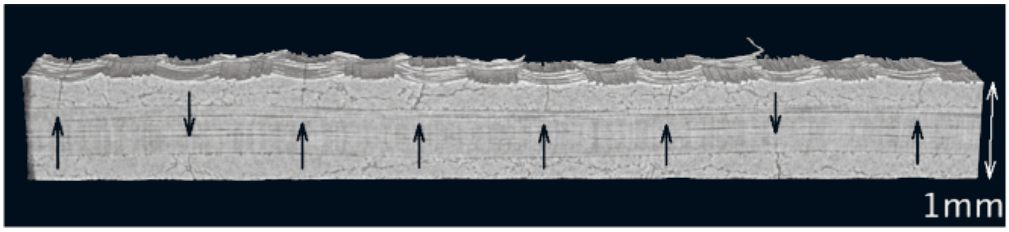

Fig. 4. Microfocus CT image of an unnotched (90/0)s graphite epoxy specimen showing transverse ply cracks, indicated by arrows.

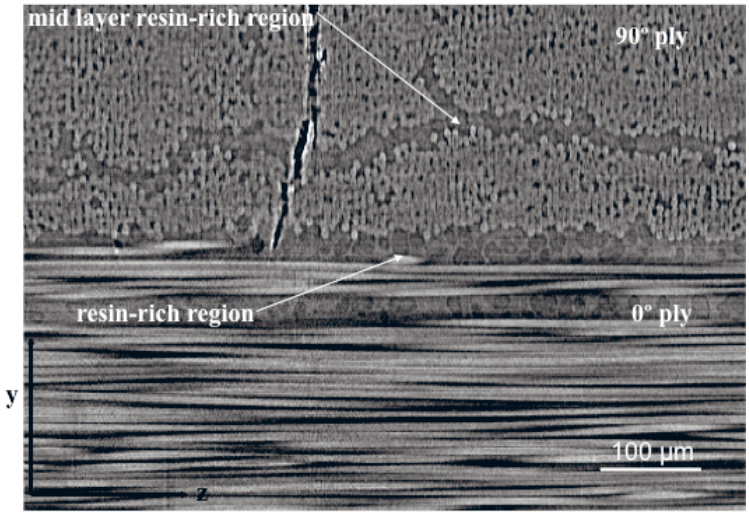

Fig. 5. SRCT cross-section of a transverse ply crack. Note the resin rich region at the interface between the 90° and 0° plies.

The cracks were segmented, and this allowed crack opening displacements to be calculated. By interpolation measurement resolutions down to approximately $1/10^{th}$ of the voxel size can be obtained. Fig. 6 shows the resulting contours of crack opening for this crack at 650 MPa and 880 MPa. Total crack opening displacements of the order of 10 – 20 µm are observed.

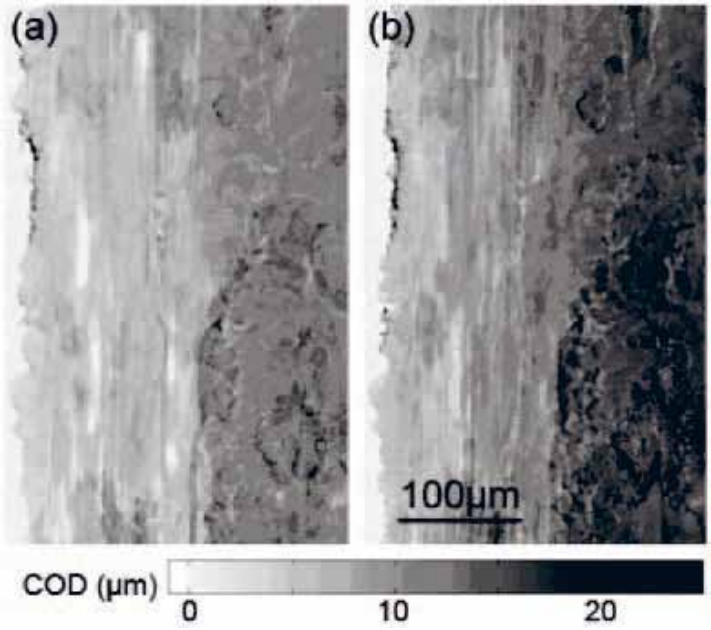

Fig. 6. Crack opening displacement contour maps for a transverse ply crack at 650 MPa and 880 MPa. Both images are of an identical region. The interface with the 0° ply is on the left hand side of both images and the free surface is to the right. Crack opening is indicated by a grey scale.

A 2-D finite element model was constructed in order to explore the ability to compare the quantitative CT data to mechanics model results. In addition to the schematic shown in Fig. 7, the model allowed for the insertion of a resin-rich region at the ply interface, and the introduction of non-linear properties for this region to reflect the non-linear constitutive behavior of this material.

Fig. 8 shows a comparison of the experimentally-measured crack opening displacements, averaged over the crack area, with the predictions of the finite element model for the baseline case without a resin rich region, a resin rich region with linear elastic properties and a plastically-deforming matrix. The crack opening displacement is the incremental displacement between the applied stress levels of 650 and 880 MPa, so as to eliminate the effect of residual stresses. It is clear that in all cases the modeling under-predicts the average crack opening displacement, with the closest prediction for the case where the inelastic resin-rich region is included. This provides a clear demonstration of the possibilities for comparing micro/meso-mechanical models to data in a way that has hitherto been impossible. Although the agreement between experiment and model is not exceptional, there is clearly scope for a more refined model, which would incorporate the details of the microstructure more fully as well as its three-dimensional character.

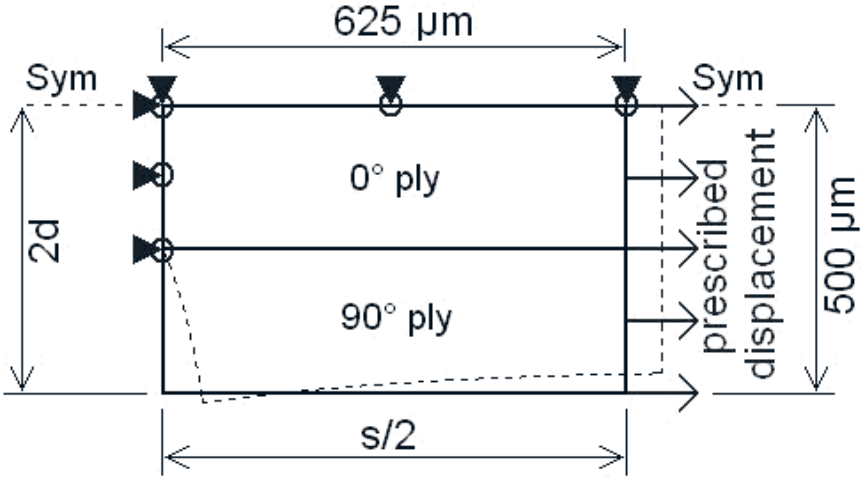

Fig. 7. Schematic of 2-D finite element model of a unit cell containing a transverse ply crack in the 90° ply. Other meshes introduced a resin-rich region at the 0/90 ply interface.

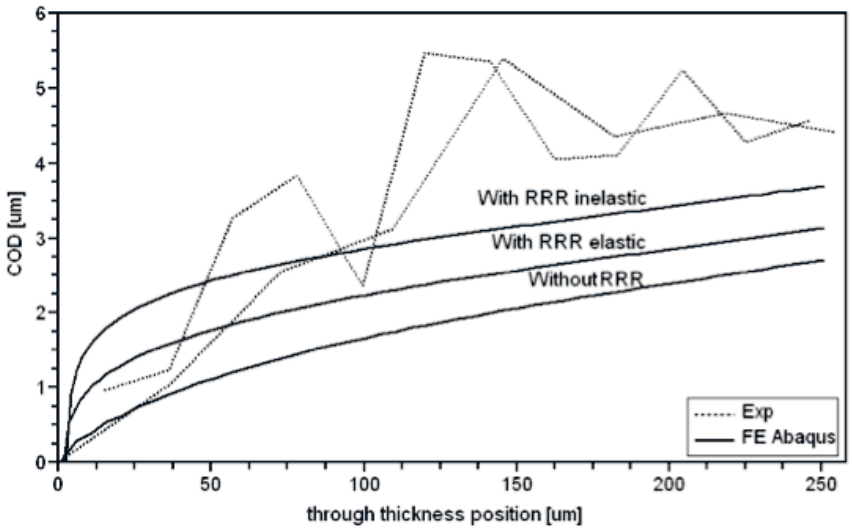

Fig. 8. Comparison of experimental results and finite element model predictions for the crack opening displacement through the 90° ply thickness. Model results are shown for the baseline model without a resin-rich region, and for a resin-rich region with elastic and inelastic properties.

4. SPLIT GROWTH FROM NOTCH TIPS.

As noted in section 2 the majority of the *in situ* loading studies conducted to date have used double edge notched specimens. A critical damage mode in such specimens is shear driven splitting of the 0° plies. This is illustrated in Fig. 9. As for the case of transverse ply cracks crack opening (and shear) displacements can be measured directly and in 3-D by segmenting out the crack volume and using appropriate image processing tools to infer the relevant displacements. Such experimental data, averaged over the split area is shown in Fig. 10. In a similar way to the case of the transverse ply cracking a finite element model was constructed to mimic the observed damage. Due to the 3-D nature of splits, and the importance of both the notch tip geometry and the confining 90° plies, 2-D modeling was not desirable (although this has been utilized in the past, see Spearing et al. 1992). Unlike the case of transverse ply cracking a linear elastic orthotropic material model was used throughout. The resulting predictions for crack opening displacement are shown in Fig. 10, and can be compared with the experimental measurements. As for the case of transverse ply cracking, measurements are made at two load levels and are subtracted in order to eliminate the effect of residual stresses. Again, this form of comparison has been hitherto not possible. The comparison between model and experiment is quite good, suggesting that the modeling approach taken captures the key physical aspects of the problem.

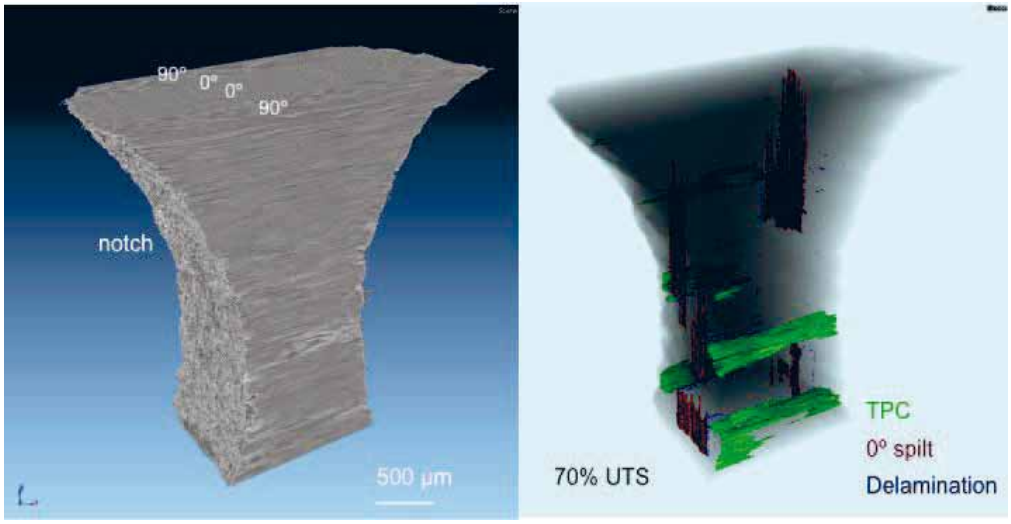

Fig. 9. SRCT images of the region between the notch tips in a double edge notched specimen. The right hand image shows the microstructure rendered opaque and the damage segmented and coloured. Transverse ply cracks are shown in green, delaminations in blue and splits in red.

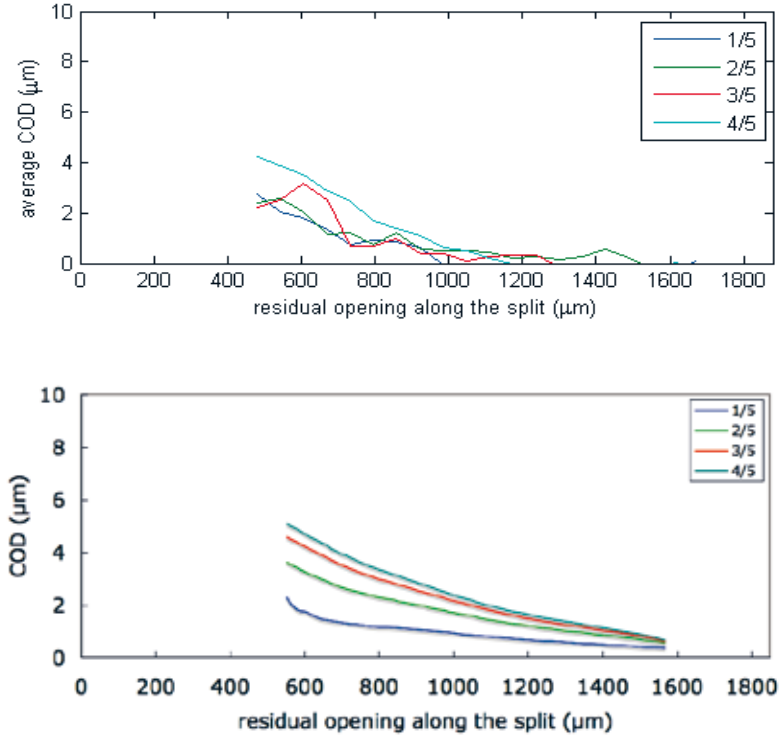

Fig. 10. a) SRCT measurements of relative average crack opening displacements for notch tip splits. b) predictions from a 3-D FE model. The curves show the relative position across the half-width of the ply containing the split.

5. FIBRE FRACTURE

Fibre fracture is the key failure mode in tensile loading of 0° dominated laminates. High resolution CT imaging combined with in situ loading provides a unique means to observe the development of broken fibres as a function of load. In particular the technique offers the opportunity to correlate broken fibres with microstructural features as well as the tendency for broken fibres to develop as clusters. Fig. 11 shows a 3-D SRCT image of the distribution of fibre breaks through the notch tip region of a double edge notched specimen. There is no correlation of the fibre breaks with the matrix-dominated damage. Fig. 12 shows a comparison between observed fibre fractures, expressed as their number density as a function of applied load. This experimental data is compared with a model for tensile failure (Blassiau et al. 2009), which includes prediction of the evolution of fibre fracture. The model predicts a comparable accelerating trend in fibre damage evolution, but underpredicts the precise number by a factor of two. Work is continuing to understand the source of this discrepancy and to develop more robust modeling techniques.

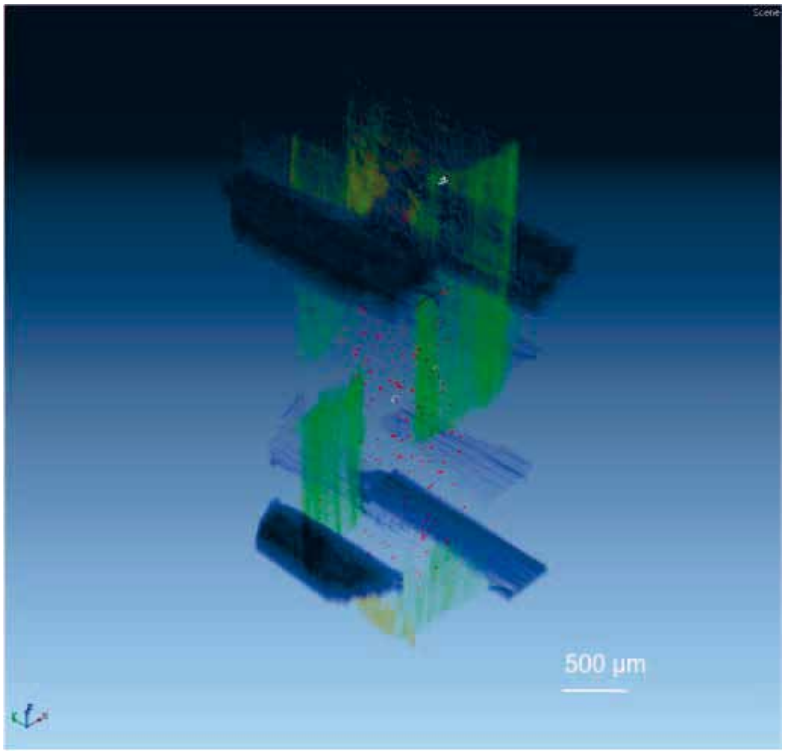

Fig. 11. Broken fibres in a double edge notched specimen at 100% of the nominal failure load. Broken fibres are shown as red points. Clusters of broken fibres are shown in white. Splits are shown in yellow, delaminations in green and transverse ply cracks in blue.

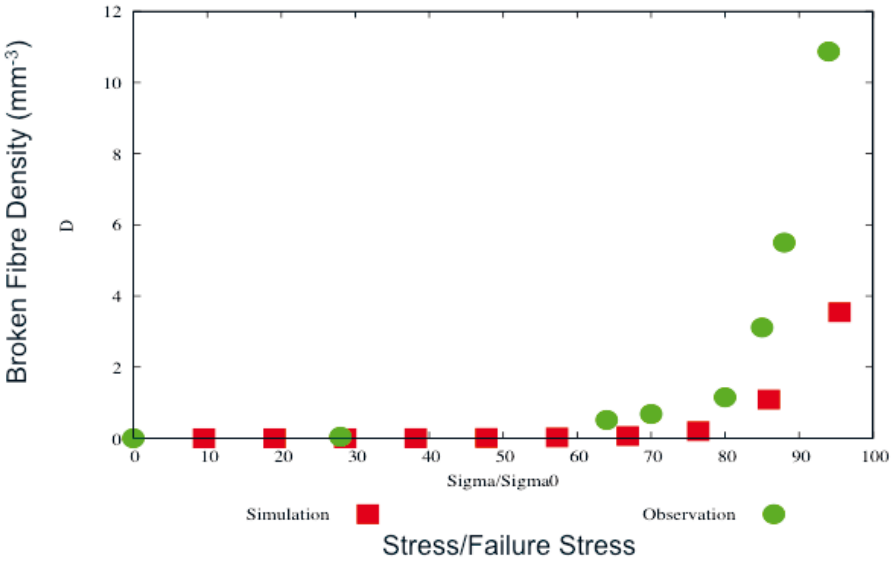

Fig. 12. Data for fibre fracture evolution with applied stress (normalized to the failure stress) compared to model predictions (Scott et al. 2011, Blassiau et al. 2009).

Fibre fracture is a useful metric for the service history of composite structures. Figure 13 shows an SRCT image of a cross-section of a filament wound composite cylinder subjected to an internal pressure loading. The cylinder consists of an aluminium liner over-wound with a sequence of hoop, helical, hoop plies of carbon fibre. From Fig.13 it is clear that the inner hoop ply contains a much higher density of broken fibres than the other plies. This correlates with the local fibre volume fraction achieved by the manufacturing process and with the predicted variation in ply level stresses. It is also clear that there is no correlation between fibre fracture and either matrix damage or fabrication-induced voids. This study illustrates the potential to use high resolution computed tomography to infer the load history experienced by parts extracted from service as well as the effect of local stress concentrations.

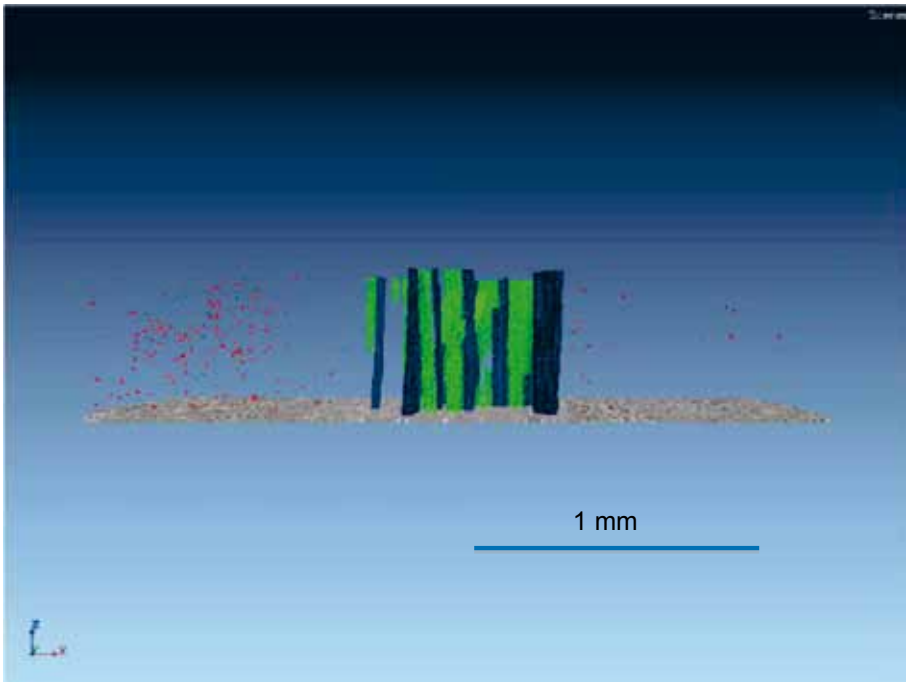

Fig. 13. Fibre fractures (shown in red) in the three plies of a filament wound cylinder loaded by internal pressure. The inner hoop layer is to the left, helical in the middle and outer hoop to the right. Matrix cracks are shown in green, and voids in blue.

6. DISCUSSION

In the preceding examples a number of common themes recur. In particular the ability to image at high resolution allows for direct measurements of displacements, and in principle, strains to be obtained. This allows for an unprecedented opportunity to inform and validate micro- and "meso-mechanics" models for composite deformation and failure. Measurements can be obtained throughout the imaged volume. With the available resolution the location and damage state of every fibre or other relevant microstructural feature can be tracked and mapped. This capability allows the notion of "data rich mechanics", a term that we have coined to recognize that our ability to develop and calibrate models is no longer limited by the ability to obtain independent micromechanical data. This has the potential to move the modeling capability for composite failure beyond the largely phenomenological models utilized in the "World-Wide Failure Exercise" (Hinton et al. 2004).

There are significant challenges associated with taking advantage of the data rich mechanics opportunity. There is a continual trade-off between achieving high resolution and obtaining a representative field of view. This requires that effort is made to ensure that information obtained from small scale specimens is representative of the behaviour of materials in large-scale structures. In the present work this has been achieved by use of multi-scale imaging approaches, combining micro-focus and SRCT images, but also using combinations of *in situ* imaging and extraction of samples from larger specimens or structures. There is still

considerable work to be done on developing robust feature recognition algorithms to allow for the identification and tracking of material microstructure and damage. Most of the images obtained in the current work relied upon human intervention to confirm and/or adjust the results from automated methods. The data sets obtained can be very large. A typical reduced SRCT image file is in excess of 4GB in size. This presents significant data handling and storage challenges, particularly when several files are required to track damage development in an experiment using *in situ* loading. A related challenge is the development of methods to compare large data sets with model predictions in 3-D. The key here is probably to identify the most sensitive parameters, and to focus on these rather than to attempt to cover the entire volume.

In addition to the data rich mechanics there are also more direct opportunities afforded by the use of high resolution CT imaging. The 3-D interactions of damage modes can be assessed in a way that has not previously been possible. For instance the correlation of fibre fractures with other damage modes or features such as voids and notches can be assessed. For the systems that are reported in this paper there is relatively little influence of these features on the development of fibre breaks. Conversely, voids do play a clear role in initiating intralaminar cracks and delaminations. Also, delaminations result from the interactions between transverse ply cracks and splits and seem to occur by the coalescence of fibre-matrix debonds at a very small scale. The high resolution also allows a fundamental understanding to be obtained of microstructural phenomena such as matrix toughening, fibre debonding and fibre failure. Not presented herein, but a focus of other work undertaken by the authors and their collaborators is the opportunity to understand the fundamental mechanisms affecting fatigue life and durability of composite structures. Of particular interest is the opportunity to conduct accelerated testing by virtue of the ability to identify mechanisms at high resolution. Comparisons between damage states can be made at much earlier stages of a specimen or structure's lifetime when damage can be identified at high resolution, in 3-D throughout a specimen volume. Finally, the ability to identify all damage events with a loaded volume provides a hitherto impossible opportunity to validate non-destructive evaluation (NDE) and structural health monitoring (SHM) techniques. The output of NDE and SHM techniques, which can detect down to individual delaminations, intralaminar cracks and fibre fractures can be verified against "gold standard" data sets.

5. CONCLUSIONS

This paper has presented results from in situ fracture tests using high resolution computed tomography imaging. Key damage modes have been imaged in three dimensions, resulting in new insights regarding their development and interaction. The work has focused on transverse ply cracking, notch tip splitting and distributed fibre fracture. Data for local deformations, particular crack opening displacements, has been obtained and used to compare with numerical models for composite deformation and failure has been demonstrated. This has great potential for allowing increasingly physically-based models for predicting composite failure and durability.

ACKNOWLEDGEMENTS

The authors wish to thank many collaborators and Ph.D students who have contributed to the work described herein. Funding from the UK's Engineering and Physical Sciences Research Council is gratefully acknowledged.

REFERENCES

S. Blassiau, A. Thionnet and A. R. Bunsell (2009), "Three-dimensional analysis of load transfer micro-mechanisms in fibre/matrix composites," *Comp. Sci. Tech*. **69**(1), 33-37.

M. J. Hinton, A. S. Kaddour, P. D. Soden (2004), "A further assessment of the predictive capabilities of current failure theories for composite laminates: comparison with experimental evidence", *Comp. Sci. Tech,* **64**(3-4), 549-588.

A. J. Moffat, P. Wright, J.Y. Buffiere, I. Sinclair and S. M. Spearing (2008), "Micromechanisms of damage in 0 degrees splits in a $[90/0]_s$ composite material using synchrotron radiation computed tomography," *Scripta Mater.*, **59** (10), 1043-1046.

A. J. Moffat, P. Wright, L. Helfen, T. Baumbach, G. Johnson, S. M. Spearing, I. Sinclair (2010), "In situ Synchrotron Computed Laminography of damage in Carbon Fibre Epoxy (90/0)s Laminates," *Scripta Materialia,* **62**(2), 97-100.

A. Renault, A. J. Moffat, P. Wright, I. Sinclair and S. M. Spearing (2011), "Direct Measurement of Transverse Ply Crack Opening Using Synchrotron X-ray Computed Tomography and Comparison with Models". Submitted to *Journal of Composite Materials*.

A. E. Scott, M. Mavrogadarto, P. Wright, I. Sinclair, S. M. Spearing (2011), "In situ fibre fracture measurement in carbon fibre-epoxy laminates using high resolution computed tomography," *Comp. Sci. Tech.* Accepted for publication.

S. M. Spearing, P. W. R. Beaumont and M. F. Ashby (1992), "Fatigue Damage Mechanics of Composite Materials II: A Damage Growth Model," *Composite Science and. Technology,* **44**, 169-177.

P. Wright, X. Fu, I. Sinclair, S. M. Spearing (2008) "Ultra high resolution computed tomography of damage in notched carbon fiber-epoxy composites," *J. Comp. Mater.* **42**(19), 1993-2002.

P. Wright, A. Moffat, I. Sinclair, S. M. Spearing (2010), "High resolution tomographic imaging and modeling of notch tip damage in a laminated composite," *Comp. Sci. Tech.* **70**(10), 1444-1452.

Proceedings of the 32nd
Risø International Symposium on Materials Science:
Composite materials for structural performance:
Towards higher limits
Editors: S. Fæster, D. Juul Jensen,
B. Ralph, B.F. Sørensen
Risø National Laboratory for Sustainable Energy,
Technical University of Denmark, 2011

MOVING THE LIMITS OF COHESIVE ZONE MODELING - FROM IDEALIZED TO ACTUAL COHESIVE LAWS

B.F. Sørensen

Materials Research Division, Risø National Laboratory for Sustainably Energy, Technical University of Denmark, Frederiksborgvej 399, DK-4000 Roskilde, Denmark

ABSTRACT

Cohesive laws form a relatively new type of material law, encompassing both strength and fracture toughness. Cohesive laws are particularly well suited for describing delamination of laminated composites, sandwich structures and adhesive joins. This paper provides an overview of the current status for cohesive laws for the modelling of fracture in engineering materials and structures. Topics covered are pure Mode I cohesive laws, Mixed Mode cohesive laws as well as the use of a cohesive law for describing rate-dependent fracture and cyclic crack growth (fatigue). Selected experimental results are presented. Measurement methods, models and unresolved issues are discussed.

1. INTRODUCTION

1.1 Background. The concepts of strength, dating back to Galileo in the seventeen century (Timoshenko 1953) and fracture energy, introduced by Griffith (1921), are likely to be replaced by the concept of cohesive laws as the unifying, universal fracture-controlling concept for materials and structures. A cohesive law is a traction-separation relationship that represents the mechanics of fracture. Although introduced by Dugdale (1960) and Barenblatt (1962) about 50 years ago, cohesive laws did not gain widespread use until introduced in the modelling by the finite element methods (Needleman 1987). First, cohesive zone modelling was used in micromechanical modelling and in fundamental studies of the effect of crack tip plasticity on overall fracture toughness (Tvergaard and Hutchinson 1992). However, by the use of cohesive laws for the modelling of structural components such as adhesive joints (Yang, Thouless and Ward 1999; Mohammad and Liechti 2000; Sørensen 2002), cohesive laws were established as being measureable from experiments and used modelling for reliable predictions of load-carrying structures. From then on, cohesive laws were no longer just elegant, academic concepts. Cohesive laws were material laws.

The power of the cohesive law concept is its generality and versatility: It can be used at many length scales to represent fracture; it can be used for a number of different failure mechanisms; it can be used for modelling crack initiation as well as crack propagation under static as well as cyclic loads. Unlike e.g. the concept of critical stress intensity factor (Irwin, Kies and Smith 1958) - which is a linear elastic fracture mechanics (LEFM) concept - cohesive zone modelling is not restricted to linear elastic material behaviour, the existence of a crack, the limitations to a small scale fracture process zone and small scale yielding. Cohesive laws can be used for problems undergoing large-scale plasticity and possess a large scale (planar) fracture process zone, such as large scale bridging.

The outset for this paper is that cohesive laws are the pertinent laws to represent fracture. We will not treat strength and fracture toughness as independent material properties but consider them as being special properties derived from a cohesive law, which is the basic material law for fracture. We will attempt to view any type of material or structural failure through cohesive laws, irrespective of whether failure occurs under a monotonically increasing load, a constant load (possibly leading to creep) or a cyclic load (fatigue). Particular emphasis will be on large scale crack bridging problems that are frequently encountered in composite materials and structures.

The motivation is to use of cohesive law for reliable strength prediction of real engineering structures, such as adhesive joints, sandwich structures and composite laminates, e.g. in cars, boats and wind turbine blades. This idea follows a top down approach to fracture. That is, cohesive laws are treated as phenomenological continuum mechanics laws to be determined experimentally, not from fundamental atomistic simulations. That is not to say that the coupling to smaller length scales is not useful. Coupling from the macroscale to the microscale is particularly useful for the study of what makes materials tougher - this is of great relevance for materials science aiming at the development of new materials having superior properties. For instance, the shape of a cohesive law represents information of the underlying microscale toughening mechanism (Sørensen and Kirkegaard 2006). However, for the prediction of the load-carrying capability of structures and components, macroscale cohesive laws are sufficient. So, in order to be able to use cohesive zone modelling for real structural applications, one must (1) measure the relevant cohesive laws of the materials involved and the interfaces, and (2) devise a robust and consistent theoretical cohesive law formulation and (3) and implement the cohesive laws in a (numerical) model of the structure.

1.2 Motivation: Moving the limits. A better understanding of cohesive laws of real materials can move the limits in two ways. First, since the shape of a cohesive law reflects the underlying microscale failure mechanisms, accurate measurements of cohesive laws provide information that can be used for uncovering the dominating toughening mechanism in a real material (or interfaces between dissimilar materials). Then, it may be easier to perform microscale optimization, enhance specific material properties, i.e., moving the *limits of the materials*. Second, a more accurate cohesive law description (meaning that materials strength properties can be described and modelled more correctly) will increase the accuracy of strength predictions, i.e., creating more accurate *design limits*. Then, the reliability of strength prediction increases and partial safety factors can be reduced.

1.3 Purpose and content of paper. The present paper aims to present a brief summary of the current state-of-the-art and give a a view to what is needed for cohesive zone modelling for a number of different problems such as Mode I cracking under monotonically increasing load, Mixed Mode cohesive laws, crack growth under cyclic loading (fatigue), and the effects of opening rate (visco-elasticity and creep). We will pay attention to experimental observations and point out when there are significant difference between idealized cohesive laws and the real

physical fracture mechanism. Focus will be on problems that involve a large scale fracture process zone, exemplified with large scale fibre bridging zones typically encountered in composites and composite structures.

2. PURE MODE COHESIVE LAWS

2.1 Definition of cohesive zone and cohesive law. First, a brief introduction to cohesive laws will be given. To do so, we consider a Mode I problem in some detail. That is a problem where the material, the specimen and loads are all symmetric about the specimen mid-plane, such that the fracture evolves along the mid-plane of the specimen. Then, due to symmetry, the fracture process zone only deforms in the direction normal to the fracture plane (typically denoted Mode I cracking).

A *fracture process zone* is a zone developing damage (usually due to the stress concentration near a crack tip or a notch), i.e., locally the strength of the material is reduced as indicated in Fig. 1. It is thus implicit assumed that the material possesses a finite tensile strength, $\hat{\sigma}_n$. This is physically realistic, since, far ahead of the crack where the stress is below $\hat{\sigma}_n$, the material should remain undamaged. We define the *macroscopic crack tip* as the position where there is no physical connection between the crack faces (position $x_1 = -L$ in Fig. 1a). Ahead of the macroscopic crack tip the stress has increased to $\hat{\sigma}_n$. At this position, the material develops damage. The fracture process zone thus covers the zone given by $-L < x_1 < 0$. In this fracture process zone, the material weakens and its ability to transfer stress decreases, while an opening, δ_n, develops. Loaded sufficiently high, the material will fail completely at $x_1 = -L$, such that its ability to transfer stresses between the crack faces vanishes. This critical value of the end-opening, δ_n^* (the value of δ_n at $x_1 = -L$), is denoted δ_n^0.

In cohesive zone modelling, the mechanical behaviour of the fracture process zone is modelled as follows. A *cohesive zone* is specified along the anticipated fracture process zone path. In the cohesive zone, the stress transfer between the two fictitious crack faces are described in terms of a cohesive law, which is a traction-separation relation. The traction-separation law is assumed to be the same at any position along the cohesive zone; the local traction, σ_n, is assumed only to be a function of the local separation, δ_n. The Mode I cohesive law formulation:

$$\sigma_n = \sigma_n(\delta_n), \tag{1}$$

implies that during a monotonic opening, the traction at any x_1-position depends only on the local separation at that point.

Two crack tips can be considered in this "fictitious crack" model: the *damage front* at $x_1 = 0$ and the macroscopic crack tip at $x_1 = -L$. It is the *active* part of the cohesive zone, i.e., the part of the cohesive zone for which the cohesive zone has separated ($-L < x_1 < 0$ in Fig. 1), that corresponds to the fracture process zone.

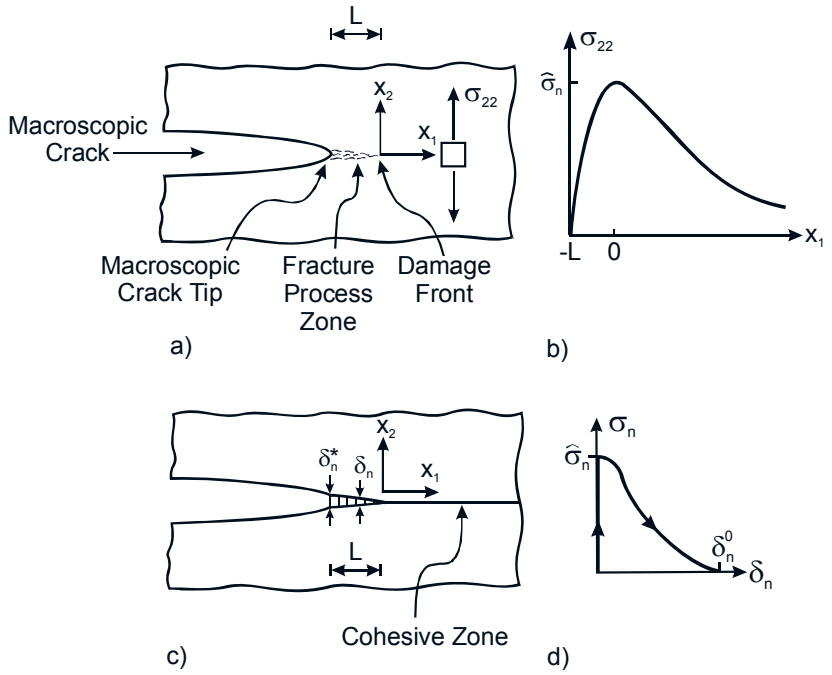

Fig. 1. Schematics of (a) a fracture process zone and the stress distribution within it (b), (c) the associated cohesive zone model and (d) cohesive law (traction-separation law).

Connections can be made between the cohesive law and *the fracture resistance* by the integration-path-independent J integral (Rice 1968a). Evaluating the J integral locally around the cohesive zone gives

$$J_R = \int_0^{\delta_n^*} \sigma_n(\delta_n)\, d\delta_n . \tag{2}$$

Equation (2) can be interpreted as the work (per unit fracture area) of the cohesive tractions at the position of the end-opening. Note that it is the end-opening, δ_n^*, not the active cohesive zone length, L, that appears as the upper limit in the integral. The end-opening corresponds to the so-called crack tip opening displacement, CTOD, used to characterise the ductile fracture of metals (Hutchinson 1983).

The relationship between the cohesive law and the resulting fracture resistance is shown schematically in Fig. 2. The normal traction is assumed to decay to zero when the end-opening δ_n^* reached the critical value, δ_n^0. The fracture resistance rises to a steady-state level, denoted J_{ss}, when δ_n^* reaches, δ_n^0 (sometimes called the *critical separation*). The cohesive zone is then said to be *fully developed*. Then, J_R has reached a steady-state value, J_{ss}:

$$J_{ss} = \int_0^{\delta_n^0} \sigma_n(\delta_n)\, d\delta_n \tag{3}$$

J_{ss} is called the *work of separation* or the fracture energy.

It is also appropriate to define the term *steady-state cracking*. Steady-state cracking implies that the fracture process zone (or, in the language of cohesive zone modelling, the active cohesive zone) is fully developed ($\delta_n^* = \delta_n^0$) and retains the same steady-state length, L_{ss}, and translates along the specimen in a self-similar fashion under constant conditions. Some fracture mechanics test specimens are steady state specimens, some are not. Note that steady-state cracking is *not* merely a specimen with a fully develop active zone ($\delta_n^* = \delta_n^0$) for which the fracture resistance is at its steady-state value.

Note also that the result (3) is independent of the active cohesive zone length. It also holds for specimens that are not steady-steady specimens; all that is required is that the active cohesive zone is fully developed.

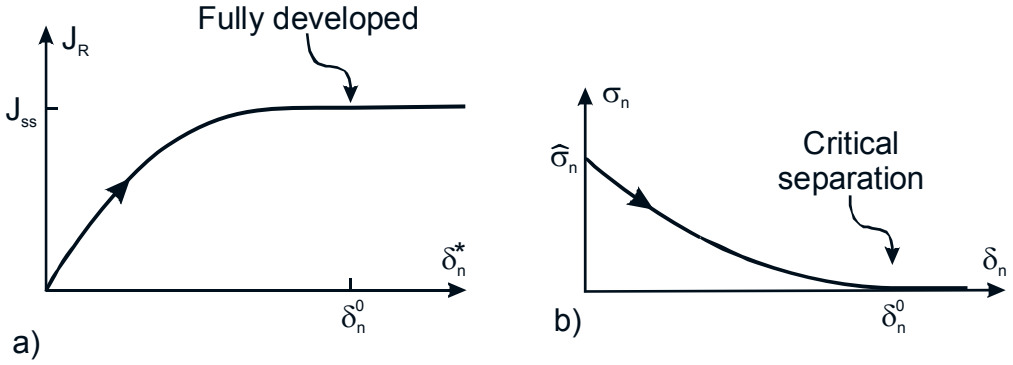

Fig. 2. Schematic illustration showing (a) the fracture resistance, J_R, as a function of the end-opening, δ_n^*, and (b) the underlying cohesive law.

Equations (2) and (3) are valid for both small and large scale fracture process zone sizes (Suo, Bao and Fan 1992). For small scale fracture process zones, LEFM apply, and J_{ss} is the fracture energy. Then, under the premises of LEFM (small scale fracture process zone size, small scale yielding), details of the cohesive law (peak traction, critical separation, cohesive law shape) are not of importance (Rice 1968b). However, for materials exhibiting a large scale fracture process zone, such as concrete and fibre composites, LEFM is insufficient and a cohesive law should be taken as the basic fracture controlling material law.

2.2 Idealised Mode I cohesive laws. A number of different idealised cohesive laws have been proposed for cohesive zone modelling. Some examples are given in Fig. 3. Most of these are purely hypothetical in the sense that they are based on neither measurements nor theoretical considerations, but are chosen for their simplicity and for numerical convenience. For instance, the trapezoidal cohesive law proposed by Tvergaard and Hutchinson (1992) has a plateau of the peak traction, $\hat{\sigma}_n$, which - relative to the yield stress of the surrounding bulk material - has a dominant role in the development of a plastic zone. Notable exceptions are cohesive laws that based on theoretical considerations or micromechanical models. Examples are the exponential

decaying cohesive law used by Xu and Needleman (1993), which is based on a fit to atomistic calculations, the square root law, which comes from a a micromechanical model of crack bridging by aligned, frictional slipping fibres oriented perpendicular to the cracking plane (Budiansky, Evans, Hutchinson 1995) and the inverse square-root law obtained from a micromechanical model of crack bridging by intact ligaments of aligned fibres parallel to the cracking plane (Spearing and Evans 1992; Sørensen and Jacobsen 1998). The last two are thus particularly relevant for the modelling of crack bridging in composites with long, aligned fibres.

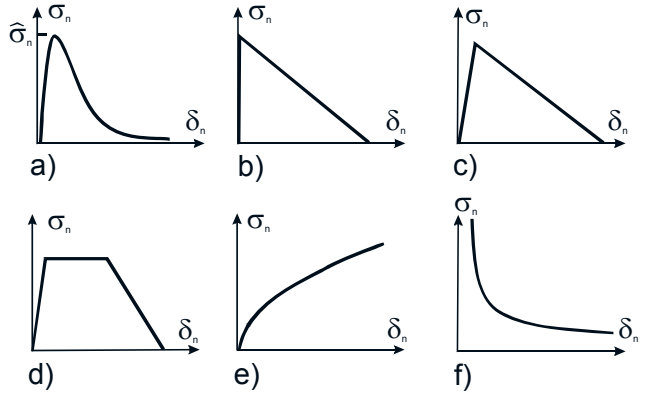

Fig. 3. Different types of idealised cohesive laws. (a) exponential decay, (b) linear softening, (c) bilinear softening (d) trapezoidal, (e) square root, ((f) inverse square root.

2.3 Measurement methods. At the present stage, realistic cohesive law parameters can only be obtained from mechanical testing of real materials and structures. The determination of cohesive laws is a rather new challenge in experimental mechanics. LEFM fracture tests and analyses are not directly usable for cohesive law determination. Importantly, in order to determine the complete cohesive law, the specimen must give a stable crack growth so that the opening of the cohesive zone occurs stably from zero to critical separation. New approaches, shown in Fig. 4, are briefly described below.

The most obvious and intuitive experimental method for the determination of a Mode I cohesive law is the direct tension method (Brenet, Conchin, Fantozzo, Reynaud, Rouby and Tallaron 1996). The experiment is designed such that the specimen develops a localisation (separation) zone in the gauge section. During the experiment, the applied stress and the displacement difference between two sides of a localized zone are recorded. This gives the traction-separation law directly. Although attractive and simple in principle, the test method has in practice a serious weakness: Often, the separation starts for one edge resulting in non-uniform separation so that it becomes impossible to get a stable and uniform separation across the specimen width. The measured traction-separation law is then inaccurate.

A second approach for experimental determination of cohesive laws is to perform numerical simulations of tested specimens undergoing cracking. A number of simulations are made using different trial cohesive law types. Cohesive law parameters are varied iteratively and the trial cohesive law that gives the best agreement with the overall experimental data (e.g. the load-displacement curve (Yang *et al*. 1999) or the near-tip displacement field (Mohammad and Liechti 2000)) is then regarded as being the "true" cohesive law. An advantage of this approach is that also problems involving large scale plasticity can be addressed. A drawback of this iterative approach is that the cohesive law cannot be identified better than the variety of assumed trial cohesive laws allows.

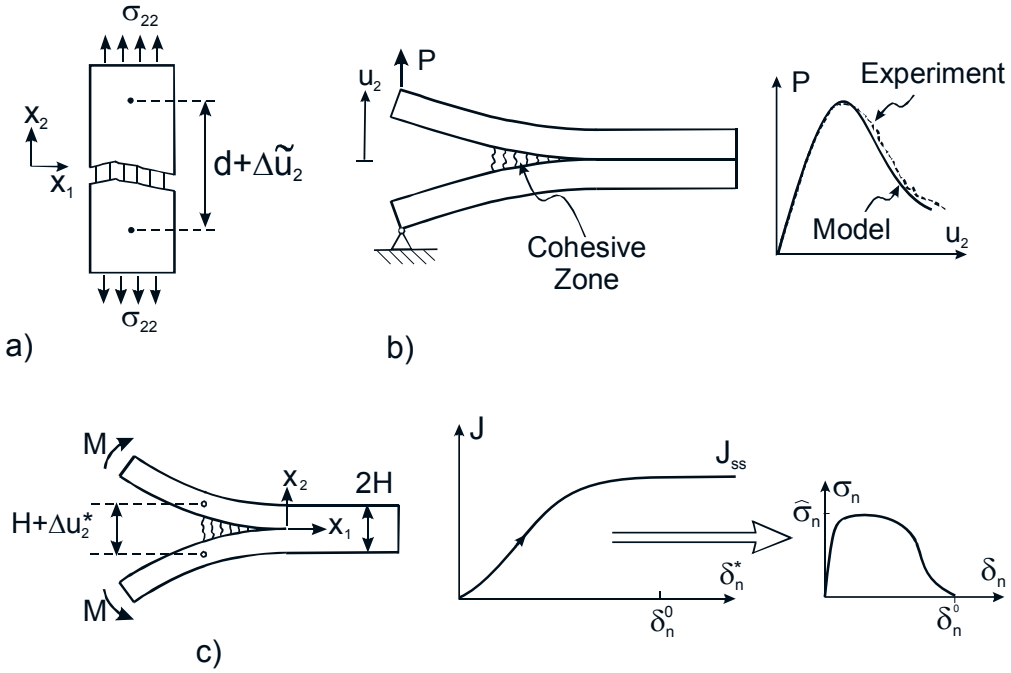

Fig. 4. Commonly used approaches for the experimental determination of macroscale cohesive laws: (a) measurement of localised deformation during direct tension, (b) measurement and modelling of the load-displacement relationship, (c) the J integral approach using DCB specimens loaded with pure bending moments.

A third approach builds on the J integral (Rice 1968a). The J integral and the end-opening of the cohesive zone, δ_n^*, must be recorded during the experiment. The cohesive law is obtained by differentiation according to (Li and Ward 1997; Suo *et al*. 1992)

$$\sigma_n\left(\delta_n^*\right)=\frac{dJ_R}{d\delta_n^*}. \tag{4}$$

An advantage of this approach is that it is fairly easy to do the differentiation (e.g., numerically or to a smooth curve fitted to measured $J_R-\delta_n^*$ data). A drawback is that a J integral solution must be known for the test specimen configuration. For problems involving a large scale fracture process zone, LEFM handbook solutions for stress intensity factors are not applicable since the LEFM relationship between J and stress intensity factors is not valid for a specimen having a large scale fracture process zone. A well-suited specimen configuration for the J integral approach is the double cantilever beam (DCB) specimen loaded with pure bending moments. This specimen is a steady-state specimen. For this test configuration, the equation for the J integral evaluated along the external boundaries is independent of crack length and cohesive law details also for large scale crack bridging (Suo *et al*. 1992). The J integral approach (4) can then be used. The standard DCB specimen loaded by wedge forces is not a steady-state specimen (Suo *et al*. 1992). However, still the J integral can be calculated from measurements of the applied force and the beam rotations - which must then be measured experimentally (Paris and Paris 1988; Olsson and Stigh 1989) since the rotation will depend on the details of the cohesive law; the cohesive law can then be obtained using (4).

2.4 Numerical implementation. Having determined a cohesive law from experiments or micromechanical modelling, the next step is to use it in models of real structures, e.g. by the finite element method. Some commercial finite element programs now have built-in cohesive laws. Alternatively, cohesive laws can be formulated as a user element subroutine in which the program inputs node displacements and a subroutine calculates the element node tractions and tangential stiffness properties.

2.5 Selected results. Obviously, many cohesive law parameters are adjustable (peak traction value, shape, fracture energy, etc.). Since the cohesive law parameters must be specified as a part of a model simulation, it is good to know which ones are the most important ones. This also determines how accurate each cohesive law parameter needs to be measured.

It has been shown that under the premise of a small scale fracture process zone and small scale yielding, the two most important parameters are the peak traction value and the fracture energy (area under the traction-separation law) (Tvergaard and Hutchinson 1992). Other studies have shown that when the active cohesive zone is large, the shape of the cohesive law can have some effect on the predicted strength value (Gu 1995; Scheider and Brock 2003; Jacobsen and Sørensen 2001). More work is therefore needed to establish more well founded rules for the important of cohesive zone parameters.

Studies aiming at relating microscale bridging mechanisms to macroscale toughening are scarce. Sørensen and Jacobsen (1998) studied intra-laminar cracking of a unidirectional carbon-fibre/epoxy composite. The fracture resistance increase was attributed to crack bridging in the form of cross-over bridging. The cohesive law was determined using the J integral approach given by (4). The cohesive law was found to have an inverse square-root dependence. The inverse square root dependence is consistent with the micromechanical prediction by a micromechanical model of cross-over bridging (Spearing and Evans 1992; Sørensen and Jacobsen 1998).

2.6 Pure Mode II. The previous sections concerned pure Mode I cohesive laws. However, much of the comments are also valid for characterisation and modelling of pure Mode II cohesive laws. Therefore, no further comments will be given here to the concepts, measurement methods and modelling of pure Mode II cohesive laws, although obviously, other test specimen configurations are required for the determination of Mode II cohesive laws than for Mode I cohesive laws. For instance, the ENF (end notch flexure) specimen was used by Leffler, Alfredsson and Stigh (2007) to derive the Mode II cohesive law for an epoxy adhesive bonded to steel adherents using a J integral approach similar to (4). The shape of the cohesive law was found to resemble the trapezoidal shape of Tvergaard and Hutchinson (1992). Both the Mode II peak traction and the critical separation were higher than the corresponding values for the Mode I cohesive law for the same adhesive. It can be noted that the ENF specimen is not a steady-state specimen.

2.7 Moving the limits - some unresolved issues. Experimental characterisation, theoretical analysis and modelling of pure mode cohesive laws have reached a relative mature state. Improvements in the form of cohesive law measurements under well-defined conditions are still desired. Micromechanical modelling is not so mature that cohesive laws can be derived entirely from micromechanical models. It is, however, important to establish and validate micromechanical models, so that more fracture-resistant composite materials can be developed. Therefore, the connection between macroscale cohesive laws and microscale parameters (e.g. through microscale observations and theoretical, micromechanical models) needs much further attention. Eventually, it should become possible to design composite microstructural parameters for optimal fracture resistance.

3. MIXED MODE COHESIVE LAWS

3.1 Basic concepts. Under Mixed-Mode cracking, the crack opening displacements consist of both normal and tangential crack opening displacements, δ_n and δ_t. Likewise, both normal and shear stresses, σ_n and σ_t, are transmitted between the crack plane within a fracture process zone. In general, it must be assumed that both σ_n and σ_t depend on both δ_n and δ_t, i.e.:

$$\sigma_n = \sigma_n(\delta_n, \delta_t) \quad \wedge \quad \sigma_t = \sigma_t(\delta_n, \delta_t) , \tag{5}$$

which are expected to reduce to uncoupled laws under pure normal and pure tangential opening. Furthermore, the shear traction is assumed to be zero under pure Mode I, and the normal traction is assumed to be zero under pure Mode II. Again, the J integral can be useful for large scale crack bridging problems. Evaluating the J integral along an integration path around the cohesive zone gives (Sørensen and Kirkegaard 2006):

$$J_R = \int_0^{\delta_n^*} \sigma_n(\delta_n, \delta_t)\, d\delta + \int_0^{\delta_t^*} \sigma_t(\delta_t, \delta_t)\, d\delta_t , \tag{6}$$

where δ_t^* is the end-sliding.

3.2 Idealised Mixed Mode cohesive laws. Mixed-Mode cohesive laws have been formulated in a number of ways. Often, simple linear, bi-linear or trapezoidal traction-separation relations are assumed. The normal and shear tractions are sometimes taken to be independent of each other (Yang and Thouless 2001). Then, the normal traction depends only on the normal opening displacement, and the shear traction depends only on the tangential opening displacement. Such cohesive laws can be called *decoupled cohesive laws*. Another approach is to derive coupled cohesive tractions from a potential function (Needleman 1987; Tvergaard and Hutchinson 1992). Coupled Mixed Mode cohesive laws can also be formulated such that they are not derived form a potential function (Tvergaard 1990; van den Bosch, Schreuers and Geers 2006). Then, however, the work of cohesive tractions depends on the opening-path history. Some Mixed-Mode cohesive laws possess the same work of separation for all opening modes (Needleman 1987; Xu and Needleman 1994; Tvergaard and Hutchinson 1992), while other models have a larger Mode II fracture energy than the Mode I fracture energy (Camanho, Davilia and de Mousa 2003).

3.3 Mixed Mode measurement methods. With a great variety of idealised Mixed Mode cohesive laws available, it is of importance to have ways of identifying which cohesive law formulations that are most suitable for a given fracture problem. Obviously, approaches that rely on measurement of only pure Mode I and pure Mode II cohesive laws and interpolation for Mixed Mode, are not sufficient for the generation of information for such a choice. It is necessary to perform some Mixed Mode experiments analyse the data theoretically in order to determine Mixed Mode cohesive laws with as few presumptions as possible. As discussed under Mode I testing, a requirement is that the crack growth should be stable. Not many Mixed Mode specimens fulfil this requirement. For instance, crack growth can be unstable for the well known MMB (mixed mode bending) specimen (Shivakumar, Crews and Avva 1998). Furthermore, as elaborated in Section 2, for structures and materials exhibiting a large scale fracture process zone, LEFM solutions for stress intensity factors are not sufficient for the calculation of *J* along the external boundaries. This limits the number of suitable test specimen configurations.

Assuming that the cohesive tractions are driveable from a potential function, the Mixed Mode cohesive laws can be obtained by (Sørensen and Kirkegaard 2006):

$$\sigma_n\left(\delta_n^*,\delta_t^*\right)=\frac{\partial J_R\left(\delta_n^*,\delta_t^*\right)}{\partial \delta_n^*} \qquad \sigma_t\left(\delta_n^*,\delta_t^*\right)=\frac{\partial J_R\left(\delta_n^*,\delta_t^*\right)}{\partial \delta_t^*}. \tag{7}$$

Thus, Mixed Mode cohesive laws can be obtained by simultaneous measurements of the fracture resistance, J_R, the end-opening, δ_n^*, and the end-sliding, δ_t^* for various different Mixed Mode experiments, e.g., by fitting a smooth (differential) function to the J_R-δ_n^*-δ_t^* data and performing partial differentiation according to (7).

A prerequisite for use of the J integral approach is that a J integral analysis must be at hand for the Mixed Mode specimen of interest. As for Mode I, under large scale bridging LEFM solutions for stress intensity factors cannot be used for the calculation of J along the external boundaries. This author prefers a test configuration of a DCB specimen loaded with uneven bending moments (DCB-UBM), see Fig. 5, since J along the external boundaries can be obtained in closed analytical form also under large scale cohesive zone (Sørensen, Jørgensen, Jacobsen and Østergaard 2006). The DCB-UBM gives stable crack growth. Furthermore, it is a steady-state specimen.

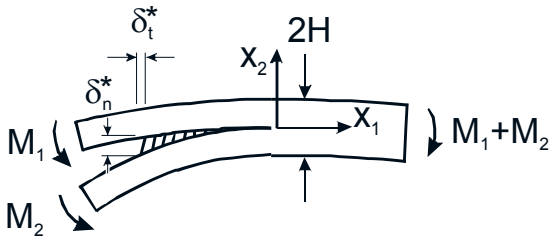

Fig. 5. Schematics of the DCB specimen loaded with uneven bending moments (DCB-UBM).

3.4 Examples of measurements. In the following, selected experimental results for Mixed Mode cohesive laws will briefly be reviewed. Differences and similarities between idealised and measured cohesive laws will be pinpointed.

Results for delamination crack growth in a unidirectional glass fibre/polyester composite tested by the DCB-UBM specimens (Sørensen and Jacobsen 2009) are shown in Fig. 6 and Fig. 7. The fracture resistance increase was attributed to cross-over bridging. The fracture resistance curves in Fig. 6 fall into two groups. For Mode I dominated experiments ($M_1/M_2 \leq 0.5$), the curves raise significantly for small openings (due to fibre bridging) and flatten out, attaining steady-state values for openings at about 2 mm. Such behaviour corresponds well with expectations. The fracture resistance curves do not flatten out for Mode II dominated experiments ($M_1/M_2 \geq 0.7$), but take a near-constant slope. This behaviour (no steady-state) is an unexpected result.

The associated end-opening/sliding histories are shown in Fig. 7. Note, that it is impossible to obtain a pure tangential opening (i.e., $\delta_n^* = 0$ $\delta_t^* \neq 0$) even for M_1/M_2 very close to unity. Although unexpected, such behaviour is not unrealistic. The formation of multiple shear cracks under dominating Mode II can create a rough fracture surface. Roughness would wedge the crack faces open, i.e. creating a normal opening, which will cause interfacial dilatation. Such

"interfacial dilatation" is not predicted by classic cohesive laws, but may be of importance for cracking problems that are controlled by displacements (e.g. parts in tight-fitting contact).

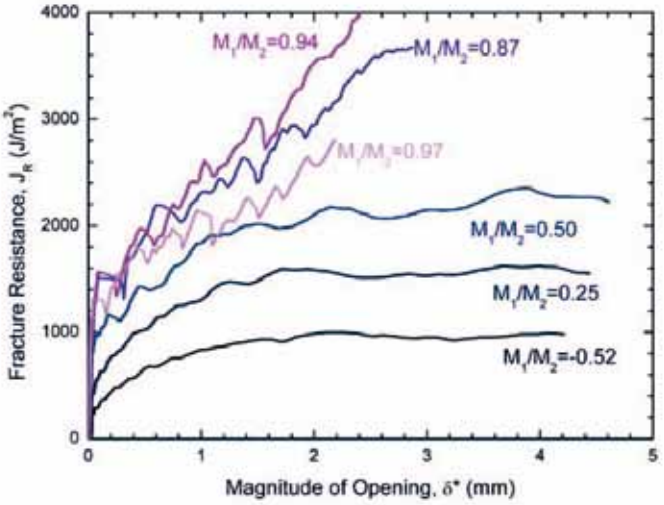

Fig. 6. Measured Mixed-Mode fracture resistance, J_R, as a function of the end-opening, δ^*, for various moment ratios. From Sørensen and Jacobsen (2009).

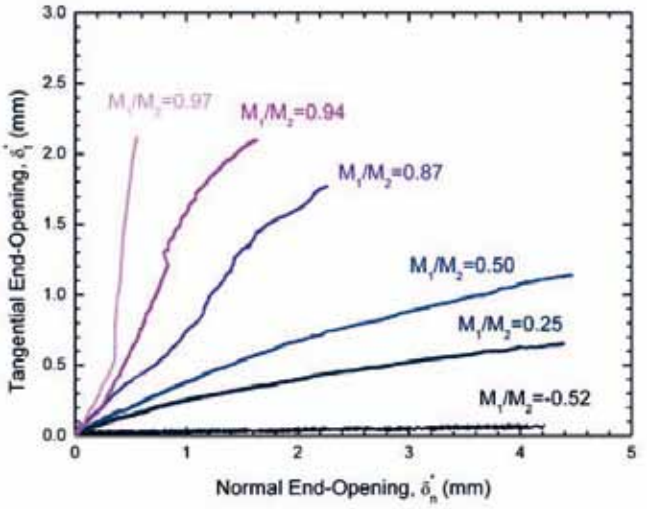

Fig. 7. Relationship between the normal end-opening, δ_n^*, and the tangential end-opening, δ_t^*, measured for various Mixed-Mode experiments. From Sørensen and Jacobsen (2009).

Calculation of Mixed Mode cohesive tractions, using the J integral approach, equation (7), revealed two major finding for Mode II dominated openings (Sørensen and Jacobsen 2009): (1) The normal traction takes a negative value (compression) for small openings and (2) the shear traction does not decay to zero, but attains a near-constant value. No Mixed Mode cohesive law in the published literature describe these effects.

Inspired by the above mentioned results, Sørensen and Goutianos (2011) developed a Mixed Mode cohesive law that includes the roughness effect. The key feature is that an imposed tangential opening displacement, δ_t, should induce a displacement in the direction normal to the cracking plane, δ_n for a small tangential displacement. For tangential displacements beyond a characteristic value, $\widetilde{\delta}_t$, the resulting normal displacement takes a constant value, $\widetilde{\delta}_n$, corresponding to that the roughness mechanism is in full operation.

Model predictions using the model of Sørensen and Goutianos (2011) are shown in Fig. 8 and Fig. 9 together with typical experimental results of Fig. 6 and Fig. 7. In these figure, the labels α_1- α_4 indicate four different sets of parameters. It is seen from Fig. 8 and Fig. 9 that the parameter set given by α_4 fits the experimental results reasonably well.

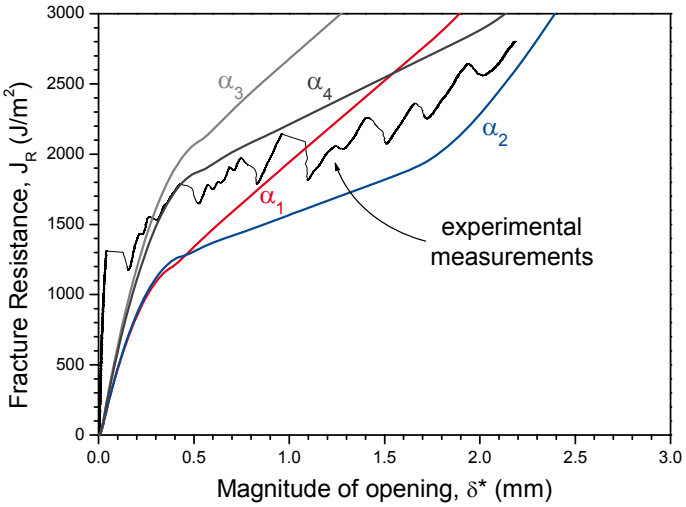

Fig. 8. Comparison of predicted and measured fracture resistance as a function of the magnitude of the end-opening for $M_1/M_2 = 0.97$.

3.5 Moving the limits - some unresolved issues. There are several issues with respect to Mixed Mode cohesive laws that need further attention. As the example above shows, actual Mixed Mode cohesive law may differ significantly from the way idealised Mixed Mode cohesive laws are. Such features can only be discovered by careful experiments covering many Mixed Mode loadings. As mentioned, some Mixed Mode cohesive laws are taken to be uncoupled (i.e., independent Mode I and Mode II laws), others are coupled in a particular manner. Aiming at that Mixed Mode cohesive law models should mimic the behaviour of real fracture process zones, models of cohesive laws should incorporate a coupling that corresponds to the nature of the real fracture process zone in focus. Therefore, in order to determine which models are most accurately describing real problems, experimental methods (test specimen configurations and data analysis approaches) are required for accurate determination of a Mixed Mode cohesive

law.

The J integral approach seems to work well in connection with the DCB-UBM test configuration. A major advantage of the J integral approach is that no assumptions need to be made regarding the specific dependence of the cohesive tractions on the normal and tangential separations, equation (5). If the data is sufficiently accurate, the peak tractions, cohesive law shapes and couplings will come directly out of the analysis. In practice, however, there can be situations where it is impossible to obtain the long and slender beams required for the DCB specimen. Therefore, it would be useful if J integral solutions, valid for large-scale bridging, were developed for more test specimen configurations.

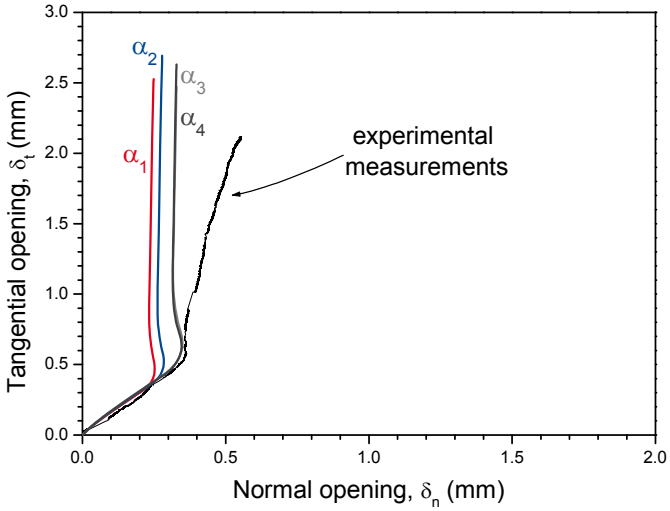

Fig. 9. Comparison of predicted and measured end-opening and end-sliding for M_1/M_2 = 0.97.

Furthermore, the J integral approach is based on the presumption that the Mixed Mode cohesive tractions are derivable from a potential function. This presumption needs to be validated. The assumptions is fulfilled if, at anytime during a fracture test, the fracture resistance - equation (6) - depends on the end-openings only, not the opening history. Therefore, the potential function assumption can be tested by performing Mixed Mode fracture mechanics tests having different opening-path histories. A systematic investigation aimed at uncovering this has, as far as the author knows, not yet been published. Testing approaches for applying different opening-path histories are thus needed. The consequences of the outcome of such experiments can be profound for Mixed Mode cohesive zone modelling. If it turns out that Mixed Mode cohesive tractions are strongly opening-path dependent and cannot be derived from a potential function, Mixed Mode cohesive laws of the form (5) are not sufficient. Instead, the cohesive laws should be modelled as opening-history-dependent (in the manner the measurements show), perhaps in incremental form. This issue is somewhat analogous to the question in plasticity whether the constitutive laws for non-linear stress-strain behaviour should be based on deformation theory or incremental J_2 flow theory (Budiansky 1959).

4. CREEP AND LOADING RATE EFFECTS

4.1 Basic concepts. Many materials, in particular polymers, have time-dependent mechanical

properties, including loading rate-dependent fracture properties (Atkins, Lee and Caddell 1975; Webb and Aifantis 1995). The rate-dependency can be in both the intrinsic fracture toughness or extrinsic toughening. In the language of cohesive zone modelling, the intrinsic toughness is the work of separation of the cohesive tractions. The extrinsic toughening is energy dissipation due to a nonlinear zone in the bulk outside the cohesive zone. The toughening can be due to non-reversible stress-strain history as an element is loaded and unloaded as the crack tip passes by. One example is volume expansion due to cavitation in polymers, as observed in rubber-modified epoxy, (Du, Thouless, and Yee 2000). In the particular case, the fracture toughness decreased with increasing loading rate. The rate-dependence was attributed to a rate-dependent intrinsic fracture toughness (Du *et al*. 2000). The opposite effect, an increasing steady-state fracture resistance were found for interfacial cracking along elastomer adhesive/steel interfaces (Liechti and Wu 2001; Sørensen 2002). Examples of measured Mode I cohesive laws are shown in Fig. 10. Rate-dependent Mode II cohesive laws for cohesive failure of an elastomer adhesive show a similar trend (Zhu, Liechti and Ravi-Chandar 2009).

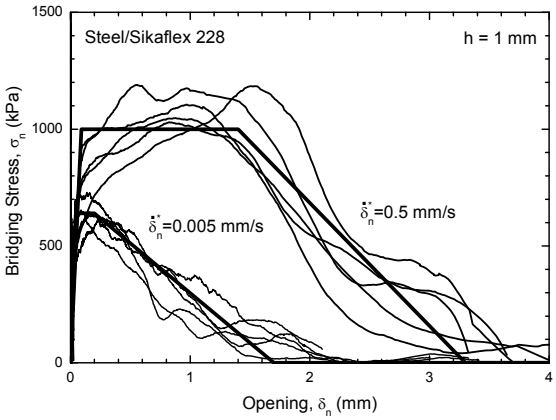

Fig. 10. Mode I traction-separation relations for two opening rates of a polyurethane/steel interface (Sørensen, 2002). The end-opening rates, $\dot{\delta}_n^*$, are indicated. The thin lines were obtained by numerical differentiation; the thick lines represent a trapezoidal cohesive law fitted to the $\sigma_n - \delta_n^*$ data.

4.2 Idealized rate-dependent cohesive laws. Opening rate-dependent traction-separation laws have been formulated for Mode I and Mixed Mode. The model of Landis, Pardoen and Hutchinson (2000) includes two rate-dependent parameters, a characteristic opening rate and a rate exponent. A Kelvin unit (a non-linear spring coupled in parallel with a dashpot) was used by Bazant and Li (1997) and Liechti and Wu (2001) for modelling the rate effect in Mode I. The dashpot was characterized by an increasing viscosity, described in terms of three viscosity coefficients. Wang, Qin, Kang, Li and Rong (2010) proposed a Mixed Mode visco-elastic cohesive law based on two Kelvin units (one for normal separation and one for tangential separation). They calibrated the model against experimental results and obtain a good agreement between measurement and model predictions.

4.3 Moving the limits - some unresolved issues. With relatively few studies addressing rate effects, there is a need for measurement methods for an experimental determination cohesive

law at constant, pre-specified opening rates. A particular challenge is to separate the effects of a rate-dependent cohesive law and rate-dependent effects of bulk (stress-strain) phenomena.

A determination of rate-dependent cohesive laws under Mixed Mode conditions is also needed. The approaches must be critically examined, e.g. by determination of rate-dependent cohesive laws from measurements using test specimens and validate the rate-dependent cohesive laws by predicting (modelling) and experimental testing of another specimen of different size, geometry and loading.

5. COHESIVE LAW FOR CYCLIC CRACK GROWTH

5.1 Basic concepts. The following section describes cyclic crack growth, taking cohesive laws as the basic material law for both small and large scale fracture process zones. For a small scale fracture process zone, crack growth can be predicted reasonably well by LEFM, e.g. using the Paris-Erdogan relation (Paris and Erdogan 1963). However, LEFM is not sufficient for the characterization and modelling of cracking problems that involve a large-scale fracture process zone, such as large-scale crack bridging. Therefore, the main challenge lies in large-scale crack bridging problems.

First, consider what happens at a fixed material point within a fracture process zone (or equivalently, an active cohesive zone) of a specimen subjected to cyclically changing loads. In the increasing part of the first loading cycle, the traction follows the cohesive law corresponding to a monotonically increasing load (i.e., the "static" cohesive law). However, upon unloading, the crack closes, so the local opening at the point of interest decreases. Next follows a reloading, causing the crack to open, the traction increases again and upon unloading the crack closes again, leading to a decrease in the cohesive traction again, etc. However, under cyclic crack growth, the fracture process zone must move to cause a *crack growth rate*, da/dN (here a is the crack length measured to the damage front and N is the number of load cycles). Thus, the local maximum opening must also increase cycle by cycle. This causes the cohesive traction at a given point to change cycle by cycle. It is also reasonable to assume that the cohesive tractions at a given point will gradually degrade as a result of the cyclic opening and closing, as illustrated in Fig. 11. In general, all points within the fracture zone may experience different cyclic opening history. The challenge is to measure and formulate an evolution law for the cohesive law as a function of the number of cycles, incorporate the effects of the decrease in strength, stiffness degradation ("damage") and possibly permanent crack opening ("plasticity"), see Fig. 12.

Steady-state specimens (see Section 2.1) are particularly useful since they can create cyclic crack growth under steady-state conditions. Consider an experiment being conducted between a fixed maximum and minimum values of J. Then, in the first few load cycles, the crack is practically unbridged, and the crack growth is controlled entirely by the cyclic crack growth rate of the crack tip. In the subsequent cycles, the damage front moves along, cracking a bridging zone between the damage front and the original crack tip (completely analogous to the development under monotonic opening, Fig. 1), except that bridging ligaments at different positions have experienced a different number of cycles. As the bridging zone length increases, the end-openings increases, so that the part of the applied J that is taken by the bridging zone increases, effectively decreasing the J around the tip of the damage front, J_{tip} (equations (2) and (6) still hold when the appropriate "cyclic" cohesive laws are used). This in turn decreases the crack growth rate. Eventually, as the fracture process zone length takes a constant, steady-state length, L_{ss}, the crack growth rate also attains a constant value. Then, under a cyclic steady-state

situation, the fracture process zone is expected to be invariant; it merely translates along the specimen with the crack tip. Then, all bridging ligaments will be subjected to the same cyclic loading history and the distribution of the bridging tractions within the fracture process zone will remain invariant. This distribution of bridging tractions at maximum load can thus be regarded as being a steady-state "cyclic" cohesive law.

The steady-state fracture process zone length, L_{ss}, is associated with a characteristic number of cycles, N_{ss}, which is the number of cycles a bridging ligament undergoes as it passes through the fracture process zone from the damage front to the end-opening.

Knowing the associated steady-state crack growth rate, $(da/dN)_{ss}$, a characteristic number of cycles, N_{ss}, can be calculated from:

$$N_{ss} = \frac{L_{ss}}{(da/dN)_{ss}}, \tag{8}$$

Since this is the number of cycles that each point within the fracture process zone expiriences, it can be expected to be the major parameter controlling the evolution of fatigue damage evolution in a bridging zone. Consequently, fatigue under large scale crack bridging may be characterized in terms of a steady-state "cyclic" cohesive law (that is a function of the characteristic number of cycles, N_{ss}) acting in the bridging zone, i.e., as

$$\sigma_n^c = \sigma_n^c(\delta_n, N_{ss}), \tag{9}$$

(superscript c indicates "cyclic" cohesive law) and the crack tip stress intensity range, that is expected to control the crack tip growth rate, e.g. following a Paris-Erdogan relation (Paris and Erdogan 1963).

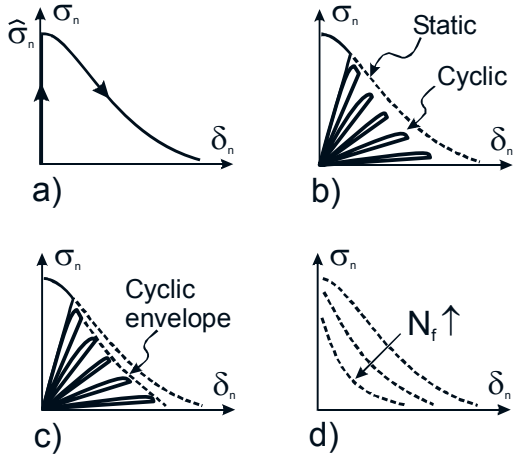

Fig. 11. Hypothetically changing traction-separation relations: (a) monotonic opening, (b) cyclic opening-closing, (c) envelopes for steady-state cyclic traction-separation relations for a given N_f, (d) envelopes for several different values of N_f.

5.2 Modelling of cyclic crack growth with cohesive law. Several attempts have been made to model cyclic crack growth using cohesive laws in finite element programs (Yang, Mall and

Ravi-Chandra 2001; Nguyen, Repetto, Ortiz and Radovitzky 2001; Adul-Baqi, Schreurs and Geers 2005; Maiti and Geubelle 2005; Turon, Costa, Camanho and Davilia 2007; Harper and Hallett 2010). All modes include a damage evolution law (sometimes called a kinetic law) that describes how the cohesive law changes from that associated with the the first load cycle (the static cohesive law) as a function of load cycles. The models differ in the way the cyclic damage evolution law is formulated.

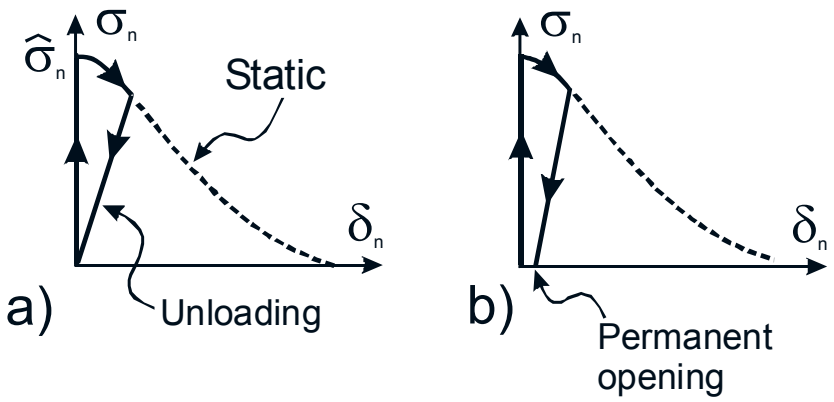

Fig. 12. Schematics of different types of unloading traction-separation relations. (a) unloading without permanent opening ("damage"-like behaviour), (b) unloading with permanent opening ("plastic"-like behaviour).

A different approach was proposed by McMeeking and Evans (1990) and Cox (1993). They studied cyclic crack growth of a Mode I crack having a sharp tip (singular crack tip stress field) having a crack bridging zone in the wake. Setting up the mathematical equations for the calculation the change in the crack tip stress intensity factor, they noticed that the mathematical form of the mathematical equation for the cyclic problem was identical to the form of the equation for the crack tip stress intensity factor for a static problem. Thus, instead of performing the cycle-to-cycle calculation, e.g. using finite element modelling, it may be possible to calculate the cyclic crack growth rate by solving the associated static problem. Although this approach only holds for traction-separation relations of a power-law form, it may be a convenient way of approaching cyclic crack growth. The approach has, as far as this author knows, not been used in connection with experimental investigations and a practical validation of the approach is thus missing.

5.3 Moving the limits - some unresolved issues. Modelling using LEFM (i.e., calculating changes in stress intensity factors and estimation of the crack growth rate using the Paris-Erdogan law) is routinely used for the estimation of cyclic crack growth rates in materials that possess a small scale fracture process zone. Probably the major use of cohesive zone modelling with in cyclic crack growth is for large-scale bridging problems. As indicated above, a consistent approach to fatigue crack growth using a cohesive law has not yet been demonstrated for large scale fracture process zones. One of the most important challenges is to perform cyclic crack growth experiments in steady-state, in order to uncover steady-state cyclic cohesive laws, as described above. The identification of cyclic cohesive laws then sets the stage for how damage evolution laws for cyclic crack growth should be formulated.

Next, such experimental results should be consistently be implemented in a numerical model

and crack growth rates should be predicted for a structure of another size, geometry and loading configuration. The accuracy of model predictions should then be evaluated by comparison with experimental investigation of cyclic crack growth in the larger structures.

The analytical approach of transforming a cyclic crack growth problem with large-scale bridging to a static problem (McMeeking and Evans 1990; Cox 1993) holds great potential if the approach can convincingly be demonstrated, e.g. by a coupled model-experimental study. Validation of such approaches is of great importance since it will enable new design tools in the analysis of engineering design and thus move the design limits.

Another important challenge is to characterize and model cyclic crack growth of large-scale crack bridging problems under Mixed Mode conditions. This topic requires much more attention before cohesive zone modelling can be used for accurate model prediction of cyclic crack growth.

6. SUMMARY

This paper has attempted to provide a modern view to fracture, using the concepts of cohesive laws as the basic strength-controlling constitutive law. Although developed primarily for static crack growth problems, more advanced fracture topics such as creep and loading rate effects as well as cyclic crack growth can be described in terms of cohesive laws.

For static crack growth under Mode I, both experimental and modelling tools are now so advanced that the crack growth of larger structures can be predicted fairly accurately from cohesive laws measured from laboratory specimens using idealised cohesive laws. Still some features are missing from the idealised cohesive laws. The formulation and implementation of more realistic cohesive laws is assumed to lead to more accurate model predictions. Effects like interfacial roughness and opening rate-dependent cohesive laws are examples of issues that are not yet well modelled.

The largest remaining challenge for cohesive zone modelling seems to be the modelling of cyclic crack growth. Characterising and modelling cyclic crack growth for large scale bridging are still in their early life. A strong interaction between experimental work and modelling is a necessity. Interestingly, it seems that the field of cohesive zone modelling is more advanced than the field of experimental determination of cohesive laws.

ACKNOWLEDGEMENTS

This work was supported by the Danish Centre for Composite Structures and Materials for Wind Turbines (DCCSM), grant no. 09-067212, from the Danish Strategic Research Council.

REFERENCES

Adul-Baqi, A., Schreurs, P.J.G., and Geers. M.G.D. (2005). Fatigue damage modelling in solder interconnects using a cohesive zone approach, Int. J. Solids Structures 42, 927-42.

Atkins, A.G., Lee, C.S., and Caddell, R.M. (1975). Time-dependent fracture toughness of PMMA. Part 1, Journal of Materials Science 10, 1391-93.

Barenblatt, G.I. (1962). The mathematical theory of equilibrium cracks in brittle fracture Advances in Applied Mechanics 7, 55-129.

Bazant, Z.P., and Li, Y.-N. (1997). Cohesive crack with rate-dependent opening and viscoelasticity: I. mathematical model and scaling, Int. J. Fract. 86, 247-65.

Brenet, P. Conchin, F., Fantozzo, G., Reynaud, P., Rouby, D., and Tallaron, C. (1996). Direct measurement of the crack bridging tractions: A new approach of the fracture behaviour of ceramic-matrix composites, Comp. Sci. Techn. 56, 817-23.

Budiansky, B. (1959). A reassessment of deformation theories of plasticity. J. Appl. Mech. 81, 259-264.

Budiansky, B., Evans, A. G., and Hutchinson, J. W. (1995). Fiber-matrix debonding effects on cracking in aligned fiber ceramic composites., Int. J. Solids Struct. 32, 315-28.

Camanho, P.P., Davilia, C.G., and de Moura, M.F. (2003). Numerical simulation of mixed-mode progressive delamination in composite materials, Journal of Composite Materials 37, 1415-1438.

Cox, B.N. (1993). Scaling for bridged cracks, Mechanics of Materials 15, 87-98.

Du, J., Thouless, M.D., and Yee, A.F. (2000). Effects of rate of crack growth in a rubber-modfieed epoxy, Acta Mater. 48, 3581-92.

Dugdale, D.S. (1960). Yielding of steel sheets containing slits, Journal of the Mechanics and Physics of Solids 8, 100-4.

Griffith, A.A. (1921). The phenomena of rupture and flow in solids, Proc. Royal Soc. Lond. A221, 163-98.

Gu, P. (1995). Notch sensitivity of fibre-reinforced ceramics, Int. J. Fracture 70, 253-66.

Harper, P.W., and Hallett, S.R. (2010). A fatigue degradation law for cohesive interface elements - Development and application to composite materials, Int. J. Fatigue 32, 1774-87.

Hutchinson, J.W. (1983). Fundamentals of the phenomenological theory of nonlinear fracture mechanics, J. Applied Mechanics 50, 1042-51.

Irwin, G.R., Kies, J.A., and Smith, H.L. (1958). Fracture strength relative to onset and arrest of crack propagation, Proc. of the American Society for Testing Materials 58, 640-57.

Jacobsen, T.K., and Sørensen, B.F. (2001). Mode I Intra-laminar crack growth in composites - modelling of R-curves from measured bridging laws, Composites part A 32, 1-11.

Landis, C.M., Pardoen, T., and Hutchinson, J.W. (2000). Crack velocity dependent toughness in rate dependent materials, Mechanics of Materials 32, 663-78.

Leffler, K., Alfredsson, K.S., and Stigh, U. (2007). Shear behaviour of adhesive layers, International Journal of Solids and Structures 44, 530-45.

Li, V.C., and Ward, R.J. (1989). A novel testing technique for post-peak tensile behaviour of cementitious materials, in Fracture toughness and fracture energy - testing methods for concrete and rocks (eds. H. Mihashi, H. Takahashi and F. H. Wittmann), A. A. Balkema Publishers, Rotterdam, 183-95.

Liechti, K.M., and Wu., J.-D. (2001). Mixed mode, time-dependent rubber/metal debonding, Mech. Phys. Solids 49, 1039-72.

Maiti, S., and Geubelle, P.H. (2005). A cohesive model for fatigue failure of polymers, Engr. Fract. Mechn. 72, 691-708.

McMeeking, R.M., and Evans, A.G. (1990). Matrix fatigue cracking in fibre composites, Mechanics of Materials 9, 217-27.

Mohammad, I., and Liechti, K.M. (2000). Cohesive zone modelling of crack nucleation at bimaterial corner, Journal of the Mechanics and Physics of Solids 48, 735-64.

Needleman, A. (1987). A continuum model for void nucleation by inclusion debonding, J. Appl. Mechn. 54, 525-531.

Nguyen, O., Repetto, E. A.,Ortiz, M., and Radovitzky, R.A. (2001). A cohesive model of fatigue crack growth, Int. J. Fracture 110, 351-69.

Olsson, P. and Stigh, U. (1989). On the determination of the constitutive properties of thin interphase layers - an exact solution, Int. J. Fracture 41, R71-6.

Paris, P., and Erdogan, F. (1963). A critical analysis of crack propagation laws, Journal of Basic Engineering, Series D 85, 528-34.

Paris, A.J., and Paris, P.C., (1988). Instantaneous evaluation of J and C*, Int. J. Fracture 8, R19-R21.

Rice, J.R. (1968a), A path independent integral and the approximate analysis of strain concentrations by notches and cracks, J. Appl. Mech. 35, 379-86.

Rice, J.R. (1968b), Mathematical analysis in the mechanics of fracture, in Fracture, An Advanced Treatice II (ed. H. Liebowitz), Academic Press, New York and London, 191-311.

Scheider, I., and Brocks, W. (2003). The effect of the traction separation law on the results of cohesive zone crack propagation analyses, Key Engineering Materials 251-2, 313-318.

Shivakumar, K.N., Crews, J.R.Jr., and Avva, V.S. (1998). Modified mixed-mode bending test apparatus for measuring delamination fracture toughness of laminated composites, J. Comp. Mater. 32, 804-28.

Sørensen, B.F. (2002). Cohesive law and notch sensitivity of adhesive joints. Acta Mater. 50, 1053-61.

Sørensen, B.F., and Goutianos, S. (2011). Mixed mode cohesive law with interface dilatation, manuscript in preparation.

Sørensen, B.F., and Jacobsen, T.K. (1998). Large scale bridging in composites: R-curve and bridging laws, Composites part A 29, 1443-51.

Sørensen, B.F., and Jacobsen, T.K. (2009). Delamination of fibre composites: determination of mixed mode cohesive laws. Comp. Sci. Techn. 69, 445-56.

Sørensen, B.F., Jørgensen, K., Jacobsen, T.K., and Østergaard, R.C. (2006). DCB-specimen loaded with uneven bending moments, International Journal of Fracture 141, 159-172.

Sørensen, B.F., and Kirkegaard, P. (2006). Determination of mixed mode cohesive laws, Engineering Fracture Mechanics 73, 2642-61.

Spearing, S.M., and Evans, A.G. (1992). The role of fibre bridging in the delamination resistance of fibre-reinforced composites, Acta Metall. Mater. 40, 2191-9.

Suo, Z., Bao, G., and Fan, B. (1992). Delamination R-curve phenomena due to damage, J. Mech. Phys. Solids. 40, 1-16.

Timoshenko, S.P. (1953). History of strength of materials, Dover Publishing, Inc. New York.

Turon, A., Costra, J., Camanho, P.P., Dávilia, C.G. (2007). Simulation of delamination in composites under high-cycle fatigue, Composites part A 38, 2270-82.

Tvergaard, V. (1990). Effect of fibre debonding in a whisker-reinforced metal, Mater. Sci. Engr. A125, 203-13.

Tvergaard, V., and Hutchinson, J.W. (1992). The relation between crack growth resistance and fracture process parameters in elastic-plastic solids J. Mech. Phys. Solids 40, 1377-97.

Tvergaard, V., and Hutchinson, J.W. (1993). The influence of plasticity on mixed mode interface toughness, Journal of the Mechanics and Physics of Solids 41, 1119-35.

Van den Bosch, M.J., Schreurs, P.J.G., and Geers, M.G.D. (2006). An improved description of the exponential Xu and Needleman cohesive zone law for mixed-mode decohesion, Engineering Fracture Mechanics 73, 1220-34.

Wang, J., Qin, Q.H., Kang, Y.L., Li, X.Q., and Rong, Q.Q. (2010). Viscoelastic adhesive interfacial model and experimental characterisation for interfacial parameters, Mechanics of Materials 42, 537-47.

Webb, T.E., and Aifantis, E.C. (1995). Oscillatory fracture in polymer materials, Int. J. Solids Structures 32, 2725-43.

Xu, X.-P., and Needleman, A. (1994). Void neucleation by inclusion debonding in a crystal matrix, Modell. Simul. Mater. Sci. Engng. 1, 111-132.

Yang B., Mall, S., and Ravi-Chandar, K. (2001). A cohesive zone model for fatigue crack growth in quasibrittle materials, Int. J. Solids Structures 38, 3927-44.

Yang, Q.D. and Thouless, M.D. (2001). Mixed-mode fracture analysis of plastically-deforming adhesive joints, Int. J. Fracture 110, 175-87.

Yang, Q.D., Thouless, M.D., and Ward, S.M. (1999). Numerical simulations of adhesively-bonded beams failing with extensive plastic deformation, J. Mech. Phys. Solids 47, 1337-53.
Zhu, Y., Liechti, K.M., and Ravi-Chandar, K. (2009). Direct extraction of rate-dependent traction-separation laws for polyurea/steel interfaces, Int. J. Solids. Struct. 46, 31-51.

Proceedings of the 32nd
Risø International Symposium on Materials Science:
Composite materials for structural performance:
Towards higher limits
Editors: S. Fæster, D. Juul Jensen,
B. Ralph, B.F. Sørensen
Risø National Laboratory for Sustainable Energy,
Technical University of Denmark, 2011

NUMERICAL SIMULATION OF COMPOSITES AT VARIOUS LENGTH SCALES: WHERE ARE THE LIMITS

Q.D. Yang*, X.J. Fang*, and B.N. Cox**

*Mech. & Aerospace Engin., University of Miami, Florida
**Teledyne Scientific Co LLC, Thousand Oaks, California

ABSTRACT

High-fidelity strength prediction of composites requires advanced numerical methods that can explicitly represent the multiple damage processes and their nonlinear coupling at various scales. Nonlinear fracture models such as cohesive zone models are critical for damage descriptions and they need to be properly embedded in a numerical framework so that correct coupling between different damage process zones can be guaranteed. This paper reviews the recent developments in advanced numerical methods that have the potential to address the important issue of progressive damage evolution in composites. Candidate FE-based numerical methods, including X-FEM, A-FEM, and phantom node methods are reviewed and their capabilities in handling the multiple damage coupling in composites are assessed. Successful simulations of composites at various scales using the framework of A-FEM are presented and the numerical and material issues associated with these high-fidelity analyses are highlighted. Finally, we address the question of how to integrate all these different scale analyses into a single multiscale numerical framework by using Arlequin coupling method.

1. INTRODUCTION

The use of advanced composites in lieu of traditional metals has been considerably expanded over the last couple of decades. Recent examples include the new commercial airplanes such as the Boeing 787 Dreamliner and the Airbus 380 and several other high profile military applications (Joint Strike Fighters of the US Air Force and the DD-X multi-mission destroyer of the US Navy, for example), all featuring high use of composite materials. Compared to structural metals, composites offer several key advantages such as significant weight savings, better reliability and durability, and lower manufacturing and maintenance costs.

However, owing to the highly heterogeneous nature of composites, predicting composite strength and durability directly from constituent material properties (i.e., matrix, fiber, and matrix-fiber interfacial properties) remains unresolved despite decades of intensive research. In the past, many strength criteria based on various homogenization theories have been proposed.

To name a few, Hashin's mechanism based criterion, Tsai-Wu criterion, and many continuum damage mechanics (CDM) based criteria such as in (Chang, Liu, and Chang 1991; Chaboche, Lesne and Maire 1995; Shokrieh and Lessard 2000; McCartney 2003). The success of these phenomenological criteria in assessing composite strength has been limited. A recent report on blind failure prediction of unidirectional PMCs revealed rather disturbing predictive capabilities of composite theories based on such strength criteria: virtually none of these homogenized composite theories can predict laminate strength satisfactorily under general loading conditions. Discrepancies among different theoretical predictions are more than 100% and up to 1500% in extreme cases (Kaddorur, Hinton and Soden 2004).

A distinctive feature of composite failure is that it is a progressive process involving many types of damage initiating and propagating in a strongly coupled fashion until final, catastrophic failure occurs. In composite laminates, the damage manifests as ply cracking, delamination, fiber rupture (in tension), and kink band formation (in compression), etc. Strength criteria calibrated from individual damage modes cannot account for the nonlinear coupling of the many complex damage systems.

Continuum damage mechanics (CDM) has also been used to better account for the progressive damage in composites. This approach considers the gradual reduction of load-bearing capability due to damage by introducing a damage parameter (or a tensor) into the material constitutive relation, which leads to irreversible damage evolution (Chang, Liu et al. 1991; Chaboche, Lesne and Maire 1995; de Borst, Pamin, Peerlings and Sluys 1995; Chaboche, Girard Levasseur 1997; Shokrieh and Lessard 2000). The CDM based theories can be conveniently formulated into traditional finite element programs. But there are two inherent difficulties associated with this approach: 1) it cannot deal with highly concentrated crack-like damage, which is universal in composites; and 2) damage parameters calibrated from individual modes do not account for multiple damage mode coupling. Linear elastic fracture mechanics (LEFM) and its computational form virtual crack closure technique (VCCT) have been used to study delamination cracks in laminated composites. But this method requires pre-existing cracks of finite size; therefore cannot deal with damage initiation from pristine materials (Tay 2003).

A multiscale hierarchical modeling approach based on unit cell (UC) or representative volume element (RVE) analyses and followed by homogenization from one scale to the next higher level scale (hierarchical model) has also been pursued to account for the progressive damage evolution on macroscopic composite properties (Oden, Vemaganti and Moes 1999; Fish and Ghouali 2001; Ladeveze 2004; Reddy 2005; Gonzalez and LLorca 2006; Tang, Whitcomb, Kelkar and Tate 2006; Inglis, Geubelle, Matous, Tan, and Huang 2007). But without explicit inclusion of the multiple damage coupling, the homogenization process will have to rely on either theoretical hypotheses or costly experimental programs to calibrate key parameters (and there are many of them!). To further illustrate this important point, let's review the progressive damage evolution recorded for a double-notched tension specimen reported in (Hallett and Wisnom 2006), which is replicated in Figure 1.

When this double-notched [0/90]s laminate was loaded at about 25% of the final load, a splitting crack in 0^0-ply and a transverse crack in 90^0-ply were already formed at the notch-root (Fig 1a). As the load increased, the splitting crack propagated gradually towards the loading boundary and was accompanied by the generation of many transverse cracks (vertical lines in Fig 1b). Meanwhile, delamination cracks were also formed around the splitting cracks in a self-similar fashion (dark triangular regions in Fig 1b & 1c). The delaminating shape and transverse crack density are results of complex interplay of the different types of cohesive damage while they evolve (Fang, Zhou, Cox and Yang 2011). It is possible to model the splits and transverse cracks

using a CDM-based material degradation model. However, in doing so, the evolving nonlinear interaction between the ply cracks and delamination cannot be followed. As a result, the delamination shape and area, as well as the splitting crack growth rate as a function of the applied stress would be inaccurate (Yang and Cox 2005; Cox and Yang 2006).

Explicit representations of all important damage modes need to be included in a structural model to achieve a faithful strength prediction. Several important numerical and material barriers therefore need to be overcome: 1) a full understanding of the mechanisms that control the initiation and propagation of these different types of damage and the length scales they operate on; 2) an accurate accounting for the interaction among the co-evolving damage modes; 3) faithfully generating the multiple transverse cracks without knowing their locations a priori. In this paper, we shall review and discuss the recent development of advanced numerical methods that can meet the challenge of faithfully simulating the coupled multiple damages at various scales in composite materials.

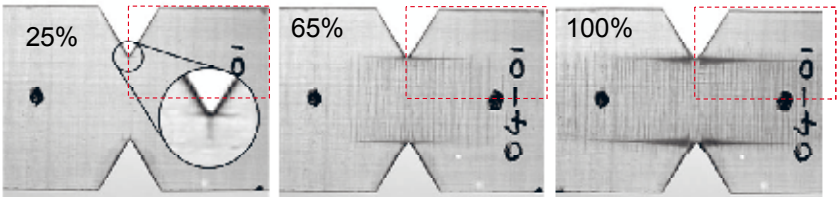

Figure 1: X-ray radiography reveals damage mechanisms viewed through the ply stack in a double-notch tension specimen with symmetric orthogonal ply stack ($[0/90]_s$) (Hallett and Wisnom 2006).

2. NONLINEAR COHESIVE ZONE MODELS FOR COMPOSITE FRACTURE

Most damage modes in composites are in the form of crack-like entities and they interact with each other at various scales as evidenced in Figure 1. When dealing with multiple crack interactions the nonlinear cohesive zone models (CZMs) are essential because they unify the processes of crack initiation and growth within a single physically-consistent model (Dugdale 1960; Barenblatt 1962). Most fracture process zones in PMCs are of size 0.1 – 1.0 mm. As will be seen shortly, the cohesive zone models allow for correct accounting of the nonlinear interaction of different fracture processes, while linear elastic fracture mechanics (LEFM), due to its non-physical nature at the limit of small crack length, cannot guarantee such correct coupling (Needleman 1990; Corigliano 1993; Wisnom and Chang 2000; Elices, Guinea, Gomez, and Planas 2002; Moës and Belytschko 2002; de Borst 2003; Remmers, de Borst, and Needleman 2003; Yang and Cox 2005; Cox and Yang 2006; Parmigiani and Thouless 2006).

Figure 2 gives an example that strongly supports this view point. In Figure 2(a) the load-displacement of a bonded polycarbonate (PC) specimen with a pre-existing notch with root angle 120^0 under three-point bending test is shown. The bond-line is at an angle of 30^0 to the specimen longitudinal direction and the fracture toughness along the bond-line is at least three times smaller than that of the PC. The LEFM, which simply compares the energy release rates (ERR) ratio of the interface crack to its toughness (G_i / Γ_{ic}), against the ERR ratio of a local mode-I kink crack (G_k / Γ_{kc}) (He and Hutchinson 1989), predicts a complete interfacial crack

propagation. However, repeated tests showed that kinking crack would form as shown in Figure 2(b). Only with cohesive zone modeling and with proper consideration of crack branching (Fang, et al. 2011; Yang and Fang 2011), were the fracture behavior and load-displacement curves correctly predicted (Fig 2a & 2c).

This example on bonded bulk PC specimens has a significant implication on composite fracture analyses because such crack kinking and coalescence processes are quite universal in laminated or textile composites. For example, crack jumping from one interface to another (Ling, Fang, Cox and Yang 2011) involves both transverse crack kinking (from one interface into a transply) and crack merging (from transply into another interface). One of the important messages from this study is that, crack branching is a competition between two fracture process zones and a careful numerical treatment is needed to ensure proper stress and deformation coupling between the two fracture process zones. The LEFM view that a kinking process is purely determined by the two competing ERR-toughness ratios is non-physical. Both the ERRs and cohesive strengths play an important role in determining whether an interfacial crack should kink into the neighbouring ply (a similar observation has also been made by Thouless and colleagues in (Parmigiani and Thouless 2006; Parmigiani and Thouless 2007). The above successful simulation was done using an augmented cohesive element (ACZ) recently developed by Fang, et al. (2011), which will be introduced in more detail shortly. We note that the common practice of coupling X-FEs or A-FEs with standard CZ elements, as has been done in many previous analyses cannot yield a correct response in this case (Van de Meer and Sluys 2009; Van de Meer, Oliver, and Sluys 2010).

While the cohesive zone models are excellent in describing the fracture processes in composites, they need to be incorporated into numerical platforms such as FE programs as special elements. This implementation has a major shortcoming because it needs a crack path to be known a priori so that the CZ elements can be properly defined in a numerical model. However, in composites such information is not available. For example, the location and spacing of the transverse cracks in Figure 1 cannot be known before the analysis. Recent developments in advanced numerical methods for introducing arbitrary discontinuity in a continuum have made it possible to include most cohesive descriptions of major crack systems in structural models to account for the progressive damage. This will be reviewed in more detail in the next section.

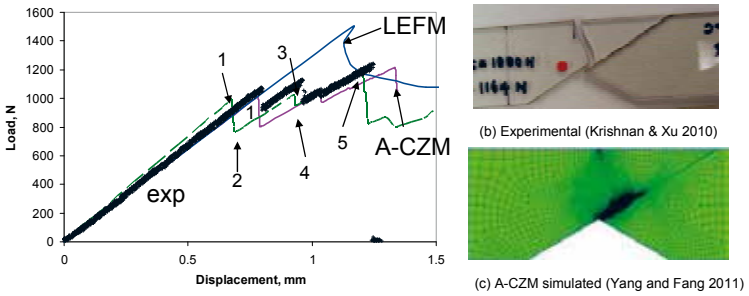

Figure 2 (a) comparison of experimentally measured, CZM simulated, and LEFM predicted load-displacement curve of an adhesively-bonded, prenotched PC specimen under three-point bending. (b) experimental observation of kinked crack; and (c) simulated kinking using nonlinear cohesive zone model.

3. ADVANCED NUMERICAL METHODS FOR ARBITRARY CRACKING

3.1 Extended finite element method (X-FEM). Standard FEM cannot adequately describe a discontinuous displacement field within an element because the shape function for intra-element displacement interpolation is continuous. This can be seen from the standard elemental interpolation below:

$$\mathbf{u}(\mathbf{x}) = \sum_{i=1}^{n_e} \left(\sum_{j=1}^{m_e^i} N_j^i(\mathbf{x}) \mathbf{u}_j^i \right) \tag{1}$$

where $\mathbf{u}(\mathbf{x})$ is the approximate displacement field. m_e^i is the number of nodes in element i and n_e is the total number of elements. Since the shape functions, $N_j^i(\mathbf{x})$, are continuous, such a formulation cannot describe intra-element discontinuities. Any discontinuities have to be arranged along inter-element boundaries. Recently, this difficulty has been successfully overcome by the X-FEM proposed by Belytschko and colleagues (Belytschko and Black 1999; Moës, Dolbow, and Belytschko 1999; Daux, Moës, Dolbow, Sukumar and Belytschko 2000). X-FEM treats a crack explicitly by introducing local enrichment to cracked elements. The local enrichment procedure, which is based on the partition-of-unity finite element method (PUFEM) first proposed by Melenk & Babuška (1996), employs the known asymptotic displacement field for crack tip regions and the generalized Heaviside function for the crack wake region. In such cases, the displacement field can be expressed in a general form as follows:

$$\mathbf{u}(\mathbf{x}) = \sum_{j}^{n} N_j(\mathbf{x}) \mathbf{u}_j + \sum_{j=J_k} N_j(\mathbf{x}) \left(d_{j_k} H(\mathbf{x}) \right) + \sum_{j=J_l} N_j(\mathbf{x}) \left(\phi_{jl} p_l(\mathbf{x}) \right) \tag{2}$$

where n is the total number of nodes; J_k is the node set that contains the nodes that are cut by traction free cracks; and J_l is the node set that is influenced by a crack-tip singular displacement function (enrichment function) $p_k(\mathbf{x})$. $H(\mathbf{x})$ is the generalized Heaviside function. d_{jk} and ϕ_{jl} are the associated DoFs to $H(\mathbf{x})$ and $p_k(\mathbf{x})$, respectively. Note that in Eqn (2) the $\mathbf{u}_j$ is not the complete nodal displacement, but the continuous part of it. The discontinuous part is accounted for by $d_{jk}H(\mathbf{x})$ and $\phi_{jl}\, p_k(\mathbf{x})$. For a moving cohesive crack, by introducing $H(\mathbf{x})$ and $p_k(\mathbf{x})$ as enrichment functions, Eqn (2) can fully account for the discontinuous displacement field. Moreover, the discontinuity treatment is local in the sense that only those nodes whose support domains are cut by a crack need to be enriched. An inconvenience associated with the X-FEM is that this enrichment process requires the addition of extra DoFs dynamically assigned to these nodes, i.e., it requires nodal DoFs be adjustable depending on whether a node is being completely cut or not (Moës et al. 1999; Dolbow, Moës, and Belytschko 2000; Remmers et al. 2003; Budyn 2004; de Borst, Remmers, and Needleman 2006; Fries and Belytschko 2006; Hettich, Hund and Ramm 2008). This makes it somewhat cumbersome in dealing with multiple cracks[1].

Although it has been demonstrated that the X-FEM is very efficient in dealing with arbitrary cracks in homogeneous materials, successful reports of X-FEM in analyzing arbitrarily cracking

[1] The X-FEM feature in commercial packages such as ABAQUS (v. 6.9 & later) can only handle stationary cracks or single propagating cracks.

heterogeneous materials such as laminated or textile composites remain relatively few (Hettich et al. 2008). The major difficulty comes from the inconvenient handling of both the material heterogeneity and the crack coalescence/bifurcation within the X-FEM framework. First of all, analytical forms of enrichment functions for bi-material interfaces may not be readily available; secondly for multiple crack interaction the enrichment level will be unduly high and it quickly becomes intractable when the crack number increases.

A more efficient and promising method for composite fracture appears to be the phantom node method, or its variation, the augmented finite element method (A-FEM), which will be described below.

3.2 Augmented finite element method (A-FEM). An alternative numerical method that can also treat the arbitrary cracking problem is the phantom-node method, first developed by Belytschko and colleagues (Song, Areias, and Belytschko 2006) based on the initial work of Hansbo and Hansbo (2004). The essence of this method is to use overlapping paired elements to describe a strong or weak discontinuity in a physical element that is bisected by a discontinuity. One of the advantages of this method is that it uses only standard finite element (FE) shape functions (i.e., more compatible with existing FE programs) and it can conveniently consider both weak and strong discontinuities. Based on this concept, Ling et al. (2009) recently proposed an element with one or multiple copies of element nodes, to account for an arbitrary intra-element crack but otherwise remain a standard finite element. This so-called augmented finite element (A-FE) is fully compatible with existing FE programs and has been implemented into a commercial FE program as a user-defined element (Yang, et al. 2010; Fang, et al. 2011; Ling, et al. 2011). Below we briefly introduce the A-FEM formulation with embedded cohesive damage descriptions.

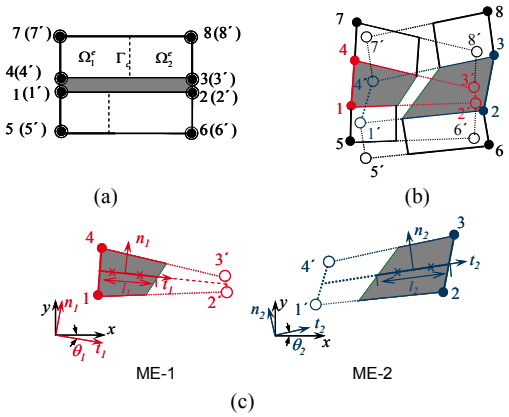

Figure 3 (a) Two bonded A-FEs bonded by a ACZ element before deformation, all with doubly-assigned nodes for possible intra-element cracking. (b) after deformation (assuming both solid A-FEs are cracked, the ACZ will be augmented into two mathematical elements with their own local coordinates as shown in (c). For each ME, the two Gaussian points are indicated by the two symbols "×", which are located in the ME's active cohesive integration domain (shaded area). The interface is exaggerated for illustration purposes (Fang, et al. 2011).

Referring to Figure 3(a), two bonded solid elements are assigned two sets of corner nodes (4-3-8-7-4′-3′-8′-7′ for the top element and 5-6-2-1-5′-6′-2′-1′ for the bottom element). For each A-

FE, the first four nodes are physical nodes and the next four nodes with superscript " ′ " are ghost nodes. If the prescribed crack initiation criterion is met, one or both of the solid A-FEs will be augmented to allow for displacement discontinuity across the intra-element crack(s) (Figure 3b). For example, the top A-FE will be augmented into two mathematical elements (MEs), i.e., ME1 with 4-3′-8′-7 and ME2 with 4′-3-8-7′. The two MEs may be connected by nonlinear spring elements or cohesive tractions for a cohesive crack. Both MEs employ standard FE shape functions for elemental displacement interpolation, i.e.:

$$\mathbf{u}_\alpha(\mathbf{x}) = \mathbf{N}_\alpha(\mathbf{x})\mathbf{d}_\alpha \tag{3}$$

where $\mathbf{N}_\alpha(\mathbf{x})$ are the standard FE shape functions and $\mathbf{d}_\alpha$ (α =1 and 2) are the nodal displacements of ME-α. Eqn (3) now allows for different displacement fields in physical domains Ω_1^e and Ω_2^e , which makes it possible to account for the discontinuous displacements (or displacement jumps) across the cohesive crack $\mathbf{\Gamma}_c$. The displacement jumps across the crack in the A-FE can be simply obtained as:

$$\boldsymbol{\delta}(\mathbf{x}) = \mathbf{u}_2(\mathbf{\Gamma}_c) - \mathbf{u}_1(\mathbf{\Gamma}_c) = \mathbf{N}(\mathbf{\Gamma}_c)(\mathbf{d}_2 - \mathbf{d}_1) \tag{4}$$

If the two MEs are connected by a cohesive crack, the displacement jumps are the cohesive opening displacement expressed in global coordinates. Denote by **R** the rotational matrix that links the global coordinates to the local coordinates defined by the solid crack direction and the direction normal to it, i.e.:

$$\mathbf{R} = \begin{bmatrix} \cos\theta & -\sin\theta \\ \sin\theta & \cos\theta \end{bmatrix}$$

with θ being the angle between crack line and global x-direction. The local displacement jumps can be written as:

$$\boldsymbol{\delta}' = \{\delta_n' \quad \delta_s'\}^T = \mathbf{R}\boldsymbol{\delta} \tag{5}$$

The superscript "T" denotes a matrix transpose. It follows that the cohesive traction associated with the solid crack is:

$$\mathbf{t}' = \{\tau' \quad \sigma'\}^T = \{f_t(\boldsymbol{\delta}') \quad f_n(\boldsymbol{\delta}')\}^T \tag{6}$$

where τ' and σ' are shear and tensile cohesive stresses in the local coordinates, respectively, and $f_t(\boldsymbol{\delta}')$ and $f_n(\boldsymbol{\delta}')$ are traction-separation relations for the shear and opening mode, respectively.

Substituting the above displacement and cohesive tractions into the virtual work principle and following the standard procedure, the weak form of the equilibrium equations for static analysis can be derived Ling, et al. (2009):

$$\int_{\Omega_1^e} \mathbf{B}^T\boldsymbol{\sigma}\mathrm{d}\Omega + \int_{\Gamma_c} \mathbf{N}^{\mathrm{T}}\mathbf{t}\mathrm{d}\Gamma = \int_{\Gamma_{F1}} \mathbf{N}^{\mathrm{T}}\mathbf{F}_1\mathrm{d}\Gamma \tag{7a}$$

$$\int_{\Omega_2^e} \mathbf{B}^T\boldsymbol{\sigma}\mathrm{d}\Omega - \int_{\Gamma_c} \mathbf{N}^{\mathrm{T}}\mathbf{t}\mathrm{d}\Gamma = \int_{\Gamma_{F2}} \mathbf{N}^{\mathrm{T}}\mathbf{F}_2\mathrm{d}\Gamma \tag{7b}$$

where $\mathbf{B}$ is the strain matrix, $\boldsymbol{\sigma}$ is the stress matrix, $\mathbf{F}_\alpha$ (α =1 and 2) are the external forces applied on ME-α, and $\mathbf{t}(\boldsymbol{\delta}) = \mathbf{R}^T\mathbf{t}'(\boldsymbol{\delta}')$ is the cohesive traction array. Since $\mathbf{t}(\boldsymbol{\delta})$ is typically nonlinear, Eqn (7) typically needs to be linearized. But it is straightforward to linearize the equation using an incremental scheme. The incremental form of the equilibrium equations is:

$$\begin{bmatrix} \mathbf{K}_{11} & \mathbf{K}_{12} \\ \mathbf{K}_{21} & \mathbf{K}_{22} \end{bmatrix} \begin{Bmatrix} \Delta\mathbf{d}_1 \\ \Delta\mathbf{d}_2 \end{Bmatrix} = \begin{Bmatrix} \int_{\Gamma_{F1}} \mathbf{N}^{\mathrm{T}} \Delta\mathbf{F}_1 \mathrm{d}\Gamma \\ \int_{\Gamma_{F2}} \mathbf{N}^{\mathrm{T}} \Delta\mathbf{F}_2 \mathrm{d}\Gamma \end{Bmatrix} \tag{8a}$$

where $\Delta\mathbf{d}_\alpha$ and $\Delta\mathbf{F}_\alpha$ (α = 1, 2) are incremental nodal displacements and external loads, respectively. The matrices $\mathbf{K}_{ij}$ are:

$$\begin{aligned} \mathbf{K}_{11} &= \int_{\Omega_1^e} \mathbf{B}^T\mathbf{D}_1\mathbf{B}\mathrm{d}\Omega + \int_{\Gamma_c} \mathbf{N}^{\mathrm{T}}\mathbf{R}^T\mathbf{D}'_{coh}\mathbf{R}\mathbf{N}\ \mathrm{d}\Gamma; \\ \mathbf{K}_{22} &= \int_{\Omega_2^e} \mathbf{B}^T\mathbf{D}_2\mathbf{B}\mathrm{d}\Omega + \int_{\Gamma_c} \mathbf{N}^{\mathrm{T}}\mathbf{R}^T\mathbf{D}'_{coh}\mathbf{R}\mathbf{N}\ \mathrm{d}\Gamma; \\ \mathbf{K}_{12} &= \mathbf{K}_{21} = -\int_{\Gamma_c} \mathbf{N}^{\mathrm{T}}\mathbf{R}^T\mathbf{D}'_{coh}\mathbf{R}\mathbf{N}\ \mathrm{d}\Gamma \end{aligned} \tag{8b}$$

where $\mathbf{D}_\alpha$ (α =1 and 2) is the stiffness matrix of the bonded solid element and $\mathbf{D}'_{\mathrm{coh}}$ is the tangential stiffness matrix of the cohesive law (in local coordinates), i.e.:

$$\mathbf{D}'_{coh} = \begin{bmatrix} \partial f_t / \partial \delta_t' & \partial f_t / \partial \delta_n' \\ \partial f_n / \partial \delta_t' & \partial f_n / \partial \delta_n' \end{bmatrix}. \tag{9}$$

The above stiffness integration within a mathematical element is performed on the active material domain (i.e., Ω_1^e for ME1 or Ω_2^e for ME2), rather than on the entire elemental domain Ω^e ($=\Omega_1^e \cup \Omega_2^e$). This is important because it offers extra flexibility in handling material heterogeneity across the discontinuity: simply using different $\mathbf{D}_\alpha$ during the integration will achieve this purpose. Subdomain integration is needed for the stiffness integration of Eqn (8) and we employed the triangularization scheme used in Moës, et al. (1999).

3.3 Augmented cohesive zone (ACZ) element for crack bifurcation and coalescence. The above A-FEM with embedded cohesive fracture description can effectively deal with multiple arbitrary cracks within any lamina (i.e., transply cracks). However, in laminated PMCs the interface delamination is often strongly coupled with the transply cracks. As discussed above, such strongly coupled process zones need a special numerical treatment to guarantee correct stress coupling during crack bifurcation and coalescence. If traditional cohesive element were used together with the A-FEM or X-FEM, the local stress transfer during the nonlinear interaction will be in significant error, as demonstrated in (Fang, et al. 2011). Fortunately, with the idea of augmented FEM, it is possible to develop augment cohesive zone (ACZ) elements that can allow for arbitrary separation according to the cracking configuration in the abutting solid elements to achieve accurate load transfer.

The ACZ element can be defined with two sets of corner nodes shared with the abutting solid A-FEs (e.g. 1-2-3-4-1′-2′-3′-4′ as shown in Figure 3(a)). If neither of the solid A-FEs is cracked, all the ghost nodes are tied with the corresponding real nodes and both the solid A-FEs and ACZ element behave like standard FE and traditional CZ element. However, if either or both of the abutting solid elements are cracked and the crack-tip(s) reaches the interface, the cohesive

element will be augmented accordingly. Figure 3(b) shows the augmented configuration when both solid A-FEs have cracked. In this case, the element can be augmented into two MEs for cohesive stress integration with 1-2′-3′-4 for ME-1 and 1′-2-3-4′ for ME-2 as shown in Figure 3(b and c). The respective cohesive stress integration domains for the MEs are shown in the figure by shaded areas.

For each ME-α (α=1 or 2), a local coordinate system can be established by defining the tangential direction ($\mathbf{t}_\alpha$) along the line that connects the mid-points of edge 14 and 2′3′ for ME-1, or, that connects the mid-points of 1′4′ and 23 for ME-2, as shown in Figure 3(c). The respective normal directions ($\mathbf{n}_\alpha$) are perpendicular to $\mathbf{t}_\alpha$. Thus the rotational matrix for each ME, can be obtained as $\mathbf{Q}_{i\alpha} = Diag\{\mathbf{R}_{i\alpha}, \mathbf{R}_{i\alpha}, \mathbf{R}_{i\alpha}, \mathbf{R}_{i\alpha}\}$. Here $\mathbf{R}_{i\alpha}$ is computed using the rotation angle θ_α of cohesive ME-α as shown in Figure 3(c). Note that from here on we shall denote all quantities associated with the ACZ interface element with subscript "*i*".

The nodal displacements of ME-α in local coordinates can be obtained as:

$$\mathbf{d}_{i\alpha}' = \mathbf{Q}_{i\alpha}\mathbf{d}_{i\alpha} \tag{10}$$

The local displacement jumps (crack displacements) across the ME-α can be obtained as:

$$\boldsymbol{\delta}_{i\alpha}' = \{\delta_t' \quad \delta_n'\}_{i\alpha}^T = \mathbf{N}\mathbf{d}_{i\alpha}' = \mathbf{N}\mathbf{Q}_{i\alpha}\mathbf{d}_{i\alpha} \tag{11}$$

where $\mathbf{N} = \begin{bmatrix} -N_1 & 0 & -N_2 & 0 & N_2 & 0 & N_1 & 0 \\ 0 & -N_1 & 0 & -N_2 & 0 & N_2 & 0 & N_1 \end{bmatrix}_\alpha$ is the interpolation matrix consisting of 1D standard nodal shape functions, i.e., $N_1 = (1-\xi)/2$ and $N_2 = (1+\xi)/2$ with $\xi \in [-1,1]$.

The incremental form of the interfacial cohesive stresses can be obtained from interfacial cohesive laws, $g_{ti}(\boldsymbol{\delta}_i')$ and $g_{ni}(\boldsymbol{\delta}_i')$, as follows:

$$\Delta\boldsymbol{\sigma}_{i\alpha}' = \mathbf{D}'_{\text{i coh}}\,\Delta\boldsymbol{\delta}_{i\alpha}' = \mathbf{D}'_{\text{i coh}}\,\mathbf{N}\mathbf{Q}_{i\alpha}\Delta\mathbf{d}_{i\alpha} \tag{12}$$

where $\mathbf{D}'_{\text{i coh}}$ is the tangential stiffness matrix of the interface cohesive law (in local coordinates), which can be obtained from Eqn (9) by replacing $f_t(\boldsymbol{\delta}')$ and $f_n(\boldsymbol{\delta}')$ with interfacial cohesive laws, $g_{ti}(\boldsymbol{\delta}_i')$ and $g_{ni}(\boldsymbol{\delta}_i')$, respectively.

From the principle of virtual work the equilibrium equation of the ME-α in incremental form can be derived straightforwardly as below:

$$\left(\int_{l_\alpha} \mathbf{Q}_{i\alpha}{}^T\mathbf{N}^T\mathbf{D}'_{\text{i coh}}\,\mathbf{N}\,\mathbf{Q}_{i\alpha}\mathrm{d}l\right)\Delta\mathbf{d}_{i\alpha} = \Delta\mathbf{F}_{i\alpha} \tag{13}$$

The integral in "()" is the tangential stiffness of the ME-α. In this study, Gaussian integration is used. For each ME-α, the two Gaussian points are located in the active cohesive integration segment only and they are indicated in Fig 3 (c) by the symbol "×".

4. A-FEM SIMULATION OF COMPOSITES AT VARIOUS LENGTH SCALES

The A-FEM and ACZ elements described above enables high-fidelity analyses of composite at various scales. In this section, we shall introduce several recent successful examples. Discussions will be focused on numerical issues that need to be addressed regarding the nonlinear fracture processes and their coupling behavior at different length scales.

4.1 Structural scale damage coupling. We first analyze the progressive damage evolution in the double notch tension specimen shown in Figure 1. The simulation was done at coupon level with each ply modeled by plane-stress A-FEM elements to allow for multiple ply cracks and ACZ elements for delamination and correct coupling. All possible damage modes of importance to structural integrity, i.e., splitting, transply cracking, inter-ply delamination, and fiber rupture, were included in a single structural model as shown in Fig 4(b). In addition, continuous plasticity that represents irreversible damage occurring in small volumes of the polymer matrix (at micrometer scales) was included.

A detailed account of how the elastic/plastic properties and cohesive fracture properties were calibrated from literature data has been given in Fang, et al. (2011), where the excellent mesh independent results were also demonstrated for specimen compliance, splitting crack growth rate, transverse crack spacing, and delamination shape and area.

A direct comparison of the simulated and experimental results is summarized in Figure 4. The A-FEM simulation successfully reproduces all the important features observed experimentally on the three cracking systems. The self-similar delamination zone angle is predicted to be 8^0, in agreement with the experimental value of 7^0-10^0. The splitting crack growth rate (as a function of applied stress), and multiple transverse cracks and their spacing are also well captured. In particular, the gradual decrease of specimen stiffness due to multiple transverse cracking in the load-displacement curve is accurately captured.

We emphasize that, to achieve this unprecedented level of fidelity it is critical to include the multiple transverse cracking in the simulation. Had this not been included, the predicted delamination area and shape would be significantly different from the experiment (c.f. the curve in Figure 4a labeled as “no transverse cracking”). Another important finding is that the continuous shear plasticity must be included. Otherwise the delamination crack propagation rate and shape would be in significant error. Evidence of crack-tip shear nonlinearity has recently been confirmed by μCT data of similar specimens Wright, Moffata, Sinclaira, and Spearing (2010).

In the above structural level simulations, it is implicitly assumed that, once a transverse crack or splitting crack is initiated, it immediately propagates as a steady-state crack, because the *in-situ* strength is derived from steady-state crack analysis based on LEFM and the assumption that the interface remains fully bonded (tunneling or channeling crack mode) (Davila, Camanho, and Rose 2005; Camanho, Davila, Pinho, Iannucci, and Robinson 2006). Judging from the simulated results, this assumption appears valid at least for the current analysis. However, whether this should be true for other composites remains a question. This question can be answered from a more detailed analysis at a smaller scale, which will be described as follows.

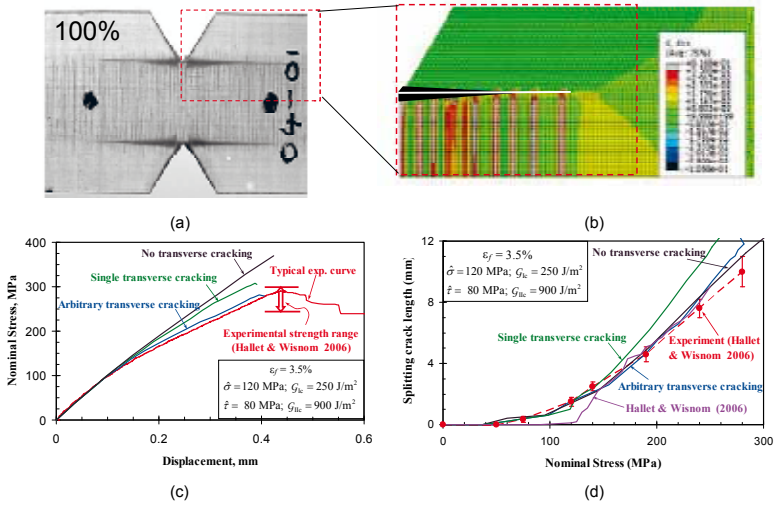

Figure 4: (a) Image taken immediately before specimen failure with clearly coupled splitting cracks, transply cracks, and wedge-shaped delamination zones. (b) predicted damages closely follow the experimentally-observed damage pattern. (c) comparison of measured and predicted load-displacement data; and (d) comparison of splitting crack length as a function of applied stress Fang et al. (2011).

4.2 Damage Coupling at Sublaminar Scale. To focus on coupling between delamination and an individual transply crack, the sublaminar level model shown in Figure 5 was studied. The transverse crack is bounded in one direction by the ply thickness, but extends along the fiber direction.

Simulations revealed that tunneling crack initiation can occur either from an arbitrarily located small flaw as a penny-shaped crack or from a free edge. However, even if initiation occurs first from the flaw, the cohesive crack at the free edge initiates before the penny-shaped crack reaches the ply interfaces; then the two quickly link up and propagate in unison towards the interfaces and thus form a mature tunneling crack (Zhou et al. 2010). Depending on the mode-II to mode-I toughness ratio and cohesive strength, there may be two tunneling modes. For PMCs, which typically have mode II toughness several times larger than mode I toughness, transply cracks will not trigger significant local delamination during their initiation and propagation (as channeling or tunneling cracks). Rather, delamination occurs after transply cracking processes are completed and upon further loading, which is indicative from the experimental images of Figure 1. In such condition, the transply crack initiation stress is only 5% less than the steady-state propagation stress (Zhou, et al. 2010).

LEFM is inaccurate in predicting the stress for initiating the delamination crack that is subsequently triggered by the transverse crack, which depends on both the toughness ratio and cohesive strength ratio and is heavily influenced by the presence of a free edge (Zhou, et al. 2010). This again highlights the need of using nonlinear cohesive models for delamination of composites, especially in cases that there are no large-sized preexisting delamination cracks.

The other mode, i.e., the unstable tunneling with delamination mode, is not commonly seen in typical PMCs, but observations have been reported of analogous cracks in other material systems such as in thin films bonded to thick substrates (Dvorak and Laws 1987; Ho and Suo 1992; Cox and Marshall 1996). Direct observation of the tunneling mode of propagation has not

been made for transverse microcracks in laminates, which calls for new experimental observation techniques.

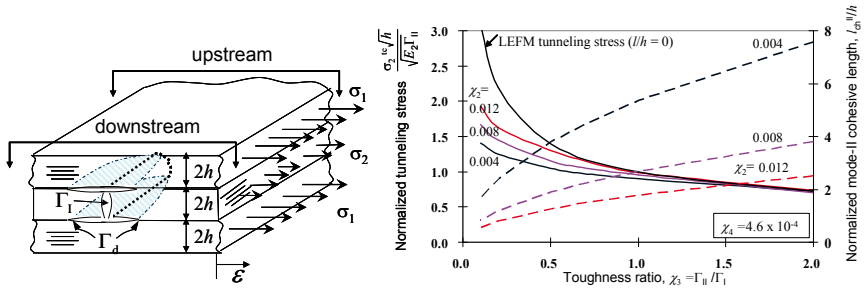

Figure 5. (a) A [0/90/0] laminate with a tunneling crack that is accompanied by four delamination cracks . (b) Numerically determined tunneling initiation stress (left Y-axis) and delamination process zone size (right Y-axis) as functions of toughness ratio Γ_{II}/Γ_{I}. (Zhou, et al. 2010)

The question that naturally follows from this sublaminar model analysis is whether one can predict fracture toughness and cohesive strength based on the properties of the matrix, fibers, and fiber-matrix interface? To answer this, one increases modeling resolution to the microscopic scale, with explicit representation of matrix, fibers and the interfaces that bond them. Such an analysis is given below.

4.3 Microscopic Fiber/Matrix Interaction. At the microscopic level (single fiber scale), stochastic matrix and fiber properties need to be considered. A-FEM is well positioned to address this issue. Figure 6 gives an example of a failure analysis of a representative volume containing 28 randomly distributed fibers embedded in a matrix (fiber volume 50%) under uniaxial tension. A-FEM elements were used for the matrix and ACZ elements were used to join the matrix domain and elastic fibers.

The simulation reveals multiple cracking in the matrix domain before a final cracking path is chosen by connecting microcracks in the matrix with fiber-matrix interfacial debonds (inset of Fig 6). It is also found that the fiber position, which is a random variable due to the manufacturing process, significantly influences the final cracking path and is responsible for the observed sample-to-sample variation of measured toughness, which is typically 10-15%.

The nominal stress-separation curves of several such simulations are given in Fig 6. In this case, the assigned toughness and strength are: for the matrix, 200 J/m^2 and 100 MPa; for interfaces, 100 J/m^2 and 60 MPa. The predicted peak strength (cohesive strength) of 80 MPa is bounded by the matrix and interfacial strength and is relatively insensitive to fiber randomness. However, the derived fracture toughness, i.e., the energy dissipation divided by the nominal crack area, predicted to be 180 ± 20 J/m^2, is significantly influenced by fiber positioning because a different fiber organization leads to significantly different final cracking paths. Thus the microscopic analysis at least offers the possibility of predicting nonlinear cohesive laws that can be used at the sublaminar or structural level.

However, note that the fidelity of such microscopic analyses depends strongly on accurate input for the material properties of the matrix, fibers, and interfaces at the microscopic scale, which is

not easily obtained. In the future, this problem may benefit from molecular dynamics analyses to determine atomic-scale behavior.

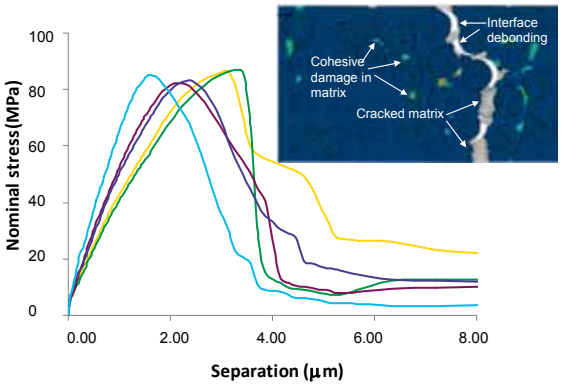

Figure 6 A-FEM simulated progressive failure of a microscopic representative volume element with explicit consideration of matrix cracking, fiber/matrix debonding, and randomly located fibers. The five nominal stress vs. separation curves are different runs with randomly assigned fiber organizations. The inset shows the multiple cohesive damage in matrix and the final cracking path of connected microcracks in matrix and fiber/matrix interfaces (Yang, et al. 2011).

5. FURTHER DISCUSSIONS ON MULTISCALE APPROACHES

It is desired to unify the different scale analyses into a single multiscale framework so that the structural level (global) deformation and those local damage processes are seamlessly coupled. Given sufficient computational resources, the A-FEM with cohesive damage descriptions, facilitated with ACZ for handling material boundaries, is inherently multiscale and can achieve faithful global-local coupling. Nevertheless current computational power limits our analysis at coupon level structural scales.

To improve numerical efficiency, one possibility is to develop multiscale hierarchical modeling approaches based on unit cell (UC) or representative volume element (RVE) analyses and followed by homogenization from one scale to next higher level scale (hierarchical model), such as those in (Oden, et al. 1999; Fish and Ghouali 2001; Ladeveze 2004; Reddy 2005; Gonzalez and LLorca 2006; Tang, et al. 2006; Inglis, et al. 2007). However, as emphasized previously any attempt to homogenize discrete damage processes leads to loss of direct damage coupling, which has been shown critical for composite strength analyses (section 4.1).

A recent report on two scale modeling using X-FEM and level set functions shed a promising light (Hettich, et al. 2008), where the authors demonstrated that it is possible to use two sets of meshes, a coarse mesh for structural responses and a fine mesh allowing for microscopic details of material heterogeneity and localized damage, to achieve global-local coupling with much reduced computational cost while maintaining reasonable simulation fidelity. The two sets of meshes were coupled through a variational multiscale method (VMM) which guarantees energy balance across the coarse-fine mesh boundaries; but the displacements were enforced in a weak

sense. A similar effort is undergoing and we shall report the results elsewhere.

Another alternative is to use the Arlequin method (Ben Dhia and Rateau 2005) to directly couple critical areas (with high-resolution A-FEM & ACZ elements) to non-critical areas (with low resolution regular elements). The most attractive feature of the Arlequin method is that it can couple two different mechanical states accurately and the numerical coupling cost is minimal. We have recently developed a suite of Arlequin coupling elements, including 2D-2D, 1D-2D, 1D-3D, 2D-3D, and shell-3D. These elements are compatible with commercial package ABAQUS (Qiao, Yang, Chen and Zhang 2011).

An example of a simulated four-point shear/bend test with A-FEM and Arlequin coupling is given in Figure 7. In Figure 7(a) the finer mesh region was A-FEs while the coarse mesh region is standard FEs. The two regions were coupled with two layers of Arlequin coupling elements. With such a set up, the simulated load vs. crack mouth sliding displacement were correctly captured with a saving of computational time of 60% as compared to the case of using a fine mesh only. A further study on adapting the method into a two-scale or even multiscale modeling approach is currently ongoing.

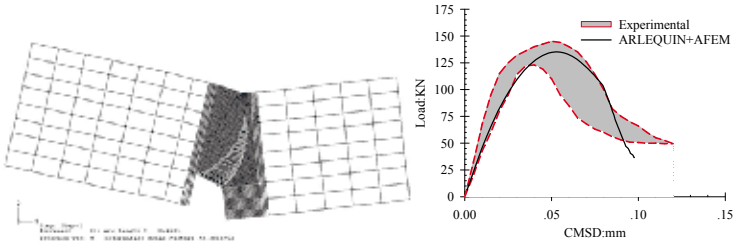

(a) (b)

Figure 7 (a) A-FEM simulated fracture of a 4-point shear test of a notched specimen. (b) comparison A-FEM predicted and experimentally-measured load vs. crack-mouth shear displacement (CMSD) curve.

6. CONCLUDING REMARKS

In this paper, the necessity of explicitly addressing multiple damage processes and their nonlinearly coupled evolution at various length scales to achieve high-fidelity strength prediction of composite materials has been highlighted. This requires advanced numerical simulation frameworks that can 1) explicitly account for major damage modes and their nonlinear coupling; 2) seamlessly integrate nonlinear material failure modes such as CZMs at different length scales; and 3) adequately account for global-local coupling so that direct influence functions between local damage events and global structural integrity can be established.

Recent developments in advanced numerical methods that can meet these challenges, including the X-FEM framework, phantom node method and its variant, the A-FEM framework have been reviewed. All these methods can adequately handle the arbitrary crack generation and propagation which is critical to describe discrete damage in composites. However, A-FEM has the advantage of easy handling of material heterogeneity and the nonlinear coupling of multiple cracking systems. In particular, the augmentation method can apply to cohesive interface elements so that they can correctly resolve the stress coupling when cracks merge or bifurcate.

Detailed formulations of an 8-node A-FE and the associated A-CZ element have been given. Successful application of this framework to composite failure analyses on three distinct length scales, i.e., structural level, sublaminar level, and microscopic level, has been demonstrated. The associated numerical and length scale issues have been discussed. Finally, the Arlequin method that has the potential to establish a tightly coupled multiscale approach to adequately account for global-local coupling has been reviewed. This method can potentially lead to the establishment of direct influence functions between local damage events and global structural integrity.

ACKNOWLEDGEMENTS

The A-FEM development and DNT specimen analysis in work were supported by NASA under Contract No. NNL08AA19C; the ACZ element and the microscopic RVE analysis were supported by National Hypersonic Science Center for Materials and Structures under AFOSR Contract No. FA9550-09-1-0477.

REFERENCES

Barenblatt, G.I. (1962). The mathematical theory of equilibrium cracks in brittle fracture. Advances in Applied Mechanics. H. L. Dryden and T. Von Karman, Academic Press. 2**:** 55-129.

Belytschko, T. and T. Black (1999). "Elastic crack growth in finite elements with minimal remeshing." International Journal for Numerical Methods in Engineering 45: 601-620.

Ben Dhia, H. and G. Rateau (2005). "The Arlequin method as a flexible engineering design tool." International Journal for Numerical Methods in Engineering 62: 1442-1462.

Budyn, E.R.L. (2004). Multiple crack growth by the extended finite element method[D]. Evanston, Illinois, Northwestern University. Ph. D. Thesis

Camanho, P.P., C.G. Davila, S.T. Pinho, L. Iannucci, and P. Robinson (2006). "Prediction of in situ strengths and matrix cracking in composites under transverse tension and in-plane shear." Composite Part A: Applied Science and Manufacturing 37: 165-176.

Chaboche, J.L., R. Girard, J. Levasseur (1997). "On the interface debonding models." International Journal of Damage Mechanics 6: 220-256.

Chaboche, J.L., P.M. Lesne, J.F. Maire (1995). "Continumm Damage Mechanics, Anisotropy and Damage Deactivation for Brittle Materials Like Concrete and Ceramic Composites." International Journal of Damage Mechanics 4: 5-22.

Chang, K.Y., S. Liu, F.K. Chang (1991). "Damage Tolerance of Laminated Composites Containing an Open Hole and Subjected to Tensile Loadings." Journal of Composite Materials 25: 274-301.

Corigliano, A. (1993). "Formulation, identification and use of interface models in the numerical analysis of composite delamination." International Journal of Solids and Structures 30: 2779-2811.

Cox, B.N. and D.B. Marshall (1996). "Crack initiation in brittle fiber reinforced laminates." Journal of the American Ceramic Society 79: 1181-1188.

Cox, B.N. and Q.D. Yang (2006). "In Quest of Virtual Tests for Structural Composites." Science 314: 1102-1107.

Daux, C., N. Moës, J. Dolbow, N. Sukumar, and T. Belytschko (2000). "Arbitrary branched and intersecting cracks with the extended finite element method." International Journal for Numerical Methods in Engineering 48: 1741-1760.

Davila, C.G., P.P. Camanho, and Rose (2005). "Failure Criteria for FPR Laminates." Journal of Composite Materials 39: 323-345.

de Borst, R. (2003). "Numerical aspects of cohesive-zone models." Engineering Fracture Mechanics 70: 1743-1757.

de Borst, R., J. Pamin, R.H.J. Peerlings, and L.J. Sluys (1995). "On gradient-enhanced damage and plasticity models for failure in quasi-brittle and frictional materials." Computational Mechanics 17: 130-141.

de Borst, R., J.J.C. Remmers, and A. Needleman (2006). "Mesh-independent discrete numerical representations of cohesive-zone models." Engineering Fracture Mechanics 73: 160-177

Dolbow, J., N. Moës, and T. Belytschko (2000). "Discontinuous enrichment in finite elements with a partition of unity method." Finite Elements in Analysis and Design 36: 235-260.

Dugdale, D.S. (1960). "Yielding in steel sheets containing slits." Journal of the Mechanics and Physics of Solids 8: 100-104.

Dvorak, G.J. and N. Laws (1987). "Analysis of progressive matrix cracking in composite laminates II. First ply failure." Journal of Composite Materials 21: 309-329.

Elices, M., G.V. Guinea, Gomez, and Planas (2002). "The cohesive zone model: Advantages, limitations and challenges." Engineering Fracture Mechanics 69: 137-163.

Fang, X.J., Q.D. Yang, B.N. Cox, and Z.Q. Zhou (2011). "An Augmented Cohesive Zone Element for Arbitrary Crack Coalescence and Bifurcation in Heterogeneous Materials." International Journal for Numerical Methods in Engineering in press: DOI: 10.1002/nme.3200.

Fang, X.J., Z.Q. Zhou, B.N. Cox, and Q.D. Yang (2011). "High-Fidelity Simulations of Multiple Fracture Processes in a Laminated Composites in Tension." Journal of the Mechanics and Physics of Solids 59: 1355-1373.

Fish, J. and A. Ghouali (2001). "Multiscale analysis sensitivity analysis for composite materials." International Journal for Numerical Methods in Engineering 50: 1501-1520.

Fries, T.P. and T. Belytschko (2006). "The intrinsic XFEM: a method for arbitryr discontinuities without additional unknowns." International Hournal for Numerical Methods in Engineering 68: 1358-1385.

Gonzalez, C. and J. LLorca (2006). "Multiscale Modeling of fracture in fiber-reinforced composites." Acta Materialia 54: 4171-4181.

Hallett, S.R. and M.R. Wisnom (2006). "Experimental Investigation of Progressive Damage and the Effect of Layup in Notched Tensile Tests." Journal of Composite Materials 40: 119-141.

Hansbo, A. and P. Hansbo (2004). "A finite element method for the simulation of strong and weak discontinuities in solid mechanics." Computational methods in Applied Mechanics and Engineering 193: 3523-3540.

He, M.-Y. and J.W. Hutchinson (1989). "Crack Deflection at an Interface Between Dissimilar Materials." International Journal of Solids and Structures 25: 1053-1067.

Hettich, T., A. Hund, and E. Ramm (2008). "Modeling of failure in composites by X-FEM and level sets within a multiscale framework." Computer Methods in Applied Mechanics and Engineering 197: 414-424.

Ho, S. and Z. Suo (1992). "Microcracks tunneling in brittle matrix composites driven by thermal expansion mismatch." Acta Metallurgica et Materialia 40: 1685-1690.

Inglis, H.M., P.H. Geubelle, K. Matous, H. Tan, and Y. Huang (2007). "Cohesive modeling of dewetting in particulate composites: micromechanics vs. multiscale finite element analysis." Mechanics of Materials 39: 580-595.

Kaddorur, A.S., M.J. Hinton, and P.D. Soden (2004). "A comparison of the predictive capabilities of current failure theories for composite laminates: Additional contributions." Composites Science and Technology 64: 449-476.

Ladeveze, P. (2004). "Multiscale Modelling and computational strategies." International Journal for Numerical Methods in Engineering 60: 233-253.

Ling, D.S., X.J. Fang, B.N. Cox, and Q.D. Yang (2011). "Nonlinear fracture analysis of delamination crack jumps in laminated composites." Journal of Aerospace Engineering 24: 181-188.

Ling, D.S., Q.D. Yang, and B.N. Cox (2009). "An augmented finite element method for modeling arbitrary discontinuities in composite materials." International Journal of Fracture 156: 53-73.

McCartney, L.N. (2003). "Physically based damage models for laminated composites." Journal of Materials: Design and Applications **217**(3): 163-199.

Melenk, J.M. and I. Babuška (1996). "The partition of unity finite element method: Basic theory and applications." Computer Methods in Applied Mechanics and Engineering 139(1-4): 289-314.

Moës, N. and T. Belytschko (2002). "Extended finite element method for cohesive crack growth." Engineering Fracture Mechanics 69: 813-833.

Moës, N., J. Dolbow, and T. Belytschko (1999). "A finite element method for crack growth without remeshing." International Journal for Numerical Methods in Engineering 46: 131-150.

Needleman, A. (1990). "An Analysis of Decohesion along an Imperfect Interface." International Journal of Fracture 42: 21-40.

Oden, J.T., K. Vemaganti, and N. Moes (1999). "Hierarchical modeling of hetrogeneous solids." Computer Methods in Applied Mechanics and Engineering 172: 3-25.

Parmigiani, J. and M.D. Thouless (2006). "The Roles of Toughness And Cohesive Strength on Crack Deflection at Interfaces." Journal of the Mechanics and Physics in Solids, 54: 266-287.

Parmigiani, J. and M.D. Thouless (2007). "The Effects of cohesive strength and toughness on mixed-mode delamination of beam-like geometries." Engin. Fract. Mech. 74: 2675-2699.

Qiao, H., Q.D. Yang, W.Q. Chen, and C.Z. Zhang (2011). "Implementation of the Arlequin method into ABAQUS: Basic formulation and applications." Advances in Engineering Software 42: 197-207.

Reddy, J.N. (2005). Multiscale computational model for predicting damage evolution in visoelastic composites subjected to impact loading**:** NTIC Report. http://handle.dtic.mil/100.2/ADA431014

Remmers, J.J.C., R. de Borst, and A. Needleman (2003). "A cohesive segments method for the simulation of crack growth." Computational Mechanics 31: 69-77.

Shokrieh, M.M. and L.B. Lessard (2000). "Progressive Fatigue Damage Modeling of Composite Materials, Part I: Modeling." Journal of Composite Materials 34: 1056-1080.

Song, J.H., P.M.A. Areias, T. Belytschko (2006). "A method for dynamic crack and shear band propagation with phantom nodes." International Journal of Numerical Methods in Engineering 67: 868-893.

Tang, X.D., J. Whitcomb, A.D. Kelkar, and J. Tate (2006). "Progressive failure analysis of 2x2 briaded composites exhibiting multiscale heterogeneity." Composite Science and Technology 66: 2580-2590.

Tay, T.E. (2003). "Characterization and Analysis of Delamination Fracture in Composites: An Overview of Developments from 1990 to 2001." Applied Mechanics Review 56: 1-32.

Van de Meer, F.P., C. Oliver, and L.J. Sluys (2010). "Computational analysis of progressive failure in a notched laminate including shear nonlinearity and fiber failure." Composite Science and Technology 70: 692-700.

Van de Meer, F.P. and L.J. Sluys (2009). "A phantom node formulation with mixed mode cohesive law for splitting in laminates." International Journal of Fracture 158: 107-124.

Wisnom, M.R. and F.K. Chang (2000). "Modelling of splitting and delamination in notched cross-ply laminates." Composites Science and Technology 60: 2849-2856.

Wright, P., A. Moffata, I. Sincliare, and S.M. Spearing (2010). "High resolution tomographic imaging and modelling of notch tip damage in a laminated composite." Composites Science and Technology 70: 1444-1452.

Yang, Q. and B.N. Cox (2005). "Cohesive Models for damage evolution in laminated composites." International Journal of Fracture 133: 107-137.

Yang, Q.D., B.N. Cox, Fang, X.J., and Z.Q. Zhou (2011). "Virtual Testing for Advanced Aerospace Composites: Advances and Future Needs." Journal of Engineering Materials and Technology 133: 11002-11008.

Yang, Q.D. and X.J. Fang (2011). "Revisiting crack kinking in cohesive materials." Journal of the Mechanics and Physics of Solids to be submitted.

Yang, Q.D., X.J. Fang, Z.Q. Zhou, and B.N. Cox (2010). "A-FEM for complex multi-scale damage evolution in laminated composites , May 2010." Proceedings of SAMPE Technical Conference, Paper #465 42: 1-8.

Zhou, Z.Q., X.J. Fang, B.N. Cox and Q.D. Yang (2010). "The evolution of a transverse intra-ply crack coupled to delamination cracks." International Journal of Fracture 165: 77-92.

Proceedings of the 32nd
Risø International Symposium on Materials Science:
Composite materials for structural performance:
Towards higher limits
Editors: S. Fæster, D. Juul Jensen,
B. Ralph, B.F. Sørensen
Risø National Laboratory for Sustainable Energy,
Technical University of Denmark, 2011

REAL TIME MONITORING OF COMPONENT TESTING WITH ACOUSTIC EMISSION

A. Antoniou*, F. Sayer*, M. Löhr** and A. van Wingerde*

*Fraunhofer IWES, Am Seedeich 45, 27572 Bremerhaven, Germany
**Physical Acoustics BV-Deutschland, Postfach 701344, 22013 Hamburg, Germany

ABSTRACT

A cantilever beam test has been developed in order to characterize structural bondlines, especially between shear webs and spar caps of a wind turbine rotor blade. The structural integrity was monitored during static and cyclic tests with the acoustic emission (AE) technique, detecting and linearly locating the developed damage at the bondline while discriminating between different failure modes. The AE during the tests is acquired with experimental equipment supplied from Physical Acoustics, with 10 MHz maximum sampling frequency and a wideband sensor network located on the the tested component.

1. INTRODUCTION

Mechanical properties of composite materials used in the design of wind turbine rotor blades are normally determined with uni-axial tests using prismatic or other more sophisticated coupon geometries as in the public funded project OPTIMAT BLADES (2006). However, the complexity of a blade structure introduces further issues that strongly affect the final failure, e.g. complex stress states, cohesion between adhesive bonding and substrates, stress concentrations due to local geometrical effects and volume - dependent flaw concentration. Towards closing the gap between coupon and full scale blade testing, evaluating structural integrity properties, an additional test is proposed. Following an idea introduced and developed for aerospace applications as described by Potter et al (2001), component and sub-component testing is currently developed for the wind sector.

In the current research a cantilever I-beam test is studied, developed in a close collaboration between the Henkel AG & Co KGaA and the Fraunhofer IWES and used during the UpWind project (2011). The aim was characterize structural bondlines especially between shear webs and spar caps of a wind turbine rotor blade as described by Sayer et al (2010). The structure has been designed based on the stress data of a commercial rotor blade, simulating the most critical complex axial – shear stress ratio developed along the blade bond line. The subcomponent is

asymmetrically tested in three point bending and its final failure is considered when the whole structure cannot sustain further loading due to extended damage in the bond line i.e. adhesion, cohesion or mixed failure along the beam length.

Nonetheless, composite structures are damage tolerant, accumulating failure developed during service or testing. Thus damage onset does not generally coincide with the ultimate failure neither temporal nor in mode pattern. Therefore, towards structural integrity monitoring, the ultrasound method has been widely used in order to identify the formed damage and record its accumulation. Techniques based on ultrasound physics i.e. pulse-echo and acousto-ultrasonics are implemented for locating defects such as delaminations in thick composite laminates and disbonds between shear web and shell structures as described by Antoniou et al (2004). These are based on an active trigger of the structure with ultrasound pulses but they do not provide with a real-time indication when a failure occurs. Instead, Acoustic Emission can be used in real time applications for monitoring damage onset and propagation in large structures as described by Dutton et al (2000). The technique is already mature in the aerospace sector, Finlayson (2000), as a global indicator of failure onset, while the same concept is currently developed for monitoring wind turbine blades.

In this research, two sub-components were tested in asymmetric three point bending, one statically and one in fatigue. Both were monitored with Acoustic Emission (AE), linearly locating failure onset and progress and discriminating between different modes in fatigue. The implemented AE equipment was supplied by PAC, providing with a maximum sampling frequency of 10 MHz and a wideband sensor network. AE findings were validated with visual inspection.

2. TESTING SET-UP & PROCEDURE

The beam test rig is illustrated in Fig. 1. The structure is supported with two bolts at one end and is loaded through a bolted frame and a hydraulic cylinder at the other end.

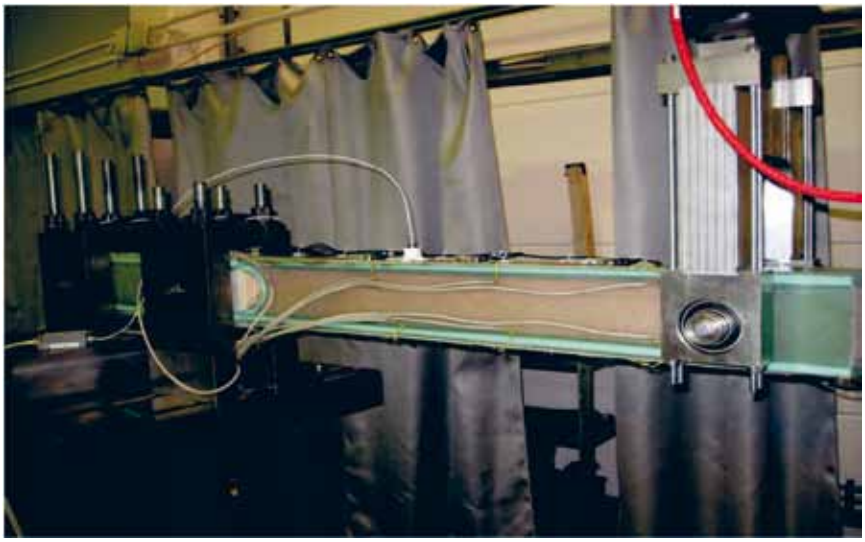

Fig. 1. Asymmetric three point bending

In Fig. 2 the beam support and load points are described while the axial and shear stress components developed at the bondline during the 3 point bending test is illustrated in Fig. 3. Their maximum ratio is developed in the area between 600 – 900mm. Therefore, this specific region, being of special interest, was monitored with the Acoustic Emission system.

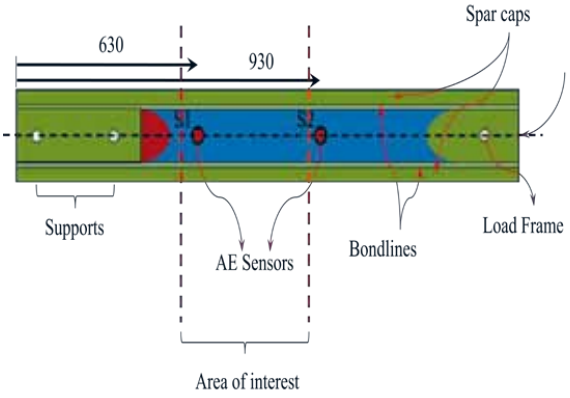

Fig. 2. Schematic of the beam structure

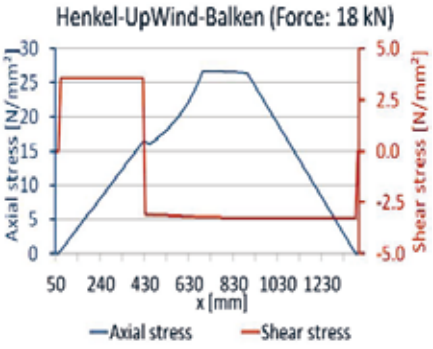

Fig. 3. Developed axial and shear stresses along the beam

General information about the acoustic emission experimental set-up, for the location of the sensors and the AE software used for the component testing can be found in Table 1.

Table 1. Setup of the Acoustic Emission measuring system

Sensors	PAC- WD (100 kHz to 1.000 kHz)					
Sensor position	Sensor	1	2	3	4	5
	Static test					
	X [mm]	630	930			
	Fatigue test					
	Upper Bondline X [mm]			608	810	1010
	Lower Bondline X [mm]	695	895			
Coupling media	Grease and tape for fixing the sensors					
Pre-amplification (filter)	20 dB_{AE} (100 kHz – 1200 kHz) by a PAC 2/4/6					
Measuring system: Hard and Software	Static: PAC PCI-2, 2 channel system					
	Fatigue: Samos, 8 channel system					
	Software: AEWIN for PCI-2 3.42					
Software-Filter	100 kHz – 1.000 kHz					
Threshold	Static: 40 dB AE, Fatigue: 60 dB AE					
Hit/ linear located event-based Data	Amplitude in dB AE and Source Amplitude in dB AE and absolute energy in aJ (atto=10^{-18})					

Waveform acquisition	2 MHz, 256 μs pre- trigger, max. length: 7,68 ms							
Linear Location	Velocity: 3.000.000 mm/s, Event Definition Value: 300 mm, Event Lockout Value: 0, Overcal: 30 mm							
Attenuation measurement with Hsu- Nielsen Source 2H 0,5 mm	Mm	20	50	100	150	200	250	300
	dB	95	84	77	80	68	65	61

One beam was statically tested up to failure. The load was applied in loops of ramp-up, hold, ramp-down and relax sequence, with incrementally increased steps of 3kN. The ramp-up reached the local maximum level in 20 seconds, then a load hold for 3 minutes was applied, followed by an unload in 20 seconds. The material was relaxed for 3 minutes without loading. This procedure was repeated until failure.

Both bondlines were monitored simultaneously with two Wide Band (WD) Acoustic Emission (AE) sensors attached on one side of the shear web at the middle of its height. In order to provide the distance source to sensor – corrected amplitude (source amplitude) out of the linear location, a preliminary attenuation measurement was conducted breaking leads in between the sensors. The average attenuation values from both sensors are shown in Table 1.

The second beam was tested in fatigue and R=-1. The maximum axial strain was 0.36% on the spar caps outermost surface, resulting in a 26.7MPa axial and 3.25MPa shear stresses in the bondline. The test was stopped every 25000 cycles, the load was rumped down to zero followed by a pseudo static load sequence. For the first 150000 cycles the test was stopped during the night and restarted during the day since some other manual measurements should be conducted. After that point the test continued without stop.

A 10 second ramp – up to the 76% of the fatigue load was followed from a 10 s hold and then rump – down at zero load, the so called proof test loading, before applying again the alternating load sequence. The AE sensors located on one side of the shear web, Table 1, were assembled in two groups, sensors 1 and 2 monitoring the lower bondline and sensors 3, 4 & 5 monitoring the upper one. Linear location was applied separately in both groups.

3. TEST RESULTS

In the static test the beam was loaded incrementally up to failure as can be seen from the green line in Fig. 4.

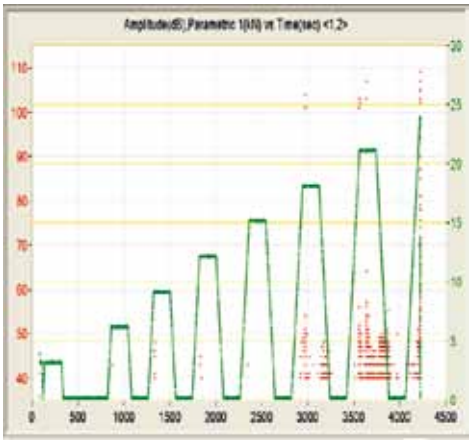

Fig. 4. Static load sequence and amplitude of the AE hits

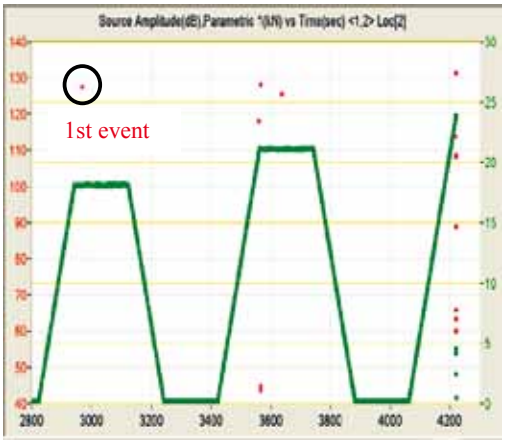

Fig. 5. Static load sequence and source amplitude of the AE located events (zoom in)

Although emission started at low loads, see red dots in Fig. 4, these hits were of low amplitude coming possibly from the test rig and were not located from the sensors. The first audible event occurred at 18kN and was located from the AE system at 843.8mm, see Fig. 5. This was a crack in the adhesive, transverse to the lower bondline longitudinal axis. The visual inspection confirmed the incipient and the following cracks all along the beam length, see Fig. 6 and Table 2. All locations were calculated with precision lower than 2%.

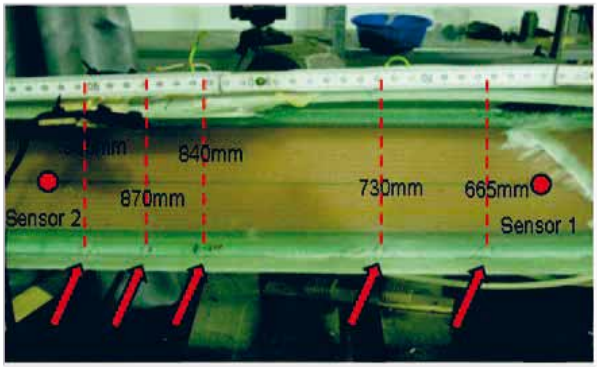

Fig. 6. Measured locations of the tranverse cracks on the bondline, developed during the static test

Table 2. List of linear located events during static test (time-descending)

Event no	x- calcul. [mm]	x- measur. [mm]
1	843.8	840
2	671.3	665
3	735	730
4	877.5	870
5	905.6	905

In the fatigue test the failure sequence observed with visual inspection is described in Fig. 7. Incipiently, transverse cracks due to the axial loading occurred at the bondline. These started to develope around 10% of the beam life. Subsequently, a local disbond with the laminate

substrate started at their tip. This could be monitored from the top of the laminate, looking as a milky whitening area, indicating the delamination. Finally, when few of these disbonds were met a catastrophic failure occurred. The intermediate and final failure can be seen in Fig. 8. Transverse and interfacial cracks are marked with different colors corresponding to separate cycle numbers. The same fracture modes can be seen in both the upper and lower bondline, however the upper one failed first leading to the component ultimate damage.

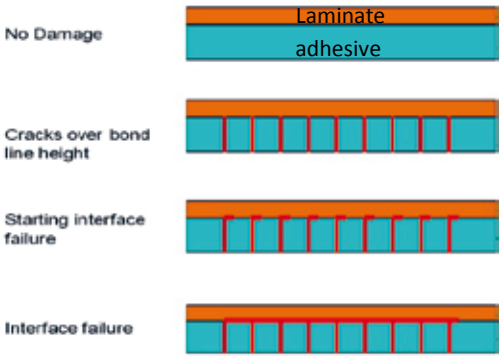

Fig. 7. Damage progress during fatigue loading

Fig. 8. Intermediate and final component failure modes modes

The acoustic emission findings from the upper and lower linear location groups indicates a change in the structural performance. Thus, the total time of the experiment can be divided in three sub – areas according to these results, see Fig. 9 and Fig. 10.

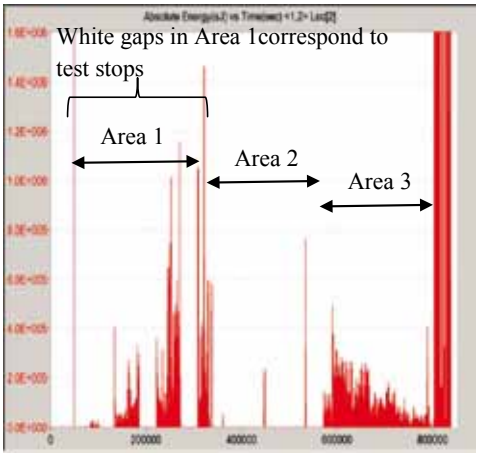

Fig. 9. Absolute located events energy content vs. time (lower bondline)

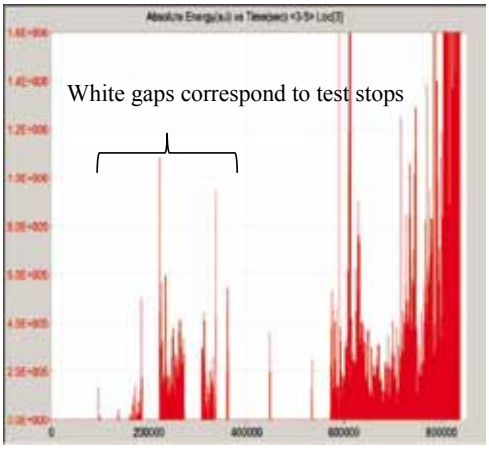

Fig. 10. Absolute located events energy content vs. time (upper bondline)

In the lower bondline the first area indicates a significantly higher energy events content than the other two. The second area is more silent than the first one; probably the intensity of the AE activity from the beam is lower there and under the detection threshold. In the last area the energy seems to decrease before the last few thousand cycles and the final failure. The same is valid for the upper bondline group except in the last area that the energy increases almost continuously till the ultimate failure. A direct correlation was performed between areas 1, 3 and visual inspection, see Fig. 11 and Fig. 12.

Fig. 11. Transverse cracks along the bond line

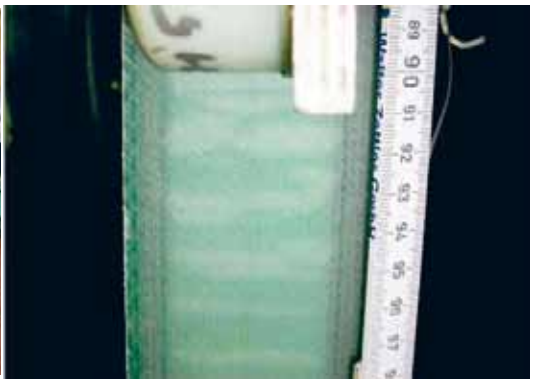

Fig. 12. Disbond between adhesive and spar cap substrate

The first area coincided with the development of transverse cracks along the bondline while the third area started just at the moment that disbonds were developed between the adhesive and the spar cap substrate.

4. CONCLUSIONS

The structural integrity of component - beam tests was successfully monitored in-situ in two separate tests, one static and one fatigue, with the Acoustic Emission technique. The experiment was performed without any noise interference being a very good platform for wave propagation signal evaluation. The AE system was able to locate the failure initiation and development, providing with strong software tools for post analysis and discrimination between different failure modes.

ACKNOWLEDGEMENTS

This work is conducted in the framework of the German public project Better Blades, funded from BMU under the official contract 0325169. The beam test development was conducted in a close collaboration between the Henkel AG & Co. KGaA and the Fraunhofer IWES. Further investigations were done in the framework of the European public funded project UpWind, were the Fraunhofer IWES participated in by a German funding from the BMU (contract number: 0327620).

REFERENCES

OPTIMAT BLADES (2001-2006). Reliable optimal use of materials for wind turbine rotor blades, ENK6-CT-2001-00552, http://www.wmc.eu/optimatblades.php

Potter, K.D., Davies, R., Barrett, M., Godbehere, A., Bateup, L., Winsom, M., and Mills, A. (2001). Heavily loaded bonded composite structure: design manufacture and test of an 'I' beam specimens. Compos. Struct. 51. 389-399

UpWind project (2007-2011). Contract number: SES6-019945, http://www.upwind.eu/

Sayer, F., Antoniou, A. and Kleiner, F. (2010). Sub-Component Testing of Adhesive Bond lines for Wind Turbine Blade. DEWEK 17th – 19th of November in Bremen, Germany

Antoniou, A.E., Assimakopoulou, T.T. and Philippidis, T.P. (2004). Delamination detection in thick composite laminates using ultrasonic waves. Proceedings of ECC11

Dutton, A.G., Blanch, M., Vionis, P., Kolovos, V., van Delft, D.R.V., Joosse, P., Anastassopoulos, A., Kouroussis, D., Kossivas, T., ter Laak, J., Philippidis, T.P., Kolaxis, Y.G., Fernando, G., Zheng, G., Liu, T., Proust, A., (2000) Acoustic emission monitoring from wind turbine blades undergoing static and fatigue testing. 15th WCNDT 2000 Rome, Italy

Finlayson, R.D., Cole, P., Lenain, J.C., (2000). Health monitoring of aerospace structures with acoustic emission and acousto-ultrasonics. 15th WCNDT 2000 Rome, Italy

Proceedings of the 32nd
Risø International Symposium on Materials Science:
Composite materials for structural performance:
Towards higher limits
Editors: S. Fæster, D. Juul Jensen,
B. Ralph, B.F. Sørensen
Risø National Laboratory for Sustainable Energy,
Technical University of Denmark, 2011

EFFECT OF DELAMINATION ON THE STRESS DISTRIBUTION OF PIN-LOADED HOLES IN COMPOSITE LAMINATES

A. Ataş*,** and C. Soutis*

*Department of Mechanical Engineering, University of Sheffield,
Sheffield, S1 3JD, UK
**Department of Mechanical Engineering, Balıkesir University,
10145, Balıkesir, Turkey

ABSTRACT

A three-dimensional (3D) finite element (FE) model of a pin-loaded hole in a $[0^{\circ}/90^{\circ}]_s$ carbon fiber-epoxy composite laminate is developed. Contact based cohesive zone elements (CZE) inserted between the layers were used to investigate the effect of delamination on the stress distribution around the fastener hole. The radial stress distribution before delamination onset around the pin-loaded hole is verified with the widely used cosine stress distribution curve and delamination evolution is quantitatively compared with previous experimental results. It is concluded that delamination damage can significantly affect the contact stress distribution and its magnitude around the pin-loaded hole which can have an effect on strength predictions.

1. INTRODUCTION

Mechanical fastening (rivet/bolt) is the most common joining method of structural aircraft composite materials and its failure usually initiates at the hole boundary because of the high fastener/laminate hole contact stresses (Atas, Demircioglu, Arslan and Soutis 2010). The strength predictions of mechanical joints usually utilize these stresses around the hole boundary (Chang 1986) and therefore, accurate stress prediction is of prime importance in order to obtain reliable strength predictions. It is shown that the stress distributions significantly affected by laminate elastic properties, friction and clearance (Hyer, Klang and Cooper 1987). Delamination is a common failure mechanism in laminated composites due to their relatively low interlaminar strength and fastener holes provide preferential areas for delamination due to the high stress/strain gradients (in-plane and out-of-plane). The compressive nature of the stresses at the loaded part of the hole boundary makes the joint's strength more susceptible to delamination since fiber microbuckling is initiated after the loss of lateral support as a consequence of delamination (Soutis and Fleck 1990). Thus, it is clear that delamination could influence the stresses and hence failure around the hole boundary. Although the CZE has been used between the metal and composite laminate layers with pin/bolted connections of fiber metal laminates

(FMLs) (Frizzell, McCharty and McCharty 2011; Hundley, Hahn, Yang and Facciano 2011), a detailed investigation of the delamination on the stress distributions has not been fully addressed neither for FMLs nor FRP laminates.

One approach to model the onset and growth of delamination is the use of CZE placed at the interface between layers. These elements use a failure criterion that combines aspects of stress-based analysis to predict the onset of the softening process, and a fracture mechanics based approach to predict the growth of delamination (Turon, Davila, Camanho and Costa 2007; Yang and Cox 2005). This approach overcomes some of the difficulties of other methods, such as the Virtual Crack Closure Technique (VCCT), in that a pre-defined crack path and complex moving mesh technique is not required (Rybicki and Kanninen 1977).

The aim of the present study is to perform the stress analysis and model the delamination failure with CZE quantifying its influence on the stress distributions around the pin-loaded hole.

2. FINITE ELEMENT MODELLING

Three-dimensional FE modeling is performed using the commercial FE code, ANSYS v12.1 (Release 12.1, 2009). The boundary and loading conditions are shown in Fig. 1. Symmetric boundary conditions are imposed along the two orthogonal planes (*xy* - *xz*). All degrees of freedom are constrained at the fixed end of the laminate to simulate the fully clamped end. Pin displacement is applied along the (negative) x-direction.

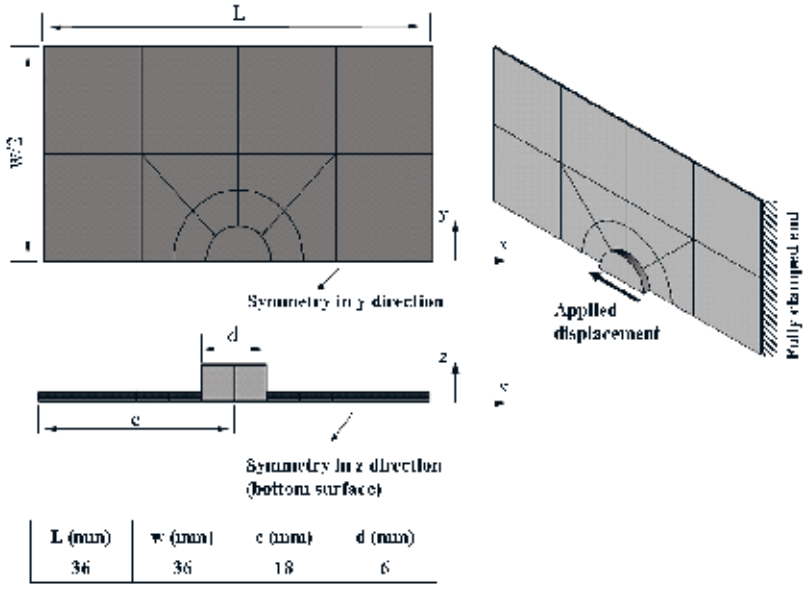

Fig. 1. Pin loaded model dimensions, boundary and loading conditions

Each composite layer, of 0.125 mm thickness, was modeled separately and was discretised with one element in the thickness direction (mesh refinement may have an effect on stresses but this is not considered in this study). Equivalent orthotropic material properties are assigned to each

unidirectional composite layer according to a pre-defined local coordinate system; see Table 1 (Harper and Hallett 2008). The fiber direction of the 0˚ layer coincides with the loading direction. Linear elastic material behavior is assumed for the composite laminate and material non-linearities such as nonlinear shear stress-strain behavior are not taken into account (Dano, Gendron and Picard 2000), although they can be important in estimating failure load of the laminate.

Table 1. Orthotropic unidirectional material properties (Harper and Hallett 2008)

E_{11} (MPa)	$E_{22}=E_{33}$ (MPa)	$G_{12}=G_{13}$ (MPa)	G_{23} (MPa)	$v_{12}=v_{13}$	v_{23}
120000	10500	5250	3480	0.3	0.51

The loading pin is modeled as a steel solid deformable body with elastic properties of *E=210 GPa* and *v=0.3*. A perfect fit is assumed between the pin and the laminate and the friction coefficient is assumed to be zero (although these simplifications may have an effect on the local stress field). Surface-to-surface deformable standard contact algorithms are defined between the pin and the carbon fiber reinforced plastic (CFRP) laminate hole boundary (Oskouei, Keikhosravy and Soutis 2009). Details of the FE modeling are given in (Atas, Mohamed and Soutis 2011).

Zero thickness 4-node contact elements are embedded between adjacent composite layers, i.e. the nodes of the adjacent elements are initially coincident at the interface. After a standard contact is established, the bonded contact option is selected and the CZE properties (Harper and Hallett 2008), as listed in Table 2, are inserted in the model.

Table 2. Interfacial properties for composite laminate (Harper and Hallett 2008)

G_{IC} (N/mm)	G_{IIC} (N/mm)	σ_{max} (MPa)	τ_{max} (MPa)	K_n (N/mm^3)	K_t (N/mm^3)
0.26	1.002	30	60	$1x10^5$	$1x10^5$

A bi-linear traction–separation law proposed by Alfano and Crisfield (2001) was used, which ensures a linear elastic response up to delamination initiation, followed by a linear softening phase. The interaction of relative contact stresses in normal and tangential directions was accounted for when calculating mixed-mode delamination initiation using the following governing relations (ANSYS, Release 12.1, 2009):

$$P = K_n u_n (1 - d_m) \tag{1a}$$

$$\tau_t = K_t u_t (1 - d_m) \tag{1b}$$

where:

P = normal contact stress, K_n = normal contact stiffness, u_n = contact gap, τ_t = tangential contact stress, K_t = tangential contact stiffness, u_t =tangential slip distance.

The debonding parameter d_m is defined as:

$$d_m = \left(\frac{\Delta_m - 1}{\Delta_m} \right) \chi \tag{1c}$$

with $d_m = 0$ for $\Delta_m \leq 1$ and $0 < d_m \leq 1$ for $\Delta_m > 1$ and Δ_m and χ are defined below:

$$\Delta_m = \sqrt{\Delta_n^2 + \Delta_t^2}\ ,\ \chi = \left(\frac{u_n^c}{u_n^c - \bar{u}_n} \right) = \left(\frac{u_t^c}{u_t^c - \bar{u}_t} \right) \tag{1d}$$

where $\bar{u}_{n,t}$ = contact gap at the maximum normal and tangential contact stress, $u_{n,t}^c$ = contact gap at the completion of debonding, $\Delta_n = u_n / \bar{u}_n$, $\Delta_t = u_t / \bar{u}_t$.

Total fracture energy at the completion of a mixed mode delamination is the sum of both normal and tangential contact stresses and a power law based energy criterion is used to define the completion of delamination (ANSYS, Release 12.1, 2009) where the values of α and β exponents are set to 1.0:

$$\left(\frac{G_n}{G_{cn}} \right)^{\alpha} + \left(\frac{G_t}{G_{ct}} \right)^{\beta} = 1 \tag{2a}$$

$$G_n = \int P du_n \tag{2b}$$

$$G_t = \int \tau_t du_t \tag{2c}$$

The normal and tangential critical fracture energies are computed as:

$$G_{cn} = \frac{1}{2} \sigma_{\max} u_n^c \tag{3a}$$

$$G_{ct} = \frac{1}{2} \tau_{\max} u_t^c \tag{3b}$$

where:

$\sigma_{\max}$ = maximum normal contact stress and $\tau_{\max}$ = maximum tangential contact stress.

Delamination modeling is also a nonlinear process which is prone to convergence problems and an artificial damping coefficient $\eta = 5 \times 10^{-4}$ is used (based on experience) in order to overcome these problems. This coefficient has the units of time and should be smaller than the minimum time increment which is necessary to be quite small in order to capture the delamination evaluation accurately. In this study, the time increment is selected to have at least three interpolation points in the descending part of the bilinear traction-separation curve after the maximum contact stress is reached (delamination onset) (Barthold 2009).

3. VERIFICATION OF THE FE PREDICTIONS

Accurate prediction of delamination is strongly dependent in capturing the stresses around the fastener hole. The cosine radial stress distribution, given in Eq. 4, gives a good idea of magnitude and distribution of pin/laminate contact stresses around the hole boundary (Crews, Hong and Raju 1981) (the angle θ is measured clockwise from the x loading axes) and is expressed as:

$$T_\theta = -\frac{4P}{\pi Dt}\cos\theta \qquad \left(-\frac{\pi}{2} \le \theta \le \frac{\pi}{2}\right) \tag{4}$$

where T_θ is the radial stress, P is the applied load, D is the hole diameter and t is the laminate thickness; it should be noted though that this expression doesn't account for the laminate anisotropy. For consistency, radial contact stresses are normalized by $4P/\pi Dt$. The applied load P is obtained as the sum of the nodal reaction forces at the clamped end of the laminate.

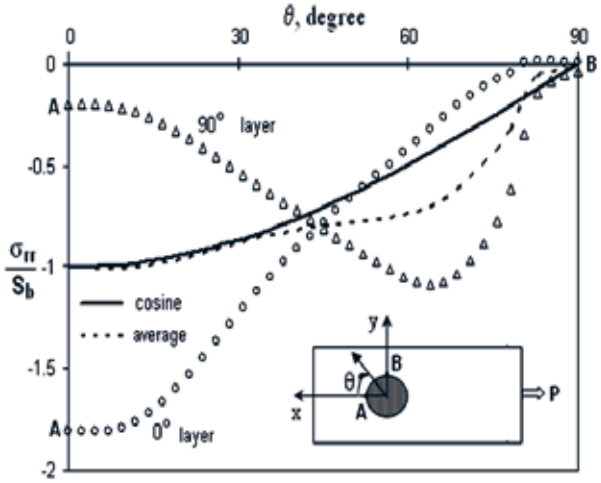

Fig. 2. Predicted and cosine radial contact stress distributions around the cross-ply $[0^\circ/90^\circ]_s$ composite pin-loaded hole at an applied pin displacement of 1.25%

A comparison of the predicted and cosine radial contact stress distributions around the pin-loaded hole in the cross-ply $[0^\circ/90^\circ]_s$ composite laminate is given in Fig. 2 at a pin displacement of 1.25%, before delamination onset. The pin displacement is expressed as $\Delta L/D$; where, ΔL is the applied pin displacement and D is the pin diameter. Predicted stress distributions are given separately for each individual layer as well as their average distribution (for the whole laminate). The average stress distribution is similar to the cosine distribution that gives confidence in the present model although there are differences due to laminate anisotropy which is not captured by the simple equation (4) (Chang 1986).

A cross-ply $[90^\circ/0^\circ]_s$ composite laminate with a centre notch is modeled in order to investigate the delamination prediction capability of the current FE model. A previous experimental study (Spearing and Beaumont 1992) shows that intra-laminar splitting (cracks parallel to the fiber direction) within the 0° layers are initiated at the notch tips and grow along the fiber length which is accompanied by delamination between adjacent layers. They are the dominant failure mechanism and they form generally a triangular shape as schematically depicted in Fig. 3. CZE

inserted between the 90˚/0˚ layers and within the 0˚ layer at the notch tip where splitting and delamination damage modes are expected. All modeling and material properties used are the same as of (Wisnom and Chang 2000) except the non-linear shear stress-strain behavior. Also, a more realistic bilinear traction separation curve is used in the present study instead of an idealized elastic-perfectly plastic curve.

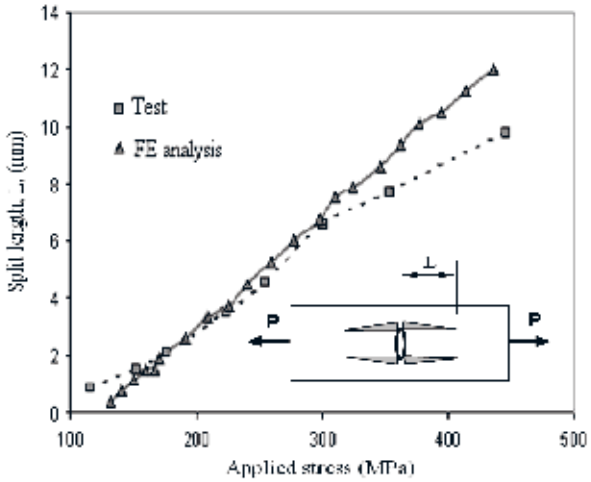

Fig. 3. Comparison of FE analysis predictions and test results for split length as a function of applied stress (test data by Spearing and Beaumont 1992).

Figure 3 shows the split length versus applied stress for FE model predictions and experimental results (Spearing and Beaumont 1992). The good agreement of split length predictions together with the good correlation of the contact stress distributions confirm that the delamination onset and growth of the pin-loaded hole in a $[90^{\circ}/0^{\circ}]_s$ composite laminate can be predicted relatively well giving confidence to the assumptions made in the present study.

4. RESULTS

Delamination onset and growth at the 0˚/90˚ interface of the $[0^{\circ}/90^{\circ}]_s$ laminate is predicted at an applied pin displacement of 2.45% and occurs at about 40˚ to the loading axis, as shown in Fig. 4. The angle at which delamination occurs can be explained by the intersection of the in-plane shear stress components of 0˚ and 90˚ layers where the average shear stress reaches its maximum at 40˚ (Atas, Mohamed and Soutis 2011). The delaminated area develops an elliptical shape which grows in a non-self similar manner with increasing pin displacement.

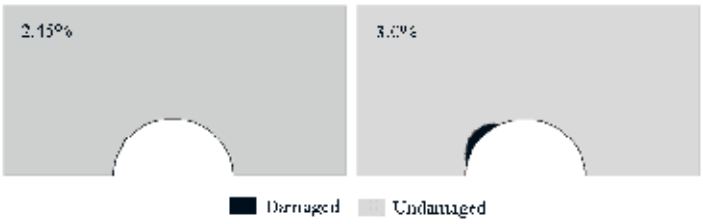

Fig. 4. Delamination onset and growth at the 0˚/90˚ interface at 2.45 and 3% pin displacement

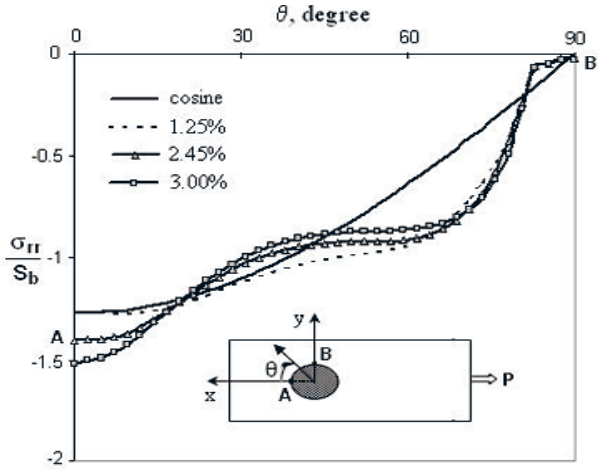

Fig. 5. Effect of delamination on the radial contact stress distributions around the pin-loaded hole; the cosine solution corresponds to an applied displacement of 1.25%.

Figure 5 shows the radial contact stress distributions at 1.25%, 2.45% and 3% pin displacement around the loaded part of the pin hole (*A-B quadrant*) as a function of the angle θ. 1.25% pin displacement corresponds to the undamaged laminate whereas 2.45% and 3% pin displacements corresponds to the onset and growth of the delamination, respectively. The cosine stress distribution is also included. For consistency, contact stresses are normalized by bearing stress, $S_b=P/Dt$. The undamaged laminate average radial contact stress follows the cosine distribution but not exactly since equation (4) is independent of laminate anisotropy. Deviation from the cosine contact stress distribution becomes more pronounced at the onset of delamination. The magnitude of the deviation increases as delamination grows. At 3% applied pin displacement the radial contact stress value is maximum at $\theta=0^\circ$ and reduces to similar values as those of a lower applied pin displacement between 25˚-90˚. These changes may be due to the transfer of the shear stresses carried by the undamaged interface at around 40˚ to the hole periphery after delamination onset.

5. CONCLUSIONS

A 3-D FE model is presented which predicts the delamination onset and growth by employing cohesive zone elements (CZE) around a pin-loaded hole in a cross-ply $[0^\circ/90^\circ]_s$ composite laminate. To simplify the analysis a perfect fit is assumed between the pin and the laminate and the friction coefficient is assumed to be zero, but it has been shown in earlier work (Berbinau and Soutis 2001) that a gap between the plate and the pin does affect local stresses. Bonded contact elements are embedded between each layer with an assumed bilinear traction-separation law (which is supported by experimental data). The current model effectively captures the delamination onset as well as the non-self similar growth.

The predicted radial contact stress distributions differ from the well known cosine stress distribution especially for $\theta>30^\circ$ and this difference becomes more pronounced after delamination onset and propagation. This indicates the importance of delamination on the stress distribution around the hole and consequently strength predictions of mechanical joints in composite structures, a topic that is currently under investigation by the authors.

ACKNOWLEDGEMENTS

The authors wish to acknowledge the Turkish Council of Higher Education and Balıkesir University for the PhD scholarship awarded to Mr Akın Ataş.

REFERENCES

Alfano, G., and Crisfield, MA. (2001). Finite element interface models for the delamination analysis of laminated composites: Mechanical and computational issues. Int. J. Numer. Meth. Eng. 50(7),1701-1736.

ANSYS® Academic Research, Release 12.1. (2009). Swanson Analysis Systems.

Atas, A., Demircioglu, T.K., Arslan, N., and Soutis, C. (2010). Progressive failure analysis of bolted carbon fibre/epoxy composite plates. 2. National Design, Manufacturing and Analysis Congress, Balikesir,Turkey. p. 138-148.

Atas, A., Mohamed, G., and Soutis, C. (Submitted May 2011). Modelling delamination onset and growth in pin loaded composite laminates. Submitted to Compos. Sci.Technol..

Barthold, U. (2009). Cohesive Element Applications. Germany: CADFEM GmbH.

Berbinau, P., and Soutis C. (2001). A new approach for solving mixed boundary value problems along holes in orthotropic plates. Int. J. of Solids & Structures 38(1), 143-159.

Chang, F-K. (1986). The effect of pin load distribution on the strength of pin loaded holes in laminated composites. J. Compos. Mater. 20, 401-408.

Crews, J.H., Hong, C.S., and Raju I.S. (1981). Stress-concentration factors for finite orthotropic laminates with a pin-loaded hole. NASA Technical Paper 1862.

Dano, M.L., Gendron, G., and Picard, A. (2000). Stress and failure analysis of mechanically fastened joints in composite laminates. Compos. Struct. 50(3), 287-296.

Frizzell, R.M., McCharty, C.T., and McCharty, M.A. (2011). Predicting the effects of the geometry on the behaviour of fibre metal laminate joints. Compos. Struct. 93(7), 1877-1889.

Harper, P.W., and Hallett, S.R. (2008). Cohesive zone length in numerical simulations of composite delamination. Eng. Fract. Mech. 75(16), 4774-4792.

Hundley, J.M., Hahn, H.T., Yang, J-M., and Facciano, A.B. (2011). Three-dimensional progressive failure analysis of bolted titanium-graphite fiber metal laminate joints. J. Compos. Mater. 45(7), 751-769.

Hyer, M.W., Klang, E.C., and Cooper, D.E. (1987). The Effects of Pin Elasticity, Clearance, and Friction on the Stresses in a Pin-Loaded Orthotropic Plate. J. Compos. Mater. 21(3), 190-206.

Oskouei, R.H., Keikhosravy, M., and Soutis, C. (2009). Estimating clamping pressure distribution and stiffness in aircraft bolted joints by finite-element analysis. P. I. Mech. Eng. G-J. Aer. 223(G7), 863-871.

Rybicki, E.F., and Kanninen, M.F. (1977). Finite-Element calculation of stress intensity factors by a modified crack closure integral. Eng. Fract. Mech. 9(4), 931-938.

Soutis, C., and Fleck, N. (1990). Static compression failure of carbon fibre T800/924c composite plate with a single hole. J. Compos. Mater. 24, 536-558.

Spearing, S.M., and Beaumont, P.W.R. (1992). Fatigue damage mechanics of composite materials. I: Experimental measurement of damage and post fatigue properties. Compos. Sci.Technol. 44, 159-168.

Turon, A., Davila, C.G., Camanho, P.P., and Costa, J. (2007). An engineering solution for mesh size effects in the simulation of delamination using cohesive zone models. Eng. Fract. Mech. 74(10), 1665-1682.

Yang, Q., Cox, B. (2005). Cohesive models for damage evolution in laminated composites. Int. J. Fracture. 133:107-137.

Wisnom, M.R., Chang, F-K. (2000). Modelling of splitting and delamination in notched cross-ply laminates. Compos. Sci.Technol. 60, 2849-2856.

Proceedings of the 32nd
Risø International Symposium on Materials Science:
Composite materials for structural performance:
Towards higher limits
Editors: S. Fæster, D. Juul Jensen,
B. Ralph, B.F. Sørensen
Risø National Laboratory for Sustainable Energy,
Technical University of Denmark, 2011

PREDICTION OF IMPACT INDUCED DELAMINATION IN COMPOSITE PLATES USING COHESIVE ELEMENTS: A COMPARISON OF 3D SOLID AND SHELL FE MODELS

F. Aymerich, A. Cerioni and D. Feng

Department of Mechanical Engineering, University of Cagliari
Piazza d'Armi – 09123 Cagliari, Italy

ABSTRACT

The structural and damage response of cross-ply laminated plates subjected to low-velocity impact was investigated in this study by means of finite element models based on cohesive interfacial elements. FE models of the composite laminates were developed using cohesive elements for the simulation of the delamination at the interface between layers, and 3D solid, continuum shell, or conventional shell elements for the modeling of the layers. The analyses were carried out using the explicit solver of the commercial software Abaqus 6.10. The numerical results obtained by the various models are discussed and compared with experimental observations from previous investigations with the aim of exploring potential and capabilities of FE models based on the combined use of cohesive and shell elements for impact damage simulation in composite structures.

1. INTRODUCTION

Laminated composite materials have been increasingly used in primary structures because of their high specific strength and stiffness, good fatigue performance and corrosion resistance. Composite laminates are however highly sensitive to transverse impact loads, which are likely to occur during manufacturing, transport, operation and maintenance. Damage in composite materials consists of a combination of different damage modes such as intralaminar matrix cracks, interlaminar delamination and fiber failure. Delamination between layers, which is often difficult or even impossible to detect by visual inspection (BVID - Barely Visible Impact Damage), is one of the most critical damage modes, since its presence may greatly reduce the strength of the composite material, especially under in-plane compression loads. Appropriate models and reliable numerical procedures are thus strongly needed for predicting the mechanical performance and the damage response of laminated structures under impact. A number of predictive methods have been proposed in the literature to simulate initiation and growth of delamination in impacted composite structures (Elder, Thomson, Nguyen and Scott 2004).

Although stress-based continuum damage mechanics approaches have been used in the past to study delamination in composites [Allix, Ladeveze and Corigliano 1995; Tay, Liu, Tan, Sun and Pham 2008], these techniques are not particularly suited to model discrete failure events such as interlaminar cracks, characterized by highly localized stresses at geometrical discontinuities. For this reason, the use of conventional fracture mechanics has become common practice to analyse the progression of interlaminar cracks by means of finite element (FE) based procedures (such as the crack closure technique) able to calculate the strain energy release rate and the separated mode I, mode II and mode III components. The results obtained by the crack closure technique (CCT) are however very sensitive to mesh geometry and element size, and the approach relies on the preliminary assumption of the presence of an initial crack in the material. Furthermore, the technique requires the use of adaptive remeshing routines when the delamination does not propagate in a self-similar way (Tay 2003).

Surface cohesive approaches, which incorporate both strength-based criteria (to predict damage initiation) and fracture mechanics energy criteria (to simulate damage propagation and subsequent fracture), are attracting considerable interest in recent years because of their potential to address the main limitations of CCT analyses [Cui and Wisnom 1993; Mi, Crisfield, Davies and Hellweg 1998; Camanho, Davila and De Moura 2003; Borg, Nillson and Simonsson 2004; Wisnom 2010]. In particular, pre-existing cracks are not needed, since damage onset is explicitly modeled in the cohesive elements, and requisites on mesh geometry and mesh density are less demanding than those required by CCT methods (Harper and Hallett 2008). Furthermore, cohesive elements may easily deal with the effects of the interaction between multiple failure modes, such as those likely to occur between adjacent intralaminar and interlaminar matrix cracks (Hallett, Jang, Khan and Wisnom 2008).

The majority of the FE analyses based on the adoption of cohesive interface elements for prediction of impact-induced delamination in composite laminates have been carried out with the use of solid 3D elements for modeling the behaviour of individual layers; in contrast, only a limited number of studies have been conducted to investigate and explore performance and capabilities of FE models combining the use of cohesive and shell elements [Dávila, Camanho and Turon 2008; Borg, Nillson and Simonsson 2004, Johnson, Louca and Mouring 2006].

In a previous investigation, cohesive interface elements in combination with 3D solid elements were successfully used to simulate the impact damage response of $[0_3/90_3]$s cross-ply laminates (Aymerich, Dore and Priolo 2008). The specific stacking sequence investigated exhibits a rather simple damage process primarily involving a central tensile matrix crack associated to a single delamination on the adjacent interface. In this study, the predictive capabilities of FE models built using cohesive interface elements for simulation of the interface between layers and shell elements for the modeling of unidirectional layers are investigated and discussed. The quality of FE results and delamination predictions obtained with the use of shell elements are compared to those achieved by full 3D models to assess the potential of shell elements in association with cohesive interface elements for damage prediction in laminates subjected to low-velocity impact

2. EXPERIMENTAL

The impact response of $[0_3/90_3]$s laminates was examined in this study. Laminates were prepared with HS160/REM graphite/epoxy prepreg tapes (61.5% fibre content in weight) cured in autoclave at 160 °C under 8 bar pressure for 2.5 hours. Rectangular specimens 65 mm × 87.5 mm in size and with an average thickness of 2.0 mm were cut from the consolidate panels and tested with an instrumented drop-weight testing machine. The specimens were simply supported on a steel plate having a 45 mm × 67.5 mm rectangular opening and

impacted using a 2.3 kg falling mass with a 12.5 mm diameter hemispherical tup. The impact force signal was acquired by a semiconductor strain-gauge bridge bonded to the tup, while impact and rebound velocities were measured by an infrared emitter/receiver.

Internal damage was characterized by X-radiography and ultrasonics at various impact energies. As visible in the X-radiographs of Fig. 1, the damage process is initiated by a tensile matrix crack in the 0° layers at the back side of the laminate, followed by a peanut-shape delamination at the lower 90°/0° interface. Shear matrix cracks also develop in the central 90° layers around the impact region while no delamination occurs on the top 0°/90° interface up to an impact energy of about 7 J.

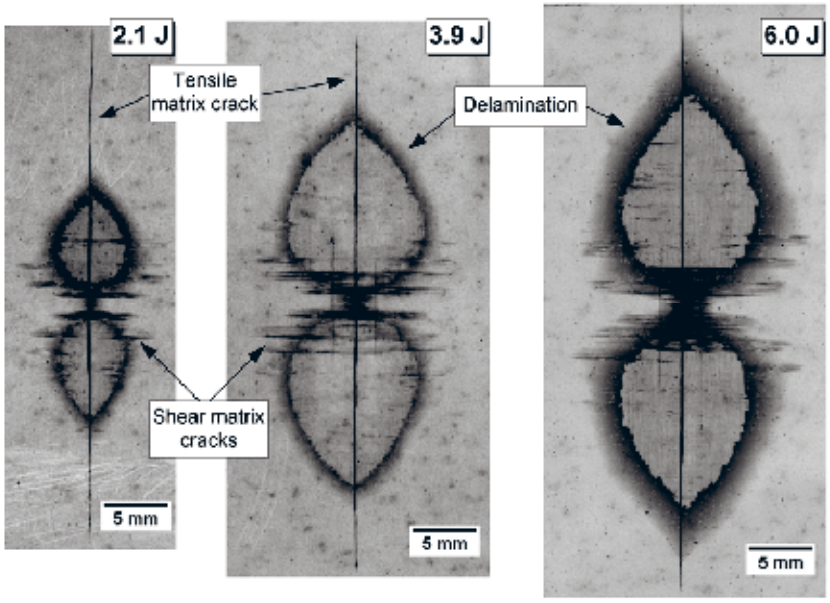

Fig. 1. X-radiographs of internal damage at three impact energies.

3. FE MODELS

Finite element analyses were carried out with the parallel explicit solver of the commercial code Abaqus 6.10 using reduced integration elements. Because of symmetry, only one quarter of specimen was modeled and analyzed (Fig. 2). 0_3 and 90_3 sublaminates were represented through their thickness with C3D8R solid elements in full 3D models, and with either SC8R continuum shell elements or S4R conventional shell elements in shell models. SC8R elements are 8-node shell elements that are defined with a solid element topology but use a shell element formulation. The continuum shell elements have only displacement degrees of freedom and can be stacked to provide more refined through-thickness response, thus providing an attractive modeling alternative over 3D solids.

In all models, COH3D8 zero thickness cohesive elements were inserted at the two interfaces between layers with different fiber orientations (i.e. at the top 0°/90° and bottom 90°/0° interfaces). Vertical cohesive interface elements were also placed on the symmetry plane

parallel to the 0° direction to simulate the development of the tensile matrix crack in the bottom 0° plies. It should be observed that shear matrix cracks occurring in the 0° layers of the laminates (see Fig. 1) were not simulated in the analyses, since previous studies carried out with full 3D FE models showed that the delamination induced by impact can be correctly predicted, in this class of laminates, without accounting for the pattern of matrix cracks developing in central layers.

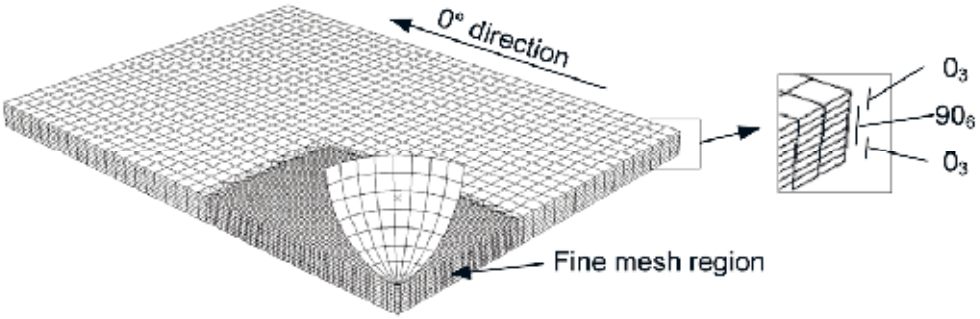

Fig. 2. 3D FE model of the laminated plate.

A simple bilinear constitutive law was chosen to describe the cohesive behaviour of the interface elements. The cohesive law was implemented in a user-defined material subroutine (VUMAT) with the elastic and fracture properties listed in Table 1. Cohesive properties, in particular, were obtained in a previous study (Aymerich et al. 2008) by calibration with experimental results of standard DCB and ENF tests. The same values of fracture properties adopted to characterize the interface between layers were used for the cohesive elements modeling the tensile matrix crack.

An empirical stress-based prediction scheme accounting for the strengthening effect of through-thickness compression on the shear strength of the interface and based on the criterion proposed by Hou, Petrinic and Ruiz [2001] was adopted for prediction of delamination initiation. The criterion predicts the initiation of interlaminar damage by the use of the following equations:

$$\begin{aligned}
&\left(\frac{t_n}{N}\right)^2+\left(\frac{t_s}{S}\right)^2+\left(\frac{t_t}{S}\right)^2=1 \qquad \text{for } t_n \geq 0 \\
&\left(\frac{t_s}{S}\right)^2+\left(\frac{t_t}{S}\right)^2-8\cdot\left(\frac{t_n}{S}\right)^2=1 \qquad \text{for } -\sqrt{\frac{t_s^{\,2}+t_t^{\,2}}{8}} \leq t_n < 0 \\
&\text{NO DELAMINATION} \qquad \text{for } t_n < -\sqrt{\frac{t_s^{\,2}+t_t^{\,2}}{8}}
\end{aligned} \tag{1}$$

where t_n is the normal stress and t_s, t_t are the shear stresses acting on the interface.

The linear interaction criterion of equation (2) was used for prediction of delamination growth.

$$\left\{\frac{G_I}{G_{IC}}\right\}+\left\{\frac{G_{II}}{G_{IIC}}\right\}+\left\{\frac{G_{III}}{G_{IIIC}}\right\}=1 \quad (2)$$

The impactor was modeled as a quarter of a rigid hemispherical body, with an assigned mass of 2.3/4 kg; impacts of different energies were simulated by imposing appropriate impactor velocities at the instant of contact. The interaction between the plate and the indentor was simulated by contact pairs with penalty constraints. Unless otherwise stated, an in-plane element size of 0.3 mm by 0.3 mm was used in the fine mesh region (12 mm × 18 mm; see Fig. 2). No mass scaling was used in the analyses.

Table 1. Values of elastic and cohesive properties used in the FE analyses

Layer properties	Interface properties
E_{11} = 93.7 GPa; $E_{22} = E_{33}$ = 7.45GPa	k_N = 120 GPa/mm; $k_S = k_T$ = 43 GPa/mm
$G_{12} = G_{23} = G_{13}$ = 3.97 GPa	N = 30 MPa; S = T = 80 MPa
$\nu_{12} = \nu_{23} = \nu_{13}$ = 0.261	G_{IC} = 520 J/m^2; $G_{IIC} = G_{IIIC}$ = 970 J/m^2

4. RESULTS AND DISCUSSION

Figs. 3 and 4 compare force histories and delaminated areas predicted for an impact of 3.9 J with the use of FE models built respectively with 3D solids (C3D8R), continuum shells (SC8R), or conventional shells (S4R). In all models the 0_3 and 90_6 sublaminates were represented with 2 elements and 4 elements respectively through the thickness. In models built with conventional shells, appropriate offsets were applied to the reference surface of relevant S4R elements so as to allow the use of shared nodes between the shell and the contiguous cohesive interface element. Surface-to-surface tie constraints were used to enforce a rigid connection between adjacent shells with the same fiber orientation.

Fig. 3 shows that the different FE models predict very similar force-time curves, with a good general agreement between numerical results and experiments. All models under investigation predict correctly the sequence of damage events, with the development of the matrix crack preceding the growth of the delamination at the neighboring interface, and simulate with reasonably good accuracy both size and shape of the 90°/0° delamination (Fig. 4; see also Fig. 1), with its typical peanut shape elongated in the fiber direction of the lowermost layer. In agreement with experimental evidence, it is also seen (Fig. 4) that no delamination is predicted to occur on the top interface by FE models using C3D8R and SC8R elements, while, in contrast, the FE model based on conventional S4R shells simulates the growth of a large delamination on the top 0°/90° interface. This discrepancy may be attributed to the lower accuracy in evaluation of normal cohesive stresses in the FE model with S4R elements, which may result in serious restrictions to the combined use of conventional shells and cohesive elements for impact damage modeling. On the other hand, SC8R elements show potential for simulation of impact damage in layered structures and, as compared to full 3D elements, have the advantage of allowing the use of 2D failure criteria and damage progression schemes natively implemented in Abaqus.

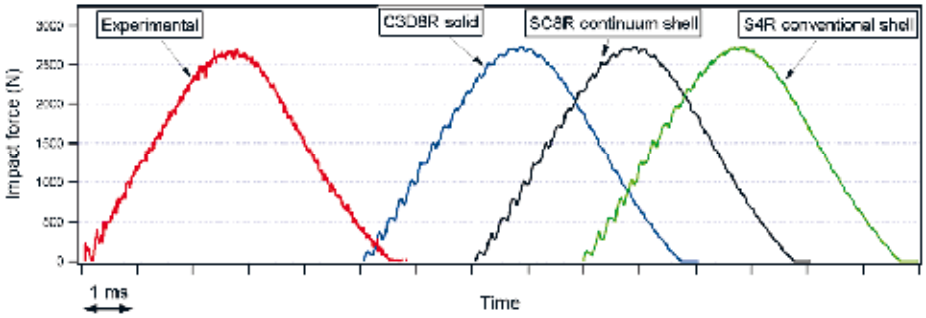

Fig. 3. Comparison between numerical and experimental force-time histories (impact energy = 3.9 J).

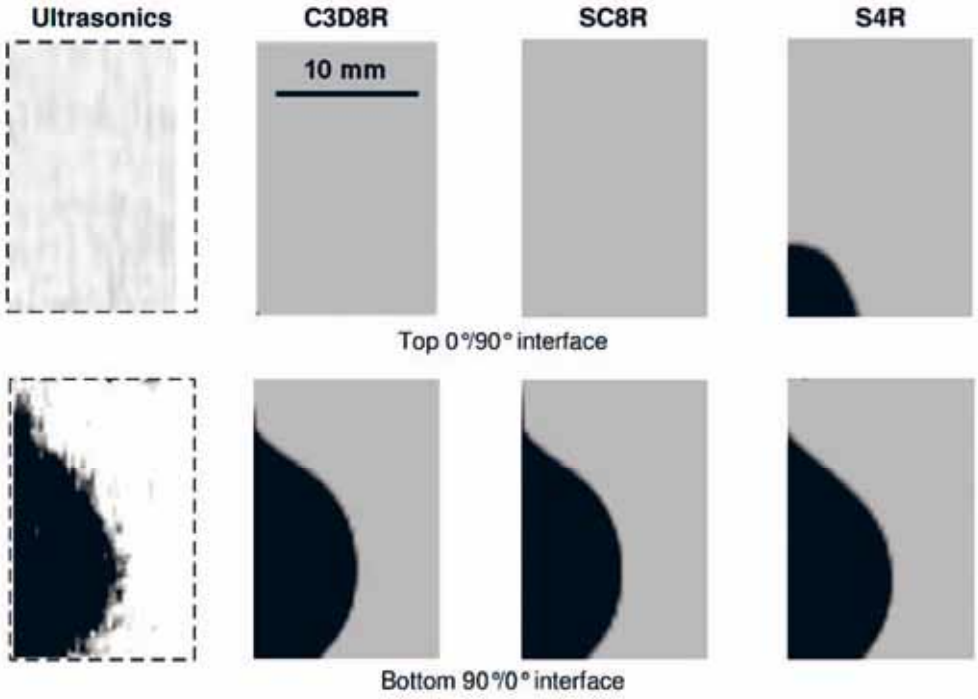

Fig. 4. Comparison between delamination areas at the two interfaces as characterized by ultrasonics and predicted by FE analyses (impact energy = 3.9 J).

Further comparisons between numerical predictions obtained with the use of C3D8R or SC8R elements and experimental results (such as those illustrated in Fig. 5, which reports peak forces and delaminated areas calculated or measured for various impact energies) indicate that FE models based on continuum shell elements provide numerical predictions which are practically coincident with those achieved by the use of full 3D models and in good agreement with experimental measurements. In addition, both the solid and the continuum shell FE models show relatively low sensitivity to mesh density (either through the thickness or in the laminate plane),

which was observed to have a negligible effect on delamination predictions provided by the models.

Similarly, FE models built with solids or continuum shells offer very similar predictions when analysing thicker laminates, as summarized in Fig. 6, which reports the delaminated area predicted for a 4 mm thick $[0_6/90_6]$s laminate. In this respect, it should be remarked that only the tensile matrix crack and the delaminations at the two interfaces were explicitly simulated as possible failure mechanisms in the FE models. On the other hand, even though no impact testing was performed on $[0_6/90_6]$s plates, the development of additional failure modes not accounted for in the models (such as matrix crushing and fiber fracture, typically occurring on the contact region of thick laminates) is to be expected in real laminates.

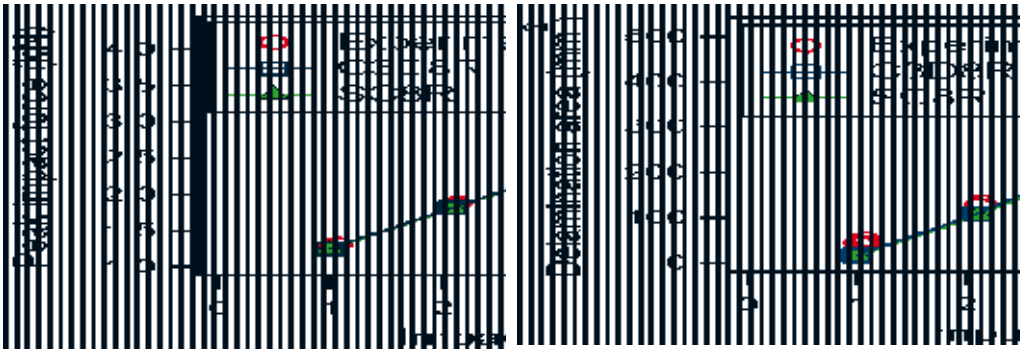

Fig. 5. Comparison between predicted and measured peak force (left) and delaminated area (right) at various impact energies (8 through-thickness elements).

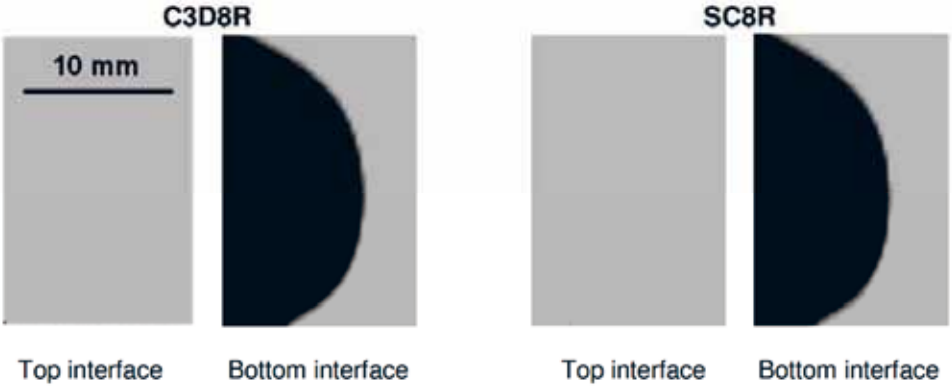

Fig. 6. Comparison between delaminated area predicted for a 4 mm thick $[0_6/90_6]$s laminate (impact energy = 3.9 J; 8 through-thickness elements).

5. CONCLUSIONS

FE models based on the use of cohesive elements for the simulation of the delamination between layers, and 3D solid, continuum shell, or conventional shell elements for the modeling of the unidirectional layers were developed in this study to analyse the performance of shell elements for impact damage prediction in composite plates. Almost coincident results were obtained with

the use of 3D solid and continuum shell (SC8R) elements in terms of simulation of delamination size and location, while largely inaccurate predictions of delamination at the interface near the impact side were provided by the model based on conventional shells (S4R). Continuum shell elements appear an attractive modeling choice as an alternative to full 3D models and further investigations are in progress to characterize predicting capabilities of shell models under more complex impact damage patterns.

ACKNOWLEDGEMENTS

This work has been supported by the EU funded FP7-ITN-Marie Curie project SYSWIND (Grant No. FP7-PEOPLE-ITN 238325).

REFERENCES

Allix, O., Ladeveze, P. and Corigliano, A. (1995). Damage analysis of interlaminar fracture specimens. Composite Structures 31(1), 61-74.

Aymerich, F., Dore, F. and Priolo, P. (2008). Prediction of impact-induced delamination in cross-ply composite laminates using cohesive interface elements, Composites Science and Technology. 68(12), 2383-2390.

Borg. R., Nilsson, L. and Simonsson, K. (2004). Simulation of low velocity impact on fiber laminates using a cohesive zone based delamination model. Composites Science and Technology 64, 279–88.

Camanho, P.P., Davila, C.G. and De Moura, M.F. (2003). Numerical simulation of mixed-mode progressive delamination in composite materials. Journal of Composite Materials 37(16), 1415–38.

Cui, W. and Wisnom, M.R. (1993). A combined stress-based and fracture-mechanics-based model for predicting delamination in composites. Composites 24(6), 467—474.

Dávila, C.G., Camanho, P.P. and Turon A. (2008). Effective simulation of delamination in aeronautical structures using shells and cohesive elements. Journal of Aircraft 45(2), 663-671.

Elder, D.J., Thomson, R.S., Nguyen, M.Q. and Scott, M.L. (2004). Review of delamination predictive methods for low speed impact of composite laminates. Composite structures 66, 677-683.

Hallett, S.R., Jiang, W.G., Khan, B. and Wisnom, M.R. (2008). Modelling the interaction between matrix cracks and delamination damage in scaled quasi-isotropic specimens. Composites Science and Technology 68, 80-89.

Harper, P.W. and Hallett, S.R. (2008). Cohesive zone length in numerical simulations of composite delamination. Engineering Fracture Mechanics 75(16), 4774--4792.

Hou, J.P., Petrinic, N. and Ruiz C. (2001). A delamination criterion for laminated composites under low-velocity impact. Composites Science and Technology 61, 2069-2074.

Johnson, H.E., Louca, L.A. and Mouring, S.E. (2006). Current research into modelling of shock damage to large scale composite panels. Journal of Materials Science 41, 6655-6672.

Mi, Y., Crisfield, M.A., Davies, G.A.O. and Hellweg, H.B. (1998). Progressive delamination using interface elements. Journal of Composite Materials 32(14), 1246–1272.

Tay, T.E., Liu, G., Tan, V.B.C., Sun, X.S. and Pham, D.C. (2008). Progressive failure analysis of composites. Journal of Composite Materials 42(18), 1921-1964.

Tay, T.E. (2003). Characterization and analysis of delamination fracture in composites: an overview of developments from 1990 to 2001. Applied Mechanics Reviews 56, 1-32.

Wisnom, M.R. (2010). Modelling discrete failures in composites with interface elements. Composites Part A: Applied Science and Manufacturing 41(7), 795-805.

Proceedings of the 32nd
Risø International Symposium on Materials Science:
Composite materials for structural performance:
Towards higher limits
Editors: S. Fæster, D. Juul Jensen,
B. Ralph, B.F. Sørensen
Risø National Laboratory for Sustainable Energy,
Technical University of Denmark, 2011

COMPRESSIVE STRENGTH OF THICK COMPOSITE PANELS

K. Branner and P. Berring

Wind Energy Division, Risø National Laboratory for Sustainable Energy, Technical University of Denmark, Denmark

ABSTRACT

The aim of this study is to investigate how much the compressive strength of thick composite panels is reduced due to delaminations and to investigate under which conditions a delamination will grow. Understanding of this is essential in order to move forward the design limits used in the structural design process.

Results obtained from finite element modeling analyses are compared with an experimental test campaign performed on flat composite panels with and without delaminations.

1. INTRODUCTION

In wind turbine blades, the flapwise bending loads are typically carried by thick, solid and slightly curved composite panels extending the whole length of the blade. These load-carrying thick laminates are the flanges in the main spar of the blade (see Fig. 1) and experience compressive loading when the blade is bending towards that side. It may therefore be critical when delaminations occur in these load carrying laminates.

In Toft, Branner, Berring and Sørensen (2011) two stochastic models for the distribution of delaminations in wind turbine blades are analyzed. The reliability is estimated for a generic wind turbine blade model both with and without delaminations. It is found that the probability of failure for this particular blade and analysis assumptions increases 5-11 times when delaminations are included.

A panel with a delamination, subjected to compressive loading may buckle and fail in two different ways. The panel may buckle in a local buckling mode, where the sublaminate on mainly one side of the delamination buckles, which typically occurs when the delamination is large in size and positioned close to one of the surfaces. The other buckling mode is global buckling where both the sub-laminate and the remaining panel buckle toward the same side of the panel, which typically occurs when the delamination is small and deep in the laminate. In the local buckling mode, the buckling may drive a growth of the delamination leading to panel

failure (buckling-driven delamination).

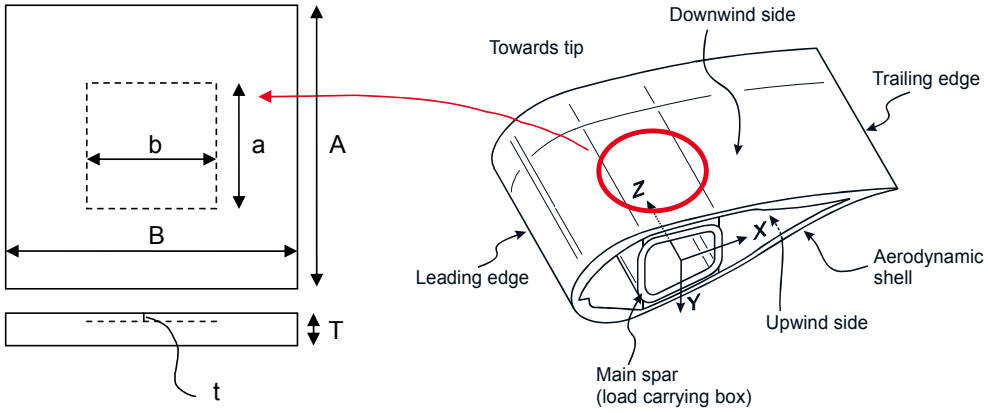

Fig. 1. Definition of panel and delamination geometry. Panels are somewhat similar to the load carrying laminate in the main spar of a typical wind turbine blade.

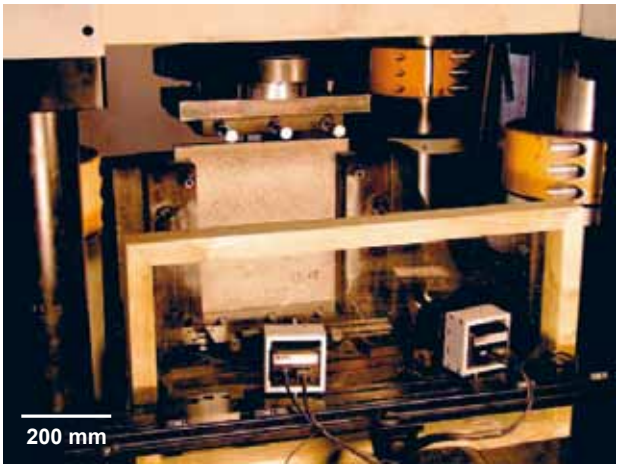

Fig. 2. Panel inserted in the test rig. Note the black speckle pattern on the panel and the two cameras that are used by the digital image correlation (DIC) measurement system to calculate deflections. Scale bar specifies the size of the panel.

2. EXPERIMENTAL RESULTS

A large number of flat composite panels with and without delaminations have been tested until failure as reported in Sørensen, Branner, Lund, Wedel-Heinen and Garm (2009) and Sørensen, Toftegaard, Goutanos, Branner, Berring, Lund, Wedel-Heinen and Garm (2010).

The test specimens are approximately 400x380x20 mm rectangular composite panels made of

glass fiber reinforcement plastic (see Fig. 1). The lay-up is symmetric with approximately 90% of the reinforcement in the load direction and the remaining reinforcement in the ±45º directions. Two different types of panels were tested. One type (PP) was made with prepregs and the other type (VI) was made using the vacuum infusion technique. Even though the specimens were made similar to the load carrying laminate in a typical wind turbine blade, the material properties do not correspond to those in real wind turbine blades, as the specimens were produced in a laboratory under different conditions.

For both types, some of the panels were manufactured with no intentional defects or imperfections, while others had slip sheets embedded to simulate delaminated rectangular areas of a different size and depth. A specially designed test rig (Sørensen et al. 2009) was used in a 5 MN Instron testing machine as shown in Fig. 2. The rig is designed to limit rotation and out-of-plane deflection of the edges of the panels. The panels are supported by steel blocks along the edges on both sides, so the panel area free to experience out-of-plane deflections is approximately 320-325 mm in both the vertical and horizontal direction. The panels were loaded in compression to ultimate failure and a digital image correlation (DIC) measurement system were used on one side of the panel to monitor full field displacements and conventional displacement transducers was used on the other side to monitor the opening of the delamination under the entire load history.

As described above, the compressive loaded panels are subjected to the two different buckling modes; the global buckling mode and the local buckling mode. The following buckling responses were observed during the experiments:

a) Global buckling.

b) Local buckling without growth. The delaminated zone “pops out” and very little growth of the delaminated zone is observed before ultimate failure.

c) Local buckling with growth. The delaminated zone “pops out” and substantial growth of the delaminated zone is observed before ultimate failure.

d) Global buckling with mode jump. The buckling begins in the 1st global mode shape. At failure a mode-jump is observed and the panel fails in an s-shape.

e) Local buckling causes instant failure. The panel fails right after the delaminated zone “pops out”. This typically occurs at high loading.

Table 1 lists the main results from the experimental panel tests. The panels have delaminations of different sizes and through thickness positions (see Fig. 1). For a few of the panels, a strange behavior was observed or measuring equipment was not running properly. These panels are not included here. In Table 1, average results are shown for between 2 and 4 specimens of each type.

2.1 Method to determine buckling load. In Sørensen et al. (2009) a method was developed in order to determine the buckling load. In this method the buckling load was defined as the in-plane load where the tangent to the out-of-plane displacement curve (as a function of the in-plane load) intersects the zero out-of-plane displacement. However, it was found that this method is too sensitive to scatter in the experimental data. In order to ensure consistency for all delamination sizes and through thickness positions, a more robust method for estimating the buckling load proposed in Sørensen et al. (2010) was applied in both the experimental and numerical studies. The normalized in-plane force was plotted vs. the normalized in-plane

displacement. In the beginning of the load history, the response of the panels is linear, but as the panels start to buckle, the response becomes nonlinear.

A linear curve is determined by the first 30% of this load history and then offset by 2.5%. The buckling load is then found as the load at the intersection between this linear curve and a spline interpolation of the entire load history as shown in Fig. 3.

Table 1. List of the tested specimens with delamination sizes and through thickness positions. The prevailing observed buckling modes are listed together with the measured reduced strength, calculated as the average buckling load for that delamination (P_i) relatively to the average buckling load for that type of panel without delamination (P_n).

Test panels					**Failure**	
Code	Specimens	a/A	b/B	t/T	Type	P_i/P_n
VI 2	3	0,33	0,40	0,20	Local	-
VI 3	3	0,25	0,30	0,20	Global	-
VI 4	2		None		Global	100%
VI 5a	3	0,48	0,39	0,31	Global	81%
VI 5b	4	0,47	0,39	0,21	Local	87%
VI 6a	2	0,36	0,30	0,31	Global	87%
VI 6b	4	0,35	0,30	0,21	Local	83%
VI 7a	2	0,42	0,34	0,25	Global	92%
VI 7b	4	0,41	0,34	0,16	Local	82%
PP 1	3	0,52	0,65	0,30	Local?	-
PP 2	3	0,43	0,55	0,35	Local?	-
PP 3	3	0,51	0,65	0,35	Local?	-
PP 5	3		None		Global	100%
PP 6	3	0,82	0,64	0,29	Local	54%
PP 7	3	0,63	0,49	0,29	Local?	63%
PP 8	2	0,68	0,54	0,25	Local?	57%

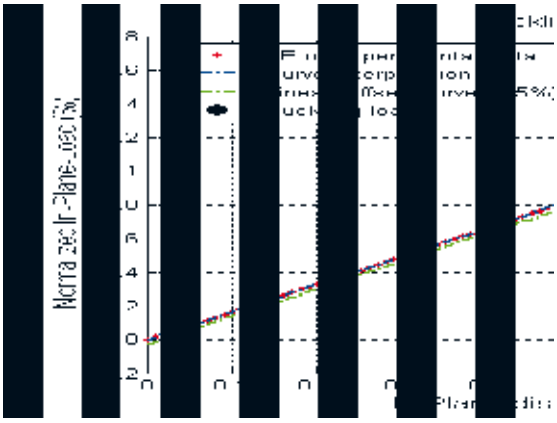

Fig. 3. Robust method to determine the buckling load.

The buckling load was determined for each panel using this robust method. The average buckling loads for the small series of each panel type are denoted P_i and the average buckling loads for panels without delaminations are denoted P_n. The two different series of panels with respect to the manufacturing process were treated separately meaning that they have different P_n. The measured average buckling loads (P_i) with respect to P_n are listed in Table 1.

For some of the early tests the measured buckling loads are not reported in Table 1. These tests were done on an earlier test rig (Sørensen et al. 2009), which has more flexible boundary conditions for the panels. The measured buckling loads are consequently not comparable with those obtained on the newer test rig and therefore not considered here.

3. NUMERICAL MODELING APPROACH

The panels modeled are relatively thick with a thickness to width ratio of about 0.067. They consist entirely of unidirectional (UD) layers with all fibers in the loading direction and are somewhat similar to the load-carrying laminate in a typical wind turbine blade where approximately 90% of the fibers are in the lengthwise direction.

A 3D solid finite-element modeling approach was used with 20-node orthotropic elements. Two or three elements were used through the thickness depending on the through thickness position of the delamination.

A small out-of-plane displacement corresponding to the first buckling mode shape was applied as an initial imperfection of the delaminated sub-laminate. The amplitude of the initial imperfections was approximately 0.5‰ of the panel thickness for the flat panels.

The elements were all joined in the interfaces, except for the delaminated area where quadratic contact conditions were applied to prevent penetration. The panels were simply supported in the midline of all their edges. Therefore, all panel models have nodes at these midlines. The load was applied by forcing a uniform in-place displacement of the short top edge and constraining the opposite edge (B edges in Fig. 1).

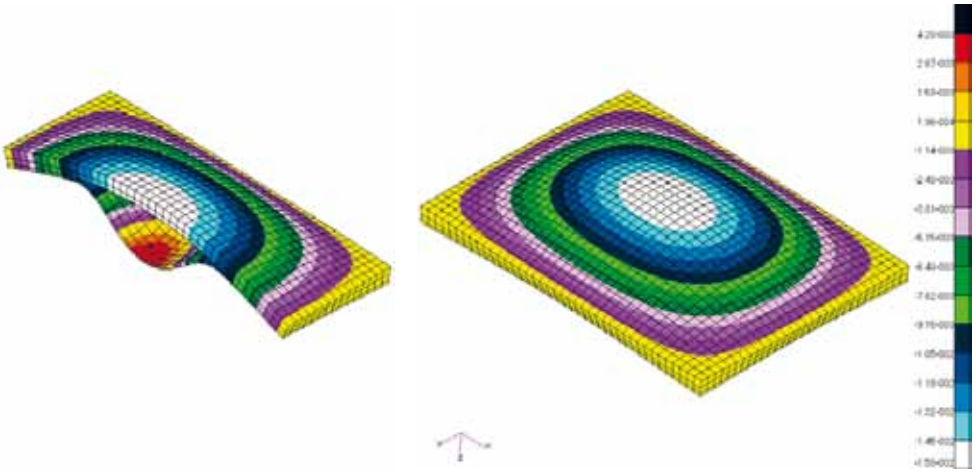

Fig. 4. A typical finite element model showing local buckling behavior.

The average number of degrees of freedom (DOFs) was approximately 150.000. Nonlinear geometric analyses were performed using an implicit solution algorithm and typical results are shown in Fig. 4.

A large numerical parameter study was performed to investigate the buckling response and reduction of strength due to different sizes of delaminations and locations through the thickness of the panels.

In the numerical studies the out-of-plane displacement of two nodes were compared to evaluate which buckling mode the panel had. One node was located at the center of the panel and one node was located at the center of the sub-laminate. In the experimental tests the out-of-plane displacements of the front panel were obtained by applying the DIC measurement system, while the out-of-plane displacement of the back of the panel was measured by applying traditional distance transducers. The displacements of the front and back of the panels were compared to determine if the panel buckled locally (opening of the delamination) or if it buckled globally (no opening of the delamination).

Results from the finite element analyses show that combinations of the global and local modes can also appear as so-called combined modes or sub-modes (see a more detailed description in Sørensen et al. (2009)). The sub-modes occur for large and deep delaminations.

In both the numerical and experimental studies the buckling load of a "perfect" panel was determined based on the robust method described earlier. The reduction of strength resulting from the delamination was determined by performing a normalization based on the results obtained from the "perfect" panels.

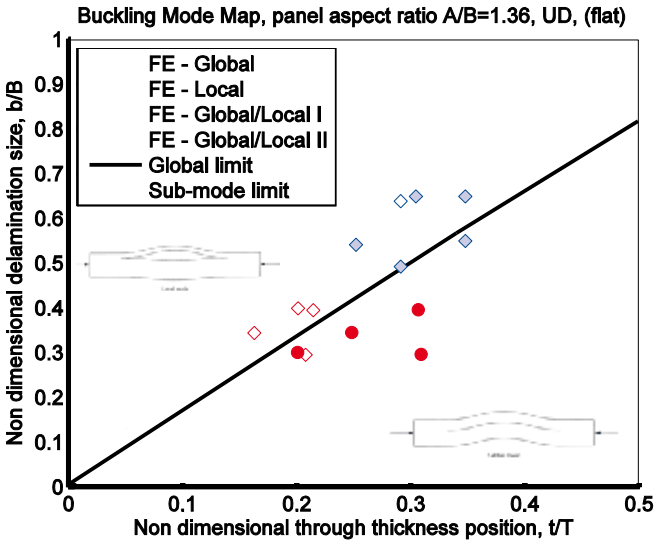

Fig. 5. Buckling mode map for flat UD panels with experimental results included. Type PP panels are blue and type VI panels red. Solid circles mean global buckling while diamonds mean local buckling. The light blue colored diamonds mean that the local behavior is uncertain or the panels sometime show global behavior.

4. COMPARISON

In Fig. 5 the buckling behavior is shown for flat UD panels and compared with the experimental results for the panels tested. It is found that there generally is a good agreement between the predicted buckling behavior and the observed behavior during the experiments. The numerical analyses give a quite sharp borderline between the local and global buckling modes. For the experiments this borderline cannot be expected to be sharp and the experiments also indicate that there is band along the borderline where both local and global buckling behavior can be expected. This band seems to be wider as the delaminations get bigger and deeper in the panels. This also agrees with the sub-mode area found for the numerical analyses. However, more experiments and analyses are needed to obtain more solid conclusions on this band.

The buckling mode map in Fig. 5 is similar to those reported by Short, Guild and Pavier (2001). However, in Short et al. (2001) only local and global modes were considered.

The reduced compressive strength caused by delaminations in the flat UD panels is shown in Fig. 6, where the results from the solid element models are compared with the experimental data. It is generally found that the reduced compressive strength is larger for the experiments than that predicted by the FE-analyses. This is particularly true for the PP type panels, where the strength is reduced more due to delaminations than found for the VI type panels. This may be due to the fact that the experimental and numerical modeled boundary conditions are not the same, but the manufacturing process for the PP type panels may also result in higher sensitivity against delaminations than seen for the VI type panels. More experiments and in-depth analyses are needed in order to make more solid conclusions on the higher observed strength reduction.

In Gaiotti, Rizzo, Branner and Berring (2011) a shell element approach is compared with this solid element approach and in Branner, Berring, Gaiotti and Rizzo (2011) the shell element approach is also compared with these experimental results.

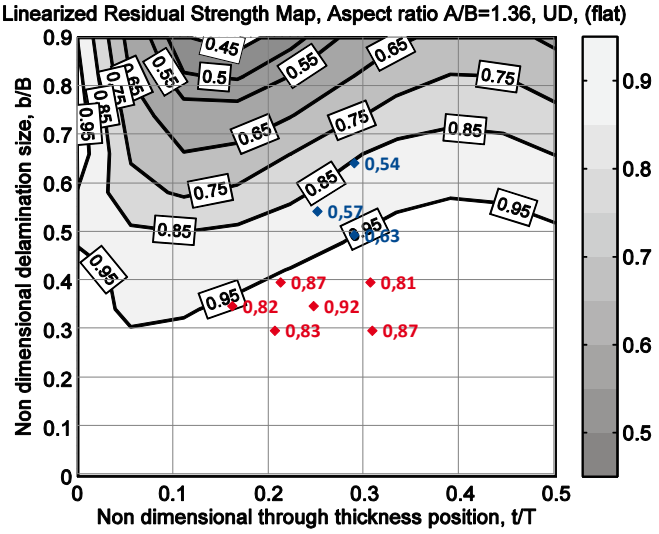

Fig. 6. Reduced compressive strength for flat UD solid element panels with experimental data included. Type PP panels are blue and type VI panels red. The labels indicate the average reduced buckling load factor from the experiments.

5. CONCLUSIONS

Test results from a large number of thick flat composite panels with and without delaminations are presented in this paper and compared with finite element analyses using solid elements. It is found that the compressive strength of thick composite panels is reduced significantly due to delaminations. The reduction of compressive strength is found to be larger for the experiments than predicted by the FE-analyses. This may be due to differences in boundary conditions.

The tests also show that large and deep delaminations caused local buckling and instant failure, while smaller delaminations closer to the surface in some cases are found to give stable delamination growth. When large and deep delaminations open, much elastic energy is released driving a rapid growth of the delamination. These deep delaminations are therefore found to be more dangerous than delaminations closer to the surface where the released elastic energy may not be high enough to drive a growth of the delamination.

ACKNOWLEDGEMENTS

The work is partly supported by the Danish Energy Authority through the 2007 Energy Research Programme (EFP 2007). The supported EFP-project is titled “Improved design of large wind turbine blades of fiber composites – phase 4” and has journal no. 33031-0078.

The work is also partly supported by the Danish Agency for Science, Technology and Innovation through the Danish Centre for Composite Structures and Materials for Wind Turbines (DCCSM) (project no. 09-067212). The support is gratefully acknowledged.

REFERENCES

Branner, K., Berring, P., Gaiotti M. and Rizzo, C.M. (2011) Comparison of Two Finite Element Methods with Experiments of Delaminated Composite Panels, in: Proc. of 18th International Conference of Composite Materials (ICCM), 21-26 August 2011, Jeju Island, Korea.

Gaiotti, M., Rizzo, C.M., Branner K. and Berring, P. (2011). Finite Elements Modeling of Delaminations in Composite Laminates, in: Proc. of 3rd International Conference on Marine Structures (MARSTRUCT), 28-30 March 2011, Hamburg, Germany.

Short, G.J., Guild F.J. and Pavier. M.J. (2001) The effect of delamination geometry on the compressive failure of composite laminates, Composites Science & Technology, 61, 2075-2086.

Sørensen, B.F., Branner, K., Lund, E., Wedel-Heinen J. and Garm. J.H. (2009). Improved design of large wind turbine blade of fibre composites (phase 3). Summary Report, Risø-R-1699(EN), Risø National Laboratory for Sustainable Energy, Denmark.

Sørensen, B.F., Toftegaard, H., Goutanos, S., Branner, K., Berring, P., Lund, E., Wedel-Heinen J. and Garm. J.H. (2010). Improved design of large wind turbine blade of fibre composites (phase 4). Summary Report, Risø-R-1734(EN), Risø National Laboratory for Sustainable Energy, Denmark.

Toft, H.S., Branner, K., Berring P. and Sørensen, J.D. (2011). Defect Distribution and Reliability Assessment of Wind Turbine Blades, Engineering Structures, 33(1), 171-180, DOI: 10.1016/j.engstruct.2010.10.002.

Proceedings of the 32nd
Risø International Symposium on Materials Science:
Composite materials for structural performance:
Towards higher limits
Editors: S. Fæster, D. Juul Jensen,
B. Ralph, B.F. Sørensen
Risø National Laboratory for Sustainable Energy,
Technical University of Denmark, 2011

ADVANCES IN FINITE ELEMENT ANALYSIS AND OPTIMIZATION OF COMPOSITE STRUCTURES INCLUDING NON LINEARITIES

M. Bruyneel, J.P. Delsemme, P. Jetteur and A. Remouchamps

SAMTECH s.a., Liège Science Park, Angleur, Belgium

ABSTRACT

In this paper, we present recent results obtained with the SAMCEF Finite Element code for the solution of composite structures analysis and optimization, when non linearities are taken into account. It is explained how delamination, progressive ply failure, buckling, post-buckling and collapse analyses are conducted. Optimization of stiffened composite panels including buckling and collapse is also studied.

1. INTRODUCTION

Taking into account non linearities in the analysis and optimization of composite structures is becoming more and more important. Modeling large displacements as well as inter and intra-laminar damages, is a condition to better understand how composite materials and structures work, and is necessary to further reduce the weight and provide designs which are not too conservative. This paper presents recent advances and results obtained in the non linear finite element analysis and structural optimization of multi-layered thin-walled stiffened panels, which provide a reliable answer to the industrial needs for the aeronautics and wind turbine industries. First, a numerical procedure for assessing the progressive failure of composites is presented, which takes into account delamination, intra-laminar ply degradation, post-buckling and collapse (Brauner et al., 2009; Bruyneel et al., 2009b). The CPU issues are discussed on an industrial application, and the significant gains obtained with parallel solution procedures are presented, showing that it is now possible to conduct advanced finite element simulations in a reasonable computational time. Models for inter and intra-laminar damages are briefly discussed, especially with respect to the problems of damage localization and sensitivity of the results with the mesh density. Then, optimization of stiffened composite panels taking into account buckling, post-buckling and collapse is presented (Bruyneel et al., 2010). It is shown how optimization can be used to tailor the non linear structural response and the equilibrium path, therefore controlling the buckling and collapse load of the structure.

2. ADVANCED NONLINEAR ANALYSIS OF COMPOSITES

2.1 Buckling, post-buckling and collapse analyses of composite structures. As far as compression and shear are present in a thin-walled structure, it must be designed to withstand buckling. Classically the buckling load factors are obtained by solving an eigen-values problem around a linearised configuration. In the formalism of the finite elements, it comes that:

$$\left(\mathbf{K} - \lambda_j \mathbf{S}\right)\mathbf{\Phi}_j = 0 \qquad j = 1,\ldots,m \tag{1}$$

where **K** and **S** are the stiffness and initial stress stiffness matrices, respectively. λ_j and $\mathbf{\Phi}_j$ are the buckling load factors and buckling modes, respectively. The reliability of a linear buckling analysis is questionable for structures capable of withstanding large displacements observed in the post-buckling range, or assuming a limit point in the equilibrium path. To simulate such behaviours and approach reality, a non linear analysis is needed, which requires a specific continuation method (Riks et al., 1996) for identifying the collapse (limit) load of the structure. In this case, a non linear system of equations is solved, together with an additional constraint imposing to stay on the equilibrium path, even if it is unstable:

$$\mathbf{F}(\mathbf{q},\lambda) = \mathbf{F}^{\text{ext}}(\lambda) - \mathbf{F}^{\text{int}}(\mathbf{q}) = 0 \tag{2}$$

$$\beta(\mathbf{q},\lambda,s) = 0 \tag{3}$$

In (2) and (3), λ is the load factor, **q** are the nodal displacements, and *s* is the arc-length, controlled over the iterative process instead of the load factor or the displacements. Figure 1 illustrates the results obtained after a linear buckling analysis and a non linear analysis. A stiffened composite panel is considered, with a stacking sequence made of conventional plies (0, 45, -45 and 90° angles). Shell elements are used to model the skin and the longitudinal omega (hat) stiffeners, which are assembled with the skin using specific rivets finite elements. The structure is simply supported on the edges with additional locked rotations, in order to simulate an embedded component. It is loaded in shear along the four edges, and subjected to longitudinal compressive forces along the curved boundaries and the stiffeners.

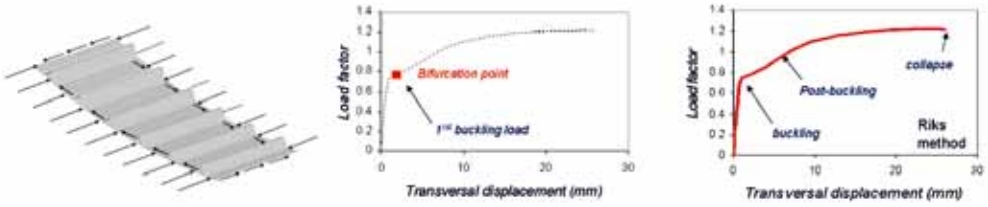

Fig. 1. Linear and non linear stability analysis of a stiffened composite panel.

2.2 Delamination in composites. Inter-laminar failure analysis can be conducted with a pure fracture mechanics approach. In that case, the Virtual Crack Extension method (VCE) can be used. In this approach, the total energy release rate G_T is first computed as a semi-analytical derivative of the total potential energy π with respect to a crack advance, ΔA (4). Then, based on sensor nodes measuring the relative displacements U_i (i = 1,,2,3) at the crack lips in local axes and on the reactions R_i to the crack opening, this total energy release rate G_T is distributed over the 3 modes (5). It is noted that only one structural analysis is required to obtain the energy release rates at the nodes of the crack fronts. Relation (4) is indeed computed with an internal re-

generation of the elements, and no additional load cases are required.

$$\frac{d\pi}{dA} \cong \frac{(\pi_{pert} - \pi_{init})}{\Delta A} \tag{4}$$

$$G_j = \frac{U_j R_j}{\sum_{i=I,II,III} U_i R_i} G_T, \qquad j = I, II, III \tag{5}$$

A solution for the SLB test case is provided in Figure 2. The results of VCE obtained with SAMCEF are compared to the solution obtained in (Krueger and Goetze, 2006) with VCCT (this last method not being available in SAMCEF). Details are given in Bruyneel et al. (2009b), Krueger and Goetze (2006) and Bruyneel et al. (2009c).

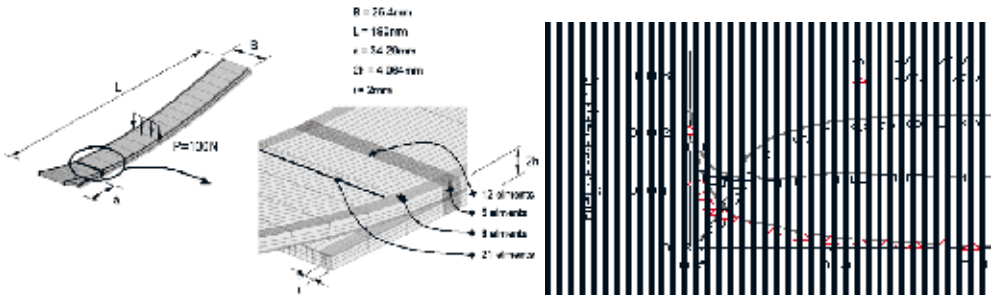

Fig. 2. Solution of the SLB test case with VCE

Cohesive elements can also be used to study the progressive delamination in laminates. In SAMCEF, the potential assigned to the interface elements is based on (6), where three damage variables d_I, d_{II} and d_{III} , related to modes I, II and III, are defined:

$$E = \frac{1}{2}\left[k_I^0 \langle \varepsilon_{33} \rangle_-^2 + k_I^0 (1 - d_I) \langle \varepsilon_{33} \rangle_+^2 + k_{II}^0 (1 - d_{II}) \gamma_{31}^2 + k_{III}^0 (1 - d_{III}) \gamma_{32}^2 \right] \tag{6}$$

k_i^0 in (6) are undamaged stiffnesses. The thermodynamic forces Y_i (i=I,II,III) are obtained by deriving (6) with respect to d_i. For mixed loading, the damage evolution is related to the three inter-laminar fracture toughness G_{IC}, G_{IIC} and G_{IIIC} corresponding to opening (I), sliding (II) and tearing (III) modes. The equivalent thermodynamic force Y takes the following form:

$$Y = \sup_{\tau \le t} G_{IC} \left\{ \left(\frac{Y_I}{G_{IC}} \right)^\alpha + \left(\frac{Y_{II}}{G_{IIC}} \right)^\alpha + \left(\frac{Y_{III}}{G_{IIIC}} \right)^\alpha \right\}^{1/\alpha} \tag{7}$$

The three damage variables have the same evolution over the loading, and a unique damage d is therefore managed for modeling delamination, that is $d = d_I = d_{II} = d_{III}$. The damage variable d is related to the equivalent thermodynamic force Y with a function of the form $g(Y)$. In SAMCEF, three different functions $g(Y)$ are available (Bruyneel et al., 2009b), leading to three cohesive laws, i.e. exponential, bi-triangular and polynomial. With this approach, it is possible to estimate the critical cracks, the propagation load, the maximum load that the structure can sustain before a significant decrease of its strength and stiffness, and the residual stiffness during

the inter-laminar cracks propagation. However, the analysis is non linear, and the iterative scheme can sometimes significantly increase the computational time needed to find a solution. In order to save time, a parallel solution procedure can be used.

VCE, the cohesive elements approach and VCCT are compared in the DCB test case in Figure 3. It is seen that for VCCT, the results obtained in Krueger (2007) with another commercial finite element code present oscillations during the crack propagation. For VCE and the cohesive elements approach, a solution is obtained without such oscillations. A complete discussion on these methods, as well as the solution of an industrial test case, can be found in Bruyneel et al. (2009b). A general observation is that VCE and VCCT require a very fine mesh in the crack front neighborhood in order to provide accurate results, while the cohesive elements approach can be used with coarser meshes.

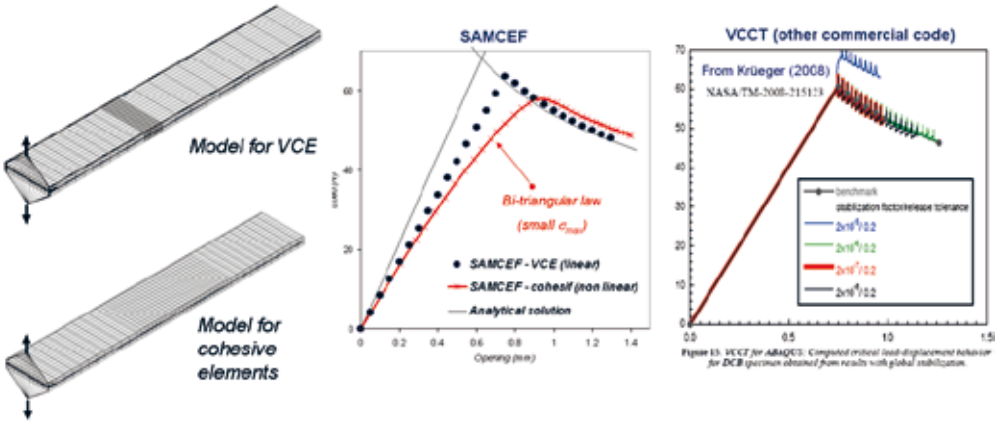

Fig. 3. Comparison of VCE, VCCT and the cohesive element approach for the DCB test case

The gain obtained in the computational time when a parallel solution procedure is used is illustrated on an industrial application. The details of the model are given in Bruyneel et al. (2009b). The structure is submitted to a pull test. It includes 54 initial crack front, and the cohesive elements are defined in the extensions of theses initial flaws. A bi-triangular cohesive law is used. A static analysis with imposed displacements is conducted. Multi-layered volume elements are used. The different mesh refinements are illustrated in Figure 4, and the resulting load-displacement curves are reported in Figure 5. The CPU times are given in Table 1. A speed up of 3 (efficiency of 75%) is observed when 4 processors are used for the finest model.

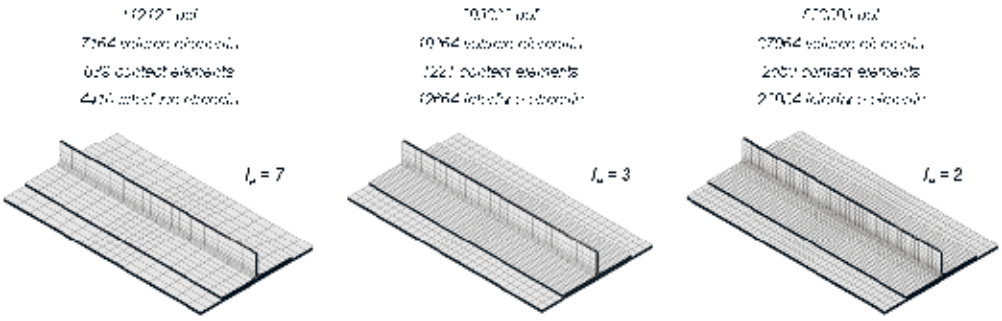

Fig. 4. Different mesh refinements of the model (l_e = average in-plane element length)

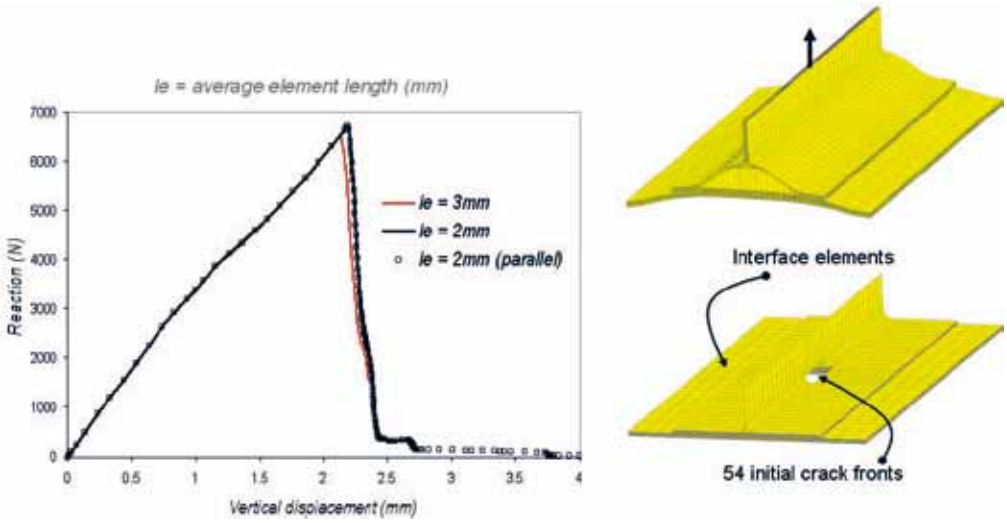

Fig. 5. Load-displacement curves for different mesh refinements of the model

Mean l_e (mm)	Number of processors	Size of the problem (dof)	Maximum load (N)	CPU to reach 2.35mm (minutes)
2	4	553889	6700	285
2	1	553889	6700	854
3	1	293332	6530	524
7	1	112122	6720	44

Table 1. Computational times (in minutes) for the solution of the industrial problem

2.3 Intra-laminar damage of composites. Although delamination is certainly the most frequent mode of failure in laminated composites, in practical applications it is necessary to consider the ply degradation as well. Besides the classical failure criteria such as Tsai-Hill, Tsai-Wu and Hashin, an advanced degradation model is available in SAMCEF. This ply damage model relies on the development proposed in Ladeveze and LeDantec (1992). For intra-laminar damage, the following potential is used:

$$E = \frac{\sigma_{11}^2}{2(1-d_{11})E_1^0} - \frac{\nu_{12}^0}{E_1^0}\sigma_{11}\sigma_{22} - \frac{\nu_{13}^0}{E_1^0}\sigma_{11}\sigma_{33} + \frac{\langle\sigma_{22}\rangle_+^2}{2(1-d_{22})E_2^0} + \frac{\langle\sigma_{22}\rangle_-^2}{2E_2^0} + \frac{\langle\sigma_{33}\rangle_+^2}{2(1-d_{22})E_3^0} + \frac{\langle\sigma_{33}\rangle_-^2}{2E_3^0} - \frac{\nu_{23}^0}{E_2^0}\sigma_{22}\sigma_{33} + \frac{\sigma_{12}^2}{2(1-d_{12})G_{12}^0} + \frac{\sigma_{13}^2}{2(1-d_{12})G_{13}^0} + \frac{\sigma_{23}^2}{2(1-d_{22})G_{23}^0} \quad (8)$$

where d_{11}, d_{22} and d_{12} are the damages related to the fibers, the transverse and the shear directions, respectively. The thermodynamic forces are derived from this potential and manage the evolution of the damages, via relations such as $d_{11} = g_{11}(Y_{11})$, $d_{22} = g_{22}(Y_{12},Y_{22})$ and $d_{12} = g_{12}(Y_{12},Y_{22})$. A delay can also be defined for the occurrence of the damages. Moreover, non linearities are introduced in the fibre direction. Finally the model can be coupled to plasticity with isotropic hardening (Jetteur, 2007).

Even if the model proposed in (8) performs well and provided accurate solutions for industrial applications (Bruyneel et al., 2009a), the representation of the damage is local, and a high

dependency of the solution with respect to the mesh density may be observed. In the non local damage law developed in SAMCEF (Jetteur, 2011) and based on the ONERA model (Germain, 2006), the thermodynamic loads become additional unknowns, whose values are constrained by equations defining regions of influence of the damage. A characteristic length is added to the problem, in order to define the size of these regions of influence. Now, the value of the damage in a given point depends on the damages occurring in its neighborhood. The damage can vary from ply to ply, but is now constant across the ply thickness. In the new model, the inter-laminar failure (i.e. delamination) can also influence the evolution of the damage in the ply. Figure 6 illustrates the nearly mesh-independent solution obtained with the non local model.

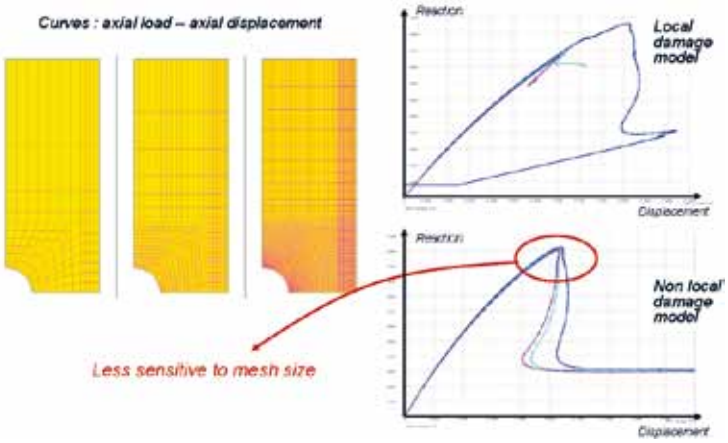

Fig. 6. Comparison of local and non local intra-laminar damage definition

3. ADVANCED OPTIMIZATION OF COMPOSITES

In aeronautics, we are mainly interested in minimizing the structural weight, while satisfying structural requirements on strength, stiffness and stability. Minimizing the weight in a stability problem is very delicate, as reported in Bruyneel et al. (2008), when local modes appear in the solution. We consider here the structure illustrated in Figure 7 (see also Figure 1). The curved stiffened panel is made of 6 super-stiffeners, each one consisting of a hat stiffener and a portion of panel. Each super-stiffener includes 6 design variables, which are the thicknesses related to the plies oriented at 0°, ±45° and 90°, for the stiffener and for the panel. The problem then includes 36 design variables. The optimization problem is written in (9), where w is the structural weight to be minimized, λ_j is the j^{th} buckling load, $\lambda_{collapse}$ is the collapse load, and $\mathbf{t}$ is the set of ply thicknesses, which must satisfy the side constraints. At the optimum, the buckling and collapse loads must be larger than prescribed values $\underline{\lambda}$ and $\underline{\lambda}_{collapse}$, respectively.

$$\begin{aligned} &\min_{\mathbf{t}} w(\mathbf{t}) \\ &\lambda_j(\mathbf{t}) \geq \underline{\lambda} \qquad j = 1,...,m \\ &\lambda_{collapse}(\mathbf{t}) \geq \underline{\lambda}_{collapse} \\ &\underline{t}_i \leq t_i \leq \bar{t}_i \qquad i = 1,...,36 \\ &\mathbf{t} = \left\{ t^{\theta}_{i\_skin}, t^{\theta}_{i\_stiff}, i = 1,...,6 ; \theta = 0°,90°,45° \right\} \end{aligned} \tag{9}$$

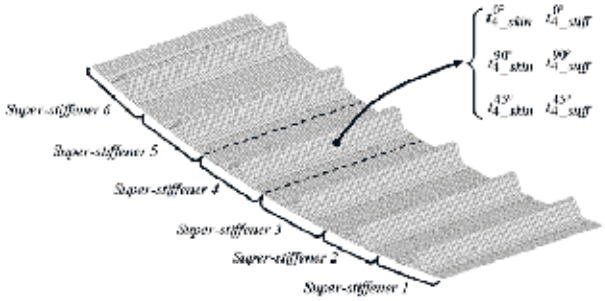

Fig. 7. The stiffened composite panel and its design variables for the optimization problem

The gradient-based method used in the paper belongs to the Sequential Convex Programming methods (Bruyneel, 2006). These are not purely Mathematical Programming methods, which would require too many iterations (and therefore structural analyses) to obtain the solution, but rather an approach where the solution of the initial non linear optimization problem is replaced by the solution of successive convex approximated problems, based on specific Taylor-series expansions. Details can be found in Bruyneel et al. (2008) and Bruyneel (2006). Since gradient-based methods are used to solve the optimization problem (9), a sensitivity analysis must be carried out. Details are given in Bruyneel et al. (2008, 2010).

In Figure 8, besides the linear buckling, a non linear analysis is performed, in order to describe the post-buckling behaviour and to identify the collapse load. In the optimization problem (9), the bound on the collapse load is set to 1.2, while local buckling is allowed during the nominal loading since the bound on λ_j is set to 0.8. Assigning the bifurcation point (with the linear buckling analysis) and the collapse load (with the non linear analysis) allows us to control the shape of the equilibrium path. Doing so, the optimal structure is lighter, and local buckling modes occur between the stiffeners before the global collapse mode appears. Optimizing with respect to geometric non linearities clearly allows to save weight (gain of 39% here instead of 31% obtained with the buckling optimization only).

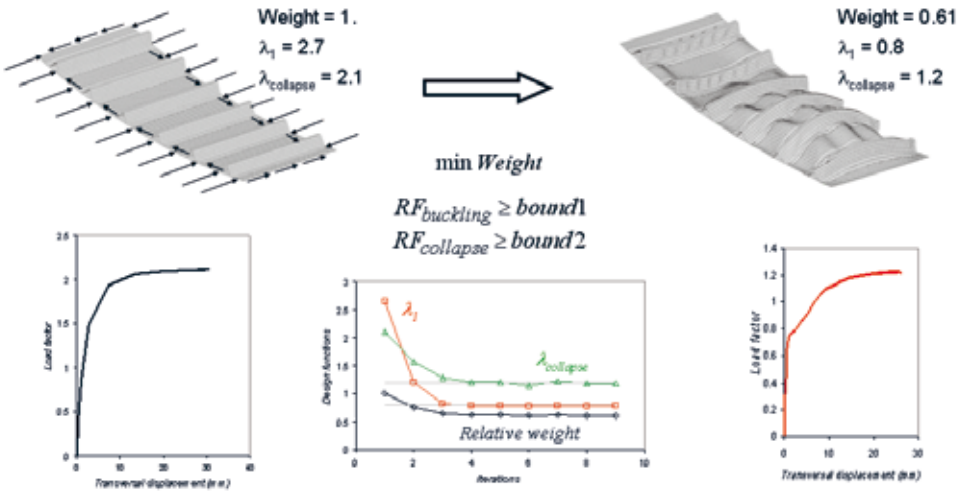

Fig. 8. Solution of the buckling and collapse optimization

4. CONCLUSIONS

Recent developments carried out in the SAMCEF finite element code were presented. They aim at proposing advanced tools for non linear analysis of composite structures, including post-buckling, collapse, inter and intra-laminar damages.

Optimization of composite panels taking into account buckling, post-buckling and collapse was then presented. It was shown how optimization can be used to tailor the non linear structural response and the equilibrium path, controlling the collapse load of the structure, and saving additional weight.

REFERENCES

Brauner C., Delsemme J.P., Jetteur P., Bruyneel M., Kuhlmann G. (2009). Non linear failure analysis of a reinforced composite curved beam with delamination and ply degradation. NAFEMS World Congress, June 16-19, Creta, Greece.

Bruyneel M. (2006). A general and effective approach for the optimal design of fibre reinforced composite structures. Composite Science & Technology, 66, pp. 1303-1314.

Bruyneel M., Colson B. and Remouchamps A. (2008). Discussion on some convergence problems in buckling optimization, Structural & Multidisciplinary Optimization, 35, pp. 181-186.

Bruyneel M., Degenhardt R., Delsemme J.P. (2009a). An industrial solution to simulate post-buckling and damage of composite panels. JEC Composites Magazine, 48, pp; 38-39.

Bruyneel M., Delsemme J.P., Jetteur P., Germain F. (2009b). Modeling inter-laminar failure in composite structures : illustration on an industrial case study. Applied Composite Materials, 16(3), pp. 149-162.

Bruyneel M., Delsemme J.P., Jetteur P., Germain F. (2009c). Modeling delamination of composite structures for industrial applications. 2nd International Carbon Composite Conference, Aerospace Valley, Arcachon, France, October 27 - 29, 2009.

Bruyneel M., Colson B., Delsemme J.P., Jetteur P., Grihon S., Remouchamps A. (2010). Exploiting semi-analytical sensitivities from linear and non-linear finite element analyses for composite panel optimization. International Journal of Structural Stability and Dynamics, 10(4), pp. 885-903.

Germain N. (2006). Modélisation non locale de l'endommagement dans les structures composites. PhD Thesis, ONERA.

Jetteur P. (2007). Modèle matériau pour le pli. SAMTECH Internal Report 248.

Jetteur P. (2011). Introduction de modèles de dommage non locaux dans SAMCEF. SAMTECH Internal Report 268.

Krueger R. and Goetze D. (2006). Influence of finite element software on energy release rates computed using the virtual crack closure technique, NASA/CR-2006-214523 – NIA Report N° 2006-06.

Krueger R. (2007). An approach for assessing delamination propagation capabilities in commercial finite element code, American Society of Composites 22nd Annual Technical Conference, September 17-19, University of Washington, Seattle, WA.

Ladeveze P. and Le Dantec S. (1992). Damage modelling of the elementary ply for laminated composites, Composites Science & Technology, 43, pp. 257-267.

Riks E., Rankin C. and Brogan F. (1996). On the solution of mode jumping phenomena in thin walled shell structures, Computer Methods in Applied Mechanics and Engineering, 136, pp. 59-92.

Proceedings of the 32nd
Risø International Symposium on Materials Science:
Composite materials for structural performance:
Towards higher limits
Editors: S. Fæster, D. Juul Jensen,
B. Ralph, B.F. Sørensen
Risø National Laboratory for Sustainable Energy,
Technical University of Denmark, 2011

INTERFACE SHEAR STRENGTH CHARACTERIZATION IN A METAL-POLYMER SYSTEM USING THE SINGLE FILAMENT FRAGMENTATION TEST METHOD

S. Charca and O.T. Thomsen

Department of Mechanical and Manufacturing Engineering
Aalborg University, Pontoppidanstræde 101, DK-9220 Aalborg East, Denmark

ABSTRACT

The single filament fragmentation test method was implemented to assess the mechanical properties of the resin-filament interface of steel filaments embedded in an unsaturated polyester resin. The main advantages of the single filament fragmentation test include simple sample manufacturing, simple testing procedure, and finally the large amount of data that can be obtained from one single test. The results show that the tensile strength of the filaments remains relatively constant with varying testing gauge length. The thermal gradient during sample manufacturing was relatively low, and therefore the thermal stresses may neglected. Small fragment lengths were obtained which indicates very high values of the estimated interfacial shear strength.

1. INTRODUCTION

Fiber-matrix interfaces are crucial in determining the mechanical properties of composite materials. For the polymer composite materials there are several test methods to characterize the interfaces properties such as fiber pull out, micro-tension, and micro-indentation (Feih, Wonsyld, Minzari, Westermann and Lilholt 2004; Piggott 2002; Pitkethly, Favre, Gau, Jakubowski, Mudrich, Caldwell, Drzal, Nardin, Wagner, Di Landro, Hampe, Armistead, Desaeger and Verpoest 1993; Rao, Herrera-Franco, Ozzello and Drzal 1991; Herrera-Franco, Rao and Dzral 1999). The single fiber fragmentation test appears to be simpler in the sense of sample manufacturing, the experimental setup and more reliable than the other methods mentioned (Feih et al. 2004; Piggott 2002; Herrera-Franco et al. 1999). A significant advantage is that a large number of fragments are typically obtained from one single sample test, thus enabling a consistent statistical analysis and estimate of the interfacial shear strengths (Feih et al. 2004). The single fiber fragmentation test was first proposed by Kelly and Tyson (1965) to estimate the interfacial shear strength of material systems with tungsten fibers embedded in a

copper matrix. Since then, the fragmentation test method has been extensively used for characterization of composite systems with carbon and glass fibers. The most important features of the single fiber fragmentation test are the alignment of the fiber (or filament) in the matrix and the failure strain of the matrix which should be at least three times higher than the failure strain of the fiber (Feih et al. 2004; Pitkethly et al. 1993; Herrera-Franco and Drzal 1992) The fiber fragmentation experiment is performed with a single or multiple fibers embedded in a matrix (dogbone shaped specimen). As the tensile load is increased during the test the stresses are transferred from the matrix to the fiber through the matrix/fiber interface. Since the fiber has a lower failure strain, the fiber will break before the matrix. When the fiber has fractured, the stress at the point of the fiber breakage becomes zero. As the applied load is further increased the stress transferred from the matrix to the fiber will increase, causing new fiber breaks and increasing the number of fragments. This will continue until the fragments become so short that the stress transferred to the fiber fragments is not sufficient to cause further fiber failure (Feih et al. 2004). The average shear stress in the matrix-fiber interface can be estimated by balancing the forces in the single matrix-fiber system and expressed by (Feih et al. 2004; Kelly et al. 1965)

$$\tau = \frac{\sigma_{fl_c} d}{2 l_c} \tag{1}$$

where σ_{flc} is the tensile strength of the fiber corresponding to the critical fragment length, d is the fiber diameter, and l_c is the critical fragment length. Several researchers have used the critical fragment length, which is obtained from the assumption that the average fragment length is between $l_c/2$ and l_c, and then the following relation can be found (Feih et al. 2004)

$$l_{avg} = \frac{3}{4} l_c \tag{2}$$

The requirements of low cost and reliable composite materials are the main motivation to explore the potential use of steel filament (or cords) as a reinforcement material for polymer composite materials. The main advantageous features of steel filaments are high mechanical properties and ductility when compared to more traditional reinforcement systems like glass and carbon fibers. A significant “challenge” is the polymer matrix-steel interfacial properties. The main subject of this research is to characterize the matrix/steel-filament interfacial properties using the single fiber/filament fragmentation test method. The methodology of sample manufacturing, experimental setup and procedure for two filament diameters are defined. Furthermore the damage and failure mechanisms in the fragmentation process will be discussed, and the interfacial shear strength will be estimated using the classic Kelly and Tyson relation (Feih et al. 2004; Kelly et al 1965)

2. MATERIALS AND EXPERIMENTAL SETUP

Two different diameters of zinc coated high strength steel filaments were used as the fibers and unsaturated polyester was used as matrix. The mechanical properties of the constituent materials are shown in Table 1. The dogbone fragmentation samples were manufactured by casting the resin into a silicone rubber mould which contained the cleaned filament. To avoid misalignment of the filament a 200g of weight was applied for the 0.1mm filament, whereas no pre-strain was applied for the 0.04mm filament. A temperature sensor was placed next to the filament (in the middle of the casting sample) to measure the real-time temperature and to assess the thermal stresses induced in the filament. The minimum cross sectional area required for the fragmentation samples were calculated using the rule of mixtures and assuming linear elastic

material behavior. The minimum cross sectional areas were estimated to be 0.27 and 2.33mm^2, respectively for the 0.04mm and 0.1mm of filaments. However, to avoid premature failure and to obtain reliable results cross sectional area of ~10 and ~90mm^2, respectively, were used. The effective testing gauge lengths for the samples were 60 and 220mm, respectively.

Table 1: Mechanical properties of ultra high strength steel filaments and the unsaturated polyester

	Steel Filament		Unsaturated Polyester
Diameter [mm]	0.1	0.04	-
Longitudinal tensile modulus [GPa]	209	209	1.289§
Tensile strength [MPa]	3016	3000	45.75§
Strain to failure	~0.021	~0.02	~0.06*§
Poisson's ratio	0.30	0.03	0.375§
§ Tested at 0.05mm/min * Non-linear ultimate strain			

Ten specimens were manufactured using the 0.1mm filaments, and five with 0.04mm filaments. To assess the effect of the manufacturing process and the test repeatability, five samples with 0.1mm filament diameter were made at Risø National Laboratory for Sustainable Energy (Technical University of Denmark) and five were made at AAU.

The 0.1mm filament diameter fragmentation tests were performed using an electric Zwick/Z100 tensile testing machine operated in deformation control. Based on the preliminary tests a loading rate of 0.05mm/min was demonstrated to be appropriate to achieve filament fragmentation. For the 0.04mm of filament diameter samples a homemade tensile test machine was used at deformation control (0.1mm/min). During the testing, the filament damage and failure process was monitored using a 50× stereomicroscope. Moreover, for the 0.1mm fiber diameter filament specimens, a photoelasticity technique was employed to observe the birefringence phenomena induced in the transparent resin by the development of local stress concentrations around the filament fragment ends. This facilitated the identification of the areas/points where the filament fragmentations occurred. Fig. 1 shows the experimental setup used.

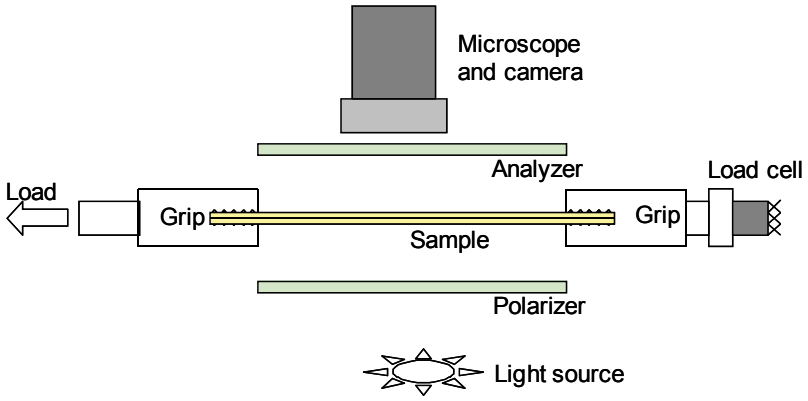

Figure 1: Schematic representation of the experimental setup

3. RESULTS AND ANALYSIS

During the curing process of the unsaturated polyester, residual stresses were induced in the specimens (especially pronounced for thick specimen samples). This is caused by two main sources: a temperature gradient developed during the curing process (exothermic reaction), and the volumetric shrinkage of the polyester caused by the chemical cross-linking polymerization reaction (Bogetti and Gillespie 1990). Fig. 3 shows the temperature monitored during the curing process of the unsaturated polyester at the centre of a fragmentation test specimen and on the outside of the specimen. The maximum thermal gradient temperature reached is relatively low (~5^{o}C), and the residual stress caused by the thermal effect is neglected accordingly. The volumetric shrinkage was quantified during the curing process to be ΔV_{shr} = 8% which is too large to be ignored in the interpretation of the results.

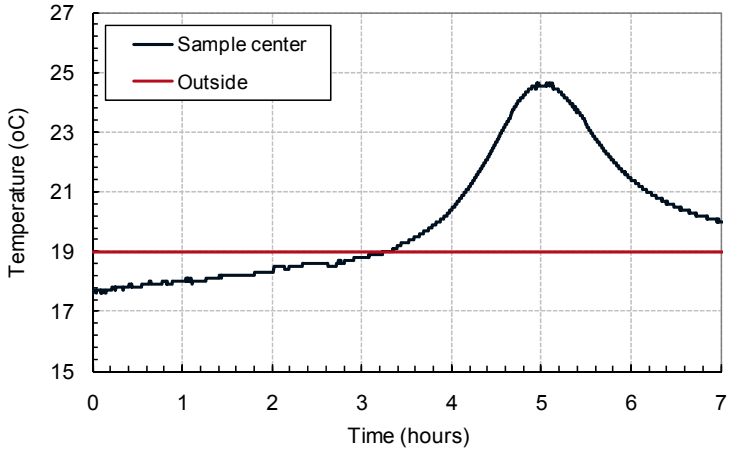

Figure 2: Measured temperatures during the curing process of the polyester resin

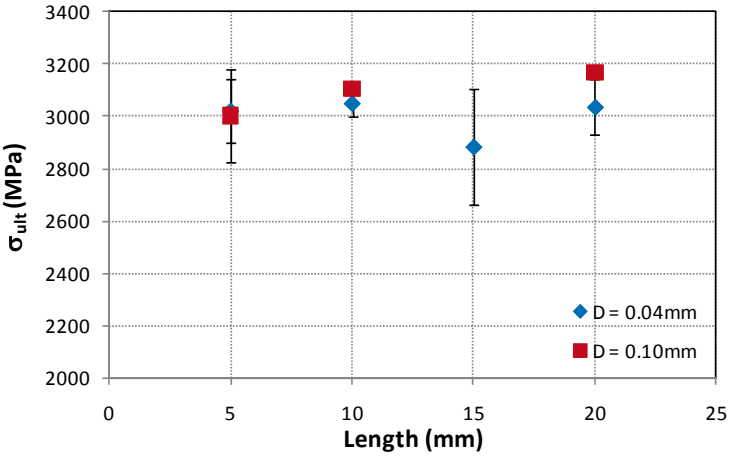

Figure 3: Tensile strength for the 0.04 and 0.1mm diameter of steel filament

According to previous investigations, the tensile strength of carbon, glass and kevlar filaments increase when the filament gauge length is reduced (Dai and Piggott 1993). Single steel filaments were tested at 5, 10, 15, and 20mm gauge lengths and the results are shown in Fig. 3. It is observed that the tensile strength as a function of the gauge length remains relatively constant, which is different than for other commercial fibers (Dai et al. 1993).

3.1. Failure mechanisms. Fig. 4 shows the sequences of failure mechanisms observed for steel filaments embedded in an unsaturated polyester resin in the fragmentation tests. Four categories were defined according to the images: debonding, partially necking, complete necking and failure. However, debonding and initial necking appeared to occur almost simultaneously, and in reality it was not possible to clearly identify which one occurred before the other. For glass and carbon fibers embedded in polymeric resin the debonding and the fiber failure happens at the same time, while no necking is observed (Kim and Nairn 2002; Nairn and Wagner1997).

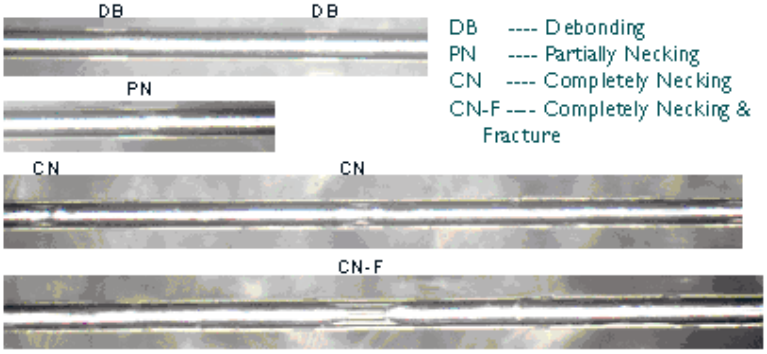

Figure 4: Steel filament failure mechanisms observed during fragmentation testing of the 0.1mm filament diameter sample.

Careful monitoring using an optical microscope of the filament fragmentation process was conducted during the loading process utilizing the photoelastic birefringence of the polyester resin. The microscopic observations showed that at first debonding/necking started at an extensional strain of approximately ~4.9%, and that complete saturation was reached between 6.4-6.9% extensional strain. Fig. 5 shows an image obtained using light polarization for a 0.1mm filament diameter sample, where the high stress concentration areas are associated with a colour change (light or dark, depending of the alignment of the polarizer and analyzer). A closer view reveals a high colour intensity change around the filament ends thus indicating the position of the filament fragmentations as showing Fig. 5.

Figure 5: Photoelastic birefringence caused by stress concentrations induced around a steel filament during fragmentation test (filament diameter 0.1mm)

3.2. Fragment lengths. After the fragment lengths were measured in the samples manufactured using the 0.1mm filament diameter it became clear that the observed fragmentation lengths did not in all cases correspond to the true saturation limit. Accordingly a careful data discrimination

process was needed. It was observed for all specimens that the cross-section was not uniform along the lengths as sketched in the lateral view in Fig. 6. During testing this leads to a non-uniform strain development along the sample length, and zones with higher strain levels reach the saturation limit faster than zones where the strain level is lower. The result of this was that there were zones in the tested specimens where the saturation limit had not been reached. The overall fragment lengths ranged between 0.5 to 15mm, and this was subdivided into the three sub-ranges 0.5-5mm, 5-8mm, and 8-15mm, respectively. Based on the experimental observations the fragments in the lengths range of 8-15mm were located in zones where saturation was not achieved, and consequently these data were omitted from the analysis. In addition, samples manufactured using 0.04mm diameter filaments were grinded and polished prior to the fragmentation test. As the cross section is uniform along the sample, the fragment lengths are distributed uniformly, and data discrimination was not needed.
Fig. 7 and 8 show the histograms obtained using the fragmentation data obtained for the 0.1mm filament diameter after omission of the 8-15mm fragment lengths range, and the raw data observations obtained for the 0.04mm filament samples. Detailed statistical fitting tests were performed on the fragment length data using the Kolmogorov-Smirnov and Chi-square method. The results of the statistical analyses show that the best fit was obtained using the Gumbel distribution, but it is also observed that both the Weibull and Gamma distributions gave acceptable fitting parameters.

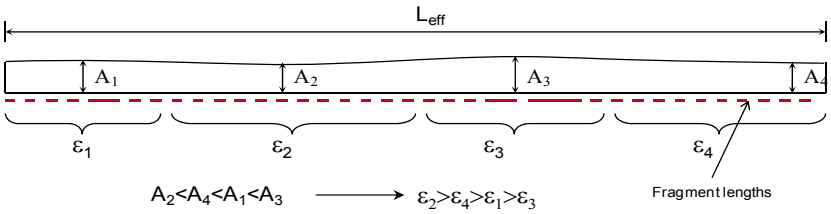

Figure 6: Schematic representation of the fragment length distribution along a specimen length

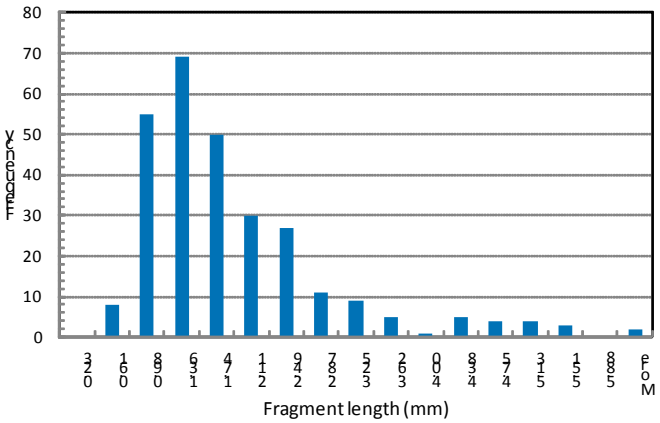

Figure **7**: Histogram of the observed fragment length distribution for 0.1mm filament diameter

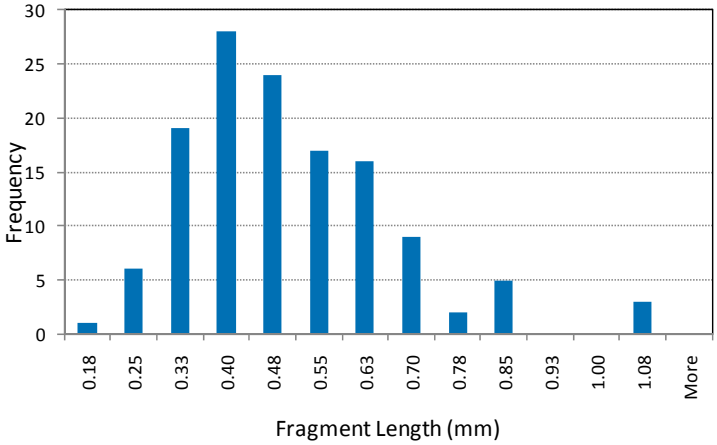

Figure 8: Histogram of the observed fragment length distribution for 0.04mm filament diameter

Table 2 shows a summary of the results of the fragmentation tests, where SD is the standard deviation. The critical fragment length was calculated according to Eq. (2), and this was then used to estimate the shear strength of the steel filament-resin interface as specified by Eq. (1). In Eq. (1) σ_{fl_c} is the tensile strength of the filament obtained for the critical fragment length, and this quantity is not easy to obtain experimentally. However, the tensile strength was determined experimentally as a function of gauge length (Fig. 3) and established to be independent of gauge length. Consequently the value showed in Table 1 can be used directly into the Eq. (1). The estimated shear strength values are very high and much higher than observed for glass or carbon fiber based polymer systems.

Table 2: Summary of fragmentation test results

D [mm]		Fragment Length [mm]	K & T Shear Stress [4/3L_{av}, MPa]
0.04	Average	0.533	84.9
	SD	0.215	
0.10	Average	1.703	67.1
	SD	0.964	

4. CONCLUSION

The single filament fragmentation test method was successfully implemented to assess the interfacial shear strength of composite systems with high strength steel filaments embedded in unsaturated polyester resin. It was observed that the tensile strength of the filaments does not display a significant variation with respect to the gauge length tested. The temperature gradient observed during the curing process was low, and therefore thermal stresses can be neglected. The obtained fragment length data showed a good fit with extreme statistical distributions. Furthermore the average fragment lengths obtained were very small, which indicated a high

value of the estimated steel filament-polyester interfacial shear strength according to the classic Kelly and Tyson relation.

ACKNOWLEDGMENTS

The research reported was sponsored by the Danish National Advanced Technology Foundation. The financial support is gratefully acknowledged. The authors wish to thank Dr. Jakob I. Bech, Dr. Hans Lilholt, Mr. Tom L. Andersen, Dr. R.T. Durai Prabhakaran at the Risø National Laboratory for Sustainable Energy, Technical University of Denmark, for inspiring discussions

REFERENCE

Bogetti, T.A., Gillespie Jr. J.W. (1990) Residual Stress and Deformation in Thick Laminate Composites Undergoing Chemical Hardening and Shrinkage. SPI Composite Institute's 45th Annual Conference Proceedings

Dai, S.R., and Piggott, M.R., (1993) The Strengths of Carbon and Kevlar Fibers as a Function of Their Lengths. Compos Sci Technol 49, p. 81

Feih, S., Wonsyld, K., Minzari, D., Westermann, P., Lilholt, H., (2004) Testing Procedure for the Single Fiber Fragmentation Test. RISO-Report 1483.

Herrera-Franco, P.J., Rao V., and Dzral, L.T., (1999) Bond Strength Measurement in Composites – Analysis of Experimental Techniques. Compos Eng 2, p. 31.

Herrera-Franco, P. J., and Drzal, L. T., (1992) Comparison of Methods for the Measurement of Fiber/Matrix Adhesion in Composites. Composites, vol. 23, No. 1, p. 2.

Kelly, A., and Tyson, W.R. (1965). Tensile properties of fiber-reinforced metals: copper/tungsten and copper/molybdenum. J. Mech. Phys. Solids, 13: 329–350.

Kim, B.W., and Nairn, J.A., (2002) Observations of Fiber Fracture and Interfacial Debonding Phenomena Using the Fragmentation Test in Single Fiber Composites. J Compos Mater 36, p. 1825.

Nairn, J.A., and Wagner, H.D., (1997) A Revised Shear-Lag Analysis of an Energy Model for Fiber-Matrix Debonding. Advanced Composites Letters 5, p. 131.

Piggott, M., (2002) Load Bearing Fiber Composites. 2nd Edition ed, ed. K.A. Publishers. New York: Springer.

Pitkethly, M.J., Favre, J.P., Gaur, U., Jakubowski, J., Mudrich, S.F., Caldwell, D.L., Drzal, L.T., Nardin, M., Wagner, H.D., Di Landro, L., Hampe, A., Armistead, J.P., Desaeger, M. and Verpoest, I. (1993) A Round-Robin Programme on Interfacial Test Methods. Composites Science and Technology, 48, p.205

Rao, V., Herrera-Franco, P., Ozzello, A.D., and Drzal, L.T. (1991) A Direct Comparison of The Fragmentation Test and the Microbond Pull-Out Test for Determining the Interfacial Shear Strength. J. Adhesion,34, No. 1, p. 65

Proceedings of the 32nd
Risø International Symposium on Materials Science:
Composite materials for structural performance:
Towards higher limits
Editors: S. Fæster, D. Juul Jensen,
B. Ralph, B.F. Sørensen
Risø National Laboratory for Sustainable Energy,
Technical University of Denmark, 2011

OPTIMIZATION OF THE OPERATING CONDITIONS USED TO PRODUCE NEW BIOMASS-BASED COMPOSITE MATERIALS BY A DOUBLE-VACUUM BAG TECHNIQUE

J.C. Domínguez and B. Madsen

Materials Research Division, Risø National Laboratory for Sustainable Energy, Technical University of Denmark, 4000 Roskilde, Denmark

ABSTRACT

The selection of a suitable technique for the manufacturing of composites with a polyfurfuryl alcohol matrix is carried out in this work. The chosen technique, based on a knowledge of the behavior of the resin during curing and its physicochemical properties is the double-vacuum-bag technique. The design of the devices needed to produce composites and the optimization of some of the operating conditions for using the double-vacuum-bag technique is also assessed in this work. Finally, a design of experiments is proposed to optimize the operating conditions of the cure cycle employed during the manufacturing of the material.

1. INTRODUCTION

One of the most important present challenges of the composite industry is the design of new composite materials with a low environmental impact, low cost and high mechanical properties comparable to the mechanical properties of traditional composites. Following these criteria, a new generation of partially and fully bio-based resins that include modified epoxy, phenolic and furan resins are under development (Alonso, Oliet, Rodríguez, Astarloa, Echeverría 2004; Guigo, Mija, Vincent, Sbirrazzuoli 2010). These resins have been designed to be used as matrixes together with traditional fibers, but also together with natural fibers, such as flax and jute fibers, to produce fullly-biobased composites, the so-called bio-composites.

Furfuryl alcohol resins, also called furan resins, have been used extensively in the production of metal-casting cores and moulds, corrosion-resistant coatings, polymer concretes, wood adhesives and binders, sand consolidation and well plugging, materials possessing low flammability and low smoke release, and carbonaceous products comprising industrial graphitic electrodes (Gandini and Belgacem 1997). Typically, these resins have been manufactured employing furfural derived from agricultural byproducts such as corncobs and wheat bran, and

using an acid catalyst to carry out the curing of the resin (Guigo, Mija, Vincent, Sbirrazzuoli 1969). Nowadays, novel polyfurfuryl alcohol (FA) bioresins are under development. These new FA bioresins are based on furfuryl alcohol which can be obtained from pentosan-rich biomass, such as bagasse (a wasteproduct from sugar cane production) (Gandini and Belgacem 1997; Guigo et al. 2010). Thus, the FA resin is a new type of bioresin with an attractive profile of being eco-friendly and with low cost. However, these resins present an important drawback during the manufacturing of composite materials. The water generated by the condensation reactions, that take place during the curing process (Choura, Belgacem, Gandini, 1996), might lead to materials with a high porosity content, and therefore also with low mechanical properties.

The use of these new bioresins as matrices for composite materials requires knowledge about the curing process including kinetics, rheokinetics, viscosity dependence on temperature, flow behavior and expansion-shrinkage in order to minimize the cycle time, and improve the quality and the performance of the resulting composite materials. A study of the kinetics of the curing process of the FA resin allows predicting the evolution of its curing degree. Therefore, these methods used for predicting the curing behavior of the FA resin can be use in the design of a cure cycle for the manufacturing of a composite material as well as to obtain the optimal amount of catalyst based on a pure kinetic criterion. Rheokinetics allows obtaining the time required to reach the gel point of the FA resin at different temperatures and that can be used for modeling. Complementary studies concerning the chemorheological behavior of the FA resin for the pre and post-gel curing stages and the viscosity dependence on temperature have already been reported in a previous work (Domínguez and Madsen 2011). This obtained background for the FA resin provides useful information both to select a proper manufacturing technique for a desired composite material among the traditional techniques and to identify the modifications of typical manufacturing techniques required to reach the specifications of the new materials.

In the present work, a detailed study on the development of a suitable manufacturing technique is presented. The study includes the selection of a proper manufacturing technique as well as the modifications required in the concrete case of the FA resin used together with glass fibers to improve the quality of the material.

2. MATERIALS

A polyfurfuryl alcohol (FA) resin under development (Furolite 050915A), and an acid catalyst based on p-toluenesulfonic acid dissolved in water (45 % aqueous solution) ("S type + D"), were supplied by Transfurans Chemicals BVBA (Belgium). According to the supplier's datasheet, the specifications of the FA resin are: water content 5.40 %, viscosity 3480 cPs at 25 ºC, and monofurfuryl alcohol content below 1 %. A +/- 45º glass fibre biaxial fabric was used for each of the layers of the composite material produced. The density of the fibres, and the area weight of the fabric were 2.66 $g.cm^{-3}$ and 450 $g.m^{-2}$, respectively.

3. EXPERIMENTAL PROCEDURE

The calorimetric measurements were performed on a STA 449 F1 Jupiter TGA-DSC equipment using low pressure pans with two holes in the lid. Differential scanning calorimetry (DSC) runs were carried out from 30 to 250 ºC using seven different heating rates: 4, 6, 8, 10, 12, 16 and 20 $K.minute^{-1}$. Sample weight was between 30 and 35 mg. Three different amounts of catalyst were used to cure the resin: 2, 4 and 6 % w/w. Experiments were conducted under an Ar atmosphere.

Rheological runs were performed using an AR Rheometer 2000ex (TA Instrumets©) with a 25 mm diameter upper plate and a Peltier lower plate for analysis of the rheokinetics of the FA resin curing process. Normal force was zeroed and fixed during the tests to prevent contact loss between the sample and plates. Isothermal curing runs at 60, 65, 70, 75, 80, and 85 ºC using a 2 and 4 % w/w amount of catalyst were carried out for 60 minute for a range of frequencies from 1 to 10 Hz (6 frequencies-logarithm scale) and a 0.5 % strain. A 20 K.minute^{-1} heating ramp from a starting temperature of 20 ºC was programmed to reach the curing temperature for all the performed tests. Samples were stabilized at 20 ºC for 2 minutes before the heating step. All the measurements were performed within the linear viscosity region of the FA resin.

4. RESULTS AND DISCUSSION

In order to overcome the problem of the high water content of FA resins and to obtain low porosity content materials, the commonly-used single-vacuum bag (SVB) manufacturing technique has been substituted by a double-vacuum bag (DVB) manufacturing technique, which has been used previously for other resins, such as polyimides and phenolics that are cured by similar condensation reactions (Hou and Jensen 2008). The advantage of the DVB technique, compared to the SVB technique, is that the water produced during the curing process can be removed from the material instead of being trapped inside, and thereby the final porosity content is considerably reduced.

After having selected the manufacturing technique, the operating conditions, and the devices used to perform the curing of the material by this technique, as well as the materials employed in the manufacturing of some of the devices, then still have to be tested and optimized for this particular case. The improvement of the DVB technique is carried out in this work through a series of cure cycles proposed to produce a composite material with a FA resin matrix together with glass fibers.

Before designing the cure cycles used in the manufacture of composite materials, studies of the kinetics of the curing of the FA resin and of its rheokinetics have been performed. The evolution of the curing degree of the resin was calculated from the thermograms obtained for each heating rate used during testing by DSC. Kissinger Akahira Sunose (KAS), Flynn-Wall-Ozawa (FWO), and Vyazovkin (VA) *model-free-kinetics* methods have been applied to the experimental data to obtain the kinetic parameters of curing of the FA resin. As shown in Fig. 1a, as an example at a heating rate of 10 K.minute^{-1}, the methods were suitable for predicting the profiles of the curing degree of the resin.

The gel times of the FA resin have been measured under isothermal conditions at different curing temperatures and the Macosko model has been applied to the results. As shown in Fig. 1b, the model was suitable to predict the gel times. Thus, this model can be used for the design of the cure cycles employed in the manufacturing of the composites with a FA resin as the matrix.

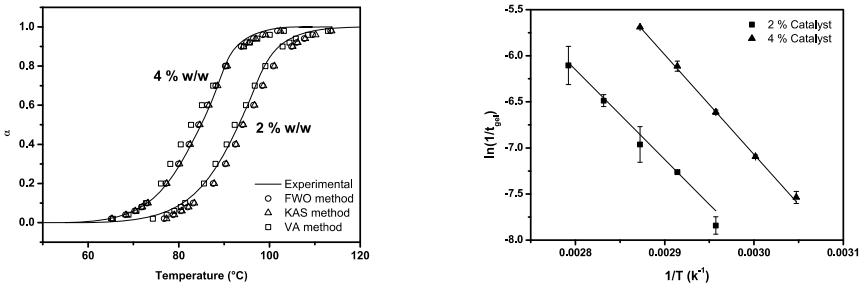

a) b)

Fig. 1. a) Experimental and predicted values of the curing degree of the FA resin with different amounts of catalyst, and a heating rate of 10 K.minute-[1], b) Experimental values of the gel time of the FA resin and fits to the Macosko model.

Three different cure cycles were employed to produce the composite plates (Fig. 2). The design of the cure cycles was performed in two stages. Firstly, the resin was cured until its gel point was reached; gel times for each temperature were calculated by the Macosko model obtained for this FA resin. During this first stage, a full vacuum was applied in the outer bag, and 60 % of the full vacuum was applied in the inner bag. Under these conditions, the inner bag was lifted up and it was in touch with a metal box. This creates an "empty" space where the "physical" water − water content from the resin and the catalyst added to the material − and the "chemical" water – water released during the curing reaction of the polymer from the condensation reaction that take place − can be removed from the composite plate. Secondly, the resin was cured for 30 minutes at 90 ºC until it was fully cured. During this stage, the vacuum was completely removed from the outer bag and it was increased in the inner bag until a full vacuum was reached. The inner bag was lowered becoming in touch with the plate and applied some pressure on the composite plate, therefore the second stage is somehow a consolidation stage of the material. A porous foil was used in the inner bag to let out the water produced in the surface of the material. Two temperatures, 60 ºC and 40ºC, which defined a short and long time cure cycle, were selected for the first stage of the cure cycle when using a low amount of catalyst (2 % w/w). A single cure cycle operating at 40ºC during the first stage of the cycle was tested using a 4 % w/w amount of catalyst. The highest temperature of the first stage used for 2 % w/w catalyst was not tested for the 4 % w/w due to the low time (20 minutes) required in reaching the gel point of the resin and the relatively long time required to prepare the samples. Thus, during the preparation of the sample the curing degree of the material could be quite advanced and an important part of the time before gelation consumed, reducing the time available during the cycle to remove the water content of the material.

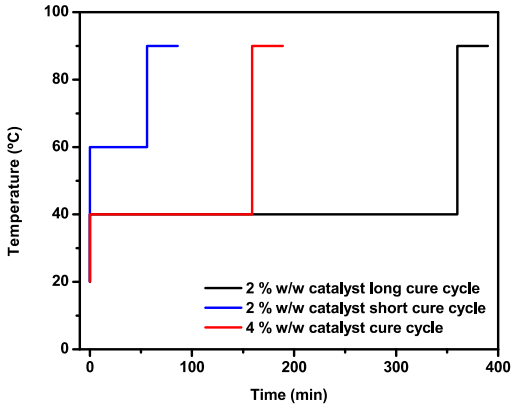

Fig. 2. Temperature profiles of the cure cycles used in the manufacturing of the composite plates by the DVB system.

A first device was manufactured according to the description of a DVB system (Fig. 3) to carry out the cure cycles for the manufacturing of the composite material. A perforated steel box was produced to hold the two stretchable plastic bags used as vacuum-bags, outer and inner, and sealed using sealing tape. A Ceran 500 heating plate was used as heat source to reach the required curing temperature of each cycle when using the DVB system (Fig. 3).

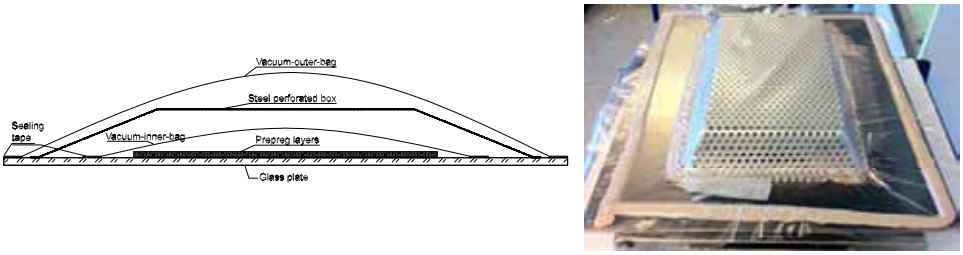

Fig. 3. DVB system: a) schematic assembly, b) and manufactured device. A heating plate was used as heat source (300x250 mm metal box).

This device presented several drawbacks that had to be solved. The heating system produced temperature gradients in the material therefore the curing of the material took place in a heterogeneous way. Also, the time required to reach the temperature until the second stage of the cure cycle was reached was quite long due to the lack of insulation of the operating environment (room temperature). Moreover, the high energy required to increase the temperature of the plate, which was increased partially by the low conductivity of the glass plate compared with other materials, also could produce a heat shock that could break the glass plate when non-special glass was used. Furthermore, the use of two vacuum bags led to a difficult to solve problem while conducting the experiments: leaks in the inner bag. Finally, the preparation of the samples took quite long times due to the difficulty of accomplishing all the parts of the DVB system.

In order to solve all the inconveniences caused by the first tested DVB system, a modification of the original DVB system also found in the literature was selected to carry out the manufacturing of the composite material (Fig. 4a) (Hou and Jensen 2008). A MMM-Vacucell vacuum oven was used as a substitute of the outer vacuum bag. Therefore, two of the problems found previously were solved: leaks were easily fixed since the single vacuum bag was accessible; the curing of the material was performed in a close homogeneous environment. In addition, the sealing of the first device was quite time-consuming. The time needed was reduced considerably by using four clamps to hold a new steel box for the modified DVB system (Figs. 4b-c). Another modification was that the original glass plate was substituted by a steel plate. However, beside the good thermal conductivity and thermal resistance of the steel plate, it presented two important new inconveniences. Firstly, the FA resin foamed intensively when it was in contact with the metal. This was solved by using a plastic coating. Secondly, the bottom surface of the plates produced contained a large amount of random bubbles and the steel plate did not allow observing how they were produced. Due to these problems and because the main drawbacks found previously for the glass plate were already solved, the steel plate was discarded and the original option of a glass plate was taken again.

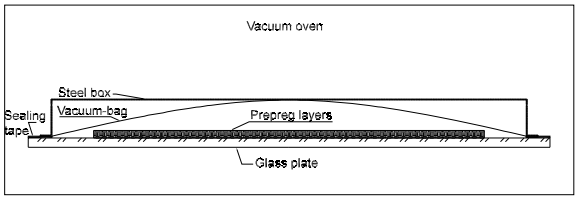

a)

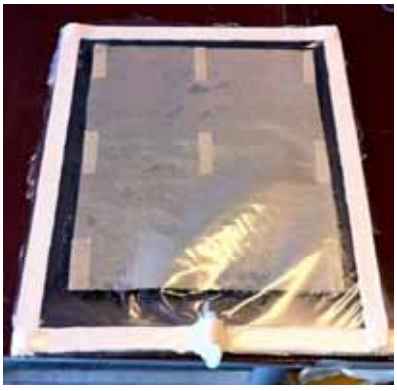

b)

c)

Fig.4. DVB system: a) schematic assembly of the concept implemented in a vacuum oven, b-c) and the manufacturing device.

Once the new system and the developed device were optimized, a series of experiments using the proposed cure cycles were performed. In Fig. 5, both sides of one of the resulting composite plates are shown.

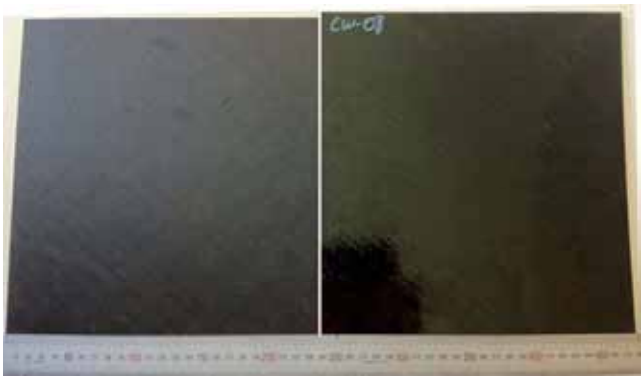

Fig. 5. Top (left) and bottom (right) of a composite plate produced using the double-vacuum-bag system inside a vacuum oven.

The manufactured plates will be cut into specimens that will be tested in tension, analyzed by microscopy, and their density and porosity content will be measured. At present, all these analyses have not been finished. However, some quantitative and qualitative information was extracted from the composite plates.

The mass loss of the plates, which is assumed to be mostly water released by the material, is about 5-6 % w/w, as shown in Table 1 for some of the samples produced. The total water content of the resin is predicted to be approx. 10 % w/w. Nonetheless, some of the water content remains trapped in the resin after its gelification, as mentioned. Therefore, a significant amount of water is removed by the modified DVB technique. The porosity of the samples, calculated through the density of the resin and the fibers, the area of the plates, and the weight fraction of resin and fibers, is lowered to below 5 %. Part of this porosity is caused by the hand-made layup, as it was identified when looking through the glass plate. This porosity produced during the hand-rolling of the layers of the material in the preparation of the pre-impregnated fibers can be reduced as more experience is accumulated but can only eliminated when the process is automated.

Table 1. Properties of the manufactured composite plates.

Sample	Dimensions of the plate (mm)	Fibre weigth fraction (%)	Mass loss (%)	Nominal porosity (%)
CW-06	320x260	43.9	5.5	25.5
CW-07	320x275	45.9	6.3	10.0
CW-08	305x280	42.5	5.3	2.5

The composite plates show a different color depending on the amount of catalyst used. Those plates manufactured using a 4 % w/w catalyst are significantly darker than when using a 2 % w/w catalyst. The colors obtained go from dark black to brown, respectively. This fact is in agreement with some results reported in previous works that showed a lower curing heat of the resin when the amount of catalyst was 2 % w/w (Domínguez and Madsen 2011). The lower curing heat was related to a lower cross-linking density of the material. The new findings support this previous assumption. However, when analyzing the results of the mechanical tests these assumptions will be more conclusive.

Finally, it is found that those plates produced with the higher amount of catalyst are clearly more

bent than those obtained using the lower amount of catalyst. Apparently, the bending of the plates also increases when the curing conditions during the first stage of the cure cycle are more intense, which is assumed to be related to the lower cross-linking density previously mentioned that leads to a lower shrinkage/expansion of the resin and lower accumulated stresses during the manufacturing of the material. A proposed solution to reduce/eliminate this bending is a post-curing process of the plates applying some pressure on them and using a slow cooling ramp.

5. FURTHER WORK

Once the selection of a proper manufacturing technique has been made, and a device is optimized to make the preparation of the sample as simple as possible and to carry out the curing of the material in a homogeneous way, some operating conditions, such as the temperature and pressure at each stage of the cure cycle, will be optimized to improve the final properties of the material and to reduce the energy consumption of the process. The optimization of these operating conditions has been traditionally performed by a trial-and-error methodology based on practical experience. However, this methodology is expensive and time-consuming, especially for new materials and manufacturing techniques, due to a lack of experience, which eventually will lead to unsuccessful results. Based on the present study, an experimental design methodology is proposed as a further investigation. This is a useful alternative to the trial-and-error methodology. A more scientific method based on a statistical approach is a design of experiments. This design can be use to obtain optimal values for the operating conditions.

Temperature at the first stage of the cure cycle, which in principle is more relevant than the post-gel curing stage, is one of the experimental variables proposed to be optimized; the pressure – vacuum level − during this stage is a second variable to study. Two levels, low and high, will be fixed for each variable – 2^2 tests −, and therefore a range of studies can be defined. In the case of temperature, the actual values, 40 and 60 ºC, are recommended to be selected as the low and high level, respectively. The vacuum level should be selected according to the boiling pressure of water at the highest operating temperature to avoid a too intense evaporation of the water released during the curing process. In addition, two central points and four star points should be performed to complete the ten tests needed for the design of experiments (Table 2).

Table 2. Proposed design of experiments.

Tests	Temperature (ºC)	Vacuum (atm)
2^2	40	0.40
	40	0.60
	60	0.40
	60	0.60
Central	50	0.50
	50	0.50
Starts	39.2	0.50
	60.8	0.50
	50	0.39
	50	0.61

The stiffness, strength, and density of the materials produced are some of the response variable that can be tested to identify the operating conditions that lead to a material with the best mechanical behavior. The dependence of these response variables on the operating conditions

will be identified through the contour surfaces obtained for all of them. These contour surfaces can be used as a powerful tool to design "ad hoc" composite materials with specific properties.

ACKNOWLEDGEMENTS

The authors are grateful for the support from "Ministerio de Educación" (Spanish Government) for financial support (Programa Nacional de Movilidad de Recursos Humanos del Plan Nacional de I-D+i 2008-2011). The research has been funded by the European Community's Seventh Framework Programme (FP7/2007-2013) under grant agreement nº 210037 (WOODY).

REFERENCES

Alonso, M.V., Oliet, M., Rodríguez, F., Astarloa, G., Echeverría, J.M. (2004). Use of a methylolated softwood ammonium lignosulfonate as partial substitute of phenol in resol resins manufacture. J. Appl. Polym. Sci. 94, 643-650.

Choura, M., Belgacem, N.M., Gandini, A. (1996). Acid-catalyzed polycondensation of furfuryl alcohol mechanisms of chromophore formation and cross-linking. Macromolecules. 29, 3839-3850.

Domínguez, J.C., Madsen, B. (2011). Furolite 050915A resin. Curing behaviour and chemorheology. Un-published Report, (Risø-DTU, Roskilde).

Gandini, A., Belgacem, M.N. (1997). Furans in polymer chemistry. Prog. Polym. Sci. 22, 1203-1379.

Guigo, N., Mija, A., Vincent, L., Sbirrazzuoli, N. (2010). Eco-friendly composite resins based on renewable biomass resources: Polyfurfuryl alcohol/lignin thermosets. Eur. Polym. J. 46, 1016-1023.

Hou, T.H., Jensen, B.J. (2008). Double-vacuum-bag technology for volatile management in composite fabrication. Polymer Composites. 29, 906-914.

Wewerka, E.M., Walters, K.L., Moore, R.H. (1969). Differential thermal analysis of furfuryl alcohol resin binders. Carbon. 7, 129-141.

Proceedings of the 32nd
Risø International Symposium on Materials Science:
Composite materials for structural performance:
Towards higher limits
Editors: S. Fæster, D. Juul Jensen,
B. Ralph, B.F. Sørensen
Risø National Laboratory for Sustainable Energy,
Technical University of Denmark, 2011

NEW DEVELOPMENTS FOR AN EFFICIENT SOLUTION OF THE DISCRETE MATERIAL TOPOLOGY OPTIMIZATION OF COMPOSITE STRUCTURES

P. Duysinx*, T. Gao*, W. Zhang**,
C. Fleury* and M. Bruyneel***

*LTAS University of Liege, Belgium
**Northwestern Polytechnical University, Xi'an, China
***SAMTECH s.a. Belgium

ABSTRACT

Optimal design of composite structures can be formulated as an optimal selection of material in a list of different laminates. Based on the seminal work by Stegmann and Lund (2005), the optimal problem can be stated as a topology optimization problem with multiple materials. The research work carries out a large investigation of different interpolation and penalization schemes for the optimal material selection problem. Besides the classical Design Material Optimization (DMO) scheme and the recent Shape Function with Penalization (SFP) scheme by Bruyneel (2011), the research introduces a generalization of the SFP approach using a bi-value coding parameterization (BCP) (Gao, Zhang, and Duysinx, 2011) The paper provides a comparison of the different parameterization approaches. It also proposes alternative penalization schemes and it investigates the effect of the power penalization. Finally, we discuss the solution aspects in the perspective of solving large-scale industrial applications. The conclusions are illustrated by a numerical application for the compliance maximization of an in-plane composite ply.

1. INTRODUCTION

Taking the best of composite material high strength and stiffness to weight ratios is essential to improve the efficiency of wind turbines and renewable energy systems. To this end, the discrete optimal orientation optimization is a fundamental problem of composite structure optimization, which can be applied to solve different problems of interest, for instance, the optimal orientation distribution problem of plies, or the optimal stacking sequence of multiple-layer laminated structures.

The Discrete Material Optimization (DMO) approach proposed by Stegmann and Lund (2005) has opened a breakthrough in composite optimization. The fundamental idea is to formulate the

composite optimization problem as an optimal material selection problem in which the different laminates and ply orientations are considered as different materials and to solve it as a topology optimization problem using continuous variables. This approach can be regarded as a generalization of the multi-phase topology optimization proposed in Thomsen (1992) and in Sigmund and Torquato (2000). To transform the discrete problem into a continuous one, one introduces a suitable parameterization to express the material properties as a weighted sum of the candidate material properties. Some difficulties of the discrete material selection using topology optimization are 1/ to find efficient interpolation and penalization schemes of the material properties and 2/ to be able to have efficient solution algorithms to handle very large scale optimization problems with many design variables. Besides the seminal work by Stegmann and Lund (2005), we extend and generalize the work by Bruyneel (2011) with the alternative SFP scheme by using a bi-value coding parameterization (BCP) (Gao, Zhang, and Duysinx, 2011). The present research work carries out a large investigation of different interpolation and penalization schemes for the optimal material selection problem. In particular, the work considers the solution aspects in the perspective of solving large-scale industrial applications.

2. DISCRETE MATERIAL OPTIMIZATION MODELS

The discrete optimal orientation design of the laminate can be treated as an optimization material selection problem with multiple materials. Following the idea by Lund and Stegmann (2005), the Discrete Material Optimization (DMO) consists in writing the linear anisotropic material stiffness matrix $\boldsymbol{C}_i$ of a composite ply noted 'i' as a weighted sum over the stiffness of some candidate materials {j} (i.e. plies with different orientations):

$$\mathbf{C}_i = \sum_{j=1}^{m} w_{ij} \mathbf{C}_i^{(j)}, \tag{1}$$

where the weighting function w_{ij} associated with the jth material phase should satisfy

$$0 \le w_{ij} \le 1 \qquad \sum_{j=1}^{m} w_{ij} \le 1 \qquad w_{ik} = 0 \left(k \ne j\right) \text{ when } w_{ij} = 1 \tag{2}$$

From the conditions (2), it comes that no additional constraint is needed to ensure the presence of a single material phase at each design element if one end up with a 0/1 design satisfying the constraints. This is achieved by using a penalization of the intermediate densities.

2.1 Discrete Material Optimization (DMO). Stegmann and Lund (2005) presented several Design Material Optimization (DMO) interpolation schemes, among which the most usual one (usually called DMO4) is:

$$w_{ij} = x_{ij}^p \prod_{\substack{\xi=1 \\ \xi \ne j}}^{m_v} \left(1 - x_{i\xi}^p\right) \quad \text{with} \quad 0 \le x_{ij} \le 1, \tag{3}$$

In this scheme, the number of design variables attached to each designable element or region just equals the number of candidate material phase, i.e., m_v=m. The design variables range from 0 to 1, meaning the presence or absence of material i. As in the SIMP method, the penalization factor p is applied to push the design variables to their extreme values 0 and 1.

2.2 Shape Function with Penalization (SFP). More recently, Bruyneel (2011) presented an alternative parameterization model named SFP based on the finite element shape functions. For a design problem with 0°, 90°, -45° and 45° plies, the shape functions of four-node finite elements are introduced as:

$$
\begin{aligned}
&w_{i1} = \left[\frac{1}{4}\left(1-x_{i1}\right)\left(1-x_{i2}\right)\right]^p \quad w_{i2} = \left[\frac{1}{4}\left(1+x_{i1}\right)\left(1-x_{i2}\right)\right]^p \\
&w_{i3} = \left[\frac{1}{4}\left(1+x_{i1}\right)\left(1+x_{i2}\right)\right]^p \quad w_{i4} = \left[\frac{1}{4}\left(1-x_{i1}\right)\left(1+x_{i2}\right)\right]^p \\
&-1 \le x_{ij} \le 1, \quad j = 1,2,3,4
\end{aligned}
\tag{4}
$$

Obviously, the SFP interpolation scheme also satisfies the conditions (2). As in the SIMP method, the penalization factor p is applied to push the design variables to their extreme values +/-1. When compared to the DMO scheme, SFP introduces only two variables for four fibre orientations. In SFP, the presence of one material phase is characterized by a specific combination of design variables taking bi-values of +1 and/or -1. The smaller number of design variables in SFP is an advantage over the DMO schemes to reduce the size of the optimization problem.

As indicated in Bruyneel (2011), even if it may be quite difficult, it is possible, in principle, to extend the SFP to more than four materials by building complex shape functions related to 'n' node finite elements satisfying the conditions (2).

2.3 Binary Coded Parameterization (BCP). The bi-valued coding parameterization (BCP) scheme generalizes the SFP scheme and provides an alternative to the classical DMO interpolation scheme. To overcome the shortcoming of the SFP scheme, one can abandon the idea of finite element shape functions and keep in mind only the idea of defining the shape function using bi-values of +1 and -1. Thus, a new BCP scheme is proposed here as the material parameterization model for 'm' material phases,

$$
w_{ij} = \left[\frac{1}{2^{m_v}} \cdot \prod_{k=1}^{m_v}\left(1+s_{jk}x_{ik}\right)\right]^p \quad \text{with} \quad -1 \le x_{ik} \le 1 \quad \text{and} \quad k = 1,\mathrm{L}\ ,m_v \tag{5}
$$

where m_v, the number of design variables is an integer defined by the ceiling function of $m_v = \log_2 m$. In other words, the BCP scheme makes it possible to interpolate between $2^{(m_v-1)}+1$ and 2^{m_v} material phases with m_v design variables. For example, for m_v=3 one can interpolate between m materials with 5≤m≤8. The s_{jk} values are given at Tables 1 and 2 for 2 and 3 binary coding variables. The values of s_{jk} are equal to 1 or -1. For m_v=2 obviously the BCP material parameterization recovers exactly the SFP scheme (4). To illustrate the "coding" clearly, a sketch is shown in Fig. 1. Each candidate material phase locates at the vertex of the square or of a cube in the 2D or 3D spaces.

Table 1 s_{jk} values (m_v=2, m=4)

k \ j	1	2	3	4
1	-1	1	1	-1
2	-1	-1	1	1

Table 2 s_{jk} values (m_v=3, m=8)

k \ j	1	2	3	4	5	6	7	8
1	-1	1	1	-1	-1	1	1	-1
2	-1	-1	1	1	1	1	-1	-1
3	-1	-1	-1	-1	1	1	1	1

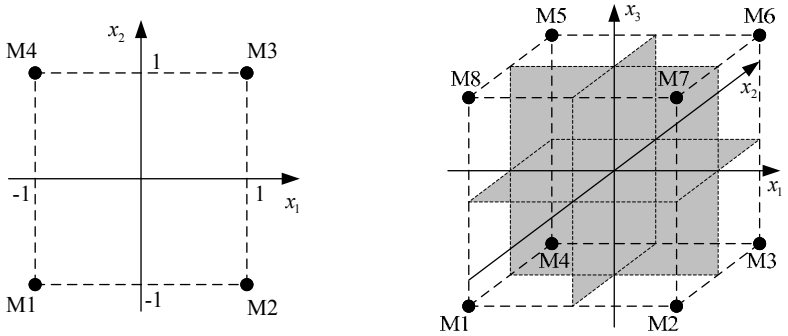

(a) m_v=2, m=4 (b) m_v=3, m=8

Fig. 1 Illustrations of the BCP scheme

2.4 Penalization of intermediate densities. In eq. (3), (4) and (5), the power penalization of intermediate is used to prevent the intermediate values of the design variables at the solution, and therefore to avoid any mixture of candidate materials in the final design. The power penalization with an exponent p (Bendsøe, 1989) is very convenient but this choice is not unique. Other penalization schemes have been explored successfully by the authors: If the intermediate values of a variable χ must be penalized, the following schemes have been investigated:

- SIMP $$f(\chi) = \chi^p \quad (6)$$
- RAMP (Stope and Svanberg, 2001) $$f(\chi) = \frac{\chi}{1 + p(1-\chi)} \quad (7)$$
- Halpin Tsai: (Halpin & Tsai, 1969) $$f(\chi) = \frac{r\chi}{(1+r)-\chi} \quad (8)$$
- Polynomial (Zhu, Zhang and Beckers, 2009) $$f(\chi) = \frac{\alpha - 1}{\alpha}\chi^p + \frac{1}{\alpha}\chi \quad (9)$$

Basically, one can find equivalent penalizations of intermediate densities by a proper choice of the penalization parameter in each scheme. For instance, the parameters p = 3 for SIMP, r = 0.269 for Halpin-Tsai and α = 16 for the polynomial scheme provide similar penalization schemes. Our numerical experiments showed that the different schemes conduct to similar results for equivalent penalization profiles. However when considering density dependent loads, one has to consider schemes with non-zero derivatives in zero density as pointed out by Bruyneel and Duysinx (2005). The authors also investigated continuation procedures in which the penalization is progressively increased. Despite the presence of many local optima, it was

not possible to find out a general strategy that improves the optimization process. The objective function was sometimes even worse when using a continuation approach.

3. LAMINATE STIFFNESS OPTIMIZATION PROBLEM

Here, the minimum compliance design of a laminated composite is considered with fibre angles to be optimized. With a discrete material parameterization , the optimization problem of a laminate can be stated as follows:

$$\begin{aligned} &\text{find:} && \{x_{ik}\} \quad (i=1,\mathrm{L}\ ,n;\ k=1,\mathrm{L}\ ,m_{\mathrm{v}}) \\ &\text{minimize:} && C=\mathbf{F}^{\mathrm{T}}\mathbf{u} \\ &\text{subject to:} && \mathbf{F}=\mathbf{K}\mathbf{u} \end{aligned} \tag{10}$$

One notices that no volume constraint is included because we consider an optimum orientation problem. For fixed loads, the sensitivity of the compliance can be generally expressed as:

$$\frac{\partial C}{\partial x_{ik}}=2\mathbf{u}^{\mathrm{T}}\frac{\partial \mathbf{F}}{\partial x_{ik}}-\mathbf{u}^{\mathrm{T}}\frac{\partial \mathbf{K}}{\partial x_{ik}}\mathbf{u}=-\mathbf{u}^{\mathrm{T}}\frac{\partial \mathbf{K}}{\partial x_{ik}}\mathbf{u} \tag{11}$$

For each finite element, the element stiffness matrix is calculated using one of the interpolation schemes (3), (4) or (5) so that the partial derivative can be calculated with:

$$\frac{\partial \mathbf{K}_i}{\partial x_{ik}}=\sum_{j=1}^{m}\frac{\partial w_{ij}}{\partial x_{ik}}\mathbf{K}_i^{(j)} \tag{12}$$

Obviously, from the sensitivity expression, the sensitivity $\partial C/\partial x_{ik}$ might be positive or negative due to the summation expression of the stiffness interpolation scheme, which means the objective function can be non-monotonous and many local solutions might exist. The large-scale optimization problem is solved by applying the well-known concept of sequential convex programming (SCP), in which one resorts to a sequence of convex subproblems of (10). In this paper, the structural analysis is carried out using SAMCEF finite element software and the MMA family optimizer by Bruyneel, Duysinx and Fleury (2002) is adopted to seek the optimal solution of each subproblem.

4. NUMERICAL APPLICATION

In this section, we consider one numerical application to illustrate and compare the different interpolation schemes. The maximum in-plane compliance problem (10) is solved by selecting the optimal orientation of the ply. An orthotropic composite material (whose properties are listed in Table 4). The local ply orientation can be searched in a list of discrete orientation angles (see Table 3). A square structural domain consisting of a single ply is considered (see Fig. 2). The model is meshed with 16×16 quadrangular finite elements. The structure is clamped along the left edge and a pin point vertical load is applied at the lower right corner. Besides, 16 separate designable patches are considered. This means that all elements of each patch have the same orientation, while the orientations might be different between patches. The DMO, SFP and BCP schemes are adopted to parameterize the material properties.

Design model with 4×4 patches Loads and boundary conditions

Fig. 2 Model of the square plate under vertical force

Table 3 Orientations

Number of material phases (m)	Number of design variables for each region (m_v)	Discrete orientation angle (°)
4	2	90/45/0/-45
9	4	80/60/40/20/0/-20/-40/-60/-80
12	4	90/75/60/45/30/15/0/-15/-30/-45/-60/-75

Table 4 Material properties

E_x	E_y	G_{xy}	v_{xy}
146.86GPa	10.62GPa	5.45GPa	0.33

The case of four orientations (m=4) is considered. For this problem, four design variables per patch are needed using the DMO scheme; while only two variables are required for SFP and BCP schemes. The optimization results by DMO, SFP and BCP schemes are given in Fig. 3. All solutions are nearly the same even though small differences exist. Actually, BCP and SFP schemes result in exactly the same solution because both schemes are identical in this particular case. The optimum compliance using the SFP/BCP scheme is a little better. However, the gradient-based algorithms used in the sequential convex programming optimization algorithms can not guarantee the global optimum convergence.

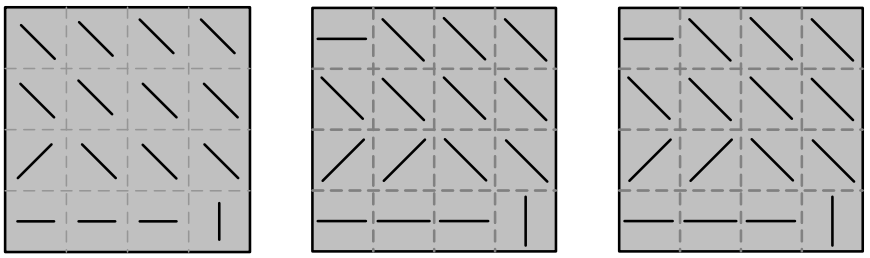

(a) DMO (C=1.220×10^{-4}) (b) SFP (C=1.182×10^{-4}) (c) BCP (C=1.182×10^{-4})

m_v=4 m_v=2 m_v=2

Fig. 3 Optimization results of the square plate under vertical force (m=4)

Using the BCP scheme, the iteration histories of the weights w_{ij} for patch 16 are plotted in

Fig. 4. At the starting point, all weights are exactly the same. Finally, the orientation -45° emerges as the optimum choice for this patch with a unit weight, while the weights of the other orientations gradually diminish to zero for the elimination of their effect.

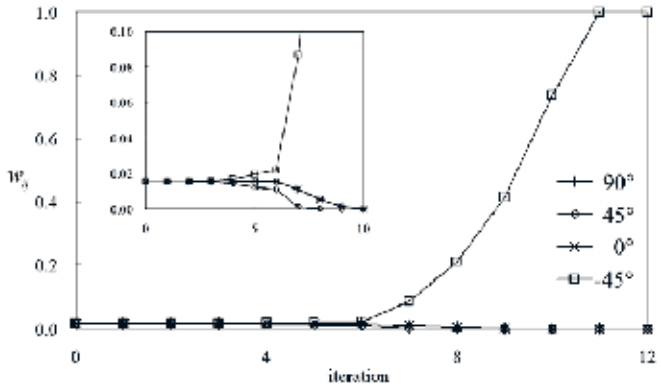

Fig. 4: Iteration histories of the weight for patch 16 (BCP m=4)

The influence of the penalization factor p on the optimization results is investigated in Fig. 5. For different values of p, the optimization iterations are quite stable, but the compliances and orientation layouts are different in the optimization results. As in topology optimization, a smaller penalization factor leads to stiffer design optimums. However, a too small penalization factor 'p' makes the optimization iteration converge quite slowly. In the cases of p=2 and p=1.5, the optimization processes have not converged after 30 iterations, while the other tests need about 10 to 15 iterations. Besides, there are still some patches consisting of "mixed" material for these two tests after even 50 iterations, as shown in Fig. 5. As a conclusion, the suggested value for the penalization factor is $p \in [2.5, 4]$.

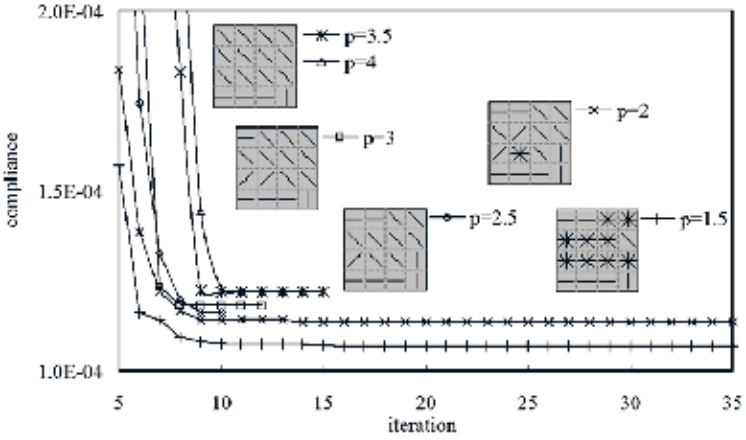

Fig. 5: Influence of the penalization factor p of the BCP scheme upon the optimization results

5. CONCLUSIONS

In this paper, we present a novel parameterization scheme based on a bi-value coding for solving the discrete material optimization of composite structures. With a reduced number of design variables, the BCP scheme generalizes the SFP scheme by Bruyneel (2011) and is a challenger to the classic DMO for large-scale problems. Furthermore, the BCP formulation provides a well-posed problem for an efficient solution using sequential convex programming algorithms. Different penalization functions of intermediate densities have been proposed and the choice of the penalization parameters has been discussed. The on-going work is devoted to extend the application of this novel parameterization scheme to larger problems involving industrial composite structures including compliance, displacement, stress constraints but also buckling and perimeter constraints.

ACKNOWLEDGEMENTS

This work was supported by the Walloon Region of Belgium and SKYWIN (Aerospace Cluster of Wallonia), through the project VIRTUALCOMP.

REFERENCES

Bendsøe, M. P. (1989). Optimal shape design as a material distribution problem. Structural Optimization, 1 (4), 193-202.

Bruyneel, M. (2011). SFP – a new parameterization based on shape functions for optimal material selection: application to conventional composite plies. Structural and Multidisciplinary Optimization. 43 (1), 17-27.

Bruyneel, M. and Duysinx, P. (2005). Note on topology optimization of continuum structure including self-weight. Structural and Multidisciplinary Optimization. 29 (4), 245-256.

Bruyneel, M. Duysinx, P., and Fleury, C. (2002) A family of MMA approximations for structural optimization. Structural and Multidisciplinary Optimization, 24 (4), 263-276.

Gao, T., Zhang, W. and Duysinx, P. (2011). A bi-value coding parameterization scheme for the discrete optimal orientation design of the composite laminate. Submitted for publication in Int. J. for Num. Methods in Engng.

Halpin, J.C. and Tsai, S.W. (1969). Effect of environmental factors on composite materials. AFML-TR, 67-423, June 1969.

Lund, E. and Stegmann, J. (2005). On structural optimization of composite shell structures using a discrete constitutive parametrization. Wind Energy, 8, 109-124

Sigmund O. and Torquato S. (2000). Design of materials with extreme thermal expansion using a three-phase topology optimization method. Journal of the Mechanics and Physics of Solids, 45 (6), 1037-1067.

Stegmann J. and Lund E. (2005). Discrete material optimization of general composite shell structures. Int. J. for Num. Methods in Engng. 62 (14), 2009-2027.

Stolpe M. and Svanberg K. (2001). An alternative interpolation scheme for minimum compliance topology optimization. Structural and Multidisciplinary Optimization, 22 (2), 116-124.

Thomsen, J. (1992). Topology optimization of structures composed of one or two materials, Structural Optimization, 5(1-2): 108-115.

Zhu, J., Zhang W., and Beckers P. (2009). Integrated layout design of multicomponent systems. Int. J. for Num. Methods in Engng, 78 (6), 631-651.

Proceedings of the 32nd
Risø International Symposium on Materials Science:
Composite materials for structural performance:
Towards higher limits
Editors: S. Fæster, D. Juul Jensen,
B. Ralph, B.F. Sørensen
Risø National Laboratory for Sustainable Energy,
Technical University of Denmark, 2011

PHYSICS-BASED FATIGUE LIFE PREDICTION OF COMPOSITE STRUCTURES

R.S. Fertig and D.J. Kenik

Firehole Composites, 210 South 3rd Street, Suite 202, Laramie,
WY 82010, USA

ABSTRACT

Widespread use of composite materials across many industries has created a need for modeling tools to accurately predict the behavior of structures comprised of these materials. In many applications, composite fatigue life is the primary factor limiting the design of a structure. However, commercial tools for predicting composite fatigue life have not been available. We present a multiscale physics-based fatigue life prediction methodology for composite structures that is computationally efficient, requires minimal fatigue characterization, and accounts for arbitrary loads and load histories. The approach has been developed to work seamlessly with structural finite element codes.

Because it is physics-bases, this method requires minimal composite characterization data. Furthermore, the method predicts fatigue life for any load history, load ratio, and loading mode. And it naturally accounts for the effects of mean stress and frequency variation on composite fatigue life. This method has been recently commercialized and is currently used to drive the fe-safe/Composites™ fatigue module. We present results using this tool where short beam shear fatigue life of a composite laminate is predicted based on lamina-level fatigue characterization.

1. INTRODUCTION

Composite materials are becoming ubiquitous in large structures such as wind turbine blades, airframes, racecars, and watercraft. Many of the applications for which composites are now used require the composite structure to perform under cyclic loading. Thus, fatigue life prediction in composite structures is an important part of composite design, but analysis tools have not been readily available until now.

For polymer-matrix composites, fatigue failure is primarily a matrix-dominated event. Fatigue

damage begins with microcrack accumulation in the polymer. These microcracks accumulate most rapidly in the early stages of fatigue life, with the accumulation rate slowing with increasing number of cycles. Ultimately, the microcracks coalesce to form a macroscopic crack that quickly causes catastrophic failure. Accurate fatigue life prediction thus requires capturing the accumulation of microcracks per cycle. The ultimate catastrophic failures typically fall into one of three categories: off-axis failure, on-axis failure, and delamination. The focus of the method described here is off-axis fatigue failure, which occurs when composite tensile loading is more than a few degrees from the fiber axis (Hashin & Rotem 1973). Ultimate failure is characterized by matrix cracking parallel to the fiber (Awerbuch & Hahn 1981; Petermann & Plumtree 2001) or by debonding between the fiber and matrix interface. In the case of a composite laminate, delamination is possible. We consider delamination as a final event so that results from accumulated matrix microcracking, thus accounting for the accumulation of matrix microcracks is sufficient for predicting fatigue failure due to delamination[1].

In this paper, we outline a methodology in which, composite fatigue is modeled as a matrix phenomenon using matrix-specific physics. After outlining this approach, it is used to predict short beam shear fatigue life using only interlaminar tension fatigue data for calibration, demonstrating the appropriateness of the applied physics.

2. MODEL DEVELOPMENT

2.1 Overview. Structural level, physics-based modelling of composite fatigue requires three separate modeling processes: a multiscale model to link composite stresses and strains to matrix stresses and strains, a physics-based model to predict fatigue damage of the matrix material, and a link between the physics-based model and the macroscopic fatigue failure of the composite. A portion of these modeling efforts have been described by Fertig (2009). Figure 1 shows a high-level overview of the information flow in this approach. First, a finite element (FE) model is used to compute composite stresses at the peak load P_{ref} of a fatigue cycle. The element stresses from the FE model results are extracted for use in the physics-based methodology described in this paper, which is encapsulated in the software module, fe-safe/Composites™. As shown in Figure 1, the only required inputs to the model are composite strengths, the elastic properties of the composite and its constituents, fatigue material properties extracted from a single calibration S-N curve, and the load history $P(t)$.

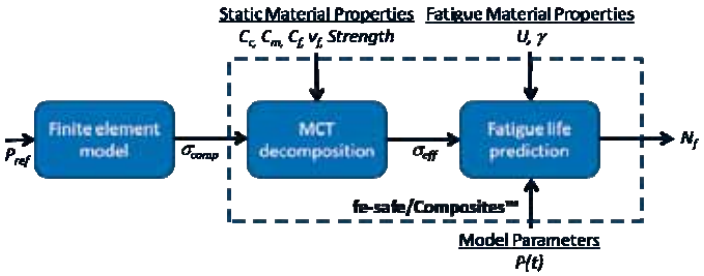

Fig. 1. Schematic showing the processes involved in predicting composite fatigue failure using fe-safe/Composites®.

[1] In the case where delaminations are present *before* initiation of fatigue loading, built-in FEA tools for crack propagation should be used rather than Helius:Fatigue.

The multiscale modeling approach employed for linking composite stress/strain behavior with constituent stress/strain behavior is multicontinuum theory (MCT). Briefly, MCT provides an exact mapping of volume average composite stresses/strains to volume average constituent stresses/strains. So any arbitrarily complex composite stress state can be mapped to its corresponding matrix stress state. This matrix stress is converted to an effective matrix stress that can be used in an appropriate physics-based model.

The relevant physics describing the fatigue of a polymer matrix is the kinetic theory of fracture (KTF) (Regel & Tamuzh 1977; Regel, Lekovskii, Slutsker & Tamuzh 1972; Kireenko, Lekovskii & Regal 1971; Sauer & Richardson 1980; Coleman 1956), which treats fracture as a thermally activated process. We modify the baseline equations of KTF in order to accurately model the effect of different stress ratios on fatigue loading.

Using KTF in conjunction with MCT gives a rate of microcrack accumulation in the matrix. The remaining effort is to link the bond breaking rate with a macroscopic measurement of composite damage. We extend the work of Hansen and Baker-Jarvis (1990) and use a damage parameter n that describes microcrack density accumulated as a percentage of the microcrack density at failure.

These steps are outlined in the subsections below.

2.2 Multicontinuum theory. Multicontinuum theory, as developed for two-constituent composite materials by Garnich and Hansen (1997a, 1997b), provides an elegant and computationally-efficient method to extract volume-averaged stresses of the matrix and fiber from the composite stress state. Here we are interested in matrix-dominated fatigue failure, so the average matrix stress is the physically- relevant parameter. The exact value of average stress in the matrix $\boldsymbol{\sigma}_\mathbf{m}$ can be written as:

$$\boldsymbol{\sigma}_\mathbf{m} = \mathbf{Q}_\mathbf{m}\boldsymbol{\sigma}_\mathbf{c} - \boldsymbol{\psi}_\mathbf{m}(\Delta T) \tag{1}$$

Where:

$$\begin{aligned}
\mathbf{Q}_\mathbf{m} &= \mathbf{C}_\mathbf{m}\left\{\mathbf{C}_\mathbf{c}\left(\phi_m\mathbf{I} + \phi_f\mathbf{A}\right)\right\}^{-1} \\
\boldsymbol{\psi}_\mathbf{m} &= \mathbf{C}_\mathbf{m}\left\{\phi_f\left[\left(\mathbf{C}_\mathbf{c} - \mathbf{C}_\mathbf{f}\right)\left(\phi_m\mathbf{I} + \phi_f\mathbf{A}\right)\right]^{-1}\mathbf{a} + \boldsymbol{\eta}_\mathbf{m} - \left(\phi_m\mathbf{I} + \phi_f\mathbf{A}\right)^{-1}\boldsymbol{\eta}_\mathbf{c}\right\} \\
\mathbf{A} &= -\frac{\phi_m}{\phi_f}\left(\mathbf{C}_\mathbf{c} - \mathbf{C}_\mathbf{f}\right)^{-1}\left(\mathbf{C}_\mathbf{c} - \mathbf{C}_\mathbf{m}\right) \\
\mathbf{a} &= \mathbf{C}_\mathbf{c}\boldsymbol{\eta}_\mathbf{c} - \phi_f\mathbf{C}_\mathbf{f}\boldsymbol{\eta}_\mathbf{f} - \phi_m\mathbf{C}_\mathbf{m}\boldsymbol{\eta}_\mathbf{m}
\end{aligned} \tag{2}$$

In Equations (1) and (2) boldface variables indicate non-scalar quantities, $\boldsymbol{\sigma}_\mathbf{c}$ is the six-component composite stress vector; ΔT is the temperature change from the stress-free state; $\mathbf{C}_\mathbf{i}$ ($i = c, f, m$) are the reduced stiffness matrices for composite, fiber, and matrix, respectively; ϕ_f and ϕ_m are the fiber and matrix volume fractions, respectively; and $\boldsymbol{\eta}_\mathbf{i}$ ($i = c, f, m$) are the thermal expansion coefficients of the composite, fiber, and matrix, written as six-component strain vectors where the shear components are zero.

In order for the matrix stress obtained in Equation (1) to be used in the kinetic theory of fracture, it must be mapped to an effective stress. This is procedure has been described elsewhere (Fertig 2009). Essentially, the strength-life equal rank assumption is employed such that a failure criterion that utilizes matrix-averaged stresses is converted to an effective stress

$$\sigma_{eff} = \sqrt{A_t \{I_{m,t}\}^2 + \sigma_{m,12}^2 + \sigma_{m,13}^2 + A_S \left(\tfrac{1}{4}\left(\sigma_{m,22} - \sigma_{m,33}\right)^2 + \sigma_{m,23}^2\right)}, \quad (3)$$

where A_S and A_t are functions of static failure coefficients, $\sigma_{m,ij}$ is the *ij*-component of the matrix stress tensor, and I_t is the maximum matrix tensile stress normal to the fiber direction. This effective matrix stress is used to drive the physics-based equations described below.

2.3 Kinetic theory of fracture. The kinetic theory of fracture (KTF) describes the process of bond breaking via thermally activated processes. Our composite fatigue methodology uses KTF to predict fatigue failure in the matrix constituent, which translates to composite failure. KTF for polymers has been described in detail in the published literature (Regel & Tamuzh 1977; Kireenko et al. 1971; Regel', Pozdnyakov & Amelin 1975; Regel 1971; Coleman 1956; Zhurkov 1965). We briefly outline its development here.

All atoms and molecules at temperatures greater than absolute zero oscillate with a frequency proportional to $\frac{kT}{h}$ given by Planck's Law, where h is Planck's constant and kT is the thermal energy, described by the product of the Boltzmann constant k and the absolute temperature T. But because the thermal energy associated with oscillation is not a single number but rather a distribution, there is always a statistical likelihood that any given oscillation will have sufficient energy to overcome an energy barrier U to move from one equilibrium state to another. The likelihood of this occurring for any oscillation is given by the familiar exponential form $\exp\left(-\frac{U}{kT}\right)$. Thus, the rate of any thermally activated process can be written simply as:

$$K = \frac{kT}{h}\exp\left(-\frac{U}{kT}\right). \quad (4)$$

For the purposes of fracture and fatigue, one equilibrium state is the un-microcracked state and the other is the microcracked state. The process is illustrated schematically in Figure 2 (left).

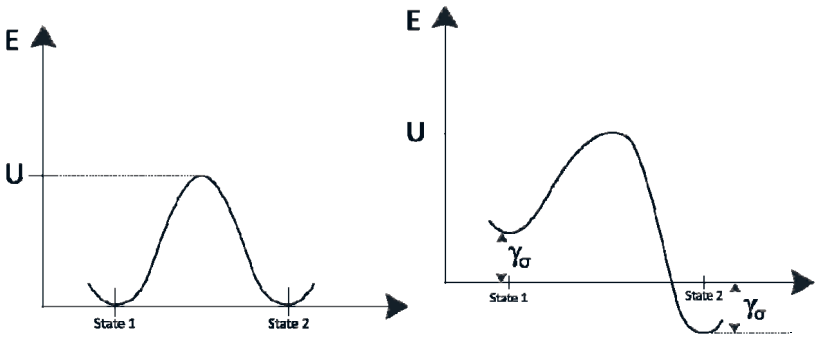

Fig. 2. (Left) Energy barrier with activation energy U for transition from State 1 to State 2. (Right) Energy barrier with activation energy U-γσ for transition from State 1 to State 2.

Now consider the effect of an applied stress on the bond breaking rate described in equation (4). in this context it is more helpful to think of stress in terms of energy per unit volume rather than

force per unit area. thus, if the stress is acting to facilitate the bond-breaking process it should reduce the energy barrier to bond-breaking. The amount of this reduction depends on the volume of material γ, the activation volume[2], over which the process occurs so that the reduction in the activation energy is simply the product of activation volume and the stress. Figure 2 (right) shows how an applied stress modifies the activation energy. Taking the activated process to be microcrack accumulation and modifying Equation (4) to reflect the effect of an applied time-varying stress gives:

$$K_b(t) = \frac{kT}{h}\exp\left(-\frac{U-\gamma\sigma(t)}{kT}\right), \tag{5}$$

which is the baseline KTF equation for predicting composite fatigue. Equation (3) is used to map the average matrix stress tensor into an effective stress that is used in Equation (5).

We now turn to the problem of how to account for oscillating stress. The nomenclature of stress ratio R and mean stress σ_m are typically introduced to describe simple sinusoidal loadings that vary from some minimum stress σ_{min} to some maximum stress σ_{max}, where rupture rate. This method successfully predicted the strength of polymers subjected to a wide range of stress rates.

We use a differential equation describing the evolution of n that is similar to the one proposed by Hansen and Baker-Jarvis:

$$\frac{dn}{dt} = (n_0 - n)^{\lambda} K_b, \quad n(0) = 0. \tag{6}$$

n_0 is a parameter that is determined by enforcing the condition:

$$\int_0^1 \frac{dn}{(n_0 - n)^{\lambda}} = 1 \tag{7}$$

Combining Equations (9) and (5) and assuming a constant nominal temperature gives the starting equation for determining the fatigue life of a polymer:

$$\frac{dn}{dt} = (n_0 - n)^{\lambda} \frac{kT}{h}\exp\left(-\frac{U-\gamma\sigma(t)}{kT}\right), \quad n(0) = 0 \tag{8}$$

Solving Equation (8) yields the evolution of the damage parameter with time, which can be written as:

$$\begin{aligned} n(t) &= n_0\left(1 - \exp\left\{-\frac{kT}{h}\exp\left(\frac{-U}{kT}\right)\int_0^t \exp\left(\frac{\gamma\sigma_{eff}(\tau)}{kT}\right)d\tau\right\}\right), \quad \lambda = 1 \\ n(t) &= n_0 - \left\{n_0^{1-\lambda} - (1-\lambda)\frac{kT}{h}\exp\left(\frac{-U}{kT}\right)\int_0^t \exp\left(\frac{\gamma\sigma_{eff}(\tau)}{kT}\right)d\tau\right\}^{\frac{1}{1-\lambda}}, \quad \lambda \neq 1 \end{aligned} \tag{9}$$

In order to use Equation (9) to predict fatigue failure, the values of U and γ must be calibrated. This is accomplished by calibrating Equation (9) to a single off-axis S-N curve.

---

[2] The precise definition of activation volume is somewhat ambiguous for the process of polymer fracture because it is much larger than, say, the atomic volume. Thus, it is typically only defined as the volume over which the activated process occurs.

3. VALIDATION: PREDICTION OF SHORT BEAM SHEAR FATIGUE LIFE

To demonstrate the capability of this methodology, we use it to predict the fatigue life of a short beam shear specimen and compare these results with experimental results from Makeev Nikishkov, Seon & Lee,(2009). A finite element model of the short beam shear specimen was created in Abaqus according to the geometric descriptions described by Makeev et al (2009). Figure 4 shows an illustration of this model. The FE model was run for applied loads of varying magnitude corresponding to peak loads of sinusoidal load histories with f = 10 Hz and R = 0.1. The results of the finite element analysis were used by fe-safe/Composites™, which embodies the methodology described in this paper, to predict fatigue life:

$$\begin{aligned} R &= \frac{\sigma_{\min}}{\sigma_{\max}} \\ \sigma_m &= \frac{\sigma_{\min} + \sigma_{\max}}{2} \end{aligned} . \tag{10}$$

Consider the load histories shown in Figure 3 for R = 0.1 and R = 0.6. It can be shown by integrating Equation (7) that for the same σ_{max} the average bond breaking rate $\langle K_b \rangle$ is greater for R = 0.6 than for R = 0.1. Thus KTF as presented in Equation (5) predicts that increasing the mean stress by increasing σ_{min} would increase the mean bond breaking rate for a fixed σ_{max}, which would result in a shortening of the fatigue life with an increasing value of R. But experiments on unidirectional composites have shown that an increase in σ_{min} causes an *increase* in the fatigue life (Kawai & Suda 2004). Thus, the oscillatory nature of the stress presents an additional physical phenomenon that is not present under constant load.

The additional physical feature is the temperature change in the polymer during cycling. Experiments on pure polymers have shown that significant heating of the polymer occurs with an increase in the oscillating stress amplitude (Sauer & Richardson 1980; Kireenko, Leksovskii & Regel, 1971) or an increase in the frequency (Sauer, Foden & Morrow, 1977). In order for kinetic theory to properly predict the fatigue life for any load history, this temperature increase must be accounted for. For a sinusoidal cycle, the rate of energy dissipated per second $\dot{E}$ is given by (Sauer & Richardson 1980):

$$\dot{E} = \pi f J'' \sigma_a^2, \tag{11}$$

Where f is the oscillation frequency, J'' is the loss compliance, and σ_a is the stress amplitude. We assume that the temperature increase is proportional to the energy dissipated. The temperature T used in Equation (5) is calculated from the nominal temperature T^* such that:

$$T = T^* + \psi \sum_{i=1}^{n} \frac{\left(\Delta\sigma_{eff}\right)^2}{\Delta t} , \tag{12}$$

Where ψ is a constant of proportionality, $\Delta\sigma_{eff}$ is the magnitude of effective stress change over a span of time Δt, and n is the number of different stress ranges per cycle.

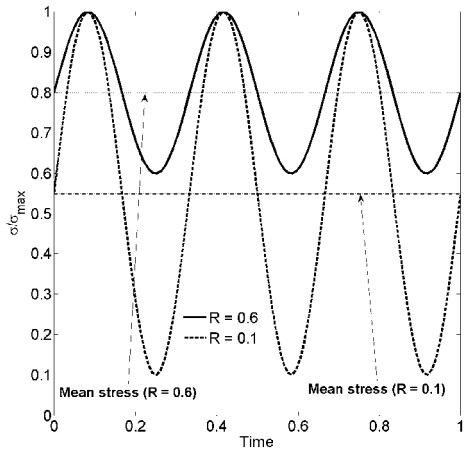

Fig. 3. Two load histories with the same maximum stress but different values of R and mean stress.

3.1 Fatigue damage accumulation in a composite. The final piece of the composite fatigue puzzle is linking the rate of microcrack accumulation with macroscopic failure of the composite. Hansen and Baker-Jarvis (1990) linked KTF with macroscopic damage by introducing a damage parameter *n* that represented the percentage of microcrack density relative to the microcrack density at failure. The damage variable, which represents the fraction of microcrack density required for macroscopic fracture, is zero initially and is unity at failure. In their formulation, they introduced a differential equation for the evolution of a damage variable *n* with time *t*, where the evolution of the damage variable is directly related to the bond rupture rate. This method successfully predicted the strength of polymers subjected to a wide range of stress rates.

We use a differential equation describing the evolution of *n* that is similar to the one proposed by Hansen and Baker-Jarvis

$$\frac{dn}{dt} = \left(n_0 - n\right)^{\lambda} K_b, \quad n(0) = 0. \tag{9}$$

n_0 is a parameter that is determined by enforcing the condition

$$\int_0^1 \frac{dn}{\left(n_0 - n\right)^{\lambda}} = 1 \tag{10}$$

Combining Equations (9) and (5) and assuming a constant nominal temperature gives the starting equation for determining the fatigue life of a polymer.

$$\frac{dn}{dt} = \left(n_0 - n\right)^{\lambda} \frac{kT}{h} \exp\left(-\frac{U - \gamma\sigma(t)}{kT}\right), \quad n(0) = 0 \tag{11}$$

Solving Equation (11) yields the evolution of the damage parameter with time, which can be written as:

$$\begin{aligned} n(t) &= n_0\left(1 - \exp\left\{-\frac{kT}{h}\exp\left(\frac{-U}{kT}\right)\int_0^t \exp\left(\frac{\gamma\sigma_{eff}(\tau)}{kT}\right)d\tau\right\}\right), \quad \lambda = 1 \\ n(t) &= n_0 - \left\{n_0^{1-\lambda} - (1-\lambda)\frac{kT}{h}\exp\left(\frac{-U}{kT}\right)\int_0^t \exp\left(\frac{\gamma\sigma_{eff}(\tau)}{kT}\right)d\tau\right\}^{\frac{1}{1-\lambda}}, \quad \lambda \neq 1 \end{aligned} \tag{12}$$

In order to use Equation (12) to predict fatigue failure, the values of U and γ must be calibrated. This is accomplished by calibrating Equation (12) to a single off-axis S-N curve.

4. VALIDATION: PREDICTION OF SHORT BEAM SHEAR FATIGUE LIFE

To demonstrate the capability of this methodology, we use it to predict the fatigue life of a short beam shear specimen and compare these results with experimental results from Makeev et al. (2009). A finite element model of the short beam shear specimen was created in Abaqus according to the geometric descriptions described by Makeev et al, (2009). Figure 4 shows an illustration of this model. The FE model was run for applied loads of varying magnitude corresponding to peak loads of sinusoidal load histories with f = 10 Hz and R = 0.1. The results of the finite element analysis were used by fe-safe/Composites™, which embodies the methodology described in this paper, to predict fatigue life.

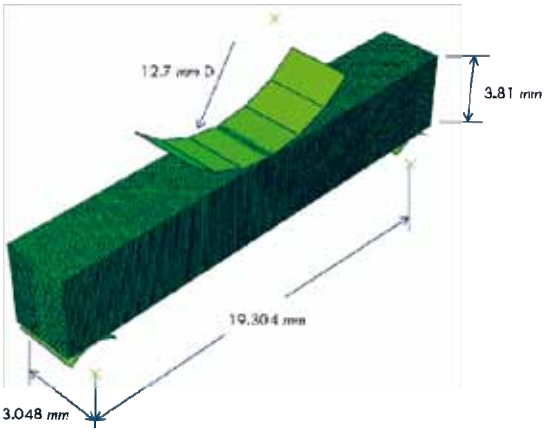

Fig. 4. Illustration of the short beam shear finite element model.

The composite material modelled was the carbon/epoxy IM7/8552 material system. Composite properties for this system are given in Table 1 and come from the reported properties by Makeev et al (2009). Constituent properties, also shown in Table 1, come from previous analyses using similar materials. The tensile and compressive transverse composite strengths along with the in-plane shear strength are also required for the fatigue analysis. These values were taken to be: ${}^{+}S_{22}$ = 82.7 MPa, ${}^{-}S_{22}$ = 260.0 MPa (taken from a similar material), and S_{12} = 110.0 MPa. In addition to static properties, lamina fatigue calibration data is required to properly calibrate the parameters in the KTF equations. The interlaminar tension fatigue data presented by Makeev et al, (2009) were used to calibrate the model parameters.

Material	**E_{11} (GPa)**	**$E_{22} = E_{33}$ (GPa)**	**$\nu_{12} = \nu_{13}$**	**ν_{23}**	**$G_{12} = G_{13}$ (GPa)**
Composite	154	8.96	0.32	0.5	5.32
Fiber	268	15	0.23	0.2	49
Matrix	3.3	3.7	0.43	0.37	1.6

Table 1. Elastic material properties for the IM7/8552 composite and its constituents.

Using fe-safe/Composites™ in conjunction with Abaqus, contour plots of the fatigue life in the short beam shear tests were generated. The contour plot for a maximum stress of 55 MPa (calculated according to the method described by ASTM D 2344 (2006) is shown in Figure 5. The number of cycles to failure for the specimen was taken to be the lowest number of cycles along a vertical line equidistant between the center load point and the support (shown in Figure 5).

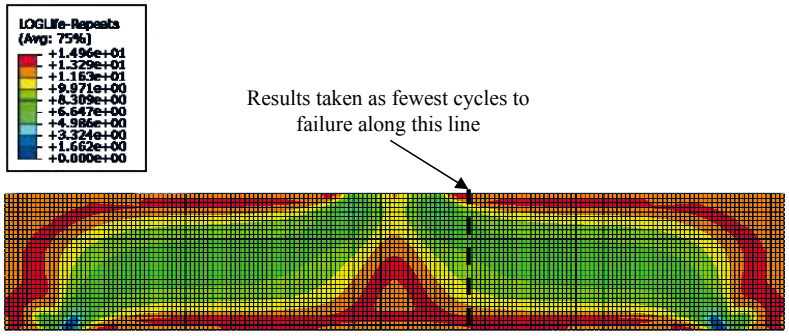

Fig. 5. Contour of the number of cycles to failure for S_{max} = 55 MPa**.**

Figure 6 shows the predicted number cycles to failure computed for various peak loadings compared with the published data from Makeev et al. (2009). Although the model prediction is slightly conservative, the agreement is remarkable. *Tension* fatigue data was used to calibrate the model; but the model was successfully used to predict *shear* behavior. This excellent correlation with experiment suggests that the composite physics is being correctly modeled and opens the door to accurate fatigue prediction for larger composite structures.

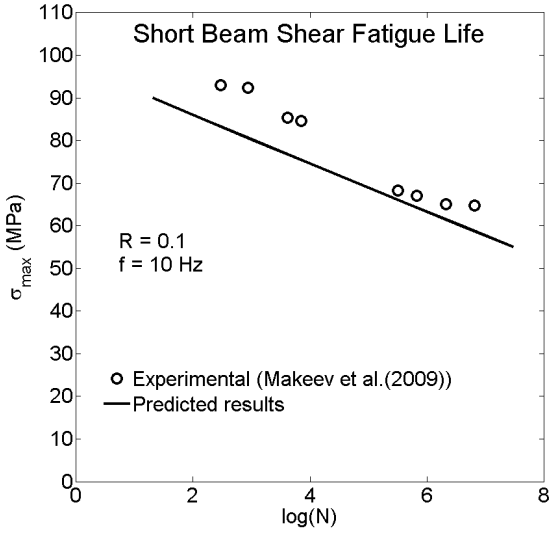

Fig. 6. Comparison of predicted fatigue life with experimental values

5. SUMMARY AND CONCLUSIONS

We have outlined a physics-based model that is computationally efficient and is easily incorporated into finite element modeling. The framework presented in this paper is commercially packaged as Helius:Fatigue™ and is used to power the fe-safe/Composites® module. The methodology utilizes multicontinuum theory to extract the matrix stress in the composite from the composite stress state. The kinetic theory of fracture was chosen to model the appropriate physics of composite fatigue, where the matrix stress is used to drive the fatigue of the composite.

This methodology was used to predict the short beam shear fatigue life given only standard static composite properties and a single interlaminar tension curve. Excellent agreement was obtained between model results and experiment, suggesting that the applied physics is appropriate and that the method is suitable for fatigue modelling of larger composite structures.

REFERENCES

ASTM D2344/D2344M-00, (2006). Standard Test Method for Short-Beam Strength of Polymer Matrix Composite Materials and Their Laminates,

Awerbuch, J. & Hahn, H., (1981). Off-axis fatigue of graphite/epoxy composite. In San Francisco: ASTM, pp. 243-273.

Coleman, B., (1956). Time dependence of mechanical breakdown phenomena. Journal of Applied Physics, 27(8), pp.862-866.

Fertig, R., (2009). Bridging the gap between physics and large-scale structural analysis: a novel method for fatigue life prediction of composites. In: SAMPE Fall Technical Conference Proceedings: Global Material Technology: Soaring to New Horizons, Wichita, KS, October 19-22, (2009). Society for the Advancement of Material and Process Engineering, CD-ROM—14pp.

Garnich, M.R. & Hansen, A.C., (1997). A Multicontinuum Approach to Structural Analysis of Linear Viscoelastic Composite Materials. Journal of Applied Mechanics, 64(4), pp.795-803.

Garnich, M. & Hansen, A., (1997). A Multicontinuum Theory for Thermal-Elastic Finite Element Analysis of Composite Materials. Journal of Composite Materials, 31(1), pp.71-86.

Hansen, A. & Baker-Jarvis, J., (1990). A rate dependent kinetic theory of fracture for polymers. International Journal of Fracture, 44, pp.221-231.

Hashin, Z. & Rotem, A., (1973). A fatigue failure criterion for fiber reinforced materials. Journal of Composite Materials, 7, p.448.

Kawai, M. & Suda, H., (2004). Effects of non-negative mean stress on the off-axis fatigue behavior of unidirectional carbon/epoxy composites at room temperature. Journal of Composite Materials, 38, pp.833-854.

Kireenko, O.F., Leksovskii, A.M. & Regel', V.R., (1971). Polymer fractography and fracture kinetics 3. Fractographic method of estimating the local heating at the ends of cracks in cyclically loaded polymers. Mechanics of Composite Materials, 7(5), pp.776-780.

Makeev, A. et al., (2009). Fatigue structural substantiation for thick composites. In: Proceedings of ICCM-17 17th International Conference on Composite Materials. ICCM-17 17th International Conference on Composite Materials. Edinburgh, UK.

Petermann, J. & Plumtree, A., (2001). A unified fatigue failure criterion for unidirectional laminates. Composites: Part A, 32, pp.107-118.

Regel, V.R. & Tamuzh, V.P., (1977). Fracture and fatigue of polymers and composites (survey). Mechanics of Composite Materials, 13(3), pp.392-408.
Regel', V.R. et al., (1972). Polymer breakdown and fatigue. Mechanics of Composite Materials, 8(4), pp.516-527.
Regel', V.R., Pozdnyakov, O.F. & Amelin, A.V., (1975). Investigation of the processes of thermal and mechanical degradation of polymers using mass spectrometers. Review. Mechanics of Composite Materials, 11(1), pp.13-26.
Regel, V., (1971). Kinetic theory of strength as a scientific basis for predicting the lifetime of polymers under load. Mechanics of Composite Materials, 7(1), pp.82-93.
Sauer, J. & Richardson, G., (1980). Fatigue of polymers. International Journal of Fracture, 16(6), pp.499-532.
Sauer, J., Foden, E. & Morrow, D., (1977). Influence of Molecular Weight on Fatigue Behavior of Polyethylene and Polystyrene. Polymer Engineering & Science, 17(4), pp.246-250.
Zhurkov, S., (1965). Kinetic Concept of the Strength of Solids. International Journal of Fracture, 1, pp.311-323.

Proceedings of the 32nd
Risø International Symposium on Materials Science:
Composite materials for structural performance:
Towards higher limits
Editors: S. Fæster, D. Juul Jensen,
B. Ralph, B.F. Sørensen
Risø National Laboratory for Sustainable Energy,
Technical University of Denmark, 2011

CORRUGATED COMPOSITES AS FLEXIBLE STRUCTURES THEORY AND FEM ANALYSIS

P. Ghabezi and M. Golzar

Department of Mechanical Engineering, Tarbiat Modares University,
Tehran, Iran.P.O.Box 14115-143

ABSTRACT

Corrugated structures are flexible in one direction and stiff in the transverse direction. They could have wide applications in engineering and science. The bidirectional stiffness properties are due to special geometries of corrugations. In this paper, the elongation and equivalent stiffness in longitudinal and transverse directions of different corrugated structures (trapezoidal, rectangular, triangular and sinusoidal) and flat composites are calculated and compared together. Different geometries are investigated for a unidirectional composite of E-glass/Epoxy. FEM models were used to simulate the characteristics of the corrugated composites. Results of FEM and analytical simulation show that how the corrugated composite can afford obviously larger deformation than the flat one.

1. INTRODUCTION

Corrugated structures are widely used as the cores of the sandwich structures (e.g. sandwich composites and card board)(Torre and Kenny 2000). In engineering such structures have been used over many decades in civil, naval, automotive and aerospace applications due to their efficient performance, i.e. low mass to stiffness (along corrugations) ratio (Sun and Spencer 2005, Perel and Libove 1978, Shanley 1947). The crushing and buckling behavior of corrugated structures made from composite materials such as tubes and panels respectively has been analyzed by (Abdewi, Sulaiman, Hamouda and Mahdi 2008) and (Rao 1987). Some studies have been undertaken on composite corrugated aircraft box structures with a consideration for energy absorption during impact (Wiggenraad, Michielsen Santoro, Lepage, Kindervater and Beltran 1999, Wiggenraad, Santoro, Lepage, Kindervater and Climent Mañez 2001). More recently, composite corrugated laminates have been suggested for use as an aircraft morphing wing skin solution (Yokozeki, Takeda, Ogasawara and Ishikawa 2006, Thill, Etches, Bond, Potter, Weaver 2007,2008).Because of their extremely anisotropic behavior: they are stiff along the corrugations and relatively compliant transverse to the corrugation direction. Corrugated composites may be applicable to morphing wing structures in the manner that the corrugation direction aligns to the chord direction. Morphing wings manufactured from corrugated

composites are expected to withstand the bending loads in the span direction and change shape easily in the chord direction.

2. ANALYTICAL MODEL

Corrugated composites can be designed depending on the corrugated appearance (e.g. wave height, wave spacing). A simple analytical model is developed to predict longitudinal and transverse stiffness of the corrugated structure. For evaluation of the effective stiffness of a laminate, one can calculate the effective extensional (A_{11} and A_{22}) and flexural (D_{11} and D_{22}) stiffness of the fabrics.

The extensional stiffness matrix [A] relates the resultant in-plane forces to the in-plane strains, and the bending stiffness matrix [D] relates the resultant bending moments to the plate curvatures. The coupling stiffness matrix [B] couples the force and moment terms to the mid-plane strains and mid-plane curvatures. Fig 1 shows analytical area of a sinusoidal element. The effective properties of the corrugated composites are formulated using the effective properties of fabrics and geometric parameters. In the perpendicular direction of the corrugation, the effective extensional and flexural properties of the corrugated composites can be evaluated by considering the volume fraction and the moment of inertia of the fabrics in the analytical area, respectively. The effective properties in the direction of corrugations can be predicted based on Castigliano's theorem using a curved Bernoulli–Euler beam as shown in Fig. 2.

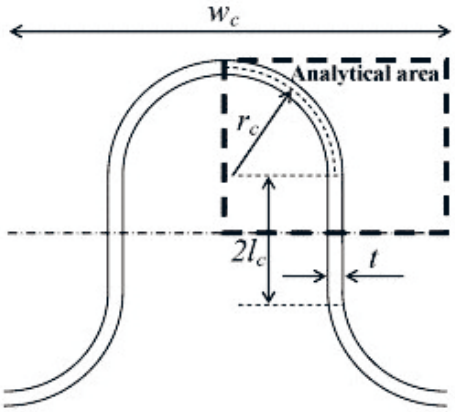

Fig. 1. Sinusoidal element.

In this paper the direction of the wave and perpendicular of the wave direction called longitudinal and transverse directions, respectively. In order to predict the longitudinal modulus of corrugated composites, a curved Bernoulli–Euler beam is considered as shown in Fig 2. Calculation of the deflection or rotation angle at the end point of the beam leads to a formulation of the longitudinal modulus based on Castigliano's theorem. The deflection of the end point due to load P, δ, can be described as:

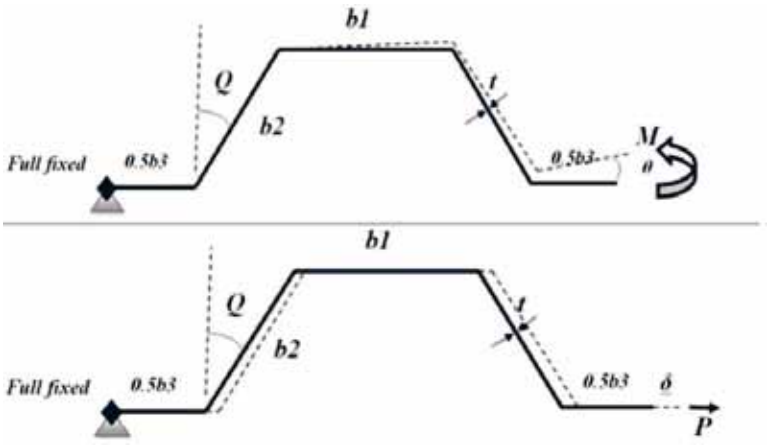

Fig. 2. Trapezoidal element

$$\delta = \frac{P(b_1 + b_2)}{E_L.W.t} + \frac{8.P.b_2.h^2}{E_L.W.t^3} + \frac{12.P.b_1.h^2}{E_L.W.t^3} + \frac{2P(\sin Q)^2 b_2}{E_L.W.t} \quad (1)$$

The longitudinal Young's modulus of the corrugated composites, E_{Leff}, can be calculated by equation 2.

$$E_{Leff} = \frac{P.L}{W.h.\delta} \quad (2)$$

In the same way, the rotation angle at the end point due to moment M, θ, is:

$$\theta = \frac{1}{D_{11}}(b_1 + 2b_2 + b_3).M \quad (3)$$

The effective longitudinal flexural modulus per width of the corrugated composites, D_{Leff}, can be expressed as:

$$D_{Leff} = \frac{D_{11}(b_1 + 2b_2 \sin Q + b_3)}{b_1 + 2b_2 + b_3} \quad (4)$$

For an estimation of the transverse flexural modulus of the corrugated composite, by calculating the moment of inertia of the cross-sectional area, we can express the effective transverse flexural modulus per width of the corrugated composite, D_{Teff}, as :

$$D_{Teff} = \frac{A_{22}.I}{t(b_1 + 2b_2 \sin Q + b_3)} \quad (5)$$

Where:

$$I = \frac{b_1.t^3}{12} + b_1.t\left[\frac{h.(b_2 + b_3)}{b_1 + 2b_2 + b_3}\right]^2 + \frac{b_3.t^3}{12} + b_3.t\left[\frac{h.(b_1 + b_2)}{b_1 + 2b_2 + b_3}\right]^2 + \frac{b_2.\sin^2(\theta).t^3}{\phi} + \frac{b_2^2.\cos^2(\theta).t}{\phi} \quad (6)$$

The effective transverse Young's modulus of the corrugated composite, E_{Teff}, is expressed as:

$$E_{Teff} = \frac{(b_1 + 2b_2 + b_3).A_{22}}{(b_2 \cos Q).(b_1 + 2b_2 \sin Q + b_3)} \quad (7)$$

Substituting $b_1 = b_3 = 0$, for a triangle and $Q = 0$, for a rectangle, in the relative equations of trapezoidal extracted effective stiffness for triangular and rectangular corrugated sheets. In the same way, we can calculate the effective tensional and flexural stiffness for a sinusoidal element that is shown in Appendix.

3. RESULTS AND DISCUTION

In this study, the equivalent extensional and flexural stiffness of a corrugated composite are for a unidirectional composite properties (E-glass/Epoxy).The width of a corrugated sheet is 0.02m, and the ply thickness is 0.5mm. Using these effective properties of unidirectional fabrics, the tensile and flexural stiffness of the corrugated composites were calculated using the above equations for sinusoidal and trapezoidal corrugated composites. Comparison between analytical and FEM results are shown in Fig. 3, Fig 4 and Fig. 5. Although there are very slight differences between analytical and FEM values, the mechanical properties of corrugated composites can be simply estimated using the present analytical model.

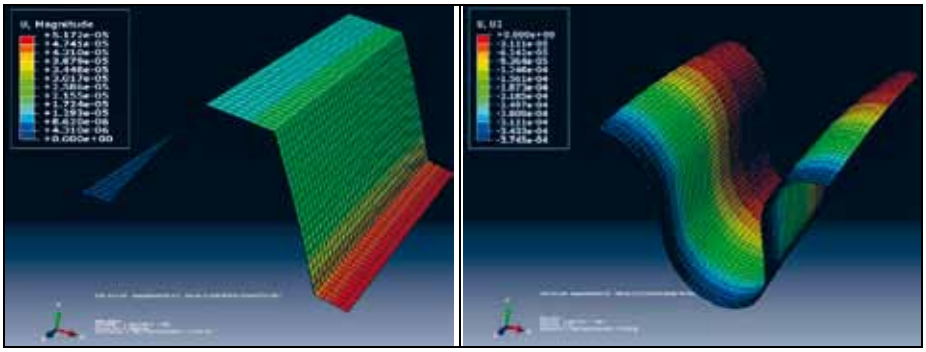

Fig 3. Finite element results for trapezoidal and sinusoidal corrugated element.

After analytical formulation of the stiffness and deformation finite element analysis, one can validate the initial studies on corrugated composites and asymmetric lay-up. However, it is time-consuming to model the nonlinear deformation by FEM. Results of FEM in various lay-up sequences, both symmetric and asymmetric give a good agreement to the analytical results.

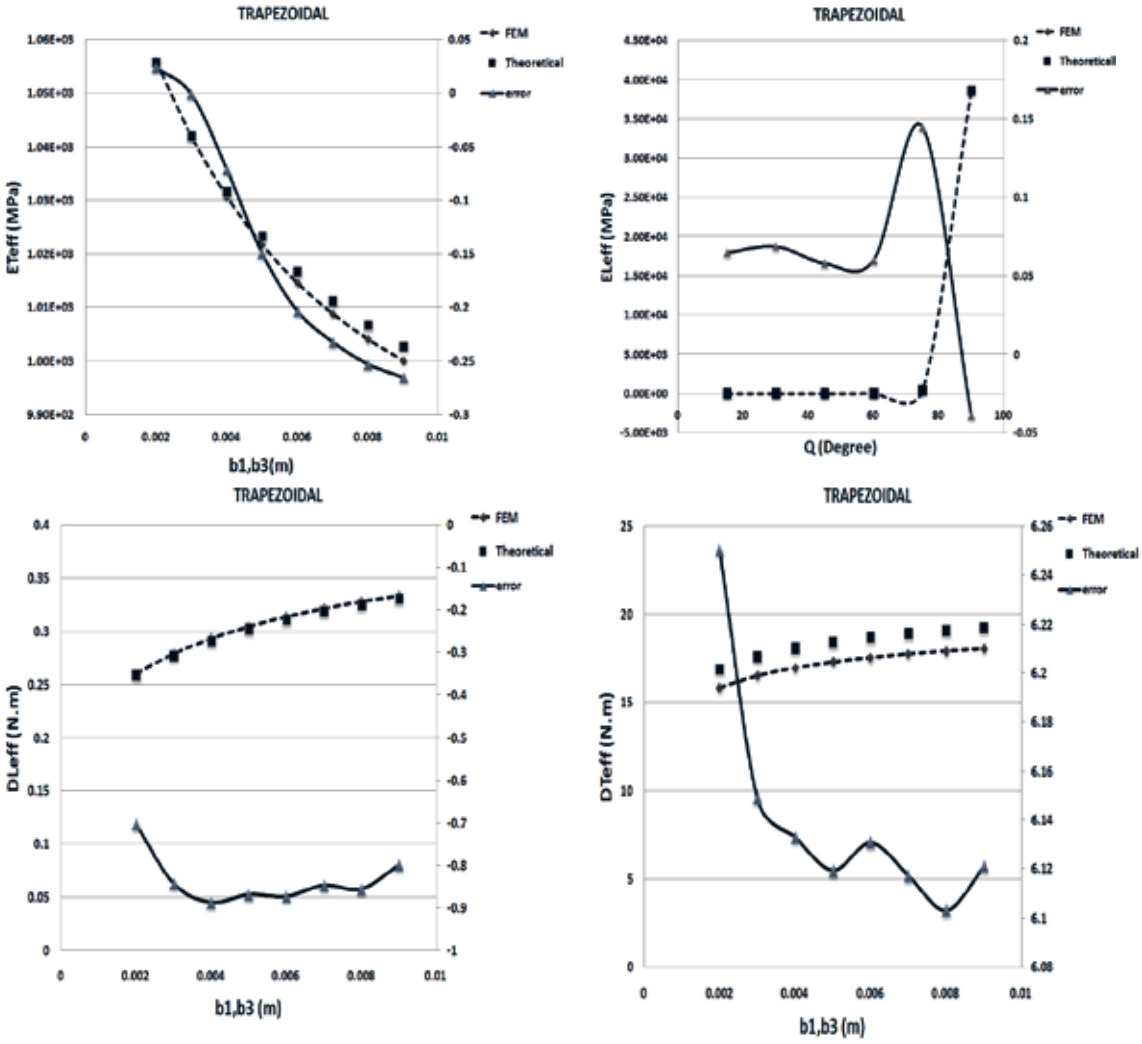

Fig 4. Comparison between analytical and FEM results for trapezoidal corrugated composites

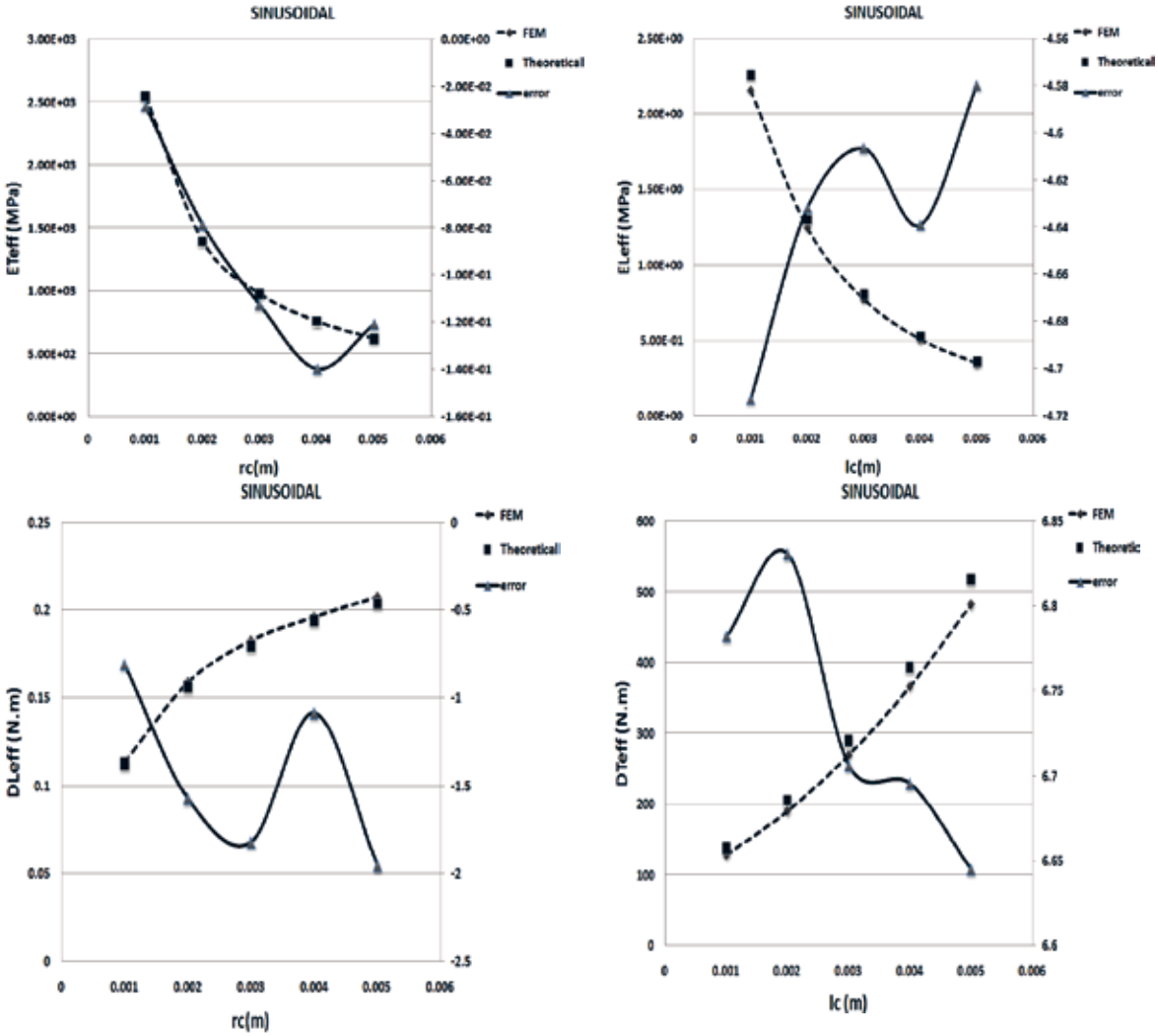

Fig. 5. Comparison between analytical and FEM results for sinusoidal corrugated composites.

4. FUTURE WORK

In future work woven fabric will be compared to UD to obtain the elastic response of a corrugated composite. Also symmetric and asymmetric laminates will be investigated. The experimental work will be focused on validation of the analysis.

REFERENCES

Abdewi, E.F., Sulaiman, S., Hamouda, A.M.S. and Mahdi, E., Quasi-static axial and lateral crushing of radial corrugated composite tubes, Thin Wall Struct 46 (3) (2008), pp. 320–332.

Perel, D. and Libove, C., Elastic buckling of infinitely long trapezoidally corrugated plates in shear, J Appl Mech 45 (3) (1978), pp. 579–582.

Rao, K.P., Shear buckling of corrugated composite panels, Compos Struct 8 (3) (1987), pp. 207–220.

Shanley, F.R., Cardboard-box wing structures, J Aeronaut Sci 14 (12) (1947), pp. 713–715.

Sun, H.-H. and Spencer, J., Buckling strength assessment of corrugated panels in offshore structures, Mar Struct 18 (7–8) (2005), pp. 548–565

Thill, C., Etches, JA., Bond, IP., Potter, KD., Weaver, P., Corrugated composite structures for aircraft morphing skin applications. In: 18th International conference of adaptive structures and technologies, Ottawa, Ontario, Canada; 2007.

Thill, C., Etches, JA., Bond, IP., Weaver, PM., Potter, KD., Experimental and parametric analysis of corrugated composite structures for morphing skin applications. In: 19th International conference on adaptive structures and technologies (ICAST). Ascona, Switzerland; 2008.

Torre, L. and Kenny, M.K., Impact testing and simulation of composite sandwich structures for civil transportation, Compos Struct 50 (2000), pp. 257–267.

Wiggenraad, J.F.M., Michielsen, A.L.P.J., Santoro, D., Lepage, C., Kindervater, C.and Beltran, F., Development of a crashworthy composite fuselage structure for a commuter aircraft, National Aerospace Laboratory NLR (1999).

Wiggenraad, J.F.M., Santoro, D., Lepage, F., Kindervater, C. and Climent Mañez, H., Development of a crashworthy composite fuselage concept for a commuter aircraft, National Aerospace Laboratory NLR (2001).

Yokozeki, T., Takeda, S., Ogasawara, T. and Ishikawa, T., Mechanical properties of corrugated composites for candidate materials of flexible wing structures, Compos Part A: Appl Sci Manuf 37 (10) (2006), pp. 1578–1586.

APPENDIX

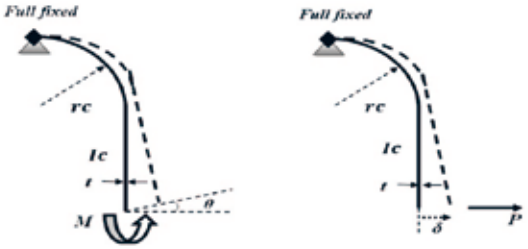

Fig. 6. Sinusoidal element.

Table.1 shows the effective stiffness for sinusoidal corrugated composite sheets. r_c is the radius of curvature of the curved section and l_c is the length of the straight section.

Table.1. effective stiffness for sinusoidal corrugated composite

Effective transverse flexural modulus	$D_{Teff} = \frac{A_{22}\{16l_c^3 + 24\pi l_c^2 r_c + 3\pi r_c(4r_c^2 + t^2) + 8l_c(12r_c^2 + t^2)\}}{48r_c}$
Effective transverse Young's modulus	$E_{Teff} = \frac{2\pi r_a + 4l_a}{w_a . h_a} . A_{22}$
Effective longitudinal flexural modulus	$D_{Leff} = \frac{r_a D_{11}}{\frac{\pi}{2} r_a + l_a}$
Effective longitudinal Young's modulus	$E_{Leff} = \frac{w_a . P}{4 h_a \delta}$

Where:

$$\delta = \frac{1}{D_{11}}\left[\frac{l_a^3}{3} + r_c\left\{\frac{\pi}{4}\left(2l_a^2 + r_a^2\right) + 2l_a r_a\right\}\right] . P \quad (8)$$

Proceedings of the 32nd
Risø International Symposium on Materials Science:
Composite materials for structural performance:
Towards higher limits
Editors: S. Fæster, D. Juul Jensen,
B. Ralph, B.F. Sørensen
Risø National Laboratory for Sustainable Energy,
Technical University of Denmark, 2011

EXPERIMENTAL AND THEORETICAL INVESTIGATION OF THERMOPHYSICAL AND MECHANICAL PROPERTIES OF THE EPOXY-CLAY NANOCOMPOSITE

T. Glaskova, A. Aniskevich, K. Aniskevich, Ye. Faitelson,
and V. Korkhov

Institute of Polymer Mechanics, University of Latvia, Riga, Latvia

ABSTRACT

The paper generalizes results of complex research of mechanical and thermophysical properties of epoxy-based nanocomposites (NC). The kinetics of moisture absorption of epoxy matrix and epoxy-based NC were previously studied experimentally. The mechanical properties of NC were experimentally investigated in tensile quasistatic and creep tests. Application of dilatometry analysis allowed establishing basic regularities for glass transition temperature for NC. The interrelation of thermophysical and mechanical characteristics of epoxy-clay NC having absorbed moisture was estimated with the structural changes accompanying deformation at various schemes of loading and temperatures.

1. INTRODUCTION

Moisture absorption of epoxy resins leads to time-dependent change in their structure and subsequent deterioration of properties. In order to minimize this negative effect of moisture on functional, structural, and mechanical properties of polymer composites the scientific and industrial interest is devoted to polymer/layered silicate nanocomposites (NC). The excellent barrier capability with significantly reduced permeability of moisture and gases is one of the most attractive and useful properties that have not been fully explored in the past. The key to such performance rests in the ability to exfoliate and disperse individual, high aspect ratio silicate platelets within the polymer matrix (Fornes, Yoon, Hunter, Keskkula, and Paul 2002). The complete dispersion of clay nanolayers in a polymer optimizes the number of available reinforcing elements for carrying an applied load and deflecting cracks. The coupling between the tremendous specific surface area of clay ($S \approx 800$ m^2/g) and a polymer matrix facilitates stress transfer to the reinforcement phase, allowing for tensile and toughening improvements (LeBaron, Wang, and Pinnavaia 1999).

Epoxy resins widely used as composite matrix are very attractive due to their high strength and

stiffness, high temperature resistance, low volatility, creep and shrinkage, good adhesion to metal and ceramic substrates. Nevertheless epoxy resins have a major drawback of moisture absorption, which in turn degrades the functional, structural and mechanical properties of the composites (Vlasveld, Groenevold, Bersee, Mendes, and Pichen 2005).

It is essential to investigate mechanical, thermal and barrier properties of NC and to estimate their steadiness to environmental effects. The improved stability of polymer NC could broaden their application in techniques and construction.

Therefore the aim of the work is to generalize the results obtained of a complex investigation of sorption, mechanical and thermophysical properties of epoxy-clay NC and to establish a correlation between mechanical and thermophysical properties of the NC investigated during moisture absorption.

For this purpose the following objectives have been set:

1. To verify the effect of moisture on mechanical properties of epoxy-clay NC incorporating silicate nanoparticles in uniaxial tensile quasistatic and creep tests;

2. To establish basic thermophysical regularities of epoxy-clay NC and to estimate structural changes of the NC investigated due to moisture absorption;

3. To establish the interrelation of thermophysical and mechanical characteristics of epoxy-clay NC having absorbed moisture with the structural changes accompanying deformation at various schemes of loading and temperatures.

2. MATERIALS AND METHODS

Bisphenol A epoxy resin hardened by polypropylene oxide filled with particles of montmorillonite clay (filler content 2, 4 and 6% by weight) was investigated in the work.

The homogeneity of the filler particles' dispersion in the polymer resin is approved by the transparency of all NC specimens. Additional microscopic methods such as scanning electron (SEM) and transmission electron microscopy (TEM) are applied for the microstructural analysis.

The kinetics of moisture sorption was experimentally investigated using a sorption method in atmospheres with relative humidities φ = 24, 77 and 98% using desiccators with silica gel and saturated solution of salts NaCl and K_2SO_4 respectively (Glaskova, Aniskevich 2009). According to the results obtained the average equilibrium moisture content reached in 437 days for NC was approximately -0.4, 1.7, and 3.2% for φ = 24, 77, and 98 % with an increase by approximately 7 % for a filler content changed from 0 to 6 % wt. It was experimentally confirmed that the sorption process in NC passed more slowly than in the pure epoxy resin, for the highest filler content the diffusivity was reduced by about half of the diffusivity for the epoxy resin. It could be caused by clay nanoparticles as they act as efficient barriers against moisture transport. The increase in equilibrium moisture content observed with an increase of the clay weight content in the NC was explained by the growth of interphase layer content. The sorption capacity of the interphase layer in NC with 1 % of filler was determined and the sorption isotherm of the interphase was derived.

The investigation of NC mechanical properties was performed by quasistatic tension tests by the use of a Zwick 2.5 testing machine with a crosshead rate of 5 mm/minute at room temperature (Glaskova, Aniskevich 2010). It was shown that the effect of absorbed moisture on the mechanical properties is substantial. The tensile strength of moistened composite decreased about twice. The elastic modulus both of moistened pure epoxy resin and NC was reduced approximately 1/3 in comparison to the initial state. Halpin-Tsai equations were applied in order to estimate the effective elastic modulus of NC conditioned in atmospheres of different relative humidities. The results obtained for specimens conditioned in a dry atmosphere were used for moistened NC and provided an opportunity to estimate the structural changes of the polymer resin due to moisture absorption.

Creep and creep recovery were examined at a constant tensile load equal to 50% of the breaking loads for each NC and at each value of the equilibrium (Aniskevich, Glaskova, Aniskevich, and Faitelson 2010). The tests were carried out at room temperature. The creep and creep recovery tests lasted for 7.5 and 17 h, respectively. The sets of creep recovery curves were approximated by the Boltzmann-Volterra linear equation with an account of the principle of the moisture-time analogy. The variation in the spectrum of retardation time of the epoxy resin with introduction of the nanofiller was estimated. It was shown that the moisture-time reduction function correlates with the changes in the forced rubber-like elasticity and the volume of nanocomposite specimens upon their moistening.

The changes of structure and properties of the materials investigated were studied by means of dilatometry analysis using a UIP-70M device with specimens heated to 150 ^{o}C at a heating rate 2 K/minute with subsequent cooling (Faitelson, Glaskova, Korkhov, and Aniskevich 2010). It was revealed that the presence of clay nanoparticles (up to 6 % wt.) didn't influence the temperature of structural transitions and doesn't cause a substantial strengthening effect. The absorbed moisture plastisized the NC and decreased its glass transition temperature by 10 ^{o}C. The specific features of the thermophysical behavior of NC upon their tensile prestrain and creep are due to the formation of an oriented structure. These results were also proved by X-ray diffractometry tests using a DRON - 3M device with photography in transmitted light using $Cu_{K\alpha}$ radiation.

3. MICROSTRUCTURAL CHARACTERIZATION OF EPOXY-CLAY NC

The behavior and properties of NC are dependent not only on the properties of its structural components, but also on the material microstructure: the dispersion and orientation of filler particles, and the interactions between filler particles and the polymer matrix. Nevertheless one of the main parameters that affects the behavior of the nanosystem is the effectiveness of the dispersion of filler particles within the polymer matrix.

One way to check the morphological peculiarities of clay nanoparticles in a solvent, before incorporating them to a matrix, is to observe their dispersion by TEM. A typical image of an acetone suspension of clay nanoparticles is shown in Fig. 1a.

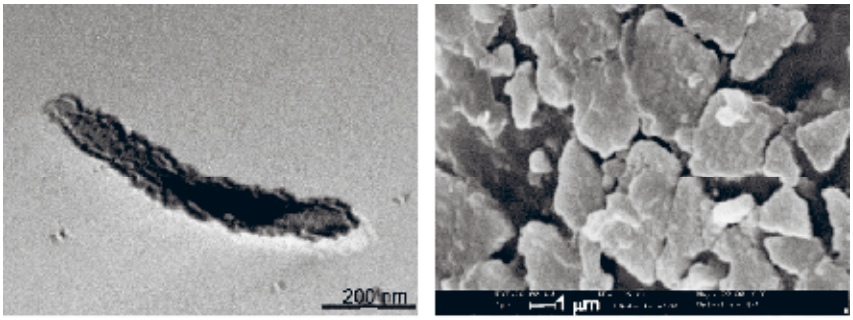

Fig. 1. Typical TEM image of an acetone suspension of clay nanoparticles. The nanoclay appears in black (a); SEM micrograph of fracture surface of NC with c = 2% (b).

It is obvious from the Fig. 1a that the observed aggregate should be a stack of clay platelets having a layered structure and a high aspect (diameter to thickness) ratio (50). The aspect ratio of the platelet stack as observed from Fig. 1a is about 7.

Moreover the platelet shape of the filler particles could be confirmed by a SEM micrograph of the fracture surface of a NC specimen with c = 2 % (Fig. 1b). It could be seen that the transverse dimension of the filler aggregates is much smaller than longitudinal ones.

4. RESULTS OF EXPERIMETS

4.1 Quasistatic tensile tests. Experimentally measured stress-strain curves of NC with c = 6 % moistened at φ = 24, 77 and 98 % RH are shown in Fig. 2. From these curves it could be observed that the effect of moisture on the mechanical behavior is substantial. Absorbed moisture essentially plasticizes the NC and changes its fracture character from brittle in a dry atmosphere to plastic in wet atmospheres.

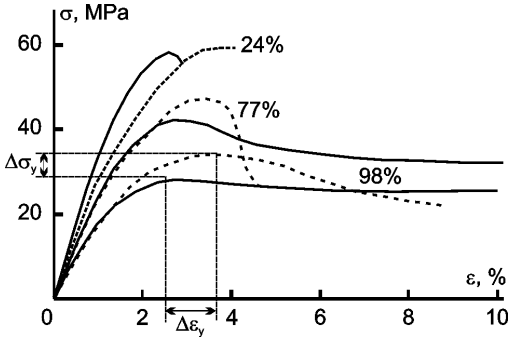

Fig. 2. Typical stress-strain curves at a fixed rate of deformation (5 mm/minute) for neat epoxy resin (dotted line) and NC with c = 6% (solid line) and different φ (numbers on the curves).

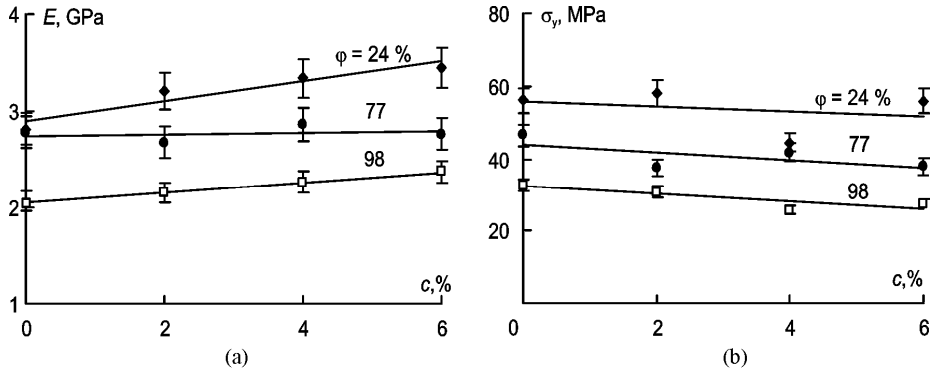

Fig. 3. Elastic modulus (a) and yield stress (b) of NC in relation to the filler mass content for different φ (numbers on the curves).

As seen from the data of Fig. 3, as a result of filling the epoxy binder with MMT particles, the elastic modulus of the dry material increases by about 30%, but the yield stress and strain decreases by about 1/3. The increased moisture content in the material of either the epoxy binder or the NC is responsible for the decreased elastic modulus and yield stress; the yield strain practically does not vary with moisture content in the material. The dry (held in an atmosphere with φ = 24%) specimens fail in a more brittle way than the moistened (with φ = 98%) ones. The strength of the first specimens exceeds two fold that of the last ones. The intermediate values of strength are observed for the specimens held in an atmosphere with φ = 77%.

4.2 Creep and creep recovery tests. The results of short-term (7.5 h) creep of a dry material showed that the creep compliances (but not the instantaneous ones $I_0 = 1/E$) of the NC without a filler and at c = 4% practically coincided (Fig. 4a), i.e., the effect of filler showed up as a filler content-dependent instantaneous compliance (or elastic modulus). The moistening of a material leads to a marked increase in the creep compliance (Fig. 4a). This is obviously caused by the fact that the state of the material is close to a highly elastic one. The experiments on creep recovery showed that the deformations did not return back to zero after a 17 h observation, but their tendency to decrease in time still persisted (Fig. 4b)

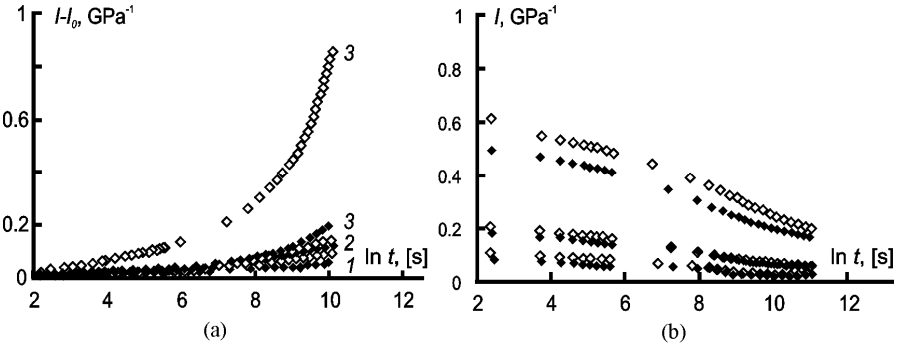

Fig. 4. Compliance curves of the NC with filler contents c = 0 (♦) and 4 (◊)% for φ = 24 (*1*), 77 (*2*) and 98% (*3*) in creep (a) and creep recovery (b).

4.3 Dilatometry and X-ray structural analysis. The investigation of NC with different filler content and moisture showed that (Fig. 5) with an increase of the moisture content in the NC its

glass transition temperature lowered from 45 to 35 °C. The variation in the glass transition temperature of NC in relation to the filler content, in an atmosphere with a fixed humidity, was insignificant (fell within the limits of the scatter of experimental data).

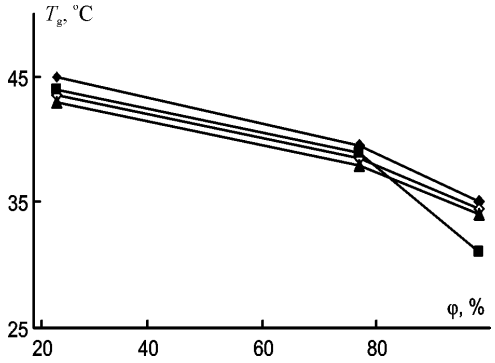

Fig. 5. Glass transition temperature as a function of the atmospheric humidity for NC at c = 0 (♦), 2 (◊), 4 (▲), and 6% (■).

The glass transition temperature of the epoxy resin and epoxy-clay NC shifts towards the region of temperatures exceeding the room temperature only by 10-20 °C, i.e., the temperature at which the mechanical tests were carried out. Therefore the application of a load can cause the epoxy resin to pass to the region of high elasticity, characterized by large deformations.

In order to establish the relationship between the thermal characteristics and the structural changes attending the NC deformation process, dilatometry analysis has been applied to epoxy-based NC specimens after quasistatic (Fig. 2) and creep tension experiments (Fig. 4). For this purpose moistened specimens from an atmosphere with φ = 98% RH were pre-deformed in air in the regime of quasi-static tension with $\dot{\varepsilon}$ = constant and creep with σ = constant until the whole of the working part material went into a "neck." Then the specimens were cut along and across the direction of stretching. From the analysis of the dilatometry curves (Fig. 6a) it is seen that the thermal expansion of the NC specimens cut in mutually perpendicular directions differs markedly and there are anisotropic changes in the thermomechanical characteristics. Analogous results have also been obtained for specimens upon creep tests. For heated NC specimens cut along the stretching direction, in both quasi-static tension and creep experiments, their clear similarity to the TMA curves is observed (Fig. 6b). For instance, in the glass transition temperature range their linear sizes sharply decrease. However, specimens oriented in the creep regime (curve *2*) shrink to a greater extent and the process proceeds in a narrower temperature range than for specimens oriented under quasi-static tension (curve *1*). Next, when temperatures of 37 °C (under creep) and 64 °C (under quasi-static tension) are attained, the process of their spontaneous stretching begins as sharply as shrinkage.

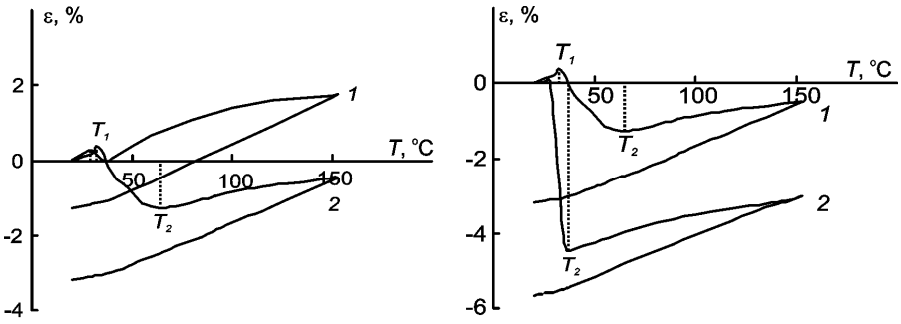

(a) (b)

Fig. 6. Dilatometry curves of NC specimens cut across (*1*) and along (*2*) the stretching directions under quasi-static tension (a) and specimens cut along the stretching direction under quasi-static tension (*1*) and creep (*2*) (b).

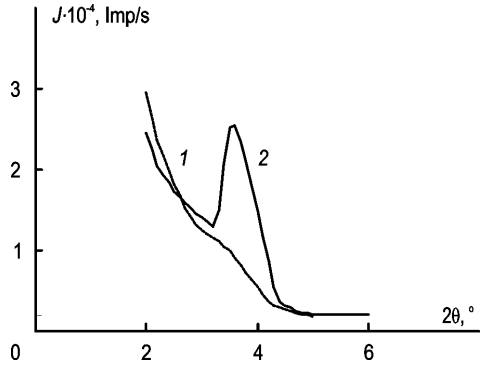

Fig. 7. Diffraction patterns of a tension pre-deformed NC specimen with c = 6% cut from the "neck" region: meridian (1); equator (2).

The data of X-ray structural analysis correlate well with the assumptions about structural changes in the NC at its deformations to high values. Fig. 7 presents meridian and equatorial diffraction patterns of NC specimens pre-stretched to failure. It is seen that in the region of small angles on the equatorial diffraction pattern a peak caused by the crystalline phases is present, while it is absent from the meridian diffraction pattern. This effect can be explained by the fact that at large stretches the material acquires an almost completely fibrillated oriented structure.

5. GENERAL CONCLUSIONS

The results of complex investigations on sorption, mechanical and thermophysical properties of various epoxy resins and epoxy-clay nanocomposite are summarized as follows:

1. A substantial effect of moisture on mechanical properties was shown. Absorbed moisture essentially plasticized the composite changing its fracture character. The tensile strength of moistened composite decreased twice. The elastic modulus both of moistened pure epoxy resin and NC was reduced approximately 1/3 in comparison to the initial value.

2. The results of short-term creep of a dry material showed that the creep compliances of

the NC practically coincided, i.e., the effect of filler showed up as a filler content-dependent instantaneous compliance. The moistening of a material leads to a marked increase in the creep compliance. This is obviously caused by the fact that the state of the material is close to a highly elastic one.

3. Moisture sorption causes plasticization of NC and leads to a decrease of glass transition temperature by 10 ^{o}C. The deformation mechanism of NC changes significantly under the effect of moisture. Large plastic deformations and the formation of transition regions to the orientated state ("necking") is revealed during tension of moistened specimens of NC. The thermal expansion of the NC specimens cut in mutually perpendicular directions after tensile quasistatic and creep tests differs markedly and there are anisotropic changes in the thermomechanical characteristics. The data of X-ray structural analysis correlates well with the assumptions about structural changes in the NC at its deformations to high values.

4. Incorporation of impenetrable clay nanoparticles with high mechanical characteristics doesn't reduce the negative effect of absorbed moisture on the mechanical properties of NC. But since the value of the elastic modulus of epoxy resin is improved on the filler content up to 20%, epoxy resin modified by impenetrable stiff montmorillonite clay nanoparticles can be applied in environments with a higher-operating relative humidity.

ACKNOWLEDGEMENTS

The authors wish to thank the European Social Fund for the financial support (Projects No. 2009/0209/1DP/1.1.1.2.0/09/APIA/VIAA/114 and 2010/0296/2DP/2.1.1.1.0/10/APIA/VIAA/049).

REFERENCES

Aniskevich, K. K., Glaskova T. I., Aniskevich A. N., Faitelson Ye. A. (2010). Effect of moisture on the viscoelastic properties of an epoxy-clay nanocomposite. Mechanics of Composite Materials 46, 573-582.

Faitelson, E. A., Glaskova, T. I., Korkhov, V. P., Aniskevich, A. N. (2010). Structural changes in a clay-containing nanocomposite with a different moisture content caused by its deformation. Journal of Engineering Physics and Thermophysics 83, 443-451.

Fornes, T. D., Yoon, P. J., Hunter, D. L., Keskkula, H., Paul, D. R. (2002). Effect of organoclay structure on nylon 6 nanocomposite morphology and properties. Polymer 43, 5915-5933.

Glaskova, T. I., Guedes, R. M., Morais, J. J., Aniskevich, A. N. (2007). A comparative analysis of moisture transport as applied to an epoxy binder. Mechanics of Composite Materials 43, 377-388.

Glaskova, T., Aniskevich A. (2009). Moisture absorption by epoxy/montmorillonite nanocomposite. Composites Science and Technology 69, 2711-2715.

Glaskova, T., Aniskevich A. (2010). Moisture effect on deformability of epoxy/montmorillonite nanocomposite. Journal of Applied Polymer Science 116, 493-498.

LeBaron, P., Wang, Z., Pinnavaia, T. J. (1999). Polymer-layered silicate nanocomposites: an overview. Applied Clay Science 15, 11-29.

Vlasveld, D., Groenevold, J., Bersee, H., Mendes, E., Pichen, S. J. (2005). Analysis of the modulus of polyamide-6 silicate nanocomposites using moisture controlled variation of the matrix properties. Polymer 46, 6102-6113.

Proceedings of the 32nd
Risø International Symposium on Materials Science:
Composite materials for structural performance:
Towards higher limits
Editors: S. Fæster, D. Juul Jensen,
B. Ralph, B.F. Sørensen
Risø National Laboratory for Sustainable Energy,
Technical University of Denmark, 2011

INFLUENCE OF TRANSVERSE PROPERTIES IN THE MODELING OF DEBOND PROPAGATION IN SINGLE CARBON FIBER COMPOSITES

E. Graciani*, J. Varna**, V. Mantič*, A. Blázquez* and F. París*

* Grupo de Elasticidad y Resistencia de Materiales. E.T.S. Ingeniería.
Camino de los Descubrimientos s/n. 41092 Sevilla. Spain.
** Polymerteknik. Luleå Tekniska Universitet. SE-97187 Luleå.
Sweden

ABSTRACT

A Finite Elements analysis of the single fiber fragmentation test, using cohesive elements, is presented in order to elucidate the significance of transversal carbon fiber properties in debond propagation. A good agreement is found in the numerical results obtained with Finite Elements employing actual carbon fiber properties and fictitious isotropic fiber properties. A Boundary Elements analysis of the single fiber fragmentation test, using fictitious isotropic fiber properties and Linear Elastic Fracture Mechanics to study crack propagation, also yields a remarkable agreement with the abovementioned results.

1. INTRODUCTION

The Single Fiber Fragmentation Test (SFFT) introduced by Kelly and Tyson (1965) is extensively used at present for the characterization of fiber-matrix interfaces in composite materials. In previous studies published by the authors, the growth of interfacial cracks in a sample containing one single glass fiber embedded in epoxy matrix has been analyzed using, firstly, an approach based on Linear Elastic Fracture Mechanics (LEFM), see Graciani, Mantič, París and Varna (2009), and, secondly, an approach based on Cohesive Zone (CZ) models, see Graciani, Blázquez, París and Varna (2010).

The LEFM based approach employs a numerical solution of the elastic state within a typical fragment of the sample, obtained using a Boundary Elements (BE) model, to determine the Energy Release Rate (ERR) associated with debond growth. The ERR is evaluated from the near-tip elastic solution using an expression in which the effect of interfacial friction along crack faces is taken into account, see Graciani, Varna, Mantič, Blázquez and París (2011).

The CZ based approach simulates debond onset and propagation employing a non-linear Finite

Elements (FE) model. Typical bilinear cohesive elements are placed along the fiber-matrix interface and the fiber plane of failure.

As shown in Graciani (2010) results obtained with both approaches are very similar, specially for large debond lengths, which validates the linearization assumed in the LEFM based approach.

An efficient method for the simultaneous evaluation of the interfacial friction coefficient and interfacial mode II fracture toughness in single glass fiber samples, using SFFT measurements of debond and fragment lengths and numerical simulations employing the LEFM based approach, has recently been presented in Graciani et al. (2011).

Evaluation of interfacial properties requires a much higher numerical effort when the CZ based approach is used instead of the LEFM based approach. By contrast, applying the CZ analysis of the SFFT to the case of single carbon fiber samples is a straightforward task, since cohesive elements and transversely isotropic material behavior are available in most commercial FE codes, while extending the LEFM based approach may be cumbersome, since the BE formulation for transversely isotropic material behavior must be developed and implemented prior to the numerical simulation.

For that reason, in this paper the possibility of employing fictitious isotropic carbon fiber properties, instead of its actual transversely isotropic properties, in the numerical analysis of the SFFT is explored. Three distinct numerical simulations have been carried out and compared: a CZ based approach has been employed in two distinct situations, one of them using actual carbon fiber properties and the other using fictitious isotropic carbon fiber properties, and a LEFM based approach has also been employed using fictitious isotropic carbon fiber properties.

In the following, firstly, the common aspects of the models created with the two approaches are described. Secondly, the particular aspects of the FE model and the BE model are explained and, finally, numerical results are shown and compared.

2. GEOMETRY AND MATERIAL PROPERTIES

Periodicity in the elastic solution in the vicinity of all fragment ends has been assumed. Thus the geometry of the model consists in the radial section of the sample portion corresponding to one half of a typical fragment, as shown in Fig.1, where the boundary conditions and the dimensions employed are indicated.

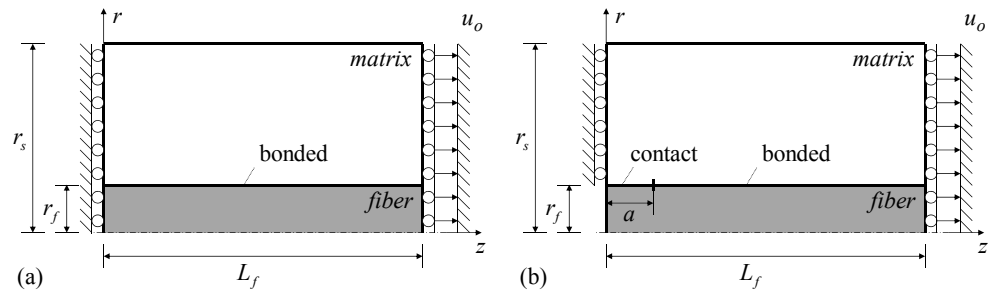

Fig. 1. Geometry and boundary conditions employed in the models: (a) before fiber breakage, and (b) after fiber breakage.

As depicted in Fig.1, symmetry conditions are employed in the plane where the fiber crack will appear and uniform displacements, corresponding to the average strain of the sample, are prescribed in the opposite side of the model. After fiber failure, the debond crack grows along the fiber-matrix interface, starting from the fiber crack tip. Since the tendency to shrink in the radial direction is larger in the matrix than in the fiber, the fiber-matrix interface is compressed in the whole length. Thus propagation of the debond crack takes place under pure fracture mode II and frictional contact between debond crack faces must be considered.

The treatment of the thermal residual stresses and the procedure employed for analyzing debond crack propagation, which are different it the two approaches employed, will be described in the following sections.

The main dimensions of the sample are: fiber radius, $r_f = 3.5\,\mu\text{m}$, sample radius, $r_s = 1\,\text{mm}$, fragment length, L_f, and debond length a. Although L_f and a are, respectively, the semi-fragment length (since only one half of the fragment is modeled) and semi-debond length (since the debond crack grows symmetrically at the other side of the fiber crack also) they will be named fragment length and debond length throughout this paper for the sake of simplicity.

During the SFFT the fiber fragments become shorter as the load is increased. In this paper, a sufficiently long fragment has been considered, having a constant length $L_f = 500\,\mu\text{m}$. However, the difficulties associated with modeling the decreasing average fragment length with the two approaches employed will also be addressed in the following sections. Material properties, obtained from the literature (Kim and Nairn 2002), are summarised in Table 1.

Table 1. Material properties employed in the analyses.

Property	carbon fiber		fictitious fiber	epoxy matrix
	Axial	Transverse		
Young's modulus (GPa)	231	40	231	2.6
Poisson's ratio	0.2	0.25	0.2	0.35
Shear modulus (GPa)	20	16	–	–
Thermal exp. coeffcient (K^{-1})	$-0.7\cdot10^{-6}$	10^{-6}	10^{-6}	$4\cdot10^{-6}$

According to the experimental measurements presented in Kim and Nairn (2002), the average debond length varies in the range $0 < a < 80\,\mu\text{m}$ when the axial strain applied at the fragment ends is increased from 1% to 2.5%. Interfacial properties selected for the present study (described in the following sections) produce results within the mentioned range.

3. FEM MODEL

Two distinct FE models have been employed, in order to determine the influence of the transversely isotropic behavior of the carbon fiber in the growth of the debond cracks. In the first model actual properties of the carbon fiber have been defined while fictitious isotropic properties have been used in the second, (see Table 1).

The onset and propagation of the cracks is modeled using cohesive elements. Therefore, for each assumed set of interfacial properties, the solution is obtained in a single non-linear analysis. Two successive load steps are considered in order to take into account the thermal residual stresses. Boundary conditions employed in both steps are depicted in Fig.1(a). In the first load step a uniform decrease of temperature $\Delta T = -125K$ has been prescribed in all elements, along with an average shortening of the sample $u_o = \varepsilon_{\Delta T} L_f$, with $\varepsilon_{\Delta T} \approx -0.5\,\%$. In

the second load step the temperature is maintained constant while an external applied strain $0 \le \varepsilon \le 2.5\,\%$ is applied. Therefore, displacements imposed at the right side of the sample during the second load step are given by: $u_o = (\varepsilon_{\Delta T} + \varepsilon) L_f$.

The present analysis has been carried out using Marc & Mentat® 2008 commercial codes. Four-node, isoparametric quadrilateral axisymmetric element type 10 is employed to mesh the fiber and matrix and four-node axisymmetric cohesive element type 190 is employed to simulate crack onset and progress. The FE mesh employed for the analyses is depicted in Fig.2. As can be seen a uniform mesh (in which the length of the element side is r_f) is employed in the whole sample, except for left side of the fiber (and the surrounding matrix zone) where a fine uniform mesh (in which the length of the element side is $\frac{1}{16} r_f$) is employed. A quick mesh transition is employed between both zones.

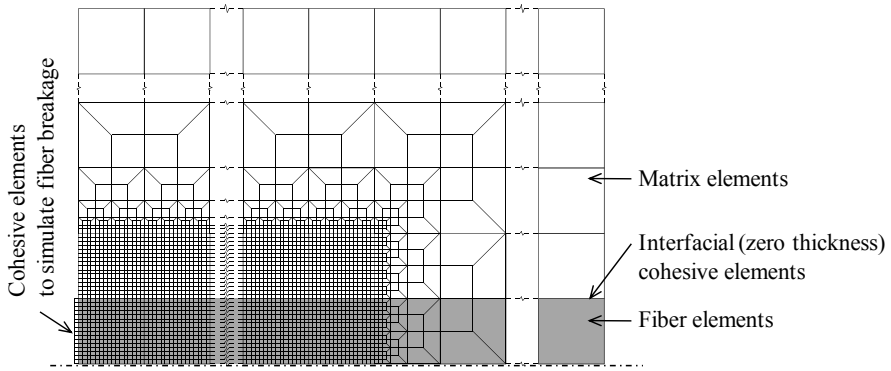

Fig. 2. Sketch of the mesh employed in the FE models.

Bilinear cohesive elements are employed to simulate fiber breakage, which takes place at an average applied strain of the order of $\varepsilon = 0.8\,\%$. In the same way, bilinear cohesive elements are placed along the interface to simulate the debond crack propagation. Simultaneously, contact conditions are employed between fiber and matrix nodes to take into account the frictional contact between crack faces after the crack is fully developed (Graciani et al. 2010).

Different interfacial properties (described in a following section) have been employed to define the behavior of the interfacial cohesive elements. In all cases, the extent of the fracture process zone is of the order of the fiber radius.

Using this approach, the length of the debond crack as a function of the applied strain is determined simply monitoring the damage of the cohesive elements along the interface during the second load step.

4. BEM MODEL

The alternative procedure for modeling the SFFT employs a BE model for evaluating the near-tip elastic solution. The BE mesh employed for the analyses is depicted in Fig.3 where the advantages of only needing a boundary mesh can clearly be appreciated. As in classical LEFM analysis, pre-existing fiber and debond cracks are assumed prior to the application of the loads. Thus, for each assumed set of interfacial properties, a set of models in which the length of the debond crack a is successively increased is needed to study crack propagation.

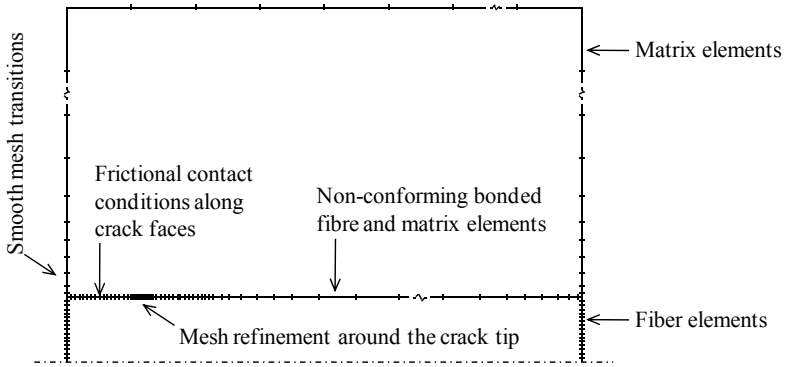

Fig. 3. Sketch of the mesh employed in the BE models.

Boundary conditions employed in the BE analyses are depicted in Fig.1(b). Two distinct load cases are employed for each of the debond lengths considered. In the first load case, a uniform decrease of temperature $\Delta T = -125K$ has been prescribed in both solids, along with an average shortening of the sample $\varepsilon_{\Delta T} \approx -0.5\,\%$. In the second load case the temperature is maintained constant while an external applied strain $\varepsilon_0 = 1\,\%$ is applied. The solution for an external applied strain ε in the range $0 < \varepsilon < 2.5\,\%$ is obtained linearly combining the above mentioned load cases. Therefore:

$$u_\alpha(r,z) = u_\alpha^{(1)}(r,z) + \varepsilon\, u_\alpha^{(2)}(r,z) \quad \text{and} \quad \sigma_{\alpha\beta}(r,z) = \sigma_{\alpha\beta}^{(1)}(r,z) + \varepsilon\, \sigma_{\alpha\beta}^{(2)}(r,z), \tag{1}$$

where u_α and $\sigma_{\alpha\beta}$ are respectively the components of the displacements and the stress tensor, with $\alpha = r, z$. Superscripts refer to the solution of each of the defined load cases.

In order to study crack growth, the following propagation criteria is employed:

$$\widetilde{G}_{II}(\Delta a) = G_{IIc}, \tag{2}$$

where G_{IIc} is the mode II interfacial fracture toughness and $\widetilde{G}_{II}(\Delta a)$ is the ERR associated to a finite increment of the crack of length Δa (a constant value of $\Delta a = 0.45\,\mu\text{m}$ has been employed throughout this paper), which can be evaluated as (Graciani et al. 2011):

$$\begin{aligned} \widetilde{G}_{II}(\Delta a) = {} & \frac{1}{2\Delta a}\int_0^{\Delta a} \sigma_{rz}(r, a+\rho)\, \Delta u_z(r, a-\Delta a+\rho)\, d\rho + \\ & + \frac{1}{2\Delta a}\int_0^{\Delta a} \sigma_{rz}(r, a-\Delta a+\rho)\, \Delta u_z(r, a-\Delta a+\rho)\, d\rho. \end{aligned} \tag{3}$$

In view of (1) and (3), it can be clearly appreciated that (2) is, in fact, a quadratic equation which yields the applied strain ε needed to cause debond growth for each of the debond lengths considered.

5. NUMERICAL RESULTS

Five distinct sets of interfacial properties have been considered (see Table 2). In three sets a constant value of the interfacial mode II fracture toughness G_{IIc} = 10 J/m^2 has been employed and the interfacial friction coefficient has been varied in the range $1 \le \mu \le 2$. In other three sets a

constant value of the interfacial friction coefficient $\mu = 1$ has been employed and the interfacial mode II fracture toughness has been varied. When the interfacial mode II fracture toughness has been changed, the maximum shear stress defined in the cohesive law has been also modified in order to keep reasonably constant the extent of the fracture process zone.

Table 2. Interfacial properties employed in the analyses.

Mode II fracture toughness (J/m^2)	10	10	10	5	20
Max. interfacial shear stress (MPa)	141.4	141.4	141.4	100	200
Friction coefficient	2	1.5	1	1	1

Numerical results showing the position of the fracture process zone (FPZ) during the loading of the sample, obtained with the CZ based approach, are shown in Fig.4. Two cases have been considered, one in which the actual carbon fiber properties are employed and another in which fictitious isotropic properties are defined (see Table 1).

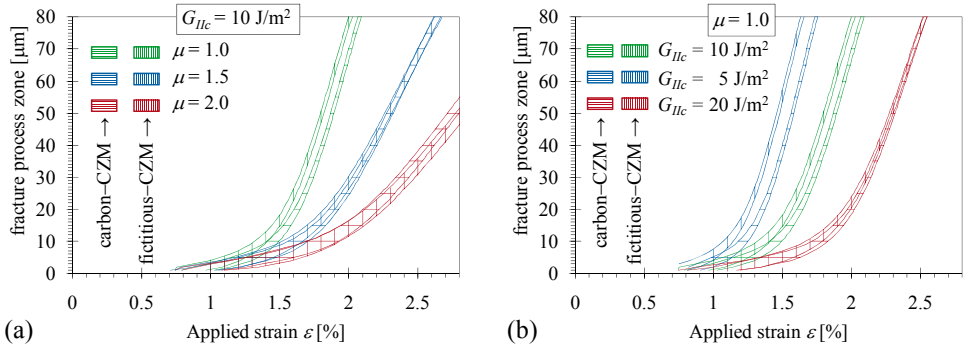

Fig. 4. Position of the FPZ using CZ based approach with actual and fictitious fiber properties: (a) varying μ and (b) varying G_{IIc}.

In Fig.4(a) the influence of changing μ, keeping G_{IIc} constant, is shown. As can be seen, the crack propagation is delayed when μ increases (i.e., it takes place at higher applied strains) and when the self-similar crack growth stage is reached (i.e., when the position of the FPZ has a linear dependency upon the applied strain) the slope is lower for higher values of μ. Analogously, in Fig.4(b) the influence of changing G_{IIc}, keeping μ constant, is shown. Obviously, the crack propagation is delayed when G_{IIc} increases. When a self-similar crack growth stage is reached the propagation curves become roughly parallel.

Additionally, as can be appreciated in Fig.4, changing interfacial properties has a more significant effect on crack propagation than changing the actual carbon fiber properties for the fictitious isotropic properties.

In Fig.5 the results obtained for debond propagation, employing the CZ based approach (with carbon fiber properties) and the LEFM based approach (with fictitious isotropic fiber properties), are shown.

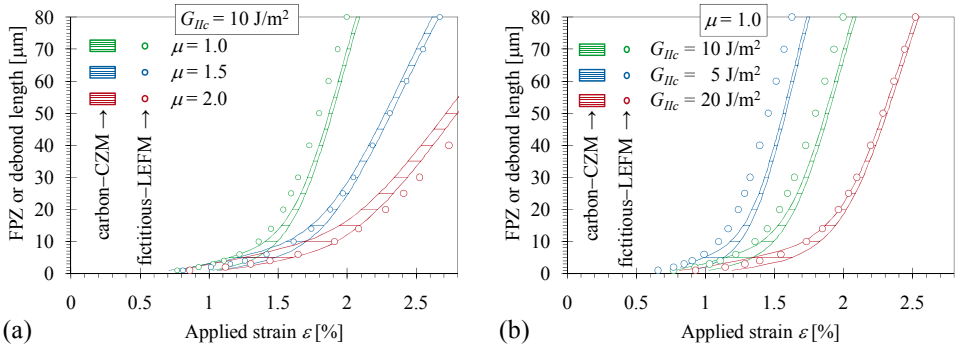

Fig. 5. Position of the FPZ using CZ based approach with actual fiber properties and debond length using LEFM based approach with fictitious fiber properties: (a) varying μ and (b) varying G_{IIc}.

The influence of changing μ, keeping G_{IIc} constant, is shown in Fig.5(a) while the influence of changing G_{IIc}, keeping μ constant, is shown in Fig.5(b). As can be seen, the results obtained with CZ and LEFM based approaches are similar, the influence of changing interfacial properties being more significant than the change in the modeling approach or the use of fictitious fiber properties.

For validation purposes, the results obtained for debond propagation employing CZ and LEFM based approaches, both of them using fictitious isotropic fiber properties, are shown in Fig.6. Numerical results show the remarkable agreement between the results obtained with the two approaches considered, as obtained in a previous analysis in which glass fiber properties were considered, see Graciani (2010).

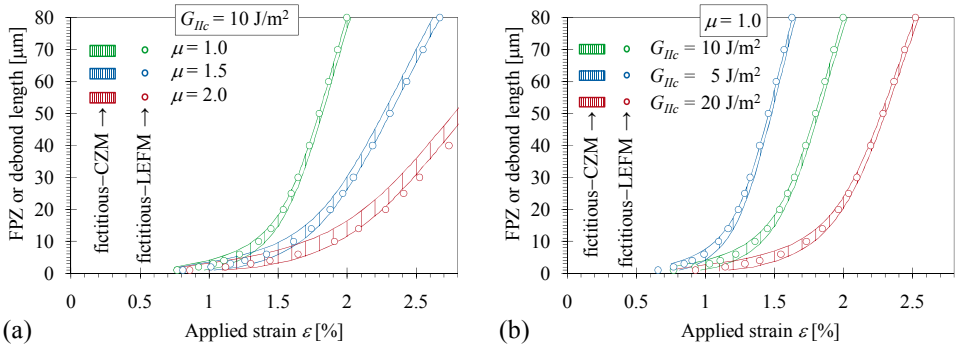

Fig. 6. Position of the FPZ using CZ based approach and debond length using LEFM based approach using fictitious fiber properties: (a) varying μ and (b) varying G_{IIc}.

Numerical simulations using CZ models like the ones shown in Fig.4 can be employed to determine interfacial properties by best fit between experimental measurements and numerical simulations. However, this approach has two important disadvantages. First, from 10^4 up to 10^5 steps, depending on the case, are needed to accurately reproduce crack onset and propagation in the examples shown and, second, the effect of the decreasing average fragment length as a function of the applied strain has not been taken into account. In order to take into account this effect, for each of the interfacial properties considered, different models having distinct fragment lengths should be considered and combined statistically, according to the experimental

measurements. Therefore, a vast amount of computational resources are needed to determine interfacial properties by inverse analysis using the CZ based approach.

By contrast, the linearization assumed in the LEFM based approach makes the numerical analysis more efficient, since only two linear load cases have to be solved for each set of values considered for the interfacial friction coefficient and the debond length. As described in Graciani et al. (2011), where glass fiber samples are analyzed, including the effect of shortening of the fragments does not increase significantly the amount of work to be carried out because the relation between the crack length and the average fragment length is known from the experimental measurements carried out during the test.

6. CONCLUDING REMARKS

Two distinct numerical analyses of the SFFT have been carried out in order to elucidate the significance of transversal carbon fiber properties in debond propagation along the fiber-matrix interface. Firstly, using a FE model with cohesive elements, the location of the fracture process zone as a function of the applied strain has been obtained using both actual and fictitious isotropic fiber properties. A good agreement is found in the results obtained in the two cases for all the interfacial properties considered. Secondly, using a BE model with fictitious isotropic fiber properties and employing LEFM to study debond propagation, the debond length as a function of the applied strain has been determined. A good agreement is also found in the results obtained with this approach for all the interfacial properties considered. Results presented validate the use of a LEFM based approach, which requires lower computational resources, for obtaining interfacial properties by best fit between test measurements and numerical simulations following the procedure described in Graciani et al. (2011). If fictitious isotropic fiber properties are used, results obtained by this technique may be validated using a FE model with cohesive elements.

ACKNOWLEDGEMENTS

The authors wish to thank Dr. L. Távara and J. L. Alarcón for their help in setting up the computer cluster employed for the numerical simulations. This work has been partially funded by project P08-TEP-04051 (Proyecto de Excelencia de la Junta de Andalucía).

REFERENCES

Graciani, E., Mantič, V., París, F., and Varna, J. (2009). Numerical analysis of debond propagation in the single fibre fragmentation test. Compos. Sci. Technol. 69,2514-2520.

Graciani, E., Blázquez, A., París, F., and Varna, J. (2010). Numerical analysis of the single fibre fragmentation test using cohesive elements. In: ECCM15, 14th European Conference on Composite Materials Proceedings.

Graciani, E. (2010). Numerical analysis of the single fiber fragmentation test including the effect of interfacial friction. Doctoral Thesis, Luleå University of Technology.

Graciani, E., Varna, J., Mantič, V., Blázquez, A. and París, F. (2011). Evaluation of interfacial fracture toughness and friction coefficient in the single fiber fragmentation test. In: ICM11, 11th International Conference on the Mechanical Behaviour of Materials (submitted).

Kelly, A., and Tyson, W.R. (1965). Tensile properties of fiber-reinforced metals: copper / tungsten and copper / molybdenum. J. Mech. Phys. Solids. 13,329-350.

Kim, B.E., and Nairn, J.A. (2002). Experimental verification of the effects of friction and residual stress on the analysis of interfacial debonding and toughness in single fiber composites. J. Mater. Sci. 37,3965-3972.

Proceedings of the 32nd
Risø International Symposium on Materials Science:
Composite materials for structural performance:
Towards higher limits
Editors: S. Fæster, D. Juul Jensen,
B. Ralph, B.F. Sørensen
Risø National Laboratory for Sustainable Energy,
Technical University of Denmark, 2011

FATIGUE DAMAGE COMPUTATION OF A COMPOSITE MATERIAL BLADE USING A "MIXED NON-LINEAR FEM AND SUPER ELEMENT APPROACH"

A. Heege*, G. Adolphs**, P. Lucas***, J.L. Sanchez*, P. Bonnet* and Fco. Diez*

*SAMTEC H Iberica
E-08008 Barcelona
**Owens Corning Technical Fabrics
E-08295 Sant Vicenç de Castellet
***Owens Corning Technical Fabrics
F-7300 Chambery

ABSTRACT

The central point of the present publication is a methodology for non-linear fatigue damage computation of dynamically loaded wind turbine components in the time domain. The proposed method is founded on a coupled aerodynamic, structural FEM and Multi-Body-System approach and permits to compute mechanical component stresses directly during the transient aero-elastic analysis of the wind turbine.

1. INTRODUCTION

Basic input for a fatigue damage computation are, on the one hand, the Rainflow Matrix of stress cycles which classifies the stress transients of all relevant design load cases in terms of mean stress and associated stress cycle amplitudes and, on the other hand, the S-N material curves (Sutherland, 1999).

Several approaches are commonly used for the computation of the Rainflow Matrix of stress cycles. These alternatives include equivalent static FEM and dynamic FEM in the time domain. If dynamic spectral methods in the frequency domain are applied, the stress history is approximated through the corresponding Probability Density Function/PDF. As ~~it~~ will be further commented in section 2, most engineering approaches for fatigue damage evaluations rely on a specific hypothesis in order to reduce the computational cost for the estimation of the fatigue stress spectrum. The respective hypothesis which was adopted in the computation of the Rainflow Matrix of stress cycles, or respectively the PDF of stresses if the fatigue analysis is performed in frequency domain, have a crucial impact on the resulting fatigue damage.

A “mixed FEM and Super Element/SE approach” was developed, in order to evaluate Rainflow Stress Matrices of dynamically loaded wind turbine components without adopting specific

hypothesis in the computation of the fatigue stresses. This numerical approach computes stress transients in hot spots of a wind turbine component directly during the global aero-elastic simulation and permits accounting for the following features:

-Aero-elasticity, further structural dynamic coupling effects and controller variables like the blade pitch transients are accounted in the stress analysis.

-Rainflow Stress Matrices (or respectively the Markov Matrix of stress cycles) are derived directly from Rainflow Counting/RFC of stress transients in time domain (Sutherland, 1999).

-The computational speed permits computation of stress transients in hot spots of wind turbine components for time series of 10 minutes real-time within a few hours CPU time on a standard Personal Computer.

2. FATIGUE ANALYSIS BASED ON DECOUPLED AERO-ELASTIC AND STRUCTURAL STRESS ANALYSIS

In most engineering practices for the fatigue dimensioning of wind turbine components, the computation of the dynamic fatigue load spectrum and the computation of the corresponding component stress cycles were performed separately in a decoupled manner. In this design practice, the global fatigue load spectrum is computed first by aero elastic analysis using simplified structural wind turbine models. Then a decoupled FEM analysis of the considered mechanical components is performed in order to estimate the stress cycles which occur during specific load cases of the aero-elastic analysis.According to commonly applied certification standards (Germanischer Lloyd Industrial Services, 2005), (IEC-61400-1, 2007), the fatigue relevant load spectrum of wind turbine components is derived from hundreds of transient aero-elastic load cases. Most of these aero-elastic load cases have a duration of 10 minutes real time and as a consequence, an equivalent stress analysis based on FEM in the time domain is prohibitive in CPU time. In order to reduce the CPU cost, generally only a reduced set of equivalent static or dynamic load cases is extracted from the fatigue load spectrum. The stress analysis of the components is then performed for the chosen reduced number of equivalent load cases and some hypothesis is necessary in order to derive from the reduced stress results, the Rainflow Stress Matrices which approximate the entire fatigue stress spectrum.

2.1 Decoupled computation of fatigue stress spectrum. In the decoupled approach, the boundary conditions are extracted from the aero-elastic analysis results and equivalent static and dynamic FEM approaches are applied in order to estimate the corresponding spectrum of stress cycles (ANSYS Theory Reference Manual V9.0, 2004), (MSC/NASTRAN, 1998). It is anticipated that decoupled static or dynamic fatigue procedures (either in time or frequency domain) are founded generally on some hypothesis about the statistical distribution of stress cycles. An inconvenience of such decoupled approaches is that the resulting fatigue damage is strongly dependent on the adopted hypothesis about the correspondence of stress results obtained from some load cases and the extrapolation to a stress spectrum which corresponds to the dynamic loads of the entire service life. If decoupled equivalent static analysis is applied, dynamic stress cycles related to local component resonances might be missed.

2.2 Linear spectral fatigue analysis in frequency domain. In spectral fatigue analysis the accelerations and/or the load transients are extracted from the aero-elastic simulation for each DOF of the component junctions of the wind turbine and the transients are processed in order to derive the corresponding Power Spectrum Densities/PSD. The boundary conditions for the

spectral analysis are constructed in terms of an input PSD matrix of loads and accelerations which dimension corresponds to the number of degrees of freedom of all component junction points. Results of the spectral FEA are the PSD of stresses and strains. For the final fatigue damage computation, there is required a model which relates PSD of stresses and the corresponding Probability Density Function/PDF of stress. That hypothesis about the statistical distribution of stress cycles enters the fatigue model in terms of spectral moments and has as a crucial impact on the final damage prediction (Bendat, 1964), (Bishop, 1990), (Sutherland, 1999), (Heege, Hemmelmann, Omiciuolo ,Sanchez, 2010).

The application of spectral methods require that the mechanical sub-system is described by a linear transfer function and the system's excitations and response correspond to linear, stationary random processes with a zero mean value. These requirements are not fulfilled in the case of the examined rotor blade hot spots and as a consequence the impact of the mean stress on the fatigue properties of composite materials cannot be accounted for in a straightforward manner. As a consequence, spectral fatigue methods are judged to be less suited for the present application.

3. COUPLED AERO-ELASTIC, STRUCTURAL DYNAMIC FEM AND MBS ANALYSIS

In the past decade, most load computations had been performed with aero-elastic programs, which were founded on the Modal Approach for the modeling of structural components and on the Blade Element Momentum/BEM Theory for an evaluation of aerodynamic loads. Frequently, the flexibility of these wind turbine models was restricted to the blades, the tower including its foundation and a few degrees of freedom for the flexibility of the power train (Bossanyi, 2004), (Larsen, 2006), (Jonkman, Buhl, 2005), (Oye, 1996).

The present state of the art approaches for the aero-elastic analysis of wind turbine are based on some thousands of Degrees of Freedom/DOF and couple implicitly FEM and Multi-Body-System/MBS functionalities (Samcef-Mecano, 2009), (Geradin, Cardona, 2001), (Heege, Bertran, Radovcic, 2007), (Simpack Reference Manual, 2008), (Elliott, Wright A.D., 1998). These aero-elastic wind turbine models include flexible component models through dynamic Finite Element models, or respectively in their condensed form as Super Elements. Further on, the most relevant mechanisms like pitch and yaw drives or detailed power train models are included in the same aero-elastic analysis model.

An accurate approach for the computation of component stress cycles is to include the considered flexible components in terms of non-linear dynamic FEM models in the global wind turbine model. Functionality is offered by the applied non-linear dynamic FEM-MBS solver SAMCEF-Mecano (Samcef-Mecano, 2009), (Geradin, Cardona, 2001), (Heege, Bertran, Radovcic, 2007), but leads to high CPU times, if a large number of DOF are included in the aero-elastic wind turbine model through the FEM component models. A common approach for the reduction of a component DOF is to condense the FEM model to a Super Element and to integrate the later into the aero-elastic wind turbine model. The Super Element approach is very efficient in order to include in an aero-elastic wind turbine model global component flexibilities and inertial properties. However the Super Element approach is not a computationally efficient solution for the computation of stress transients. This is because the computational cost for recovering at discrete time instances of the aero-elastic analysis from the condensed Super Element solution the deformation and stress transients of the uncondensed FEM model, is comparable to the cost of including directly uncondensed FEM components in the aero-elastic model.

4. BLADE MODELING BY A "MIXED FEM & SUPER ELEMENT APPROACH"

The structural blade model of the wind turbine model is loaded aero-dynamically at discrete blade section nodes through the application of the Blade Element Momentum/BEM theory. The aero-elastic coupling is performed in the case of the Super Element blade model at the retained blade SE nodes which are located at the ¼ chord length positions of 15 equally spaced blade sections.Figure 1 illustrates schematically the adopted "retained Super Element nodes", if 1 hot spot at the spar cap is modeled. The blade Super Element model is connected at retained node number 1 to the rotor hub model of the global aero-elastic model. The aero-dynamic load elements which are based on the BEM theory are implicitly coupled through retained nodes 2 to 16 to the structural blade model. Finally, Super Element nodes 17 to 20 are retained in order to model a hot spot in the region of the spar cap by a composite material FEM shell element. As depicted in Figure 2, these retained SE nodes at the ¼ chord length positions were connected to the FEM-nodes of the exterior blade skin through "averaged weighted kinematic constraint equations" (also denominated in practice RBE3 or Mean Elements). In that approach "averaged weighted kinematic constraint equations" are applied in order to couple the retained slave nodes which are retained for the aerodynamic coupling at the ¼ chord length positions and the master nodes located on the exterior blade skin. The weights of the kinematic constraint equations define the transfer of the discrete aero-dynamic load vectors from the ¼ chord length positions to the exterior blade skin and have a crucial impact on the local stress distribution. Ideally, these weights of the coupling constraints should be chosen such that realistic aerodynamic pressure & viscous load distribution is roughly approximated. An inherent feature of the Super Element method is that the computational model is linear with respect to a moving reference frame and material non-linearities or stress induced stiffening is not accounted for.

In the case of the "mixed FEM & SE method", the hot spot is presented through full FEM modeling and all non-linearities are accounted for and specific features of the solver SAMCEF-Mecano for advanced composite modelling can be exploited (Samcef-Mecano, 2009), (Bruyneel, Delsemme, Jetteur, German, 2009).

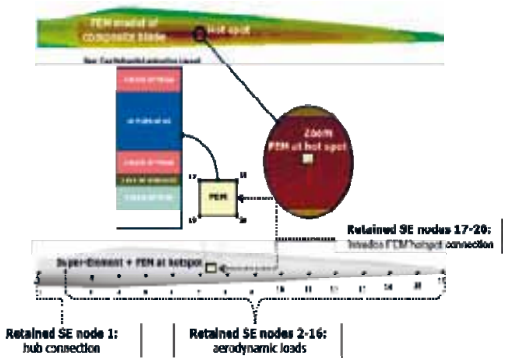

Fig. 1. Definition of retained nodes of "mixed FEM and Super Element blade model"

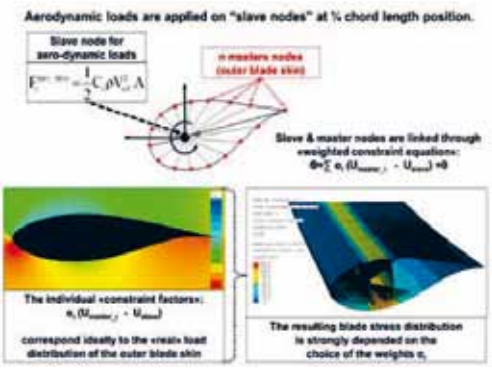

Fig. 2. Coupling of aero-dynamic "slave load node" & "master nodes"

Component models which are subjected to fatigue evaluations have to be specifically prepared and integrated into the wind turbine model in order to include FEM modeling at the hot spots which are to be evaluated. This requires prior to the aero-elastic analysis of fatigue relevant design load cases that hot spots are identified and component models updated correspondingly.

It is emphasized that the "mixed FEM & Super Element component models" might include several non-condensed domains in order to preserve full FEM modelling simultaneously in different hot spots. However, since the resulting Super Element matrices are fully occupied, for computational efficiency the total number of retained Super Element nodes should stay inferior to some hundred nodes. In the blade model presented, 4-noded composite material shell FEM elements are applied for the discretization of the hot spots and, as a consequence, about 25 hot spots might be analyzed efficiently with a "mixed FEM & Super Element component model".

The required manpower for the preparation of a "mixed FEM & Super Element component model" can be summarized by the following basic steps:

- Identification of the hot spots
- Generation of the Super Element model which retains all required nodes in the hot spots for full FEM modeling, as well as the nodes required to connect the component model to the global aero-elastic wind turbine model.

Anticipating that the original FEM component model is pre-existing, an experienced analyst requires a few days work in order to adapt and generate the "mixed FEM & Super Element model" and in order to integrate the updated component model in the global aero-elastic wind turbine model.

5. HOT SPOT IDENTIFICATION FOR THE PREPARATION OF COMPONENT MODELS

Generally, either equivalent static or dynamic FEM methods are applied in order to identify the most fatigue relevant areas. As follows some experiences in the hot spot identification will be discussed.

5.1 Stress computation by super element recovery. The Super Element Restitution permits computation through a "back-transformation" of the condensed solution vector which is associated to the DOF's of the Super Element, the corresponding solution of the original FEM model (Ansys Theory Reference Manual V9.0, 2004), (Bendat, 1964), (Craig, Bampton, 1968), (SAMCEF-Dynam, 2009). As depicted in Figure 3, if component models are integrated in the aero-elastic wind turbine model through Super Elements, the full FEM solution of the component model is obtained through the Super Element restitution process at any time step of the transient analysis,. That approach accounts for all the dynamic effects, but not for material and not for geometric non-linearities like stress induced stiffening. It is emphasized that the stress recovery by the Super Element restitution is only performed in order to localize the hot spots of the component model. As outlined in Figure 4, the stress computation for the fatigue analysis is performed through the updated wind turbine model which incorporates the specifically adapted "mixed FEM & Super Element" component model.

5.2 Equivalent static analysis based on pressure mapping. For the identification of the blade hot spots, as an alternative to the Super Element restitution, an uncoupled static approach was applied. In that equivalent static approach, the discrete aerodynamic load vectors at the "retained Super Element nodes at the ¼ chord length positions" are mapped into a 3D pressure distribution which is applied on the blade skin of the uncondensed FEM blade model. In that approach, the 3D pressure distributions are obtained from the extrapolation of 2D pressure profiles along the blade span. The equivalent 2D pressure profiles were computed by the program Xfoil (Drela, Giles, 1987) by a panel method.

In that equivalent static FEM analysis, viscous drag effects are neglected and gravity and centrifugal loads are approximated through external boundary conditions.

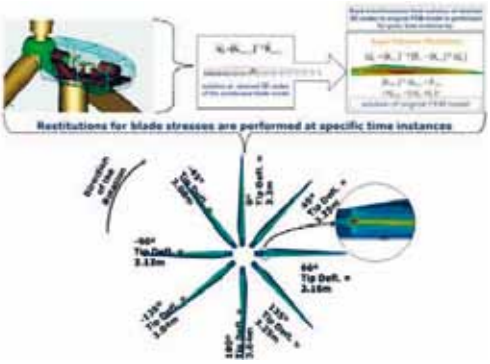

Fig. 3. Tsai-Wu stress criteria at critical plies computed from Super Element recovery

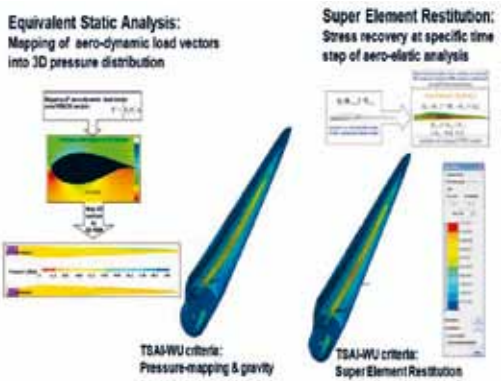

Fig. 4. Hot spot identification by "Pressure Mapping" and "Super Element Restitution"

5.3 Hot spot identification at spar cap and at trailing edge. As shown in Figure 3 in terms of the Tsai-Wu stress criteria at the critical ply, the FEM solution obtained either by Super Element Recovery from the aero-elastic analysis, or respectively by an equivalent static analysis showed qualitatively very similar results and identified the same locations of the hot spots at the blade root, at the spar cap and at the trailing edge.

However, even if the qualitative stress results showed good agreement, differences in quantitative hot spot stresses of up to 15% where obtained by both methods. It is emphasized that these deviations in quantitative stress results are of minor importance as they do not enter the final fatigue computation, but are used only to identify the hot spots. As illustrated in Figure 4, the stress transients which are finally computed with the updated aero-elastic wind turbine model rely on a non-linear dynamic FEM modeling of the hot spots. As a consequence, all non-linear dynamic effects can be accounted in the hot spots.

6. FATIGUE ANALYSIS OF A ROTOR BLADE BASED ON THE "MIXED FEM AND SUPER ELEMENT APPROACH"

According to the computational scheme presented in Figure 5, the stress transients for the final fatigue evaluation were computed according to a sub-set of IEC-61400 design load cases (IEC-61400-1, 2007) which includes turbulent wind fields in the range of 4[m/s] to 25 [m/s]. Figure 6 shows the computed stress transients in the direction of lamination for different plies at the spar cap hot spot side-extrados.

As depicted in Figure 5, the Rainflow Matrix of major principal stresses is obtained through the RFC of stress cycles where each cycle is decomposed into a mean stress (compression or traction) and the associated stress amplitude.

The stress transients, who are depicted in Figure 6 for the hot spot at the spar cap side extrados for different material plies, are computed directly from the global aero-elastic wind turbine model. It is mentioned that the stress transients shown in Figure 6 correspond to an IEC-61400 design load case of a mean wind speed of 13 [m/s] and a turbulence intensity of 18.9%. The

Rainflow stress matrix depicted in Figure 7, is constructed by Rainflow Counting of the stress transients which were computed for a sub-set of IEC-61400 design load cases which include turbulent wind fields of mean speeds from 4 [m/s] to 25 [m/s].

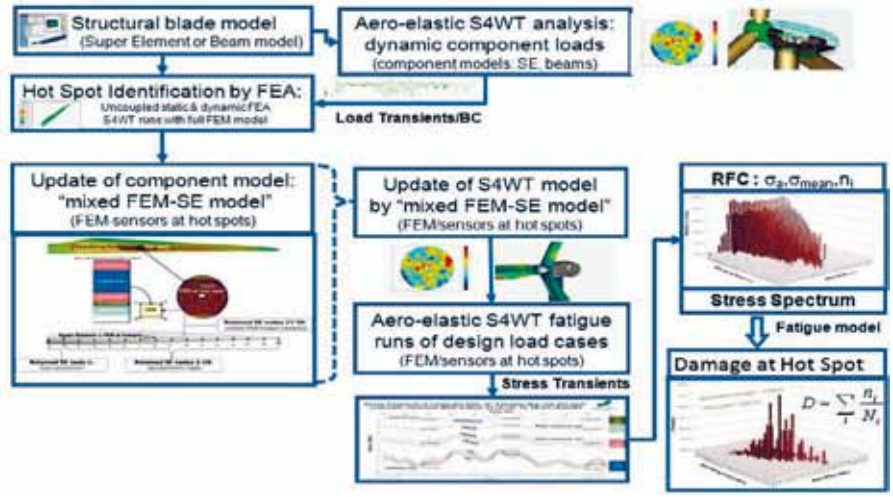

Fig. 5. Fatigue damage computation based on "mixed FEM and Super Element" blade model

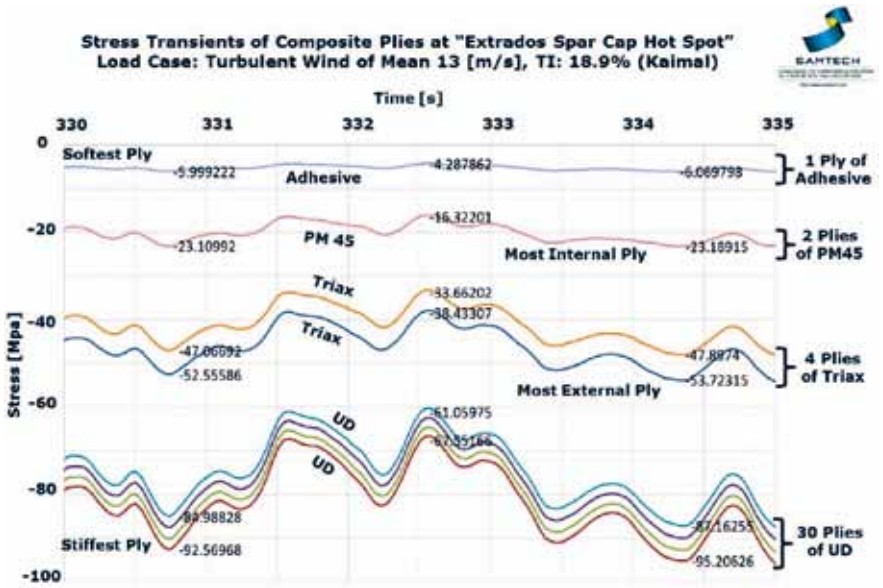

Fig. 6. Stress transients at the extrados hot spot of the spar cap for different plies

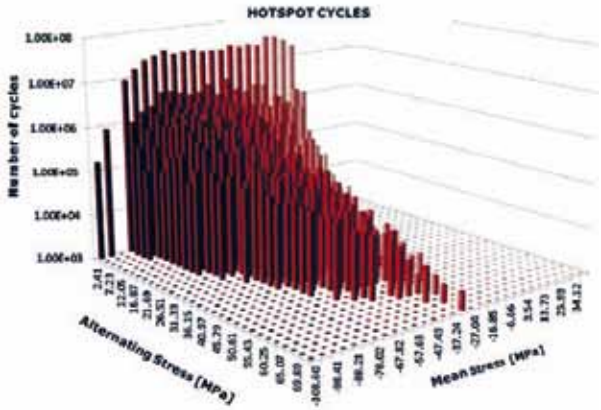

Fig. 7. Rainflow Matrix of stresses of critical ply at the extrados hot spot of spar cap

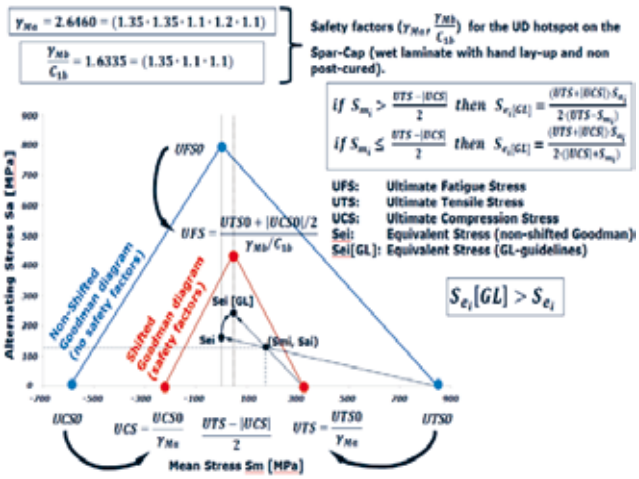

Fig. 8. Shifted Goodman diagram according to Germanisher Lloyd certification guidelines

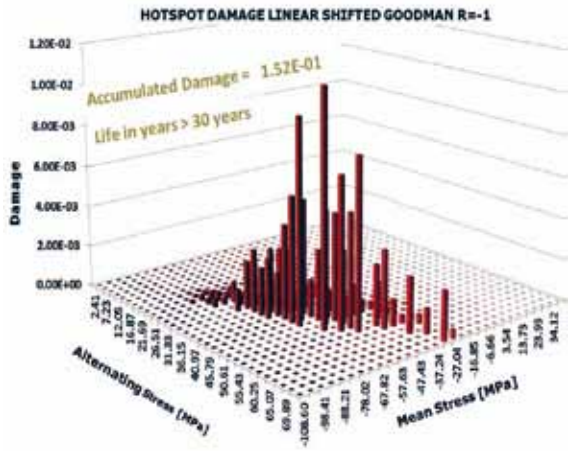

Fig.9. Matrix of damage contributions of critical ply at the extrados hot spot of the spar cap

The final fatigue damage is computed by the Palmgren-Miner rule and the use of shifted Goodman diagrams which are constructed from experimental uni-directional S-N curves. As illustrated in figure 8, the applied safety factors have a crucial impact on the final computational fatigue damage. In Figure 9 is depicted for the spar cap hot spot (side extrados) the damage contribution which is computed for each classification bin of the original Rainflow Stress Matrix. It is mentioned that the fatigue damage computation presented in figure 9 is based on a shifted Goodman diagram (see figure 8) according to the safety factors proposed by the Germanischer Lloyd certification guidelines (Germanischer Lloyd Industrial Services, 2005).

6.1 Principal stress and fiber direction. In the case of uni-directional/UD glass fiber composite materials, the accumulation of fatigue damage is determined essentially by the amplitude of stress cycles, the sign and value of mean stresses (compression or tension) and the angle in between the fiber direction and the direction of the principal stress. In certification guidelines special emphasis is put on the fatigue safety factors which are to be applied on Goodman diagrams in order to account for compression mean stresses and for the "Principal Stress-Fiber Angle" in between the UD fiber direction and the major principal stress direction.
The distribution of the "Principal Stress-Fiber Angle" is depicted in Figure 10 for the hot spot at the spar cap and in Figure 11 for the hot spot at the trailing edge for a turbulent IEC load case of 13[m/s] mean speed [3]. It is deduced from Figure 10 that the "principle angle" in between the principal stress direction and the UD-fiber direction is about 5 [degrees] at the extrados spar cap hot spot.

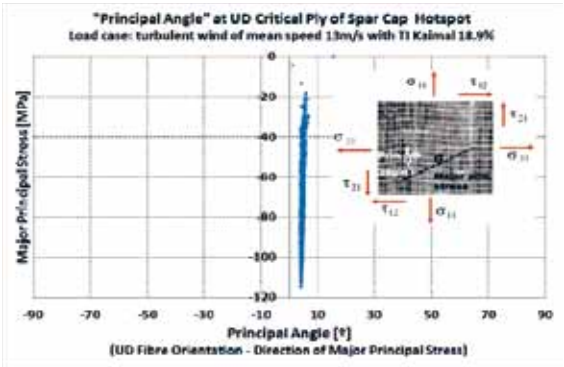

Fig. 10. Angle in between direction of major principle stress & UD fiber direction at spar cap

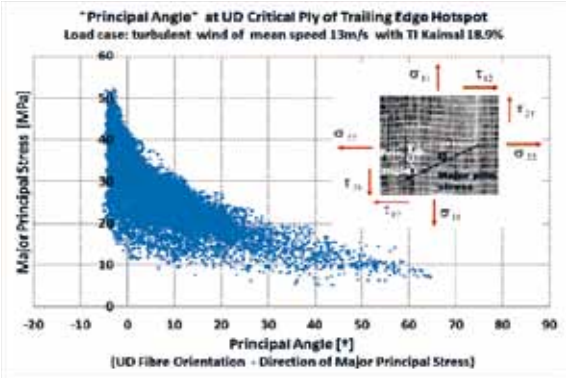

Fig. 11. Angle in between direction of major principle stress & UD fiber direction at trailing edge

Since the value of the principle angle is small and practically constant, it is concluded that the UD fibers at the investigated spar cap hot spot are orientated correctly in order to absorb properly the examined operational loads of the blade. It is deduced from Figure 11 that for the hot spot at the trailing edge, the direction of the major principal stress deviates up to 65 [degrees] with respect to the UD fiber direction. It is concluded for the trailing edge hot spot that the UD composite material is not loaded exclusively in the fiber direction. As a consequence, in order to account for the reduced fatigue properties of the matrix material, further correction factors should be applied on the uni-directional S-N material curves.

7. CONCLUSIONS

The presented "mixed FEM & Super Element approach" combines the inherent advantages of an implicit non-linear dynamic FEM method for accurate stress computation in the time domain and the advantages of the Super Element Method for CPU efficient modeling of flexible components. Since non-linear FEM modeling is preserved in the rotor blade hot spots considered, the "mixed FEM & Super Element approach" permits the computation of multi-axial "stress/strain tensor cycle data" in each ply of the composite material laminates. However, even if multi-axial stress/strain tensor cycle data can be computed efficiently by the proposed methodology, for precise fatigue damage predictions of composite materials, further development of fatigue laws and experimental testing are necessary.

The initiation of fatigue failure mechanisms of composite structures include inter-laminar delamination and crack propagation which can be of intra-laminar and inter-laminar characteristics. Both phenomena might be induced by excessive compressive stresses which can produce local buckling and eventually matrix failure or delamination. A misalignment of the principal fiber orientation and the direction of major principal stress cycles might result in important shear stresses and damage specifically the binder. These two failure mechanisms can be roughly estimated if the applied fatigue methodology accounts for:

- Rainflow matrices of stress/strain cycles which are derived from dynamic stress/strain transients of the examined component hot spots.
- Fatigue models which account for mean stress/strain and the associated stress/strain cycle amplitudes like for example Goodman corrected S-N diagrams.
- Extended S-N material curves and RFC based damage evaluations which account in addition to the mean stress/strain and associated cycle amplitudes, as well for the "principal angle" in between the fiber direction and major principal stress/strain cycles.

The presented fatigue damage computation, was based on experimental uni-directional S-N material fatigue curves of the commercial UD fibers OCV/Advantex© & OCV/HP-epoxy©. All fatigue evaluations were performed according to GL certification standards (Sutherland, 1999) using Goodman corrected S-N diagrams which had been shifted in order to account for reduced compression strength and for further safety factors which are due to the respective fabrication process. For the investigated hot spots in the spar cap (sides intrados & extrados), for both mentioned UD materials, the "Principal Stress-Fiber Angle" was generally below 15 [deg.] and a fatigue life superior to 40 years was computed for both UD fiber layouts, even if conservative safety factors were applied.

In the case of the stress hot spot at the trailing edge, the authors are less confident about the precision of the fatigue prediction. This is because the computed distribution of the "Principal Stress-Fiber Angle" revealed dynamically alternating stress misalignments with respect to the

principal fiber directions and thus loading substantially the matrix (epoxy) of the composite layers. The applied fatigue model does not account for dynamically alternating multi-axial stress states and only uni-directional S-N material curves are presently available. As a consequence, the fatigue evaluation is based on S-N curves which include safety and corrections factors, but little knowledge about these corrections is available. Further investigation is required in order to improve the understanding of fatigue damage produced by cyclic misalignment of UD fiber orientations w.r.t. the principal stress directions, as was observed in the investigated trailing edge hot spots. This will require further experimental fatigue testing and future investigations will be focused on uni-directional S-N material curves which are derived for different UD fiber orientations. It is anticipated that further fundamental investigations will be required in order to approximate damage mechanisms produced by multi-axial stress cycles of composite materials.

Analogously to the impact of the R=σmin/ σmax value on S-N material curves, the "Principal Stress-Fiber Angle" might be incorporated in the future as a further variable in the fatigue model.

REFERENCES

Sutherland, H.J. (1999). On the Fatigue Analysis of Wind Turbines, SAND99-0089, Sandia National Laboratories P.O. Box 5800 Albuquerque, New Mexico 87185-0708.

Germanischer Lloyd Industrial Services GmbH (2005): Guideline for the Certification of Offshore Wind Turbines.

IEC-61400-1, Ed. 3, 2005-8. 2007). Wind Turbine Design requirements.

ANSYS Theory Reference Manual V9.0. (2004). www.ansys.com.

MSC/NASTRAN Numerical Methods User's Guide V70.5. (1998). www.mscsoftware.com.

Bendat, J.S. (1964). "Probability functions for random responses". NASA report on contract NAS-5-4590.

Bishop, N.W. and Sherratt, F. (1990). A theoretical solution for the estimation of rainflow ranges from power spectral density data. Fatigue Fract. Engng Mater. Struct., Vol. 13, pp. 311-326.

Heege, A., Hemmelmann, J., Omiciuolo M., Sanchez, J.L. (2010).Comparison of wind turbine component damage computed by linear and fully non-linear fatigue methodologies. EWEC 2010 Proceedings

Bossanyi, E. A. (2004). GH-Bladed User Manual, Issue 14, Garrad Hassan and Partners Limited, Bristol, UK.

Larsen, TJ. (2006). HAWC2 User Manual version 1.4, Risø National Laboratory.

Jonkman, J.M., Buhl M.L. Jr. (2005).FAST User's Guide, Technical Report NREL/EL-500-38230.

Øye, S. (1196). FLEX 4 - Simulation of Wind Turbine Dynamics. Proceedings 28th IEA Meeting of Experts "State of the Art of Aeroelastic Codes for Wind Turbine Calculations", pp. 71-76, Technical University of Denmark, Lyngby, Denmark, April 11-12

Samcef-Mecano User Manual V.13. (2009). Samtech SA,www.samcef.com.

Geradin, M. and Cardona, A. (2001). Flexible Multibody Dynamics: A Finite Element Approach. John Wiley and Sons Ltd.

Heege A., Betran J., Radovcic Y. (2007). "Fatigue Load Computation of Wind Turbine Gearboxes by Coupled Finite Element, Multi-Body-System and Aerodynamic Analysis", Wind Energy, vol. 10:395-413.

Simpack Reference Manual V8.805. (2008) INTEC GmbH, Germany.

Elliott, A. S. and Wright, A. D. (1198). Adams/WT 2.0 User's Guide, Mechanical Dynamics Inc. (Ann Arbor, Michigan, US) and National Renewable Energy Department (Golden, Colorado, US).

Bruyneel M., Delsemme J.P., Jetteur Ph., Germain F. (2009). Modeling inter-laminar failure in composite structures: illustration on an industrial case study, Applied Composite Materials, 16(3), pp. 149-162.

Craig, R. and Bampton, M. (1968). "Coupling of substructures for dynamic analysis", AIAA Jnl., Vol. 6 no. 7. pp.:1313-1319.

SAMCEF-Dynam User Manual, version 13.1-01. (2009). www.samtech.com.

Drela, M. and Giles, M.B. (1987). Viscous-Inviscid Analysis of Transonic and Low Reynolds Number Airfoils, AIAA Journal, 25(10), pp.1347-1355.

Proceedings of the 32nd
Risø International Symposium on Materials Science:
Composite materials for structural performance:
Towards higher limits
Editors: S. Fæster, D. Juul Jensen,
B. Ralph, B.F. Sørensen
Risø National Laboratory for Sustainable Energy,
Technical University of Denmark, 2011

MECHANICAL AND THERMAL PROPERTIES OF CARBON FIBER/EPOXY COMPOSITES FOR THE ARM OF A MOBILE ROBOT

M. Janiszewska, A. Boczkowska and Z. Pakiela

Warsaw University of Technology
Faculty of Materials Science and Engineering
Woloska 141 str., 02-507 Warsaw, Poland

ABSTRACT

Several types of samples with various fiber orientations were produced for the measurement of the orientation influence of carbon fiber on the composite strength and stiffness. For this purpose, composites reinforced with unidirectional carbon fibers, as well as 2D fabrics, plain and twill were manufactured. It was found that samples of unidirectional reinforced composite had the highest strength. The average value of tensile strength of these samples was about 1080 MPa. It was also found that the composites reinforced with plain weave fabrics have higher strength and Young's modulus than composites with twill weave fabrics.

In regard of a planned working temperature of the robot ranging from -50ºC to 150ºC in case of continues work and up to 650 ºC temporarily, thermo gravimetric analysis (TGA) and differential scanning calorimetry (DSC) tests of the material degradation were made. This temperature is defined as a temperature of 5% loss of a sample mass. It was found that this temperature for the investigated material is in the range of 315 ºC - 320 ºC. DSC studies allowed an evaluation of glass transition temperature T_g were also performed. The thermal analysis allowed measurement of the temperature fabricated composites. It was found the average Tg of the tested materials is about 95ºC.

1. INTRODUCION

Attractive properties of carbon fiber/epoxy composites make them very useful in various applications particularly in cases where high stiffness and specific strength are expected. One of such applications is the arm of a mobile robot for special tasks during rescue operations. Replacement of usually used aluminum alloys with carbon fiber/epoxy composites can cause

mass reduction of the robot arm and consequently an increase of the robot load capacity.

Application of carbon/ epoxy composites requires an investigation of the mechanical and thermal properties of the material at different load directions. For the purpose of the study four types of samples with various fibers orientations were produced. These samples were used for the measurement of the orientation influence of carbon fibers on the composite strength and stiffness. Two different composites reinforced with unidirectional carbon fibers, as well as composites reinforced with 2D fabrics, plain and twill were manufactured.

2. EXPERIMENTAL DETAILS

2.1 Materials. Carbon fiber/epoxy composites were used for testing. The samples were made using the EPIKOTE resin MGS LR 285 produced by the Hexion Specialty Chemicals company and the carbon fibers produced by INTERGLAS TECHNOLOGIES [www.Hexion.com]. All samples were air-cured at room temperature. Characteristic parameters of the composites used are presented in Table 1.

Table 1 Characteristic parameter of the composite materials used

Samples symbols	Dimensions l l x b x h [mm]	Type of reinforcement	Number of layers	Direction of fibers	Fibers content		Resin /Hardener
					mass	volumetric	
R	149.9x14.5x1.2	KDU 1007, unidirectional tape,	4	T	0.51	0.41	MGS 285/286
S	10.15x9.95x2.2	KDU 1007, unidirectional tape,	7	T	0.51	0.41	MGS 285/286
SC	150x24.6x2.4	fabric 98130, plain weave,	10	X	0.50	0.40	MGS 285/286
SP	150x24.6x2.2	fabric 98130, twill weave	10	X	0.50	0.40	MGS 285/286

2.2 Experimental procedure. Composites labeled R, SC and SP were used for static tensile tests at room temperature. These tests were performed according to standards [PN - EN ISO 527; PN - EN ISO 14129; ASTM D3479/D3479M-96]. MTS 810 testing machine was used. Deformation was measured in two perpendicular axes using a digital image correlation (DIC) method. Tensile tests were carried out with a constant displacement velocity a 2 mm/minute. The tests allowed measuring such materials parameters as: tensile strength, Young's modulus, Poisson's ratio. For calculation of the Poisson's ratio deformation measurements in two directions, along the tensile direction and in the perpendicular direction were done.

Thermo gravimetric analysis (TGA) was used to determine the temperature of 5% weight loss. The test was performed using a TA instrument TGA Q500 at heating rate of 283.15 K minute^{-1}. The samples were heated from room temperature to 650 ºC in an argon atmosphere. The

samples were cut into small pieces using a Buehler's "Isomet" low speed saw. The mass of the sample used was about 7 – 10 mg. These samples were placed into aluminum crucibles and placed inside the TGA chamber.

The glass transition temperature was measured by a differential scanning calorimeter (DSC) using a Q1000 TA instruments. The mass of the samples used was approximately 10 mg. The test was conducted using a heating-cooling-heating scheme of testing, in the temperature range from -50 ºC to 150 °C. The heating rate of samples was 283.15 K minute^{-1}, while cooling 278.15 K minute^{-1}. The tests were conducted in an argon atmosphere.

Microscopic observations of samples after tensile tests were carried out using a SEM (Hitachi TM-3000).

3. RESULTS AND DISCUSSION

3.1 Tensile tests. The results of the tensile tests of three types of composites are shown in Fig.1 and in Table 2

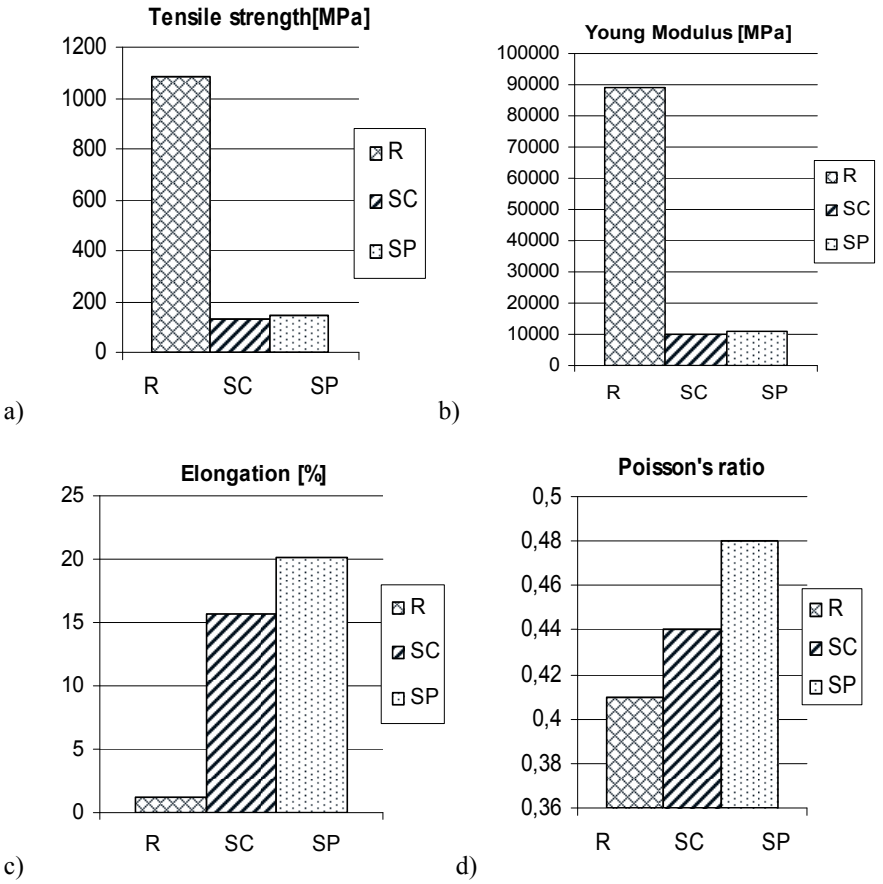

Fig. 1 The results of the tensile tests: a) tensile strength; b) Young's modulus; c) elongation; d) Poisson's ratio

Table 2. Mechanical properties of the tested composites

Samples symbols	Tensile strength [MPa]	Standard deviation [MPa]	Elongation [%]	Standard deviation	Young's modulus [GPa]	Standard deviation [GPa]	Poisson ratio	Standard deviation
R	1084	28.5	1.2	0.34	89.2	22.0	0.41	0.06
SC	134	2.1	15.7	3.35	10.0	1.1	0.44	0.02
SP	142	8.7	20.2	1.91	10.8	0.7	0.48	0.05

Samples with unidirectional tape reinforcement had the highest strength. The average value of the tensile strength of these samples was about 1080 MPa. For this type of composites, the measured elongation did not exceed 2%. It was also found that the composites reinforced with plain weave fabrics have a higher strength and Young's modulus than composites with the twill weave fabrics. Elongation to failure was bigger than in unidirectional reinforced composite and equals about 15-20%.

3.2 Thermal analysis. TGA measurements were carried out for an estimation of the thermal stability of various composite systems.

The type of reinforcement has a weak effect on the degradation temperature. The effect of reinforcement type on 5% weight loss temperature was observed on TGA curves. Figure 2 shows the TGA of four types of composites considered in this study. The following trend can be observed: with the number of reinforcement layers where an increase in the rise of the thermal resistance was observed (Fig. 3).

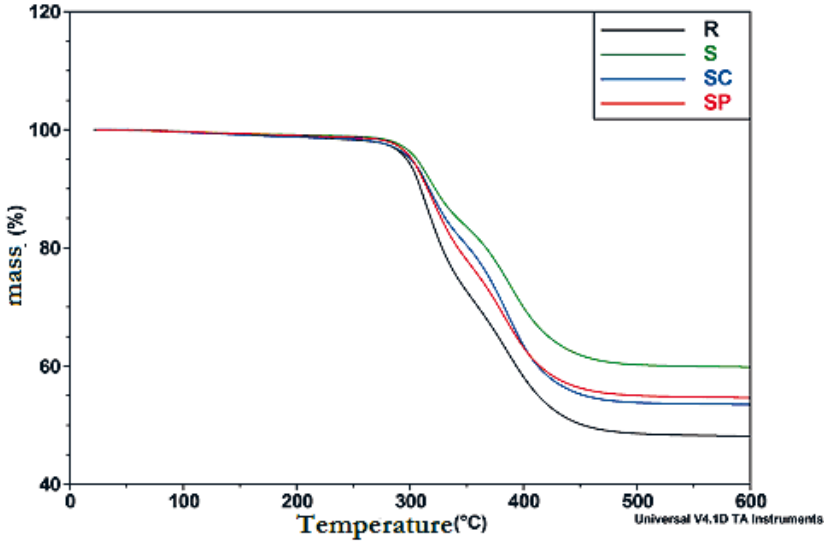

Fig. 2. Weight loss during heating

Increasing the number of reinforcement layers increases the thermal resistance temperature and the peaks of weight loss rate temperature. However, this effect is not very strong. Only a small temperature increase (about 6°C) was observed.

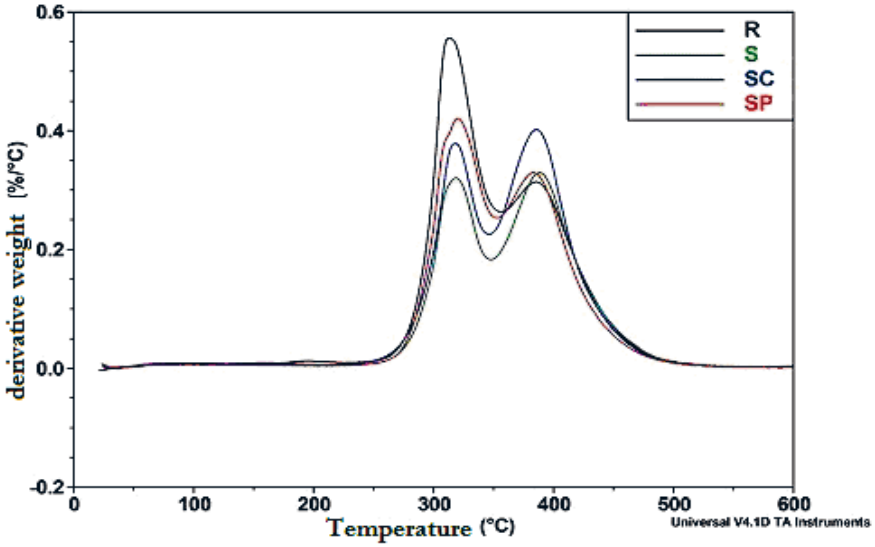

Fig. 3. Weight loss rate of the samples during DSC examination

The results of the DSC measurement of four types of composites are shown in Table 3.

Table 3. The characteristic materials parameters measured by DSC

Samples	5% weight loss [ºC]	1st pick [ºC]	2nd pick [ºC]	residue [%]	residue [mg]	T_g [ºC]
R	297.0	313.8	386.2	48	4.2	91.2
S	305.9	318.6	389.0	59	5.1	95.2
SC	300.6	317.8	385.4	54	4.3	92.3
SP	301.6	320.4	382.5	55	5.5	97.5

The type of composite reinforcement has not affected the glass transition temperature. There were not observed an influence of the direction of fiber arrangement, or the type of carbon fiber fabric on the T_g (Fig.4). In contrast, the contents of fibers affected the value of T_g of the resin used. Therefore the T_g value declared by the manufacturer is higher than the T_g measured for the composites containing about 40% vol. of fibers.

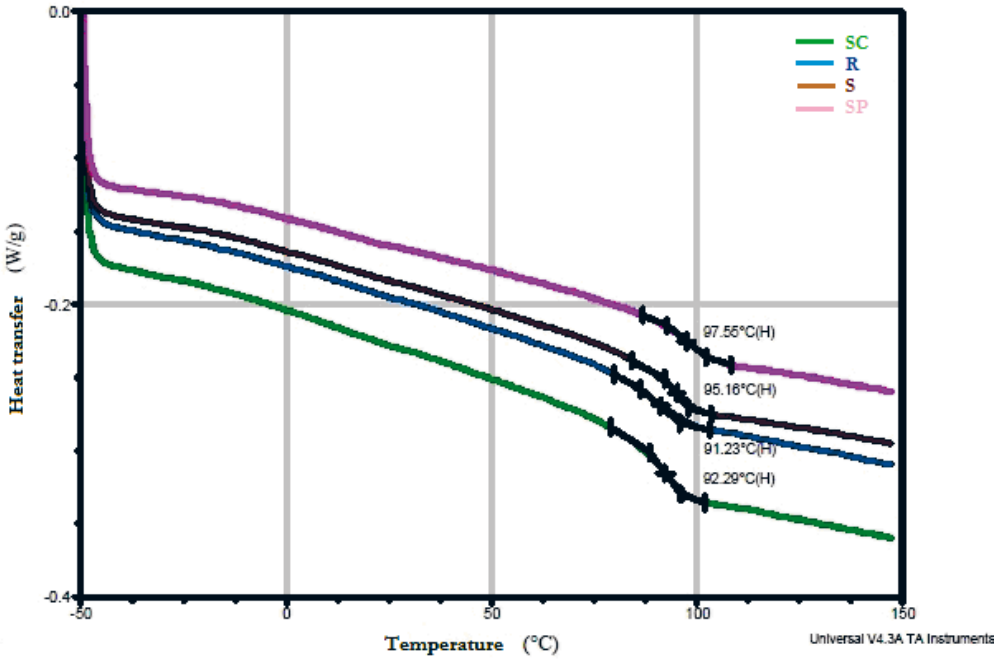

Fig. 4 Glass transition temperature determined by the DSC

3.3 Microscopic observations. For microstructure observations the samples after static tensile tests at room temperature were used (Fig.5). All the observed samples of composites were delaminated. The composites of epoxy-carbon fiber with plain weave fabric reinforcement were broken in an irregular manner. In the twill weave fabric reinforcement composites there were observed the various strands of fibers. The samples reinforced by unidirectional tape were damaged perpendicularly to loading direction but also cracks along the fibers parallel the loading direction were observed.

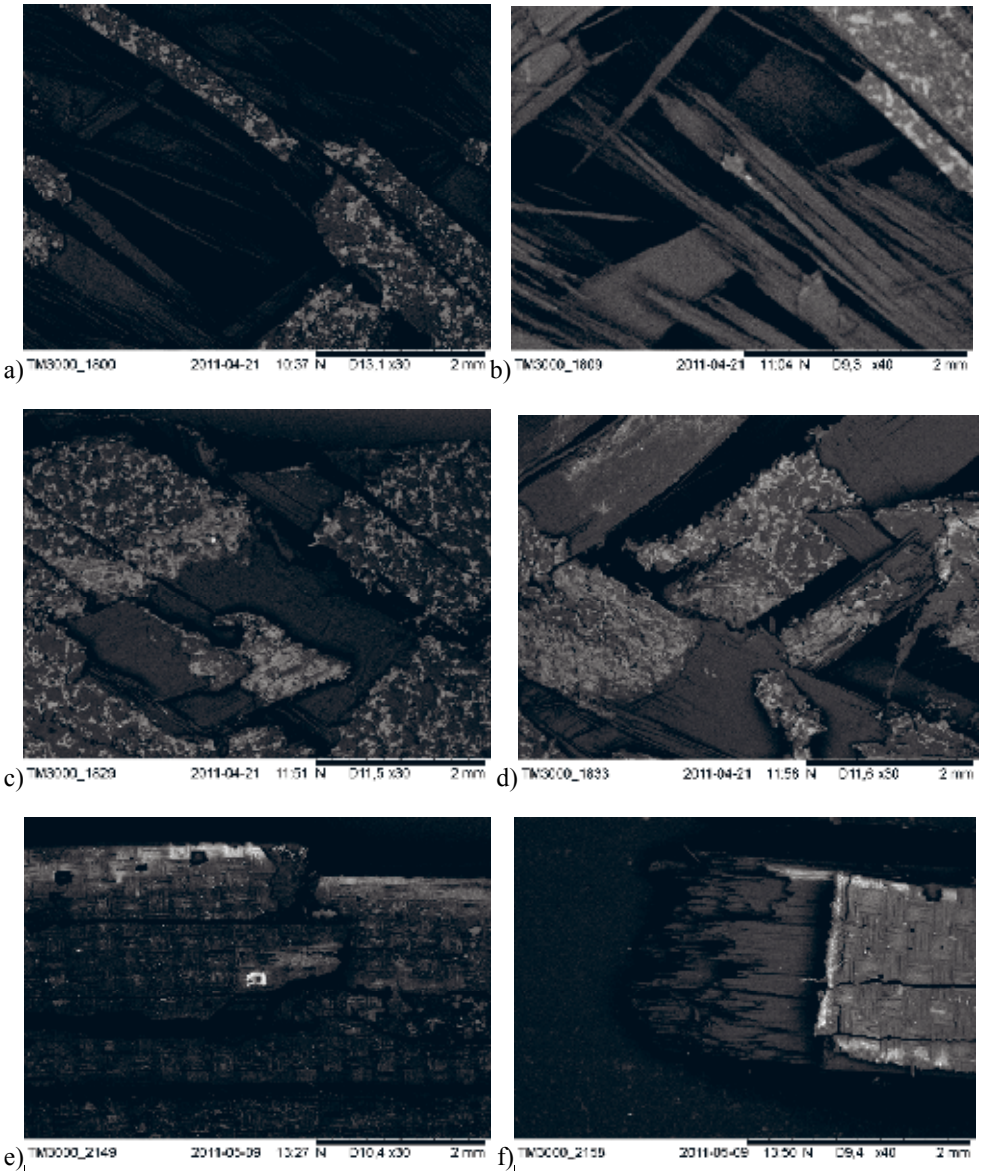

Fig. 5. SEM image: a-b) plain weave fabric; c-d) twill weave fabric; e-f) unidirectional tape

4. CONCLUSIONS

It was found that samples of unidirectional reinforced composite had the highest strength. The average value of the tensile strength of these samples was about 1080 MPa. It was also found that the composites reinforced with plain weave fabrics have a higher strength and Young's modulus than composites with the twill weave fabrics.

It was found that temperature of 5% loss of a sample weight for the investigated materials is in the range of 315 ºC - 320 ºC. The glass transition temperature T_g of fabricated composites measured by the DSC method is about 95ºC.

Scanning electron microscopy observations of composites revealed that the fracture surface type strongly depends on the reinforcement arrangement.

REFERENCES

EPIKOTE™ Resin 862 Data Sheet. http://www.Hexion.com/products.

ASTM D3479/D3479M-96. Standard test method for tension-tension fatigue of polymer matrix composite materials; 2007.

PN - EN ISO 527 Tworzywa sztuczne -- Oznaczanie właściwości mechanicznych przy statycznym rozciąganiu -- Część 5: Warunki badań kompozytów tworzywowych wzmocnionych włóknami jednokierunkowo

PN - EN ISO 14129 Kompozyty tworzywowe wzmocnione włóknem -- Oznaczanie naprężenia ścinającego i odpowiadającego odkształcenia, modułu ścinania i wytrzymałości podczas rozciągania pod kątem +- 45 stopni

ACKNOWLEDGMENTS

The authors would like to gratefully acknowledge the support of the european regional development fund within the framework of the 1. priority axis of the innovative economy operational programme, 2007-2013, submeasure 1.1.2 "strategic r&d research". Contract no. poig.01.02.01-00-014/08.

Proceedings of the 32nd
Risø International Symposium on Materials Science:
Composite materials for structural performance:
Towards higher limits
Editors: S. Fæster, D. Juul Jensen,
B. Ralph, B.F. Sørensen
Risø National Laboratory for Sustainable Energy,
Technical University of Denmark, 2011

FAILURES IN TRAILING EDGE BONDLINES OF WIND TURBINE BLADES

F.M. Jensen*, J.D. Sørensen*, **, P.H. Nielsen*,
P. Berring* and S. Flores*

*Wind Energy Division, Risø National Laboratory for Sustainable Energy, Technical University of Denmark
**Department of Civil Engineering, Aalborg University, Denmark

ABSTRACT

Bonded joints in composite structures are often an object for concern. This is also true for wind turbine blades, where damage occurs in the trailing edge due to fatigue loads. Reliability of wind turbines becomes increasingly important when used offshore, where operation and maintenance costs constitute a significant part of the cost per kWh produced. However, the wind turbine industry is reluctant to share statistical values for damages, and this makes it more difficult to assess the reliability. Instead of analyzing the joint and reinforce the connection, research at Risø DTU has shown, that it possible to reduce the deformation of the trailing edge panels and thereby reduce the peeling stresses in the trailing edge joint. A basic solution patented by Risø DTU is presented. The research is based on a combination of numerical analysis and full-scale testing. The research has shown the need for improved full scale testing.

1. INTRODUCTION

Out-of-plane deformations of wind turbine blade trailing edge panels are important since they can cause peeling stresses in the bondlines. These effects are thought to be the main reason for fatigue failure in trailing edge adhesive joints, see Fig. 1 from Jensen, F. M. (2008).

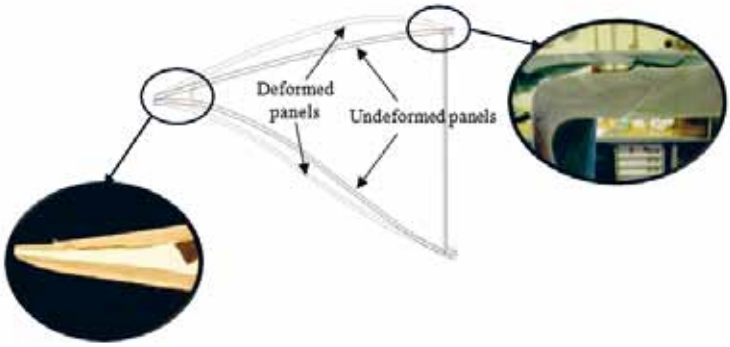

Fig. 1. Sketch of the trailing edge shells with out-of-plane deformations. The close ups show failure at the trailing edge as well as debonding of the outer skin on the box girder.

It is well-known from the literature that bondlines have a low strength when exposed to peeling stresses compared to the other loading directions, e.g. the fracture energy is approximately a factor 8-10 higher for mode 2 (shearing) than for mode 1 (peeling) loading.

For decades, wind turbine blades have been tested in full-scale tests, required by the certification bodies, e.g. GL and DNV, see Germanischer Lloyd WindEnergie GmbH. (June 2005) and Det Norske Veritas (October 2010). Static tests with extreme loads are required in both flap and edgewise directions. DNV also requires a 20 year fatigue test, see Det Norske Veritas (October 2010).

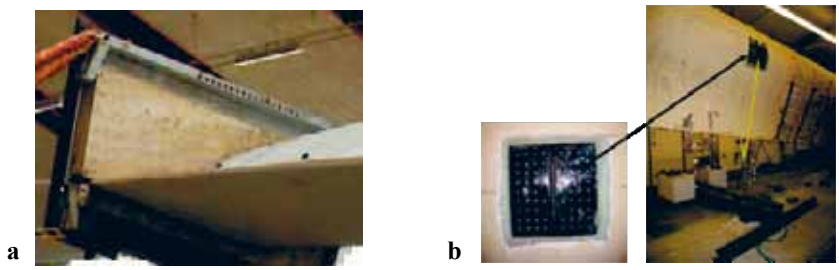

Fig. 2. a) Traditional method for load application often used in commercial tests. b) Novel loading method used at the Risø DTU test facility.

Both for static and fatigue tests the loading clamps shown in Fig. 2a are usually used. A newly-developed load application system employs anchor plates glued to the airfoil as illustrated in Fig. 2b. In the 'traditional' test method the loads are applied by means of a wooden clamp surrounding the blade's cross section which results in unrealistic local stiffness, since the trailing edge panels are not free to deform out-of-plane.
This paper presents a full-scale test with a new type of reinforcement, which reduce the out-of-plane deformations 30-40% by using strings from one panel to the other as illustrated in Fig. 3. Peeling in the adhesive joints is reduced by preventing the panels deforming outward using the patented solution, Jensen, F. M. (2009). The results from the full-scale test generated by applying an advanced Digital Image Correlation (DIC) technique are compared with non-linear FE-simulations.

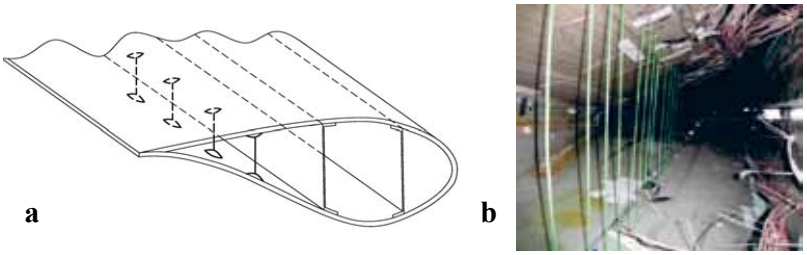

Fig. 3. Reinforcement solution with the trailing edge panels coupled. a) Sketch from Risø DTU Patent, Jensen, F. M. (2009). b) Photograph inside the blade (Trailing edge region) showing the reinforcement between the panels.

Failure of the bondlines in the trailing edge implies that repairs have to be performed. These repairs and follow-up costs can be very large for offshore wind turbines, since repairs can be very difficult to perform especially in the winter months with harsh weather conditions.

2. OBSERVATION ON WIND TURBINES

Periodic inspections of wind turbines are required either by the administrative authorities or by classification societies etc. One type of defects which are often encountered in these inspections is cracks on the surface of the blade in the vicinity of the trailing edge. The cracks occur in the blade surface coating but are an indication of defects in the underlying material which is associated with the joint in the trailing edge and the joint between the outer shell and the load-carrying box girder. Similar defects occur at the surface of the blade at the position where the shell is bonded to the internal shear web or spar. The cracks are not linked to a particular manufacturing process or manufacturer, and occur on many different sizes of blades. The cracks are difficult to repair and in severe cases, the only option is to replace the blade. Although the problem has been known for many years, it is difficult to obtain a systematic overview of the occurrence of the defects and the relation to the structural behavior of the blade due to the general market competition. For example inspections at a major Danish offshore wind turbine park have shown that almost all blades have cracks near the trailing edge, see example in Fig. 4.

Fig. 4. Left: Crack near the trailing edge discovered by periodical inspection from a Danish major offshore park. Right: Crack near the webs.

3. RELIABILITY AND OPERATION & MAINTENANCE

According to IEC 61400-1 and the partial safety factors recommended, blades are implicitly designed to a reliability level which corresponds to an annual probability of failure in the range 10^{-4} to 10^{-3}. However, as illustrated above the observed failure rates are much higher, see also Faulstich, S. and Hahn, B. (February 2009) where annual failure rates for blades of the order of 0.1 are reported. It is noted that these observed failure rates include both minor and major failures.

The level of failure rates is very important when assessing the Cost of Energy (CoE) using a life cycle approach, see Sørensen, J.D. (2009) for details. The total expected life cycle costs to operation and maintenance (OM) can be obtained by adding for each year in the lifetime the product of the

- annual probability of failure and
- the discounted costs of repair / failure, which include both direct costs (cost of repair or exchange of the blade, inclusive spare parts, equipment, transport, waiting times, etc.) and indirect costs (due to loss of electricity production).

For offshore wind turbines the costs are highly influenced by the expensive transport and harsh weather conditions implying that transport times, waiting times and loss of production can be very expensive. Thus high reliability of blades is very important, especially for offshore wind turbines. It is noted that condition monitoring, e.g. structural health monitoring (SHM) can be an efficient tool to detect and prevent smaller defects to develop into major failures.

4. EXPERIMENTAL AND NUMERCIAL INVESTIGATIONS OF TRALING EDGE SANDWHICH PANEL DEFORMATION

A 34m wind turbine blade manufactured by SSP Technology A/S is considered in this study. The blade is designed for 1.5 MW wind turbines and features a load-carrying girder bonded in between aerodynamic shells. The blade is manufactured using prepreg technology, which together with the design, results in a lightweight blade.

In order to investigate the deformation behavior of the sandwich panels in the trailing edge and the load effects that the adhesive bound is subjected to, a numerical and experimental test campaign is performed. Furthermore experimental tests are performed on the same blade with the implementation of the reinforcement described in Fig. 3 in order to study the effect of this design proposal. For a more detailed description of the full-scale tests, see (Nielsen et al. 2010).

4.1 Experimental full-scale test. In the experimental studies an advanced 3D Digital Image Correlation (DIC) measuring system is applied to capture the 3D displacements of the sandwich panels under the full load history. The system has been applied at Risø DTU for a couple of years and the accuracy of these types of measurements are within +/- 0.1mm.

The test has been performed at the full scale test facility at Risø DTU with the blade loaded in the edgewise direction from the leading edge towards the trailing edge. The loads on the blade are based on both aeroelastic calculations and previous full scale tests with the blade. These have been combined to form a 'Risø load' where 100% is the expected ultimate failure load of the blade at the evaluated direction. The 'Risø load' is 25% higher than the certification loads of the blade, see Jensen, F.M. (2008).

The experimental results presented in the following are obtained during the full-scale test campaign performed in order to investigate the influence of the reinforcement (strings) on the structural behavior of the blade cross-section, see Nielsen, M. et al. (2010) for details. The implementation of the reinforcement is shown in Fig. 3, where trailing edge panels were coupled with 6 mm nylon cord (called wires). This coupling was established in the blade between 3.5m and 4.5m from the blade root.

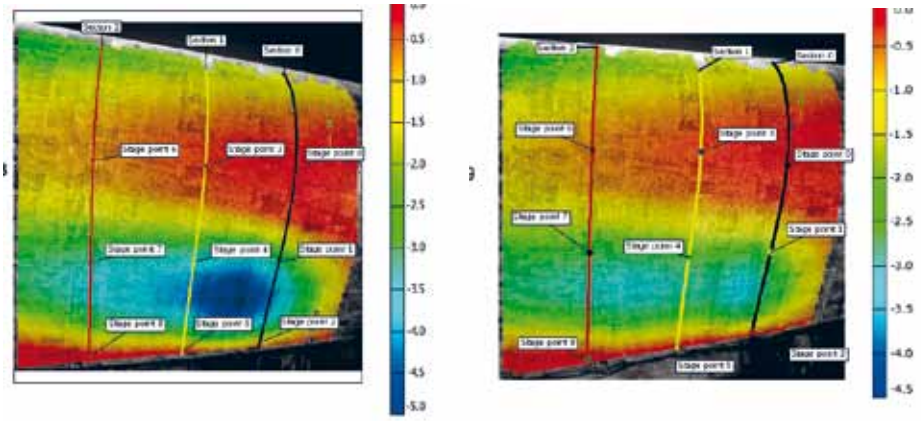

Fig. 5. Snapshot from 3.5m-5m section at 60% 'Risø load'. The load path used in the test is of the same order as the operational loads. Left) without reinforcement between the panels. Right) with reinforcement between the panels.

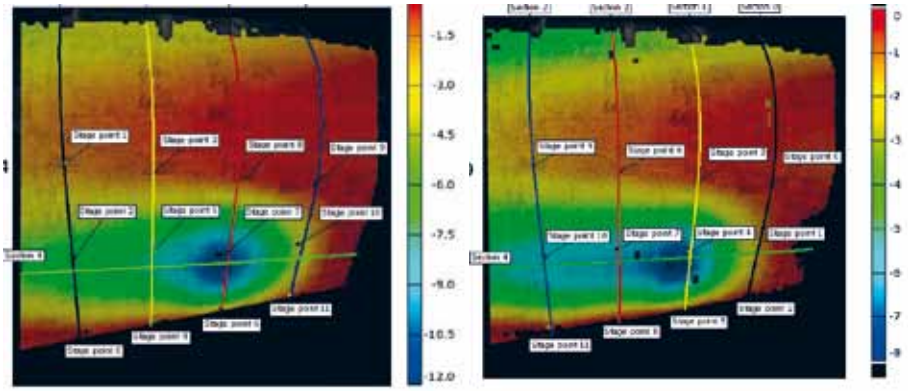

Fig. 6. Snapshot from 3.5m-5m section at 80% 'Risø load' corresponding to extreme loads. Left) without reinforcement between the panels. Right) with reinforcement between the panels.

The results show that the out-of-plane displacements of the panel are reduced when the blade is reinforced. Fig. 5 shows the results with a load corresponding to 60% 'Risø load'. The measurement was taken from 30% to 60% Risø load and this load path is in the range of the maximum operational load, see Fig. 5. When the reinforcement is inserted the amplitude of the maximal deformations decreases from 4.5mm to 3.0mm which is a reduction of 33%. When the blade is loaded up to 80%, which is similar to an extreme load (Fig. 6), the deformation is decreased from 11mm to 6-7mm. This results in a reduction at approximately 40% if the

reinforcement is used.

4.2 Numerical studies of edgewise loading. In the numerical studies a detailed finite element model of the blade is analyzed using Abaqus/CAE software. The geometry and material properties in the FE-model were defined using technical information e.g. the material data obtained from experimental coupon tests. The blade is modeled with 8-noded layered continuum shell elements. The model is densely meshed with a typical element size of approximately 80 x 70mm and the entire model has approximately 44500 elements. All FE-studies were performed by applying a non-linear geometric algorithm. The analyses are done through a computer cluster with up to 240 nodes.

The load case applied in the numerical studies is identical to the edgewise loading performed in the experimental test campaign. The three point loads are applied to the model by utilizing kinematic couplings, where the master node is coupled to the nodes in the load-carrying box. This kinematic coupling is a linear interpolation element, which does not constrain the sections. The boundary condition is applied by making the end of the blade at the root section fully fixed in all degrees of freedom.

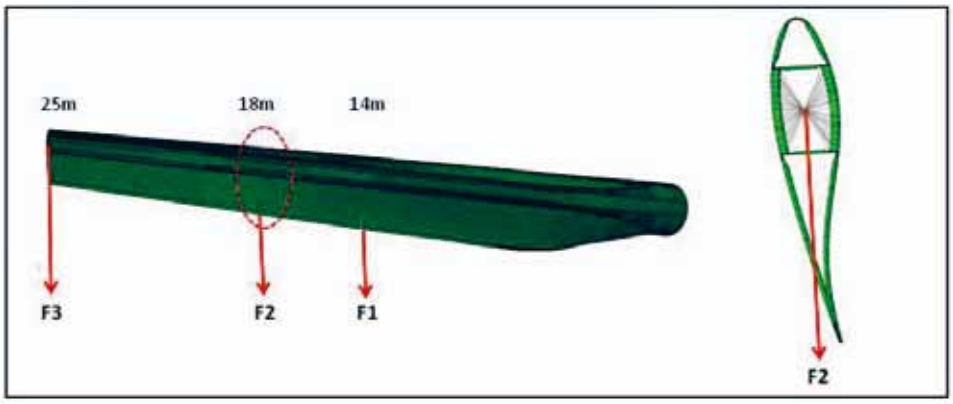

Fig. 7. FEM model with point forces and a section through the blade showing the kinematic coupling.

The experimental and numerical out-of-plan displacements of the sandwich panels have been compared and in general an excellent agreement between the results is found. Earlier studies performed at Risø DTU also show good agreement between experimental and numerical results when elastic behavior is compared. In Fig. 8 the experimental and numerical results of the out-of-plane deformation of the pressure side sandwich panel 4m form root are compared. It is seen that both the deformation behavior and the amplitude of the deformation is close to being identical.

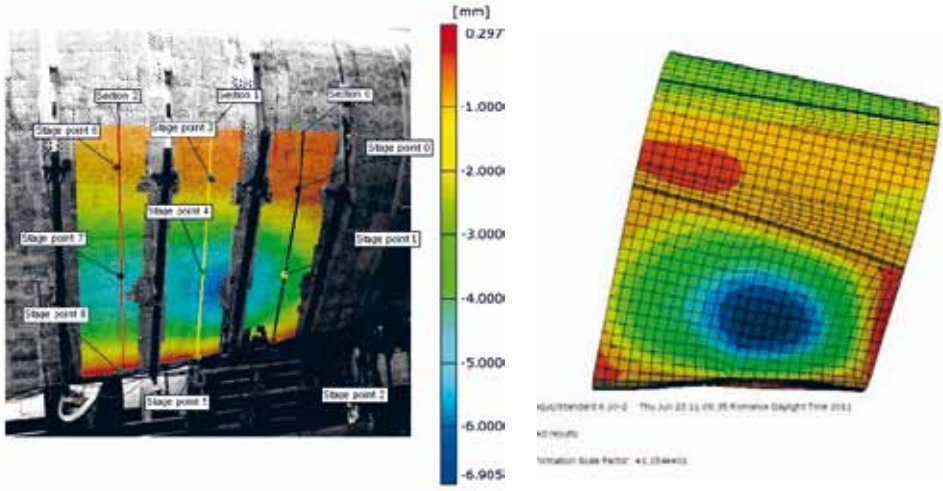

Fig. 8. Comparison of experimental and numerical results for the out of plane deformations without reinforcement, (Nielsen et al. 2010). Left) Deformation distribution obtained with Aramis. Right) FEM results from a corresponding load step in the same region. The scale has been adjusted for a better visualization of the comparison.

The edgewise loading is mainly generated by gravity loads, which during operation results in cyclic loading as the gravity forces changes sign as the blade rotates. The out-of-plane deformations of the soft sandwich panels are due to this loading and as the load changes sign the out of plane response is to some extent mirrored.

In Fig. 9, the relative out-of-plane displacements of the midpoint at the pressure side of the sandwich panel are plotted at different load levels. These displacements were calculated by selecting three nodes along the width of the pressure side panel. These points are located at the trailing edge, mid-point and at the junction of the panel with the shear web. The calculations were performed for radial positions 3m-16m. In order to only analyze the local deformations of the trailing edge shell a 3-point method is applied. By applying a 3-point method to the relative displacements of the points, the local out of plane deformations, illustrated in Fig. 9 is obtained.

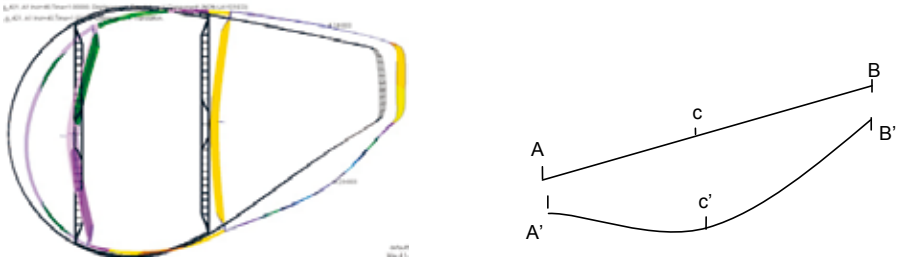

Fig. 9. Right) A deformed transverse section showing the “local” deformation of the trailing edge panel. Left) An illustration of the trailing edge panel where A and B are the “fixed” points and C the “local” point in the center of the trailing edge panel. The symbols are used in the 3-point method described below.

By applying a 3-point method to the relative displacements of the points, the local out-of-plane deformations are obtained as follows:

$$C_{local_x} = C^t_x - \frac{A^t_x + B^t_x}{2} \quad (1)$$

At the inner part of the blade the sandwich panels deform outwards at cross sections from 3.5m to 6m, while the cross section at 14m deforms inwards, when the blade is loaded towards the trailing edge. The response is mirrored when the blade is loaded towards the leading edge.

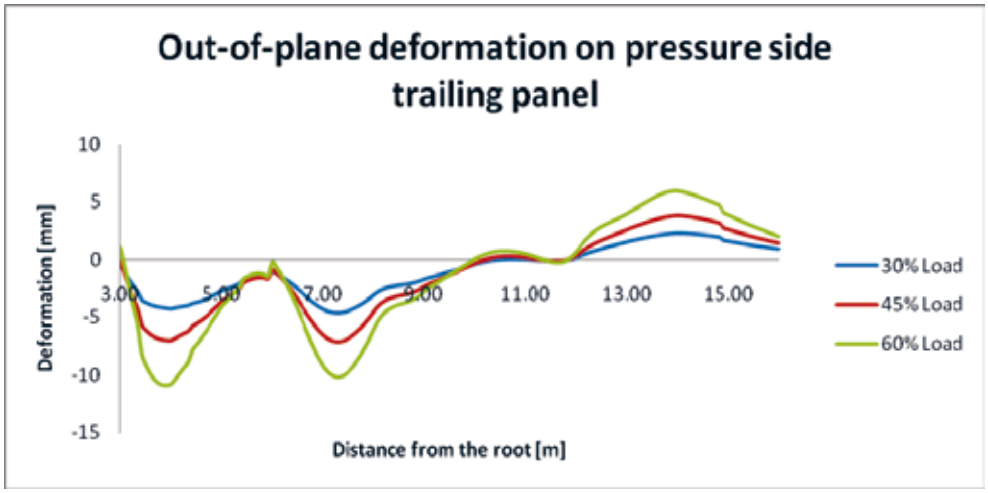

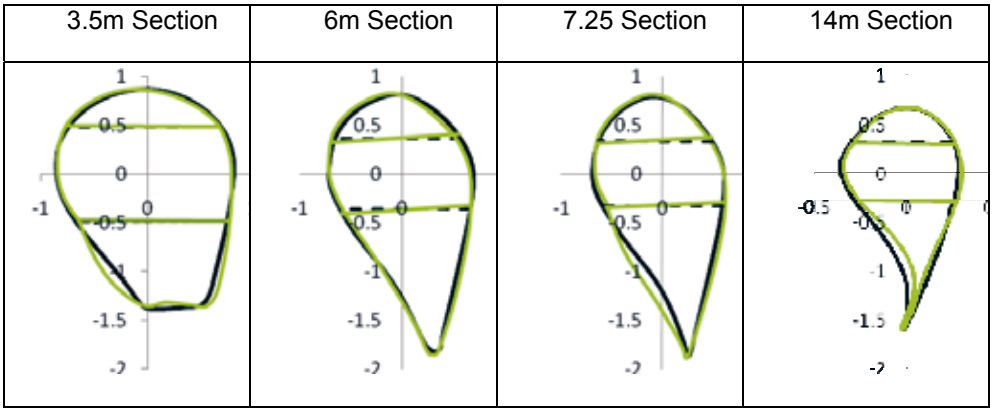

Fig. 10. Top) Out of plane displacements of the midpoint of the pressure side sandwich panel. Bottom left to right) Section through the blade with unloaded blade (black) and loaded blade (green). The deformation is plotted with a scale factor of 10.

In Roczek, A. (2009) the non-linear behavior was investigated in order to verify, if it is due to buckling or a general non-linear geometric behavior which also can happen when the panels are in tension. The conclusion from the investigation was that the panels had the mirrored out-of-plane behavior (and amplitude) which means that the out-of-plane behavior is not influenced by the in-plane compression behavior "buckling".

5. RESULTS AND CONCLUSIONS

High reliability of bonded joints in wind turbine blades is important in order to obtain a low cost of energy, especially for offshore wind turbines where the costs are highly influenced by the expensive transport and harsh weather conditions implying that transport times, waiting times and loss of production can be very expensive.

Inspections of blades at turbines in operation often show cracks on the surface of the blades. In this paper it is investigated if these can be the result of the out of plane deformations. Full-scale tests and numerical investigations are performed. The results show that the waving deformation is not caused by buckling but is purely a non-linear elastic geometric behavior which can introduce significant peeling stresses at the bonded joints.

The effect of reinforcement of the connection using a method developed and patented by Risø DTU has been investigated. The results show that it possible to reduce the out-of-plane deformations of the trailing edge panels by 30-40% using a string from one panel to the other and thereby reduce the peeling stresses in the trailing edge joint. The research is based on a combination of numerical analysis and full scale testing and has shown the need for improved full scale methods.

ACKNOWLEDGEMENTS

The research is conducted within the frame of a project entitled 'Experimental Blade Research - phase 2'. The project is financially supported by the Danish Energy Agency through the Energy Technology Development and Demonstration Programme (EUDP 2010). The support is gratefully acknowledged. The work with the 34m blade is conducted in cooperation with SSP Technology A/S and the work with repair costs for on/-offshore wind turbines is conducted with Vättenfall which is very much appreciated.

REFERENCES

DNV Standard DNV-OS-J102 - Design and Manufacture of Wind Turbine Blades. Det Norske Veritas (October 2010)

Faulstich, S. and Hahn, B. (February 2009) "Comparison of different wind turbine concepts due to their effects on reliability". Report WP7.3.2, UpWind, ISET, Kassel, Germany.

Guideline for the Certification of Offshore Wind Turbines. Germanischer Lloyd WindEnergie GmbH. (June 2005)

IEC 61400-1. Wind turbines - Part1: Design requirements. 3rd edition. (2005)

Jensen, F.M. (2008) Ultimate strength of a large wind turbine blade, Risø-PhD-34(EN), PhD thesis, Risø National Laboratory for Sustainable Energy, Technical University of Denmark.

Jensen, F. M. (June 2009) "A Reinforced Wind Turbine Blade". PCT/DK2009/000149.

Nielsen, M., Roczek, A., Jensen, F. M., Nielsen, P. H., Berring, P., Sieradzan, T., Roudnitski, V., Bitsche, R., Knudsen, H., Rasmussen, A., Rasmussen, J., Uldahl, U., Andrlová, Z., Branner, K., Bak, C., Kallesøe, B., McGugan, M., Lagerbon, M., (September 2010) "Full Scale Test SSP 34m blade, edgewise loading LTT. Extreme load and PoC_InvE Data report" Risø-R 1748(EN)

Roczek, A. (2009) Optimization of Material Layup for Wind Turbine Blade Trailing Edge Panels , master thesis. Risø DTU National Laboratory for Sustainable Energy

Sørensen, J.D. (2009) "Framework for risk-based planning of operation and maintenance for offshore wind turbines". Wind Energy, Vol. 12, pp. 493-506.

Proceedings of the 32nd
Risø International Symposium on Materials Science:
Composite materials for structural performance:
Towards higher limits
Editors: S. Fæster, D. Juul Jensen,
B. Ralph, B.F. Sørensen
Risø National Laboratory for Sustainable Energy,
Technical University of Denmark, 2011

TENSILE PROPERTIES OF CELLULOSIC FIBER/STARCH ACETATE COMPOSITES WITH VARIABLE FIBER AND PLASTICIZER CONTENT

R. Joffe*, B. Madsen** and K. Nättinen***

*Luleå University of Technology, SE-97187 Luleå, SWEDEN
**Technical University of Denmark, Risø National Laboratory for Sustainable Energy, Materials Research Division, P.O. Box 49, DK-4000 Roskilde, DENMARK
***VTT Technical Research Centre of Finland, Sinitaival 6, Tampere, P.O. Box 1300, FIN-33101, FINLAND

ABSTRACT

In this experimental study, the performance of injection-molded short cellulosic fiber/plasticized starch acetate composites is analyzed in terms of stiffness and strength. Parameters involved in the analysis are a variable fiber and plasticizer content. The measured strength of the composites varies in the range 12–51 MPa, whereas the stiffness varies in the range 1.1-8.3 GPa, which is significantly higher than the properties of unreinforced matrix.

1. INTRODUCTION

Bio-based polymers are materials derived from natural and renewable resources (such as plant-based biomass), and as such, bio-polymers provide sustainable alternatives to traditional synthetic polymers. However, bio-based polymers usually have inferior properties in comparison with the synthetic competitors and suffer from sensitivity to moisture and temperature changes. One of the ways for these materials to reach acceptable performance in terms of mechanical properties is reinforcement with natural fibers, such as wood or agrofibers. The commonly used natural fiber reinforcements are flax, hemp, kenaf, jute, sisal, ramie and coir. The stiffness of e.g. bast fibers in longitudinal direction is comparable to that of glass fibers (for example flax fibers have a stiffness 50-100 GPa vs 72 GPa for E-glass fibers) (Lilholt and Lawther 2000, Joffe et al 2003, Andersons et al 2005, Summerscales et al 2010). The direct benefits of use of natural fibers in composites are light weight, reduced wear on the processing equipment and lower impact on the environment. There are also certain issues with these materials, for example, as they are of natural origin, their mechanical properties are subject to a large variation. Moreover, a common issue with bio-based composite materials is a low

chemical compatibility between the fibers and the matrix. This can result in poor performance of the composites due to low fiber/matrix bonding, nonuniform fiber/matrix dispersion, and a high content of porosity.

In order to improve the properties of bio-based composites with regard to processing and performance, miscellaneous additives are used. For example, compatibilizers are used to improve fiber dispersion and fiber/matrix adhesion, and plasticizers are employed to increase toughness of these materials. Sometimes fire retardants and UV inhibitors are also added to tailor these materials for particular applications.

Common processing methods and products of natural fiber composites include injection molding of packages, extrusion of beams for decking, and compression molding of panels for automotive use. Other methods, such as rotational molding, have also been considered, but so far not widely exploited. The advantage of the good mechanical properties of the natural fibers is perhaps best taken of in compression-molded products. However, this requires additional fiber processing to produce high quality yarns.

Generally speaking composites based on thermoplastic biopolymers (lignin, starch, PLA) reinforced with natural fibers are today established as engineering materials used in various industrial branches (Nampoothiri et al 2010, Yu et al 2006).

In this study, a bio-based composite system is used where the fibers and the matrix are naturally compatible; both the cellulosic fibers and the matrix of the starch derivative are composed of glucose units. This results in a high level of intermolecular interaction through the hydrogen bonding of the hydroxyl functionalities of the fibers and the starch derivative.

Starch, which is composed of the carbohydrate polymers amylose and amylopectin, is characterized by being highly hygroscopic and with a brittle mechanical behavior. By acetylation of some of the free hydroxyl groups in the starch, the internal hydrogen bonding is strongly reduced and the polymer becomes less brittle, and it becomes melt processable. In addition, the water sensitivity of acetylated starch is markedly reduced (Larotonda et al 2005); the polymer becomes insoluble in water. The brittleness of the polymer can be reduced even further using a plasticizing agent, such as triethyl citrate. The plasticizer content has previously been shown to be directly correlated with the mechanical properties of the starch acetate (Nättinen et al 2010).

This article is addressing bio-based composites of short cellulosic fibers in a plasticized starch acetate (PSA) matrix. The composites are produced by compounding and injection molding. This article presents analysis of the performance of these composites in tension. The fiber content, and the plasticizer content are used as experimental parameters.

2. EXPERIMENTAL DETAILS

2.1 Materials. Flax fibers were supplied by Ekotex, Poland. Amylose-rich corn starch was supplied by Gargill, USA (Cerestar Amylogel 03003: 65wt% amylose, 35wt% amylopectin). The processes of fiber pelletizing, starch acetylation, and plasticization as well as processing of composites (compounding, post-processing, and injection molding) are described in detail in (Nättinen et al 2010).

2.2 Tensile tests. Tensile properties of the neat PSA matrix and the composites were measured according to the ISO 527 standard. The tensile specimens were tested on an Instron 4505

Universal Tensile Tester with 10 kN load cell and 5 mm/min cross-head speed. Strain was measured by an Instron 2665 Series High Resolution Digital Automatic Extensometer. Testing was performed at controlled ambient conditions: 23°C and relative humidity of 50%. Cross-sectional dimensions of the gauge area section of each tensile specimen were measured with a slide gauge (+/- 0.01 mm). Values of Young's modulus (GPa, linear regression between strain of 0.0005 and 0.0025 mm/mm) and maximum stress (MPa) were determined from the average of five stress-strain curves. More details on processing of materials and characterization of the micro-structure can be found in (Nättinen et al 2010, Madsen et al 2011).

3. THEORY

It should be noted that main objective of this paper is to present data on the mechanical performance of PSA/flax fiber composites. Modeling is employed to demonstrate trends in changes of mechanical properties with respect to the parameters of the constituents of the composites (such as fiber and plasticizer contents). The stiffness modeling has been performed in previous work (Madsen et al 2011) but this is the first attempt to perform calculations of strength of these composites.

3.1 Stiffness. For composites with a non-unidirectional fiber orientation and discontinuous fibers, a porosity corrected rule of mixtures model has previously been shown to well predict the Young's modulus of a range of cellulosic fiber composites (Madsen et al 2009):

$$E_C = \left(\eta_o \eta_l V_f E_f + V_m E_m\right)\left(1 - V_p\right)^2 \tag{1}$$

where E_C is the Young's modulus of the composite, V_f, V_m, V_p are the volume fractions of fibers, matrix and porosity respectively, η_o is the fiber orientation efficiency factor, η_l is the fiber length efficiency factor.

Although it is known that natural fibers are anisotropic, for simplicity in this study only one elastic modulus is used to characterize it, thus assuming isotropic fiber and representing it by some kind of an effective elastic modulus (E_f).

The effect of discontinuous fibers is included in the model via the fiber length efficiency factor (η_l), which can be calculated by the shear lag model originally developed by Cox in 1952:

$$\eta_l = 1 - \frac{\tanh(\theta)}{\theta}, \qquad \text{and} \qquad \theta = 2\frac{L_f}{d_f}\sqrt{G_m / E_f \ln\left(\frac{\kappa}{V_f}\right)} \tag{2}$$

where L_f is the average fiber length, d_f is the fiber diameter, G_m is the shear stiffness of the matrix, and κ is a constant controlled by the geometrical packing pattern of the fibers (Tucker and Liang 1999). For hexagonal packing of fibers, which is assumed here, κ is $\pi/2\cdot\sqrt{3}$ (=0.907).

The effect of non-unidirectional fiber orientation is included in the model via the fiber orientation efficiency factor (η_o), which is based on a geometrical model originally developed by Krenchel in 1964. Typical fiber orientation distributions in composites give the following η_o values: unidirectional, η_o=1; 2-D random, η_o=3/8 (0.375); 3-D random, η_o=1/5 (0.2).

3.2 Strength. Similar to the stiffness models for these materials, many strength models for short fiber composites are also based on the "rule-of-mixtures" (Kelly and Tyson 1965, Fukuda and Chou 1982, Fu and Lauke 1996, Lauke and Fu 1999).

The strength can be expressed as:

$$\sigma_c^u = \eta_{ls}\eta_{os}\sigma_f^u V_f + (1 - V_f)\sigma_m \tag{3}$$

where σ_f^u is the fiber strength; σ_m is the stress in the matrix at the failure strain of the fiber, assuming linear elastic behavior of the fiber and matrix $\sigma_m = \sigma_f^u \cdot (E_m/E_f)$; the η_{ls} and η_{os} are the length efficiency and orientation factors respectively. The fiber length efficiency factor is calculated as follows (Kelly and Tyson 1965):

$$\eta_{ls} = \begin{cases} 1 - l_c/2l & l \geq l_c \\ l/2l_c & l < l_c \end{cases}, \text{ where } l_c \text{ is critical fiber length defined as: } l_c = \frac{\sigma_f^u d_f}{2\tau} \tag{4}$$

and τ is the interfacial shear strength (ISS).

It has been shown previously (Joffe et al 2003, Andersons et al 2005) that the strength of flax fibers, similarly to synthetic fibers (such as carbon and glass fibers), can be well described by a Weibull distribution. According to this distribution the average fiber strength is given by:

$$\sigma_f^u = \beta\left(\frac{l}{l_0}\right)^{-1/\alpha}\Gamma\left(1 + \frac{1}{\alpha}\right) \tag{5}$$

where l if the fiber length, l_0 is a normalization parameter ($l_0 = 1$ *mm*), α and β are parameters of Weibull distributions and Γ is the gamma function. Therefore, the critical fiber length l_c can be expressed as (Andersons et al 2006):

$$l_c = \left(\frac{\beta\Gamma(1 + 1/\alpha)d_f}{2\tau l_0^{-1/\alpha}}\right)^{\frac{\alpha}{1+\alpha}} \tag{6}$$

However, due to a lack of some parameters needed to calculate the composite strength (such as ISS, fiber orientation distribution, the real fiber modulus) the following assumptions will be made:

a) perfect adhesion is assumed and ISS is equal to the strength of the matrix;

b) the orientation factor will be calculated based on experimental results for stiffness;

c) since the actual fiber modulus is not known and for flax fibers it can vary within a rather wide range (50-100 GPa) (Lilholt and Lawther 2000), the stress in the matrix at the failure strain of the fiber is assumed to be equal to the matrix strength.

The orientation factor η_{os} can be obtained either directly by optical measurements or by analyzing stress-strain curves of the composite and using a rule-of-mixture expression for composite stiffness (Tomason 2002). It was shown (Tomason 2002) that all of these approaches rendered the same results for the orientation factor of short glass fiber composites with four different thermoplastic matrices. Therefore, it was decided to use a rule-of-mixture for stiffness to calculate orientation efficiency factor η_{os}:

$$\eta_{os} = (E_C - V_m E_m)/\eta_l V_f E_f \tag{7}$$

4. RESULTS AND DISCUSSION

The typical stress-strain curves from tensile tests for unreinforced starch acetate with a plasticizer (PSA) and flax fiber composites are presented in Fig. 1. The results in Fig. 1a show that the plasticizer has very strong effect on the mechanical properties of the starch matrix. The stiffness and strength of PSA are drastically reduced, whereas the strain at failure is significantly increased with an increase of plasticizer content. Similar effect of the plasticizer content is observed from the results for the composites (see Fig. 1b) but the composite properties also very strongly depend on fiber content. Higher flax fiber content increases the stiffness and strength and decreases the strain at failure. A summary of results for the unreinforced starch and flax fiber composites are presented in Table 1.

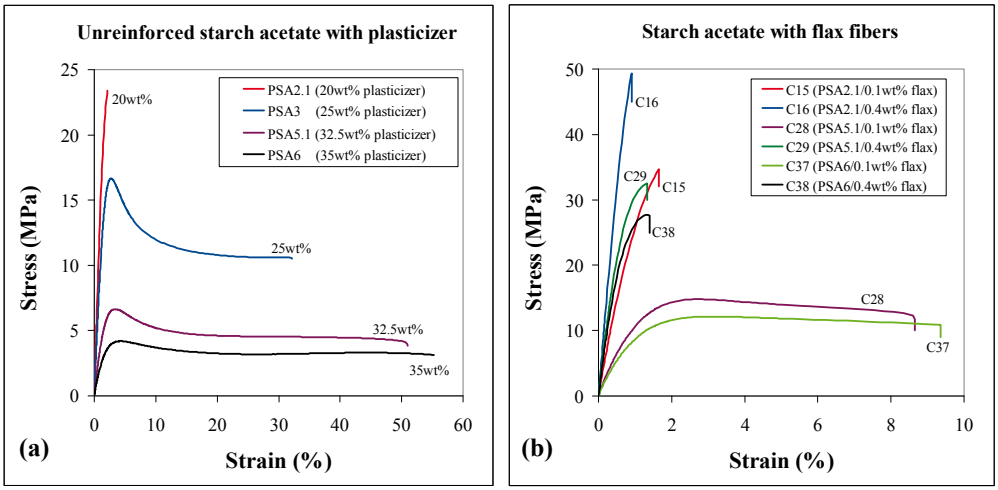

Fig. 1. Typical stress-strain curves for the unreinforced matrix (a) and composites (b).

Table 1. Summary of experimental results for PSA and flax fiber composites.

Composite	Matrix	Density (compos.) g/cm^3	Average fiber length (mm)	Av. fiber diameter (μm)	V_f (compos.)	V_v (compos.) (%)	Plasticizer (compos.) (wt%)	Stiffness (composite) (GPa)	Max Stress (composite) (MPa)	Stiffness (matrix) (GPa)	Max Stress (matrix) (MPa)
C15	PSA2.1	1.321	0.347	18	0.107	0.3 ± 0.1	20.0	3.14 ± 0.15	35.0 ± 1.4	1.66 ± 0.07	22.6 ± 1.2
C16	PSA2.1	1.372	0.151	19	0.363	1.3 ± 0.1	20.0	8.10 ± 0.90	51.0 ± 3.0	1.66 ± 0.07	22.6 ± 1.2
C17	PSA2.2	---	0.150	17	---	---	20.0	8.30 ± 0.50	51.0 ± 4.0	1.78 ± 0.07	23.2 ± 1.1
C20	PSA3	---	0.317	17	---	---	25.0	2.37 ± 0.09	24.9 ± 1.0	1.16 ± 0.06	17.1 ± 0.3
C21	PSA3	---	0.252	17	---	---	25.0	6.00 ± 0.20	45.8 ± 0.5	1.16 ± 0.06	17.1 ± 0.3
C28	PSA5.1	1.306	0.334	19	0.093	0.1 ± 0.0	32.5	1.57 ± 0.12	15.7 ± 0.4	0.45 ± 0.02	6.6 ± 0.2
C29	PSA5.1	1.370	0.293	19	0.356	0.6 ± 0.1	32.5	5.60 ± 0.70	33.7 ± 0.3	0.45 ± 0.02	6.6 ± 0.2
C37	PSA6	1.304	0.498	18	0.098	0.0 ± 0.1	35.0	1.12 ± 0.05	12.1 ± 0.1	0.27 ± 0.03	3.9 ± 0.3
C38	PSA6	1.368	0.297	17	0.356	0.5 ± 0.2	35.0	5.10 ± 0.30	28.8 ± 0.5	0.27 ± 0.03	3.9 ± 0.3

The results in Table 1 show that there is a very significant reinforcing effect of flax fibers even at a low volume content of fibers. Both, the stiffness and maximum stress of PSA are considerably increased by addition of fibers.

The experimental data along with modeling results for the composite stiffness are presented in Fig. 2. In general, all the model lines for the flax fiber composites in Fig. 2a are in good agreement with the experimental data. Assuming that models for prediction of stiffness are

reliable (good agreement with experiment) and using empirical results for fiber dimensions and the micro-structure of composites it is possible to construct a property diagram of stiffness of the composites (see more details on stiffness modeling in Madsen et al 2011). This diagram is presented in Fig. 2b.

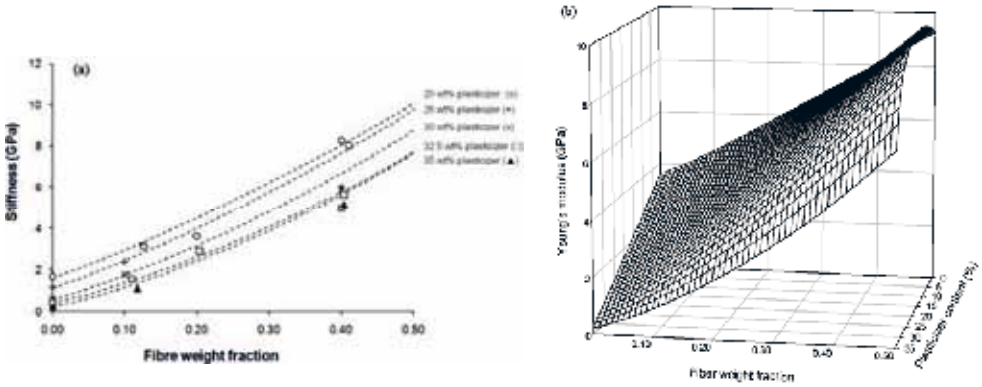

Fig. 2. Experimental values (symbols) and modeling results (lines) for composite stiffness (a). Modeling results showing stiffness dependence on fiber and plasticizer contents (b).

The diagram presented in Fig. 2b can be used to tailor the PSA/flax fiber composite stiffness based on the requirements of particular applications by adjusting the fiber and plasticizer contents. For example, a maximum stiffness of the composites of 10.0 GPa can be achieved with a plasticizer content of 16wt% and a fiber weight fraction of 0.50. The diagram suggests that even better properties can be achieved if the fiber content is increased above 0.50, although this might not be the case since other factors might interfere (e.g. an increase of porosity V_p for higher V_f, Madsen et al 2007).

The probability of failure for similar flax fibers (from the same supplier) as used in the composites are shown in Fig. 3a. These results are obtained from tensile tests of 20 mm long fibers (the detailed experimental procedure and tests data processing procedure can be found in Joffe et al 2003, Andersons et al 2005).

The experimental results presented in Fig. 3a are approximated by a Weibull distribution and the parameters of distribution are derived (α = 2.66, β = 1358 MPa). The average fiber strength as a function of the fiber length (Eq. 5) is shown in Fig. 3b (the prediction is compared with test data for 3 mm long fiber). Thus, it is indicated that the strength of the fiber of any length can be obtained by using Eq. 5.

Results of modeling of the composite strength based on assumptions described above and the available experimental data are presented in Table 2. It should be noted that the average length of fibers in the composites is well below the values of the fiber critical length. The calculations demonstrate that the reinforcing effect of fibers (which is characterized by the $\eta_{os} \cdot \eta_{ls}$) is rather low, even though perfect bonding between the fiber and matrix was assumed with an ISS equal to the matrix strength. It is reported (Fu and Lauke 1996) that for a short fiber composite with a good interface the average reinforcement factor is $\eta_{os} \cdot \eta_{ls} \approx 0.21$. As is seen from Table 2, the fiber orientation factor for the composites studied here is actually rather high (average value $\eta_{os} \approx 0.6$). However, the fibers are too short (thus, a rather low length efficiency factor η_{ls}) to ensure full utilization of their strength.

For a more convenient comparison the strength values for composites shown in Table 2 are also presented in Fig. 4.

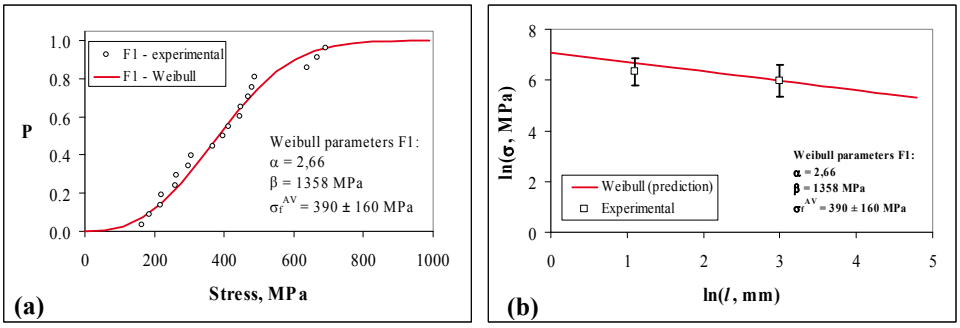

Fig. 3. Probability of survival (a) and average strength (b): test (○,□), prediction (—).

Table 2. Summary of modeling of composite strength (intermediate and final results).

Composite	Fiber length, l (mm)	σ_f^u, Eq. 5 (MPa)	l_c, Eq. 6 (mm)	η_{os}, Eq. 7	η_{ls}, Eq. 4	$\eta_{os} \cdot \eta_{ls}$	σ_c^u exp. (MPa)	σ_c^u, Eq. 3 (MPa)	$^*\sigma_c^u$, Eq. 3 (MPa)
C15	0.347	1798	0.587	0.465	0.295	0.137	35.0	46.6	40.0
C16	0.151	2459	0.611	0.784	0.124	0.097	51.0	100.9	79.2
C28	0.334	1824	1.494	0.696	0.112	0.078	15.7	19.2	15.9
C29	0.293	1916	1.494	0.610	0.098	0.060	33.7	45.1	34.9
C37	0.498	1569	2.105	0.400	0.118	0.047	12.1	10.8	9.0
C38	0.297	1906	2.020	0.640	0.074	0.047	28.8	34.4	26.4

* - fiber strength is assumed 0.75 of the initial values calculated by Eq. 5.

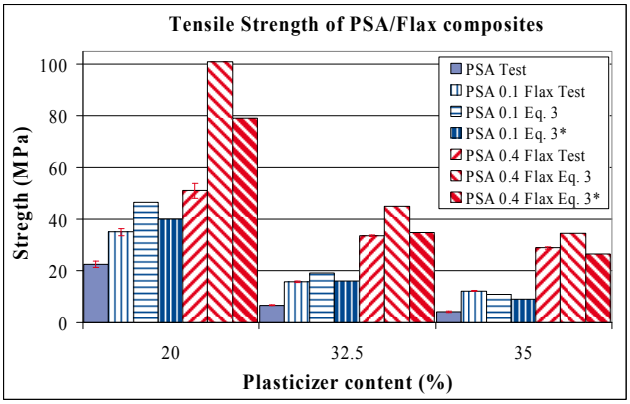

Fig. 4. Strength of PSA and flax fiber composites with different contents of fibers (test data and prediction Eq. 3) as a function of plasticizer content (Eq. 3* corresponds to the case where the fiber strength is reduced to 0.75 of the initial value obtained from Eq. 5).

The results obtained from Eq. 3 significantly overestimate the experimentally measured strength (except for the composite C37). It is expected that the model will give an upper estimate for the strength because of some assumptions made due to lack of input parameters (for example, instead of ISS and stress in the matrix at the failure strain of the fiber, the maximum stress achieved by matrix is used). However, an overestimated prediction might be the result of too high strength of the short fibers obtained from Eq. 5. Even if the strength of such short fibers is

estimated correctly, in reality fibers go through a very rough treatment during the composite manufacturing process. Therefore, not only the fiber length would be degraded but also the fiber strength can be significantly reduced. For example, assuming that the residual strength of the fiber is 0.75 of its initial value give a much better predictions for the strength of composite (see Table 2 and Fig. 4).

It is clear that modeling of the strength of composites is not as successful as predictions of stiffness. This is of course due to an insufficient amount of reliable input parameters. Therefore, at this stage no deeper analysis of the strength dependence on various factors is performed in this work. This will be done in a further investigation when a more accurate estimation of missing parameters will be achieved.

5. SUMMARY

This study presented experimental results of PSA/flax fiber composites with different plasticizer and fiber contents. It is demonstrated that the addition of flax fibers significantly improves the properties of acetylated starch. The stiffness of unreinforced PSA is 0.3-1.8 GPa and maximum achieved stress is 4-23 MPa, whereas the stiffness of the composites is in the range of 1.1-8.3 GPa and the strength is 12–51 MPa.

It is shown that the composite stiffness prediction is rather accurate by using a modified rule-of-mixture expression if the input parameters describing the internal structure of the material are known. It is possible to construct a property diagram by employing this model and use this diagram to tailor the composite stiffness depending on application needs by varying the content of constituents.

The modeling of strength was not as accurate as in case of stiffness due to a lack of information needed to evaluate important input parameters. However, an upper estimate for strength of PSA/flax composites was obtained and some limited analysis of the strength dependence on composite constituents was done. Further work is needed to increase the accuracy of the input parameters for the strength model.

ACKNOWLEDGEMENTS

This study has been partly supported by the EU Sixth Framework Programme project. ‘New classes of engineering composite materials are from renewable resources,’ BIOCOMP; contract grant number: IP 515769-2.

REFERENCES

Lilholt H., Lawther J. M., “*Natural organic fibres*” in Comprehensive Composite Materials, Vol 1. Elsevier Science, 2000.

Joffe R., Andersons J. and Wallström L., “*Strength and adhesion characteristics of elementary flax fibres with different surface treatments*”. Compos Part A, 2003:34, p. 603-12.

Andersons J., Sparniņš E., Joffe R. and Wallström L., “*Strength distribution of elementary flax fibres*”, Compos Sci & Techn, 2005:65, p. 693-702.

Summerscales J., Dissanayake N.P.J., Virk A.S., Hall W., “*A review of bast fibres and their composites. Part 1 – Fibres as reinforcements*”, Compos Part A, 2010:41, p. 1329–1335.

Nampoothiri K. M., Nair R. N., John R. P., “*An overview of the recent developments in polylactide (PLA) research*”. Bioresource Technol, 2010:101, p. 8493-8501.

Yu L., Dean K., Li L., "*Polymer blends and composites from renewable resources*". Progr in Polym Sci, 2006:31, p. 576-602.

Larotonda F.D.S, Matsui K.N., Sobral P.J.A. and Laurindo J.B., "*Hygroscopicity and water vapor permeability of Kraft paper impregnated with starch acetate*", J Food Eng, 2005:71, p. 394–402.

Nättinen K., Hyvärinen S., Joffe R., Wallström L. and Madsen B., "*Naturally compatible: starch acetate/cellulosic fiber composites. I. Processing and properties*", Polym Compos 2010:31, p. 524–535.

Madsen B., Joffe R., Peltola H. and Nättinen K., "*Short cellulosic fiber/starch acetate composites – micromechanical modeling of Young's modulus*", Accepted in J Compos Mater 2011.

Madsen B., Thygesen A., Lilholt H., "*Plant fibre composites – porosity and stiffness*", Compos Sci Technol, 2009:69, p. 1057-1069.

Cox H.L., "*The elasticity and strength of paper and other fibrous materials*", Brit J Appl Phys, 1952:3, p. 72-79.

Tucker C.L., Liang E., "*Stiffness predictions for unidirectional short-fiber composites: Review and evaluation*", Compos Sci Technol, 1999:59, p. 655-671.

Krenchel H., "*Fibre reinforcement. Akademisk forlag*", Copenhagen, Denmark, 1964. p. 16-22.

Kelly A. and Tyson W.R., "*Tensile properties of fibre-reinforced metals: Copper/tungsten and copper/molybdenum*", J. Mech Phys Solids, 1965:13, p. 329-350.

Fukuda H. and Chou T.-W., "*A probabilistic theory of the strength of short-fibre composites with variable fibre length and orientation*", J Mater Sci, 1982:17, p. 1003-1011.

Fu S.-Y. and Lauke B., „*Effects of fiber length and fiber orientation distributions on the tensile strength of short-fiber-reinforced polymers*", Compos Sci Technol, 56, 1996:56, p. 1179-1190.

Lauke B. and Fu S.-Y., "*Strength anisotropy of misaligned short-fibre-reinforced polymers*", Compos Sci Technol, 1999:59, p. 699-708.

Andersons J., Joffe R., Spārniņš E., "*Stiffness and strength of flax fiber/polymer matrix composites*", Polym Compos, 2006:27, p. 221-229.

Tomason J.L., "*Interfacial strength in thermoplastic composites - at last an industry friendly measurement method?*", Compos Part A, 2002:33, p. 1283–1288.

Madsen B., Thygesen A., Lilholt H., "*Plant fibre composites – porosity and volumetric interaction*", Comp Sci Tech, 2007:67, p. 1584-1600.

Proceedings of the 32nd
Risø International Symposium on Materials Science:
Composite materials for structural performance:
Towards higher limits
Editors: S. Fæster, D. Juul Jensen,
B. Ralph, B.F. Sørensen
Risø National Laboratory for Sustainable Energy,
Technical University of Denmark, 2011

PARAMETRIC STUDY OF COMPOSITE WIND TURBINE BLADES

T. Kim, K. Branner and A.M. Hansen

Wind Energy Division, Risø National Laboratory for Sustainable Energy, Technical University of Denmark, 4000 Roskilde, Denmark

ABSTRACT

In this paper an anisotropic beam element for a composite wind turbine blades is developed. Eigenvalue analysis with the new beam element is conducted in order to understand its responses associated with the wind turbine performances. From the results of natural frequencies and mode shapes it is obvious that the anisotropic characteristics should not be ignored to obtain accurate results.

1. INTRODUCTION

For wind turbines blades, composite materials are widely used because they can reduce the total weight while retaining the structural properties and because they have good tailoring and fatigue life characteristics. The tailoring capability of the composite blade could be used to passively control the wind turbine response and results in a decrease of fatigue loads and the risk of flutter. It is shown in Luczak, Manzato, Peeters, Branner, Berring, and Kahsin (2011) that a typical wind turbine blade has very small couplings, but that these can be introduced easily by adding angled unidirectional layers. However, the aeroelastic codes in the wind energy fields such as HAWC2 still use the classical beam models. Therefore, it cannot be used to investigate the coupling effects of anisotropic materials.

In this paper a new beam element which is able to include anisotropic characteristics of a beam is developed and implemented into the structural part of the HAWC2.

2. METHODS

The classical Timoshenko beam element is currently used in HAWC2 by considering Finite Element Analysis (FEA). In order to compute the shape functions, static equilibrium equations are solved with geometric boundary conditions. The principle of virtual displacements is used to derive the element stiffness with the obtained shape functions. More detailed equations are

represented in Petersen (1990). However, the beam model in the current HAWC2 can generally not be extended to an anisotropic beam model because the shape functions do not necessarily capture the coupled motions. Therefore, a new beam element with new shape functions should be introduced to capture coupled behaviors. Fig. 1 shows a sketch of the coordinate system in HAWC2.

Fig.1: A sketch of the coordinate system

In order to compute the element stiffness and mass matrix, the elastic energy and the kinetic energy are considered.

2.1 Stiffness matrix. The elastic energy of the beam is defined as follows:

$$2U = \int_0^L \left(\varepsilon^T S \varepsilon\right) dz\,, \tag{1}$$

where S is the cross-sectional stiffness matrix defined by a diagonal matrix into the current HAWC2.

For the classical Timoshenko beam S is addressed by the diagonal matrix as follows:

$$S = diag\{k_x GA,\quad k_y GA,\quad EA,\quad EI_x,\quad EI_y,\quad GJ\}\,, \tag{2}$$

where k_x and k_y are shear factors related to forces in x and y directions, respectively.

In Eq. (1), ε the generalized strains of the Timoshenko beam are expressed as:

$$\begin{aligned}\{\varepsilon\}^T &= \{\varepsilon_x,\quad \varepsilon_y,\quad \varepsilon_z,\quad \kappa_x,\quad \kappa_y,\quad \kappa_z\} \\ &= \{u_x' - \theta_y,\quad -u_y' - \theta_x,\quad u_z',\quad \theta_x',\quad \theta_y',\quad \theta_z'\},\end{aligned} \tag{3}$$

In FEA the displacement and rotation can be expressed by an interpolating polynomial in terms of generalized degrees of freedom as follows:

$$q(x) = \{u_x,\quad u_y,\quad u_z,\quad \theta_x,\quad \theta_y,\quad \theta_z\}^T = \underbrace{N(x)}_{6\times 6N_i}\underbrace{\alpha}_{6N_i\times 1}\,, \tag{4}$$

where N is the polynomial matrix in which, $\lfloor N \rfloor = \lfloor 1 \quad x \quad x^2 \quad \cdots \quad x^n \rfloor$ where n=1 for a linear polynomial, α are the generalized degrees of freedom, and N_i is the highest power in the polynomial + 1.

From the Eqs. (3) and (4) the generalized strain can be expanded in terms of a strain-displacement matrix and generalized degrees of freedom as follows:

$$\varepsilon = \underbrace{B(x)}_{6\times 6N_i}\underbrace{\alpha}_{6N_i\times 1}, \tag{5}$$

where B is the strain-displacement matrix which includes a polynomial matrix and its derivative terms as follows:

$$\underbrace{B(x)}_{6\times 6N_i} = B_0 N(x) + B_1 N'(x), \tag{6}$$

By substituting Eq. (5) into Eq. (1), the elastic energy of the beam can be illustrated as follows:

$$2U = \alpha^T \underbrace{\int_0^L \left(B^T S B\right) dz}_{D} \alpha, \tag{7}$$

In order to find α in Eq. (7) the boundary conditions at the beam ends are satisfied and the beam sections are in equilibrium which can be obtained when the total elastic energy is minimized. By applying boundary conditions the nodal degrees of freedom are obtained as follows:

$$\underbrace{d}_{12\times 1} = \underbrace{N_d}_{12\times 6N_i}\underbrace{\alpha}_{6N_i\times 1} = \begin{bmatrix} N_1 & N_2 \end{bmatrix}\begin{Bmatrix} \alpha_1 \\ \alpha_2 \end{Bmatrix}, \tag{8}$$

Here N_1 is a 12 by 12 matrix which is assumed to be invertible. Therefore, N_1 and N_2 become:

$$\underbrace{N_1}_{12\times 12} = \begin{bmatrix} I & 0 \\ I & LI \end{bmatrix}, \quad \underbrace{N_2}_{12\times(6N_i-12)} = \begin{bmatrix} 0 & 0 & \cdots & 0 \\ L^2 I & L^3 I & \cdots & L^{N_i-1} I \end{bmatrix}, \tag{9}$$

where L is the length of the beam element.

From Eq. (8) α_1 can be rewritten as:

$$\alpha_1 = N_1^{-1}\left(d - N_2\alpha_2\right), \tag{10}$$

Therefore α can be expressed as follows:

$$\alpha = \begin{Bmatrix} \alpha_1 \\ \alpha_2 \end{Bmatrix} = \begin{bmatrix} N_1^{-1} & -N_1^{-1}N_2 \\ 0 & I \end{bmatrix}\begin{Bmatrix} d \\ \alpha_2 \end{Bmatrix}$$

$$\therefore \underbrace{\alpha}_{6N_i\times 1} = \underbrace{\begin{bmatrix} \underbrace{I}_{12\times 12} \\ \underbrace{0}_{(6N_i-12)\times 12} \end{bmatrix}}_{A_{\alpha 1}}\underbrace{\alpha_1}_{12\times 1} + \underbrace{\begin{bmatrix} \underbrace{0}_{12\times(6N_i-12)} \\ \underbrace{I}_{(6N_i-12)\times(6N_i-12)} \end{bmatrix}}_{A_{\alpha 2}}\underbrace{\alpha_2}_{(6N_i-12)\times 1} = \underbrace{A_{\alpha 1}}_{6N_i\times 12}\underbrace{\alpha_1}_{12\times 1} + \underbrace{A_{\alpha 2}}_{6N_i\times(6N_i-12)}\underbrace{\alpha_2}_{(6N_i-12)\times 1} \tag{11}$$

$$= A_{\alpha 1}N_1^{-1}d - A_{\alpha 1}N_1^{-1}N_2\alpha_2 + A_{\alpha 2}\alpha_2,$$

To compute α vector, the total energy minimization approach in terms of α_2, $\frac{dU}{d\alpha_2} = 0$, is considered. From Eqs. (7) and (11), the total elastic energy of the beam is obtained as follows:

$$U = \frac{1}{2}\underbrace{\left(d^T N_1^{-T} A_{\alpha 1}{}^T - \alpha_2{}^T N_2{}^T N_1^{-T} A_{\alpha 1}{}^T + \alpha_2{}^T A_{\alpha 2}{}^T\right)}_{\alpha^T} D \underbrace{\left(A_{\alpha 1} N_1^{-1} d - A_{\alpha 1} N_1^{-1} N_2 \alpha_2 + A_{\alpha 2}\alpha_2\right)}_{\alpha}, \tag{12}$$

Resulting from the total energy minimization, the α_2 vector is obtained as follows:

$$\begin{aligned} &\frac{dU}{d\alpha_2} = 0 \\ &\therefore \underbrace{\left\{\left(N_2{}^T N_1^{-T} A_{\alpha 1}{}^T D A_{\alpha 1} N_1^{-1}\right) - \left(A_{\alpha 2}{}^T D A_{\alpha 1} N_1^{-1}\right)\right\}}_{P} d \\ &= \underbrace{\left\{\left(N_2{}^T N_1^{-T} A_{\alpha 1}{}^T D A_{\alpha 1} N_1^{-1} N_2\right) - \left(A_{\alpha 2}{}^T D A_{\alpha 1} N_1^{-1} N_2\right) - \left(N_2{}^T N_1^{-T} A_{\alpha 1}{}^T D A_{\alpha 2}\right) + \left(A_{\alpha 2}{}^T D A_{\alpha 2}\right)\right\}}_{Q} \alpha_2 \\ &\therefore \alpha_2 = \underbrace{Q^{-1}}_{(6N_i-12)\times(6N_i-12)} \underbrace{P}_{(6N_i-12)\times 12} \underbrace{d}_{12\times 1}, \end{aligned} \tag{13}$$

By substituting Eq. (13) into Eq. (11), the α vector as a function of the nodal degrees of freedom is represented as follows:

$$\begin{aligned} \alpha &= A_{\alpha 1} N_1^{-1} d - A_{\alpha 1} N_1^{-1} N_2 Q^{-1} P d + A_{\alpha 2} Q^{-1} P d \\ &= \left(A_{\alpha 1} N_1^{-1} - A_{\alpha 1} N_1^{-1} N_2 Q^{-1} P + A_{\alpha 2} Q^{-1} P\right) d \\ &= \underbrace{N_\alpha}_{6N_i\times 12} d, \end{aligned} \tag{14}$$

Finally, the elastic energy of the beam is obtained in terms of nodal degrees of freedom by substituting Eq. (14) into Eq. (7) as follows:

$$\begin{aligned} U &= \frac{1}{2} d^T N_\alpha{}^T \left[\int_0^L \left(B^T S B\right) dz\right] N_\alpha d \\ &= \frac{1}{2} d^T K d, \end{aligned} \tag{15}$$

where K matrix, $K = N_\alpha{}^T \left[\int_0^L \left(B^T S B\right) dz\right] N_\alpha$, is the element stiffness matrix.

2.2 Mass matrix. The method to compute the element mass matrix is similar to the definition of the stiffness matrix. The element mass matrix is obtained from the kinetic energy as follows:

$$\begin{aligned} T &= \frac{1}{2}\int_V \rho \dot{r}^T \dot{r} dV \\ &= \frac{1}{2}\int_0^L \dot{r}^T E \dot{r} dz, \end{aligned} \tag{16}$$

where ρ, $\dot{r}$, V, and E are the mass density, velocity of the body, volume of body and the cross-sectional mass matrix, respectively.

By applying the same shape function as the stiffness matrix, Eq. (16) can be extended as follows:

$$T = \frac{1}{2}\dot{d}^T N_\alpha{}^T \left[\int_0^L \left(N(x)^T EN(x)\right)dz\right] N_\alpha \dot{d} = \frac{1}{2}\dot{d}^T M \dot{d}, \tag{17}$$

where M matrix, $M = N_\alpha{}^T \left[\int_0^L \left(N^T EN\right)dz\right] N_\alpha$, is the element mass matrix.

3. RESULTS

After implementing this new beam element into HAWC2, three different cases are investigated in order to validate the new beam model. The effect of using an anisotropic material is studied as well. Three different cases are considered for this study. Fig. 2 (a), (b), and (c) show a sketch of the considered cases. Table 1 shows the detailed structural properties and cross-sectional stiffness matrix for the first example. For Case 2 and Case 3, only sectional stiffness information is displayed in Table 2. More detailed information about the material properties and geometries are addressed in Yu (2007) and Hodges, Atilgan, Fulton, and Rehfield (1991).

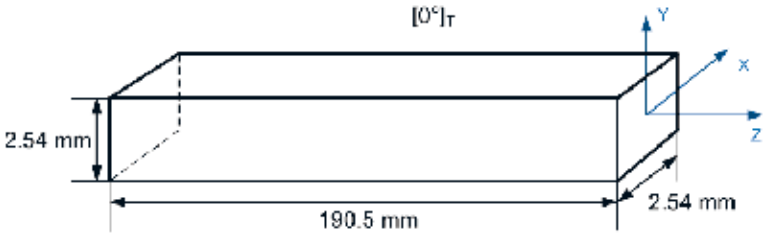

(a)

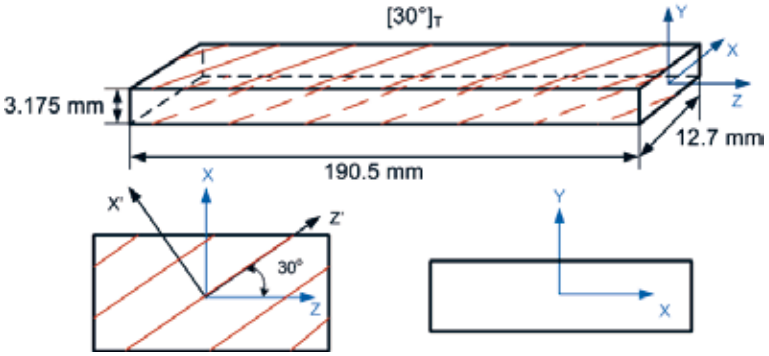

(b)

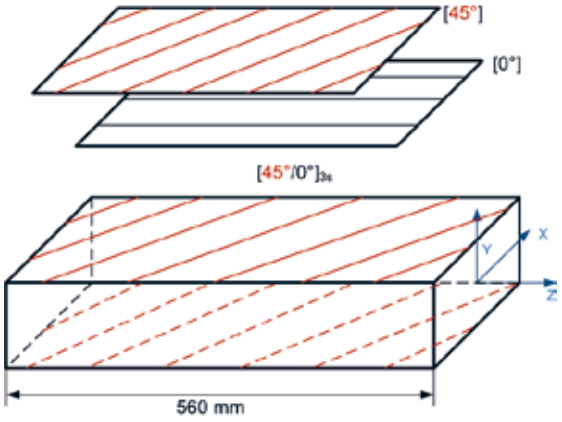

(c)

Fig.2. A sketch of considered cases. (a) Case1: $[0°]_T$ layup with arbitrary isotropic material, (b) Case2: $[30°]_T$ layup with Graphite/Epoxy, (c) Case3: $[45°/0°]_{3s}$ layups with Graphite/Epoxy.

Table 1. Structural properties of Case 1 (Blasques and Lazarov 2011)

Material	Arbitrary material
E_{11}, E_{22}, E_{33}	100 Pa
G_{12}, G_{13}, G_{23}	41.667 Pa
ν_{12}, ν_{13}, ν_{23}	0.2
ρ	1 kg/m^3
Width	0.1 m
Height	0.1 m
Length	7.5 m
Sectional stiffness of Case 1	
S_{11}, S_{22}	3.4899×10^{-1} (N)
S_{33}	1 (N)
S_{44}, S_{55}	8.3384×10^{-4} (N-m^2)
S_{66}	5.9084×10^{-4} (N-m^2)

Table 2. Sectional stiffness of Cases 2 and 3

Stiffness of Case 2 (Yu 2007)		Stiffness of Case 3 (Hodges et al. 1991)	
S_{11}	4.4702400×10^{5} (N)	S_{11}	4.1673312×10^{5} (N)
S_{13}	5.6667520×10^{5} (N)	S_{13}	-2.070544×10^{5} (N)
S_{22}	3.8404032×10^{4} (N)	S_{22}	3.0237504×10^{4} (N)
S_{33}	1.5861568×10^{6} (N)	S_{33}	3.6099968×10^{6} (N)
S_{44}	0.1313736×10^{1} (N-m^2)	S_{44}	5.314632×10^{-1} (N-m^2)
S_{46}	-9.225995×10^{-1} (N-m^2)	S_{46}	9.894628×10^{-2} (N-m^2)
S_{55}	1.1656606×10^{1}(N-m^2)	S_{55}	2.634072×10^{2}(N-m^2)
S_{66}	0.1454637×10^{1} (N-m^2)	S_{66}	3.584220×10^{-1} (N-m^2)

Case 1 is used for validating whether the new beam model is correctly implemented into HAWC2 or not. The other two cases are used for the comparisons between new HAWC2 computation with anisotropic material and the other existing results obtained from Yu (2007) and Hodges et al. (1991).

3.1 Natural frequencies and mode shapes. Eigenvalue analysis is performed for the three different cases. Table 3 shows the natural frequency comparisons of Case 1 between the new beam element before implementing HAWC2 and after implementation. They are completely identical. From this result, it may be concluded that the new beam element is successfully implemented into HAWC2.

Table 3. Natural frequency comparison of Case 1

Mode	New beam element only [Hz]	HAWC2 [Hz]
1	2.87262E-03	2.87262E-03
2	2.87262E-03	2.87262E-03
3	1.80466E-02	1.80466E-02
4	1.80466E-02	1.80466E-02
5	5.09409E-02	5.09409E-02
6	5.09409E-02	5.09409E-02
7	1.14752E-01	1.14752E-01

Table 4 shows the natural frequency comparisons between the other existing results and HAWC2 computation. The HAWC2 result shows good agreement with Yu (2007) and Hodges et al. (1991), respectively.

Table 4. Natural frequency comparisons of Cases 2 and 3

	Case 2	
Mode	HAWC2 [Hz]	Yu (2007) [Hz]
1 (flap-torsion)	52.5	52.6
2 (edge)	209.7	209.8
3 (flap-torsion)	326.1	326.3
4 (flap-torsion)	899.3	899.8
5 (edge)	1284.2	1284.9
6 (flap-torsion)	1660.9	1661.3

Mode	Case 3	
	HAWC2 [Hz]	Hodges et al. (1991) [Hz]
1 (flap-torsion)	4.66	4.66
2 (flap-torsion)	29.18	29.60
3 (flap-torsion)	81.57	84.89
4 (edge)	105.99	N/A
5 (flap-torsion)	113.35	113.43
6 (flap-torsion)	159.52	N/A

Small discrepancies in Cases 2 and 3 might occur due to converting the units from English to SI units and using different shape functions.

It is clear to see that flapwise bending-torsion and axial-edgewise deflections are coupled on the structure of Cases 2 and 3 from the Table 2. The coupling effects on the structure can be captured through the mode shape analyses. Fig. 3 shows the first 6 mode shapes of Case 2. From the mode 1, 3, 4, and 6 it is shown that the flap mode is coupled with the torsion mode.

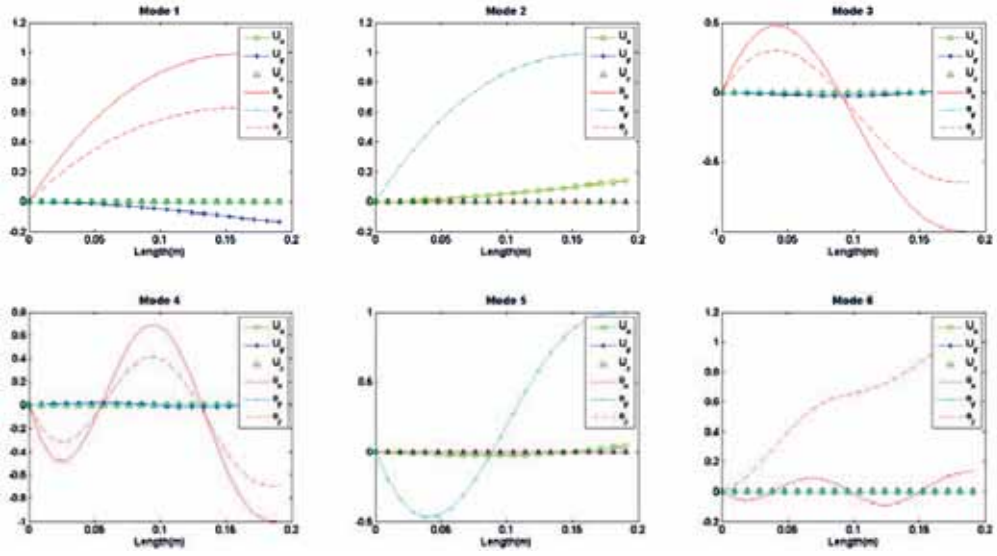

Fig. 3. First 6 mode shapes of Case 2 with anisotropic properties

Fig. 4 shows the first 6 mode shapes of Case 3. It is observed by mode 1, 2, 3, 5, and 6 that the flap mode is coupled with the torsion mode.

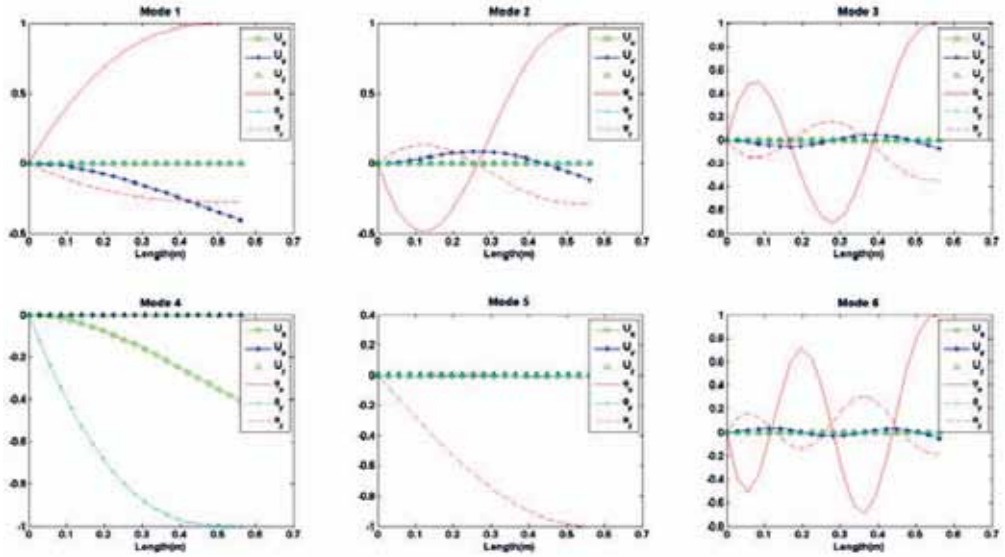

Fig. 4. First 6 mode shapes of Case 3 with anisotropic properties

From the above results of natural frequencies and mode shapes the new beam model can capture the physical behaviors of structural coupled characteristics.

An additional Eigenvalue analysis is performed with Cases 2 and 3 in order to investigate important physical differences between isotropic and anisotropic structures by using old versions (i.e. before implementing the new beam model) and new versions (i.e. after implementing the new beam model) of HAWC2. The old version of HACW2 considers the anisotropic characteristics produced by the shear center offset only (Petersen 1990; Larsen and Hansen 2007). However, its effect is ignored in this paper. Thus, it is assumed that the shear center is located at the center of the sections considered for both cases. In order to produce an isotropic structure, the off-diagonal terms in the anisotropic structural property are removed. Due to the mentioned assumption for the isotropic case the comparisons cannot offer equivalent conditions. However these comparisons may be helpful for understanding the physical differences between them.

Table 5 shows the natural frequency differences between the isotropic and the anisotropic model of Cases 2 and 3. The differences are obvious on the coupled modes because the isotropic model does not have the abilities to capture the coupling effects between modes.

Fig. 5 and 6 show the mode shapes of Cases 2 and 3 with an isotropic structure, respectively. As expected no coupled modes are observed.

Table 5. Natural frequency differences between isotropic and anisotropic model

HAWC2 simulation of Case 2			
Mode	Anisotropic [Hz]	Mode	Isotropic [Hz]
1 (flap-torsion)	52.5	1 (flap only)	70.5
2 (edge only)	209.7	2 (edge only)	210.0
3 (flap-torsion)	326.1	3 (flap only)	436.1
4 (flap-torsion)	899.3	4 (flap only)	1196.6
5 (edge only)	1284.2	5 (edge only)	1296.5
6 (flap-torsion)	1660.9	6 (torsion only)	1675.0
HAWC2 simulation of Case 3			
Mode	Anisotropic [Hz]	Mode	Isotropic [Hz]
1 (flap-torsion)	4.66	1 (flap only)	4.78
2 (flap-torsion)	29.18	2 (flap only)	29.97
3 (flap-torsion)	81.57	3 (flap only)	83.81
4 (edge only)	105.99	4 (edge only)	106.01
5 (flap-torsion)	113.35	5 (torsion only)	113.34
6 (flap-torsion)	159.52	6 (flap only)	163.95

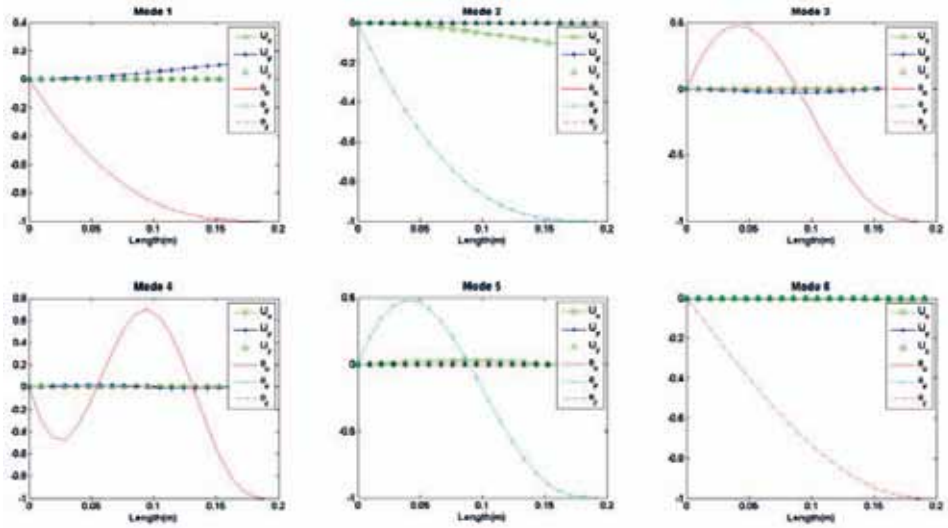

Fig. 5. First 6 mode shapes of Case 2 with isotropic properties

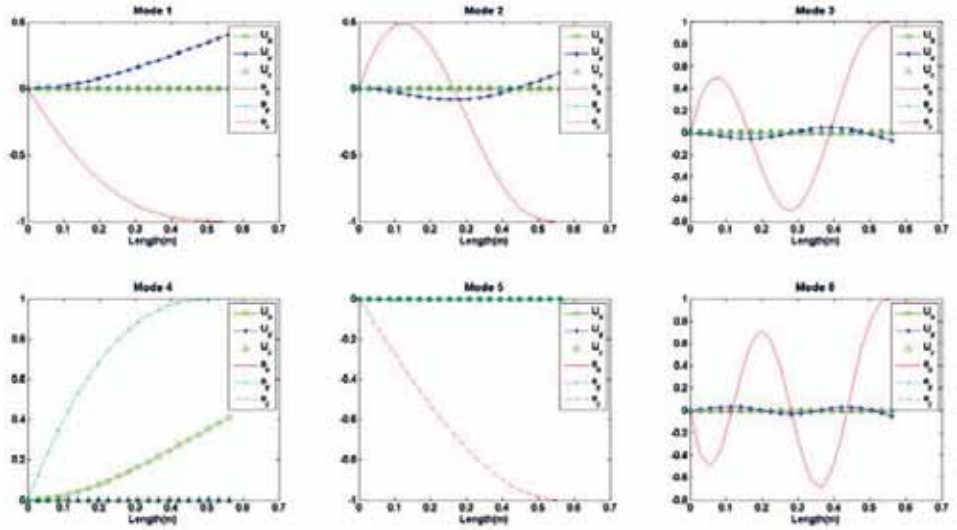

Fig. 6. First 6 mode shapes of Case 3 with isotropic properties

As we have investigated above there are differences between isotropic and anisotropic results for both the natural frequencies and mode shapes. Both are very important parameters when designing wind turbines. In that sense, the anisotropic behavior should be included in the relevant aeroelastic numerical tool if the blades have structural couplings.

4. CONCLUSIONS

In this paper, a new beam element which is able to consider the anisotropic behaviors is developed and implemented into HAWC2. Validations for the beam model and implementation are performed with 3 different cases. Eigenvalue analyses are performed. From the results the anisotropic characteristics show different behaviors compared to the isotropic ones. A new torsion mode, for instance, can be introduced by using bending-twist coupling of the anisotropic case. This additional effect may be used for developing new types of blades such as blades with less pitch control.

ACKNOWLEDGEMENTS

The work is partly supported by the Danish Energy Authority through the 2007 Energy Research Programme (EFP 2007). The supported EFP-project is titled “Anisotropic beam model for analysis and design of passive controlled wind turbine blades” and has journal no. 33033-0075. The support is gratefully acknowledged and highly appreciated.

REFERENCES

Blasques, J. P., and Lazarov, B. (2011). A Cross Section Analysis Tool for Anisotropic and Inhomogeneous Sections of Arbitrary Geometry. Risø-R-1785.

Hodges, D. H., Atilgan, A. R., Fulton, M. V., and Rehfield, L. W. (1991). Free-Vibration Anaysis of Composite Beams. Journal of the American Helicopter Society. 36(3), pp. 36-47.

Larsen, T.J., and Hansen, A.M. (2007). How 2 HAWC2, the user’s manual. Risø-R-1597(EN).

Luczak, M., Manzato, S., Peeters, B., Branner, K., Berring, P. & Kahsin, M. (2011). Dynamic Investigation of Twist-bend Coupling in a Wind Turbine Blade. Journal of Theoretical and Applied Mechanics, 49(3)

Petersen , J.T. (1990). Kinematically Nonlinear Finite Element Model of a Horizontal Axis Wind Turbine- Part 1: Mathematical Model and Results. Ph.D. Thesis. Technical University of Denmark.

Yu, W. (2007). Efficient High-Fidelity Simulation of Multi-body Systems with Composite Dimensionally Reducible Components. Journal of the American Helicopter Society. 52(1), pp. 49-57.

Proceedings of the 32nd
Risø International Symposium on Materials Science:
Composite materials for structural performance:
Towards higher limits
Editors: S. Fæster, D. Juul Jensen,
B. Ralph, B.F. Sørensen
Risø National Laboratory for Sustainable Energy,
Technical University of Denmark, 2011

FATIGUE BEHAVIOR OF COMPOSITE PRESSURE VESSELS WITH ALUMINUM ALLOY LINERS

S.-T. Kim**, K.-M. Lee* and J.-S. Park*

**School of Mechanical Engineering, Yeungnam University, Gyongsan, Korea
*Korea Institute of Machinery and Materials, Changwon, Korea.

ABSTRACT

The composite pressure vessel with an aluminum liner is widely used for high pressure gas storage these days. In the manufacturing process of composite cylinders with a metal liner, the autofrettage treatment, which induces a compressive residual stress on the liner of a composite pressure vessel, is one of the important methods for increasing the fatigue life of the pressure vessel. In this study, the fracture location and fatigue life of the composite pressure vessel with an aluminum liner were analyzed with the finite element method and verified through a fatigue test of the liner material and a pressure cycling test of composite cylinders. The nonlinear finite element analysis shows that the autofrettage pressure increases the fatigue life of the liner. The leak position was changed from the cylinder to the dome knuckle part, and from the dome knuckle part to the boss neck part. The change of the leak position can be explained with the change of maximum strain. This FEM analysis results, also, agree with the results of cyclic pressurizing test. The method applied in this study will be a good example for finding out the optimum condition of the autofrettage pressure for a composite pressure vessel and can be applied to the different vessels with larger sizes.

1. INTRODUCTION

There have been numerous studies of the application of composite materials to the structure of pressure vessels. A composite pressure vessel fully over-wrapped with carbon/epoxy composite layers over an aluminum liner is the most ideal and safe high pressure gas container due to the light weight, performance and the leak-before-burst characteristics [Kim et al 1997; James et al 1987; Sun et al 1999]. An autofrettage process was applied at the end of the manufacturing process of a cylinder for the purpose of improving the fatigue life, where the cylinder is once over pressurized to a certain pressure usually beyond its test pressure and yield limit of the aluminum liner. This process induces a compressive residual stress on the liner when it goes back to zero pressure, resulting in noticeable improvement in cycling life of the cylinder. During service, if the damage of fibers occurs in the outer composite layers, it can degrade the structural performance, reducing cycling life from the original design life. In this study, the fracture location and fatigue life of a composite pressure vessel with an aluminum liner were analyzed

with the finite element method and verified through a fatigue test of liner material and pressure cycling test of composite cylinders [Kabir 2000; Kwang 2000]. Because the finite element modeling and analysis is path dependent due to plastic deformation of the aluminum liner in the autofrettage process, a crack should be introduced after autofrettage in the analysis step considering real circumstances where a crack occurs during the use in service. The objective of this study is to establish the optimum autofrettage pressure which gives maximum cycling life and favorable failure mode with finite element analysis and to verify with the fatigue test of the liner material and pressure cycling test of composite cylinders [Koh 2000].

2. THE FINITE ELEMENT MODELING AND ANALYSIS OF COMPOSITE CYCLINDERS

The pressure vessel used in this study is a composite cylinders with an inner volume of 6.8*l* and weight of 4kg. The main use of this pressure vessel is for the respirator of a Self-Contained Breathing Apparatus(SCBA) in a toxic gas environment. Figure 1 is the cross section of the 6.8 *l* filament-wound composite cylinder. The composites were made of carbon/epoxy and the liner was made of Al6061-T6 alloy.

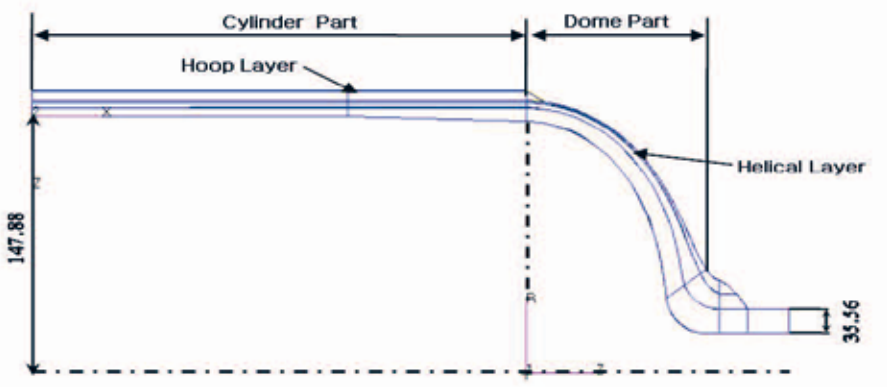

Fig. 1. Cross section of 6.8*l* filament-wound composite cylinder(dimensions in mm)

A path-dependent nonlinear finite element analysis for the cylinder was conducted to determine liner stresses accurately due to plastic deformation of the aluminum liner after the autofrettage process. It is assumed that the maximum stress would occur in the cylinder part of the pressure vessels and cracks would be located in the center of vessels. This center part of the cylinder is circularly symmetrical in the direction of the circumference and one section of vessel is used for 3D modeling with 20 nodal solid elements. Two cracks with different sizes were introduced to find out the effect of crack size on the performance of vessels. The maximum principal strain of the liner derived from the finite element analysis was taken into the stress-life technique to predict the cycling life with different levels of autofrettage pressure. The effect of the autofrettage pressure was examined in the range of 105% to 195% of the test pressure increasing by 5%. The analysis was carried out using the ABAQUS and Patran. Figure 2 shows single point and multi-point constraints for finite element model of the 6.8 *l* composite cylinder. Figure 3 is the analysis sequence considering the residual compressive stress effect by autofrettage of the linear material. It can be explained step by step as follows:

Step 1 : Loading up to the autofrettage pressure (52.5 MPa, 105%)

Step 2 : Unloading to zero pressure (0MPa)

Step 3 : Loading up to the test pressure (30 MPa)

Step 4 : Loading up to the minimum burst pressure.

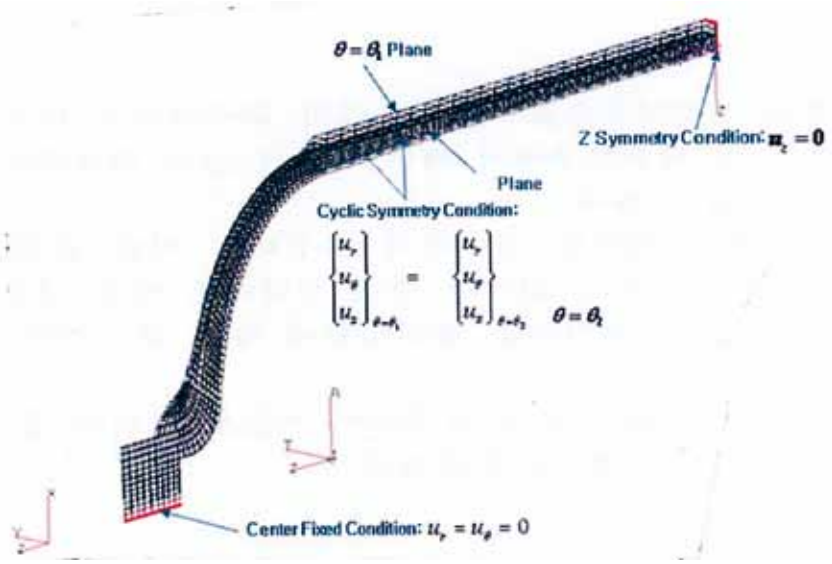

Fig. 2. Single point and multi-point constraints for the finite element model of the 6.8 *l* composite cylinder

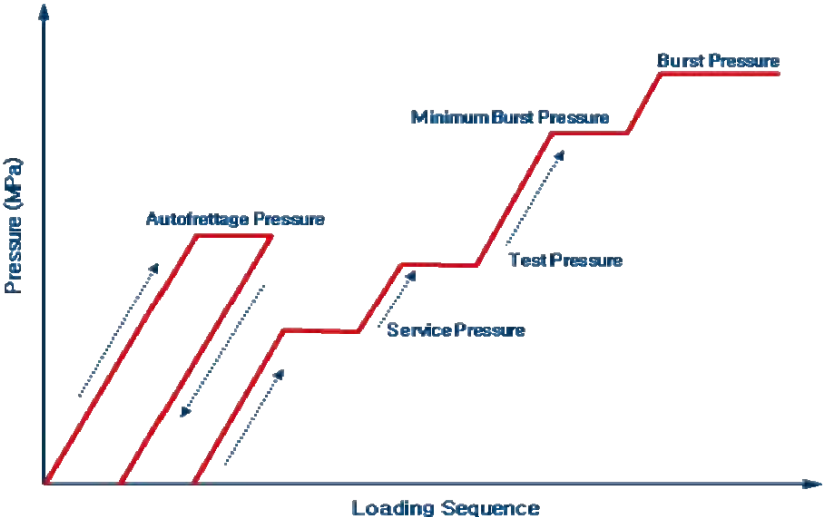

Fig. 3. Loading sequence of the FE Analysis

3. RESULTS OF THE FINITE ELEMENT ANALYSIS

The key parameters for determining the fatigue life of composite vessels are the amplitudes and distributions of the stress and strain in the liner. The stress distribution under the cyclic pressure in the liner depends on the amounts of plastic deformation and specific stiffness ratio between composites and Al liner. Fig. 4 shows the deformed shape under an autofrettage pressure (52.5 MPa) of the composite pressure vessel,

Fig. 4. Deformed shape under an autofrettage pressure (52.5 MPa) of the 6.8 *l* composite pressure vessel; 1:10 scale

A path-dependent nonlinear finite element analysis for the cylinder was conducted step by step in order to determine liner stresses accurately due to the plastic deformation of the aluminum liner after the autofrettage process. Figure 5 and Figure 6 show the Von-Mises stress distribution and the maximum principal strain distribution in the 6.8*l* composite pressure vessel with 105% (52.5MPa) autofrettage, respectively.

Fig. 5. Von-Mises stress distribution in the 6.8*l* composite pressure vessel with 105% (52.5MPa) autofrettage pressure

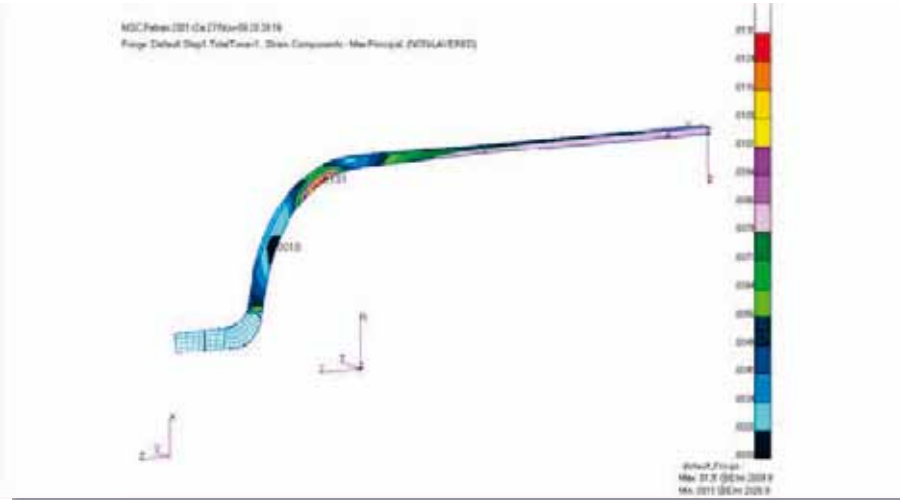

Fig. 6. Maximum principal strain distribution in the 6.8*l* composite pressure vessel with 105% (52.5MPa) autofrettage pressure

Figure 7 is the stress-strain history of the liner knuckle part in the 6.8*l* composite pressure vessel with a 30.0 MPa cyclic test pressure after the autofrettage pressure. It predicts the strain of the liner at a cyclic test pressure from zero pressure to 30 MPa**.**

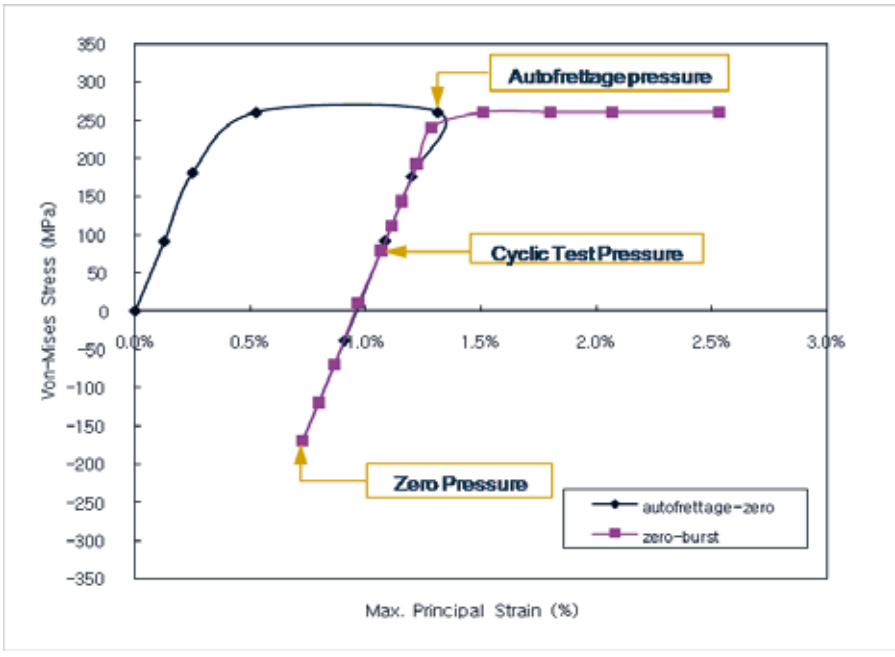

Fig. 7. Stress-strain history of the liner knuckle part in the 6.8*l* composite pressure vessel with a 30.0 MPa cyclic test pressure after the autofrettage pressure

4. EXPERIMENTAL CHARACTERIZATION

Tensile tests and fatigue tests were carried out to compare with the finite element analysis results. The plate tensile test specimens of 189 mm length, 12mm width and 2.41 mm thickness were prepared according to DOT-CFFC standards. The result of a tensile test shows the average value of the yield strength of the material is 310.7 MPa and the average stress corresponding to the maximum principal strain with an autofrettage pressure of 52.5 MPa. Also, fatigue tests were carried out with the liner coupon specimens. The stress ratio and frequency during the test were 0.1 and 3 Hz, respectively. Figure 8 shows the fatigue test results for a liner specimen of the 6.8*l* composite pressure vessel. The equation of the fatigue life vs stress value was obtained from the experimental result of stress-life test as follows:

$$\sigma = m_1 \, N_f^{\,m_2}$$

where, m_1 is 1262, m_2 is -0.16.

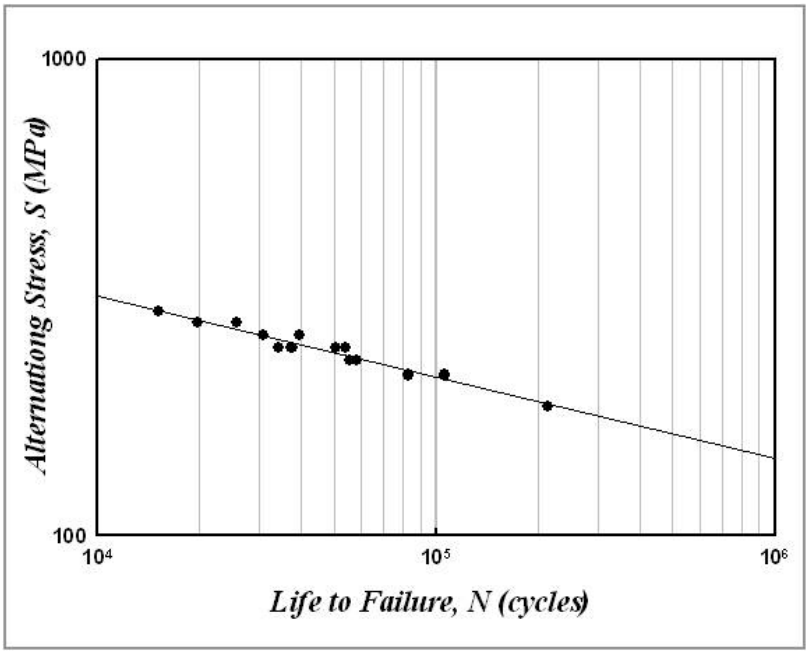

Fig. 8. Fatigue test result for the liner specimen of the 6.8*l* composite pressure vessel

Figure 9 is the fatigue test result in the total range of the autofrettage pressure (105% to 195%). Figure 10 shows the shape of vessels used in fatigue tests and a leak around the cylindrical part after failure by the pressure cyclic test in the composite cylinder.

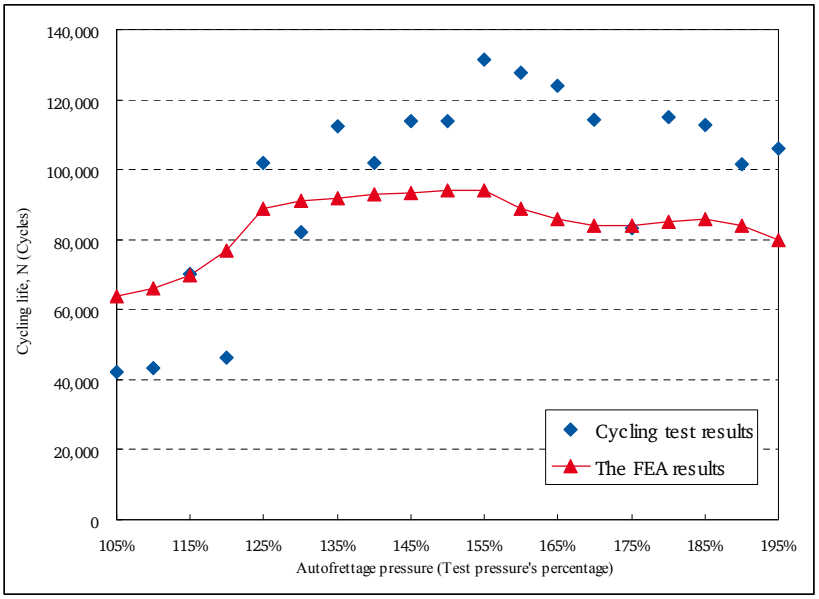

Fig. 9. Results in the total range of autofrettage pressure (105% to 195%)

Fig. 10. Shape of vessels used in fatigue tests and a leak around the cylindrical part after failure by a pressure cyclic test in the composite cylinder.

5. RESULT ANALYSIS

In the analysis, the cycling life of cylinder increased according to an increase of the autofrettage pressure up to 155 % of the test pressure, but it began to slightly decrease above 160%. Failure location by a leak was also changed from the cylinder part to the dome knuckle part in the range of 105 to 155 % pressure, and again from the dome knuckle part to the boss neck above 160%. Cyclic tests for several cylinders were also conducted to verify the analysis results. Change of cycling life and failure locations in testing showed good agreement with the analysis results in the overall trend

6. CONCLUSION

Based on the above results, It can be concluded that the compressive residual stress induced by the autofrettage pressure differs by locations, and it is the highest in the cylinder part and begins to decrease around the dome knuckle part and further decreases along the dome contour up to the boss neck in sequence. Compressive residual stress at any location of the liner increases with the increase of autofrettage pressure, but only up to compressive yield limit of the liner, and beyond that point further increasing of the autofrettage pressure does not have any effect on cycling life of that location. Consequently, a 155 % pressure was determined as an optimum autofrettage pressure which generates the maximum residual stress in the cylinder part and a moderate residual stress in the dome part, resulting in a maximum cycling life and desirable failure location of the dome knuckle part.

REFERENCES

James, D.E. and James, A.Y. (1987). Graphite epoxy pressure vessel dome reinforcement study. 32nd International SAMPE Symposium. pp. 221-237.

Kabir, X.M. (2000). Finite element analysis of composite pressure vessels with a load sharing metallic liner. Composite Structure. 49, 247-255.

Kim B.S. (1997). Developing of composite CNG pressure vessels," ICCM-11, Int'l Conf. Composite Materials, pp. 401-418.

Koh, S.K. (2000). Fatigue analysis of autofrettaged pressure vessels with radial holes," International Journal of Fatigue. 22, 717-726.

Kwang, T.K., Jung, S.K. Doh, Y.D., Cho, W.M. and Jung, B. (2000). The performance improvement of filament wound composite pressure vessels," SAMPE 2000, pp. 1427-1438.

Sun, X.K., Du, S.Y. and Wang, G.D. (1999). Bursting problem of filament wound composite pressure vessels. International Journal of Pressure Vessels and Pinging 76, 55-59.

Proceedings of the 32nd
Risø International Symposium on Materials Science:
Composite materials for structural performance:
Towards higher limits
Editors: S. Fæster, D. Juul Jensen,
B. Ralph, B.F. Sørensen
Risø National Laboratory for Sustainable Energy,
Technical University of Denmark, 2011

ELECTROSPINNING OF POLY(VINYL ALCOHOL) AQUEOUS CONTAINING TIO_2 NANOPARTICLES

W.S. Lyoo*, J.W. Cha*, M.J. Kim*, S.M. Lee*, S.H. Han*, M.K. Lee*, Y.H. Jang**, C.S. Kim**, T.H. Oh*, Y.S. Gal*** and S.K. Noh****

*Division of Advanced Organic Materials, School of Textiles, Yeungnam University, Gyeongsan 712-749, Korea
**WooJinChem Co., Ltd., Gyochon-ri, Jain-Myeon, Gyeongsan-si, Gyeongsangbuk-do 712-852, Korea
***Polymer Chemistry Laboratory, College of Engineering, Kyungil University, Gyeongsan 712-701, Korea
****School of Display and Chemical Engineering, Yeungnam University, Gyeongsan 712-749, Korea

ABSTRACT

Poly(vinyl alcohol) (PVA)/TiO_2 composite nanofibers were successfully prepared via an electrospinning technique. In this study, the effect of the addition of a TiO_2 colloidal solution on the PVA/TiO_2 composite nanofibers was performed by a series of experiments varying the processing parameters, including concentration of the PVA solution, the contents of TiO_2, the applied voltage (AV), the tip-to-collector distance (TCD). A water-based colloidal TiO_2 in PVA solution was directly mixed without any chemical or structural modification into PVA polymer fibers to form organic-inorganic composite nanofibers. The PVA/TiO_2 composite nanofibers were characterized by field emission scanning electron microscopy (SEM). A division of TiO_2 nanoparticles in the PVA/TiO_2 composite nanofibers was observed with transmission electron microscopy (TEM).

1. INTRODUCTION

Polymer/inorganic nanoparticle composites have been the focus of extensive research efforts through the past decade. The introduction of inorganic nanoparticles into a polymer matrix has proved to be an effective and low-cost method to improve the performance of existing polymer materials. The synergistic properties produced by the addition of inorganic nanoparticles include an improved modulus and dimensional stability, a lower thermal expansion coefficient and gas permeability, a higher swelling resistance, and enhanced ionic conductivity, etc. When nanometre-sized particles are applied, these benefits can be achieved at very low loading levels

as a result of their unusually large specific surface areas.

In recent years, the electrospinning process has regained great attention, as it is a simple and low cost method for fabricating pure polymer nanofibers and polymer/inorganic composite nanofibers. The incorporation of inorganic nanoparticles into polymer nanofibers can be achieved using electrospinning polymer solutions containing inorganic nanoparticles.

In this study, PVA/TiO_2 composite nanofibers were electrospun from a PVA/TiO_2 solution with small amounts of a water-based TiO_2 colloidal solution. Conventionally, the PVA solution and the TiO_2 colloidal solution were mechanically mixed to form composites. It did not require the introduction of an additional reduction or stabilizing agent because the polymer serves as both a stabilizing agent and material for forming nanofibers.

2. EXPERIMENTAL

2.1. Materials. Poly(vinyl alcohol) (PVA) with number-average degree of polymerization (P_n) of 1700 and degree of saponification (DS) of 99.9% was purchased from DC chemical Co., Ltd., Seoul, Korea. A titanium dioxide (TiO_2) nanoparticles aqueous solution was purchased from Miji tech. Co., Ltd., Korea. The concentration of the TiO_2 colloidal solution is 10,000 ppm.

2.2. Preparation of PVA and PVA/TiO_2 solution. PVA aqueous solutions (9, 11, 13 wt%) were prepared by dissolving PVA in distilled water at 90 ℃ under magnetic stirring for 2h. TiO_2 (0.1, 0.2, 0.4 wt% of the amount of PVA) nanoparticles were dropped slowly into the PVA aqueous solutions under vigorous stirring in a water bath at 30 ℃.

2.3. Electrospinning. Concentration of the PVA aqeous solution was varied from 9 to 13 wt%. The applied voltage (AV) ranged from 15 and 25 kV. The tip-to-collector (TCD) was varied from 11 to 15cm.

3. RESULTS AND DISCUSSION

SEM images of PVA/TiO_2 composite nanofibers electrospun for various concentrations of PVA (9, 11, 13 wt%) are shown in Fig. 1. With an increase in the concentration of the PVA solution, the average diameters of PVA/TiO_2 composite nanofibers were decreased. When the concentration of the PVA solution was 13 wt%, PVA/TiO_2 composite nanofibers were prepared with difficulty.

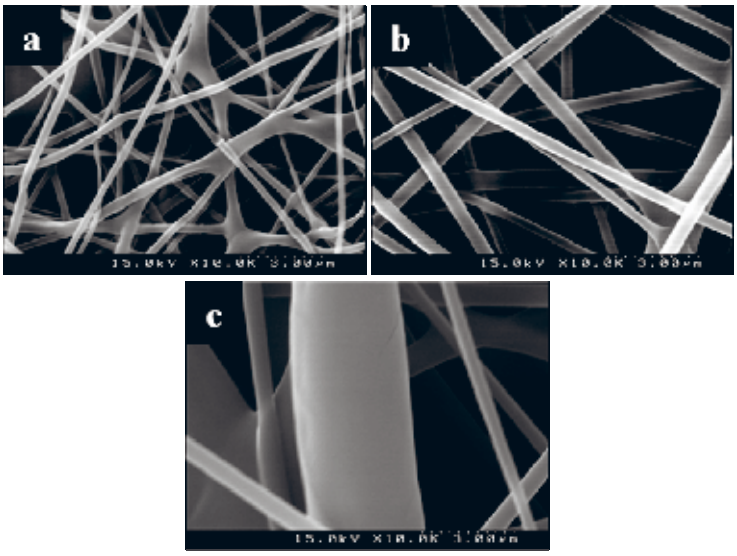

Fig. 1. SEM images of PVA/TiO_2 composite nanofibers electrospun at an applied voltage and TCD of 25kV and 13 cm, respectively, with 0.1 wt% TiO_2 colloidal solution and with various concentrations of PVA solution: a, 9 wt%; b, 11 wt%; c, 13 wt%.

SEM images of PVA/TiO_2 composite nanofibers electrospun with various applied voltages and various TCD were shown in Fig. 2 and Fig. 3, respectively. The results, the diameters of PVA/TiO_2 composite nanofibers were formed nonuniformally with an increase in the applied voltage. As the TCD increased from 9 to 12 cm, the average diameters of PVA/TiO_2 composite nanofibers were decreased.

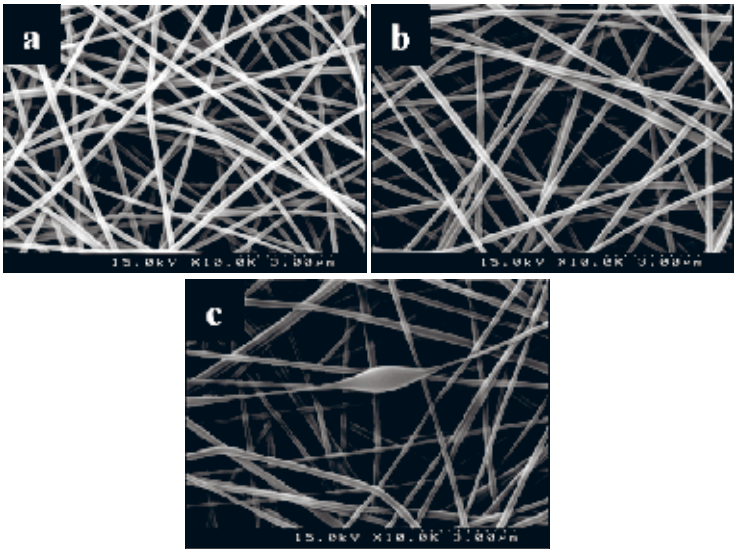

Fig. 2. SEM images of PVA/TiO_2 composite nanofibers electrospun at a TCD of 15 cm , with concentration of 9 wt% PVA solution and 0.2 wt% TiO_2 colloidal solution, with various applied voltages: a, 15 kV; b, 20 kV; c, 25 kV.

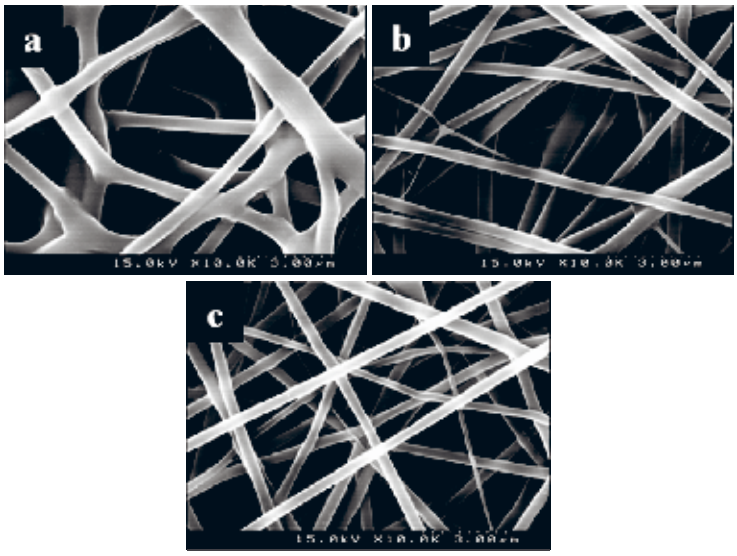

Fig. 3. SEM images of PVA/TiO_2 composite nanofibers electrospun at an applied voltage of 15kV, with a concentration of 11 wt% PVA solution and 0.2 wt% TiO_2 colloidal solution, with various TCDs: a, 11 cm; b, 13 cm; c, 15 cm.

When dopant is added to the polymer solution for electrospinning, the interaction between the dopant and polymer will make the nanofiber thicker. Fig. 4 are SEM images of pure PVA nanofibers and PVA/TiO_2 composite nanofibers. The average diameter of PVA/TiO_2 composite nanofibers increased with the TiO_2 colloidal solution content in the PVA aqueous solution. The reason is that the TiO_2 nanoparticle enters between the high molecular chains and then the interval of chains becomes wider.

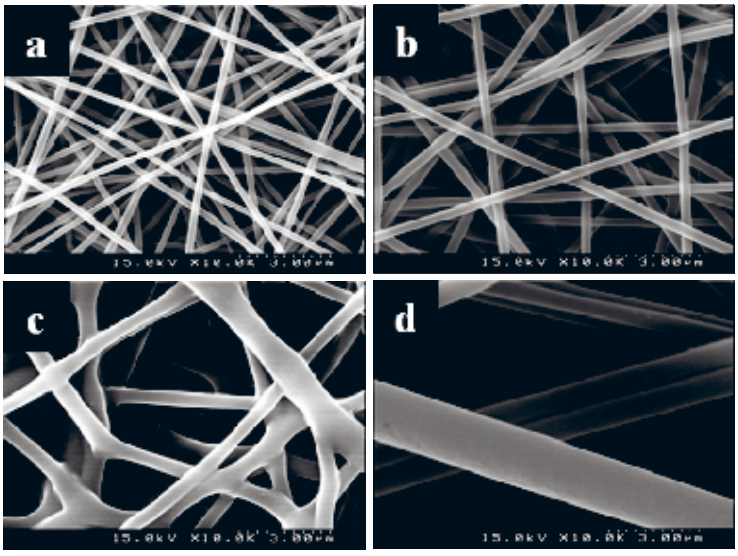

Fig. 4. SEM images of PVA/TiO_2 composite nanofibers electrospun at an applied voltage and TCD of 15kV and 11 cm, respectively, with a concentration of 11 wt% PVA solution and with various amounts of TiO_2 colloidal solution: (a) 0 wt%; (b) 0.1 wt%; (c) 0.2 wt%; (d) 0.4 wt%.

TEM images provides direct evidence that TiO_2 nanoparticles are embedded in the PVA/TiO_2 composite nanofibers. As shown in Fig. 5, the dark field TEM images indicate clearly these TiO_2 nanoparticles were contained in the nanofibers Although a cohesion phenomenon occurs a little between TiO_2 nanoparticles, the TiO_2 nanoparticles inside PVA/TiO_2 composite nanofibers were evenly distributed.

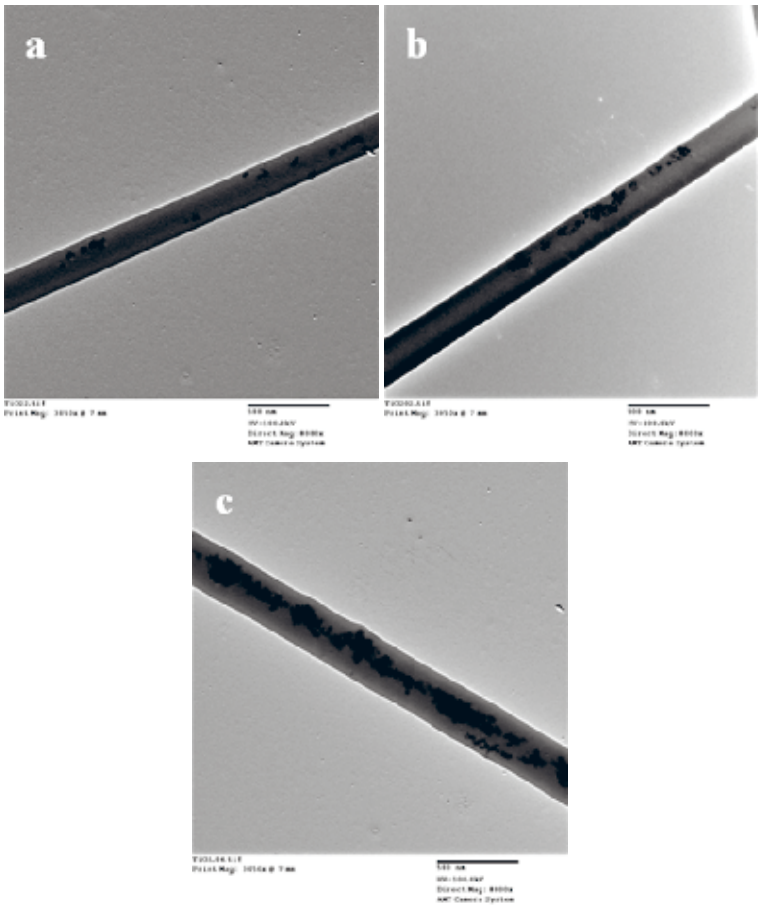

Fig. 5. TEM images of PVA/TiO_2 composite nanofibers electrospun at an applied voltage and TCD of 20kV and 11 cm, respectively, with a concentration of 11 wt% PVA solution and with various amounts of TiO_2 colloidal solution: a, 0.1 wt%; b, 0.2 wt%; c, 0.4 wt%.

ACKNOWLEDGEMENTS

This work was supported by grant No. RTI04-01-04 from the Regional Technology Innovation Program of the Ministry of Knowledge Economy (MKE).

REFERENCES

Daniel, M. C.; Astruc, D. Chem Rev **104**, 293 (2004).
Hari, P. R.; Chandy, T.; Sharma, C. P. J Appl Polym Sci **59**, 1795 (1996)
Kim, F.; Song, J. H.; Yang, P. J Am Chem Soc **124**, 14316 (2002).
Lee, H. K.; Jeong, E. H.; Baek, C. K.; Youk, J. H. Mater Lett **59**, 2977 (2005).
Lee, Y. J.; Lyoo, W. S. J Polym Sci Polym Phys **47**, 1916 (2009).
Son, W. K.; Youk, J. H.; Lee, T. S.; Park, W. H. Macromol Rapid Commun **25**, 1632 (2004).
Yonezawa, T.; Kunitake, T. Colloids Surf A **149**, 193 (1999).
Zhang, Z.; Han, M. J Mater Chem Commu **12**, 641 (2003).
Zhang, Z.; Zhao, B.; Hu, L. J Solid State Chem **121**, 105 (1996)

Proceedings of the 32nd
Risø International Symposium on Materials Science:
Composite materials for structural performance:
Towards higher limits
Editors: S. Fæster, D. Juul Jensen,
B. Ralph, B.F. Sørensen
Risø National Laboratory for Sustainable Energy,
Technical University of Denmark, 2011

APPLYING THE MECO PRINCIPLE TO ASSESS THE ENVIRONMENTAL IMPACT OF CONVENTIONAL AND BIO-BASED COMPOSITE MATERIALS IN A CASE STUDY OF A SMALL-SCALE WIND TURBINE BLADE

C.M. Markussen*, F. Bottoli**, L. Pignatti*, B. Madsen*, L.P. Mikkelsen*, P. Brøndsted* and T.L. Andersen*

* National Laboratory of Sustainable Energy Risø DTU, Denmark
** Politecnico di Milano, Italy

ABSTRACT

The MECO-principle has been used for benchmarking conventional and bio-based composite materials in an environmental impact context. Material characterisation has been performed on composites with a standard carbon fibre fabric, a flax fibre fabric and a flax/carbon hybrid fabric. All composites are made with a bio-based epoxy derived from wood processing waste. Material data results have been used as input for a FEM model constructed, to dimension a prototype small-scale wind turbine blade. Sets of blades with the different types of fabrics are manufactured while accounting for materials consumption. Consumption data is used to present a benchmarking scenario, demonstrating the feasibility of using bio-based materials for load-carrying structures in wind turbine blades. It is estimated in this study that the non-renewable energy consumption for the conventional composite is around 106,3 $[MJ]$ compared to 5,1 $[MJ]$ for the bio-based one.

1. INTRODUCTION

With increasing awareness of the planets dwindling resources, the demand for wider application of sustainable and renewable materials is becoming ever more adamant for all industrial sectors. Within the composite sector, natural reinforcements, such as flax and hemp fibres, have been used for years for non-structural parts (furniture, automotive panels etc.). Due to so far unresolved issues of predictability with the material homogeneity, porosity content and moisture resistance, these materials have not yet been used in load carrying structures. The aim of this study is to determine how well the state-of-the-art industrially-produced bio-based reinforcement materials compare with conventional materials. The application in which the materials will be evaluated, is a prototype small-scale wind turbine blade (Gaunaa, Øye and Mikkelsen (2009)). This article summarises the work carried out in the study

by Bottoli and Pignatti (2011) and further builds on the results with application of the MECO principle for environmental impact assessment of the products.

2. MATERIALS SELECTION

The fibre fabrics and matrixes selected in the present study have been procured through regular vendors, which yield an unbiased representation of what the industry standard is capable of regarding bio-based composites. Parameters for materials selection have been:

- Mechanical properties
- Price
- Degree of sustainability

Different fabric styles have been considered for the natural fibre fabrics, and the choice fell on a variety of woven fabrics and stitched UD fabrics due to their superior mechanical properties. The better performance of the stitched UD and tightly woven fabrics comes at the expense of drapability which can become an issue with the mould geometry of a wind turbine blade. For the conventional material, a carbon fibre twill weave was chosen due to its high drapability and low relative cost, and a unidirectional tape was chosen because of its good mechanical properties. An overview of the selected fabrics can be found in Table 1.

It was decided to only use one type of matrix resin to reduce the number of materials variables. The resin used is from the company Entropy Resins, more specifically the SuperSap™ 100/1000. The selected bio-epoxy contains 48% renewable materials. This is sourced from co-products and by-products derived from waste treatment of industrial processes such as wood pulp and bio-fuel production (Entropy Resins (2011)). Data from the technical datasheet for the SuperSap™ is presented in Table 2.

Fabrics Selected

Company	Fibre Type	Weave Style	Area Weight [gsm]
Biotex	Flax	Biaxial +/- 45	400
Lineo	Flax	Unidirectional	150
Lineo	Flax/Carbon	Balanced 0/90	220
GEL-TOP A/S	Carbon	Unidirectional tape	375
R&G	Carbon	Twill	160

Table 1: Selected reinforcement fabrics

3. MATERIALS FABRICATION AND TESTING

A number of flat composite plates have been manufactured. All plates have been made using the Vacuum Assisted Resin Infusion Moulding procedure (VARIM). An illustration of the technique is shown in Fig. 1. In order to investigate the tensile properties of the fibre reinforced material the standards ISO 527-4 and ISO 527-5 were used. The shear testing

SuperSap 100/1000		
Property	Unit	Value
Mix Viscosity (1000 Hardener)	[cPs]	2000-3000
Gel Time at 25C (150g mixed)	[min]	22-25
Cure time at 25C	[days]	7
Tensile Strength	[MPa]	62
Elongation at Break	[%]	7
Tg	[C]	120
Tensile Modulus	[GPa]	2,48
Density at 25C	[kg/l]	1,25

Table 2: Properties of SuperSap™ resin

procedure is carried out following the guidelines provided by the standard ASTM D 5379/D 5379M-98. For experimental setup see Fig. 2.

In this section a selection of the mechanical properties determined for the composites are presented (see Table 3). Volume fractions for reinforcement, matrix and porosities have been determined according to ISO 1172 and ASTM D2584. As expected the volume fractions for the natural fibres are significantly lower than for the carbon. Porosity content has been determined experimentally and is found to be very low. A full documentation can be found in Bottoli and Pignatti (2011). All values for the flax fibre composites correspond well with what has been reported elsewhere in litterature (Madsen and Lilholt (2003) and Goutianos et al. (2006)).

		Tensile Properties		Shear Properties	
Material	V_f [%]	E [GPa]	σu [MPa]	E [GPa]	σu [MPa]
Flax UD 0	34,5	19,93	237,87	1,56	35,84
Carbon UD 0	50,0	104,25	1970,58	3,81	43,91

Table 3: Results from mechanical testing of manufactured composite plates. Notice the difference in the achieved fiber volume fraction.

4. FABRICATION OF ROTOR BLADES

Initially a MATLAB model was used to optimise the layup of fabrics in the blade. A CAD model of the blade geometry was subsequently converted to ABAQUS and discretised. Using the material properties, found experimentally from the manufactured test specimens, as input, a FEM model was constructed. Full documentation of the method, procedure and results are available in Bottoli and Pignatti (2011). The CAD model and the resulting FEM model can be seen in Fig. 3.

In the FEM model the blades are dimensioned for stiffness, meaning they should have the same deflection given the same boundary conditions (load and constraints). With such a model it is possible to optimise the layup of fabric. Using these results an estimate can be made of the material consumption related to manufacturing. Because the carbon fibres are stronger, the laminate thickness and final composite weight can be reduced. However,

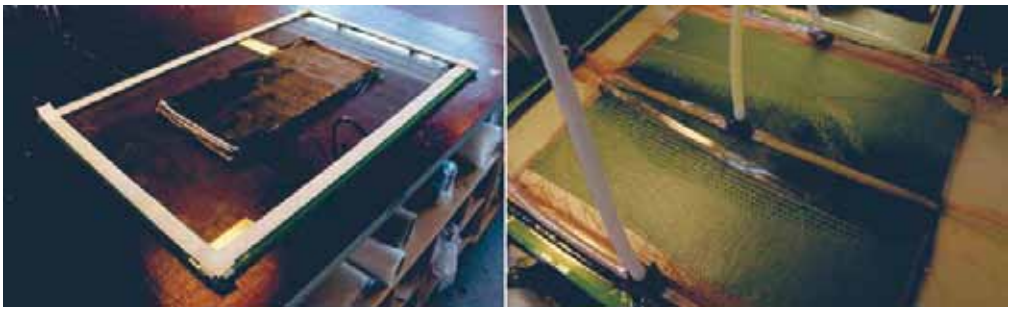

Fig. 1: The fabric layup(left) on a glass tool plate (500mm x 700mm) treated with release agent and sealant tape around the edges. A fabric layup (right) being infused with SuperSap™ 100/1000. Resin inlet is in the middle of the plate to simulate the short infusion length of the blade mould (10-15 cm crosswise).

even though the natural fibres need thicker laminates, the lower density of the flax partly compensates for this. The blade made from natural fibres still comes out heavier, principally due to the much lower fiber volume fraction ($Vol_f - \%$). But the interesting observation in this context is not the weight but rather the price, and the environmental impact of the final product.

In Fig. 4 the manufacturing process of a rotor blade prototype is shown. It can be seen that a significant amount of excess material will have to be discarded (trimmings) during the final stages of manufacture. The extent of this waste product can be of significant importance for the outcome of an environmental impact assessment. This is a subject of optimisation. Because this is a prototype, a fixed value of 10 % will instead be used as waste of the final product weight. Alternatively, the blades would suffer inappropriately compared to an optimised industrial production.

5. ENVIRONMENTAL IMPACT ASSESSMENT

With the environmental impact assessment, the aim is to uncover whether the naturally based composite can be considered a backstop technology and a marginal product to the

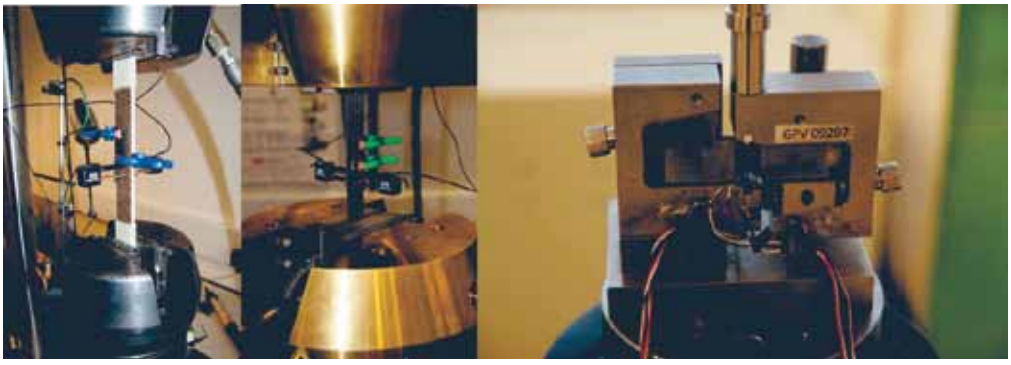

Fig. 2: Test specimens mounted for tensile testing (left) and shear testing (right)

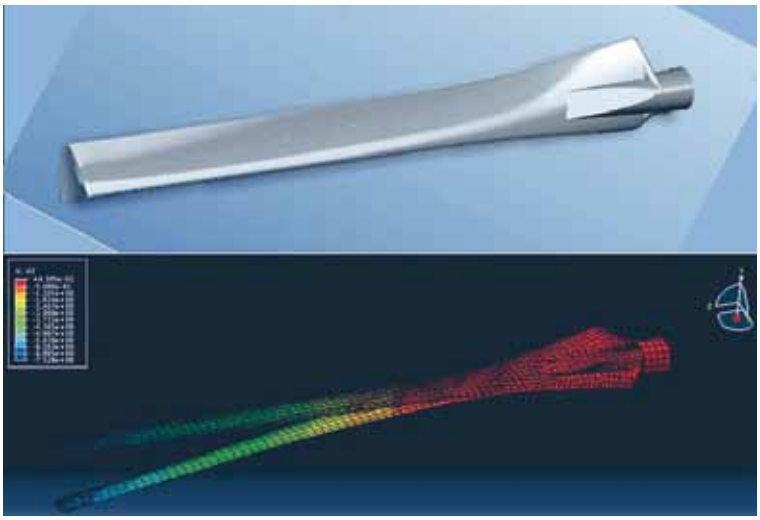

Fig. 3: CAD model (top) used as input for FEM model (bottom). The FEM model shows a load scenario with calculated deflection.

conventional petrochemically based product. Questions that must be answered in an assessment therefore are; whether the naturally sourced product has a lower negative environmental impact, and whether it is a feasible alternative?

Ideally any industrial products should have undergone a full quantitative Life Cycle Impact Assessment (LCIA) already in the design phase. Because this is rarely a feasible option, there exists a need for simplified benchmarking methods to aid the industrial designer. One such tool is the MECO principle *(Materials, Energy, Chemicals and Other)* (Wenzel, 1998). Developed in Denmark for the *EDIP* framework *(Environmental Design of Industrial Products)* the MECO principle is generally regarded as a hands-on approach for quickly organising an environmental assessment in the design phase. According to Wenzel (1998) there are three basic levels of LCIA:

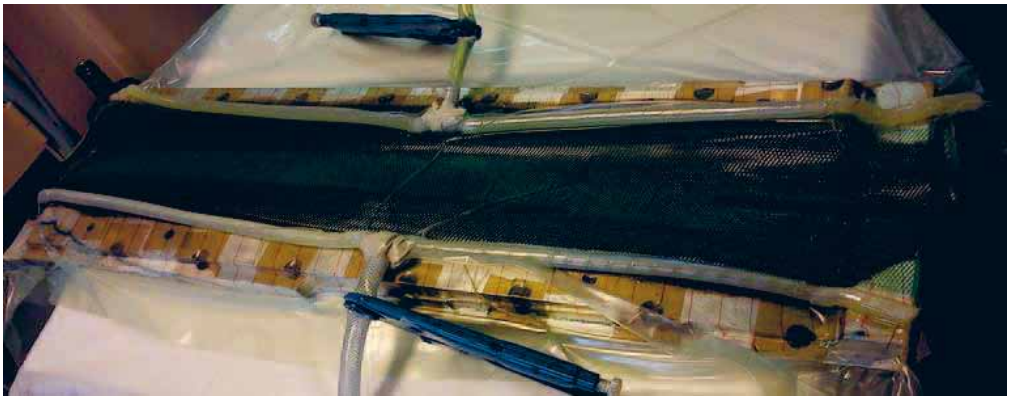

Fig. 4: Infusion of a blade section using flax fibres and bio-epoxy.

Process		Product	Material
Drying of fibres	*	Precision oven	Electricity
Cleaning of moulds		Cleaning agent (Bio)	Chemical X
Preparation of moulds		Release agent (Bio)	Chemical Y
Reinforcement	*	Bio fibre	Flax (cellulose)
Infusion material		Peel Ply	Nylon (PA6)
Infusion material		Greenflow	PolyPropylene
Infusion material		Spiral hose	PolyPropylene
Infusion material		Connectors	PolyPropylene
Infusion material		Straight hose	PolyPropylene
Infusion material		Sealant tape	Synthetic Rubber
Infusion material		Vacuum bag	Nylon (PA6)
Infusion	*	Bio epoxy	Epoxidised pine oil waste
Infusion		Mixing cup	PolyPropylene
Infusion		Mixing stick	Glass fiber reinforced plastic
Cleaning of mixing stick		Oven	Electricity
Evacuating laminate		Vacuum pump	Electricity
Elevating temperature of resin		Oven	Electricity
Vacuum degassing resin		Vacuum oven	Electricity
Post curing		Precision oven	Electricity
Post tooling		Power tools	Electricity
Bonding components		Structural adhesive	Epoxy

Table 4: Material consumption during manufacture. Only rows with * offer a variance when comparing the conventional materials over the bio-based ones. Example based on flax fibres.

- A matrix LCA; qualitative or semi-quantitative
- A screening LCA; quantitative using readily available data or semi-quantitative.
- A full LCA; quantitative and including new data inventory

There is an increasing need for quantity and quality of information when approaching a full quantitative LCA (Hochshorner and Finnveden (2003)). In the MECO-principle it is suggested that quantitative information could be used if it is easily available, and if so, a quantitative dimension can be added to the qualitative evaluation (Hochshorner and Finnveden (2003)). In theory this makes it ideal for efficiently benchmarking interchangeable products with regards to environmental impact.

In applying the MECO principle during the manufacturing stage of the blade in the present study a number of assumptions are made:

1. All processes leading to the semi-manufactures are fixed.
2. The functional unit is fixed i.e. the application of the product.
3. The products compared are interchangeable with respect to the functional unit, and the only difference is then the input/output of the manufacturing process.
4. The manufacturing procedure of the finished product is similar or identical.

	Material	Manufacture	Use	Disposal	Transport
1. Materials *a*) quantity *b*) resource					
2. Energy *a*) primary *b*) resource					
3. Chemicals					
4. Others					

Table 5: A standard MECO chart (Pommer et al. (2001))

5. There is no resource consumption related to the use of the product.

6. The resource consumption related to disposal is identical for the compared products.

Using the above assumptions, the MECO chart can be simplified from Table 5 to just include the column "Manufacture". Since the method of production is identical, this survey will exclude the consumables related to manufacturing. This leaves only the material input for matrix and reinforcements.

5.1 MECO matrix. The materials consumed during manufacture of the rotor blade prototypes are listed in Table 4. For the processes not indicated with an *, there is no difference in consumption for either material, they can therefore be omitted from the comparison. This reduces the matrix to Table 6.

Because there are many ways to compare the environmental impact, including release of solid, liquid and gaseous residues to the surroundings, eutrophication, GWP and so on, there is no clear consensus on what procedure yields the most reliable results. In this survey it was therefore chosen to compare the non-renewable energy requirements for production of the compared products. Indirectly contained in this number are also all emissions related to the energy consumption from the electricity mix at the production site.

As was shown in Diener and Schieler (1999) and reproduced in Markert (2008), the energy consumption related to the production of a flax fiber mat is only a fraction of that related

Manufacture Ressource consumption in final product + 10%.		
	Flax	Carbon
1. Materials Reinforcement	199,6 [g]	148,5 [g]
2. Energy		
3. Chemicals Bio-Epoxy	291,6 [g]	97,4[g]
4. Others		

Table 6: Materials consumed during the manufacture of the blades.

Non-renewable energy requirements for production of different fibres (MJ/kg)

Glass fiber mat		Flax fiber mat	
Raw materials	1.7	Seed production	0.05
Mixture	1.0	Fertilisers	1.0
Transport	1.6	Transport	0.9
Melting	21.5	Cultivation	2.0
Spinning	5.9	Fiber separation	2.7
Mat production	23.0	Mat production	2.9
Total	54.7	Total	9.55

Table 7: Consumption of non-renewable energy resources related to the different reinforcement materials (Diener and Schieler (1999)).

to the production of glass fiber mats (see Table 7). This is principally due to the extreme amounts of heat consumed during melting of the semi products. According to Das (2011), the energy requirement for manufacturing carbon fibres is 704 $[MJ/kg]$, again due to extreme amounts of heat, here required for carbonisation of the PAN. This however is a figure that is the subject of much debate and recent sources state values around 300 $[MJ/kg]$. It is clear that this is an area of optimisation and the producers are still improving the process. This study will use the number from Das (2011) and Diener and Schieler (1999) because their accounting methods are available for scientific evaluation. The numbers from Diener and Schieler (1999) and Das (2011) do not include the energy required for manufacturing a woven fabric. This study will not speculate on the production efficiency of this process and simply take the numbers as they are. It should therefore be clearly stated that these numbers are indicative and the results taken as such.

For the epoxy different considerations should be made as to what value would be representative to use in the calculations. As presented in Kosbar, Gelorme Japp and Fotorny (2001) and reproduced in Patel, Bastioli, Marini and Würdinger (2005) the difference in energy requirement for conventional and bio-based epoxy is quite significant (see Table 8). For the purpose of this analysis, the use of bio-epoxy is assumed interchangeable with a conventional epoxy with respect to manufacturing, which is also supported by the volume-fractions and mechanical properties of the composites. Therefore the value for total energy requirement for epoxy is chosen as conventional for the carbon and bio-epoxy for the natural reinforcements. This will better represent an actual production situation. With this information it is now possible to compare the total consumption for the finished rotor blades (see Table 9).

[MJ/kg] resin solids	Process	Feedstock	Transportation	Total
Conventional epoxy	10.0	7.16	0.68	17.8
Kraft lignin/epoxy	9.54	2.91	0.44	12.9
Organosolve lignin/epoxy	7.64	2.91	0.45	11.0

Table 8: Energy requirements for epoxy at different levels of sustainability (Kosbar et al. (2001)).

Manufacture Non-renewable energy requirement		
	Flax	Carbon
1. Materials Reinforcement	1,9 [MJ]	104,5 [MJ]
2. Energy		
3. Chemicals Bio-Epoxy	3,1 [MJ]	1,7 [MJ]
4. Others		
total	5,1 [MJ]	106,3 [MJ]

Table 9: Results of applying the MECO-principle to compare the non-renewable energy requirements for producing a small-scale wind turbine blade in bio-composite and conventional composite materials respectively.

It can be seen that the energy requirement for producing similar products is much more energy consuming in conventional composite materials than is the case for the all bio-based materials. The bio-based product only consumes 4,8% of the energy used to manufacture the same product using carbon fibres. The much larger number for a conventional carbon fibre composite can only be marginally amended if the conventional epoxy is exchanged with a bio-based one. In that case the consumption number for the carbon fibre blade is reduced to 105,6 [MJ]. It remains clear that the use of conventional reinforcements is the primary cause of non-renewable energy consumption.

6. DISCUSSION

The results from the study in applying the MECO-principle are based on a large selection of data from a variety of sources. The intention is to apply and use the principle to reliably advocate for the use of one class of material over another. Because the data used for the study is made by different people, and the work needed to gain insight in their method of accounting is prohibitive, it must, in this context, be taken at face value. It can be speculated, however, that some margin of uncertainty exists and the results should be interpreted with this in mind. However even taking the results as qualitative, there is a substantial indication of a much larger environmental impact related to the use of conventional composites compared with bio-based ones.

This study was aimed at benchmarking two classes of materials and to see which would be preferable from an environmental impact context. For this purpose, any similarity in consumption related to manufacturing was omitted in order to reduce the scale of the survey. This yielded a clear and convincing result in favour of the bio-based materials. If on the other hand all material consumption had been included, the resulting consumption numbers would have been much higher. In this case the difference separating the materials could have seemed marginal. With that in mind it is quite understandable why producers choose to be conservative, and prefer the tried and already tested material, if the economic and environmental advantages are not overwhelming.

Reflecting on the method, it is important to point out that the application of the MECO-principle was carried out by people with only little background in the field of LCA. As such

there are probably best-praxis guidelines which have not been strictly adhered to. It would however be interesting to examine the way the method has been applied in the present study, since this, in all probability, will resemble the way the people, for whom it was intended (industrial designers), will apply it. This says something of the robustness of the principle, in that it is clear and well defined in its method, so that reasonable results can be obtained within a workable time frame even for relatively inexperienced users.

7. CONCLUSION

In this study the mechanical properties measured from new bio-based materials, and conventional petro-chemically based ones, were used to dimension and fabricate prototype small-scale wind turbine blades. The resulting material consumption was accounted for and used to assess the different materials environmental impact. Here the MECO-principle was applied and the chosen indicator was the non-renewable energy consumption. It was estimated, when looking only at the difference in final product, that the use of bio-based materials consumed only 4,8% of the energy when compared to conventional materials i.e. carbon fibre / epoxy.

ACKNOWLEDGEMENT

The authors would like to thank Robert Mikkelsen of DTU Mechanical Engineering for loan of the prototype blade moulds and CAD model. Furthermore the technicians at the Risø Fiberlab for their assistance with manufacturing all composite panels and blades.

REFERENCES

Bottoli, F. and Pignatti, L. (2011). Design and Processing of Structural Components in Biocomposite Materials Case Study: Rotor Blades for Wind Turbine Cars. Master Thesis, xx pp.

Das, S. (2011) Life Cycle Assessment of Carbon Fiber-reinforced Polymer Composites. Int J Life Cycle Assess (2011) 16:268-282.

Diener, J. and Siehler, U. (1999). Ökologischer Vergleich con NMT- und GMT-Bauteilen. Die Angewandte Makromolekulare Chemie 272 (1999) 1-4 (Nr. 4744)

Entropy Resins (2011)
http : //www.entropyresins.com/sites/default/files/TDS_11_ONE01_v1_US.pdf

Gaunaa, M., Øye, S. and Mikkelsen, R. (2009). Theory and Design of Flow Driven Vehicles Using Rotors for Energy Conversion. EWEC 2009 Proceedings online, pages: 10 pages, 2009, EWEC.

Goutianos, S., Peijs, T., Nystrom, B. and Skrifvars, M. (2006) Development of Flax Fibre Based Textile Reinforcements for Composite Applications. Appl Compos Mater (2006) 13: 19921

Joshi, S.V., Drzal, L.T., Mohanty, A.K. and Arora, S. (2003). Are natural fiber composites environmentally superior to glass fiber reinforced composites? Composites Part A: Applied Science and Manufacturing Volume 35, Issue 3, Pages 371-376 (2004).

Hochshorner, E. and Finnveden, G. (2003) Evaluation of Two Simplified Life Cycle Assessment Methods. Int. J. LCA 8 (3) 119-128, 10 pp.

Kosbar, L.L., Gelorme, J.D., Japp, R.M. and Fotorny, W.T. (2001). Introducing Biobased Materials into the Electronics Industry. Journal of Industrial Ecology Vol. 4 issue 3

(2008).
Madsen, B. and Lilholt, H. (2003). Physical and mechanical properties of unidirectional plant fibre composites an evaluation of the influence of porosity. Composites Science and Technology Volume 63, Issue 9, July 2003, Pages 1265-1272.
Markert, F. (2008). Sustainability, Environmental and Safety Aspects in the Production of Biocomposites. 17th International Conference on Composite Materials.
Martin, P., Bastioli, C., Marini, L. and Würdinger, E. (2005). Life-cycle Assessment of Bio-based Polymers and Natural Fiber Composites. Biopolymers Online (2005)
Patel, M., Bastioli, C., Marini, L., Wrdinger, E. (2005). Life-cycle Assessment of Bio-based Polymers and Natural Fiber Composites. Biopolymers Online.
Pommer, K., Bech, P., Wenzel, H., Caspersen, N. and Olsen, S. I. (2001). Håndbog i miljøvurdering af produkter - En enkel metode. Miljønyt Nr. 58 2001. Miljøstyrelsen, Miljø og Energiministeriet (In Danish).
Rydh, C.J., and Sun, M. (2005). Life cycle inventory data for materials grouped according to environmental and material properties. Journal of cleaner Production, Volume 13, issues 13-14, pp. 1258-1268, (2005).
Wenzel, H. (1998). Application Dependency of LCA Methodology: Key Variables and Their Mode of Influencing the Method. Int. J. LCA 3(5) 281-288, 8 pp.

Proceedings of the 32nd
Risø International Symposium on Materials Science:
Composite materials for structural performance:
Towards higher limits
Editors: S. Fæster, D. Juul Jensen,
B. Ralph, B.F. Sørensen
Risø National Laboratory for Sustainable Energy,
Technical University of Denmark, 2011

MICROSCALE DAMAGE IN MODEL COMPOSITES

K. Martyniuk*, B.F. Sørensen*, E.M. Lauridsen*, S. Goutianos*, M. McGugan*, W. Ludwig** and S. Fæster*

*Risø DTU, National Laboratory for sustainable Energy, Materials Research Division, 4000 Roskilde, Denmark
**European Synchrotron Radiation Facility, 38043 Grenoble, Cedex 9, France

ABSTRACT

The microscale damage evolution in a glass fiber model composite is studied with the aim of establishing criteria for damage initiation and propagation. Microscale properties are known to influence the macroscopic strength of composites. However, it is not known in details how the crack initiation/propagation depends on material properties like fiber spacing or fiber/matrix interface. Therefore, this study focuses on evolution of the microscale damage in composites subjected to tensile loading perpendicular to the fiber direction. 2D and 3D in situ observations are carried using scanning electron microscopy, X-ray facilities and acoustic emission system.

1. INTRODUCTION

The amount of electricity produced by wind turbines is anticipated to grow exponentially. In order to harvest wind energy more efficiently, the size of new wind turbine must continue to increase. Consequently, their largest rotating components, the rotor blades, will be subjected to greater loads. Therefore, weight saving is of greater importance for large wind turbines. Yet, it is essential that weight saving due to design changes do not compromise the reliability of the blades. The reliability can be increased by better design criteria i.e. by improving the description of materials strength properties. Better materials models can be developed if the understanding of evaluation of damage and crack growth is increased. Therefore it is important to characterize materials' microstructures and study how micro cracks initiate and propagate. Previous studies have shown that the first modes of microscale damage in glass fiber composites are fiber/matrix debonding and matrix cracking (Holmes, Peterson, Hunston and McDonough, 2007). The process of damage initiation is influenced by the fibers spacing and interface fracture toughness. Therefore, in order to uncover the relationship between microstructure and damage evolution, it is necessary to observe the damage initiation and evolution in composites.

In this study, tensile tests of model composite fiber samples were performed by various techniques in order to observe damage initiation and crack propagation in situ. The acquired knowledge will be used for development of 3D models that can predict the mechanical properties of composites from basic properties of fiber, matrix and fiber/matrix interface.

In situ observations during tensile tests in an environmental scanning electron microscopy (ESEM) were performed in order to observe crack initiation and propagation in model composites made with a single glass fiber embedded in epoxy resin. Since ESEM studies are limited only to surface observations, the same kind of specimen was tested using X-ray computed tomography (X-ray CT). 3D images were acquired at several load steps using X-ray synchrotron radiation at the European Synchrotron Radiation Facility (ESRF, Grenoble, France). During both ESEM and X-ray tests, acoustic emission (AE) signals were recorded with the aim of correlating the AE signals with the microscale visual observations. Experimentally determined cohesive laws and fracture toughness will be later used in finite element unit cell modeling.

2. MATERIALS AND SPECIMEN MANUFACTORING

Due to the complexity of the stress distribution in composite materials and amount of different failure mechanisms involved in the damage process, it would be difficult to separate and study different failure modes by testing bulk composite samples. Therefore, model specimens were studied in order to isolate micro mechanisms of damage and study them more precisely.

The composites under investigation are model samples made of fast curing epoxy resin Epoxydharz HT 2 from Faserverbundwerkstoffe Composite Technology, with an embedded transverse single glass fiber (Fig.1). The specimen is 6 mm long with a cross section 2×2 mm. A single glass fiber with a diameter of ~50 μm provided by Ahlstrom, was placed in a rubber mould and pre-strained by applying load on both sides of the fiber. Subsequently the rubber mould was filled up with the degassed resin which was cured for 24 hours at room temperature, followed by post curing at 50° C for 10 hours. Finally, the samples were grinded with SiC papers with grain sizes: 500, 1000 and 4000, and subsequently polished precisely using diamond paste with particles sizes 3 μm and 1 μm, in order to remove any fiber breakage and prepare the surface for microscopie studies.

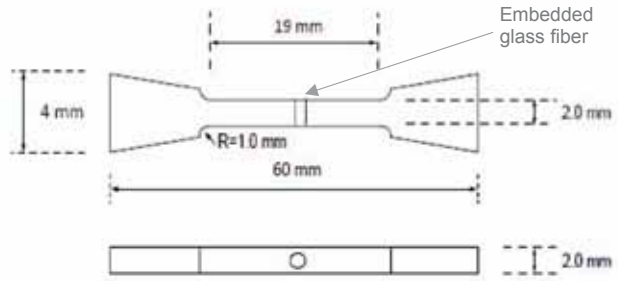

Fig. 1. Geometry and dimensions of test specimen.

In order to study the influence of the fiber spacing, different geometrical configuration of multiple fibers positioning will be studied. However, only results from single-fiber samples will be reported here.

In order to observe strain fields in the samples by means of Digital Image Correlation (DIC) techniques, we will make use of micro-sized particles added during manufacturing for a subset of the samples. For 2D observations in ESEM, the surfaces of the samples will be covered with TiO_2 micro-particles. The method is still under development. For the 3D studies carried out using X-ray CT, glass marker particles with diameter ~5µm were mixed with resin before curing. The method has been successfully applied in previous studies (Nielsen 2003).

3. TENSILE TESTING IN ESEM

3.1 Experimental method. In order to obtain an in situ observation of crack initiation under the tensile loading, mechanical tests were carried out in the vacuum chamber of an environmental electron microscope (Zeiss, EVO60), using a special in-house made tensile loading fixture (Sørensen, Horsewell and Skov-Hansen, 2002), (Fig.2), designed to be mounted in the ESEM. Additionally, an AE system, which has been proven to be useful method for the detection of failures in model composite (Ageorges, Frirdrich, Schueller and Lauke, 1998), was applied in these experiments. Macroscopic mechanical tests had been carried out previously in order to establish and to verify the applicability of AE for the subsequent microscale ESEM tests. In all macroscopic tests some "warning" AE events were detected before the final failure. To assist the controlling of the microscale loading experiment it was therefore decided to apply the AE system to ESEM experiments. During the microscale experiments, the load was applied to the specimen in increments. The tensile test was interrupted at various loads until ultimate failure. This enabled observing and capturing of images of the crack propagation using ESEM facilities.

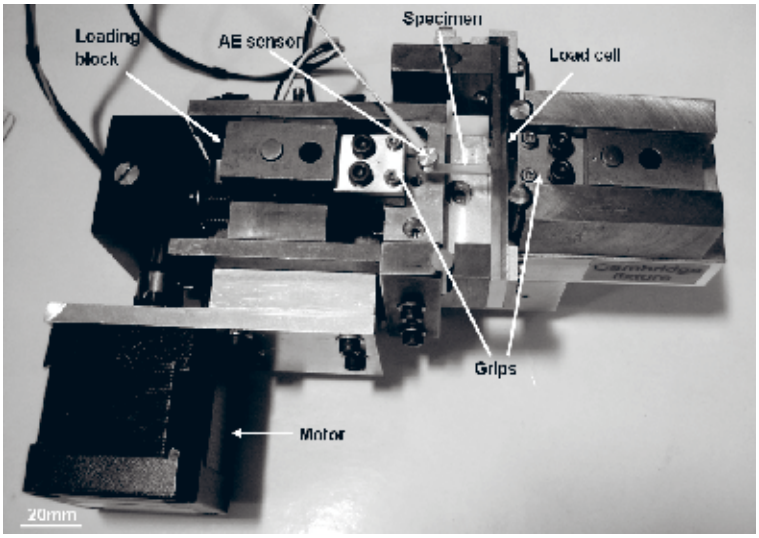

Fig. 2. Test set-up for tensile testing in ESEM. A motor drives a spindle that moves one of the loading blocks and thus one grip.

3.2 Results. The crack initiation and propagation were observed in situ during loading. The same damage sequence was observed in several samples and thus shown to be repeatable. However, prior to the testing, surface debonding was observed (probably due to the polishing procedure; however this needs to be verified). The preparation of polymer composites for microscopy

studies is somewhat difficult, since soft matrix and brittle fiber are polished at the same time. Debonding prior to testing was observed in different positions in different samples (Fig. 3).

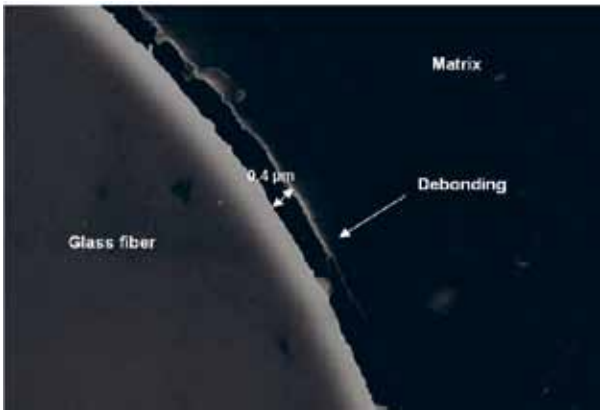

Fig. 3. Example of debonding observed in ESEM prior to loading caused by the polishing process.

However, once loading started, further debonding started to appear at angles 0° and 180° with respect to the applied tensile load direction (Fig. 4). The debonding starts to grow at ~25 MPa. Subsequently the debond crack kinks out of the interface to the matrix at a stress level ~30 MPa (Fig.5a). The kinked cracks are oriented approximately normally to the external load, which means that they run into the matrix along the direction corresponding to Mode I (Fig. 5). During subsequent loading crack growth and further penetration into the matrix was observed (Fig. 5) until ultimate failure which occurred at a stress state of ~50 MPa. The damage sequence is marked in order in Fig. 5.

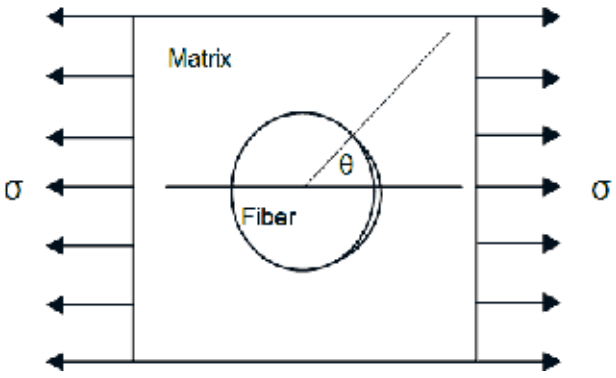

Fig. 4. Geometry of single fiber with cracked interface under a transverse load.

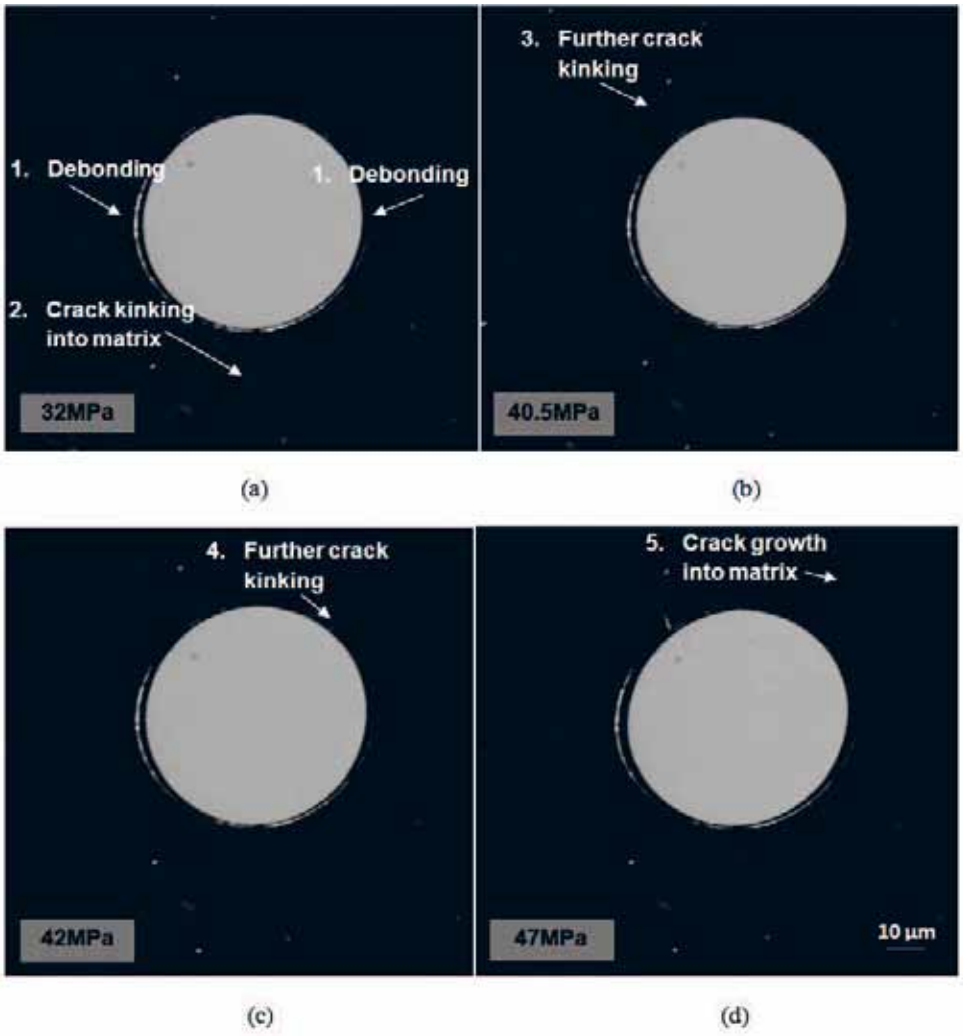

Fig. 5. 2D damage sequence in model fiber composite observed in ESEM under uniaxial transverse loading.

The AE system was able to detect the crack initiation/propagation while loading. Nevertheless not all of the cracks visible on the surface were detected by AE. This requires more studies and possibly changes in the set-up. However, most of the cracks observed on the surface were correlated with AE events. The correlation of event counts versus peak amplitude presented in Fig. 6 reveals a high density of events in the 40-50dB amplitude range. It has been confirmed before (Barre, Benzeggagh, 1994) the lowest amplitudes characterize matrix cracking which matches with the visual ESEM observations. Due to the debonding observed prior to loading, it is impossible to correlate AE events with 2D surface observations of interfacial debonding since the debonding may occur inside the material.

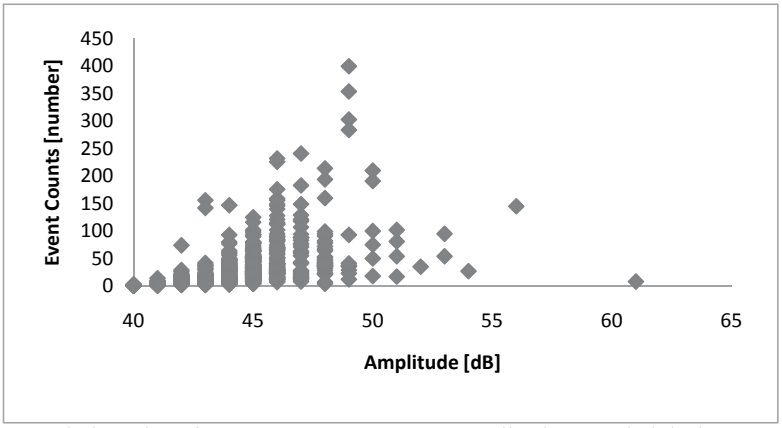

Fig. 6. Correlation plot of AE event counts versus amplitude recorded during an ESEM test.

4. IN SITU MICROTOMOGRAPHY

4.1 Experimental method. Since a complex stress state exists along the free-edges of the sample (Pagano and Pipes, 1971), the damage initiation is likely to occur here and propagate into the composite. Thus the behavior at a free surface is not necessarily representative of what occurs inside the material. It is therefore necessary to study damage evolution in composites in 3 dimensions. X-ray tomography has proven itself a very powerful tool for in situ 3D observations allowing non-destructive observation of how, damage initiation occurs and propagates inside the material (Schiling 2005). Such knowledge is fundamental for establishing a complete understanding of damage evolution and for the prediction of macroscopic material properties.
The ESEM (Fig. 5) results show that 3D studies of the proposed model composites require a sub-micron spatial resolution, since debonding was observed (prior to loading) to be in range of ~0.5 μm. Therefore, in order to observe 3D interfacial crack initiation, high resolution microtomography is needed.

An X-ray transparent loading fixture compatible with a high resolution microtomography set-up was developed in-house [Fig.7). The loading fixture was designed to allow for simultaneous acquiring of X-ray tomography data and AE events. Preliminary 3D experiments were carried out at ESRF on beamline BM05. The X-ray photon energy of the beam was 20 keV and projections were captured over a 180° of rotation, using a voxel size of 0.7 μm and 1.4 μm. The loading procedure applied in 2D ESEM studies was repeated during the microtomography tests. To avoid relaxations during the acquisition of X-ray tomography data, the specimen was unloaded ~10% after each load step. After each load increment, the sample was scanned using the X-ray microtomography.

4.2 Results. The complex test set-up was successfully applied during experiments. Although the sample was loaded manually, compared to the automatic loading in the ESEM experiments, the AE system could still successfully record relevant signals. Preliminary data analysis reveals that the contrast obtained by the glass particles in the matrix is sufficient for segmentation and the distribution of the particles in the matrix seems suitable for measurement of displacement fields and crack openings in 3D (Fig. 8) using the DIC technique.

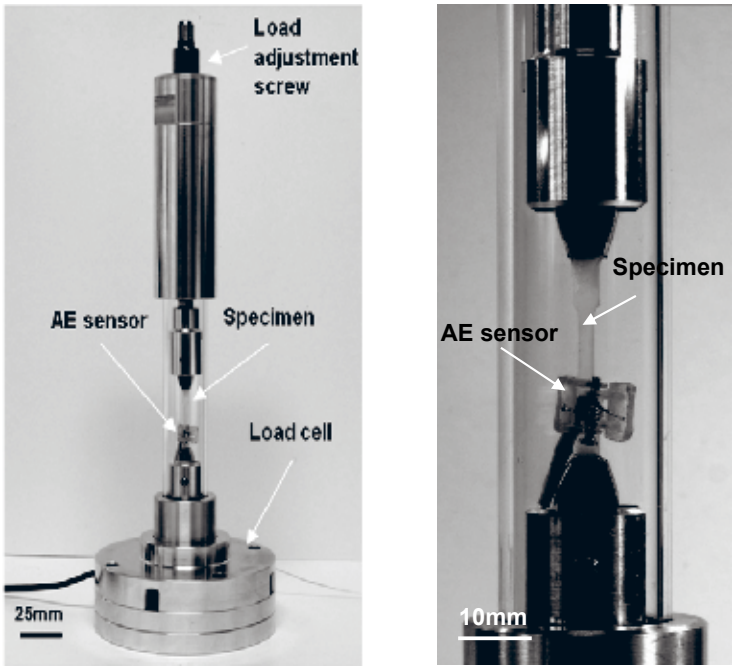

(a) (b)

Fig. 7. In-situ microtomography loading device: (a) test set-up, (b) specimen mounting-close-up.

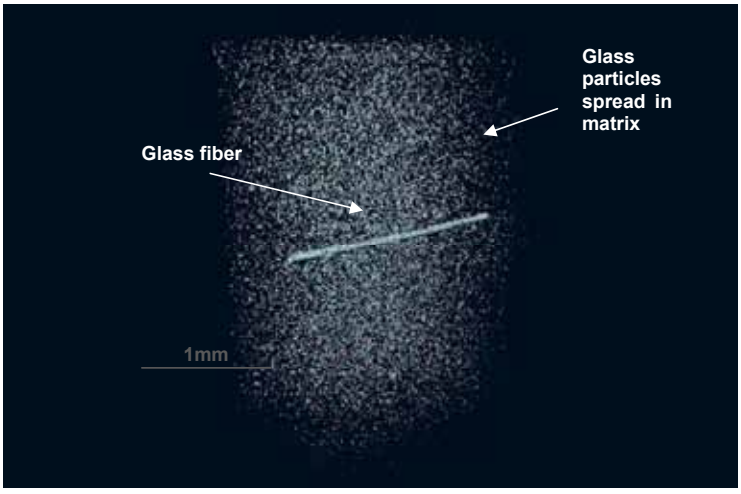

Fig. 8. Sub-set of tomography data.

5. CONCLUSIONS

Although pre-existing debonding was observed prior to loading, the crack initiation and propagation observed during experiments, match to the results of numerical studies carried out by Paris et al. using Boundary Element Method (Paris, Correa and Mantic, 2007). Due to limitations of the ESEM, it would be preferable to study full-field strain mapping using particles on the surface during the loading. That would enable studying the crack initiation by means of displacement fields, before it becomes visible in the ESEM. For 2D studies AE technique was successfully applied during experiments carried out in ESEM. However, in order to be able to correlate AE signals precisely with visual observations, it is necessary to carry out 3D experiments. The debond crack size indicates that high resolution X-ray CT is needed in order to be able to carry out 3D studies. However, specimen size needs to be optimized in order to obtain an optimum resolution.

ACKNOWLEDGEMENTS

The authors wish to thank Julie Glasscock from Risø DTU for technical assistance at scanning electron microscopy. We would also like to thank to Research Technicians: Jonas Heininge, Erik Vogeley, Christian H. Madsen, Jens Olsson, Steen J. Bang and Ebtisam Abdellahi for assistance with specimen preparation, loading device design and test set-ups for experiments. The Danish Research Council is acknowledged for funding the synchrotron experiments (via Danscatt). ESRF is thanked for beamtime.

REFERENCES

Ageorges, C., Frirdrich,K., Schueller,T., Lauke, B. (1998). Single-fiber Broutman test: fiber-matrix interface transverse debonding. Composites: Part A:applied science and manufactoring 30, 1423-1434.

Holmes, G.A., Peterson,R.C., Hunston,D.L., McDonough,W.G. (2007). E-Glass/DGEBA/m-PDA Single Fiber Composites: Interface Debonding During Fiber Fracture. Polymer Composites 28, 561-574.

Nielsen, S.F. (2003). Measurements of plastic displacement gradient components in three dimensions using marker particles and synchrotron X-ray absorption microtomography. Acta Materialia 51, 2407-2415.

Pagano, N.J. and Pipes, R.B. (1971). The Influence of Stacking Sequence on Laminate Strength. Journal of Composite Materials 5, 50–57.

Paris, F., Correa, E., Mantic, V. (2007:). Kinking of transverse interface cracks between fiber and matrix. Appl. Mech. 74, 703-716.

Barre, S., Benzeggagh, M.L. (1994) On the use of the Acoustic Emission to Investigate Damage Mechanims ini Glass-Fiber-Reinforced Polypropylen. Composites Sci. Technol. 52, 369-376.

Schiling, J.P. (2005). X-ray computer microtomography of internal damage in fiber reinforced polymer matrix composites. Composites Science and Technology 65, 2071-2078.

Sørensen, B.F., Horsewell, A., and Skov-Hansen, P. (2002). In-situ observation of crack formation Bi-2223 HTS tapes. Physica C: Superconductivity and its application 372-376,1032-1035.

Proceedings of the 32nd
Risø International Symposium on Materials Science:
Composite materials for structural performance:
Towards higher limits
Editors: S. Fæster, D. Juul Jensen,
B. Ralph, B.F. Sørensen
Risø National Laboratory for Sustainable Energy,
Technical University of Denmark, 2011

NON-DESTRUCTIVE ANALYSIS OF FIBER PROPERTIES USING 3D X-RAY TOMOGRAPHIC DATA

A. Miettinen* and M. Kataja

Department of Physics, University of Jyväskylä, FI-40014, Finland
* arttu.i.miettinen@jyu.fi, Tel. +358142602391

ABSTRACT

An algorithm for estimating the bivariate length and diameter distribution of fibers in a heterogenous fibrous material utilizing x-ray tomographic images is developed. The method is based on a granulometric approach and is applicable in arbitrarily complex fibrous structures. The algorithm is first tested for two and three-dimensional computer-generated random fiber network structures with a known fiber size distribution. Secondly, the method is applied in analysing length and diameter distribution of fibers in a wood-fiber reinforced composite material. The results indicate that the present method yields qualitatively correct bivariate and marginal distributions of length and diameter in the computer-generated test cases, and also plausible distributions for the actual composite material sample.

1. INTRODUCTION

Heterogenous fibrous or fiber reinforced materials such as paper and board, non-woven fabrics and many short fiber composites contain fibers with varying size and shape. In addition to the raw fiber material used, manufacturing process often affects the composition of the fibers in the material. Obviously, the structural properties of such materials strongly depend on the distribution of the fiber size and shape. It is therefore of interest to develop methods for analysing fiber size distributions present in the final material product. An opportunity for such analysis is provided by x-ray microtomography (X-μCT) that can give three-dimensional (3D) structural information of material samples unintrusively. The typical best resolution of the commercial laboratory-scale x-ray microtomographic scanners available is of the order of one micrometre or less. Such a resolution is sufficient for very detailed analysis of many practical fiber-based materials. Indeed, several methods based on the use of tomographic images have been recently developed for finding the distribution of *e.g.* fiber length or fiber diameter separately (see *e.g.* Kimura and Yamasaki, 2003; Avérous, Quantin, Lafon and Crespy, 1995 and references therein). In many materials, however, various fiber dimensions such as length and diameter are correlated. Analysis of such a correlation may provide valuable additional information on the structural properties

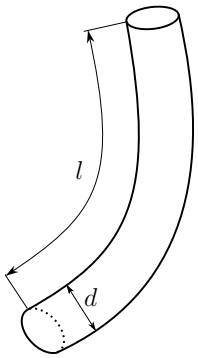

Fig. 1: Assumed fiber geometry and notations for length l and diameter d.

of the material. To this end, an algorithm for simultaneous estimation of the bivariate length and diameter distribution of fibers in a heterogenous material is developed in this work. The method is based on a granulometric approach applied on 3D x-ray tomographic images. It is applicable in virtually arbitrarily complex fibrous structures and requires no individual fiber recognition, skeletonization or analysis of the fiber network topology.

2. MEASUREMENT OF LENGTH AND DIAMETER DISTRIBUTION

The original opening operation is an image processing filter that removes small structures and preserves large structures in a binary image (Gonzalez and Woods, 2001, p. 559). The threshold size is defined by the size of the structuring element inherent in the filtering algorithm. The opening operation can be generalized to gray scale images in which case complete removal of structures is replaced by attenuation of the gray scale value associated to voxels (pixels in a two-dimensional case) that belong in small structures. Granulometry, in general, refers to a process where size discrimination is used to find the size distribution of objects in an image. In what follows, we mostly consider three-dimensional images as obtained from tomography. Application to two-dimensional images is straightforward.

Granulometric process based on an opening filter involves selecting the structuring element in a manner suitable for the present case, and performing an opening operation on the original image I_0 for varying values of size r of the structuring element. For a given value of size parameter r, the resulting image $I(r)$ contains only structures larger than r. We assume that the pixel values of the original image are normalized such that the integral of the image over the entire domain contained in the image gives the total volume of the structures in the domain. The volume $V(r)$ of objects with size larger than r can then be calculated from:

$$V(r) = \int I(r) \mathrm{d}\vec{x}, \tag{1}$$

where the integral is taken over the whole image. The size distribution of the volume is then given by:

$$\phi(r) = -\frac{\mathrm{d}V(r)}{\mathrm{d}r}. \tag{2}$$

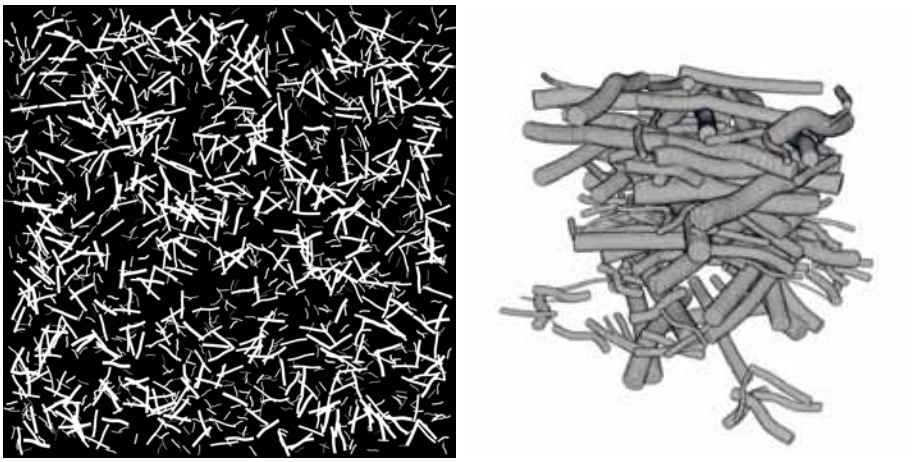

(a) (b)

Fig. 2: Two-dimensional test image containing total of 1600 individual fibers (a) and visualisation of three-dimensional test image containing a total of 200 individual fibers (b).

Traditionally, granulometry has been used to characterize the size distribution of granular particles utilizing a spherical structuring element. This amounts to fractionating the particles by their smallest dimension. Fractionation by the largest dimension of particles can be obtained by another version of the opening filter called path-opening as discussed by Luengo Hendriks (2010). In what follows, we denote by $S(d;I)$ and $P(l;I)$ the images resulting from opening operations on I based on a spherical structuring element of diameter d, and on path-opening filter with a size parameter l, respectively.

In order to estimate the bivariate size distribution $N(d,l)$ we assume that the shape of the particles is highly elongated with a constant circular cross-section, and that they are only moderately curved or twisted (see Fig. 1). In this case, the volume of the particles is approximated with a reasonable accuracy by the volume of a cylinder of length l and diameter d. Analogously with Eq. (1), we define:

$$V(d,l) = \int I(d,l)\mathrm{d}\vec{x}, \tag{3}$$

where $I(d,l) = S(d;P(l;I_0))$, *i.e.* an image obtained by first applying a path-opening operation with a size parameter l and then a regular opening with a spherical structuring element with a size parameter d on the original image I_0. It is again assumed that the original image I_0 is properly normalized and the integral is taken over the whole image $I(d,l)$. The quantity $V(d,l)$ thereby gives the volume of fibers whose length is larger than l and diameter larger than d. In other words, it is the bivariate tail distribution function of the volume, and can be given in terms of the size distribution function (probability density) $N(d,l)$ by:

$$V(d,l) = \int_l^\infty \int_d^\infty N(d,l)V_1(d,l)\,\mathrm{d}d\mathrm{d}l. \tag{4}$$

Here $V_1(d,l)$ is the volume of a single fiber of length l and diameter d. Differentiating Eq. (4)

with respect to d and l, we finally get:

$$N(d,l) = \frac{1}{V_1(d,l)} \frac{\partial V}{\partial l \partial d}. \tag{5}$$

For three and two-dimensional cases we have $V_1(d,l) \approx \frac{1}{4}\pi d^2 l$ and $V_1(d,l) \approx dl$, respectively. These relations are exact in the case that the fibers are straight circular cylinders or rectangles.

3. TEST CASE

As the first qualitative test of the method it was applied in images generated computationally using a specific fiber deposition algorithm. The fibers were modeled as three-dimensional cylindrical rods with random small curvature. The length and diameter of the fibers were chosen by sampling a predetermined bivariate distribution. The fibers were then released at a random position and orientation in a gravity field above a flat substrate. The motion

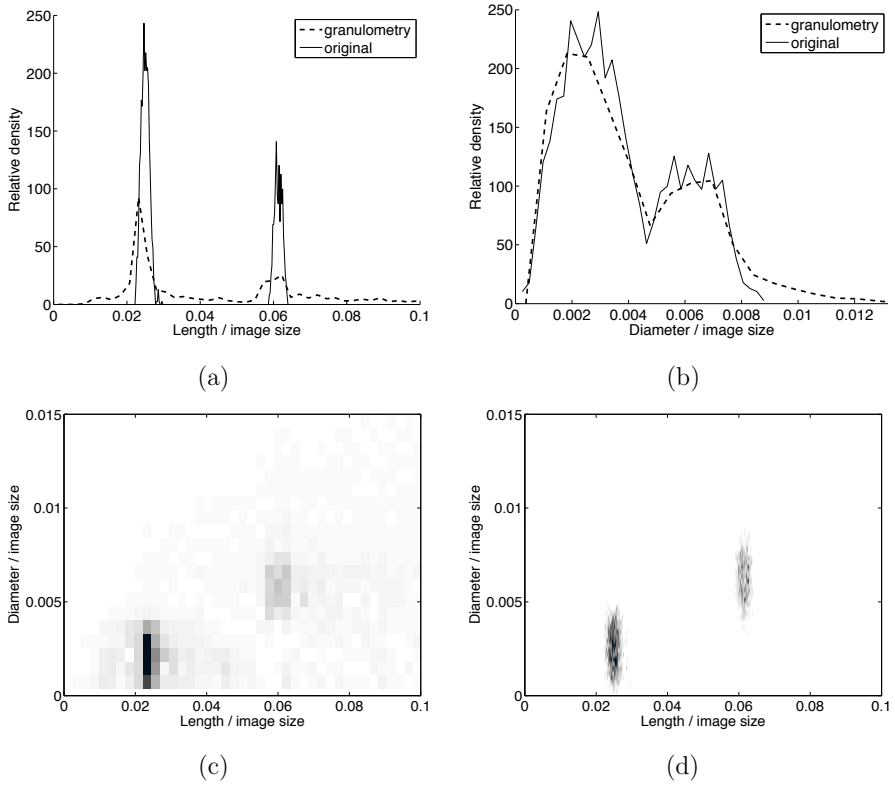

Fig. 3: Comparison of true and measured length and diameter marginal distributions in the 2D case (a,b). The bivariate diameter/length distribution found from Eq. (5) (c) and the original distribution of fibers (d). In the bivariate distributions, the gray value describes relative density white corresponding to zero. Gray values have been scaled to improve visibility.

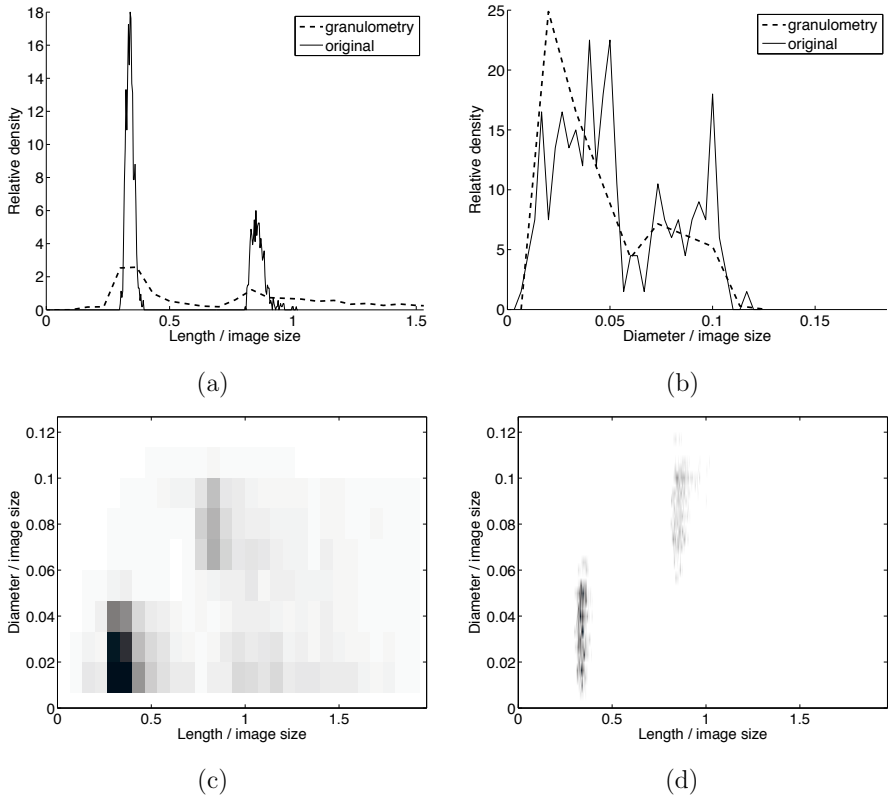

Fig. 4: As Fig. 3, but for the three-dimensional test case. Average result of eight images containing a total of 1600 fibres.

of the fiber was solved numerically while moving towards the substrate, until the movement ceased due to internal friction or collisions to the substrate or with other fibers. The position of the fiber was then fixed and a new one was deposited. The process was continued until a specified amount of fibers were deposited. The three-dimensional test image was then constructed numerically based on the final fiber network geometry. The same algorithm was also used to produce a two-dimensional test image as a projection of a similar 3D structure (but with more fibers) on the substrate plane. The resulting images of two and three dimensional fiber network structures are shown in Fig. 2. The results obtained using the granulometric method described above with comparison to the ground truth distribution given by the actual bivariate distribution of the deposited fibers, are shown in Figures 3 and 4.

It appears that the method yields plausible and qualitatively correct results at finite values of length and diameter. As is typical of granulometric methods, the size distribution given by the present method is smoothened as compared to the actual strongly peaked distribution of the original fibers. Furthermore, the method seems to produce a high l tail in the distribution as compared to the distribution of individual fibers. This is most likely due to concatenated fibers that occur in the random network structure. Notice, that a similar tailing phenomenon is not so prominent in the d direction since that would require fibers

Fig. 5: X-µCT image of a wood fiber composite material sample. The physical size of the sample is $(0.7\,\mathrm{mm})^3$. Only fibers are visualized while the PLA matrix has been made invisible.

located side by side along most of their length, which is less likely. At values of l and d approaching zero, the results become clearly inaccurate. That is as expected due to the known drawback of granulometric methods producing artefacts at a small size scale. Methods for correcting such an effect are available (Luengo Hendriks, van Kempen and van Vliet, 2007), but were not applied here. Instead, the results at lowest values of l and d were simply abandoned.

4. APPLICATION TO WOOD FIBRE COMPOSITE MATERIAL

To demonstrate the feasibility of the method in the case of a fibrous material, it was applied in an X-µCT image of a wood fiber composite sample (Fig. 5) obtained at the TOMCAT x-ray beamline at the Swiss Light Source, Paul Scherrer Institute. The material consists of kraft pulp fibers, approximately 10 % by weight, in a Polylactic Acid matrix. Physical dimensions of the sample were approximately $(0.7\,\mathrm{mm})^3$ while the 3D image voxel size was $(0.7\,\mu\mathrm{m})^3$.

The original reconstructed image was first denoised and semi-binarized by assigning the numerical value 1 for the voxels clearly inside the fibrous material (fiber walls), and value 0 for the voxels outside the fiber walls. The numerical values for voxels located at the interface between a fiber wall and matrix material were obtained by linear interpolation between zero and one. This procedure assures correct normalization of the original image as specified in section 2 (in units where the volume of a voxel is unity). The joint length and diameter distribution was obtained from the preprocessed image using Eq. (5). Figure 6 shows the resulting bivariate distribution and marginal distributions for fiber length and diameter. Also shown in Fig. 6 (b) is the result from an independent measurement of the

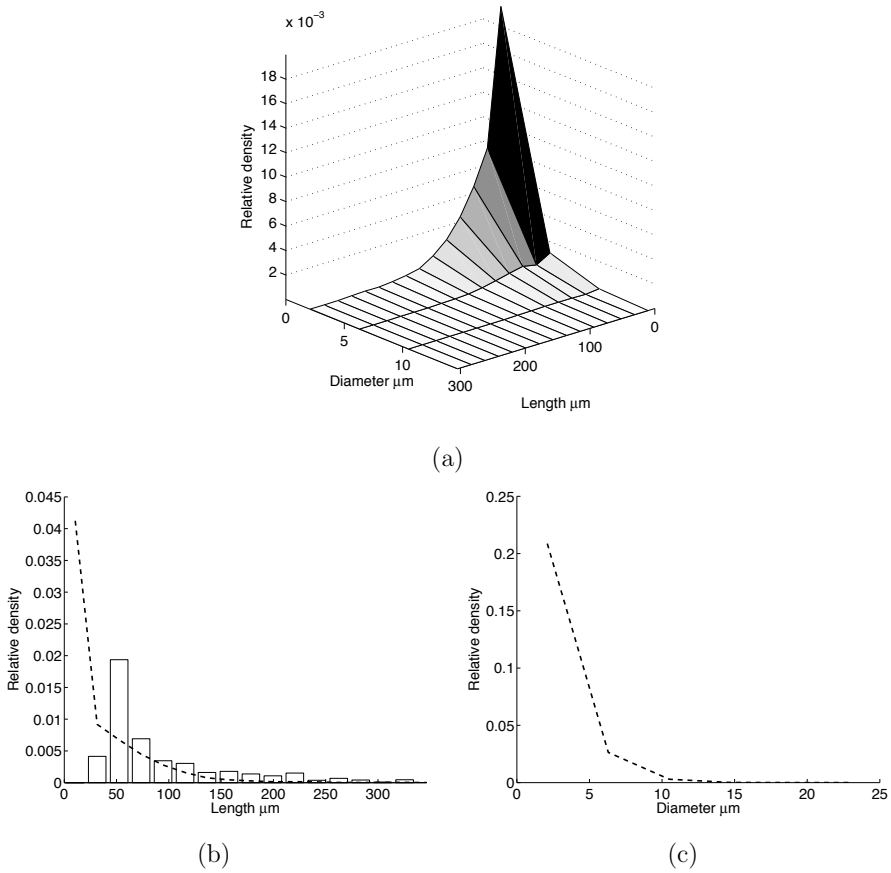

Fig. 6: Joint distribution of length and diameter for a wood fiber composite material sample (see Fig. 5) (a). Marginal distributions of fiber length (b) and diameter (c). In figure (b) also shown is the experimental distribution of fiber length for the same material (bars).

fiber length distribution obtained by dissolving the composite material in chloroform, and manually measuring the length of the extracted fibers using optical microscopy (Miettinen, Luengo Hendriks, Chinga-Carrasco, Gamstedt and Kataja, 2011). The relatively low value of the experimental point corresponding to the shortest fiber fraction is most likely due to partially omitting small fiber fragments in the visual sampling of representative fibers.

5. CONCLUSIONS

A method for estimating the bivariate distribution of fiber length and diameter of fibrous materials was developed. The method is based on two consecutive granulometric operations applied on three-dimensional x-ray tomographic images of actual material samples. According to the test cases analysed, the method seems to yield qualitatively correct and plausible results. As is typical of granulometric techniques however, the method tends to produce

a somewhat smoothened distribution, long length tail and apparently inaccurate results as length or diameter approach zero. In spite of these shortcomings, the method seems useful especially in cases of relatively complex topology of the fiber network where individual fiber recognition or detailed analysis of fiber network topology is not feasible. Although the method is primarily intended for use with fiber based materials, it can be applied in any heterogeneous material containing elongated particles with a circular cross-section.

ACKNOWLEDGEMENTS

We express our gratitude to Anne M. Reitan, Trond Karlsen and Gary Chinga-Carrasco for preparation of the wood fiber composite sample at the Paper and Fiber Research Institute, Norway and to Rajmund Mokso and Federica Marone at the Swiss Light Source for assistance and guidance during the acquisition of the image in Fig. 5.

This work was partially funded through WoodWisdom-Net under the WoodFibre3D project. The research leading to these results has received funding from the European Community's Seventh Framework Programme (FP7/2007-2013) under grant agreement nr. 226716.

REFERENCES

Avérous, L., Quantin, J.C., Lafon, D. and Crespy, A. (1995). Granulometric Characterization of Short Fiberglass in Reinforced Polypropylene. Relation to Processing Conditions and Mechanical Properties. Int. J. Polym. Anal. Charact. 4, 339–347.

Gonzalez, R.C. and Woods, R.E. (2001). Digital Image Processing (Prentice-Hall, New Jersey)

Kimura, K. and Yamasaki, S. (2003). Accurate root length and diameter measurement using NIH Image: use of Pythagorean distance for diameter estimation. Plant and Soil 254, 305–315.

Luengo Hendriks, C.L. (2010). Constrained and Dimensionality–Independent Path Openings. IEEE Trans. Im. Proc. 19, 1587–1595.

Luengo Hendriks, C.L., van Kempen, G.M.P. and van Vliet, L.J. (2007). Improving the accuracy of isotropic granulometries. Patt. Rec. Lett. 28, 865-872.

Miettinen, A., Luengo Hendriks, C.L., Chinga-Carrasco, G., Gamstedt, E.K. and Kataja, M. (2011). A non-destructive x–ray microtomography approach for measuring fiber length in short–fibre composites. In preparation.

Proceedings of the 32nd
Risø International Symposium on Materials Science:
Composite materials for structural performance:
Towards higher limits
Editors: S. Fæster, D. Juul Jensen,
B. Ralph, B.F. Sørensen
Risø National Laboratory for Sustainable Energy,
Technical University of Denmark, 2011

MECHANISMS AND MICROMECHANICS OF DEGRADATION OF WIND BLADE COMPOSITES: RESULTS OF UPWIND.TTC PROJECT

L. Mishnaevsky Jr.*, P. Brøndsted*, V. Kushch**, S. Shmegera**,
H. Zhou***, R. Peng***, A. Mukherjee**** and S. Joshi*****

*Materials Research Division, Risø National Laboratory for Sustainable Energy, DTU, Denmark
**Bakul Institute for Superhard Materials, Kiev, Ukraine
***China University of Mining and Technology (Beijing), China
****Thapar University, Patiala, India
*****National University of Singapore, Singapore

ABSTRACT

In this paper, recent investigations of micromechanisms of damage evolution in wind blade composites under loading, and methods of computational microstructural modeling of the degradation of the materials are summarized. The research studies have been carried out in the framework of the project supported by the INCO/TTC (Third Target Countries) program of the EU and realized as an extension of the EU FP6 project UpWind. The effects of fiber orientation, loading conditions, fiber clustering, misalignments, interfacial properties and other factors on the strength and lifetime of the wind turbine blade materials were investigated in the experiments and micromechanical simulations.

1. INTRODUCTION

The strength and reliability of wind turbine blades depend on the properties, mechanical behavior and strengths of the material components (glass or carbon fibers and polymer matrix), and the interaction between them under loading. In the framework of TTC (Third Target Countries) extension of the EU FP6 project UpWind, the teams from several European and non-European countries collaborated to investigate the micromechanisms of degradation of wind blade composites, and to develop micromechanical models of these materials. The answers on the following questions were sought: which physical mechanisms control the strength and failure of the wind turbine blade materials? Which parameters of microstructures of the materials influence the strength of wind turbine blade materials? How can the service properties

of the materials be improved by modifying the microscale structures? To answer these questions, advanced experimental methods (SEM/scanning electron microscope in-situ static and fatigue experiments), theoretical approaches (complex variables techniques, etc.) and numerical methods (3D finite elements, micromechanical models) were employed. The effects of fiber orientation, loading conditions, fiber clustering, misalignments, interface properties and other factors on the strength and lifetime of the wind turbine blade materials were investigated in the experiments and micromechanical simulations.

2. MICROMECHANISMS OF DAMAGE GROWTH AND DEGRADATION OF WIND BLADE MATERIALS

In order to clarify the effect of the loading direction on the wind blade strength, SEM (Scanning Electron Microscopy) in-situ experimental investigations of damage growth in glass fiber-reinforced plastics (GFRP) under three point bending, tensile, compressive (Figure 1) and (tension-tension) cyclic loadings under different angles between the loading and fibers have been carried out. The detailed conditions of the experiments are described elsewhere (Zhou, Mishnaevsky Jr, Brøndsted, Tan, Gui, 2010).

In the 3 point bending experiments, it was observed that the peak strengths, elastic strengths and elastic modulus of the composites decrease with increasing the angles between load vector and fibers almost linearly. Under compression, the peak strengths, elastic strengths and elastic modulus of the composites decrease with the increasing the angles of fibers at first, and slightly increase thereafter. Under tension-tension cyclic loading, it was observed that the cracks develop most often along the interface between main fibers and matrix.

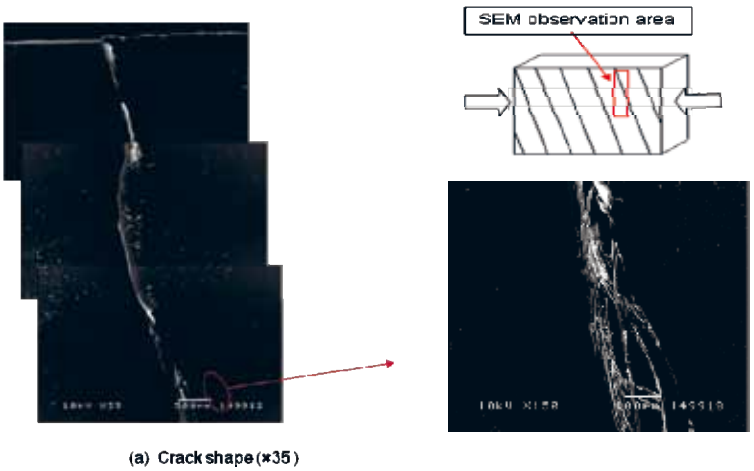

Fig. 1. Crack formation at compressive loading, Angle 75 degrees.

3. MICROSTRUCTURE OF COMPOSITES AND ITS EFFECT ON THE LONGITUDINAL STRENGTH AND DAMAGE RESISTANCE

In order to study the effect of microscale parameters of wind blade composites on their strength, a series of computational simulations has been carried out. At this stage, the damage, strength and fracture of the composites under longitudinal loading (along the fiber axes) was considered. A special software for the automatic generation of 3D computational micromechanical models of the composites was developed (Qing and Mishnaevsky Jr, 2009, Mishnaevsky Jr and Brøndsted, 2009abc, Mishnaevsky Jr., Freere, Sinha, Acharya, Shrestha, Manandhar, 2011a, . Mishnaevsky Jr, Brøndsted, Nijssen, Lekou and Philippidis, 2011b), and used in the numerical experiments. Figure 2 shows a micrograph of a composite, and the 3D finite element model as well as the crack growth schema.

The effects of the statistical variability of fiber strengths, viscosity of the polymer matrix as well as the interaction between the damage processes in matrix, fibers and interface were investigated numerically, by testing different multifiber unit cell models of the composites. It was demonstrated in the simulations that fibers with constant strength ensure higher strength of a composite at the pre-critical load, while the fibers with randomly distributed strengths lead to the higher strength of the composite at post-critical loads. In the case of randomly distributed fiber strengths, the damage growth in fibers seems to be almost independent from the crack length in matrix, while the influence of matrix cracks on the beginning of fiber cracking is clearly seen for the case of the constant fiber strength. Competition between the matrix cracking and interface debonding was observed in the simulations: in the areas with intensive interface cracking, both fiber fracture and the matrix cracking are delayed. Reversely, in the area, where a long matrix crack is formed, the fiber cracking does not lead to interfacial damage (Mishnaevsky Jr and Brøndsted, 2009abc).

Further, the effect of fiber misalignment and clustering on the compressive and fatigue strength of carbon fiber based wind blade materials was considered. In order to study the compressive strength of carbon fiber reinforced polymer composites, statistical computational model was developed, using the Monte-Carlo method and the Budiansky-Fleck fiber kinking condition (Mishnaevsky Jr and Brøndsted, 2009c). The effects of fiber misalignment variability, fiber clustering, load sharing rules on the damage in a composite were studied numerically. It was demonstrated that the clustering of fibers has a negative effect on the damage resistance of a composite. Further, the static compressive loading model is generalized for the case of cyclic compressive loading, with and without microdegradation of the matrix, and with and without random components of cyclic loading. It was observed that random variations of loading shorten the lifetime of the composite: the larger the variability of applied load, the shorter the lifetime. Considering the cases of small and large interfacial defects with different defect densities, we observed that small interfacial microcracks do not lead to a sufficient reduction of compressive strength even at an unrealistically high microcrack density. In contrast, large interfacial defects have a strong effect on the compressive strength of the composite.

4. DAMAGE EVOLUTION IN COMPOSITES UNDER TRANSVERSE LOADING

In order to analyze the damage evolution, in particular, interfacial debonding under transverse loading: analytical methods have been used. An accurate analytical method has been developed to solve for stress in the meso cell based on the Muskhelishvili's complex variables technique. The model is reduced to the well-posed infinte set of linear algebraic equations with the matrix

coefficients given by rational expressions and involving (unlike FEM or BEM) no integration (Kushch, Shmegera, Mishnaevsky Jr., 2009, 2010, 2011a, Kushch, Shmegera, Brøndsted, Mishnaevsky Jr, 2011b). The model developed of progressive interfacial debonding in FRC combines the representative (many-fiber) unit cell geometry with the adhesive zone model of an interface. Figure 3 shows the model, and the expected crack path based on the maximum stress debond techniques.

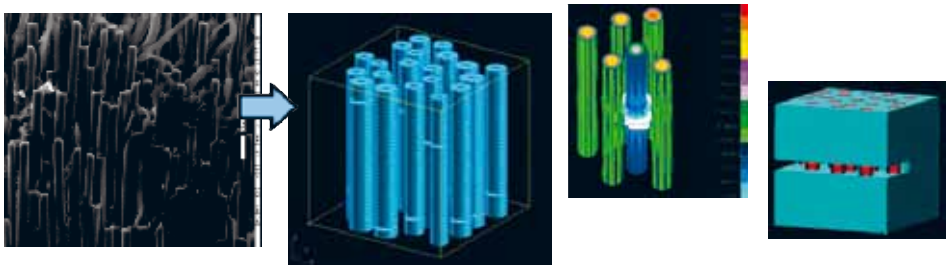

Fig 2 Micrograph of the composite, 3D FE micromechanical model, crack growth between the fibers, and fiber bridging over the matrix crack (Mishnaevsky Jr and Brøndsted, 2009a)

In the simulations, it was observed that the interfacial stress grows up rapidly in the area between the fibers perfectly bonded with matrix. One can expect an interfacial crack onset at a load well below the level predicted by the single-fiber model (Kushch et al, 2011ab). Interfacial debonding causes substantial stress re-distribution and relaxation of the peak interfacial stress on the adjacent fibers. In terms of strength, interfacial crack formation on a given fiber affects debonding the nearest neighbor fibers. The stress intensity factors and the energy release rate are greatly contributed to from elastic interaction between the fibers and are rather sensitive to their arrangement. In terms of strength, interfacial crack propagation is mediated by the neighbour fibers and cracks. In order to verify the analytical results, a finite element model of interfacial debonding under transversal loading was developed (Kushch et al, 2011a). Figure 4 shows the debonding path and the stress distribution in the composite.

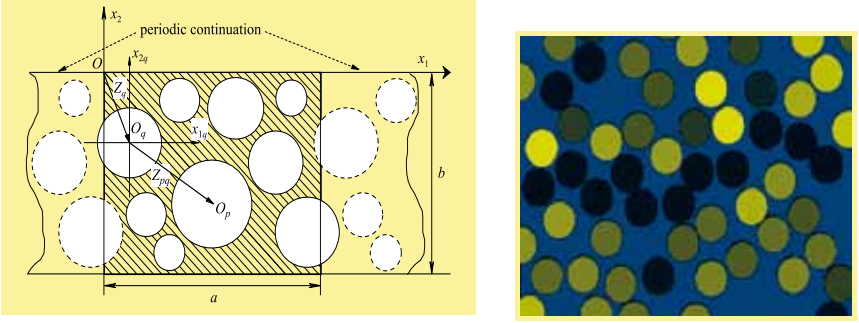

Fig.3. Model of transversal loading and the expected path of the debonded crack (Kushch et al, 2009).

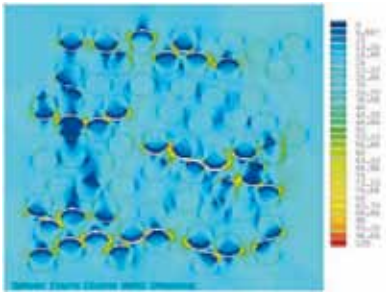

Fig. 4: Progressive debonding of composite under transverse loading (Kushch et al, 2011ab).

5. MOISTURE EFFECT

Moisture-induced interfacial damage evolution and debonding for different fiber realizations werestudied numerically using the finite element method and micromechanical modeling (Abhilash, Joshi, Mukherjee, Mishnaevsky Jr, 2011).The interplay of the two time scales (diffusion time scale and the time scale of the applied load) is considered by applying a strain rate comparable to the moisture diffusion rate (Figure 5). In the simulations, it was observed that moisture-induced degradation of the interfacial properties brought a substantial increase in the interfacial damage. It is observed that not just the damage present in the RVE is the one which contributed to the overall response, but the location and orientation of the damage to the load direction. The unit cell model of a composite subjected to loading after being saturated with moisture has been shown to decrease in the nominal stress achieved and the initial tangent modulus which is dependent on the fiber distribution in the composite .

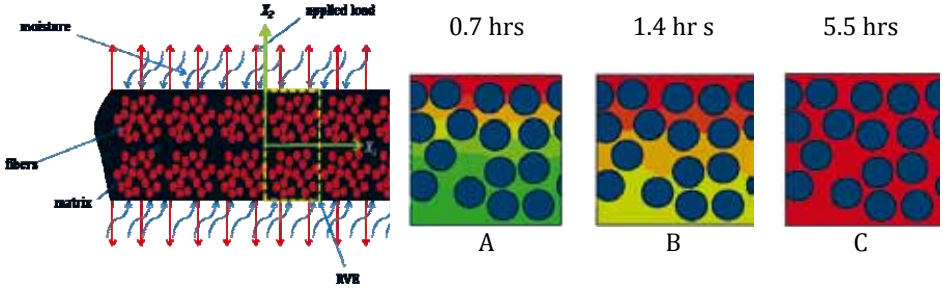

Fig. 5. Schema of the model of the moisture-induced degradation, and the shapshots of the of moisture diffusion profiles (Abhilash et al, 2011).

5. CONCLUSIONS

Summarizing the research described in this section, we can state that the strength of fiber/matrix interface, fiber misalignment and variability of fiber properties, as well as clustering of fibers are important parameters influencing the strength of blade materials. Controlling these parameters, one can improve the strength and lifetime of blade materials. Generally, the microscale analysis and microstructural optimization represent important sources for the

improvement of wind blade materials.

ACKNOWLEDGEMENTS

The authors gratefully acknowledge the financial support of the Commission of the European Communities through the Sixth Framework Programme Grant UpWind.TTC (Contract #019945) as well as of the Danish Council for Strategic Research via the Sino-Danish collaborative project "High reliability of large wind turbines via computational micromechanics based enhancement of materials performances"(Ref. no. 10-094539) and the Danish Centre for Composite Structures and Materials for Wind Turbines (DCCSM) (contract number 09-067212).

REFERENCES

A.S. Abhilash, S.P. Joshi, A.Mukherjee, L. Mishnaevsky Jr. (2011), Micromechanics of diffusion induced damage evolution in reinforced polymers, Composites Sci & Technol, Vol. 71, No. 3, pp. 333-342

P. Brøndsted, H. Lilholt, Aa. Lystrup (2005) Composite materials for wind power turbine blades. Ann. Rev. Mater. Res. 35 , 505-538

V.I. Kushch, S.V. Shmegera, L. Mishnaevsky Jr. (2009) Statistics of microstructure, peak stress and interface damage in fiber reinforced composites. J Mechanics of Materials & Structures Vol. 4, 6, 1089–1107

V.I. Kushch, S.V. Shmegera, L. Mishnaevsky Jr. (2010) Elastic interaction of partially debonded circular inclusions. I. Theoretical solution, Int J Solids and Structures, Vol. 47, No. 14-15, pp. 1961-1971

V.I. Kushch, S.V. Shmegera and L. Mishnaevsky Jr, (2011a) Explicit modelling the progressive interface damage in fibrious composite: analytical vs. Numerical approach, Composites Science and Technology, Vol.71, No.7, pp. 989-997

V.I. Kushch, S.V. Shmegera P. Brøndsted, L. Mishnaevsky Jr (2011b) Numerical simulation of progressive debonding in fiber reinforced composite under transverse loading, Int. J. Eng. Sci., Vol. 49, No.1, 2011, pp. 17-29

H. Qing, and L. Mishnaevsky Jr (2009) Unidirectional high fiber content composites: Automatic 3D FE model generation and damage simulation, Computational Materials Science, Vol. 47, 2, pp. 548-555

L. Mishnaevsky Jr and P. Brøndsted (2009a) Micromechanical modeling of damage and fracture of unidirectional fiber reinforced composites: A review, Comput Materials Science, Vol. 44, No. 4, pp. 1351-1359

L. Mishnaevsky Jr and P. Brøndsted (2009b) Micromechanisms of damage in unidirectional fiber reinforced composites: 3D computational analysis, Composites Sci & Technol, Vol. 69, No.7-8, pp. 1036-1044

L. Mishnaevsky Jr and P. Brøndsted, (2009c) Statistical modelling of compression and fatigue damage of unidirectional fiber reinforced composites, Composites Sci & Technol, Vol. 69, 3-4, pp. 477-484

L. Mishnaevsky Jr., P. Freere, R. Sinha, P. Acharya, R. Shrestha, P. Manandhar (2011a) Small wind turbines with timber blades for developing countries: Materials choice, development, installation and experiences, Renewable Energy, 36, pp. 2128-2138

L. Mishnaevsky Jr., P. Brøndsted, R. Nijssen, D. J. Lekou and T. P. Philippidis (2011b), Materials of large wind turbine blades: Recent results in testing and modelling, Wind energy, doi: 10.1002/we.470

H.W. Zhou, L. Mishnaevsky Jr, P. Brøndsted, J. Tan, L. Gui (2010), SEM in situ laboratory investigations on damage growth in GFRP composite under three-point bending tests, Chinese Science Bulletin, 2010 Vol.55 No.12: 1199−1208

Proceedings of the 32nd
Risø International Symposium on Materials Science:
Composite materials for structural performance:
Towards higher limits
Editors: S. Fæster, D. Juul Jensen,
B. Ralph, B.F. Sørensen
Risø National Laboratory for Sustainable Energy,
Technical University of Denmark, 2011

SUPERIORITY OF CFRP TO HOMOGENOUS MATERIALS FOR DEBRIS PROTECTOR

H. Miyoi*, H. Kohri*, K. Tanaka**, I. Shiota***, A. Yumoto****,
M. Kato***, S. Sasaki** and T. Yagasaki*

*Kogakuin University, 2665-1, Nakano-machi, Hachioji, Tokyo
192-0015, Japan
** ISAS/JAXA, Japan,
***Salesian Polytecnic, Japan,
****Shibaura Institute of Technology, Japan

ABSTRACT

We propose a new protector applied for an oblique collision. An oblique collision between the protector and the debris with a small impact angle will shift a moving direction and lose energy of the space debris. A fundamental experiment was performed in order to study the possibility of thin panels made of CFRP to protect from the debris by oblique collision. We observed and compared damage on the target for several collision angles between 20 to 45 degrees. CFRP and Ti-6Al-4V were used as target materials. A yarn of carbon fiber in CFRP consists of 1000 or 12000 filaments and the volume fraction of carbon fiber was 52 % in both samples. Also, we observed fragments of the projectile and the spread of the ejector after impact by the capture boards with a high speed video camera. We obtained a prospect to construct a thin and light weight debris protector.

1. INTRODUCTION

Increasing with manmade orbiting debris is recognized as a serious and growing threat to man's utilization of space. A space solar power system (SSPS) is expected as one of the countermeasures against global warming and energy issues (P.E.Glaser 1968; DOE/ER-0023 1978). The SSPS will transmit energy from space to the ground using microwaves, and consist of large-sized solar arrays, transmitting antenna and bus systems. The core system of the SSPS should be protected against space debris.

Debris larger than 10 cm in diameter is detected by ground based radars and optical observations. But it is impossible to detect debris smaller than 10 cm by ground-based observations using existing technologies. Typical debris impacts are thought to occur at a velocity of around 10 km/s. Hypervelocity impact will cause extreme damage to the spacecraft's subsystems.

A "Whipple bumper" is one of the famous conventional debris shields, which consists of a thin sacrificial metal sheet placed a small distance in front of the spacecraft wall (F.L Whipple 1947). However, a light weight debris shield is required with an increase in size of the spacecraft. Particular, SSPS is a huge system on a scale never before imagined. Shiota proposed a new concept on the debris protection system applying a principle of a stone skipping for the large space craft or the SSPS (Shiota 2010). An oblique collision between the protector and the debris with a small impact angle will shift the moving direction and lose energy of the space debris. A fundamental experiment was performed in order to study the possibility of thin panels made of CFRP and metal materials to protect from the debris by an oblique collision. In this paper, results of the oblique impact experiment using some types of CFRP plates and Ti plates as target materials are described.

2. EXPERIMENTAL SETUP

Our hyper velocity impact experiments were performed at the ISAS hypervelocity impact facility. The facility consists of a rail gun accelerator, a two stage light gas gun, a vacuum impact chamber, and a velocity measurement system. Figure 1 shows the two stage light gas gun capable of launching 7 mm diameter particles up to 7 km/s.

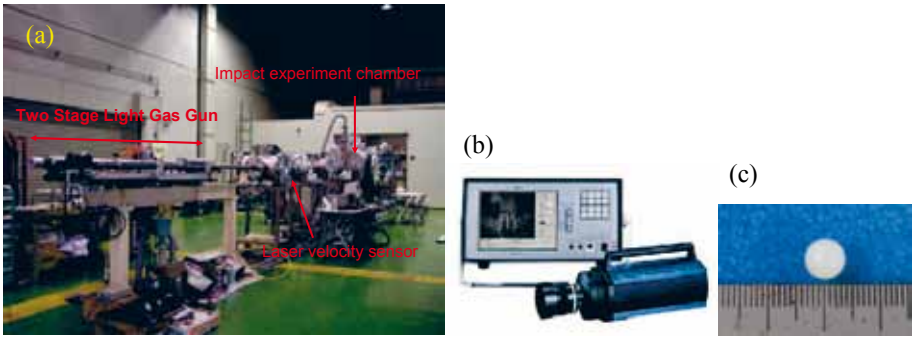

Fig. 1 ISAS hypervelocity impact facility, (a) Two-stage light Gas Gun, (b) High-speed video camera (Hyper Vision HPV-1), (c) Projectile made of Nylon66.

The chamber is evacuated to several torrs using a vacuum pump system. The typical velocity range of the projectile for our experiments was around 5 km/s. The projectile for the gas gun, which is shown in Fig.1 (c) is made of nylon 66 with a diameter of 7 mm and a weight of around 0.21 g.

The impact chamber consists of an experimental impact section with a viewing port and several feed through flanges. Optical events are monitored through a viewing port on the side of the impact chamber using a high-speed video camera (Hyper Vision HPV-1 made by Shimadzu Corporation) with a maximum recording speed of 1,000,000 fps and a spatial resolution of 312 × 260 pixels. One hundred frames can be recorded. A picture of the camera is shown in Fig.1 (b).The camera is triggered using a signal from the laser velocity sensor after a delay time.

Table 1 Target materials and test parameters.

Target	Thickness(mm)	Velocity(km/s)	Impact angle(°)	Target distance(mm)
CFRP (12k T700S)	3	5	30,45	20,40
CFRP （1k T300）	3	5	30	20
CFRP （1k M46）	3	5	30, 20	20
CFRP(IM600)	3	2, 4, 5	10, 15, 20, 25, 30	-
CFRP (12k T700S)+Al	3+5	5	45, 60	40
Ti-6Al-4V	2+1	5	30	20

Table 2 CFRP configuration

Carbon fiber	Filament	Tensile strength(MPa)	Fiber orientation	Vf(%)
T700S	12000(12K）	4900	(0/90,30/120,60/150)s	52%
T300	1000(1K)	3530	(0/90,±45,±45,0/90)6	52%
M46	1000(1K)	4200	(0/90,±45,±45,0/90)7	52%
IM600		4410	(0/-45/90/+45)3s	60%

Table.3 Area density

Target material	Thickness(mm)	Area density（g/cm）
Ti-6Al-4V	2	0.87
CFRP(12k T700S)	3	0.46
CFRP(1k t300)	3	0.49
CFRP(1k m46)	3	0.48
CFRP(IM600)	3	0.46

We used CFRP materials and Ti alloy as targets. Table 1 and 2 summarize the materials and test parameters. Schematic drawing of the target holder which defines the impact angle is depicted in Fig.2. Figure 3 shows a photograph of the target holder that includes the capture board of the ejector. Double layer targets were used in our experiment. CFRP and aluminium plates were used for the 2nd layer.

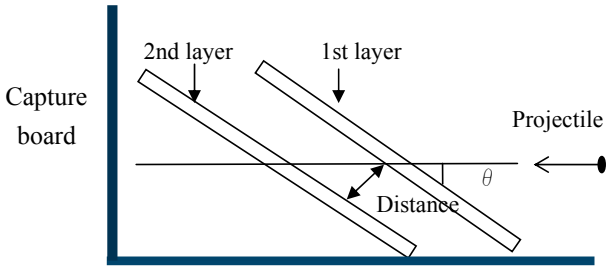

Fig.2 Definition of the impact angle

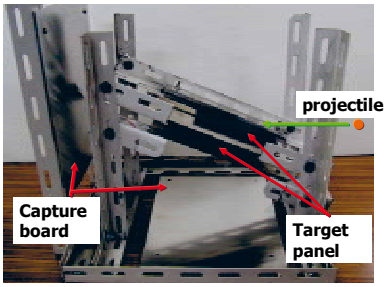

Fig.3 Target holder

3. RESULTS AND DISCUSSION

We compared the damage on the CFRP target using IM600 caused by the hyper velocity impact experiments under several impact angles and several project velocities. Figure 4 (a) and (b) show damage on the targets with impact angles of 20 and 30 degrees. The velocity of the projectile for Fig. 4 (a) was 4 km/s and that for Fig. 4 (b) was 5 km/s, respectively.

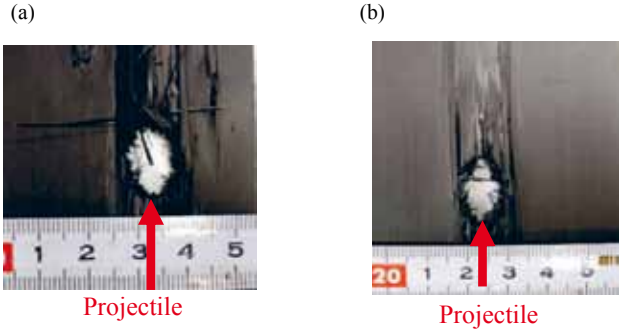

Fig.4 CFRP IM600 (a)4km/s , 30° (b) 5km/s , 20°.

A flattened through-hole was made on each target. Delaminated damage occurred along the fiber direction. Penetration on the target is considered to depend on the vertical component of the velocity of the projectile. Threshold conditions that the through-hole is made on the target are shown in Fig.5.

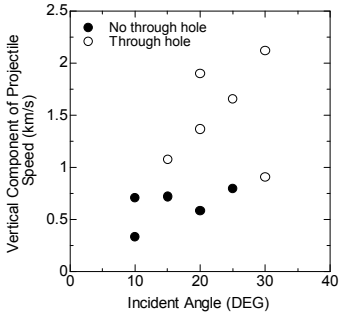

Fig.5 Formation conditions of the through hole on the target.

Figure 6 shows photographs just after and after 2 microseconds from impact by the high speed video camera. Bright cloud which travels on the target will indicate a movement of the pieces of the projectile and ejector from the target. In every shot, the ejector moves along the surface of the target.

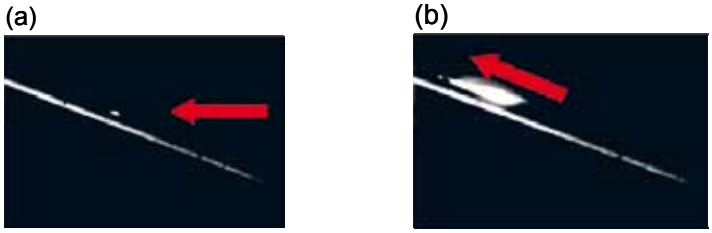

Fig.6 Photograph of the oblique Impact, (a) a moment of the impact, (b) after 2 micro seconds.

Figure 7 shows a capture panel after impact. Impact traces on the panel indicate distributions of the pieces of the projectile and the ejector.

Fig.7 Capture panel after impact.

Figure 8 shows an exploded ejector from the back side of the target. The major direction of the ejector from the back side is vertical to the surface.

Fig.8 Exploded ejector from the back side of the target.

The impact angle has to make a small angle with an increase in the impact velocity in order to prevent a through-hole. However, the major stream of the projectile or the ejector, which will make serious damage, is limited in an extension of the surface of the target. The effect of the ejector from the back side of the target is considered to be small. So, we confirmed a protective performance of a double layer structure against a hypervelocity oblique impact. CFRP and Ti-6Al-4V were used as target materials. Yarns of carbon fiber in CFRP consist of 1000 or 12000 filaments were woven to a cloth, and the volume fraction of carbon fiber was 52 % in both samples.

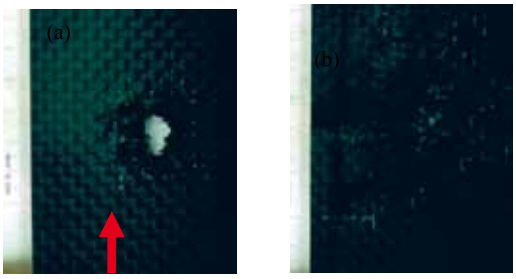

Fig.9 CFRP T700S, 45° (a) 1st layer, (b) 2nd layer.

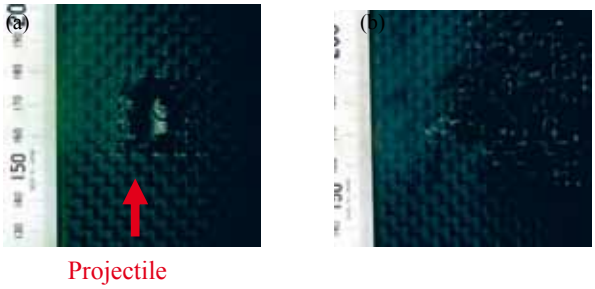

Fig.10 CFRP T700S, 30°, (a) 1st layer, (b) 2nd layer.

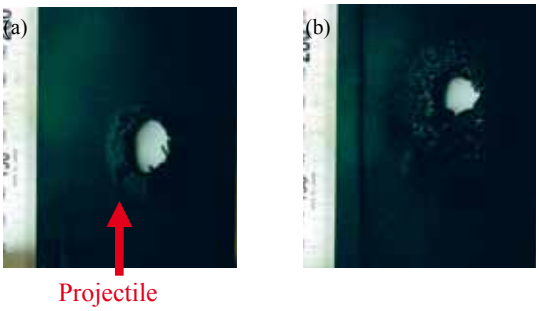

Fig11.CFRP T300, 30° (a) 1st layer, (b) 2nd layer.

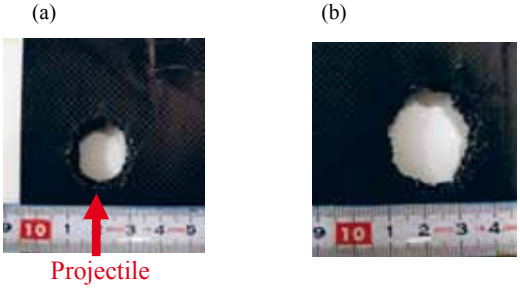

Fig.12 CFRP M46, 30° (a) 1st layer, (b) 2nd layer.

Figures 9 and 10 show the results of the impact experiment with collision angles of 30 degrees and 45 degrees using the double layer structure placed 20 mm apart. Damage on the 1st layers of the CFRP plate with 12k made by T700S filament is shown in Fig.9 (a) and Fig.10 (a). Damage on the 2nd layers is shown in Fig. 9 (b) and Fig. 10 (b), respectively. The through-hole was not observed on each 2nd layer. Damage of the 2nd layer performed with an incident angle of 30 degrees is smaller than that performed with one of 45 degrees. Impact damage on the target using the CFRP plate made with 1k is shown in Fig. 11 and Fig.12, respectively. Damages on the 1st layer are shown in Figs 11 (a) and 12 (a), and damages on the 2nd layer are shown in Figs 11 (b) and 12 (b). The through-holes on both 1st plates with 1k were larger than that on the 1st plate with 12k. A through-hole is made on each 2nd plate. Three kinds of the CFRP with T700S, T300 and M46 have almost same tensile strength. Therefore, it is considered that the protective performance depends on the number of yarns which configure the CFRP plate.

Also, we observed the spread of the ejector for the back side of the 1st layer after impact using the aluminium 2nd layer. Figures 12 (a) and (b) show the damage on the aluminium plate made by impacts with the impact angle of 45 degrees and 60 degrees, respectively. The space between the 1st layer and the 2nd layer is 40 mm. Many small craters generated by the ejector are almost distributed symmetrically. However, some large craters are concentrated in the travelling direction of the projectile. These phenomena mean that the ejector consists of two kinds of components. One is made by the elastic wave and propagates hemi-spherically. The other is affected by the parallel component of the momentum of the projectile.

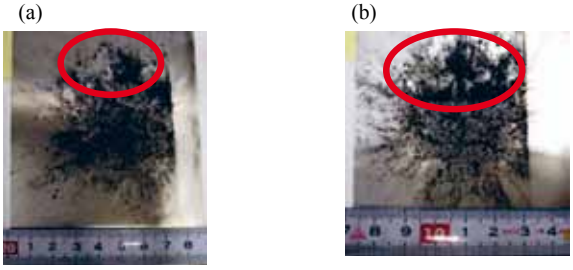

Fig.13 CFRP + Al (a) 45°, 2nd layer, (b) 60°, 2nd layer.

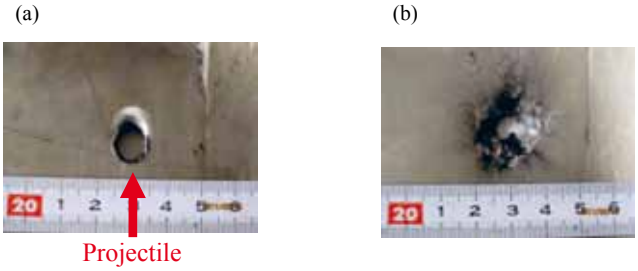

Fig.13 T-6Al-4V, 30° (a) 1st layer, (b) 2nd layer.

Figure 13 (a) and (b) show the through-hole on the 1st and 2nd layers made in the Ti alloy. The surface density of the Ti-6Al-4V plate 2 mm thick is 0.87 g/cm and that of the CFRP (12k, T700S) 3 mm thick is 0.46 g/cm. We confirmed that the CFRP plate is superior in terms of the protective performance per unit mass.

4. CONCLUSION

We carried out the hyper velocity oblique impact experiments. We confirmed that the protective performance depends on number of the yarns that configures the CFRP plate. Also, we compared and confirmed the advantage of the CFRP plate as a debris shield. We obtained a prospect to construct a thin and light weight debris protector.

ACKNOWLEDGEMENTS

The experiments were conducted and supported by the Space Plasma Laboratory, ISAS, JAXA. The authors would like to thank the Showa Metal Co. Ltd. for providing titanium materials.

REFERENCES

Glaser, P.E. "Power from the Sun: its Future", Science, 162, 857-866 (1968).

Shiota, I (2010), CFRP SHIELD AGAINST DEBRIS BY OBLIQUE COLLISION, *Materials Science and Engineering,* Technical University, Darmstadt , Germany.

U.S.Department of Energy, Satellite power system concept development and evaluation program - reference system report, DOE/ER-0023 (1978)

Whipple, F.L. Meteoroites and space travel, Astronomical Journal, 52(1161), 131 (1947).

Proceedings of the 32nd
Risø International Symposium on Materials Science:
Composite materials for structural performance:
Towards higher limits
Editors: S. Fæster, D. Juul Jensen,
B. Ralph, B.F. Sørensen
Risø National Laboratory for Sustainable Energy,
Technical University of Denmark, 2011

MOISTURE DIFFUSION IN GFRP COMPOSITES WITH A RANDOM FIBER ARRANGEMENT

Abhijit Mukherjee*
Rahul Chhibber*

Abhilash A.S Nair**
Shailendra P. Joshi**

*Thapar University, Patiala, India
**National University of Singapore, Singapore

ABSTRACT

GFRP composites undergo moisture diffusion that can be aggravated by mechanical stretching and irregular fiber arrangements. This paper reports experimental and analytical results of moisture diffusion in GFRP with random fiber arrangements. The effect of mechanical stretching on diffusion is also studied. The randomness in fiber orientation determines the nucleation of moisture diffusion that ultimately leads to mechanical failure of the GFRP. Clustering of fibers that creates large resin pockets is found to be most detrimental for the composite.

1. INTRODUCTION

GFRP composites that contain glass fibres in a resin matrix are susceptible to damage due to moisture diffusion. The moisture softens the matrix resulting in loss of composite action leading to failure. Diffusion is not uniform in the composite and often damage nucleates at locations that are rich in resin. The resin-rich regions are the result of a non-uniform distribution of fibers in the composite. Moreover, mechanical stretching of the composite creates micro-cracks in the matrix that can act as nucleation sites. Thus, the combined effect of mechanical stretching and randomness of the fiber arrangement is more detrimental. In extreme conditions, the moisture may attack the fibres. In alkaline environment, the diffusion may result in damage of the glass fibres and the capacity of the composite may be severely compromised. It has long been recognized that while polymer composites possess exceptional potential in designing light and strong structures, understanding their behavior in harsh environmental conditions during their operational life is imperative for their large scale use.

In this paper, moisture diffusion through the matrix is studied through experimentation and theoretical studies. Of special interest is the combined effect of moisture and mechanical stretching. It is noticed that moisture diffusion is higher in regions where resin pockets are formed due to non-uniform distribution of fibers in the matrix. Higher levels of stretching accelerate matrix damage and premature failure.

2. EXPERIMENTATION

GFRP composites have been fabricated from glass fiber sheets and epoxy resin by a hand layup technique. The specimens conformed to ASTM Standard D-3039 (Fig. 1). It is a flat sample of 500mm length with two tabs of length 150mm reinforcing the ends. This left an effective length of about 200 mm in the center. The samples have been tested by applying a tensile force in a Universal Testing Machine and their capacities have been determined. Another set of samples were stretched to different fractions of their ultimate capacities. The samples have been dipped in tanks containing distilled water at 40°C for varying periods of time (Fig. 2). The aim is to emulate the hot and humid tropical conditions.

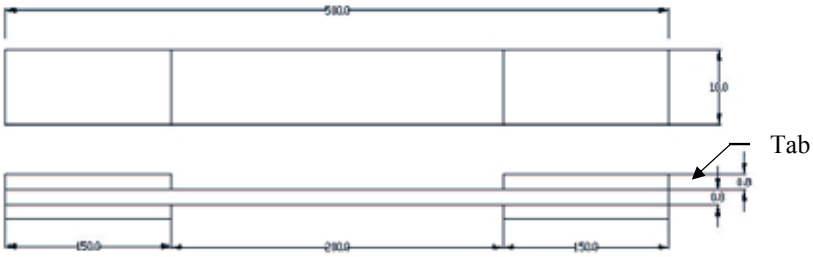

Fig. 1 Dimensions of the Specimen [1] All dimensions are in mm

Fig. 2 Experimental setup

The specimens were stretched to 20%, 40%, 60% & 80% of their failure load and their weights were noted using an electronic weighing balance. Thereafter, they were immersed in water for 1

and 2 months. After exposure for a specific time the specimens were weighed once again to determine their moisture absorption. Then the specimens were tested by applying a tensile force in a Universal Testing Machine. The onset and progression of damage during the tensile test have been carefully noted. Samples have been collected from the failure locations for carrying out microstructural studies. A scanning electron microscope has been used to find out the arrangements of fibers in the locations of failure. The spatial distribution of the fibres is characterised statistically by determining the coefficient of variation of centre to centre distance among the fibres. A detailed description is available in "Mukherjee, A., Chhibber, R., Sharma, A. and Mishnaevsky, L., Jr. (2010)".

3. MICROSTRUCTURAL CHARACTERISATION

Microstructural characterisation of composites is often done with regular fiber arrangementS. However, the experimental evidence shows that at failure locations the fiber arrangements are almost always disturbed. While one may use digitized versions of such real microstructures, a more computational approach may be adopted to generate artificial microstructural arrangements mimicking real composites. Such a strategy enables comparing a wide range of microstructures with different fiber volume fractions f, arrangements and fiber diameters, d.

(a) Random 1 (R1) (C_V=0.09)

(b) Random 2 (R2) (C_V=0.189)

(c) Random 3 (R3) (C_V=0.116)

(d) Random cluster (RC) (C_V=0.102)

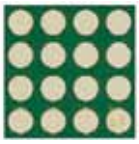

(e) Square regular (SR) (C_V=0.291)

(f) Square cluster (SC) (C_v=0.277)

Fig. 3 RVEs with different fiber arrangements with f = 0.5 and d = 10 μm.[Abhilash et al. (2011)]

The RVEs in Fig. 3 are three different random (R1, R2, R3) arrangements. Note that amongst these three the R2 arrangement has all the fibres completely inside the RVE, which means that there exists a thin *matrix-rich* layer at the edges of the RVE [Bond et al. (2005)]. Fig. 2d shows a random arrangement but with a clustering (RC) of fibres leaving what appears to be a big region in the microstructure that is matrix-rich. Fig. 2e shows a regular square (SR) arrangement, used as benchmark. Finally, Fig. 2f shows a square clustered (SC) arrangement where a set of four fibres are placed close together and this arrangement is repeated within the RVE. In this study, an attempt has been made to quantify the heterogeneity of fiber distribution (i.e. clustering) in different RVEs using the center-to-center (c-c) distance between the neighboring fibres. The neighbors of a fiber are defined such that the lines joining the centers of two fibres do not trespass other fibres. Then, the coefficient of variation C_v=($\sum/\mu$), $\sum$ = standard deviation and μ= mean) of the c-c distance can be used as a metric to quantify clustering.

Fig. 3 shows an example of a random arrangement with d =10 μm and f =0.47. Green circles are the fibres, the magenta outline represents the periodicity of the RVE, and the blue and red lines connect the centers of fibres such that none of the lines pass through an intermediate fibre. Note that the red lines connect fibres that are significantly apart from each other even though they may not necessarily communicate with each other through their stress fields, yet they can be connected topologically as far as the definition of c-c connectivity is concerned. From a topological perspective, this situation may not be uncommon in random microstructures; however, from the physical viewpoint it may not be relevant to include such remote influences.

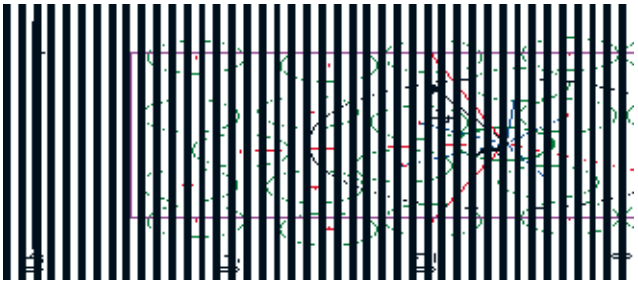

Fig. 4. Illustration showing the calculation of C_{vc} based on cut-off radius r_c for an RVE [Abhilash et al. (2011)].

The method has been applied to characterise the experimentally obtained microstructures as well. The samples have been exposed to a predetermined mechanical stress and moisture exposure. The exposed samples have been subjected to tensile load until failure. Samples have been collected from the zone of failure for studying their images in a scanning electron microscope (Fig. 5). The C_v has been calculated by measuring the central distances between the fibres as seen in the microscope images. It can be seen that fiber arrangements vary greatly in samples. However, failure locations invariably contain large matrix regions indicated by the dark patches in the images.

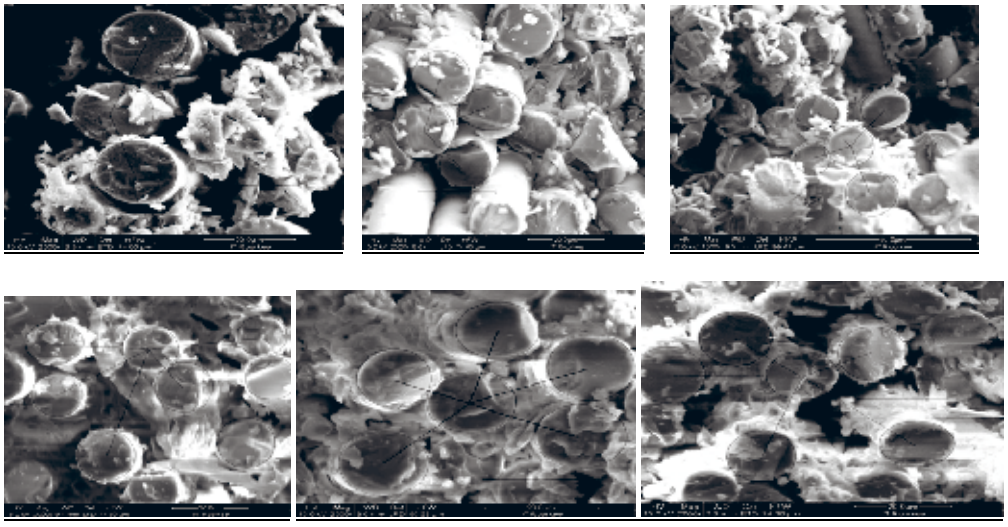

Fig. 5. SEM images of 20%, 40%, 60%, 80% pre stretched samples

3. NUMERICAL MODEL

Transient moisture diffusion, which is assumed to obey Fick's law is modeled in finite element. The Fick's law is analogous to the Fourier's heat conduction law, which is available in the ABAQUS/Standard® FE program as a coupled temperature-displacement analysis procedure. We exploit this analogy to model the transient, coupled moisture-displacement problem. The moisture diffusivity (D_m) is specified in terms of the equivalent thermal diffusivity (D_t) in ABAQUS. The temperature evolution in the RVE then resembles the moisture diffusion. Likewise, the moisture b.c. is specified in terms of the equivalent temperature[Abhilash et al. (2011)].

4. MOISTURE DIFFUSION

The moisture diffusion snapshots at different times as obtained from the numerical model are presented in Fig. 6. The microstructures that had rather fast diffusion have been presented. Clearly, the randomness of fiber arrangement affects diffusion. The diffusion was fastest through the clustered structure (RC). A large resin-rich region at the surface, resulting from clustering of fibres, facilitates moisture ingress in RC. This demonstrates the importance of the inclusion of randomness in the fiber arrangement in numerical models for moisture diffusion. The pockets of diffusion ultimately determine the long-term performance of the composite.

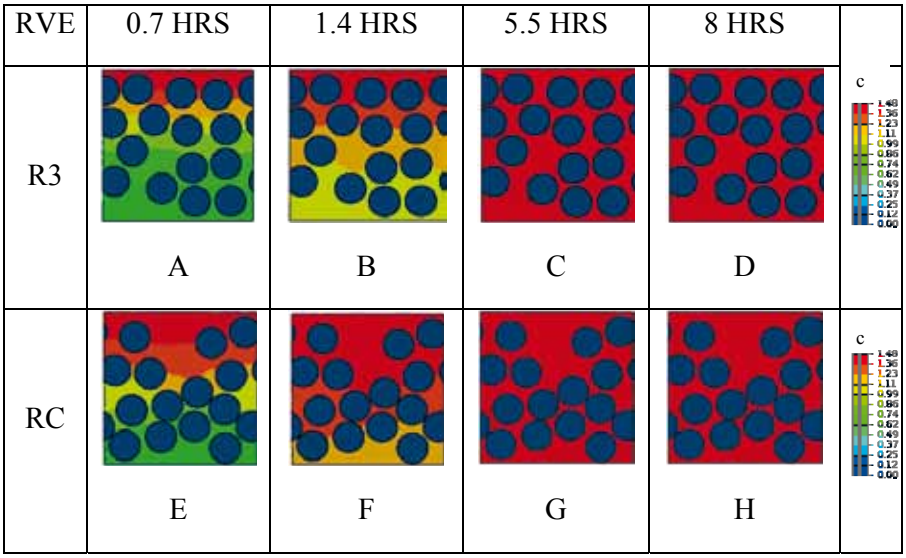

Fig. 6. Moisture diffusion snapshots from ABAQUS

In the experiments moisture diffusion has been characterised by weight gain due to exposure to water. The percent change in weight is plotted against the coefficient of variation (Fig. 7). The weight gain accelerates with an increase in C_v. However, the numerical experiment shows only C_v may not be enough in characterising the composite. A metric of clustering is needed to better characterise the composite.

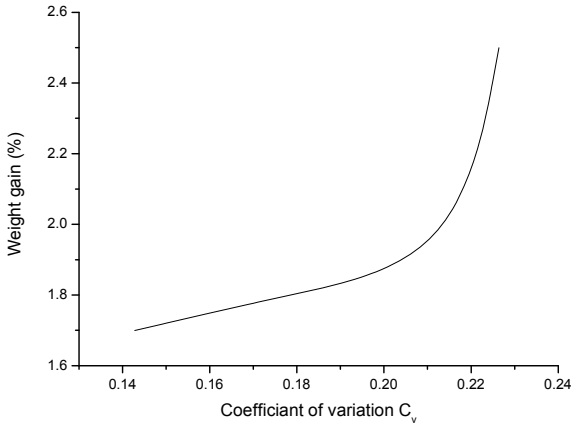

Fig. 7. Weight gain due to moisture diffusion in randomly oriented composites

Experiments were carried out with pre-stretched samples. Pre-stretching should lead to matrix cracking that would further facilitate moisture ingress. The variation of weight gain due to moisture ingress is plotted with percentage pre-stretch in Fig. 8. Clearly, there is a takeoff point in the graph at 60% pre-stretch. At this level profuse matrix cracking has been noticed in microscopic studies.

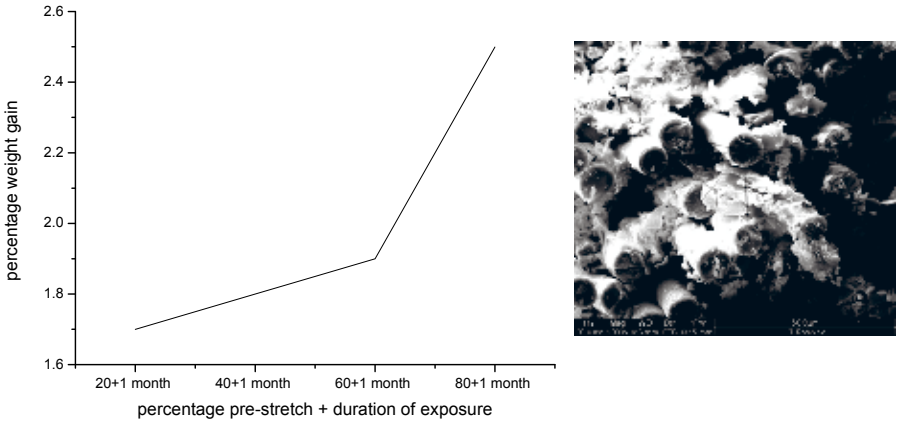

a. Variation b. micrograph

Fig. 8. Variation of moisture ingress with pre-stretch

4. CONCLUSIONS

This paper highlights the effect of randomness of the distribution of fibres in GFRP in moisture ingress. Although studies with regular fiber arrangements are ubiquitous some randomness is inevitable in fabrication of GFRP. This randomness has a seminal effect in the long-term behavior of the composite. Ingress of moisture is responsible for nucleation of failure in the

composite. Clustering of fibres that leads to creation of large resin pockets, especially those near the surface of the composite, seems to be the weakest. Experimental evidence shows that failure takes place at such locations.

The mechanical loading to a level close to the capacity load of the composite leads to cracking of the matrix. Such cracks also act as nucleation points for moisture ingress and play an important role in the long-term performance of GFRP. The present experiments have been carried out by immersing the composites in pure water. An alkaline environment is expected to be more severe as the alkali is expected to dissolve silica in the glass fibre [Mukherjee et al. (2007), Mukherjee et al. (2005)]. This is the subject of a future study.

ACKNOWLEDGEMENTS

The authors wish to thank the European Union for extending financial support for carrying out the experimentation and BASF India for providing the material requirements for this work.

REFERENCES

Abhilash, A.S., Joshi, S.P., Mukherjee, A. and Mishnaevsky, L., Jr. (2011). Micromechanics of diffusion induced damage evolution in reinforced polymers. Composites Science and Technology, doi:10.1016/j.compscitech.2010.11.

Bond, D. (2005). Moisture diffusion in a fibre-reinforced composite: Part I-non-fickian transport and the effect of fiber spatial distribution. Journal of Composite Materials. 39, 2113.

Mukherjee, A., Arwikar S.J. (2007) Performance of GFRP Sheets in Tropical Environment- II. Microstructural Tests, Journal of Composite Structures, 81, 33-40.

Mukherjee A., Arwikar S.J. (2005) Performance of GFRP Rebars in Tropical Environment- II. Microstructural Tests, ACI Structural Journal. 102 (6), 816-822.

Mukherjee, A., Chhibber, R., Sharma, A. and Mishnaevsky, L., Jr. (2010). Environmental degradation of glass fiber reinforced polymer composite, Upwind Project Report

Proceedings of the 32nd
Risø International Symposium on Materials Science:
Composite materials for structural performance:
Towards higher limits
Editors: S. Fæster, D. Juul Jensen,
B. Ralph, B.F. Sørensen
Risø National Laboratory for Sustainable Energy,
Technical University of Denmark, 2011

STRENGTH OF NCF COMPOSITE BUNDLES UNDER BIAXIAL STRESS

R. Olsson*, E. Marklund*, L.E. Asp* and N. Jansson**

*Swerea SICOMP AB, Box 104, SE-431 22 Mölndal, Sweden
**Volvo Aero Corp., Cold Structures SE-461 81 Trollhättan, Sweden

ABSTRACT

This paper presents experiments to support development of mesomechanics models for prediction of the strength of Non-Crimp Fabric (NCF) materials under tri-axial loading. Here we describe initial tests to characterise the failure envelope of the material in fibre bundles of a carbon fibre/epoxy NCF. Uniaxial loading of unidirectional off-axis specimens is used to obtain in-plane stress states ranging from highly shear dominated to fully transverse or axial tension, while future tests will include compressive stresses. The bundle material is represented by filament winding of unidirectional laminates and subsequent vacuum infusion of the resin. The resulting fibre volume fraction of 69% is representative of typical bundles in NCF materials. A modified Puck failure criterion provides reasonable predictions of the failure envelope.

1. INTRODUCTION

Fibre reinforced polymer composites are an appealing option for all structures where high performance and low weight is required. Carbon fibres provide particularly high specific stiffness and the aerospace industry has for a long time used laminates based on unidirectional (UD) carbon fibre prepreg plies, due to the superior quality and performance of such materials. Composite materials are currently introduced on a large scale in civil passenger aircraft and wind turbines and there is an increasing interest for introducing them in automotive applications.

Prepreg based manufacturing is, however, comparatively expensive and slow. For these reasons infusion of dry textile fibre preforms is preferred in production of complex parts for aeroengines and automotive structures or for large structures, such as ships and wind turbine blades. The penalty for the simplified and cheaper production is, however, a reduced in-plane performance introduced by the fibre waviness (crimp) in textile systems. Non Crimp Fabrics (NCF), based on comparatively straight continuous fibre bundles knitted or stitched together, have been introduced to reduce the significant crimp of conventional textile preforms based on woven fibre bundles. Resin Transfer Moulding (RTM) of NCF composites is now considered by Volvo Aero Corporation for various components in future aeroengines.

Stress analysis, testing and prediction of the constitutive behaviour and failure of textile composites is significantly more complex than for conventional prepreg materials, due to the inhomogeneous mesostructure with non-straight fibre bundles separated by resin pockets and stitch thread, Fig. 1. The bundle waviness is also influenced by the orientation of the neighbouring plies. Fairly accurate methods have been developed to predict the stiffness of textile composites, but this is not the case for predictions of failure initiation and strength (Marklund, Varna and Asp 2011a).

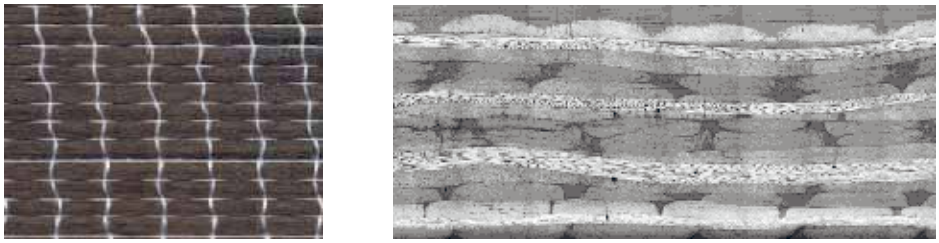

Fig. 1. Knitted UD NCF fibre bundles (left) and cross section of an NCF laminate (right)

Future composite structures, particularly those based on NCF materials and other textile composites, involve thicker laminates and more complex geometries than previously used. This increases the need to predict failure of composites under three-dimensional (3D) stress states. Furthermore, the inhomogeneity and bundle waviness of textile materials introduces local 3D stresses even under pure in-plane loading. Correct simulation of the infusion, curing and cooling of textile composites is crucial for an accurate prediction of the quality and residual stresses after manufacture.

The project ReFACT within the 5th Swedish National Aeronautical Research Program (NFFP 5) is performed in collaboration between Swerea SICOMP, Luleå Technical University and Volvo Aero Corporation, with joint funding from VINNOVA and Volvo Aero Corporation. The project is focused on carbon fibre/epoxy NCF materials for components in future aeroengines with the aims to develop methods to (i) predict the constitutive behaviour and failure and (ii) residual stresses and shape distortions resulting from processing of such materials. The current paper is related to the work to predict the constitutive behaviour and failure of NCF composites.

The strategy for the ReFACT project is to characterise the constitutive behaviour and failure of the transversely isotropic impregnated fibre bundles and the pure resin material under multiaxial stresses, and to implement these properties in a mesomechanics model based on the observed geometry of the NCF composite, Fig. 2. The mesomechanics model will then be used to predict stiffness and failure of the NCF composite material under arbitrary loading cases. The option to predict the bundle strength from micromechanics and the properties of bare fibres and resin is not pursued within ReFACT and has been given a grey background in Fig. 2. The reasons are difficulties to properly determine transverse properties of the fibres, statistical variations in the fibre distribution and the volume-dependent resin strength at a microscale (Asp, Berglund and Talreja 1996; Hobbiebrunken, Fiedler, Hojo and Tanaka 2007).

The bundle strength is particularly critical for NCF composites as fractographic studies show that matrix-dominated failure mainly occurs *within* bundles rather than in the resin pockets between bundles (Asp, Marklund and Varna 2011). The current paper is focused on the tests to characterise stiffness and failure of the fibre bundle material under combined shear and tensile loads.

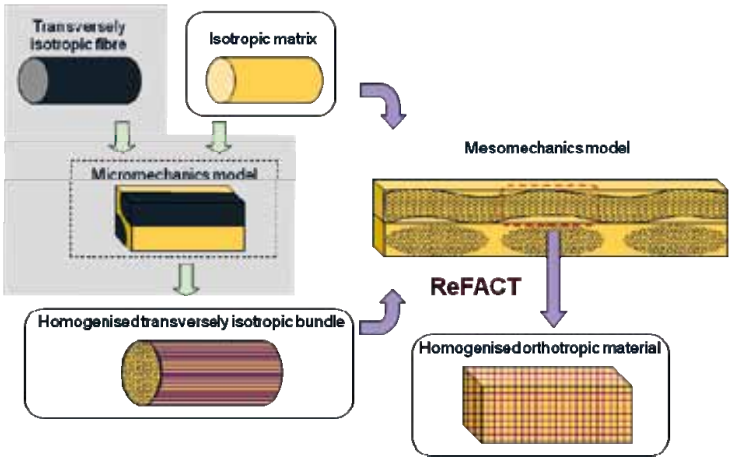

Fig. 2. Modelling strategy for NCF material in the project ReFACT.

2. SPECIMENS

The aim of this study was to mimic the transversely isotropic material in the bundles (impregnated roving) of the NCF material, consisting of Tenax HTS carbon fibre 12K roving and RTM6 epoxy matrix. This was done by winding roving with a feed of 3.1 mm per round on a 50x500x500 mm aluminium tooling plate covered with a peel ply. The winding results in a roving width of about 6 mm. A 4 mm diameter steel bar was placed between the fibres and the tool during winding to compensate for thermal and chemical deformations during processing. The steel bar was removed prior to infusion and curing. After completion of the winding the plates were covered with a peel ply and a caul plate and placed in a vacuum bag where the resin was infused along the fibres from one edge of the plate to the opposite edge using a vacuum. Two initial trials were required until essentially porous-free laminates could be manufactured. After infusion the laminates were cured at 160°C in 2.5 h + 180°C in 4 h.

The quality of the laminates after manufacture was inspected using microscopy, which indicated a homogeneous material without distinguishable bundles and a porosity of less than 1%, Fig. 3.

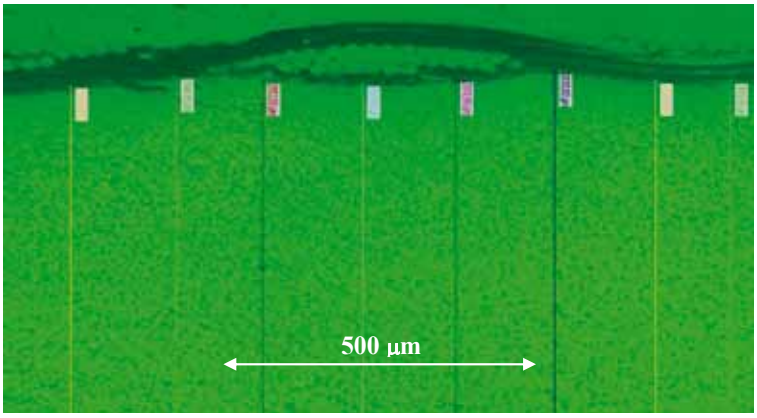

Fig. 3. Cross section close to the upper surface of one laminate.

A peel ply bundle with coarser fibres is visible in the upper part of Fig. 3. The peel ply generated a somewhat wavy surface of the specimen. Microscopy was used to determine the local thickness at several positions (shown by vertical lines in the figure) in several specimens. The resulting average thickness was typically 0.060 mm less than the peak-to-peak thickness. The thickness measured by a micrometer was therefore reduced by 0.060 mm, which resulted in an estimated average thickness of 2.14 mm for the tensile test specimens. The thickness and width of the gauge section of each specimen was measured at 2-3 lengthwise positions.

The fibre volume fraction v_f was determined indirectly from the fibre weight fraction by measuring the weight loss of small specimens after removing the matrix by a heat ramp up to 450°C for 1 h followed by 4 h at 450°C, and compensating for the weight loss of the carbon fibres in an accompanying reference tow. The measured value of v_f=69% is close to values obtained for fibre bundles of NCF laminates in the previous European project FALCOM. Thus, the fibre content of the present specimens is believed to be representative of the fibre content in bundles of typical NCF laminates.

After completion of manufacture specimens were cut in 0°, 3°, 10°, 45° and 90° angle to the fibres of the UD material. The 3° specimens will be used to study how small off-axis angles affect the axial compressive strength, and will not be discussed in the present paper. To minimise stress concentrations all off-axis specimens (i.e. other than 0° and 90°) were equipped with tabs at an oblique angle, Fig. 4, according to recommendations by Sun and Chung (1993). The angle ø between the edge of the tab end and the loading axis of the specimen is given by the following expression:

$$\cot\phi = -\bar{S}_{16}/\bar{S}_{11} \tag{1}$$

where $\bar{S}_{ij} = (\bar{C}_{ij})^{-1}$ are the compliance components of the material in a coordinate system aligned with the load. Specimens were manufactured with a 25° tab angle for 10°-specimens, and 62° for 45°-specimens, based on the *assumed* material properties E_1=155 GPa, E_2=12 GPa, G_{12}=6 GPa, ν_{12} =0.3. All specimens had a free length of 40-50 mm between tabs, satisfying the ASTM D3039 minimum requirement of two specimen widths + one gauge length (12.5 mm for the extensometer, less for strain gauges).

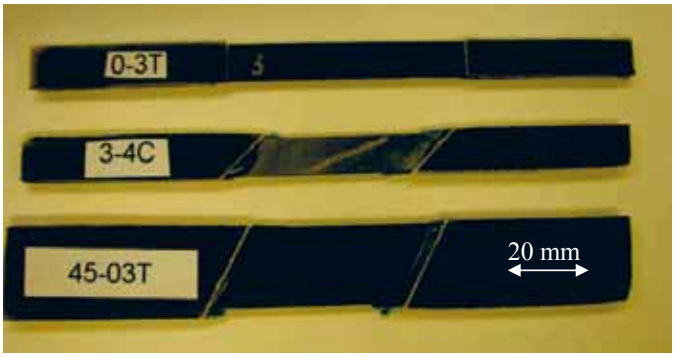

Fig. 4. Examples of test specimens with bundles in 0°, 3° and 45° angle.

3. EXPERIMENTS

A review (Olsson 2011) of methods to obtain mixed in-plane stresses indicated that off-axis specimens under uniaxial loading could provide a useful range of combined stresses. For a ply with an angle θ to a uniaxial stress σ_x in the global coordinate system *x*-*y* the local stresses in the material coordinate 1-2 system are given by:

$$\sigma_1 = \sigma_x \cos^2\theta \qquad \sigma_2 = \sigma_x \sin^2\theta \qquad \tau_{12} = -\sigma_x \cos\theta \sin\theta \tag{2}$$

Figure 5 illustrates the corresponding strain ratios for a typical UD carbon/epoxy system. A more or less pure shear failure will occur for an off-axis of about 10°, while larger angles provide matrix-controlled failure with an increasing fraction of transverse tensile strain ε_2.

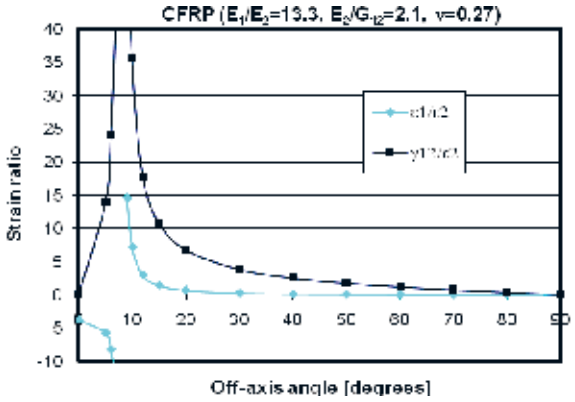

Fig. 5. Strain ratios for uniaxial loading at various off-axis angles.

All tests were done at room temperature (20-25°C) and a relative humidity of 20-30%. The specimens were loaded in tension in an INSTRON 8501 hydraulic test machine equipped with a 100 kN load cell and INSTRON 8800 software using hydraulic grips with a pressure of 75 bar. The loading rate was 0.5 mm/min for the 90°-specimens, and 1 mm/min for all other specimens. All specimens except the 90°-specimens were equipped with triaxial ("rosettes") 3 mm Kyowa KFG-3-120-D17-11 strain gauges. The axial strain on all specimens was also measured with an INSTRON 2620-601 extensometer with a 12.5 mm gauge length. Recordings were made at 10 Hz on a PC using Acqknowledge and a Microstrain collector with Agile-link V1.4.1.

4. RESULTS AND DISCUSSION

The axial stress σ_x at failure was obtained by dividing the maximum load of each specimen with the minimum cross section of the specimen, where the thickness measured with a micrometer was reduced by 0.060 mm to account for the difference between the peak-to-peak and average thickness. The local ply stresses were then calculated using Eq. (2). The properties obtained for the bundle material generally appear comparable to similar UD carbon/epoxy prepreg systems.

Three 0°-specimens were tested. The resulting average tensile strength was X_t=2215 MPa (values 2143 to 2319 MPa). The axial strain gauge signals from these specimens proved extremely unreliable, and for this reason the axial strains were based on extensometer readings. For strains between 0.1 and 0.6% the average Young's secant modulus was E_{1t}=160 GPa (values

150 to 166 GPa), and the average Poisson's ratio was ν_{12}=0.336 (±0.012). Measurements on five 90°-specimens for strains between 0.05% and 0.3 % yielded E_{2t}=9.1 GPa (values 7.1 to 10 GPa).

For the prediction of transverse matrix failure under combined stress states, the test results are being compared to a modified Puck criterion. The so called "Puck criteria", which are based on Mohr's fracture hypothesis stating that failure is exclusively created by the stresses acting on the fracture plane, are explained in detail by Puck and Schürmann (1998, 2002). Depending on if the normal stress component of the fracture plane is tensile or compressive, different quadratic criteria may be formulated. An advantageous feature of these criteria is that they provide additional information about the failure, such as the fracture plane angle, which may be important for subsequent delamination initiation predictions. It is here recognised that the criteria could be used to predict matrix failure initiation within bundles for NCF composites which, due to the inherent tow waviness, may exhibit rather significant out-of-plane stresses under in-plane loading. For a general 3D loading case, the criteria are rather complex, and require a numerical search routine for the fracture plane angle that maximises the failure index. However, under tensile normal loading, and only considering a combined σ_2-τ_{12} stress state, the modified criterion (Marklund, Varna and Asp 2011b) may be significantly simplified:

$$\left(\frac{\sigma_2}{R_{2t}}\right)^2+\left(\frac{\tau_{12}}{R_{12}-p_{NL}\sigma_2}\right)^2=1 \tag{3}$$

This expression contains a parameter p_{NL}, which represents the gradient of the failure envelope at σ_N=σ_2=0.

The relation between transverse matrix stresses and shear stresses at failure for 10°, 45° and 90° off-axis specimens is illustrated in Fig. 6. Deviating specimens with very low failure stresses have been indicated by red crosses. Several 10° specimens yield very low strengths, which may indicate difficulties in specimen preparation or tabbing. A failure envelope based on the modified Puck criterion, assuming R_{12}=80 MPa, R_{2t}=45 MPa, R_{2c}=160 MPa and a fracture angle in pure transverse compression α=53°, has been included for comparison. Due to this choice of strength values and fracture angle, we obtain p_{NL}=0.38 (Marklund, Varna and Asp 2011b). The predicted failure envelope is not significantly affected by moderate changes in R_{12} and α.

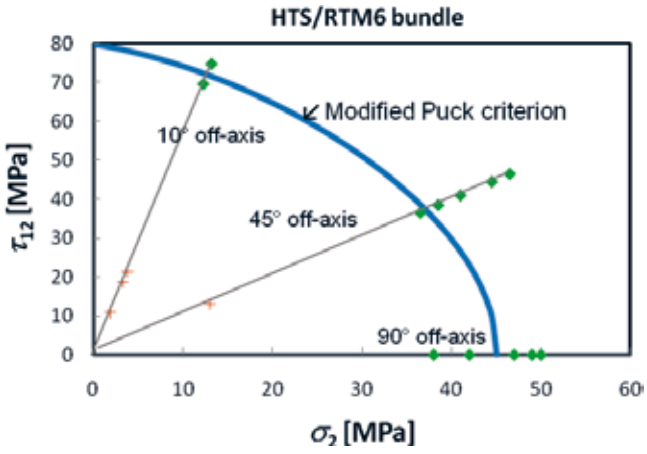

Fig. 6. Shear stress versus transverse matrix stress at bundle failure.

5. CONCLUSIONS

Previous fractographic studies indicate that both matrix dominated and fibre dominated failure in NCF composites is controlled by the strength of the impregnated fibre bundles. This paper has presented an experimental study of the elastic properties and failure envelope of HTS/RTM6 carbon/epoxy bundles in NCF materials under combined in-plane tension and shear. The properties are comparable to those of similar UD prepreg materials, although the fibre volume fraction of 69% is slightly higher than in most prepreg materials.

The measured matrix-dominated strengths are matched reasonably well by a modified Puck failure criterion but further data are required for more reliable predictions and evaluation. Ongoing and planned experiments include compression tests of similar specimens and Iosipescu shear tests. The reasons for the very low strengths of several 10° specimens need to be investigated.

The results of this study are to be used in mesomechanics models for the prediction of stiffness and failure of NCF composite materials under multiaxial loading. These mesomechanics models will be based on the current measurements of bundle properties, properties of the pure resin and a characterisation of the bundle geometry in the final NCF composite. The aim is an ability to predict failure of NCF composites with any given fibre architecture under arbitrary loads.

ACKNOWLEDGEMENTS

This work is a part of the project ReFACT within the 5th Swedish National Aeronautical Research Program (NFFP 5), and was jointly funded by VINNOVA and Volvo Aero Corporation. Funding for participation and presentation at the Risø conference was provided by the Swerea SICOMP internal SK development funds. The assistance of Runar Långström, Magnus Edin, Emil Hedlund and Greger Nilsson at the Swerea SICOMP lab is acknowledged.

REFERENCES

Asp, L.E., Marklund, E. and Varna, J. (2011). Ch. 12: Damage progression in non-crimp fabric composites. In: Non-crimp fabric composites: Manufacturing, properties and applications. Ed. S. Lomov. Woodhead.

Asp, L.E., Berglund, L.A. and Talreja, R. (1996). Prediction of matrix-initiated transverse failure in polymer composites. Compos. Sci. Technol. 56, 1089-1097.

Hobbiebrunken, T., Fiedler, B., Hojo, M. and Tanaka, M. (2007). Experimental determination of the true epoxy resin strength using micro-scaled specimens. Composites Part A 38, 814-818.

Marklund, E., Varna, J. and Asp, L.E. (2011a). Ch. 17: Modelling stiffness and strength of non-crimp fabric composites: semi-laminar analysis. In: Non-crimp fabric composites: Manufacturing, properties and applications. Ed. S. Lomov. Woodhead.

Marklund, E., Varna, J. and Asp, L.E. (2011b). Stiffness and strength modelling of non-crimp fabric composites. Proc. 52nd AIAA/ASME/ASCE/AHS/ASC Structures, Structural Dynamics and Materials Conference. Denver, Colorado. Paper AIAA-2011-1748.

Olsson, R. (2011). A survey of test methods for multiaxial and out-of-plane strength of composite laminates. Compos. Sci. Technol. 71, 773–783.

Puck, A. and Schürmann, H. (1998). Failure analysis of FRP laminates by means of physically based phenomenological models. Compos. Sci. Technol. 58, 1045–1067.

Puck, A. and Schürmann, H. (2002). Failure analysis of FRP laminates by means of physically based phenomenological models. Compos. Sci. Technol. 62, 1633–1662.

Sun, C.T. and Chung, I. (1993). An oblique end-tab design for testing off-axis composite specimens. Composites 24, 619-623.

Proceedings of the 32nd
Risø International Symposium on Materials Science:
Composite materials for structural performance:
Towards higher limits
Editors: S. Fæster, D. Juul Jensen,
B. Ralph, B.F. Sørensen
Risø National Laboratory for Sustainable Energy,
Technical University of Denmark, 2011

MATERIALS AND PROCESS LIMITATIONS FOR THERMOPLASTIC COMPOSITE MATERIALS FOR WIND TURBINE BLADES – PREFORM OF PREPREGS AND COMMINGLED YARNS

R.T. Durai Prabhakaran

Materials Research Division,
Risø National Laboratory for Sustainable Energy, Risø DTU,
Technical University of Denmark, Roskilde, Denmark

ABSTRACT

Wind turbine blades are produced based on the current thermoset resin technology, but thermoplastics can offer better potential to become the future blade materials. One of the most important goals when designing larger blade systems is to keep the blade weight under control. Thermoplastic materials offer weight saving similar to thermosets, apart from many other benefits like design flexibility, durability, cost, weight saving, and performance advantageous to the wind industry. In the current research study a detailed discussion on material and process limitations such as thermoplastic prepreg tapes and commingled yarns are presented in terms of their properties and available forms in the current markets. A critical review of thermoplastics discussed in the context of turbine blades applications.

1. INTRODUCTION

In today's industrial context thermoplastic composites are a well accepted material system used extensively for the development of several engineering products to automotive and aerospace applications. In particular, thermoplastic composites are falling under increasing scrutiny due to their potential to be easily repaired and/or reshaped, making them easier to recycle and reuse compared with thermosetting matrix composites. The high strength-to-weight and stiffness-to-weight ratios of composites make them attractive solutions for high performance structures where weight reductions can enable enhanced performance. Among the composite industries, the wind industry is interested in using thermoplastic materials in future wind turbine blades. Wind turbine rotor blades are large and consume enormous amount of material, which can form very big markets for thermoplastic materials. Material scientists and blade designers are in a

continuous hunt of inventing new and innovative blade design concepts with the new material systems like thermoplastics by properly utilize their benefits compared to thermoset composites. In recent years, development of polymer fibers reinforced with glass/carbon/aramid fiber reinforcements forming new systems called commingled/hybrid yarns are relatively new. These hybrid systems form new kind of composites which can be recycled after having been fully melted. A strong and better interface can be obtained since the reinforcement and matrix are of identical chemical composition or with a perfect degree of commingling yielding for better performance. The hybrid fabrics composed of continuous glass fibers and polymer fibers such as polypropylene (PP), have been used to fabricate thermoplastic composite blade with higher fiber volume fraction and improved performance at smaller scale blade lengths (developed by ÉireComposites, Ireland). Similar to hybrid fabrics, prepregs are used in multiple applications but the majority of uses come from aerospace (63%), industrial market (25%), sporting goods (12%) (Banks (2004)). Few industries are trying to use prepreg tapes for producing wind turbines, but the material is from thermosets. Thermoplastic materials need further development at this stage. Once the thermoplastic blade technology gets mature and fully developed similar to thermosets for longer blade lengths, one can aim for future blades with different thermoplastic materials. Hence, the current article highlights the limitations of few thermoplastic composites in terms of its material process-ability and performance related issues.

2. MATERIALS AND MANUFACTURING METHODS

In the current study, the thermoplastic polymers considered to characterize suitability for wind turbine blades are polypropylene (PP), polyethylene terephthalate (PET), polyamides (PA6), polybutylene terephthalate (PBT), and polyethylene (PE). These polymer materials are used in the form of pre-impregnated resins with a glass and fiber form to commingle with glass fibers (GF). The polymers considered in this study are semi-crystalline in nature, whereas the molecular weight and degree of cystallinity depends on the melt temperature (see Table 1). PBT and PA6 have a little higher melt temperatures compared to PP, mPET, and PE polymers. Processing of these polymers needs a very high temperature, this focuses special attention and a suitable tooling system. Therefore vacuum consolidation was chosen as a suitable process because it is relatively simple consisting of the following steps – layup, application of a vacuum, a ramp to process temperature, cool down and de-molding. There is no additional pressure needed to process the material, hence no autoclave is required. The process also resembles a vacuum infusion technique, which is the most common processing method for producing large turbine blades in several wind industries.

Table 1. Thermoplastic polymers and its properties

Sl. No.	Polymer System	Polymer Morphology	Polymer Melting Temperature (°C)	Process Temperature (°C)	Polymer Moisture Absorption (%)	Other limitations
1	Polypropylene	Semi-crystalline	160	210	0.01 – 0.1	Fiber structure: 2-D mats/3-D structural reinforcements Fiber volume fraction V_f : 50 – 60% Void/porosity volume fraction V_v: 1 – 2%
2	Polyethylene	Semi-crystalline	127 - 140	170	< 0.01	
3	Modified Polyethylene terephthalate	Semi-crystalline ??	180 - 190	220	0.16	
4	Polybutylene terephthalate	Semi-crystalline	228	240	0.1	
5	Polyamides 6	Semi-crystalline	220	260	3	

Table 2. Design requirements for a light and stiff blade (Grujicic (2010))

Function	Turbine Rotor Blade
Objective	Minimize the weight
	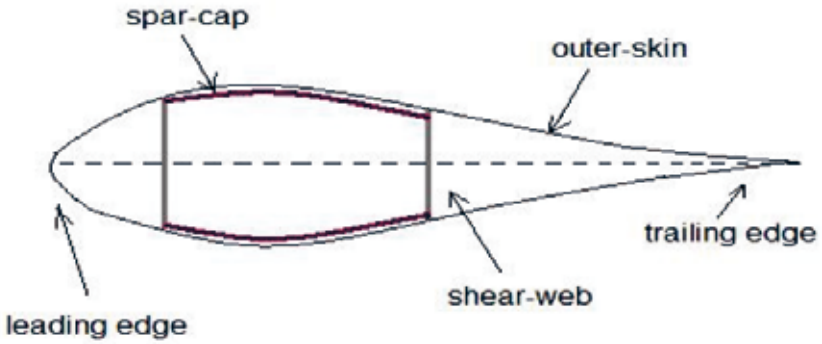
Constraints	a) Fixed geometry with a length specified design b) Deflection at the tip of the blade should not exceed 20% of the blade length c) Loading – Aerodynamic pressure and Centrifugal loading d) High fatigue strength ensuring a long life cycle of the blade
Variables	Shell thickness, Shell Layup Reinforcement combination, Material combination

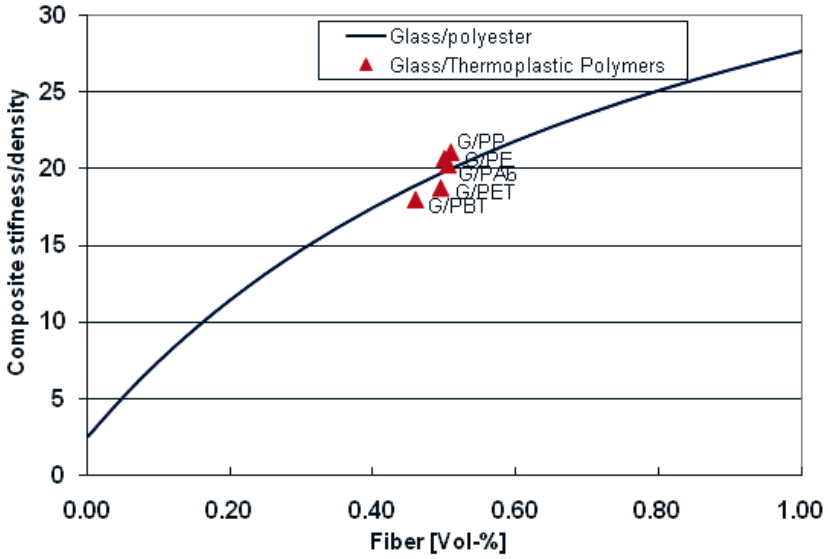

Figure 1. Material Indices – Glass/Polyester and Glass/Thermoplastic Polymers

Table 3. Material indices for the thermoplastic composites

Thermoplastic Composites	Fiber volume fraction	Theoretical modulus of composite	Theoretical density of composite	Stiffness to density Ratio	Material Indices
	V_f (%)	E_c (GPa)	ρ_c (g/cm^3)	E_c/ρ_c	$M = \frac{E^{\frac{1}{2}}}{\rho}$
GF/PP	0.51	37.3	1.77	21	3.45
GF/PE	0.50	36.6	1.77	21	3.42
GF/PET	0.50	37.2	1.98	19	3.08
GF/PBT	0.46	34.4	1.91	18	3.07
GF/PA6	0.51	38.0	1.88	20	3.29
G/Polyester	**0.50**	**37.5**	**1.89**	**20**	**3.24**

3. DESIGN REQUIREMENTS

In general the blade design is based on a stiffness-limited application satisfying – the functional requirement, geometry and material constraints having larger values of the material index (to minimize the mass, the material index should be maximized for better design aspects):

$$M = \frac{E^{\frac{1}{2}}}{\rho} \tag{1}$$

Aceves (2009) described the design selection methodology, to select an optimum composite wind turbine blade considering several factors like aerodynamic loading, computational fluid dynamics, variable structural properties including prepreg material, thickness, layup of the blade's shell and the thickness, and extent of the unidirectional material used as a spar. The solution proposed by the author satisfies the design requirements and improves on the benchmark by reducing the weight by almost 50% using prepreg unidirectional composites. Several researchers tried the Ashby approach to select the best material system as per the material indices derived considering several design factors (see Table 2). To design the blade for minimal weight the bending stiffness is considered as the main design factor. Since the mass of the blade directly scales with the average cross-sectional area, while its stiffness scales roughly with the square of its cross-sectional area, therefore the blade considered as a light and stiff beam with the highest material index is given by Equation (1). The indices for the thermoplastic laminates are given in Table 3 and can be compared with the standard glass/polyester material systems. The graph shown in Figure 1 clearly indicates that the thermoplastic composites (PP, mPET, PBT, PA6, and PE) are in the same order of material index and have the potential to replace the glass fiber reinforced polyester materials, but there are several factors which will not allow these materials to be used in practise.

On the other hand the mechanical properties of thermoplastic composites considered in the present study are in good agreement compared to glass/polyester composites as shown in Table 4. A glass/mPET commingled system and glass/PA6 have got higher compression strength compared to glass/polyester composites. In spite of its better compression properties, the fatigue resistance needs to be improved compared to the glass/polyester system. Therefore several researchers are trying to modify the polymers by adding special chemicals, nano particles, fillers etc to improve fatigue resistance. This shows that thermoplastic composites (both prepreg and commingled) have got good potential to replace glass/polyester materials in the current blade technology, but need to resolve many practical and technical issues to be used as blade materials.

Table 4. Mechanical properties - Thermoplastic prepreg and commingled composites

Sl. No.	Material System	Fiber Volume Fraction V_f (%)	Compression Modulus E^C (GPa)	Compression Strength σ^C (MPa)	Compression Strain to Failure ϵ^C (%)	Inter-Laminar Shear Strength ILSS MPa
Prepreg Laminates						
1	GF/PP	50.9	36.2	335	1.0	25.9
2	GF/HDPE	45.2	34.8	205	0.6	11.1
3	GF/mPET	49.5	32.9	372	1.2	22.6
4	GF/PBT	46.0	31.3	517	1.6	48.6
5	GF/PA6	47.0	34.6	534	1.6	59.3
Commingled Laminates						
1	GF/PP	50.3	41.4	516	1.3	37.4
2	GF/LPET	49.4	40.6	624	1.5	59.1
3	GF/PA6	47.8	39.1	577	1.5	69.8
4	GF/PBT	50.0	37.5	601	1.7	35.5
Reference Laminate						
1	GF/Polyester	50	38	570	1.5	76

4. MATERIAL AND PROCESSING LIMITATIONS

Several factors that have held back the thermoplastic composites from being used for wind turbine blades are a high process temperature (180–350°C) and difficult to adhesive join due to the high surface tension of thermoplastics. New and innovative process technologies have to be introduced, and special care is required in mould tool design including considerations regarding thermal expansion and thermal resistance. The following are the detailed explanation regarding the limitations of thermoplastic materials in terms of their processing and performance aspects.

4.1. Process temperature. The high viscosity thermoplastic polymers introduce processing challenges to composite manufacturers. The melting temperature of these polymers is very high (> 150 °C) and requires high temperatures to reduce the polymer viscosity and melt them to impregnate the fiber reinforcements in order to make very high quality composite products. In addition, the low thermal conductivity of thermoplastic materials makes achieving through thickness heating difficult using the current heating methods and gives a higher processing time. Table 1 show the processing temperatures needed for thermoplastic polymers which are of interest to future wind turbine blades. Therefore the development of new heating and processing methods are of interest to meet the upcoming challenges associated with the wind industry.

4.2. Tooling system. Rate of cooling is a crucial process parameter in determining the level of crystallinity. The chemical and mechanical properties of thermoplastic polymers used in composites are highly dependent on the degree of crystallinity. As given in Table 1, the polymers considered in this article are semi-crystalline in nature, which indicates the crystallinity never exceeds about 90%. The degree of crystallinity is determined by many factors including the type of polymer and the processing conditions used for composite development. The final properties of a composite depend on the polymer melt and its crystal formation during its cooling stage. Therefore a tooling system which can cool down the polymers from the molten state at a faster rate is highly difficult with the current tooling system. This is another big challenge to tool designers to incorporate a faster cooling rate along with the high temperature processing system.

4.3. Material quality. The prepreg tapes and commingled yarns as a raw material form can have a better storage life compared to thermosets, but these materials have a moisture absorption problem. Compared to thermosets, thermoplastic polymers are showing up a very low absorption level (except a few polymers like PBT and PA6). Table 1 shows the percentage of moisture absorption for various thermoplastic polymers at the raw material stage. This indicates some special drying of the material is needed before using the material system for processing.

4.4. Fatigue resistance. Fatigue properties were significantly analyzed at the early stages of composites. Few research studies show fatigue properties were improved to a certain level similar to glass/polyester but the processing is a big challenge for large structures (i.e. Glass/Anionic PA6 composites). Extensive research on fiber surface treatments and sizings is also under development to augment the fiber/matrix chemical bond, further increasing static and fatigue properties.

4.5. Environmental degradation. Environmental attack to composite structures such as temperature, humidity, radiation, and chemical exposure will have a significant role in the degradation of properties and finally affect the overall performance of composite structures (James (2001)). The combination of moisture absorption and change in mechanical properties may be a problem for the natural frequency and damping of composite structures.
The matrix dominated properties like the shear stiffness, the shear strength and the stiffness and strength across the fiber direction are the ones which are mostly affected by the moisture content in the material. For example for glass/PA6 composite conditioned material, the stiffness across the fiber direction drops to about 1/3, whereas the other sensitive properties drop to about ½ of the properties for the dry material. To avoid catastrophic failures of large structures one needs to analyze the material degradation by different mechanisms and consider the design data accordingly to account for the environmental resistance.

4.6. Material availability. Both prepreg tapes and commingled yarns or fabrics are readily available in the market. As per product design needs, one can demand the material supplier for a longer width and thickness of the fabrics. In spite of its availability in the present forms, fully compatible sizings on fiber reinforcements are still in the development stages for many reinforcements to better improve on interfacial bonding between fiber/matrix composites. Several researchers are trying to modify the sizing chemicals and also inventing new sizing methods to improve the fiber surface coating which can react with polymers for better bonding.

4.7. Repair methods. Repair procedures for thermoplastic composites have not yet fully matured and have not become a regular part of composite structural service. Several bonding techniques are developed these days at smaller scale product repair. But at larger scale structures like wind turbine blades joining to shells of the blade and repair methods are not available for more than

40m length blades.

4.8. Cost. The cost of thermoplastic polymers is currently high compared to thermoset resins like polyester. The wind industry is a big consumer of matrix materials, once a thermoplastic polymer is selected for future blades the material cost for huge consumption will go down. The cost of thermoplastic resin prepregs can be up to three times that of comparable epoxy prepregs. Apart from the polymer cost, tooling materials such as the vacuum bag, sealant tapes, and other miscellaneous materials used for processing the composite products under higher processing temperatures are adding up to the overall cost of the product. In order to supply high heat and a faster cooling rates a huge amount of energy consumption takes place, this also adds cost issues to the overall cost of the composite product.

The above considerations limit the use of thermoplastics in a large composite structure like wind turbine blades. The wind industry and several researchers are continuously trying to resolve the issues and use thermoplastics as future materials due to their special advantage of recyclability.

5. CONCLUSIONS

A wide range of thermoplastics are available in the market and in common use today in several applications. Thermoplastics for turbine blades are relatively new and interesting materials due to their several advantageous compared to thermoset materials. In spite of the advantageous, there are several disadvantageous to fulfill the design and production criteria for a blade design. The wind industry is trying hard to replace the current thermoset by thermoplastics or any other material system which can lower the current production cost and increase the life cycle of the blade by its high-end performance characteristics. Therefore in the current research study possible thermoplastic materials suitable for future blade were listed. The mechanical properties of these materials are good in comparison with the glass/polyester unidirectional composites. Before considering the best candidate thermoplastic material for future blades several challenges need to be resolved. The current article highlights the practical issues associated with these thermoplastic materials in terms of processing, performance and quality aspects.

ACKNOWLEDGEMENTS

The work reported was conducted in the research project sponsored by the Danish National Advanced Technology Foundation. Special thanks are due to the project partners: LM Wind Power A/S, Comfil ApS, and Aalborg University (Department of Mechanical and Manufacturing Engineering). The author would also like to thank the material (resin) supplier Cyclics Corporation, USA and Ticona Germany, Bond Laminates, Germany, Polystrand, Germany and Jonam composites ltd UK, for their support and useful discussion in carrying out this research study.

REFERENCES

Aceves, C.M., Sutcliffe, M.P.F., Ashby, M.F., Skordos, A.A., and Roman C.R. (2009), Design selection of a wind turbine blade using prepreg materials, 17th International Conference on Composite Materails (ICCM17), 27 Jul 2009 - 31 Jul 2009, Edinburgh, UK, 10 pp.

Banks, R., Mouritz, A.P., John, S., Coman, F. and Paton, R. (2004), Development of a new structural prepreg: Characterization of handling, drape, and tack properties, Composite structures, 66, 169 – 174.

Grujicic, M., Arakere, G., Subramanian, E., Sellappan, V., Vallejo, A. and Ozen, M. (2010), Structural-response analysis, fatigue-life prediction, and material selection for 1MW horizontal-axis wind-turbine blades, Journal of Materials Engineering and Performance, 19(6), 790 -801.

James, M.S., Bruce K.F., Steven, H.M., Crystal, H.N., John, W.G.J., Giuseppe R.P. (2001), Environmental issues for polymer matrix composites and structural adhesives, Clean Products and Processes, 2, 228-235.

Proceedings of the 32nd
Risø International Symposium on Materials Science:
Composite materials for structural performance:
Towards higher limits
Editors: S. Fæster, D. Juul Jensen,
B. Ralph, B.F. Sørensen
Risø National Laboratory for Sustainable Energy,
Technical University of Denmark, 2011

TENSILE AND COMPRESSION PROPERTIES OF STEEL FIBER REINFORCED COMPOSITES – EFFECT OF FIBER VOLUME FRACTION AND POROSITY

R.T. Durai Prabhakaran, T.L. Andersen, J.I. Bech and H. Lilholt

Materials Research Division,
Risø National Laboratory for Sustainable Energy, Risø DTU,
Technical University of Denmark, Roskilde, Denmark

ABSTRACT

Steel fibers are commonly used to reinforce concrete for several applications in the construction industry, whereas steel fiber reinforcement of polymers is a relatively new area in the composites field. The aims of this study were to use steel fibers in order to make unidirectional fiber reinforced composites (SFRC) by a standard manufacturing technique, vacuum infusion. The current study also considers investigating the effects of the fiber volume fraction and porosity on the mechanical properties of SFRC. An optical microscopy examination of specimens indicated small pores observed surrounding the fiber surfaces. Composites with fiber volume fractions of (V_f) - 33%, 48%, and 72% were produced and tested for mechanical properties such as tensile and compression properties. The compression strength values are significantly reduced at higher fiber volume fractions i.e. 72 vol.% due to the presence of porosity.

1. INTRODUCTION

The mechanical properties of fiber-reinforced composites depend on the strength of the fiber, the matrix and the interface bond between them. Among the fibers used in composites, steel fibers are an upcoming reinforcement material for the development of large composite structures like composite bridges. In spite of their higher density, steel fibers have a higher strength, stiffness, and much higher ductility. This can bring new benefits to the use of steel fibers in composite applications compared to other traditional reinforcement materials such as glass fibers, aramid fibers, and carbon fibers. Despite the benefits, steel fibers for the reinforcement of polymers are a relatively new application and not well reported in the literature concerning processing and property characterization.

In the present study, the effect of fiber content and porosity on the mechanical properties of steel fiber-reinforced polyester composites was examined. Mechanical strengths, and stress-strain behavior of SFRC performed under tensile and compression loading were evaluated. The laminates were made by the standard processing technique called the vacuum infusion method. In order to calculate the laminate porosities, a standard laboratory technique is used, such as to measure the density of the composite and weight fraction of steel fibers.

2. MATERIALS

High carbon steel fibers in the form of single filaments were used in the present work. The steel filament has a standard diameter 0.21mm, and was coated with a zinc layer on its surface to prevent corrosion. The properties of the steel fiber are given in Table 1. Similarly, standard polyester resin such as Polylite 400-499 grade resin were used in the current study. The physical and mechanical properties of the polyester resin are also shown in Table 1. A small percentage of hardener was used (approximately 1.5% as recommended by the supplier), in order to infuse and initiate the curing process of the polyester resin and also to provide better impregnation between the wound fibers.

Table 1. Properties of the steel fiber and polyester resin

Material System	**Density (g/cc)**	**Diameter (mm)**	**Young's Modulus (GPa)**	**Tensile Strength (MPa)**
Steel Fiber	7.85	0.21	212.5	2628
Polyester Resin	1.18	---	3.11	54.8

3. MANUFACTURING METHODS

Unidirectional (UD) steel fiber reinforced composite laminates were produced by vacuum infusion. This processing method is very simple and follows a similar procedure to the current composite industry in order to produce large structures like wind turbine blades. UD laminates made by steel filaments with perfect alignment, such as 0^0 orientation needs another important pre-processing step called filament winding.

3.1. Filament winding. As shown in Figure 1(a), a plastic mould with grooves of a certain depth equal to the thickness of the laminate was designed in order to place the steel filaments in a parallel configuration. Using the filament winding procedure (Andersen and Lystrup (1993)), laminates can be made either by using steel filaments or steel fiber bundles. The winding process gives the best possible alignment for steel filaments. Tensile and compression test specimens have been manufactured by filament winding followed by vacuum infusion with the polyester resin. The test specimens were directly wound in the grooves having dimensions of 15 mm x 2 mm, see Figure 1a) and Figure 1b).

a) Filament winding in a groove b) Vacuum infusion setup

Fig.1. Setup used for processing the UD steel fiber reinforced polyester composites

3.2. Vacuum infusion technique. The plastic mould designed for this work has three grooves and each groove can contain steel filaments wound exactly into the groove as per the calculated fiber volume fraction, and a press plate is used on top of it. The mould was placed on a flat glass plate (500 x 740 x 10 mm), which is used as the bottom tool plate. The tool plate is treated with a release agent, except around the edges where sealant tape is to be placed. To ensure easy release, a thin non-porous PTFE coated release fabric is placed on the glass plate. The layup is placed on the release fabric and sealant tape is placed along the edge of the glass tool plate. The layup is covered in a peel ply and the peel ply is extended in either end to cover the inlet and outlet hoses. A distribution mesh is placed on top of the peel ply in one end, where the infusion is performed along the length of the fibers. The vacuum is pulled slowly while the vacuum bag is pulled towards the lay-up. Manual manipulation of the vacuum bag during this step may be necessary to prevent bridging of the bag. Extra care must be taken at this step in layup, since the moulds will not yield and will frequently form high flow resin paths. Unacceptable leaks must be repaired and then the infusion process is initiated.

The infusion is carried out by straightening the Z-closure and allowing the resin to flow into the layup. It is important that the easiest flow path for the resin is through the laminate, otherwise the resin will back track into the laminate which can cause voids. In a normal infusion the resin flow front will reach the spiral hose at the outlet and be allowed to fill it and rise a little up into the outlet hose. Because of the low pressure drop over a steel fiber laminate the pump is kept connected to the system for 25 minutes allowing some resin to be pumped through the system. A vacuum trap is essential for this step to avoid resin coming into the vacuum pump.

Following the above procedure, three laminates with different fiber volume fractions (i.e. 33%, 48%, 72%) were produced and the laminates were cut into test specimens as per the standards. The composites were characterized with respect to density, fiber content, and porosity content (see Table 2). Optical microscopy shows porosities at the fiber/matrix interfaces, see Fig 2.

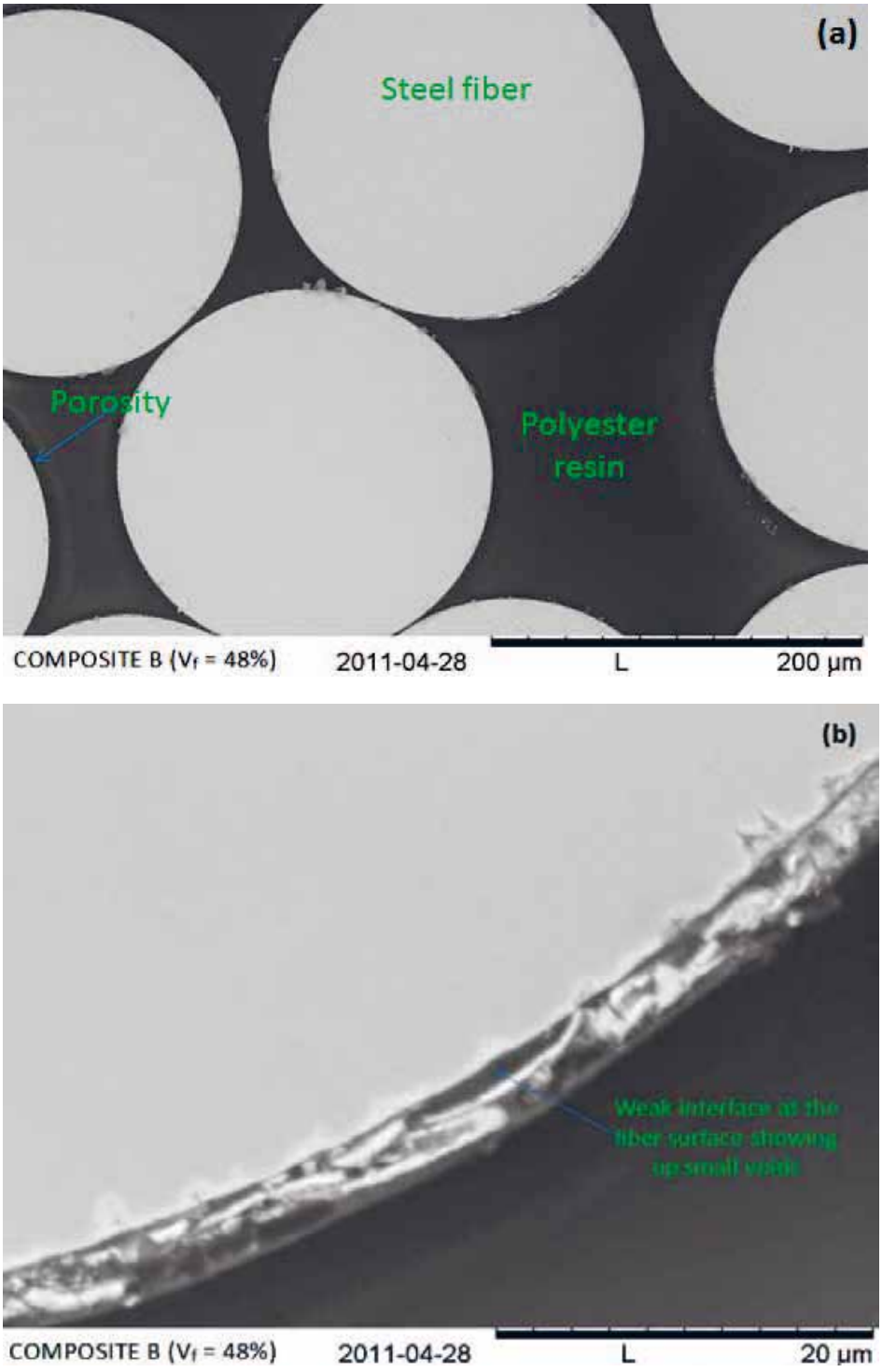

Fig.2. Micrographs showing the porosity in the laminate B (48 fiber vol.%)

Table 2. Measured density, weight fraction and porosity of steel/polyester composites

Sl. No.	Composite specimen ID	Fiber diameter (mm)	Nominal fiber volume fraction (%)	Weight fraction of the fiber (%)	Density of the composite (g/cm^3)	Measured fiber volume fraction (%)	Volume fraction of porosity (%)
1	A	0.21	31	77.4	3.35	33	2.75
2	B	0.21	52	86.7	4.35	48	2.89
3	C**	0.21	72	---	---	---	---

** For composites made with higher fiber volume fractions (i.e. C series), it was not possible to make specimens for porosity determinations. These laminates contain a very low resin content which separated from the steel filaments due to weak interfacial bonding.

4. MECHANICAL TESTS

The aim of this study is to measure the tensile and compression properties of UD steel fiber reinforced polyester composites with a varying fiber volume fraction.

4.1. Tensile Test. Tensile tests were carried out on an Instron testing machine following the ISO standards. The strain measurements were made with mechanical extensometers of a 50mm gauge length clamped directly to the tensile test specimen. The output of the extensometer was fed via a strain gauge amplifier unit. A complete stress-strain curve up to failure of the specimen was automatically obtained. Figure 3a shows the tensile test setup used, and a specimen mounted in the hydraulic grip with two extensometers. Figure 3b shows the failed specimen after the test. The tensile properties are given in Table 3. The tensile stress-strain response of composite B specimens is shown in Figure 4.

4.2. Compression Test. The compression test was conducted in accordance to ISO standards 14126 (1999). A 250 kN servo-hydraulic machine with a mechanical combined loading (MCL) test fixture designed by Risø was used to determine the compressive behaviour of the UD SFRC laminates. The compression on the UD specimens was performed at a constant compression rate of 1.5mm/minute. The specimens were tabbed at both ends and loaded in uniaxial compression. The MCL test fixture and specimen geometry were properly designed to generate a uniform stress state in the test sample. Test data such as applied load on the specimen, displacement, back-to-back longitudinal strains were recorded by a PC via a data acquisition system. The compression properties for the three different laminates with a varying fiber volume fraction are given in Table 3. The compressive stress-strain response of composite B specimens is shown in Figure 4. The longitudinal strain on the front and back faces of the specimen was initially observed as the same, however as the compressive load was increased, the strain values were different showing up some bending of the specimen; material softening can also occur due to internal damage (Hahn and Williams (1984)).

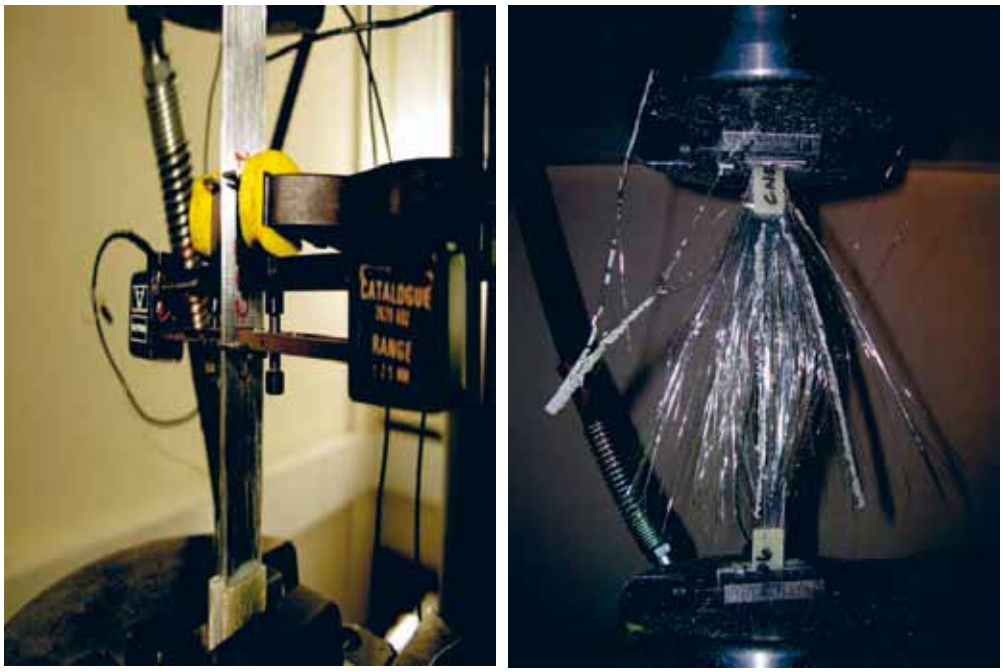

a) Tensile setup with mechanical extensometers b) Failed tensile test specimen

Fig. 3. Tensile test setup – Steel fiber/polyester specimens

The test results shown in Table 3 are based on six specimens for each set of results, the average values are listed under tensile and compression - modulus, strengths and strains. The three laminates have the same fiber diameter, the same fiber surface coating, produced under the same process conditions, but with varying fiber volume fractions.

Table 3. Tensile and compression properties of steel fiber reinforced polyester composites

SL. NO.	Composite specimen ID	Fiber diameter (mm)	Measured fiber volume fraction (%)	Tensile modulus (GPa)	Tensile strength (MPa)	Tensile strain to failure (%)	Compression modulus (GPa)	Compression strength (MPa)	Compression strain to failure (%)
1	A	0.21	33	68	789	1.28	68	592	1.04
2	B	0.21	48	110	1130	1.53	118	978	1.02
3	C	0.21	72	144	1771	1.37	157	1084	0.74

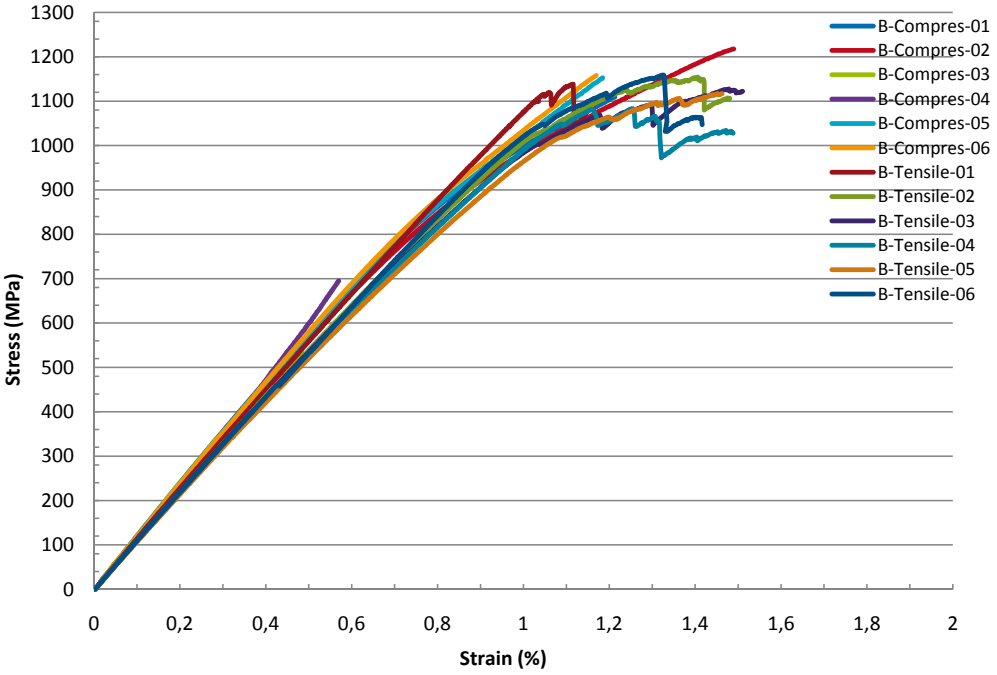

Fig. 4. Stress-strain curves of tensile and compression tests for composites with 48% V_f (The curves with "stepwise final part" before failure are tensile test data)

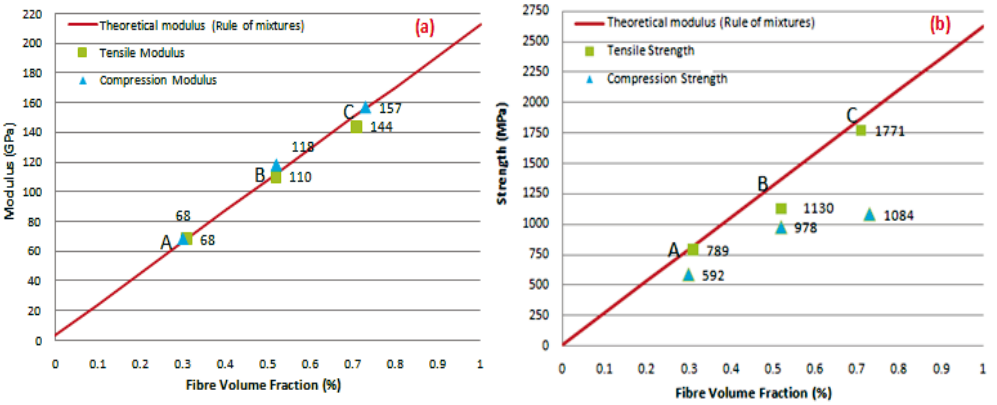

Fig. 5. Comparison of modulus and strength of three composites with the theoretical values

Figure 4 shows the combined stress strain curves of tensile tests and compression tests on the same plot for a composite with 48% fiber volume fraction. It is noted that the compressive strength is significantly lower than the tensile strength of the composite. This may be related to the matrix properties and fiber/matrix interface strength. Also the Bauschinger effect causing the compressive yield stress to be lower than the tensile yield stress of the drawn steel filaments may play a role.

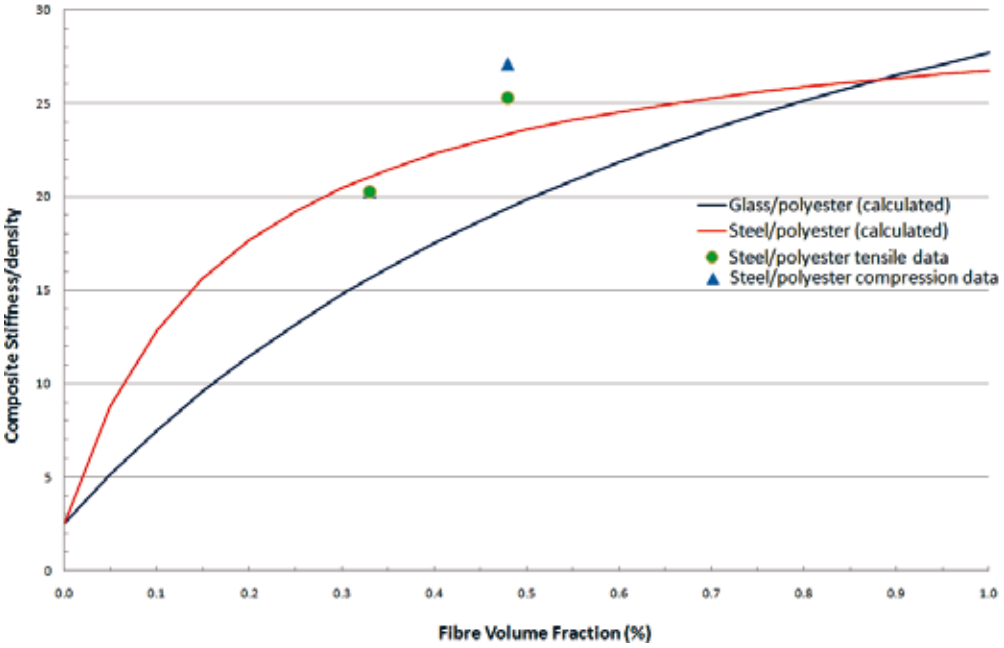

Fig. 6. Stiffness/density ratio versus fiber volume fraction for steel and glass fiber reinforced composites

5. EFFECT OF FIBER VOLUME FRACTION AND POROSITY

The effect of fiber volume fraction on the mechanical properties such as tensile and compression properties are shown in the Figure 5a and Figure 5b. The tensile and compression modulus have values almost equal to the theoretical modulus calculated as per the rule of mixtures. Table 2 shows the porosity content measured on the three laminates, which is a little higher than the acceptable values for the composites (i.e. > 2%). For the laminate C, this could not be measured due to the very high fiber volume fraction and very small content of polyester resin which does not allow taking a small sample from a composite to make porosity measurements. An optical microscopy examination of specimens indicated small pores observed surrounding fiber surfaces.

The role of pores and the fiber volume fraction have significant effects on compression strengths compared to tensile strength values. Figure 5b shows the composites with 33 and 48% fiber volume fractions have little deviation of strengths, whereas the composite laminate with 72% fiber volume fraction deviates more from the theoretical strength. This indicates the difficulty of packing a large amount of fibers in a given composite volume; the insufficient amount of matrix leads to an increased porosity content.

Figure 6 demonstrates, as the fiber volume fraction increases, that the composite stiffness relative to the density increases for steel/polyester composites compared to glass/polyester. From the literature glass/polyester can have good properties if the fiber volume fraction is between 50-60%; similarly in the present work, steel fiber/polyester composites showed relatively better properties at 48% compared to a composite having a higher fiber volume fraction (i.e. $V_f = 72\%$).

6. CONCLUSIONS

The influence of fiber volume fraction and porosity on the mechanical properties of steel fiber reinforced polyester composites were examined for an optimal use of composites in large engineering structures. A summary of the work are given below:

1. Laminates were made by filament winding and a vacuum infusion technique.
2. Three laminates with varying fiber volume fractions (33, 48, and 72%) were considered to make the process trials in the current study.
3. A standard technique was used to determine the volume fraction of porosity in the three composites, this helps to study the role of porosity on the measured mechanical properties.
4. Tensile and compression properties were measured to determine the effect of fiber volume fraction on the properties.
5. Tensile and compression modulus values are in good agreement with the theoretical modulus as per the rule of mixtures, whereas the tensile and compression strength deviated from the theoretical strengths for the composites having a very high fiber volume fraction and porosity.

This study helps to understand the process difficulties, laminate cutting procedure in making specimens for various mechanical tests, the role of the fiber volume fraction and porosity on the tensile and compression properties of steel fiber reinforced polyester composites.

ACKNOWLEDGEMENTS

The work reported was conducted at Risø DTU for a research study sponsored by the Danish National Advanced Technology Foundation. The authors would also like to thank the material suppliers. The authors would like to thank Shahid Mehmood, Jacob Christensen, and Christen Malte Markussen for supporting the experimental work in processing the laminates and porosity measurements.

REFERENCES

Andersen, T.L. and Lystrup, A. (1993). Room temperature filament winding of thermoplastic composites, Plastics, Rubber and Composites Processing and Applications, 19, 143 – 149.

Hahn, H.T. and Williams, J.G. (1984). Compression failure mechanisms in unidirectional composites, Nasa Technical memorandum – 85834, Langley Research Centre, Hampton, Virginia – 23665, 28 pp.

ISO 14126 (1999). Fiber-reinforced plastic composites – Determination of compressive properties in the in-plane direction, International Standard ISO 14126, International Organization Standard, Geneve 20, Switzerland.

Proceedings of the 32nd
Risø International Symposium on Materials Science:
Composite materials for structural performance:
Towards higher limits
Editors: S. Fæster, D. Juul Jensen,
B. Ralph, B.F. Sørensen
Risø National Laboratory for Sustainable Energy,
Technical University of Denmark, 2011

THE MIXED MODE BENDING TEST FOR FULL INTERFACE FRACTURE CHARACTERIZATION OF SANDWICH COMPOSITES

A. Quispitupa*, C. Berggreen* and L.A. Carlsson**

*Department of Mechanical Engineering, Technical University of Denmark
Nils Koppels Allé, Building 403, DK-2800 Kgs. Lyngby, Denmark
**Department of Ocean and Mechanical Engineering, Florida Atlantic University
777 Glades Road, Boca Raton FL, 33431, USA

ABSTRACT

Mixed mode fracture characterization of face/core debonds in composite sandwich structures is a crucial task for the prediction of failure. The mixed mode bending (MMB) fixture has successfully been used for debond fracture characterization of sandwich composites. However, it is currently limited at providing only negative shear loading, i.e. negative mode mixities at the crack tip. As real composite structures typically experience fully reversed cycles, the debond crack tip will be subjected to negative and positive shear loadings. In order to incorporate and apply positive shear loads at the interfacial crack tip, a modification of the MMB fixture is proposed in this paper. A parametric finite element analysis of the modified version of the MMB fixture reveals that it is actually possible to achieve positive mode mixities at the crack tip. The effect of loading condition, specimen geometry and material properties on the crack tip loading is examined.

1. INTRODUCTION

A face/core debond is a frequent type of defect that affects the reliable performance of sandwich composite structures. Such a defect is an interfacial crack between the face and core in a sandwich and reduces the load-carrying capacity of the sandwich structure. A debond may originate from manufacturing defects, cracks produced by fatigue loads or low velocity impact, stress concentration at geometrical discontinuities and material imperfections.

Despite the well known advantages of sandwich composite materials, difficulties remain in the proper assessment of debond propagation under different loading conditions. In order to assess the effect of a face/core debond on the structural reliability, several test methods have been proposed and used in the past decades (Carlsson and Kardomateas, 2011). Recent promising

candidates for full face/core debond fracture characterization under mixed mode loading are the modified tilted sandwich debond (TSD) test method (Berggreen and Carlsson, 2010), the double cantilever beam loaded with uneven bending moments (DCB-UBM) (Sørensen, Jørgensen, Jacobsen and Østergaard, 2006)) and the mixed mode bending test method (Reeder and Crews, 1990, ASTM D6671/D 6671M-06, 2006) adopted for sandwich specimens by (Quispitupa, Berggreen and Carlsson, 2009). The state of mode mixity at the crack tip is quantified by the phase angle, ψ (Hutchinson and Suo, 1990). This measure quantifies the ratio of mode II to mode I stress intensity factors in a convenient and simple manner.

The modified TSD method (Berggreen and Carlsson, 2010) uses a rectangular sandwich specimen and needs a thick and stiff metal plate attached to the upper face of the specimen in order to achieve a large range of mode mixities. Large phase angles are obtained at large tilt angles, close to ±90°. The DCB-UBM method is a highly versatile test method that employs a tall test fixture with a system of wires in order to apply moments at the cracked ends of the specimen, and also needs a relatively thick steel plate attached to the debonded face sheet. The MMB fixture (Reeder and Crews, 1990) extended to face/core debond fracture characterization (Quispitupa *et.* al 2009) provides only negative shear loadings, i.e. negative phase angles at the crack tip. For monolithic composites, this is not an issue, but for sandwich composite structures the direction of loading makes a substantial difference, thus making it necessary to incorporate positive shear loading. To accomplish this, the MMB fixture needs to be modified. This will allow performing a more comprehensive fracture characterization of face/core debonds in a sandwich structure over a wide range of positive and negative mode mixities.

2. THE MODIFIED MMB TEST FIXTURE

The original and modified version of the MMB test methods are shown in Fig. 1. Figure 1a shows the original MMB test fixture where the load is introduced at a distance c from the mid-span. In principle the MMB test fixture subjects the crack front to tensile normal (mode I) and sliding (mode II) shear loadings, as depicted schematically in the box inserted in Fig. 1a. As seen in this figure, negative shear loads ($\tau_{xy} < 0$) are imposed by the original MMB fixture, which leads to negative phase angles. The mixed mode loading is varied by changing the location of the compressive force P. Larger c values promote mode I dominated loading and smaller c values mode II dominated loading.

To achieve positive mode mixities at the crack tip requires application of an upward tensile force at a distance c from the mid-span, as depicted in Fig. 1b. The mixed mode loading at the crack tip is controlled by changing the load application point, i.e. c, where c is defined positive for the original MMB version (Fig. 1a) and negative for the modified (Fig. 1b). The stresses acting at the crack tip are shown schematically in the box inserted, i.e. opening mode (σ_y) and shearing mode ($\tau_{xy} > 0$). In Fig. 1b, shear dominated loading, i.e. larger positive mode mixity, is achieved by locating the loading point closer to the mid-span, whereas, mode I dominated loading is achieved by load application near the left end of the specimen.

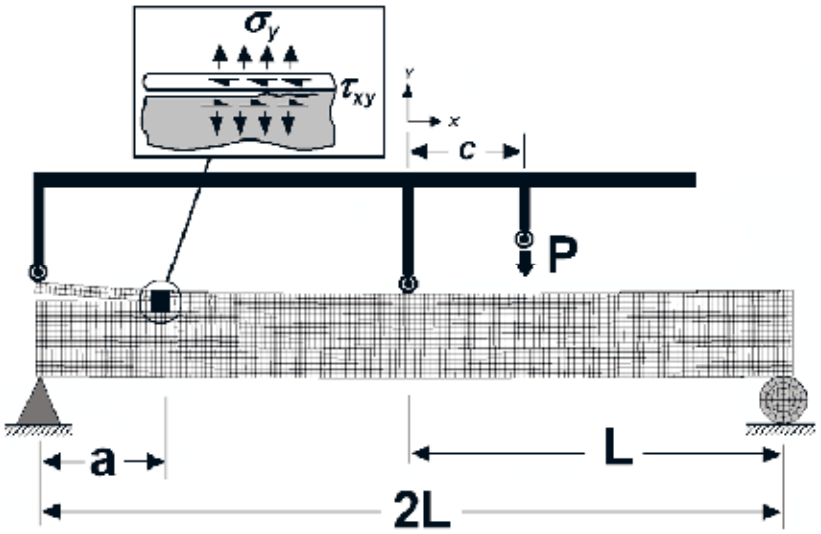

a)

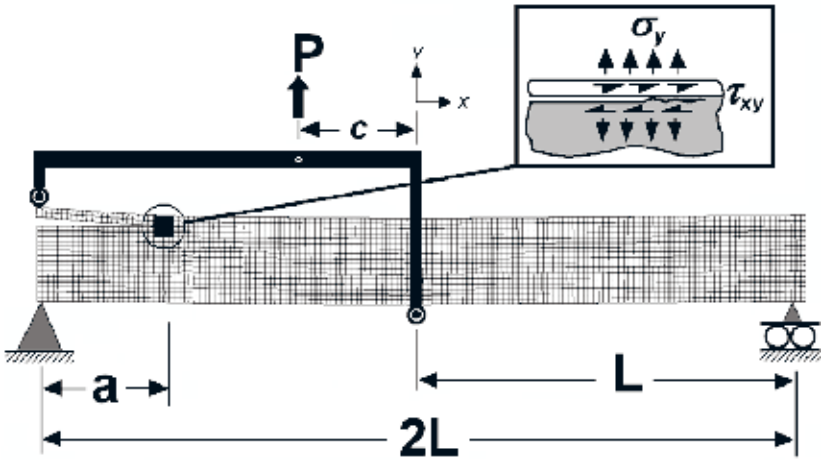

b)

Fig. 1. The MMB test fixture a) original and b) modified (the origin of the XY coordinate system is the mid-span of the MMB specimen)

In order to examine the viability of the modified version of the MMB test fixture as a fracture mechanics specimen suitable for debond fracture characterization, an extensive parametric finite element analysis is performed and presented in this paper. This helps to improve the actual design of the test fixture and understanding of the influence of loading and specimen dimensions and mechanical properties of the face and core materials on the mode mixity at the debond crack tip.

The objectives in this article are; i) propose a modified version of the MMB test fixture for full debond fracture characterization and, ii) to perform finite element analyses in order to assess the modified MMB test method.

3. MIXED MODE FRACTURE

Mixed mode fracture which involves a combination of mode I and mode II at the debond crack tip and results in a fracture toughness that is distinct from the mode I and mode II fracture toughnesses of the interface. In a sandwich composite, the face and core are largely different in terms of mechanical properties which cause the crack tip to be loaded under mixed mode even under global mode I or global mode II loading. The term global mode I or mode II is used to represent the way the loads are applied externally. Global mode I loading resembles the load configuration of a typical double cantilever beam (DCB) (Aviles and Carlsson, 2008), and global mode II that of a cracked sandwich beam (Carlsson, Sendlein and Merry, 1991). The mixed mode loading at the crack tip may be measured by the mode mixity as a phase angle (Hutchinson and Suo, 1990):

$$\psi = \tan^{-1}\left(\frac{\delta_x}{\delta_y}\right) - \varepsilon \ln\left(\frac{x}{h}\right) + \tan^{-1}(2\varepsilon), \tag{1}$$

where δ_x and δ_y are the relative opening and shearing displacements of the crack flanks at a short distance x behind the crack tip, h is a characteristic distance, set equal to the face sheet thickness in this study, and ε is the oscillatory index at the crack tip due to the elastic mismatch of the face and core across the interface. The relative nodal displacements (δ_x and δ_y) are determined from finite element analysis displacement results extrapolated to the crack tip ($x \rightarrow 0$). The mode mixity formulation presented above is termed as the full formulation as it includes the effect of the oscillatory index, ε. For completeness, the reduced mode mixity formulation which assumes that $\varepsilon = 0$, is included:

$$\psi_R = \tan^{-1}\left(\frac{\delta_x}{\delta_y}\right), \tag{2}$$

This measure suppresses the role of the oscillations by assuming β=0 (bi-material Dundurs parameter at the interface, Dundurs 1967) and provides stress intensity factors K_I and K_{II} consistent with ordinary fracture mechanics.

4. FINITE ELEMENT ANALYSIS OF THE MODIFIED MMB TEST

The modified MMB sandwich specimen and the loading configuration are shown in Fig. 1b. A 2-D plane strain finite element (FE) model of the MMB specimen was constructed using the commercial finite element code ANSYS (ANSYS ®). A highly refined mesh at the crack tip is used to accurately resolve the rapidly changing displacements. The total number of elements used in the finite element model was 6512 and the element size at the crack tip was 5μm. PLANE42 elements defined by 4 corner nodes each with two degrees of freedom were used at the crack tip. This type of element was selected since they can support large strains (ANSYS ®). The rest of the specimen was constructed with PLANE82 elements defined by 8-nodes having two translational degrees of freedom at each node. Both types of elements were configured in plane strain. To obtain the local mode mixities at the crack tip, quantified by the phase angles ψ (Eq. (1)) and ψ_R (Eq. (2)), FE analysis was conducted on sandwich specimens with E-glass fiber face sheets and a range of PVC foam cores. Three foam core materials (H45, H100 and H250) were selected for the analysis. The face and core material properties are listed in Table 1.

Table 1. Mechanical properties of face sheet and PVC foams.

	E_x, MPa	G_{xz}, MPa	v_{xz}
DBLT-850 face sheets	16400	2700	0.17
H45 foam	50	15	0.325
H100 foam	135	35	0.325
H250 foam	300	104	0.325

Note that the face sheets are considered homogenous in the finite element analysis (FEA). FEA was conducted on specimens with the following dimensions, span length $2L$ = 160mm, width b = 35mm, face sheet thickness of 2mm and core thickness of 10mm.

The mixed mode loading in the modified MMB fixture is controlled by varying the load application point, c as depicted in Fig. 1b. Figure 2a shows the phase angles (ψ and ψ_R) vs. the loading position for a specimen with H45 core. Results presented in Fig. 2a shows the phase angles provided by using both version of the MMB text fixture. It can be observed that positive phase angles are achieved by using the modified version of the MMB test fixture, whereas negative phase angles are provided by the original MMB test fixture. As seen in Fig. 2a, the phase angle, using full mode mixity formulation, ranges from $-87° < \psi < 67°$, and using the reduced formulation $-60° < \psi_R < 88°$. It can also be observed that the phase angle for both versions of the MMB fixture changes rapidly as c/L approaches 0 when shear loading at the crack tip increases.

Figure 2b present the phase angles for an MMB specimen for a range of crack lengths, a/L, at a constant lever position c/L = 0.1. For short cracks significant changes in the phase angle are observed, similar to the situation for the original MMB sandwich specimen (Quispitupa *et* al, 2009). This can be attributed to the large shear deformation in the core at short crack lengths (Carlsson et al, 1991). It can be observed that the phase angle is roughly independent of crack length for $a/L \geq 0.2$, for all core materials evaluated, similar to the original MMB test method (Quispitupa *et* al, 2009). This observation is important if fatigue tests at constant phase angles are to be performed. There are some small changes in the phase angle for the specimens with H45 and H100 cores for $a/L > 0.2$, however these are very small and can be neglected. Fracture toughness of the face/core interface does not change due to small changes of the phase angle, as shown experimentally by (Quispitupa *et* al, 2011). Based on these results, it is suggested to use an initial crack length $a/L \geq 0.2$ that promotes an approximately constant phase angle at the crack tip. Furthermore, when performing fracture experiments, a single MMB specimen can potentially be used several times as the phase angle remains constant, thus reducing testing time and number of test coupons needed for the fracture toughness characterization.

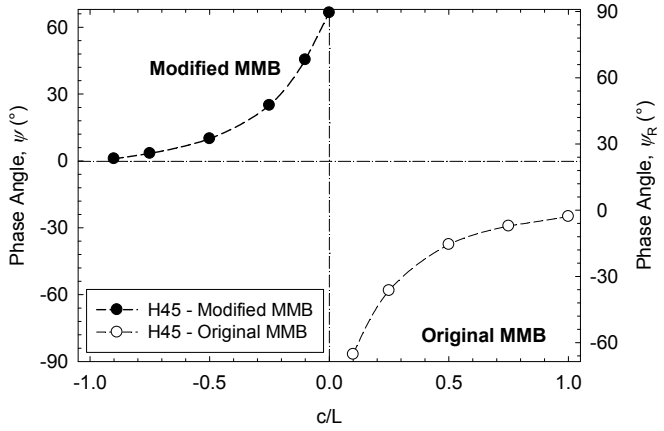

(a)

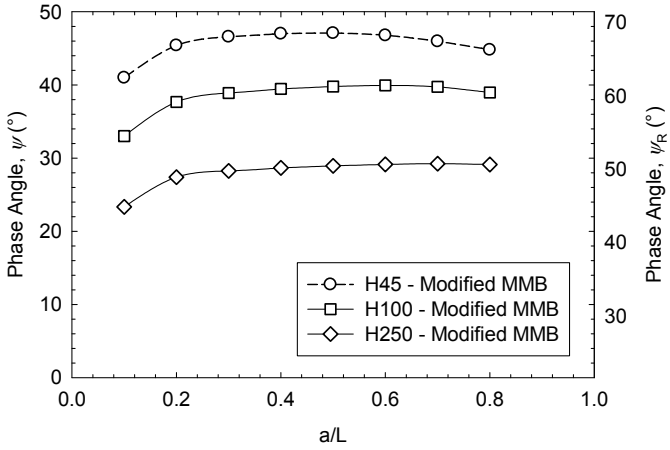

(b)

Fig. 2. Phase angle (full, ψ, and reduced, ψ_R, formulations) as function of a) loading lever position for sandwich specimen with a H45 core, and b) crack length (a load of 1N/b was applied to the specimen)

Figure 3 present the results of phase angle vs. loading lever position for both versions of the MMB test fixture for the three core materials examined. As can be observed, a wide range of phase angles, from negative to positive are achieved by the combined use of the modified and original MMB fixture. This result is very convenient as face/core debond fracture characterization of interfacial crack problems needs to be performed at a wide range of phase angles, especially during fatigue of sandwich structures subject to fully reversed load cycles. As observed in Fig. 3, the large range of mode mixities is achieved for the specimen with H45 core, i.e. materials combination with large elastic mismatch. Furthermore, for both versions of the MMB test fixture, high shear loadings are imposed at the crack tip as $c/L \rightarrow 0$.

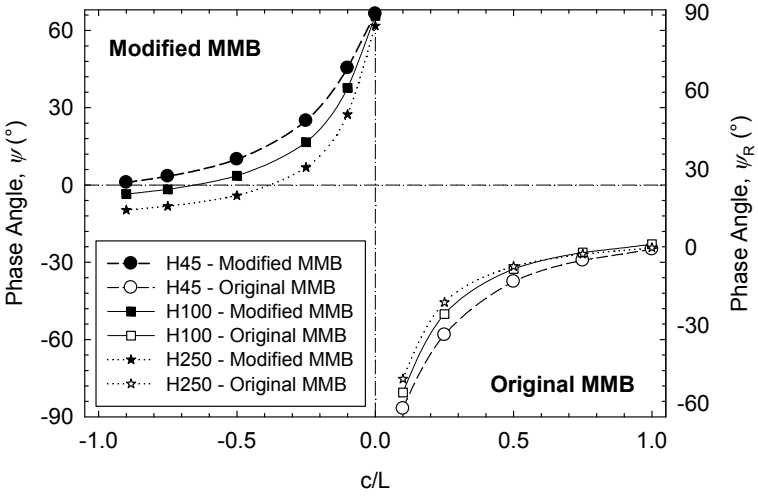

Fig.3. Phase angle (full, ψ, and reduced, ψ_R, formulations) as function of loading lever position for the modified and original MMB test fixtures. Core materials examined are H45, H100 and H250.

5. CONCLUSIONS

A modified version of the MMB test fixture for face/core debond fracture characterization under positive shear loading is proposed. Finite element analysis of the modified version of the MMB test fixture showed that it is actually possible to impose positive shear loading at the crack tip and thus positive mode mixities. It was shown that for crack lengths greater than 20% of the half span length ($a/L > 0.2$), the phase angle is independent of crack length which is very convenient for the condition of fatigue testing under constant phase angles. Finally, by using both versions of the MMB fixture, a wide range of positive and negative phase angles are achieved. This will allow performing a full face/core debond fracture characterization of sandwich composites.

REFERENCES

ANSYS 12, User Manual. Swanson Analysis System, Houston, PA.

ASTM D6671/D 6671M-06. (2006). Standard Test Method for Mixed Mode I-Mode II Interlaminar Fracture Toughness of Unidirectional Fiber Reinforced Polymer Matrix Composites. ASTM International, Philadelphia, PA.

Avilés F. and Carlsson L.A. (2008). "Analysis of the Sandwich DCB Specimens for Debond Characterization", Engineering Fracture Mechanics, 75:153-168.

Berggreen C. and Carlsson L.A. (2010) "A modified TSD specimen for fracture toughness characterization – fracture mechanics analysis and design", Journal of Composite Materials, DOI: 10.1177/0021998309360937.

Carlsson L.A. and Kardomateas G.A. (2011). Structural and Failure Mechanics of Sandwich Composites, Springer, Dordrecht.

Carlsson L.A., Sendlein L.S. and Merry S.L. (1991). "Characterization of Face/Core Shear Fracture of Composite Sandwich Beams", Journal of Composite Materials, 25(1):101-116.

Dundurs J. (1967). "Effect of Elastic Constants on Stress in Composites under Plane Deformation", Journal of Composite Materials, 1(3), 310-322.

Hutchinson J.W. and Suo Z. (1992) "Mixed Mode Cracking in Layered Materials. Advances in Applied Mechanics", J.W. Hutchinson and T.Y. Wu Eds. 29, 63-191.

Li X. and Carlsson L.A. (1999) "The tilted sandwich debond (TSD) specimen for face/core interface fracture characterization", Journal of Sandwich Structures and Materials, 1, 60-75.

Ozdil F. and Carlsson L.A. (2000). "Characterization of Mixed Mode Delamination Growth in Glass/Epoxy Composite Cylinders", Journal of Composite Materials, 34(5), 420-441.

Quispitupa A., Berggreen C. and Carlsson L.A. (2009). "On the Analysis of the Mixed Mode Bending (MMB) Sandwich Specimen for Debond Fracture Characterization", Engineering Fracture Mechanics, 76(4), 594-613.

Quispitupa A., Berggreen C. and Carlsson L.A. (2011). "Face/core Interface Fracture Characterization of Mixed Mode Bending Sandwich Specimens", Fatigue and Fracture of Engineering Materials and Structures, In press.

Reeder J. and Crews J.H. (1990). "Mixed-Mode Bending Method for Delamination Testing", AIAA Journal, 28(7), 1270-1276.

Sørensen B.F., Jørgensen K., Jacobsen T.K. and Østergaard R.C. (2006) "DBC Specimen Loaded with Uneven Bending Moments", International Journal of Fracture, 14(1), 163-176.

Proceedings of the 32nd
Risø International Symposium on Materials Science:
Composite materials for structural performance:
Towards higher limits
Editors: S. Fæster, D. Juul Jensen,
B. Ralph, B.F. Sørensen
Risø National Laboratory for Sustainable Energy,
Technical University of Denmark, 2011

WIND TURBINE BLADE TESTING UNDER COMBINED LOADING

A. Roczek-Sieradzan, M. Nielsen, K. Branner,
F.M. Jensen and R. Bitsche.

Wind Energy Division, Risø National Laboratory for Sustainable Energy, Technical University of Denmark, Roskilde, Denmark

ABSTRACT

The paper presents full-scale blade tests under a combined flap- and edgewise loading. The main aim of this paper is to present the results from testing a wind turbine blade under such conditions and to study the structural behavior of the blade subjected to combined loading. A loading method using anchor plates was applied, allowing transverse shear distortion. The global and local deformation of the blade as well as the reproducibility of the test was studied and the results from the investigations are presented.

1. INTRODUCTION

Today, wind turbine blade certification tests are based on flapwise and edgewise loading only. However, some results have indicated that loads in other directions than pure flap- or edgewise may have major importance and failure mechanisms related to transverse shear distortion discussed in (Jensen 2008) may also be sensitive to this loading direction.

The aim of this study is to investigate how combined loading can be performed on full-scale testing of wind turbine blades without limiting its possibility to deform in shear distortion. The aim is also to investigate how important shear distortion is in blade failure and how it can be prevented.

A thorough analysis of the behavior of wind turbine blades validated by testing is needed in order to improve their structural design and move the design limits. The testing and numerical simulations performed at Risø DTU, see (Berggreen, Branner, Jensen, Schultz 2007; Luczak. Manzato, Peeters, Branner, Berring, Kahsin 2007; Jensen 2008; Jensen Puri, Dear, Branner, Morris 2011) have resulted in a considerable increase in knowledge about the structural response and failure of wind turbine blades.

2. METHODS FOR BLADE TESTING

The tests presented were performed on a 34m long blade from SSP technology A/S. A more detailed description of the loading conditions, measuring methods, test setup and preparation are found in (Nielsen, Jensen et al. 2010) and in (Nielsen, Nielsen et al. 2010) the combined load definition and test methods are described in detail.

2.1 Combined Load Case Background. Under normal operation the blade profile is moving towards the wind at a small angle. The resulting aerodynamic force is therefore mainly pointing flapwise towards the suction side, and slightly angled towards the leading edge. A typical load in the flapwise direction is shown in Fig. 1.

Fig. 1. Pressure distribution on an aerodynamic profile generating the aerodynamic loads.

In the edgewise direction, the main loads are a gravity load and the dynamic loads, which e.g. result from an emergency stop of the turbine.

A part of the present project was to explore which loads and loading directions were appropriate in a combined load case examination of the blade.

For the SSP 34m blade the available loads were the extreme loads in the flap- and edgewise directions. Thus, the determination of the loading on the blade was performed from these and the magnitudes of the loads were made by vector addition of the extreme loads in flap- and edgewise directions. The loads were then applied at an angle of 30°, measured from the flapwise direction towards the leading edge.

2.2 Loading. For the combined load test the blade is mounted on the test rig as shown in Fig. 2. This loading method is based on a new concept and the process of test preparation and load application is described in more details in (Nielsen, Nielsen et al. 2010). The way the blade is positioned allows the force to be applied on the suction side of the blade pulling towards the floor, which creates an angle of 30^{o} with the flapwise plane.

The loads are defined as % of Risø loads, where 100% Risø loads represent the ultimate load where a similar blade failed in a flapwise test.

Fig. 2. The blade bolted to the test rig. The tip was truncated at 25m. The blade is loaded at a 30^{o} angle to the flapwise direction, simulating combined flap- and edgewise loads.

A load application method using anchor plates was applied as presented in Fig. 3. The anchor plates are specially shaped steel fittings attached to the blade with an epoxy adhesive.

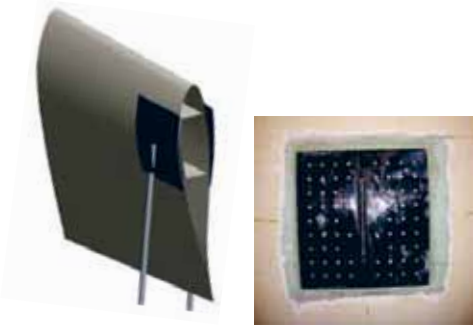

Fig. 3. Load application using anchor plates. In the performed test the anchorplates glued to the blade had a surface area of 500x500mm.

Several possibilities for the load introduction were investigated in order to allow the blade to deform freely. Considering all aspects, as presented in (Nielsen, Nielsen et al. 2010), it was decided to only use one anchor plate at each of the three loaded sections.

3 RESULTS

The results of full-scale blade testing under combined loading are presented in this section.

3.1Global Behavior. Before testing the combined load case, finite element analysis (FEA) was performed in order to predict the possible failure of the blade. It indicated buckling of the cap at approximately 8.5m from the root at a load of approximately 111% of the Risø load.

The measurement of the global displacement of the blade in the horizontal direction (parallel to the floor is presented in Fig. 4. It can be observed that the blade deflects towards the pressure side and the leading edge in the region close to the root, but towards the suction side and the trailing edge in the region close to the tip.

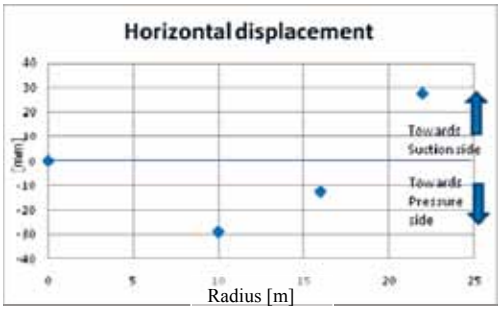

Fig. 4. Horizontal displacement measured at 55% of the Risø combined load.

The deformations at different sections were studied at 4m, 7m and 10m from the root. Fig. 5 presents the results for the 10m section. At small loads the blade section is twisting counter-clockwise as seen from the root, while it starts to twist clockwise as the load is increased. This behavior is sketched for the same section in Fig. 6.

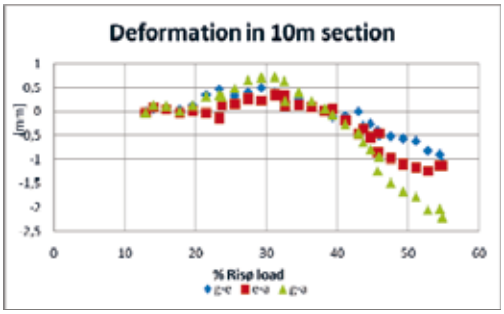

Fig. 5. Deformation of the 10m section: Difference in vertical displacement between the points *g, e* and *a* (location indicated in Fig. 6).

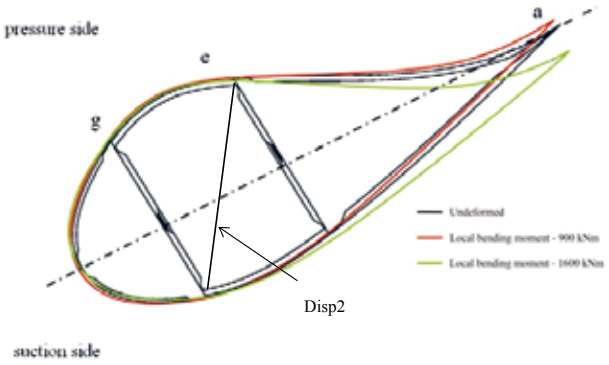

Fig. 6. Sketch of the10m section showing the blade behavior during loading. Black line: undeformed configuration, red line: local bending moment 30% Risø load, green line: local bending moment 55% Risø load.

The FEM calculations showing the change of the length of a box girder diagonal along the blade radius is confirming this observation. Fig. 7 shows the relative length change of a box girder diagonal for different load levels as predicted by the FE model. It can be observed that the radial position where the deformation of the diagonal switches sign moves outward with increasing load. At the 10m section the length of the diagonal first increases, and then decreases as the load is increased. The switch from one side to the other at the 10m section happens at approximately 40% loads, which is in agreement with the measured results presented in Fig. 5.

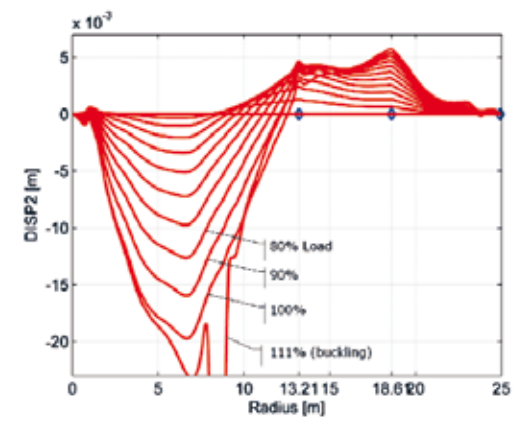

Fig. 7. Relative length change of a diagonal of the box girder for different load levels (0%, 10%, ... , 90%, 100%, 111%) as predicted by the FE model. (Buckling of the suction side cap can be observed at r=8.5m and 111% load.)

3.2 Transverse Shear Distortion. One of the focus areas of the combined load test was investigating the "transverse shear distortion", as it may be an important failure mechanism for this loading case. The phenomenon of transverse shear distortion is presented schematically in Fig. 8.

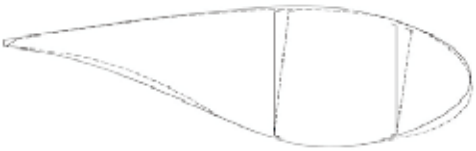

Fig. 8. Schematic presenting transverse shear distortion behavior.

The transverse shear distortion was measured for loads up to 90% Risø load. The measurements were performed in steps where the load was increased. The tests were first carried out with the blade reinforced with wires to prevent the transverse shear distortion, see Fig. 9 (red arrows). Then the wires were removed and the test was repeated. Both tests with and without reinforcement were carried out successfully without any damage to the blade.

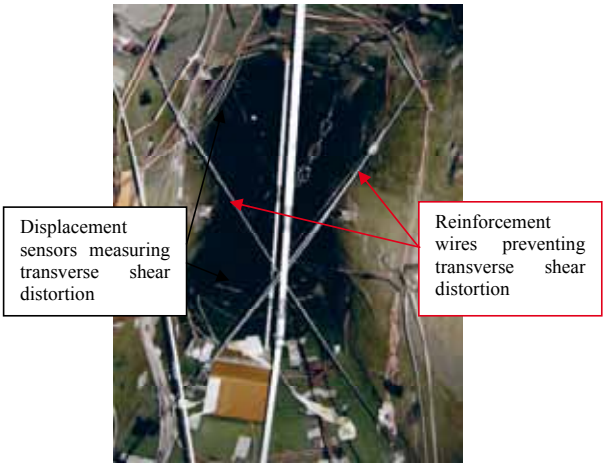

Fig. 9. Photograph taken inside the blade showing the reinforcement wires, and the measurement equipment installed between the two webs. The length of the reinforcement wires in front of the picture are approximately 2m.

Fig. 9 also shows the displacement sensors mounted inside the blade, where the diagonal lines crossing inside of the box are strings that allow measuring the distance between the corners (black arrows).

The comparison of these tests showed a reduction of the transverse shear distortion when the reinforcement was applied, see Fig. 10.

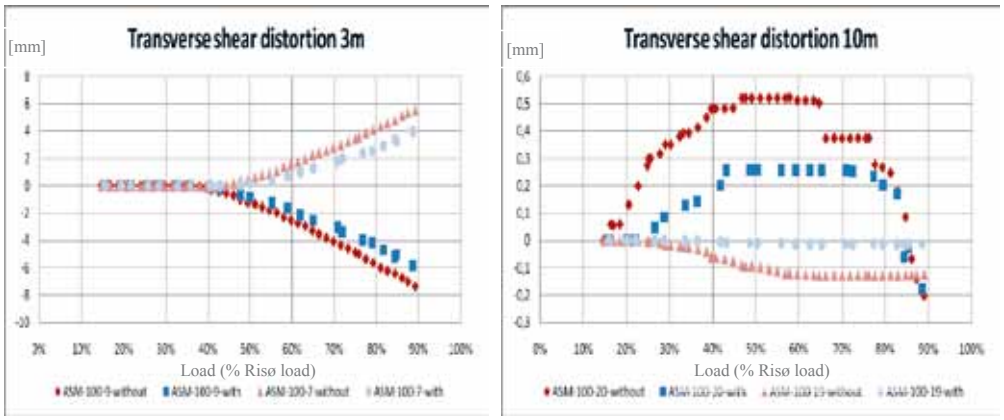

Fig. 10. Transverse shear distortion in 3m and 10m sections with (blue symbols) and without (red symbols) reinforcements.

3.3 Reproducibility of the Measurements. Some of the tests were repeated without making any changes in the measurement procedure. In Fig. 11, the transverse shear distortion (see Section 3.2) in the 3m section is presented. The tests were performed in the following order: a – b – c. The results presented here reveal that the measured deformations did not follow the same path at a lower loading value when the test was repeated.

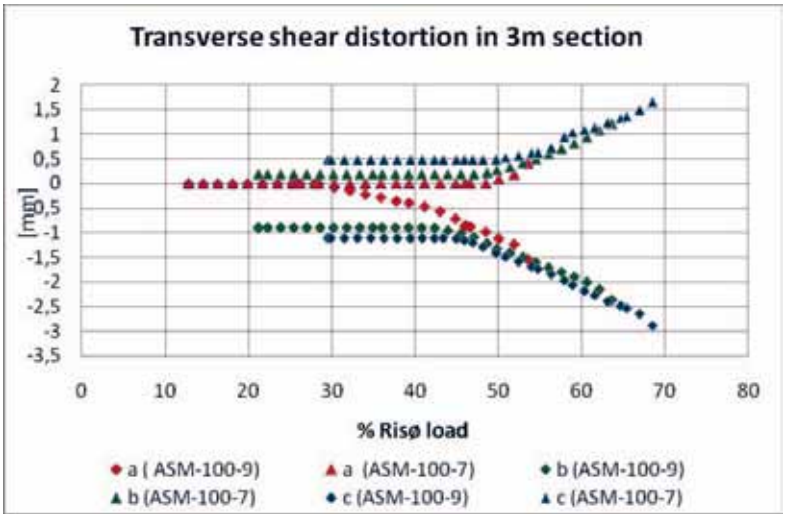

Fig. 11.Data from 3 repeated pulls showing the transverse shear distortion in the 3m section, a (red) the first pull, b (green) the second pull and c (blue) the third pull.

Such behavior was observed at many locations and for different structural components such as panels and webs, see also (Nielsen, Jensen et al. 2010).

4 CONCLUSIONS

This work presents full-scale tests of a wind turbine blade under combined flap and edgewise loading, i.e. at 30° angle from the flapwise plane towards the leading edge.

The global and local deformation of the blade as well as the reproducibility of the tests was studied and some of the results were compared to FE analyses. In this investigation, the FEA closely resembled the behavior of the blade.

Repeated measurements of local deformations indicate that these are only reproducible to some extent. The blade does not behave perfectly elastically, and the results from these measurements depend on the ways in which the blade are loaded and on the previous loading case. Measurements of local deformations has thus to be treated very carefully as the deviation might exceed 50% at a low load level and in the case the load history differs.

The tests presented in this paper provide no indication that transverse shear distortion may result in failure for this particular wind turbine blade in combined loading. It is shown that diagonal steel wire reinforcements can reduce the transverse shear distortion. Such reinforcements may be a reasonable solution, if action should be taken in order to prevent transverse shear distortion.

ACKNOWLEDGEMENTS

The authors wish to thank Per H. Nielsen and Peter Berring (both from Risø DTU) for extremely valuable input that helped performing and interpreting the measurements.

The project is supported by Danish Energy Agency through the Energy Technology Development and Demonstration Program (EUDP 2010). The supported EUDP-project is titled "Experimental Blade Research – phase 2" and has journal no. 64011-0006.The support is gratefully acknowledged.

REFERENCES

Berggreen, C., Branner, K., Jensen, J. F. & Schultz, J. P., (2007).Application and Analysis of Sandwich Elements in the Primary Structure of Large Wind Turbine Blades, Journal of Sandwich Structures and Materials, Volume 9 Issue 6, November 2007, pp. 525-552, DOI: 10.1177/1099636207069071.

Luczak, M., Manzato, S., Peeters, B., Branner, K., Berring, P. & Kahsin, M., (2011). Dynamic Investigation of Twist-bend Coupling in a Wind Turbine Blade, Journal of Theoretical and Applied Mechanics, Volume 49 Issue 3, 2011.

Jensen, F.M.,(2008). Ultimate strength of a large wind turbine blade, Risø-PhD-34(EN).

Jensen, F.M., Puri, A.S., Dear, J.P., Branner, K. & Morris, A.,(2011). Investigating the Impact of Non-linear Geometrical Effects on Wind Turbine Blade - Part 1: Current Issues and Future Challenges in Design Optimisation, Wind Energy, Volume 14 Issue 2, March 2011, pp. 239-254, DOI: 10.1002/we.415.

Nielsen, M., Jensen, F.M., Nielsen, P., Berring, P., Martyniuk, K., Roczek, A., Sieradzan, T., Roudnitski, V., Kucio, P., Bitsche, R., Andresen, P., Lukassen, T., Andrlová, Z., Branner, K., Bak, C., Kallesøe, B., McGugan, M., (2010). Full scale test of SSP 34m blade, edgewise loading LTT. Data report 1. Risø-R-1718(EN).

Nielsen, P., Nielsen, M., Jensen,F.M., Roczek-Sieradzan, A., P. Berring, Sieradzan, T., Roudnitski, V., Bitsche, R., Knudsen, H., Rasmussen, A., Rasmussen, J., Uldahl, U., Andrlová, Z., Branner, K., Bak, C., Kallesøe, B., McGugan, M., Wedel-Heinen, J., Riber. H.J., Jensen, C., Lagerbon, M., (2010). Full Scale Test of SSP 34m blade, combined edge- and flapwise loading. Data Report. Risø-R-1749(EN).

Proceedings of the 32nd
Risø International Symposium on Materials Science:
Composite materials for structural performance:
Towards higher limits
Editors: S. Fæster, D. Juul Jensen,
B. Ralph, B.F. Sørensen
Risø National Laboratory for Sustainable Energy,
Technical University of Denmark, 2011

FRACTURE LENGTH SCALES IN DELAMINATION OF COMPOSITE MATERIALS

R. B. Sills* and M. D. Thouless**, ***

* Gas Transfer Systems, Sandia National Laboratories, Livermore, CA 94550 USA
** Department of Mechanical Engineering, University of Michigan, Ann Arbor, MI 48109 USA
*** Department of Materials Science & Engineering, University of Michigan, Ann Arbor, MI 48109 USA

ABSTRACT

Cohesive zone models of fracture have seen great success in modeling delamination and debonding of composite materials (Aymerich, Dore, and Priolo 2009; Li, Thouless, Waas, Schroeder, and Zavattieri 2005b; Yang and Cox 2005). By embedding cohesive zone elements along potential crack planes, arbitrary delamination configurations can be represented without the need for an a priori knowledge of crack locations or pre-existing cracks. The stress-displacement behavior of elements in cohesive zone modeling is governed by cohesive or traction-separation laws, which dictate the tractions across the interface as a function of the crack plane separations. For mixed-mode problems, orthogonal sets of cohesive laws can define these relationships for each mode. In fibrous composites, various toughening mechanisms such as matrix cracking and fiber bridging operate at different strengths and length scales forming a complicated amalgamation of processes that are difficult to model directly. With cohesive zone modeling, these processes can be accounted for in the cohesive law via the fracture length scale. Many authors have pointed out that the shape of the traction-separation law and its associated fracture length scales is dictated by the cohesive mechanisms at work (Dávila, Rose, and Camanho 2009; Li, Thouless, Waas, Schroeder, and Zavattieri 2005a; Yang and Cox 2005) but a general framework for understanding how the evolution of these mechanisms with loading manifest themselves within the cohesive zone structure has not been presented. In this work, such a framework will be developed by defining an average fracture length scale that is a property of the load state along the crack plane. With this new length scale, the effects of cohesive law shape can be understood – allowing a direct connection between law shape and physical process.

1. INTRODUCTION

Cohesive zone models of fracture provide a broad framework for representing material behavior during fracture or delamination. By defining the normal and shear tractions across potential fracture planes, arbitrary crack configurations can be modeled without the need for an a priori knowledge of crack locations. The relationships defining these tractions are known as cohesive or traction-separation laws and they relate the tractions to the opening displacements between the planes. An example of a traction-separation law is given in Fig. 1. The area swept out under-the-curve at any increment of load is the strain energy release rate, $\mathcal{G}$, and the net area under-the-curve is the toughness of the interface, Γ. By introducing finite stresses at the crack tip, cohesive zone models of fracture provide a means for understanding the effects of cohesive strengths on fracture (Tvergaard and Hutchinson 1992; Parmigiani and Thouless 2007). Furthermore, these finite stresses introduce a length scale absent in linear-elastic fracture mechanics (LEFM) known as the fracture length scale. This length scale is generally defined as (Hillerborg, Modéer, and Petersson 1976; Bao and Suo 1992):

$$\zeta_{nominal} = \frac{\Gamma E}{\hat{\sigma}^2} \tag{1}$$

where Γ is the toughness, E is the modulus of elasticity, and $\hat{\sigma}$ is the peak stress of the traction-separation law (see Fig. 1). It has been demonstrated by numerous authors that this length scale is instructive in predicting whether the Inglis (1913) strength approach to fracture or the Griffith (1920) energy approach will predict the crack behavior (Bao and Suo 1992; Parmigiani and Thouless 2007). When the fracture length scale is small compared to all physical dimensions, energy dominates the fracture process, the assumptions necessary for LEFM are valid, and the material and geometry is said to be flaw intolerant (notch sensitive). When the length scale is large, strength is the dominating property causing net-ligament failure and flaw insensitivity. If the length scale exists between these extremes, both strength and energy will play a role.

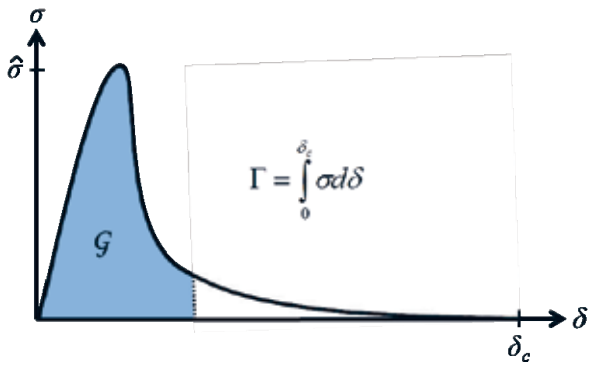

Fig. 1. A basic traction-separation or cohesive law.

Traction-separation laws can take any shape depending on the toughening and deformation processes present. Such a generality allows for the accurate depiction of a broad range of materials. In the case of fibrous composite materials numerous processes contribute to the cohesive tractions including matrix cracking, fiber breakage, delamination, and pullout, and frictional sliding. The law shape can be derived by direct measurement of tractions and displacements (Sørensen and Jacobsen 1998), performing strength and toughness characterizing

mechanical tests (Li *et al.* 2005b), or with micromechanical modeling (Sørensen, Gamstedt, Østergaard, and Goutianos 2008).

Many authors have found that in modeling material systems, details regarding the shape of the traction-separation law are of secondary importance as long as the toughness and cohesive strength (peak stress) are correct - it is upon this assumption that Eqn. 1 was derived. Sills and Thouless (2011a,b) however, demonstrated that the law shape and fracture length scale are intrinsically linked. Extending the fracture length scale concept to any increment of load, they defined an instantaneous fracture length scale as:

$$\zeta_{inst.} = \frac{\Gamma E}{\sigma_{ave}^2} \tag{2}$$

where σ_{ave} is the average stress of the cohesive law at the current load increment and displacement, δ_i, given by:

$$\sigma_{ave} = \frac{1}{\delta_i}\int_0^{\delta_i} \sigma d\delta = G(\delta_i)/\delta_i \tag{3}$$

With Eqn. 2, a linear traction-separation law will have an instantaneous fracture length scale that is independent of the load increment and inversely proportional to the slope. Any nonlinear cohesive law will have a changing fracture length scale as the system is loaded. In mixed-mode problems, each mode has its own fracture length scale given by the relevant displacement (normal, in-plane tangential, or out-of-plane tangential) and strain energy release rate component. How these fracture length scales combine and form an overall fracture length scale is not clear (Sills and Thouless 2011b), however it is clear that law shape must be accounted for in calculating the fracture length scale.

It should be noted that in the case of large scale bridging (when the length of the bridging zone becomes comparable to a characteristic physical dimension), the physical manifestation of the fracture length scale becomes dependent on a characteristic physical dimension (Bao and Suo 1992; Yang and Cox 2005). This is due to the fact that the compliance of the system limits the development of the process zone. In this work, the fracture length scale will be examined independent of specimen size and geometry.

A large effort has been put forth to understand the fracture length scale in the context of delamination in composite materials. Most of the relationships given in the literature are derived upon the assumption that law shape is of secondary importance and no work to date, to the authors' knowledge, takes into account the evolution of the fracture length scale with loading. The impetus for this work is then to understand the behavior of the fracture length scale during delamination in composites.

2. DESCRIPTION OF THE DELAMINATION PROCESS

The delamination behavior of composites can vary greatly as a function of the fiber and matrix materials, fiber volume fraction, ply composition and orientation, and the specimen geometry. In general, however, the process can be decomposed into two stages: matrix cracking and fiber bridging. Matrix cracking initiates the delamination process and is generally considered to

occur in a manner consistent with linear-elastic fracture mechanics – the toughness of the fiber-reinforced matrix dominates crack growth. Following the matrix crack, fibers can bridge the crack opening for a significant amount of growth as they undergo debonding, pull-out, and frictional sliding. The bridging portion of the crack growth process is often considered within the context of a bridging law, which dictates the tractions applied by the bridging fibers as a function of the crack face displacements in the same way a cohesive law does. Cohesive and bridging laws differ only in how their abscissa is defined – cohesive laws describe the entire delamination process while bridging laws only focus on crack growth after the matrix crack has formed; this work focuses on the former. From a computational point of view cohesive laws are more useful because they allow cracks to be modeled easily from an equilibrium (unloaded) state.

Many authors have noted that the various portions (displacement regimes) of traction-separation laws for composite materials can be thought of as representing different toughening and deformation mechanisms (Dávila *et al.* 2009; Gutkin, Laffan, Pinho, Robinson, and Curtis 2011; Li *et al.* 2005b; Yang and Cox 2005) – this work will make use of this observation as follows. Before matrix cracks develop or grow, the system behaves in a linearly elastic manner with the opening behavior being dictated primarily by the matrix and fiber moduli and the fiber volume fraction. Matrix cracks then form, either on their own or due to fiber debonds, and grow up to when the matrix strength, $\hat{\sigma}_m$, and toughness, Γ_m, are reached. The crack faces are then primarily supported by fiber ligaments that bridge between them, providing tractions that start at some peak bridging value, $\hat{\sigma}_b$, and decay to zero as the strain energy release rate approaches the sum of the matrix and bridging toughness, Γ_b. This simple description of the delamination process can be represented by the tri-linear cohesive law in Fig. 2. With this model, matrix cracking dominates the stress-displacement behavior when the opening displacement, δ, is less than δ_m. Beyond this value, fiber bridging governs the response until all of the fibers fully pull-out or break at the critical displacement, δ_c.

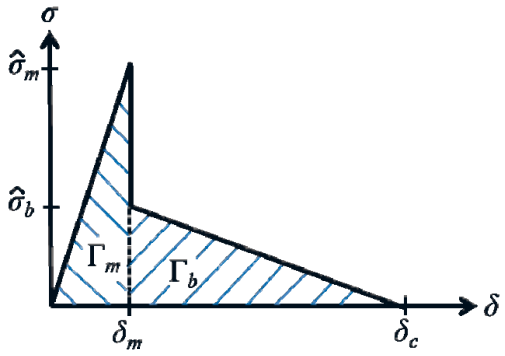

Fig. 2. The traction-separation law used to model composite delamination in this work. Subscripts *m* and *b* represent matrix cracking and fiber bridging, respectively.

3. COHESIVE LAW FORMULATION

For a general tri-linear cohesive law, the traction-separation law has the piecewise form (Gutkin *et al.* 2011):

$$\sigma(\delta)=\begin{cases}\dfrac{\hat{\sigma}_1}{\delta_1}\delta^2 & 0\le\delta\le\delta_1\\ \dfrac{\hat{\sigma}_1}{\delta_2-\delta_1}\left[\left(\dfrac{1}{R}-1\right)\delta+\left(\delta_2-\dfrac{\delta_1}{R}\right)\right] & \delta_1<\delta\le\delta_2\\ \dfrac{\hat{\sigma}_1}{R(\delta_c-\delta_2)}(\delta_c-\delta) & \delta_2<\delta\le\delta_c\end{cases} \tag{4}$$

where the subscripts 1 and 2 denote the ends of the first and second linear segments and R is the strength ratio, $\hat{\sigma}_1/\hat{\sigma}_2$. For this work, the differentiation between the displacements δ_1 and δ_2 is unnecessary and so to reduce the number of parameters all results will be derived with $\delta_1=\delta_2$.

As discussed above, the cohesive law used in this work will represent matrix cracking followed by fiber bridging. This formulation is convenient because it is a direct analog to much of the fiber bridging literature, which considers a toughness at the crack tip (matrix cracking) and a toughness and strength in the bridging zone. In order to fully define the law shape, four of the following six parameters must be specified:

$$\hat{\sigma}_m \quad \hat{\sigma}_b \quad \Gamma_m \quad \Gamma_b \quad \delta_m \quad \delta_c$$

where the first four retain the definition used above, δ_m is the displacement after full matrix crack-dominated growth, and δ_c is the critical displacement upon complete fiber-ligament failure. These variables are depicted in Fig. 2.

4. FRACTURE LENGTH SCALES

By using Eqn. (4) in Eqn. (3) and applying the result to Eqn. (2), the instantaneous fracture length scale for our model traction-separation law as a function of the opening displacement is given by:

$$\zeta/\delta_c=\begin{cases}2\left(\dfrac{E^*}{\hat{\sigma}_m}\right)\left(\dfrac{G}{R+G}\right) & 0\le\delta\le\delta_m\\ \left(\dfrac{E^*}{\hat{\sigma}_m}\right)\left(\dfrac{\delta}{\delta_c}\right)^2\left(\dfrac{G}{R+G}\left(\dfrac{1}{2}-\dfrac{1}{R}-\dfrac{G}{2R^2}\right)+\dfrac{\delta}{\delta_c}\left(\dfrac{1}{R}+\dfrac{G}{R^2}\right)-\dfrac{1}{2}\left(\dfrac{\delta}{\delta_c}\right)^2\dfrac{R+G}{R^2}\right)^{-1} & \delta_m<\delta\le\delta_c\end{cases} \tag{5}$$

where $G=\Gamma_m/\Gamma_b$, the toughness ratio, $R=\hat{\sigma}_m/\hat{\sigma}_b$, the strength ratio, and E^* is the effective modulus. Note that the two key displacements are related by $\delta_m/\delta_c=G/(R+G)$. For a bimaterial interface crack, the effective modulus is $2\overline{E}_1\overline{E}_2/\left(\overline{E}_1+\overline{E}_2\right)$, where the subscripts 1 and 2 denote the two materials (Sills and Thouless 2011b). Eqn. (5) provides a simple formulation for understanding the effects of relative changes in toughness and strength on the fracture length scale.

Fracture length scales have been calculated using Eqn. (5) for a variety of toughness and strength ratios – changing these parameters can be thought of as modifying the matrix or fiber material, or the interface between the two. Fig. 3 presents how the fracture length scale evolves with loading (displacement) for toughness ratios of G=1, 10, 100, strength ratios of R=1, 10, 25,

50, 100 and with $E^*/\hat{\sigma}_m = 1$. In all cases, the length scale starts small during the matrix cracking phase and grows with loading as fiber bridging takes over up to a peak value at fracture ($\delta=\delta_c$). For values of R less than 1, the length scale will actually shrink for some portion of loading but the overall behavior is not appreciably different. All cases begin with the length scale assuming a constant value due to the initial linear portion of the traction-separation law, as discussed above. When the matrix toughness is small relative to the fiber bridging toughness (small G), the fracture length scale at fracture is highly sensitive to the strength ratio, taking larger values as the matrix becomes significantly stronger than the bridging fibers. As the toughness ratio grows, the length scale growth becomes less pronounced and less sensitive to R eventually becoming independent of it – in the limiting case, the cohesive law has a pure linear hardening shape and the fracture-length scale is completely independent of load.

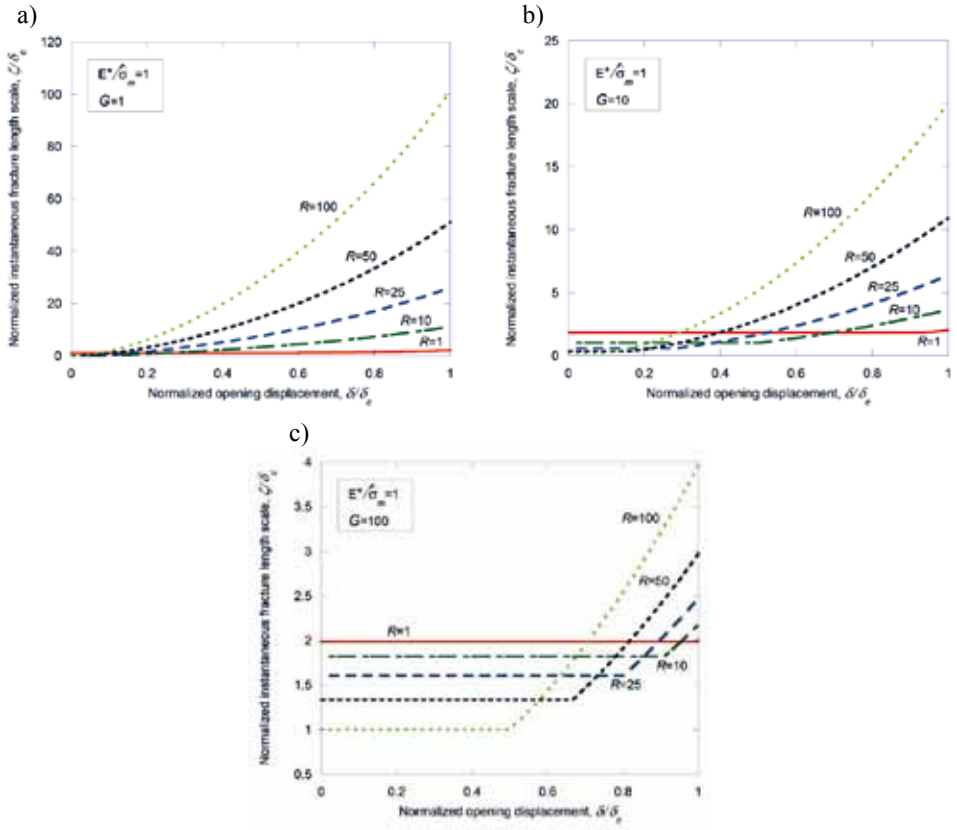

Fig. 3. The fracture length scale of the model traction-separation law depicted in Fig. 2 when $E^*/\hat{\sigma}_m = 1$, R=1, 10, 25, 50, and 100 and G=1(a), 10(b), and 100(b).

To further understand how the fracture-length scale behaves, values at fracture have been calculated and plotted in Fig. 4. In this plot, it can clearly be seen that the length scale shrinks rapidly as matrix cracking toughens relative to fiber bridging. A similar trend has been elucidated by Cox and Marshall (1994) in considering the ratio of the toughness at the crack tip to the bridging zone – their length scale assumes a bridging law with a constant bridging stress and in the notation of this work can be expressed as:

$$\zeta(\delta_c)/\delta_c = \frac{\pi}{4}\left(\frac{E^*}{\hat{\sigma}_m}\right) R\left[\sqrt{1+G}-\sqrt{G}\right]^2 \tag{6}$$

This expression applies to small-scale bridging where the fracture process is fully characterized by energy considerations – the stresses at the crack tip are singular and when G is of order unity. Eqn. (6) has also been plotted in Fig. 4 with R=1000 – the curve approximately matches the results from this work around G≈1, as expected.

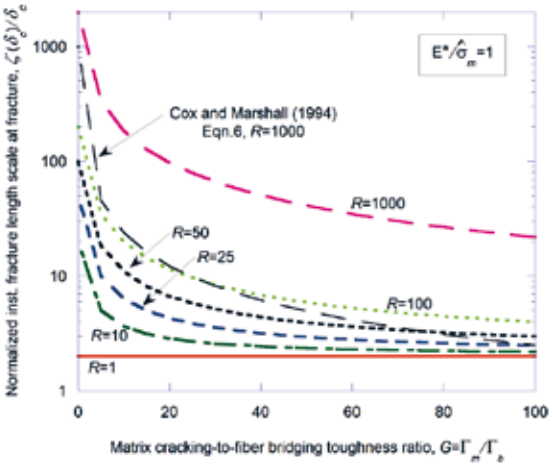

Fig. 4. The fracture length scale at fracture of the model traction-separation law depicted in Fig. 2 as a function of the toughness ratio, $G = \Gamma_m/\Gamma_b$, when $E^*/\hat{\sigma}_m = 1$ and R=1, 10, 25, 50, 100, and 1000.

It can also be seen that the strength ratio strongly affects the length scale at fracture when the toughness ratio is small – increasing the strength ratio by an order of magnitude results in a corresponding increase in the fracture length scale. This is due to the fact that when the matrix cracking strength is significantly higher than the fiber bridging strength, the interface softens significantly in transitioning between the mechanisms, and in general softening grows the fracture length scale. At large toughness ratios, the strength ratio becomes less important and in the limiting case doesn't matter at all as discussed above. It is important to keep in mind that for all of these results, the effective modulus has been held constant relative to the matrix strength.

In delamination models that use bridging laws, fracture length scales are generally only considered with respect to the bridging phenomenon. Indeed, the entire benefit in using bridging models stems from the distillation of processes at the crack tip down to a strain-energy release rate and corresponding toughness, bypassing direct modeling of the large stress gradients therein (Cox and Marshall 1994). Calculating length scales in this way, however, ignores the contribution of the finite crack tip strength. Eqn. (2) dictates that the fracture length scale is a function of the entire loading history of the system, so neglecting the crack tip can result in incorrect length scales.

Cohesive laws of the form in Fig. 2 have been derived and used by numerous authors in order to represent mode I delamination and the R-curve behavior of composites. While some authors have noted that such laws work because they accurately capture the fracture mechanisms, how

these mechanisms manifest themselves in the models has not been thoroughly explained. Fig. 3 presents evidence that these mechanisms affect the simulation by changing the fracture length scale, indicating that the length scale is a dynamic variable of the model. Therefore, the instantaneous fracture length scale provides an explanation for how cohesive zone modeling accurately captures the delamination process – the dynamics of strengthening and toughening are represented by changes in the fracture length scale.

REFERENCES

Aymerich, F., Dore, F., and Priolo, P. (2009). Simulation of multiple delamination in impacted cross-ply laminates using a finite element model based on cohesive interface elements. Comp. Sci. Tech. 69, 1699-1709.

Bao, G. and Suo, Z. (1992). Remarks on crack-bridging concepts. App. Mech. Rev. 45, 355-366.

Cox, B.N. and Marshall, D.B. (1994). Concepts for bridged cracks in fracture and fatigue. Acta metall. mater. 42, 341-363.

Dávila, C.G., Rose, C.A., and Camanho, P.P. (2009). A procedure for superposing linear cohesive laws to represent multiple damage mechanisms in the fracture of composites. Int. J. Fract. 158, 211-223.

Griffith, A.A. (1920). The phenomenon of rupture and flow in solids. Phil. Trans. Roy. Soc. A221, 163-198.

Gutkin, R., Laffan, M.L. Pinho, S.T., Robinson, P., and Curtis. P.T. (2011). Modelling the R-curve effect and its specimen-dependence. Int. J. Sol. Struct. Doi: 10.1016/j.ijsolstr.2011.02.025.

Hillerborg, A., Modéer, M., and Petersson, P.E. (1976). Analysis of crack formation and crack growth in concrete by means of fracture mechanics and finite elements. Cem. Con. Res. 6, 773-782.

Inglis, C.E. (1913). Stresses in a plate due to the presence of cracks and sharp corners. Proc. Inst. Nav. Arch. 55, 219-230.

Li, S., Thouless, M.D., Waas, A.M., Schroeder, J.A., and Zavattieri, P.D. (2005a). Use of mode-I cohesive-zone models to describe the fracture of an adhesively-bonded polymer-matrix composite. Comp. Sci. Tech. 65, 281-293.

Li, S., Thouless, M.D., Waas, A.M., Schroeder, J.A., and Zavattieri, P.D. (2005b). Use of cohesive-zone model to analyze the fracture of a fiber-reinforced polymer-matrix composite. Comp. Sci. Tech. 65, 537-549.

Parmigiani, J.P. and Thouless, M.D. (2007). The effects of cohesive strength and toughness on mixed-mode delamination of beam-like geometries. Eng. Fract. Mech. 74, 2675-2699.

Sills, R.B. and Thouless, M.D. (2011a). The effect of cohesive law shape on the strength of interfaces. (to be submitted).

Sills, R.B. and Thouless, M.D. (2011b). The effects of cohesive-law parameters on mixed-mode fracture. (to be submitted).

Sørensen, B.F., and Jacobsen, T.K. (1998). Large-scale bridging in composites: R-curves and bridging laws. Comp. Part A 29A, 1443-1451.

Sørensen, B.F., Gamstedt, E.K., Østergaard, R.C., and Goutianos, S. (2008). Micromechanical model of cross-over bridging – Prediction of mixed mode bridging laws. Mech. of Mat. 40, 220-234.

Tvergaard, V. and Hutchinson, J.W. (1992). The relation between crack growth resistance and fracture process parameters in elastic-plastic solids. J. Mech. Phys. Sol. 40, 1377-1397.

Yang, Q. and Cox, B. (2005). Cohesive models for damage evolution in laminated composites. Int. J. Fract. 133, 107-137.

Proceedings of the 32nd
Risø International Symposium on Materials Science:
Composite materials for structural performance:
Towards higher limits
Editors: S. Fæster, D. Juul Jensen,
B. Ralph, B.F. Sørensen
Risø National Laboratory for Sustainable Energy,
Technical University of Denmark, 2011

FIXTURE FOR LARGE IOSIPESCU SHEAR SPECIMENS

H. Toftegaard and H. Lilholt

Materials Research Division, Risø DTU
DK-4000, Roskilde, Denmark

ABSTRACT

The performance of an in-house fixture for in-plane shear measurements on large Iosipescu specimens has been investigated for composite laminates with continuous fibers. Large specimens have a larger test section and will be less sensitive to specimens with coarse features. Standard size specimens and double size specimens have been tested in a Wyoming fixture and in the in-house fixture, respectively, for three different biaxial $[\pm 45]_N$ polyester laminates with glass fiber fabrics (low and high area density) and aramid fabrics (low area density). Classical laminate theory is used to assess the measured shear stiffness and strength. Compared to the tests in the Wyoming fixture less twisting is seen for the specimens in the in-house fixture (Risø fixture). For the low area density laminates the stiffness and strength obtained with the in-house fixture were higher and matched the theoretical values better than those obtained with the Wyoming fixture. For the high area density glass/polyester the same stiffness and strength were obtained with the two fixtures. The in-house fixture seems to perform better than the Wyoming fixture, but should be investigated further to explore its potential for testing the shear modulus and strength of laminates and core materials with coarse features.

1. INTRODUCTION

Shear properties are important in many structural composite components such as beams and shear webs. In order to achieve higher limits test methods should be as reliable as possible so that high safety factors can be avoided. As the material properties, in general, are volume-dependent, the size of the coupon should be considered – especially regarding the strength properties.

This also applies to composite laminate in-plane shear properties that can be measured in a number of ways such as an uniaxial tension of a ±45° laminate or a 10° off-axis laminate, two-rail and three-rail shear tests, the V-notched beam (or Iosipescu) shear specimen, twisting of a flat laminate and torsion of a thin-walled tube (Hodgkinson 2000).

The Iosipescu test provides both shear modulus and shear strength, it is compatible with most material types, the data analysis is straight forward and the shear stress state is fairly uniform (Iosipescu 1967; Walrath and Adams 1983; Barnes, Kumosa and Hull 1987; Ho, Tsai and Morton 1993). The test is standardized in ASTM D 5379 specifying a standard specimen size (76 mm x 20 mm x 3-4 mm) to be tested in the modified Wyoming II fixture.

One drawback of the Wyoming fixture, however, is the tendency for specimen twisting resulting in different shear moduli measured on the specimen front and back sides (Conant and Odom 1995; Pierron 1998). An improved fixture (the University of Idaho fixture) was developed for the standard specimen size to prevent twisting (Conant and Odom 1995).

As pointed out in ASTM D 5397 the laminate material should be homogeneous with respect to the size of the test section of the standard specimen. For specimens with coarse features or an inhomogeneous structure a scale up of the specimen and fixture is possible, but is beyond the scope of ASTM D 5379. For scaled up specimens the influence on strength from a larger volume (a higher probability of a critical defect) should be taken into account (Wisnom 1999).

This paper presents a comparison between the performance of the modified Wyoming II fixture and that of an in-house (Risø) fixture intended for specimens 2 to 4 times larger than the ASTM standard specimen. The comparison is made for specimens of a standard size and specimens of double size made from 3 different types of biaxial laminates. The double size specimens tested in the Risø fixture show less twisting for all 3 types of laminates and a higher shear modulus as well as a higher shear strength for 2 of the laminate types.

2. EXPERIMENTAL

Three different laminates were manufactured from ±45° (biaxial) non-crimp fabric and ISO polyester: E-glass with an area weight of 260 g/m^2 (G260/P), aramid with an area weight of 240 g/m^2 (A240/P), and E-glass with an area weight of 850 g/m^2 (G850/P). The laminates with lay/ups $[45/\text{-}45]_{10}$ for G260/P, $[45/\text{-}45]_6$ for A240/P and $[45/\text{-}45]_4$ for G850/P measured 600 mm x 400 mm x 2 mm and were produced by vacuum infusion and post cured at 60°C.

For measurement of fiber and void fractions 4 specimens (15 mm x 15 mm x 2 mm) were cut with a diamond coated cutting wheel from each of the 3 laminates. The specimens from the glass fiber reinforced laminates (G260/P and G850/P) were analyzed by weighing the laminate specimens in air and in water, burning the laminate to remove the resin and weighing the fibers (according to ASTM D3171-09). For the A240/P laminate the resin could not be removed by burning and could not be dissolved in acid without affecting the organic aramid fibers. Instead the fiber volume fraction was assumed to be 46 % by volume as planned, and the porosity amount was estimated from microscopy of polished specimen edges.

Tab material made from 2 mm thick E-glass/epoxy cross-ply laminate was bonded to each of the 3 laminates with an epoxy adhesive (3M™ DP-460 Off-White Scotch-Weld™). Two sizes (standard and double size) of Iosipescu specimens (Fig. 1) were subsequently cut from each laminate with a water jet (a series of 6 specimens of each combination of laminate and specimen size – a total of 6 series and 36 specimens).

The specimens were equipped with ±45° strain gauge couples bonded back-to-back at the center of the major faces with cyanoacrylate adhesive. For the standard specimens 1.5 mm long gauges were used (HBM 1-XY21-1.5/350) and for the double specimens 3 mm long gauges were used (HBM 1-XY21-3/350).

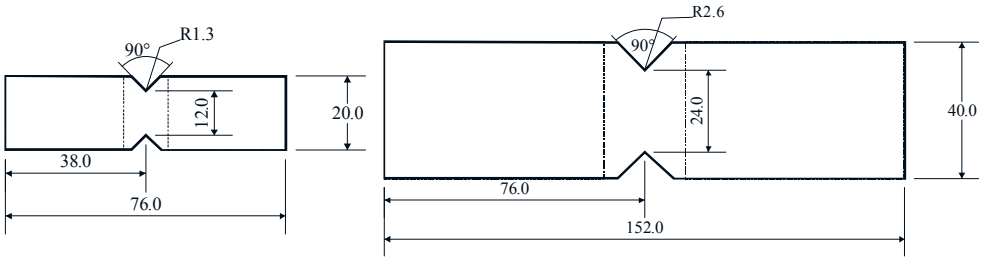

Fig. 1. The geometry used for the standard (1x) Iosipescu specimen (left) and the double size (2x) specimen (right). Laminates 2 mm thick were used for both specimen types. Tabs were bonded to both sides of the specimens and extend in full height from the ends to the vertical dashed lines on both sides of the V-notches.

Testing was performed in displacement control in a servo-electrical test machine (Instron 88R 1362) equipped with a ±100 kN load cell (UK1034). The constant cross-head speed was 2 mm/minute and the data acquisition rate was 10 Hz. The standard size specimens were tested according to ASTM D 5379-98 in the modified Wyoming II fixture (Fig. 2). The double size specimens were tested in the Risø fixture intended for specimen sizes of 2 to 4 times the standard size (Fig. 2). During testing the specimen is gripped by the left-hand and right-hand part of the fixture. The parts are positioned on a backing plate – the left-hand part is attached rigidly and the right-hand part can move vertically in two linear bearings. Testing of the specimens was continued until the load had reached a maximum and started to decrease. Five or six specimens were tested in each series in order to obtain 5 valid tests for each series.

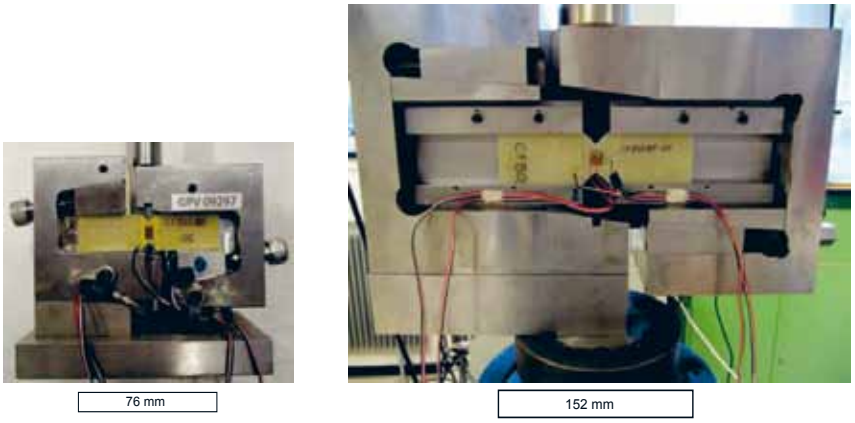

Fig. 2. The modified Wyoming II fixture used for the standard specimens (left), and the Risø fixture used for the double size specimens (right). The Risø fixture has been designed for specimens with sizes from 2 to 4 times the standard specimen.

3. RESULTS

For each Iosipescu specimen 4 normal strains were measured in the 45° and -45° directions on the major faces: $\varepsilon_{+45°}^{front}$, $\varepsilon_{-45°}^{front}$, $\varepsilon_{+45°}^{back}$ and $\varepsilon_{-45°}^{back}$. In the data analysis each of these strains was off-set to obtain a zero strain at zero load. The (engineering) shear strain on the front and back face and the average shear strain are obtained from:

$$\gamma^{front} = \varepsilon_{-45°}^{front} - \varepsilon_{+45°}^{front} \quad (1)$$

$$\gamma^{back} = \varepsilon_{-45°}^{back} - \varepsilon_{+45°}^{back} \quad (2)$$

$$\gamma^{average} = (\varepsilon_{-45°}^{front} - \varepsilon_{+45°}^{front} + \varepsilon_{-45°}^{back} - \varepsilon_{+45°}^{back})/2 \quad (3)$$

The shear stress, τ, is obtained from:

$$\tau = P/(wh), \quad (4)$$

where P is load, w is the distance between the notches, and h is the specimen thickness between the notches.

Typical shear stress-strain curves recorded for the front face and the back face together with the average stress-strain curves are shown in Fig. 3 for the 6 combinations of material and specimen size/fixture. The standard size specimens tested in the Wyoming fixture show large differences in the stress-strain curves of the front and back faces (Fig. 3a, 3b and 3c) in contrast to the curves for the double size specimens tested in the Risø fixture (Fig. 3d, 3e and 3f). The maximum stress is lower for the standard size G260/P and A240/P specimens (Fig. 3a and 3b) than for the corresponding double size specimens (Fig. 3d and 3e). The G850/P specimens (Fig. 3c and 3f) on the other hand do not show this difference.

Average shear stress-strain curves (up to maximum load) are shown for all valid tests in Fig. 4 displaying limited scatter. Typical average shear stress-strain curves can be compared in Fig. 5.

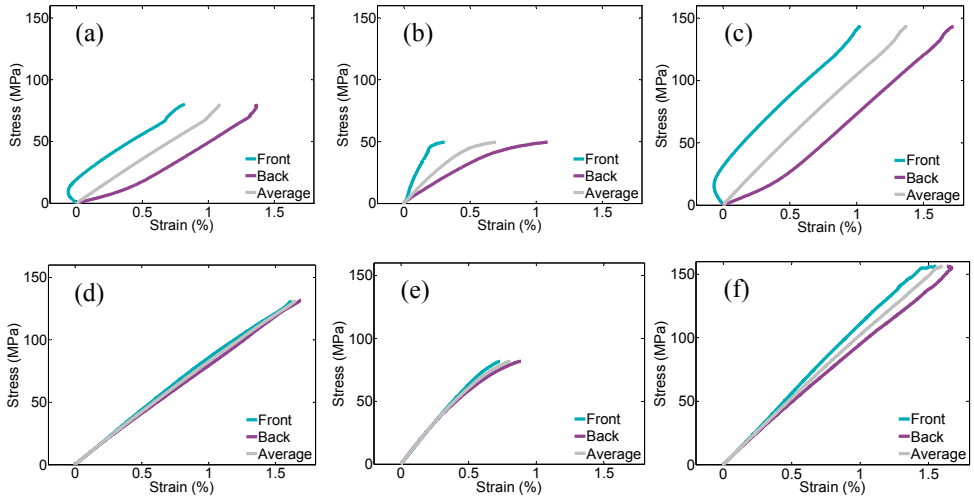

Fig. 3. Shear stress-strain curves (up to a maximum load) from strain gauge couples on the front and back together with the average stress-strain curve typical for: (a) G260/P 1x, (b) A240/P 1x, (c) G850/P 1x, (d) G260/P 2x, (e) A240/P 2x, and (f) G850/P 2x.

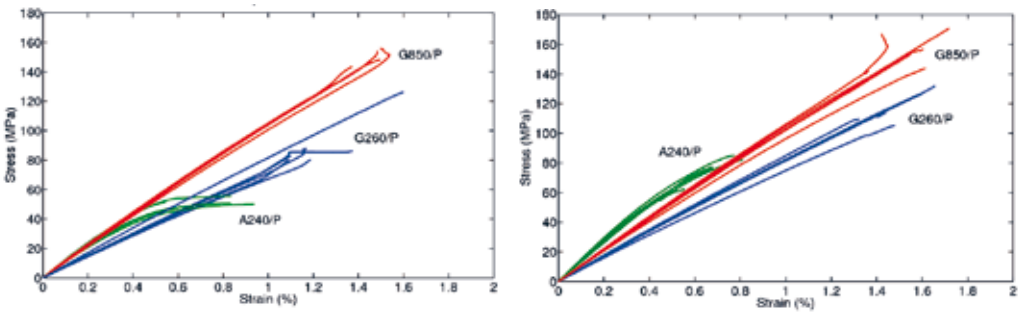

Fig. 4. Curves of shear stress versus average shear strain (up to a maximum load) obtained with all standard size specimens (left) and all double size specimens (right).

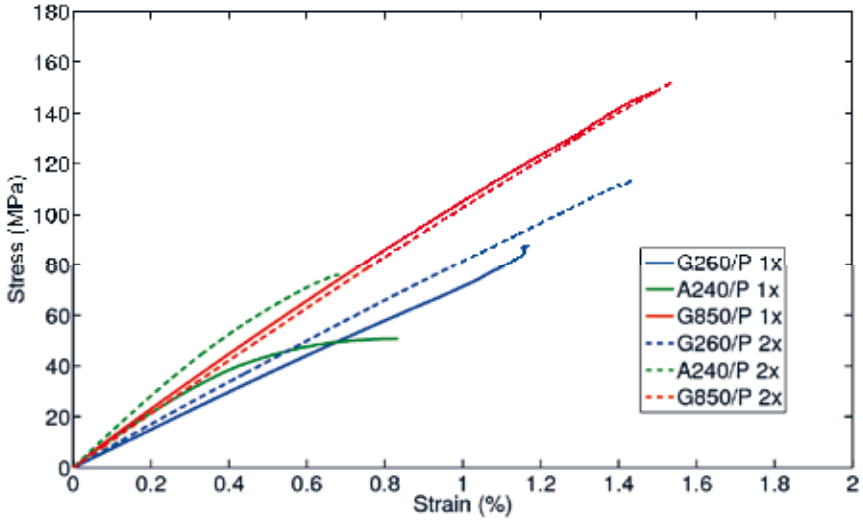

Fig. 5. Plots of shear stress versus average shear strain typical for the tested combinations of laminate materials (G260/P, A240/P and G850/P) and specimen sizes (1x and 2x).

The shear modulus G (the initial slope of the shear stress-strain curve) was calculated from a linear fit in the shear strain range from 0.1 to 0.35%. The G moduli for the stress-strain curves for the front and the back faces of the specimens are given in Table 1 in terms of the average ± the 95% confidence interval bound (the average 95% confidence interval extends from the average *minus* bound to the average *plus* bound).

The shear strength was calculated as the maximum shear stress for shear strains ≤ 5% (according to ASTM D 5379-98). The G moduli for the shear stress versus average shear strain and the shear strengths together with the measured fiber and void fractions are listed in Table 2.

Micromechanics and classical laminate theory (CLT) were used to obtain theoretical values for the G modulus and the shear strength (first ply failure). The calculations were performed with a

commercial code (CompositePro v. 2.1 from Peak Composite Innovations) using standard data for E-glass fibers, aramid fibers (Kevlar 49) and polyester together with the measured fiber volume fractions. The maximum stress failure criterion was used to predict first ply failure. The assumed fiber fractions and the predicted G moduli and shear strengths are shown in Table 2.

Table 1. Measured values of G moduli (average ± 95% confidence interval bound) for the front and back faces of the standard size specimens (1x) and the double size specimens (2x).

Property	G260/P		A240/P		G850/P	
	Front	Back	Front	Back	Front	Back
G modulus 1x (GPa)	8.0 ± 0.5	3.3 ± 0.2	11 ± 9	6.8 ± 0.7	11.7 ± 0.5	6 ± 3
G modulus 2x (GPa)	8.6 ± 0.7	8.2 ± 0.2	13.6 ± 1.2	12.1 ± 1.5	10.9 ± 0.7	10.3 ± 0.8

Table 2. Measured values of fiber and void volume fractions, G moduli (for shear stress versus average shear strain) and shear strengths (average ± 95% confidence interval bound) together with the CLT predictions and the fiber volume fractions assumed.

Property	G260/P		A240/P		G850/P	
	Measured	CLT	Measured	CLT	Measured	CLT
Fiber volume fraction (vol-%)	42.6 ± 0.3	43	-	46	52.6 ± 0.6	53
Void volume fraction (vol-%)	7.4 ± 0.6	0	7-10	0	7.6 ± 0.8	0
G modulus 1x (GPa)	7.4 ± 0.2	9.3	9.8 ± 0.9	15.2	10.8 ± 0.4	11.4
G modulus 2x (GPa)	8.4 ± 0.4	9.3	12.9 ± 0.5	15.2	10.6 ± 0.4	11.4
Shear strength 1x (MPa)	83 ± 4	133	51 ± 3	98	150 ± 9	170
Shear strength 2x (MPa)	117 ± 14	133	76 ± 11	98	158 ± 13	170

According to statistical tests (two-sample t-tests at the 5% significance level) the front and back face G moduli (Table 1) are significantly different for G260/P 1x and G850/P 1x. For A240/P 1x the large scatter for the front face G means that the hypothesis of equal G values cannot be rejected. For the double size specimens no significant difference is found between the front and back G moduli for any of the 3 laminates.

For the measurements of Table 2 the same statistical tests reveal that the G moduli for the 1x and the 2x specimens are significantly different for G260/P and A240/P, but not for G850/P. As for the G moduli the shear strengths for the 1x and 2x specimens are significantly different for G260/P and A240/P, while this is not the case for G850/P.

4. DISCUSSION

The purpose of the Risø fixture is to facilitate testing of larger specimens and minimize the effect of twisting. The investigation reported here is part of the process to validate the fixture.

The standard size specimens in the Wyoming fixture show large differences in the stress-strain curves of the front and back faces (Fig. 3a, 3b and 3c), and large differences in the G moduli for

the front and back faces (Table 1) indicating twisting of the specimens. This is in line with the findings of other investigations (Conant and Odom 1995).

In contrast, the double size specimens in the Risø fixture show small differences between the stress-strain curves of the front and back faces (Fig. 3d, 3e and 3f). The G moduli for the front and back faces (Table 1) are not significantly different for any of the 3 laminate materials G260/P, A240/P and G850/P. The small difference in stress-strain curves and the (reasonably) equal G moduli for the front and the back imply a small degree of twisting similar to the results obtained with the University of Idaho fixture for standard size specimens (Conant and Odom 1995).

The relatively small degree of twisting is probably due to the fact that (in contrast to the Wyoming fixture) the movable part of the Risø fixture is prevented from rotating out of the specimen plane by the backing plate. The scatter for the front and back face G moduli (Table 1, G 2x), however, is higher compared to the scatter on G moduli based on average strains (Table 2, G 2x) so that also for the Risø fixture strain measurements are still necessary both on the front and the back face.

The shear moduli based on the average shear strain (Table 2) show relatively little scatter for the 1x specimens tested in the Wyoming fixture despite the large scatter in shear modulus for the front of A240/P 1x specimens and for the back of the G850/P specimens. This illustrates how much averaging improves the G modulus measurement for a twisted specimen.

Another aspect of this effective averaging is apparent in Fig. 4, where the scatter in the stress-average strain curves for the 1x and the 2x specimens are seen to be comparable. The expected smaller scatter in the measured stress-strain curves for a larger specimen is thus not observed.

The differences between the shear moduli and shear strengths measured with the 1x and 2x specimens are illustrated in Fig. 5, where the measured shear moduli and shear strength are higher for the 2x than the 1x specimens for the laminates with low area weight fabric (G260/P and A240/P). For the laminates with high area weight (G850/P) the same moduli and strength values were measured for the 1x and 2x specimens. The reason for this difference in behavior of specimens with low and high area weight fabric is unresolved.

For G260/P and A240/P the moduli and strength measured with the 2x specimens are closer to the CLT predictions than the values measured with the 1x specimens. In general the CLT predictions of moduli and strengths are consistently higher than (or equal to) the measured moduli and strengths (Table 2). One reason for this could be that the relatively high void fractions were not taken into account. Instead the voids were assumed to be filled with matrix and the shear modulus and shear strength are thus overestimated to some degree.

The A240/P stress-average shear curve for the 2x specimen is straighter than the curve for the 1x specimen perhaps indicating a purer shear stress state in the 2x specimens with loading in the fiber directions (compression in the 45° direction and tension in the -45° direction).

The expected effect of a decrease in shear strength with increasing specimen volume (Wisnom 1999) was not seen. One reason could be that this effect was overshadowed by the difference in specimen response due to the two different fixtures.

Larger specimens (3x and 4x) and other laminate lay-ups as well as other material structures will have to be tested with the Risø fixture in order to validate its performance and potential for shear testing of laminates and, for example, core materials with the need of a large gauge section.

3. CONCLUSIONS

The biax G260/P, A240/P and G850/P Iosipescu specimens of 2 times the standard size tested in the Risø fixture showed less twisting than the corresponding specimens of standard size tested in the Wyoming fixture of ASTM D 5379. Compared to the specimens tested in the Wyoming fixture the specimens tested in the Risø fixture show higher and more realistic shear moduli and shear strengths for the G260/P and A240/P. For G850/P the same moduli and strength values are found with the two fixtures.

ACKNOWLEDGEMENTS

Financial support from the EU FP7 grant ACP7-GA-2008-213577 FLY-BAG is greatly acknowledged. The authors wish to thank Tord Gustafsson from APC Composite AB in Luleå, Sweden for manufacturing the laminates. The authors also thank the following staff members at the Materials Research Division at Risø for contributing to the experimental work: Mr. Jacob Christensen, Mr. Jonas K. Heininge, Mr. Troels Hoff, Mr. Christian H. Madsen and Mr. Jens Olsson.

REFERENCES

ASTM D3171-09 Constituent Content of Composite Materials, ASTM International, Pennsylvania, USA, pp 10.

ASTM D5379-98 Standard Test Method for Shear Properties of Composite Materials by the V-Notched Beam Method, ASTM International, Pennsylvania, USA, pp 13.

Barnes, J.A., Kumosa, M. and Hull, D. (1987). Theoretical and experimental evaluation of the Iosipescu shear test. Composites Science and Technology, 28, 251-268.

Conant, N.R., Odom, E.M. (1995). An improved Iosipescu shear test fixture. Journal of Composites Technology and Research, 17, 50-55.

Ho, H., Tsai, M.Y. and Morton, J. (1993). Numerical analysis of the Iosipescu specimen for composite materials. Composites Science and Technology, 46, 115-128.

Hodgkinson, J.M. editor (2000). Mechanical testing of advanced fiber composites. Woodhead Publishing Limited, Cambridge, England, p. 100-123.

Iosipescu, N. (1967). New accurate procedure for single shear testing of metals. Journal of Materials, 2, 537-566.

Pierron, F. (1998). Saint-Venant effects in the Iosipescu specimen. Journal of Composite Materials, 32, 1986-2015.

Walrath D.E., Adams D.F. (1983). The Iosipescu shear test as applied to composite-materials. Experimental Mechanics, 23, 105-110.

Wisnom, M.R. (1999). Size effects in the testing of fiber-composite materials. Composites Science and Technology, 59, 1937-1957.

Proceedings of the 32nd
Risø International Symposium on Materials Science:
Composite materials for structural performance:
Towards higher limits
Editors: S. Fæster, D. Juul Jensen,
B. Ralph, B.F. Sørensen
Risø National Laboratory for Sustainable Energy,
Technical University of Denmark, 2011

NANOTECHNOLOGY AND NANOSCIENCE FOR WIND POWER

B. Wei

Department of Energy Technology, Royal Institute of Technology,
Valhallavägen 79, Stockholm, Sweden

ABSTRACT

Currently, wind power is one of the best forms of green energy for humans to pursue a sustainable energy supply, and plays an increasingly essential role in energy systems. However, the efficiency and cost of wind energy is relatively higher than other types of energy resources, which make it less competitive. In this paper, I will analyze the usage of materials in wind energy equipment to understand the scope of improvement for wind energy materials, and utilize Nanotechnology and Nano science to propose performance improvement of wind energy devices.

1. INTRODUCTION

As a way of tackling the problems associated with climate change, wind energy has in the past decades emerged as an attractive alternative resource for electricity supply. With the development of wind energy, concerns about properties of materials used for construction are growing. In recent years, nanotechnology is involved in many areas to solve complex issues. The aim of this paper is to examine how nanotechnology can advance properties of current wind turbine blade materials, ensuring a safe and secure electricity supply from wind turbines.

2. SCOPE AND LIMITATIONS

As we know, wind power is not only a conversion of wind energy into electricity but also other types of energy with available usage, like a wind pump for elevating water, wind mills to generate mechanical power, and to power sailing ships. Although in this paper, I will only focus on electricity from wind resources. Moreover, from the point of view of improving the efficiency of overall wind energy and reduce the cost of wind energy facilities, materials will be mainly concentrated upon other than the utilizing mechanism of wind resources. Additionally, wind energy equipment for electricity production can be divided into two parts - mechanical

devices and electronics. Mechanical devices consist of three subsystems, wind turbine, nacelle, and tower. In this project, materials used only in wind turbine blade are considered.

3. METHODOLOGY

The objective of this report is to present a thorough investigation of the use of nanotechnology to improve the properties of wind turbine blade materials. First, it is necessary to introduce properties of different raw materials for the rotor blade and current wind turbine blade materials. Secondly, advantages and disadvantages are analyzed for different composite materials. Furthermore, a proposal of nanotechnology to improve the strength and stiffness of wind turbine blade materials is presented. In these three steps, the information is collected through books and the internet.

4. CONTENTS

4.1 Description of properties and material selection. As wind electricity is now becoming indispensable in an energy supply system, it is extremely significant to ensure normal operation of wind turbines and elevate the cost effectiveness of wind electricity generation. However, it is not as easy as we think to maintain wind turbine operation during high performance. Temperature, humidity, rain, hail, snow, ice, solar irradiation, lightening and salinity all affect the optimal output of wind energy and its safety operation. Therefore, improving the properties of wind turbine blades is necessary to handle these issues. The most important material properties are: specific weight (g/cm^3), strength limit (N/mm^2), modulus of elasticity (kN/m^2), breaking strength related to the specific weight (km), modulus of elasticity related to the specific weight (m^3), allowable fatigue strength after 10^7 to 10^8 load cycles (N/mm^2) (Hau, 2006). Throughout the development of wind turbine materials, (wood, aluminum, steel to modern rotor blade materials), engineers are trying their best to find materials with better strengths and stiffneses. In the starting phase of rotor blades construction, several properties for different materials should be taken into consideration. This can be seen in the Table 1.

Table 1. Strength and stiffness parameters of materials for rotor blades (Hau, 2006)

Parameter / Material	Spec. weight γ g/cm^3	Strength limit σ_B N/mm^2	Modulus of elasticity E (kN/m^2	Spec. breaking strength σ_B / γ km	Spec. modulus of elasticity E / γ 10^3km	Fatigue strength $\pm\sigma_A$ 10^7 N/mm^2
Steel St 52	7.85	520	210	6.6	2.7	60
Alloyed steel 1.7735.4	7.85	680	210	8.7	2.7	70
Aluminium AlZnMgCu	2.7	480	70	18	2.6	40
Aluminium AlMg5 (weldable)	2.7	236	70	8.7	2.6	20
Titanium alloy 3.7164.1	4.5	900	110	20	2.4	–

Fiber glass/epoxy composite	1.7	420	15	24.7	0.9	35
Carbon fiber/epoxy composite	1.4	550	44	39	3.1	100
Aramide fiber/epoxy composite	1.25	450	24	36	1.9	–
Wood (Sikta Spruce)	0.38	appr. 65	appr. 8	appr. 17	appr. 2.1	appr. 20
Wood/epoxy	0.58	appr. 75	appr. 11	appr. 13	appr. 1.9	appr. 35

4.2 The defects and merits of present wind turbine blade materials. Modern wind turbines are usually made from fiber-reinforced composite materials. Well-known synthetic resins reinforce these materials by embedding fibers to improve the strength. The different fibers available are: carbon fiber, glass fiber, and organic aramide fibers (KEVLAR). The matrix used as bonding for fiber-reinforced composite materials, is produced through two alternatives: polyester resins and epoxy resins. Table 2 and table 3 illustrate the advantages and disadvantages of these raw materials.

Table 2. Disadvantages and advantages of different fibers

Feature / Material	Advantages	Disadvantages
Organic fibers (KEVLAR)	High Strength	Hygroscopic, resulting not be used in offshore wind turbines
Carbon fiber	Longest breaking strength, high modulus (high stiffness), and good fatigue strength	High cost due to manufacture
Glass fiber	Extraordinarily high strength	Specific modulus of elasticity is not good, which means stiffness is not very high, resulting in not be used in large rotor blades

Table 3. Disadvantages and advantages of different resins

Material \ Feature	Advantages	Disadvantages
Polyester resins	Reasonable price and can handle medium stress	Low strength
Epoxy resins	Good strength, lightweight and do not exhibit any shrinkage	High cost

4.3 Nanotechnology for better rotor blade materials. In order to pursue a high performance of wind turbines, materials used for construction of the rotor blades is of extreme importance. As the list above illustrates drawbacks for various raw materials to produce rotor blades, the methods used should avoid disadvantages of these materials while maintaining or further developing their merits. With a sooner than expected development of sophisticated nanotechnology, engineers and researchers can propose new structural fiber-reinforced composite materials to meet stringent requirements, further enhancing secure and efficient wind energy supply.

Three approaches to improve the strength and stiffness of fiber-reinforced composite materials by nanotechnology are proposed below. There are carbon nanotubes for carbon-fiber-reinforced plastics (CFRP), nanosizing structures and sandwich technology.

There are mainly two types of carbon nanotubes: single wall (SWNTs) and multi wall (MWNT) nanotubes, which are shown in Figure 1. A single wall carbon nanotube is made by seamlessly rolling a cylinder of graphene sheet, which is a single layer of hexagonally arranged carbon atoms. Due to the homogeneous structure, the carbon-carbon bonds are the strongest bonds universally, leading to extraordinary mechanical properties of CNTs. The diameter of SWNT ranges from 1 nm to 2nm, and that of MWNT is 10-200 nm (Rychwalski, 2010). Due to the fact that CNTs have a high length-to-diameter ratio and other unprecedented properties, they are ideal reinforcement for polymers, plastics, etc. Therefore, nanotubes can contribute to a higher performance CFRP.

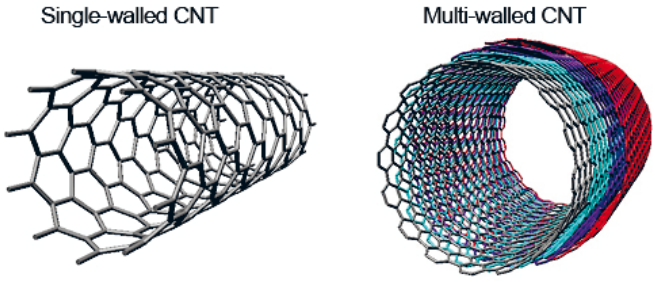

Fig 1. Single wall (SWNTs) and multi wall (MWNT) nanotubes.

Nanosized materials, which have a high surface area-to-volume ratio, increase the dominance of behavior of atoms on the surface of particles. Consequently, interaction between other particles is, in principle, influenced. That is because a higher surface area leads to a greater reaction with other particles. As a result, this structural variation of a material increases the strength, stiffness, and other factors. In addition, nano composites can offer a range of possibilities for improving the properties of conventional fiber-reinforced composite materials, for instance no fiber cracks, optical transparency, lower noise and also methods to produce conventional polymers can be applied to nano scale production of polymers.

Sandwich technology is used to process composite materials resembling a sandwich structure by bonding two relatively thin, dense, parallel high strength sheets called skins or facing with a relatively thick, lightweight core. This technical method brings two merits for composites, one is a lightweight structure with the promotion of performance and another is to lower the content of fibers in composites with a reduction of cost. A structure of a sandwich is shown in Figure 2.

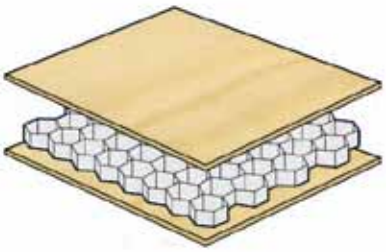

Fig 2. Structure of sandwich

With these three approaches, engineers can provide organic fibers (KEVLAR) with anti-hygroscopic properties, so that KEVLAR can be further utilized in offshore wind turbines with its advantage of high stiffness and good fatigue strength. The same way can be utilized in manufacturing nanostructured glass fibers to give it a high Young's modulus, resulting in an improvement of stiffness that can be used for large wind turbine blades. The cost of carbon fibers can be reduced, increasing its widespread use with glass fibers for high stress requirement.

4 CONCLUSIONS

This report investigates the optimization of properties for fiber-reinforced composite materials for wind turbine blades through nanotechnology. Nanotechnology can improve the anti-hygroscopic properties of KEVLAR, increase the stiffness of glass-fiber-reinforced polyester, and decrease the cost of carbon-fiber-reinforced plastics. These changes can enhance the cost effectiveness of wind turbine blades and their performance under various environmental conditions.

5 OUTLOOK

Nanotechnology can contribute to better rotor blade materials. Being an emerging technology, significant improvements can be expected from the continuous development of nanotechnology. Hence, higher strength and stiffness of fiber-reinforced composite materials and a low cost of wind turbine blades can be rationally foreseen, ensuring a more reliable and sustainable wind electricity supply.

REFERENCES

Erich Hau.: “Wind turbines”, The Springer Press, Krailing, Germany, 2006.
Rodney Rychwalski.: “Light weight polymeric (nano) materials”, Department of Materials and Manufacturing Technology, Chalmers University of Technology, 2010.
N.N.: “Foldvari Group”. URL:
http://science.uwaterloo.ca/~foldvari/images/SWNT-MWNT.jpg,updated: 2011-2-27.
N.N.: “Foldvari Group”. URL:
http://img.nauticexpo.com/images_ne/photo-g/sandwich-panels-plywood-honeycomb-244684.jpg,%20updated, updated: 2011-2-27.

Proceedings of the 32nd
Risø International Symposium on Materials Science:
Composite materials for structural performance:
Towards higher limits
Editors: S. Fæster, D. Juul Jensen,
B. Ralph, B.F. Sørensen
Risø National Laboratory for Sustainable Energy,
Technical University of Denmark, 2011

PREDICTING EFFECTIVE STRENGTHS OF BONDED LAP JOINTS WITH A FINITE FRACTURE MECHANICS CRITERION

P. Weißgraeber* and W. Becker*

* Fachgebiet Strukturmechanik, TU Darmstadt,
Hochschulstraße 1, 64289 Darmstadt, Germany

ABSTRACT

The aim of this contribution is to present a new approach for assessing the effective strength of adhesive joints. The approach is based on the hybrid failure model as postulated by Leguillon in the framework of finite fracture mechanics. In this hybrid failure model formation of cracks of finite size is predicted if a stress criterion is fulfilled over the full virtual crack area and the incremental energy release rate reaches the fracture toughness. Effective strength predictions have been performed for single lap joints using the new hybrid failure model. Besides closed-form analytical models that are based on linear elasticity solutions a numerical model using the finite element method is presented. The results of the three models are shown and compared and their limitations are discussed.

1. INTRODUCTION

Efficient and reliable predictions of failure loads of adhesively bonded lap joints are increasingly needed in order to use adhesive joints in modern engineering applications. With a utilization of the full load bearing capabilities of adhesively bonded joints weight reduction or correspondingly performance increases can be achieved. The main advantages of adhesive joints are the possibility to advantageously join thin-walled structural parts as they are often used in modern lightweight designs. The capability to join dissimilar materials and to use adapted bond geometries are distinctive advantages as well.

Currently, there are three basic approaches for assessing the effective strength of bonded lap joints: strength of material approaches, fracture mechanics approaches and cohesive zone modeling (da Silva and Öchsner (2008)).

In strength of material approaches it is typically assumed that failure occurs when an appropriately chosen function of the stress or strain tensor reaches a critical value. But as according to linear elasticity theory stress- or strain singularities occur in almost all adhesively bonded joints at sharp corners and multi-material-junctions, these approaches cannot

be applied directly. Evidence for this can be found in finite element analyses when no convergence can be achieved and the stresses increase infinitely with mesh refinement. A common way to avoid these singular stresses is to evaluate the stresses at a certain distance from the singular point. The results of such criteria will depend strongly on the chosen length parameter. In closed-form analytical linear-elasticity solutions, for example the classical works of Volkersen (1938), Goland and Reissner (1944) and Hart-Smith (1981), the stresses are typically bounded and do not show a singular behavior. But in these closed-form solutions not all geometric effects are covered adequately.

Fracture mechanics approaches consider the presence of defects in the material. Failure is assumed if an energy criterion is fulfilled. If no information on the size and orientation of the defects is available assumptions have to be made. A typical way to do this is to assume a pre-crack of a specific size. The size of this pre-crack again has a strong influence on the resulting effective strength of the adhesive bond.

In the past years many studies have focused on cohesive zone modeling, where a non-linear stress-displacement law is introduced on the assumed crack paths. This non-linear stress-displacement law includes a softening in the crack path with increasing damage. In the simplest formulation, the softening law is controlled by two parameters: a cohesive strength, which must be exceeded to initiate damage, and a released energy, represented by the integral of the stress-displacement function. Cohesive zone models are typically implemented into numerical analyses and can be applied to a wide range of problems. The resulting finite element calculations are of course non-linear and numerical issues (slow or no convergence) might occur. Another issue is the identification of well-adjusted material parameters.

The aim of the present contribution is to present a new alternative approach to assess the effective strength of bonded lap joints. This approach is based on the hybrid criterion as postulated by Leguillon (2002) in the framework of finite fracture mechanics. Finite fracture mechanics considers the sudden formation of cracks of a finite size. The failure condition requires a strict simultaneous fulfillment of a strength and an energy criterion. Hence, it is a combination of the classical strength of a material and fracture mechanics approaches. Details are given in section 2. This hybrid failure model is incorporated in three models to assess the effective strength of adhesively bonded single lap joints (SLJ). Two closed-form analytical models, that are based on linear elasticity solutions for SLJ, and a numerical model, that is based on a finite element analysis are presented in section 3. Results are compared and limitations of the models are discussed in section 4.

2. THEORY

The basic assumption of the hybrid fracture criterion is the spontaneous formation of cracks of finite size if a stress criterion is fulfilled on the complete area of the crack considered and an energy criterion is fulfilled simultaneously. The physical explanation of the hybrid criterion is that a crack will only appear if the bond forces are exceeded along its complete surface and when the energy required for the crack formation is available . In this work the hybrid criterion is specified as follows: Formation of a crack of finite size A will occur, when a stress criterion is fulfilled in all points x_i on the surface Ω_c of the crack considered and when the respective incremental energy release rate is greater than or equal to a fracture toughness parameter G_c. The stress criterion demands that a component of the stress tensor or an appropriate equivalent stress reaches or exceeds the strength. The hybrid criterion

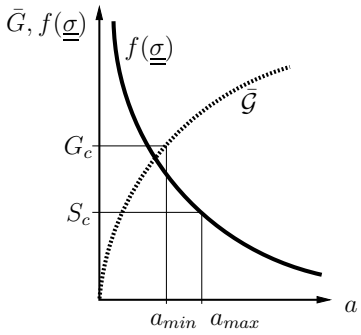

Fig. 1: The optimization problem for the failure load F_f. a_{min} and a_{max} are the upper and lower limit of the crack length resulting from the energy and the stress criterion.

can be given as:

$$f(\underline{\underline{\sigma}}) \geq S_c \quad \forall\, x_i \in \Omega_c \quad \wedge \quad \bar{\mathcal{G}}(A) \geq G_c \tag{1}$$

To determine the lowest load satisfying the criterion, the failure load, a non-linear, constrained optimization must be performed, which is a two-dimensional optimization problem: The lowest load F satisfying the criterion for an arbitrary crack area A is the failure load F_f:

$$F_f = \min_{F,A} \left\{ F \,|\, f(\underline{\underline{\sigma}}) \geq S_c \quad \forall\, x_i \in \Omega_c\,,\ \bar{\mathcal{G}}(A) \geq G_c \right\} \tag{2}$$

In this problem the strength criterion operates as an upper limit for the crack length, as with increasing distance from the stress concentration the stresses decrease. The energy condition yields a lower limit for the crack length since typically the incremental energy release rate increases with larger crack lengths. In fig. 1 the characteristic curves of the incremental energy release rate and the equivalent stress are depicted. The upper and lower limits for the crack length resulting from the stress and energy criterion are shown as well.

In essence the hybrid criterion includes Griffth's energy criterion (sharp crack) or a simple strength of materials criterion (failure of a sufficiently large body with a homogeneous stress state) as limiting cases.

The hybrid criterion has been successfully used, e.g. to study failure of notched PMMA-specimens and free-edge delaminations of laminates (Hebel, Dieringer and Becker (2010), Martin, Leguillon and Carrère (2010)).

3. MODELS

In this section the models of the mechanical behavior of adhesively bonded SLJ are briefly described. In all cases the same single lap joint with overlapping length l, width b, adherend thickness h and adhesive layer thickness t as n fig. 2 is considered. The material is assumed to behave linear elastically. The material properties of the adherends are given by Young's Modulus E and Poisson's ratio ν. The material properties of the adhesive layer are Young's Modulus E_a and Poisson's ratio ν_a. Cracks are assumed to appear at the re-entrant corners of the adherend and the adhesive layers, as known from experiments.

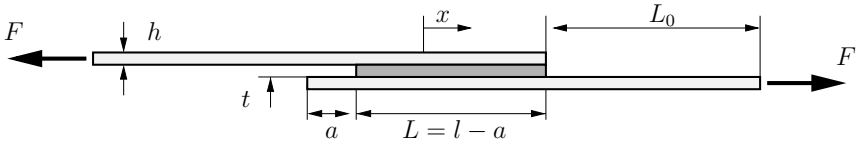

Fig. 2: Geometry of the considered SLJ. The width of the joint is denoted as b.

3.1 Closed-form models based on linear elasticity solutions. In this closed-form model two classical analytical solutions of the stress distributions in SLJ are utilized, the Volkersen model and the Goland and Reissner model. On the basis of the closed-form expressions of the stresses in the adhesive layer the incremental energy release rates are calculated under the assumption that crack initiation corresponds to a shortening of the overlapping length, cf. Krenk (1992).

Firstly the very simplifying shear lag theory by Volkersen is used. In the Volkersen model the adherends are modeled as rods with constant longitudinal stresses over the thickness and the adhesive layer is modeled as shear springs. The shear stress distribution results in:

$$\tau_{xy} = \frac{F\omega}{2lb} \frac{\cosh \omega \frac{x}{l}}{\sinh \frac{\omega}{2}} \quad \text{with} \quad \omega = \sqrt{\frac{2G}{Eht}} \cdot l. \tag{3}$$

The incremental energy release rate of the Volkersen model $\bar{\mathcal{G}}^{(V)}$ is calculated from the change of the compliance ΔC of the single lap joint in crack initiation. The compliance is given as the sum of the elongation of the adherends and the shear deformation of the adhesive layer:

$$\bar{\mathcal{G}} = \frac{1}{2} \frac{\Delta C}{A} F^2 = \frac{1}{2} \frac{C_{cracked} - C_{initial}}{ab} F^2 \tag{4}$$

$$C_{cracked} = \frac{t}{G_a} \frac{\tau_{peak}^{(L=l-a)}}{F} + \frac{l-a}{2Ehb} + \frac{a}{Ehb}; \quad C_{initial} = \frac{t}{G_a} \frac{\tau_{peak}^{(L=l)}}{F} + \frac{l}{2Ehb} \tag{5}$$

$$\bar{\mathcal{G}}^{(V)} = \frac{F^2}{4Ehb^2} \left(1 + \frac{2}{\lambda a} \left(\coth \frac{\lambda (l-a)}{2} - \coth \frac{\lambda l}{a} \right) \right) \tag{6}$$

To formulate the optimization problem of the failure load in the Volkersen model a simple maximum shear stress criterion is used.

In the Goland and Reissner solution the bending of the adherends is considered additionally. The basic idea of the analysis is to couple the shear lag analysis with an analysis of a bedded beam. Thus, besides a shear stress solution, which is similar to the Volkersen solution, a peel stress distribution is derived:

$$\tau = -\frac{F}{8b} \left(\lambda_\tau (1+3k) \frac{\cosh \lambda_\tau x}{\sinh \lambda_\tau \frac{L}{2}} + \frac{3}{L} (1-k) \right) \quad \text{with} \quad \lambda_\tau = \sqrt{\frac{8G}{Eht}} \tag{7}$$

$$\sigma_0 = \frac{Fh\lambda_\sigma}{\Psi b}\left(\left(\frac{\lambda_\sigma}{2}R_1 k + \frac{2}{L}k'\sinh\left(\lambda_\sigma\frac{L}{2}\right)\sin\left(\lambda_\sigma\frac{L}{2}\right)\right)\sinh\left(\lambda_\sigma x\right)\sin\left(\lambda_\sigma x\right)\right.$$
$$\left. \ldots + \left(\frac{\lambda_\sigma}{2}R_2 k + \frac{2}{L}k'\cosh\left(\lambda_\sigma\frac{L}{2}\right)\cos\left(\lambda_\sigma\frac{L}{2}\right)\right)\cosh\left(\lambda_\sigma x\right)\cos\left(\lambda_\sigma x\right)\right) \tag{8}$$

$$\text{with } \lambda_\sigma = \sqrt[4]{\frac{6E_a\left(1-\nu^2\right)}{Eh^3 t}}. \tag{9}$$

$$R_1 = \cosh\lambda\frac{L}{2}\sin\lambda\frac{L}{2} + \sinh\lambda\frac{L}{2}\cos\lambda\frac{L}{2};\; R_2 = \sinh\lambda\frac{L}{2}\cos\lambda\frac{L}{2} - \cosh\lambda\frac{L}{2}\sin\lambda\frac{L}{2} \tag{10}$$

$$\Psi = \frac{1}{2}\left(\sinh\lambda L + \sin\lambda L\right) \tag{11}$$

In these equations k and k' are the so called moment factors and take into account the nonlinearities arising due to bending of the adherends. Considering the comments and corrections by Tsai and Morton (1994) they can be identified as:

$$k = \frac{1}{1 + 2\sqrt{2}\tanh\left(\sqrt{\frac{3(1-\nu^2)}{2}}\frac{L}{2h}\sqrt{\frac{F}{Ehb}}\right)};\quad k' = \frac{1}{L}\left(\left(1-k\right)h + t\right) \tag{12}$$

On the basis of the given stress distributions and kinematics the incremental energy release rate is calculated as:

$$\bar{\mathcal{G}}_{(GR)} = \frac{F^2}{4Ehb^2}\frac{1}{a}\left[\left(1+6k\right)a + \frac{2\left(1+3k\right)}{\lambda_\tau}\left(\coth\left(\lambda_\tau\frac{l-a}{2}\right) - \coth\left(\lambda_\tau\frac{l}{2}\right)\right)\right.$$
$$+ \frac{6\left(1-k\right)}{\lambda_\tau^2}\frac{a}{l\left(l-a\right)} +$$
$$\left. + \frac{6k}{\lambda_\sigma}\left(\frac{\cosh\left(\lambda_\sigma(l-a)\right) - \cos\left(\lambda_\sigma(l-a)\right)}{\sinh\left(\lambda_\sigma(l-a)\right) + \sin\left(\lambda_\sigma(l-a)\right)} - \frac{\cosh\left(\lambda_\sigma l\right) - \cos\left(\lambda_\sigma l\right)}{\sinh\left(\lambda_\sigma l\right) + \sin\left(\lambda_\sigma l\right)}\right)\right] \tag{13}$$

In this model the von Mises stress is used as the considered equivalent stress. With this and the given incremental energy release rate the optimization problem given in eqn. (2) can be directly implemented in a mathematical toolbox to calculate the failure load with the hybrid criterion.

3.2 Numerical model based on a finite element formulation. As a very flexible alternative the stress analysis can be performed numerically by means of an appropriate finite element analysis. A two-dimensional model with a structured meshing is used. The mesh structure of a cracked single lap joint is shown in fig. 3. Close to the stress concentration a characteristic element length of 0.05 mm is used.

The finite element routine performs one analysis of the uncracked singe lap joint in order to obtain the stress distribution on the assumed crack path and several analyses of the cracked structure to calculate the incremental energy release for several crack lengths. The incremental energy release rate is calculated from the difference of the strain energy Π_i of the uncracked and cracked state using Clapeyron's theorem:

$$\bar{\mathcal{G}}^{(FEM)}(A) = -\frac{\Pi_i^{\text{uncracked}} - \Pi_i^{\text{cracked}}}{A} \tag{14}$$

The stresses and energy release rates from the finite element routine are obtained for a unit load F_0. To use them in the optimization problem they are multiplied by the load factor

Fig. 3: Left: Boundary conditions in the FE analysis (overscaled deformation); Right: Meshing in the area of the crack along the adherend/adhesive interface. Doubled nodes along the crack considered (shown in white).

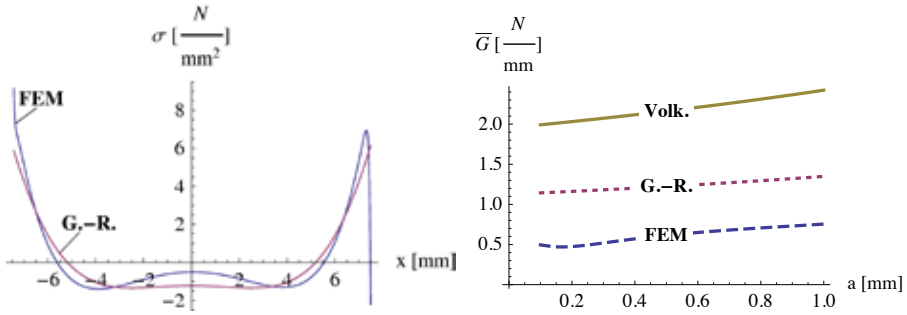

Fig. 4: Comparison of the closed-form analytical and numerical models.

$\frac{F}{F0}$ resp. its square $\left(\frac{F}{F_0}\right)^2$ and linearly interpolated to attain continuous dependences. Thus the optimization problem can easily be implemented in a mathematical toolbox to calculate the failure load.

4. RESULTS

4.1 Comparison of the models. In this section the three models are compared. Fig. 4 depicts the peel stress distribution and the incremental energy release rate. The peel stress distributions are in good agreement. The Goland-Reissner solution is symmetric, whereas in the numerical result the stresses are asymmetric. The curves of the incremental energy release rates are in the same order of magnitude and show a similar dependence on the crack length.

In fig. 5 the dependence of the failure load derived from the optimization problem given in eqn. (2) on two geometric parameters are shown. It can be seen that the effect of the adherend height is stronger in the results of the numerical model. The Volkersen model does not cover this effect at all, as it neglects the adherend bending. On the right hand side of fig. 5 the effect of the adhesive layer thickness is shown. With rising adhesive layer thicknesses the failure load decreases. This is a known effect from experiments, which is typically not covered in most of the effective strength assessments. This effect is mainly controlled by the energy release rate, which increases with thicker adhesive layer thicknesses.

4.2 Comparison to experimental results. To assess the efficiency of the present models a comparison to experimental results is performed. The results from Goglio, Rossetto and Dragoni (2008) are used. They have performed tests on SLJ with steel adherends and an

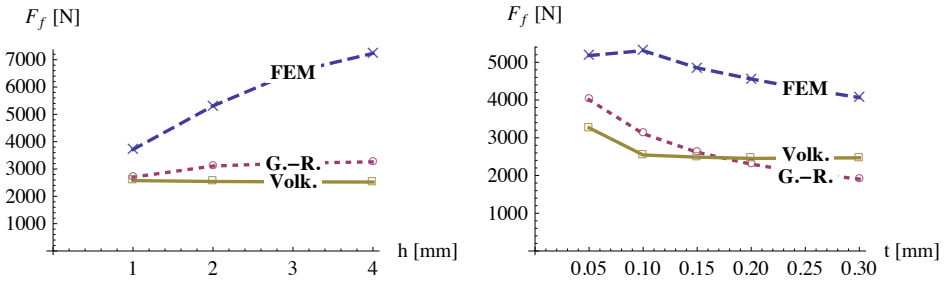

Fig. 5: Influence of the adherend h and the adhesive layer thickness t on the failure load in all three models.

acrylic structural adhesive with 12 different geometries (geometric parameters h, t, L were varied). Due to the lack of appropriate material data the material parameters S_c and G_c are obtained by a best fit to all 12 test series, in which the deviation:

$$s = \sqrt{\frac{1}{n}\sum_{i=1}^{12}\left(\frac{F_f - F_{exp}}{F_{exp}}\right)^2} \tag{15}$$

is minimized. The results of this comparison can be seen in figure 6. The achieved deviations are $s^{(Volk)} = 22,8\%$, $s^{(GR)} = 5,5\%$ and $s^{(FEM)} = 12,8\%$. The results of the Volkersen model are only slightly better than a very simple peak stress criterion (Weißgraeber and Becker 2011). The simplifications of the model, especially the neglection of adherend bending, are too strong to cover the geometric effects. The results of the Goland-Reissner model are in good agreement with the experimental results and the deviation is for almost all test series in the magnitude of the experimental scattering, which is 9.6% on average. The results of the numerical model have a larger deviation than the Goland-Reissner model, but still yield acceptable values. It can be seen, that in particular the effect of the overlapping length is not covered sufficiently. In the current finite element model only the peel stresses have been used to formulate the stress criterion. A consideration of appropriate equivalent stresses should increase the efficiency of the model significantly, as the shear stresses strongly depend on the overlapping length. Possible further improvements of the finite element model are a consideration of a plane strain condition and a more realistic geometry, e.g. fillets.

It has to be considered that only two different values of the adherend and adhesive layer thickness have been examined in the experiments. A larger set of experiments is needed to make more specific statements about the efficiency of the given criteria. In doing so it might be necessary to use enhanced closed-form analytical models, that for example consider shear deformation or stress variations over the thickness of the adhesive layer.

5. CONCLUSIONS

In this work effective strength predictions for single lap joints have been presented. The underlying hybrid criterion in the framework of finite fracture mechanics has been explained and the resulting optimization problem was shown. The resulting criterion for crack formation is a physically based criterion with two material parameters.

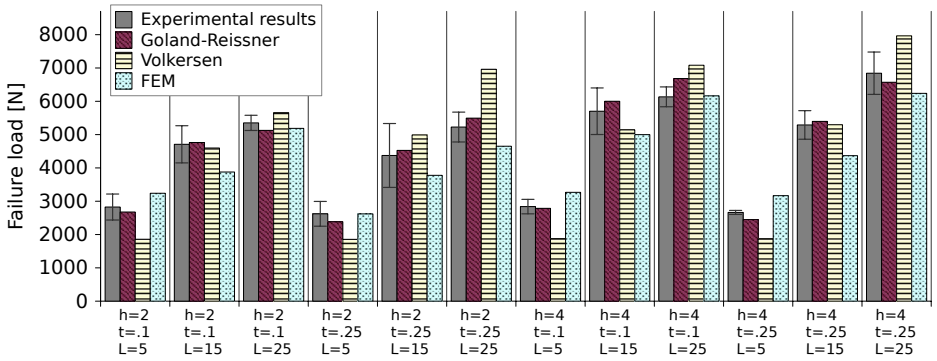

Fig. 6: Comparison of the present effective strength predictions with experimental results.

Two closed-form analytical and one numerical model were given in detail. The models have been compared and the resulting criteria are compared to experimental results. A very good agreement of the criterion based on the Goland-Reissner model with the experimental results was observed. The criterion based on the Volkersen model was not able to cover the geometric effects and in the numerical model based on the finite element formulation in particular the effect of the overlapping length was not covered sufficiently. Possible enhancements of the very simple finite element model were discussed.

REFERENCES

da Silva, L. F. M., and Öchsner, A. (2008). Modeling of Adhesively Bonded Joints (Springer-Verlag, Berlin).

Goglio, L., Rossetto, M., Dragoni, E. (2008), Design of adhesive joints based on peak elastic stresses, Int J Adhes Adhes 28-8, 427–435

Goland, M., Reissner E. (1944). The Stresses in Cemented Joints. J. Appl. Mech. 11 17–27.

Hart-Smith, L. J. (1981), Stress analysis: a continuum mechanics approach, Developments in Adhesives, (Applied Science Publishers, London).

Hebel, J., Dieringer, R., Becker, W. (2010), Modelling brittle crack formation at geometrical and material discontinuities using a finite fracture mechanics approach, Eng Fract Mech 77-18, 3558–3572.

Krenk, S. (1992), Energy release rate of symmetric adhesive joints, Eng Fract Mech 43-4, 549–559.

Leguillon, D. (2002), Strength or toughness? A criterion for crack onset at a notch, Eur. J. Mech. A-Solid 21-1, 61–72.

Martin, E., Leguillon, D., Carrère, N. (2010), A twofold strength and toughness criterion for the onset of free-edge shear delamination in angle-ply laminates, Int J Solids Struct 47-9, 1297–1305.

Tsai, M. Y., Morton, J. (1994), A note on the peel stresses in single-lap adhesive joints, J Appl Mech 61, 712–715.

Volkersen, O. (1938). Die Nietkraftverteilung in zugbeanspruchten Nietverbindungen mit konstanten Laschenquerschnitten. Luftfahrtforschung, 15: 41-47.

Weißgraeber, P., Becker, W. (2011), A new finite fracture mechanics approach for assessing the strength of bonded lap joints. Key Eng Mat 471-472, 1075–1080.

Proceedings of the 32nd
Risø International Symposium on Materials Science:
Composite materials for structural performance:
Towards higher limits
Editors: S. Fæster, D. Juul Jensen,
B. Ralph, B.F. Sørensen
Risø National Laboratory for Sustainable Energy,
Technical University of Denmark, 2011

EXAMINATION OF THE INFLUENCE OF SHEAR MICRO-GEOMETRICAL PROPERTIES ON TRANSVERSE ELASTICITY THE MODULUS OF ROVING COMPOSITE MATERIALS USED IN CRITICAL CONSTRUCTIONS

P. Wolszczak and R. Cechowicz

Lublin University of Technology, Automation Faculty, Poland

ABSTRACT

Monitoring of quality is an important task in the production process of critical supporting structures made from roving composites. Results from the research performed on the production samples of girders of helicopter blades presented in this paper, suggest that geometrical measures can be used for prediction of material strength and durability. The correlation between geometrical measurements of shear microstructure and values of the elasticity modulus determined in the transverse shear strength test by short beam method was assessed.

1. INTRODUCTION

Composites made up of fibres (glass or carbon) with a circular cross section, arranged unidirectionally and embedded in an epoxy resin matrix constitute an interesting group among machine building materials. The composite of hard, brittle fibres immersed in an epoxy resin of significantly lower strength is strongly anisotropic. Strength of the composite depends on: the direction of load in relation to the fibre axis, the strength of the components, the adhesive forces between the fibres and the resin, on the relative volume of the components and on the geometrical arrangement of fibres in a cross-section. The geometrical arrangement of fibres depends on the manufacturing process (Ochelski 2004; Śleziona 1998; German 2001; Kelly and Zweben 2000).

One of the main problems in material strength analysis is to determine the geometrical distribution of fibres in a sample and obtain a measure that can be related to material strength. A literature review assumes that the geometric properties of the microstructure are random (Kelly and Zweben 2000). However, in theoretical considerations of composite strength, the following assumptions are made (German 2001): composite components are homogeneous (there are no defects such as bubbles and impurities in the matrix volume), component materials are isotropic (anisotropy of the fibres is ignored), elastic deformation of composite ingredients is linear, a combination of fibres and matrix is ideal and the strength of the adhesion exceeds the

strength of the warp (no slip and tear), the cross-section of fibres is circular or rectangular (can be approximated with basic geometrical shapes like circle or rectangle).

There are additional simplification of the models, such as: all fibres are uniform in diameter (can be represented as points in geometrical distribution models) and there is no fibres-to-matrix adhesion (thickness of the interface is ignored). The results quoted in the literature concern models, rather than real objects which are likely be characterized by considerable randomness (Pyrz and Bochenek 1998).

A standard evaluation of the geometrical distribution of composite ingredients is made on the basis of an image of the microstructure. The evaluation is made from: number, size, shape and position of every component (Rudawska 2008; Siejka-Kulczyk, Lewandowska, Kurzydłowski 2008). Various local and global indicators are calculated from these values.

The following methods for characterizing heterogeneity of the structure of multiphase materials are mentioned (Pyrz and Bochenek 1998; Rożniatowski 2001; Kurzydłowski and Ralph 1995; Kołosow and Kljawlin 1987; Gusev, Hineb and Ward 2000; Missoum-Benziane, Ryckelynck and Chinesta 2007; Krywult 2002):

- systematically arranged test elements (secants) like: systematic scanning (grid fields, open curvilinear shapes), covariance function (parallel secants), radial distribution function (circular test elements),
- distance and angle between the neighbouring fibres,
- properties of the tessellation polygons, including: field (A_i), circuit (B_i) and number of polygon sides, the thickness of the matrix between neighbouring fibres and the aspect ratio,
- topological entropy and functions for local concentrations.

2. THE STUDY MATERIALS AND METHODS

The composites studied were made from glass fibres and epoxy resin. The samples, obtained from the production process of helicopter blades, were tested for endurance in a laboratory and then cross-sections were made for the geometrical analysis.

Laboratory tests according to the PN-EN ISO 14130:2001 (determination of the shear strength by a short-beam method) and BS-EN-ISO-14125:2001 (bending strength test) were performed on the samples. Additionally, the results of flexural strength tests according to PN-79/C-89027, performed by the manufacturer were collected. Bitmap images of the cross-sections were used for geometrical analysis. The experimental material consisted of over 1400 bitmap images taken from 81 composite samples.

As the results of the geometrical analysis of bitmap images, the following were obtained: parametrized microstructural images, fibre coordinates and their diameters, defect locations and surfaces (inclusions and gas pores). The relative volume of glass and gas pores, as well as measures characterizing the distribution of fibres were then calculated from these sets. All measurements and calculations were performed using the computerized vision system developed by the author (Wolszczak 2006). Sample results are shown in Fig. 1.

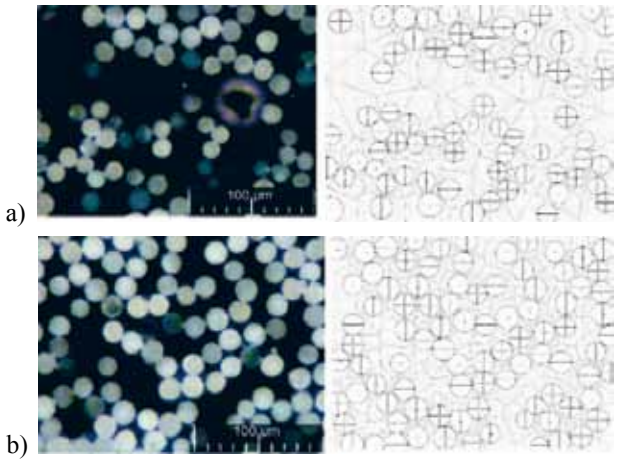

Fig. 1 a) Bitmap images of cross-sections of composite samples, parametrized microstructural images with tessellation polygons. Topological entropy values a) S = 1.59, b) S = 1.06 (author's study)

As one of the main factors determining the composite properties is the area of contact between components and the strength of adhesive forces, it seems appropriate to measure the fibre distribution homogeneity. Thus a measure of matrix film thickness was proposed, similar to those documented in (Kamiński 2005; Nairn, Liu and Galiotis 1996; Beyerlein, Zhou and Schadler 2003; Konsztowicz 1986)

The measurements characterizing composite macro-structure and design assumptions such as the relative volume of the glass Usz [%] and fibre diameter - Dw [μm] were considered during the research. Additionally, the relative volume of the gas pores [%] and fibre arrangements defined by the topological entropy S and the minimum distance between neighbouring fibres G_{1min} $[\mu m]$ were calculated.

As shown in Fig. 2, the matrix film thickness around a single fibre can be defined by G_1, G_2, G_{AB}, G_{AD} $[\mu m]$, where:

G_1 – half of the distance between neighbouring fibres,

G_2 – local film thickness measured at regular intervals along the perimeter,

G_{AD} – the average value of film thickness calculated by the formula (1):

$$G_{AD} = \frac{\sqrt{D_w^2 + 4\frac{A_o}{\pi}} - D_w}{2}, \tag{1}$$

G_{AB} – the proportion of matrix area in the tessellation polygon A_o to the fibre circuit B_w, calculated according to the formula (2):

$$G_{AB} = \frac{A_o}{\pi D_w} \tag{2}$$

The geometrical measurements documented in the literature like tessellation polygon properties (number of sides, circumference and the area of the polygon) and the ratio of the area of the

tessellation polygon and the fibre cross-section (related to the relative volume of the glass) (Krywult 2002) are illustrated in Fig 2.

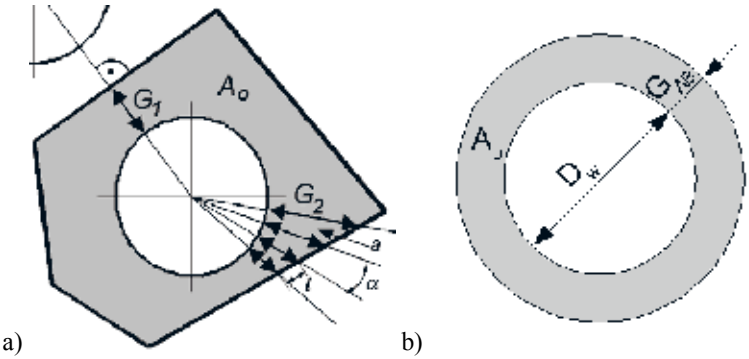

Fig. 2 a) Local thickness of the polygon layer around a single fibre, b) ring model of the matrix around fibre (author's study)

Fig. 3 presents a fragment of a geometrical model, determined for a sample composite specimen, with average matrix film thickness measures G_1, G_1, and G_{AD} represented by the circles coaxial with the corresponding fibre.

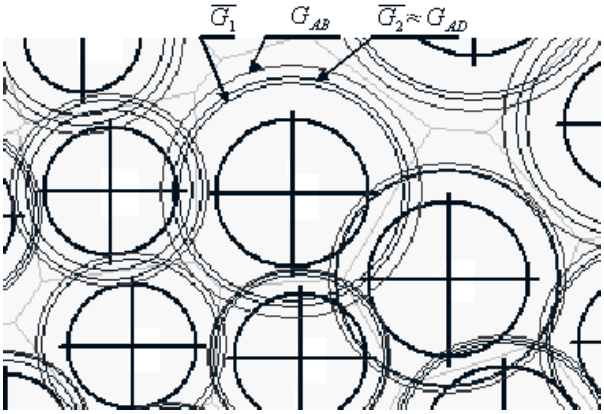

Fig. 3: Fragment of roving composite microstructural model with circles significant averages of matrix layers around singles fibres $\overline{G_1}, \overline{G_2}$, G_{AB} and G_{AD} (author's study) (Płaska and Wolszczak 2004)

Fig. 4 illustrates the how the local film thickness measured around the fibre perimeter (dashed curve) relates to the values of the corresponding average matrix film thickness measures G_1, G_1, and G_{AD} calculated for the fibre.

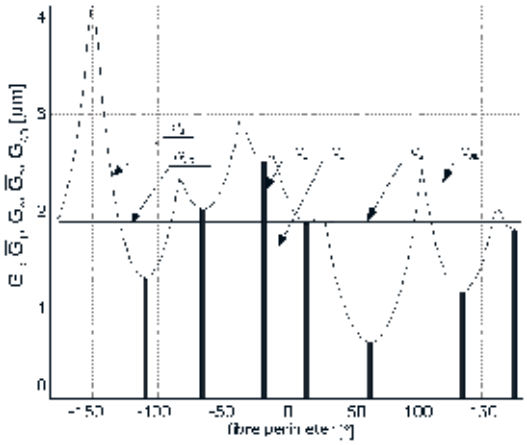

Fig. 4: Thickness of the matrix layer circumference single fibre along its perimeter (horizontal axis - angle +/-180°) defined as a measurements: $G_1, \overline{G}_1, G_2, \overline{G}_2, G_{AB}$ (vertical axis) (author's study) (Płaska and Wolszczak 2004)

3. INTERPRETATION OF THE RESULTS OBTAINED

The set of material strength characteristics contained 11 measurements, while the set of geometrical microstructural measurements had 13 values for each sample. In the final phase of the statistical correlation analysis, the geometrical measurements were tested for correlation with the material strength values obtained form shear strength tests (PN-EN ISO 2003).

The uniform high quality of the samples received, resulting from the quality control level and manufacturing standards in the aerospace industry made it difficult to determine a strong correlation between geometrical measures and strength test results. However, a comparison of two sets of samples, one containing the highest value of transverse elasticity modulus E_{2t}, (set A) and the other, containing the lowest, located on opposite sides of the E_{2t} range (set B), shows a correlation between the strength of the sample and its geometrical properties. The differentiation between the sets A and B, confirmed by a Student's t-test is illustrated in Fig. 5.

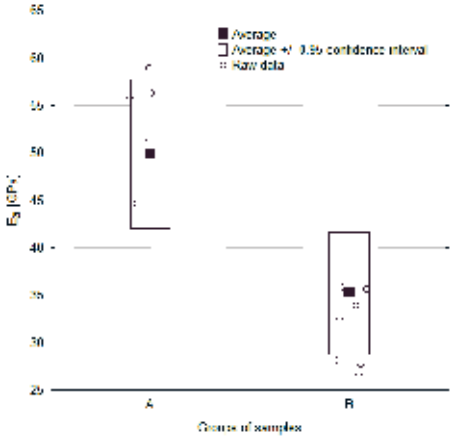

Fig. 5: Modulus of shear averaged values (□) in two groups of samples, raw data (Δ) and confidence interval ($\perp$/$\top$) (author's study)

Thus, there is a problem requiring explanation: does any of the geometrical measures correlate with the strength measurements. In the first instance the fibre diameter D_w. was analysed.

Fig. 6 shows distributions of fibre diameters $D_w[\mu m]$ in both groups of samples. The difference between average values of $D_{w(A)}$ and $D_{w(B)}$ is significantly lower than the variation $\delta_{w(A)}$ and $\delta_{w(B)}$ in both groups. That similarity indicates that no significant correlation exists between the fibre diameter and sample strength.

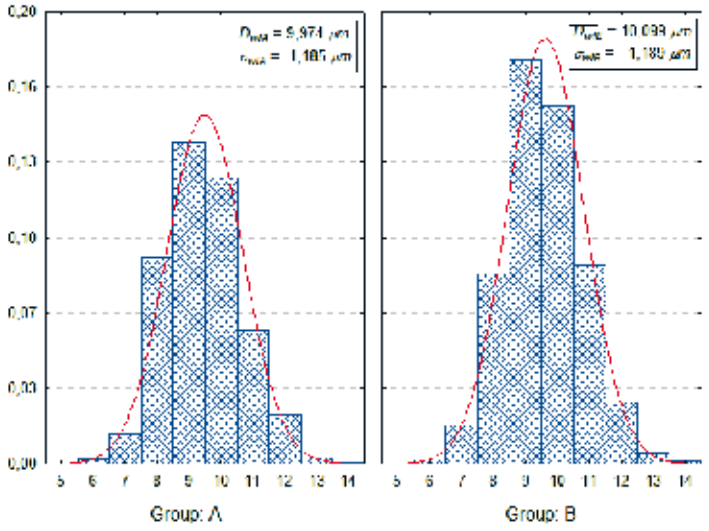

Fig. 6: Fibre diameter D_w distribution: a) set A, b) set B (author's study)

Another quantity tested for correlation was the relative volume of glass U_{sz} [%]. Fig. 7 shows the distributions of the relative volume of glass U_{sz} [%] in both sets. It was found that the average values in both sets differ, what may suggest the existence of a correlation.

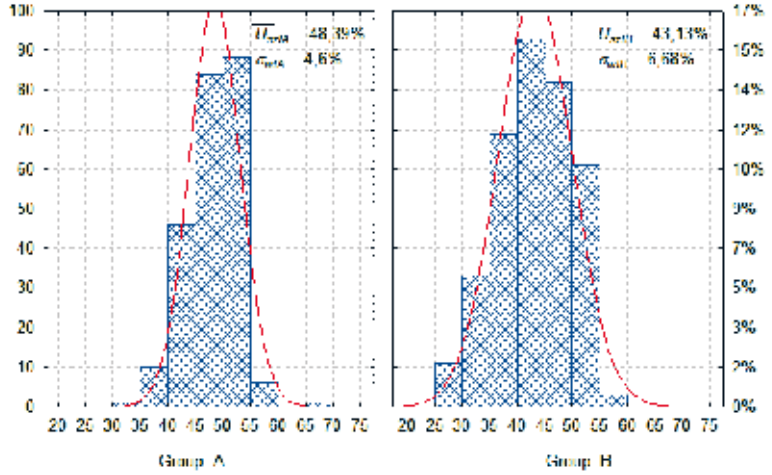

Fig. 7: Distributions of glass relative volume: a) set A, b) set B (author's study)

A discriminant function an analysis was used to determine the importance of the selected factors (Płaska 2000).

On the basis of the correlation analysis three of the total group of 13 measures were selected:

- G_{AB} - conventional matrix film thickness around a single fibre,
- G_{1min} - the minimum matrix thickness around a single fibre,
- U_{sz} - the glass relative volume of glass.

Locations of the members of the sets A and B in the space defined by variables selected in the correlation analysis [U_{sz}, G_{AB}, G_{1min}] are shown in Fig 8.

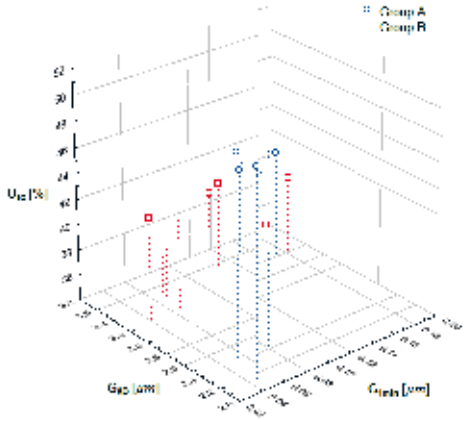

Fig. 8: U_{sz}, G_{AB} i G_{1min} values of subsets A(○) and B(□) samples (author's study)

A discriminant function for this case could be defined as:

$$D_1 = 14{,}357 + 1{,}649\ G_{AB} - 16{,}944\ G_{1min} - 0{,}396\ U_{sz}\ . \qquad (3)$$

Its significance level, as defined in a chi-square test, was p = 0.0001. The high value of the canonical correlation R = 0.9151 indicates a strong correlation between groups and the discriminant function (Stanisz 2007). Consequently, the function (3) is a good classifier for the sets A and B.

The results of the above analysis were verified by applying the discriminant function (3) to all samples. In the results, all but one of the original members of the sets A and B were classified incorrectly (93.3% accuracy).

A classification based on an evaluation of distances from individual cases to block centroids and a probability analysis of specimens classifications to appropriate groups were consistent with the results obtained by using the classification function.

The coefficients in the formula (3) were evaluated from the standardized coefficients of the discriminant function (Table 1), and structural factor coefficients (Table 2) (Płaska 2000).

Table 1: Discriminant function coefficients (author's study)

	Coefficients	
	Raw	**Standardized**
Constant	14,357	
G_{AB}	1,649	0,448
G_{1min}	-16,944	-0,746
U_{sz}	-0,396	-0,945
Eigenvalue	5,151	

The standardized coefficients of the discriminant function determine how the particular variable contributes to the group differentiation into the sets A and B. The highest standardized coefficient value in Table 1 reaches the U_{sz} characteristic, which is -0.945. It is worth noting, that the quality G_{AB} is related to U_{sz} (Konsztowicz 1986). Additionally, the coefficient of G_{AB} is inversely proportional to U_{sz}, which means that the contribution made by of one characteristic is decreased by the influence of the other. In this situation, a structural factor analysis was performed to find out the real influence of both factors (Table 2).

Table 2: Geometrical characteristics – canonical coefficient correlation (author's study)

	Element 1
G_{AB}	0,837
G_{1min}	0,188
U_{sz}	-0,810

Structural factor coefficients (Table 2) determine the individual contribution of characteristics to the value of the discriminant function (Płaska 2000; Stanisz 2007). Characteristics G_{AB} and U_{sz} have similar, high values of the coefficients (Table 2), while the correlation coefficient of G_{AB} is greater than the coefficient of U_{sz}.

As the results show, the fibre diameter quality has no significant influence on sample strength. This confirms the information contained in the histogram shown in Fig. 6. in accordance with the plan for obtaining specimens, with the same fibre diameter. While an essential influence of the relative volume of the glass U_{sz} on the variability in this group of specimens makes it difficult to analyse the effects of the fibre arrangements.

The results of the discriminant function analysis (performed on sets A and B) proved as significant the following geometrical characteristics: G_{AB}, G_{1min}, U_{sz}. Therefore, a verification of these characteristics impact on the value of the transverse elasticity modulus E_{2t} was made. The verification was carried out using a multiple regression analysis method.

The aim of this analysis was to determine whether the characteristics selected during the discriminant analysis clearly and thoroughly define the composite structure, and if the transverse elasticity modulus value E_{2t} could be determined from these characteristics.

The aim of the analysis is to find the coefficients of the function $E_{2t}(G_{1min}, G_{AB}, U_{sz})$, and their interpretation.

A linear regression equation obtained from the analysis has the following form:

$$E_{2t} = 93{,}82 - 20{,}52\ G_{AB} + 77{,}74\ G_{1min} - 0{,}0076\ U_{sz} \pm 6{,}47 \qquad (4)$$

(115,4) (13,7) (50,9) (1,7)

Below the equation, in parentheses standard errors for estimating the value E_{2t} are listed. The resulting model explains a 74.39% variation of E_{2t} in the considered specimen group.

Analysing the relationship (4) it should be noted that in the examined variability of the research material, the greatest impact on the value of E_{2t} was the average matrix thickness around fibre G_{AB}.

Given that the characteristics of composite construction are interlinked, the sense of the coefficients in the linear equation is easy to interpret and consistent with observations made during the discriminant analysis.

It should also be noted that the value of the average matrix thickness around the fibres (for example, expressed by measure G_{AB}) is related to the relative volume of glass. However, the G_{AB} value may be increased if there are gas pores in the cross-section surface. The presence of gas pores reduces the value of the transverse elasticity modulus E_{2t}. Increasing the minimum distance between neighbouring fibres G_{1min} will improve the composite elasticity (a lower number of adjoining fibre pairs). The influence of the relative volume of the glass U_{sz} on E_{2t} is not significant in relation to other characteristics. This is probably due to, the fact that the relative volume of glass is already included in G_{AB}.

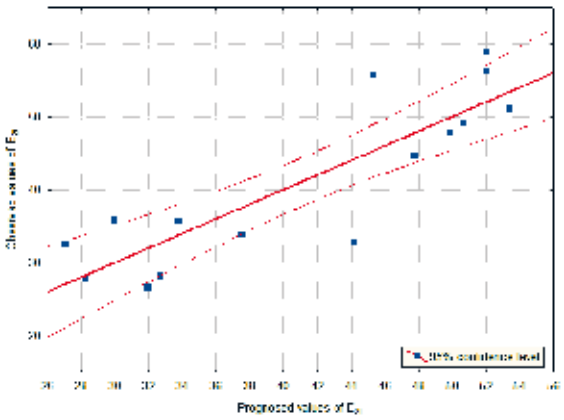

Fig. 9: Predicted and observed values E_{2t} correlation (author's study)

The results of the transverse elasticity modulus E_{2t} calculated from equation (2) and compared to the strength test results are shown in Fig 9. Most of the cases are located within the confidence limits. These results are consistent with the relation (3).

4. CONCLUSIONS

It has been shown that the strength of a roving composite defined as the transverse elasticity modulus value E_{2t}, in the range of variability of the samples examined could be classified in different groups by using the results of the geometrical analysis of the cross-section: the average matrix thickness around a fibre $\overline{G}_{AB}$, the minimum thickness of the matrix G_{1min} and the relative

volume of the glass U_{sz}. In the range of characteristics considered these quantities form a linear equation which makes it possible to predict the transverse elasticity modulus E_{2t}.
The most significant contribution to the transverse elasticity modulus comes from the average matrix thickness around a single fibre $\overline{G}_{AB}$.
A correlation of the micro-geometrical properties of the composite construction, expressed mainly by the G_{AB} to its mechanical properties (transversal elasticity modulus) was proved experimentally. The composite material should not be treated as homogeneous in cases of cross loading and strength calculations should take into account the possible variability of the average matrix thickness around a single fibre G_{AB}.

REFERENCES

Beyerlein I. J., Zhou C. H., Schadler L. S.: Int. J. Solids Struct. 2003, 40, 2171–2194.

German J. „Podstawy mechaniki kompozytów włóknistych", PK Kraków 2001.

Gusev A. A., Hineb P. J., Ward, I. M.: Compos. Sci. Technol. 2000, 60, 535–541.

Kamiński M. M. "Computational mechanics of composite materials - sensitivity, randomnes and multiscale behaviour",Springer Londyn 2005.

Kelly A., Zweben, C. "Comprehensive Composite Materials", Elsevier Science 2000.

Kołosow A., Kljawlin W.: Miechanika kompozitnych materialow 1987,6, 990-998.

Konsztowicz K. „Kompozyty wzmacniane włóknami. Podstawy technologii" AGH Kraków 1986.

Krywult B. „Wybrane problemy technologiczne i badawcze z zakresu przetwórstwa tworzyw wzmocnionych włóknem" Postęp w przetwórstwie materiałów polimerowych, Częstochowa 2002, 136-140.

Kurzeja L. Chemik 2004, 57, 162.

Kurzydłowski K. J., Ralph B. "The quantitative description of the microstructure of materials",CRC Press USA 1995.

Missoum-Benziane D., Ryckelynck D., Chinesta F. "Micro-Macro approach for mechanical problems involving microstructure" 10 ESAFORM Conference on Material Forming (pod red. Cueto E. i Chinesta F.) 2007, 1342-1347.

Nairn J. A., Liu Y. C., Galiotis C. "Analysis of stress transfer from the matrix to the fiber through an imperfect interface: application to Raman data and the single-fiber fragmentation test" ASTM STP 1290, USA, 1996.

Ochelski S. „Metody doświadczalne mechaniki kompozytów konstrukcyjnych", Warszawa , WNT Warszawa 2004.

Płaska S. „Wprowadzenie do statystycznego sterowania procesami technologicznymi", PL Lublin 2000.

Płaska S. i Wolszczak P. „Pomiar i ocena rozmieszczenia równolegle ułożonych włókien wzmacniających tworzywa" Materiały polimerowe i ich przetwórstwo. Częstochowa 2004, 65-74.

PN-EN ISO 14125:2001/AC:2003 „Kompozyty tworzywowe wzmocnione włóknem. Oznaczanie właściwości przy zginaniu".

Pyrz R., Bochenek B.: Int. J. Solids Structures 1998, 19, 2413-2427.

Rożniatowski K. „Metody charakteryzowania niejednorodności struktury materiałów wielofazowych", PTS Katowice 2001.

Rudawska A.: Polimery, 2008, 53, 452.

Siejka-Kulczyk J., Lewandowska M., Kurzydłowski K.J.: Polimery 2008, 53, 208

Śleziona J. „Podstawy technologii kompozytów", WPŚ, Gliwice 1998.

Stanisz A. „Przystępny kurs statystyki z zastosowaniem Statistica PL na przykładach z medycyny. Tom 3. Analizy wielowymiarowe", Statsoft Kraków 2007.

Wolszczak P. Przegląd Mechaniczny. 2006, 65s, 150-153.

Proceedings of the 32nd
Risø International Symposium on Materials Science:
Composite materials for structural performance:
Towards higher limits
Editors: S. Fæster, D. Juul Jensen,
B. Ralph, B.F. Sørensen
Risø National Laboratory for Sustainable Energy,
Technical University of Denmark, 2011

STIFFNESS TENSOR CALCULATION APPROACH CONSIDERING THE REINFORCEMENTS ARRANGENMENT AND ORIENTATION IN SPHERICAL PARTICULATE COMPOSITES

S. Yilmaz

Department of Mechanical Engineering
Technical University of Istanbul
34437 Istanbul
Turkey

ABSTRACT

The apparent behavior of composites is primarily determined by the respective properties of its constituents. However, the architecture of microstructure, i.e., volume fraction, size, shape, orientation and arrangement geometries of constituents, affect the stress and strain portioning of the constituents. The design of high performance, tailor made composite materials can be realized by optimizing the microstructural features. A numerical method is presented in this paper for calculation of the elastic behavior of particulate reinforced composites having a continuous metal matrix including ceramic particulates. The effects of the arrangement and orientation of ceramic particulates on the stiffness tensor of metal matrix composites were estimated. The numerical method presented can consider the arrangement and orientation effects of the reinforcement via a simple parameter named as the geometrical factor (Gf). In order to determine the geometrical factor of Gf, the projection areas of reinforcement and reinforcement embedded RVE are calculated with respect to loading direction. The geometrical factor of Gf was changed between the Gf value of the reinforcement and RVE in the implementation of numerical iterations in order to simulate the effects of the microstructural architecture. Hence, the effects of orientation and arrangement can be considered. Voronoi tessellations including a complete reinforcement were used as RVE. The Gf value of RVE was calculated with respect to the loading direction. The estimation of numerical calculations were in very good agreement with finite element method findings. An important advantage of numerical method proposed in this work is to allow the systematic and parametric investigation of the effects of the microstructure architecture on the elastic behavior of particulate composites. Further, the proposed numerical calculation approach is easy to implement and gives quick results.

1. INTRODUCTION

Particulate reinforced composites are attractive materials for many engineering applications. They have some advantages like low cost, near-isotropic properties and the possibility to be produced by traditional fabrication and forming methods. The ductility and fracture toughness of particle composites (mainly metal matrix composites) are lower, compared with that of their matrices, but improvements can be achieved in their elastic moduli and strength (Yilmaz, S., Aran A., 1998). The design of high performance tailor made composite materials can be realized by optimizing the microstructural features.

The apparent stress-strain behavior of composite is primarily determined by the respective properties of their constituents. However, the architecture of microstructure, i.e volume fraction, shape, orientation and arrangement geometries of the constituents affect the stress and strain partitioning of the constituents. The mechanical properties of composite constituents and the character of the interface can be classified as "natural parameters" of the composite domain. The volume fraction, shape, orientation, arrangement geometries of the constituents can be classified as "architectural parameters" of the composite domain. An accurate estimation method for the stress-strain behavior must consider the effects of all microstructural parameters for tailoring of composite materials. The effects of natural parameters on the stress and strain partitioning of the constituents are complex. The complexity depends on the architecture of the composite microstructure (Yilmaz, S., Aran A., 1998)

There are several analytical approaches (i.e. homogenization methods) to calculate the mechanical properties of particulate composites in the literature (Mura, 1998) . Amongst the analytical approaches, the Mori-Tanaka method (MTM) (Mori, T., Tanaka, K., 1973), which considers the inhomogenity shape and interactions by means of the Eshelby tensor (Eshelby, 1957), is one of the most sophisticated methods. The success of homogenization methods depends on the validity of the assumptions. The Finite Element Method (FEM) can consider all microstructural parameters of the composite microstructure (Yilmaz, S., Aran A., 1998) (Li, S., Wongsto, A., 2004). In this work, a numerical calculation approach considering the arrangement of spherical reinforcement was proposed to estimate the components of the stiffness tensor of the composite domain having a continuous matrix, including spherical reinforcements. The results are discussed by comparison with MTM and FEM results.

2. COMPUTATIONAL APROACH

For a composite domain having perfectly bounded double constituents, the properties lie in the upper bound-parallel loading model (Voight, 1928) and lower bound-serial loading model values (Reuss, 1929). As the volume fraction becomes very high (close to 1), the gap between the bound values is very narrow. Hence, it would be plausible to estimate the composite behavior as a weighted average of the upper and lower bounds. A matrix region including a reinforcement having a volume fraction of V_f can be built up by a collection of a nested sequence of skins as shown in Fig. 1. In that case, each skin includes a composite domain having a volume faction very close to 1. For the stiffness tensor of the composite, it was assumed that the stiffness tensor of the **ith** heterogeneous domain, as shown in Fig. 1, was calculated using the following equations:,

$$C_i = (1 - Gf)C_i^{UB} + Gf\ C_i^{LB} \tag{1}$$

$$C_i^{UB} = Vf_i^S C_m + (1 - Vf_i^S)C_{i-1} \quad \text{(Upper bound - Parallel loading model)} \tag{2}$$

$$C_i^{LB} = \frac{C_m C_{i-1}}{(1 - Vf_i^S)C_m + Vf_i^S C_{i-1}} \quad \text{(Lower bound- Serial loading model)} \tag{3}$$

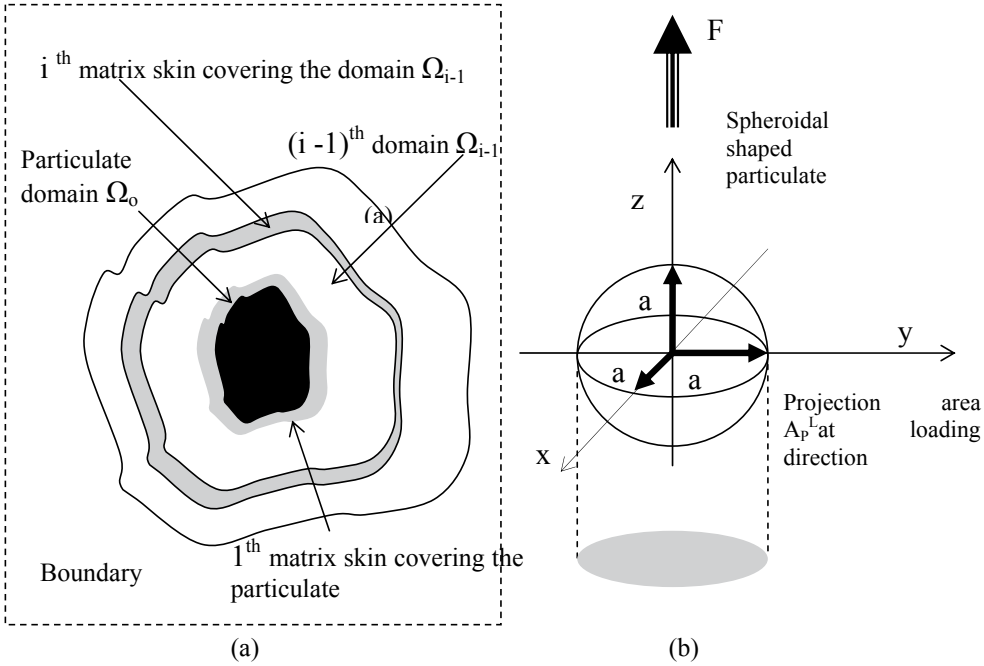

Figure 1. (a)Schematic representation of the division of the composite domain into a nested sequence. (b)Schematic representation of the projected area of the particulate in the loading direction.

where C_i^{UB} , C_i^{LB} and C_i are the upper bound value, lower bound value and weighted average value for the stiffness tensors of the i^{th} composite domain, respectively. C_{i-1} the stiffness of the inner $(i-1)^{th}$ composite domain covered by i^{th} skin; Vf_i^S the volume fraction of the i^{th} skin covering the inner $(i-1)^{th}$ composite domain. Gf is the weighted constant for the lower bound value. Apparently, the stiffness tensor of the particulate composite would be calculated by Eq. (1) for the domain covered by outermost skin.

In the present work, the ratio of the projected area to the surface area of the particulate was considered for calculating the weighted constant, Gf. The Gf value was calculated by the following equation:

$$Gf = \frac{2A_P}{As} \tag{4}$$

where A_S and A_P are the surface area and the projected area of the particulate, respectively. The multiplier 2 is necessary due to the projected area having two faces, i.e., a top side and a bottom side.

It is clear that C_{i-1} equals the stiffness of the reinforcement for the first step (i is equal to 1). A set of Visual Basic code was written in order to implement the numerical calculations mentioned above. The proposed numerical calculation approach for the projected area is named PAA in the text for simplicity. Detail of PAA calculations can be found in Ref (Yilmaz, 2010).

3. MATERIAL MODELS

The spherical shape was considered to model the mean effect of equally sized - irregularly shaped particulate as in most in particulate reinforced composites. The Gf value for a spherical geometry is 0,5.

The representative volume element (RVE) models were used for modeling the composite domain and used to examine the effects of the particulate arrangement on the stiffness tensor. At the beginning, spherical RVE systems were chosen, just like those used in the MTM, in order to remove the arrangement effect. To consider the arrangement effects, material models with an idealized arrangement of particulates were considered. In idealized arrangements, a composite domain can be assumed to have periodically distributed particulates in 3D space. Thus, a particulate-matrix packing system can be established, and a space can be built up, using unit cells (Weissenbek E., Bohm, H.J., Rammerstorfer F.G., 1994). Three different unit cells were considered. One of them was a SC unit cell having the characteristics of a non-staggered arrangement. The other ones were BCC and FCC unit cells having the characteristics of a staggered arrangement. Voronoi tessellations, which contained a complete reinforcement, were used as a RVE for the composite domain built up unit cells. SC, BCC and FCC unit cells and the corresponding RVE's are shown in Fig. 2. The shape of the Voronoi tessellation and, therefore, the shape of the RVE for domains represented by the BCC unit cell is a tetrakaidecahedron. The shape of the RVE for an FCC unit cell is a rhombic dodecahedron. In order to consider the arrangement effect, the Gf value was assumed to be equal to the value of the particulate in the first step, and then it was approached linearly to the value of the RVE, in the numerical iteration steps of the numerical calculations of the PAA proposed.

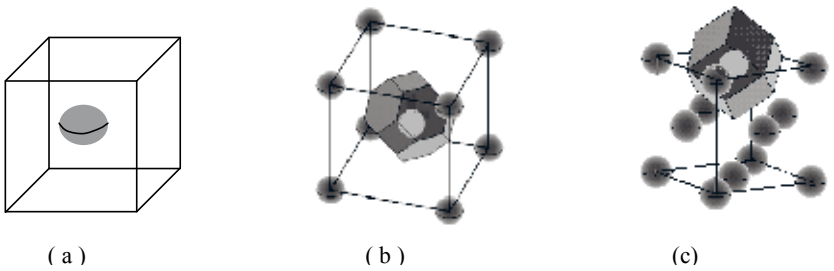

Figure 2. SC (a) , BCC (b) and, FCC(c) unit cells and Voronoi tessellations for the RVE considered for particulate arrangements.

4. RESULTS AND DISCUSSION

The stiffness tensors of composite systems were calculated by the PAA proposed. In order to clarify the health of the PAA calculation, a simple case isolating the arrangement effect was considered firstly. The MTM findings belonging to the case of a spherical particulate were compared with the results of the PAA proposed, in Fig 3. As seen from Fig. 3, the agreement between the PAA results and MTM findings were very good. The curves of the PAA calculations were close to the MTM results (Fig 3). To reveal the success of the PAA on the arrangement and orientation effect considerations, the elastic moduli of composite systems were also calculated by the PAA proposed and compared with the FEM results [5,9] given in Table 1 and Table 2. Similar to the FEM findings, PAA estimations yielded different elastic moduli values depending on the different Gf parameters representing the cases of arrangements and orientations (Table 1, Table 2). In general, the FEM analysis yielded slightly higher elastic moduli values than the PAA predictions. The mutual Poisson contraction effect of the composite components, causes a stress triaxility development in the components. FEM calculations are able to consider the effect of a triaxial

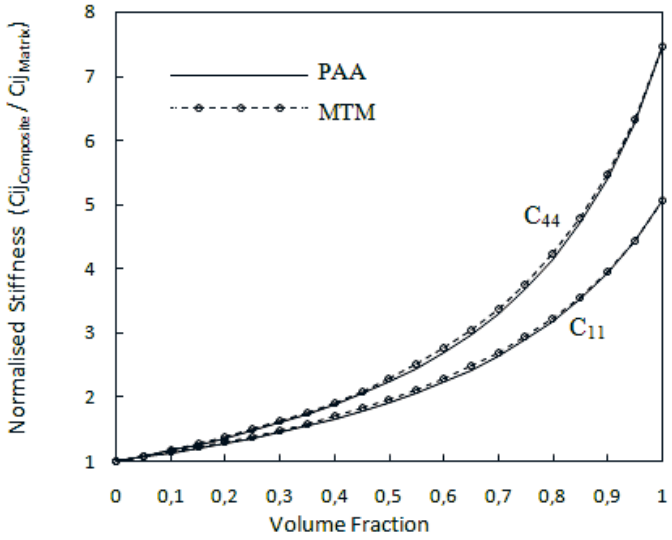

Figure 3. Normalized elastic moduli versus volume fraction. (a) PAA estimations and comparison with MTM results.

stress state development [1]. The highest stress triaxility development is in the SC arrangement [1]. Therefore, the PAA-predictions at an 001 orientation for the SC arrangement were the most different than the FEM-calculations, as expected. However, the PAA estimations for elastic moduli values were generally close to the FEM results (Table 1, Table 2).

Table 1. Elastic moduli of Al-SiC_p composite calculated for different arrangements and loading orientations by the finite element method using unit cell models and by the PAA proposed.

System	Unit Cell	FEM[9] (GPa)			PAA (GPa)			Gf^{001} for RVE	Gf^{110} for RVE	Gf^{111} for RVE
Al / 20 %SiC_p		E^{001}	E^{110}	E^{111}	E^{001}	E^{110}	E^{111}			
E_{Al}= 67.2 GPa, υ_{Al}=0.35 E_{SiCp}=429 GPa υ_{SiCp}=0.17	SC	96.4	90.2	-	94.0	90.3	89.8	0.000*	0.471	0.577
	BCC	89.9	91.1	-	90.2	90.7	90.8	0.523	0.424	0.427
	FCC	90.0	91.6	-	90.5	90.3	90.9	0.471	0.500	0.405

*See Appendix

Obviously, elastic modulus of E^{110} can be expressed in terms of E^{100} and E^{111} as:

$$\frac{4}{E^{110}} = \frac{1}{E^{001}} + \frac{3}{E^{111}} \tag{5}$$

and it is not independent [5,9]. It can also be easily proved that E^{110} always falls between E^{001} and E^{111}. It is seen from Table 1 that PAA estimated elastic moduli values also obey this rule except for the FCC case. For example, with the help of Eq. 5, using the PAA estimated elastic values given in Table 1 for 001 and 111 orientations, E^{110} values were calculated as 90.8, 90.7, 90,6 for SC, BCC and FFC arrangements respectively. These values are very close to PAA estimated E^{110} values and also indicate the success of the proposed approach. The difference seen in FCC case is explained in the Appendix.

Table . Elastic moduli of a glass-epoxy particulate composite

System	RVE		PAA (GPa)	FEM[5] (GPa)	Orientation	Gf
Epoxy resin / % 30 Glass particulate E_{Epoxy}=3.01 GPa, υ_{Epoxy}=0.394 E_{Glass}=76 GPa υ_{Glass}=0.23	SC	E_z	5.709	6.822	001	0.000
		υ_{zy}	0.3844	0.3354	001 / 010	
		G_{zy}	2.062	1.839	001 / 010	
		E'	5.269	5.064	111	0.577
	BCC	E_z	5.304	5.335	001	0.523
		υ_{zy}	0.3865	0.3736	001 / 010	
		G_{zy}	1.9127	2.150	001 / 010	
		E'	5.369	5.762	111	0.427
	FCC	E_z	5.339	5.150	001	0.471
		υ_{zy}	0.3863	0.3729	001 / 010	
		G_{zy}	1.925	2.067	001 / 010	
		E'	5.384	5.588	111	0.405
	CPH	E_z	5.384	5.810	100	0.405
		υ_{zy}	0.3861	0.3601	001 / $1\bar{2}0$	
		G_{zy}	1.942	2.003	001 / $1\bar{2}0$	
		E_y	5.318	5.681	$1\bar{2}0$	0.502
		G_{yx}	1.918	2.067	100 / $1\bar{2}0$	

Similar to the elastic moduli values, PAA estimations yielded different Poisson ratios and shear moduli values depending on the different Gf parameters representing the cases of arrangements and orientations (Table 2). Although cubic symmetry is not met in a CPH arrangement, the PAA predictions are also given in Table 2 for comparison purposes. It is seen form Table 2 that, the PAA estimations for Poison ratio and shear moduli values were also close to the FEM results (Table 2).

The agreement between results calculated with PAA and with MTM and FEM indicates the success of the PAA proposed in the current study. It is obvious that the proposed numerical approach (PAA) can estimate other physical properties of particle composites such as heat and electrical conductivities, the coefficient of thermal expansion, etc.

5. CONCLUSIONS

The stiffness tensor and thus moduli of particulate reinforced composite was estimated using a numerical calculation method. This method can consider the arrangement and orientation effects of a spherical reinforcement via a simple parameter, named the geometrical factor (Gf). There was very good agreement between the estimations of the proposed numerical approach (PAA) and results of the analytical MTM calculations and also results of the FEM simulations. The numerical calculation method proposed in this work allows the systematic and parametric investigation of arrangement geometry on the composite elastic behavior. Furthermore, the proposed numerical calculation approach is easy to implement and gives quick results.

REFERENCES

Eshelby, C. C. (1957). The determination of the elastic field of an ellipsoidal inclusion, and related field. *Proc. R. Soc. Lond.*, (s. A241, 376-396).

Mori, T., Tanaka, K. (1973). , Average stress in the matrix and average elastic energy of materials with misfitting inclusions. *Acta Metall. Mater., 21* , 571-574.

Mura, T. (1998). *Micromechanics of Defect in Solids.* the Netherlands, : Kluwer.

Reuss, A. (1929). Berechung der fliessgrenzen von mischkristallen aurf grund der

plastiizitatsbedingug fur einkristalle. *Zeitschrift fur angewandte mathematik und mechanik, 9* , 49-58.

Li, S., Wongsto, A. (2004). Unit cells for micromechanical analyses of particle-reinforced composites. *Mech. Mat., 36* , 543-572.

Voight, W. (1928). *Lehrbuch Der Kristallphysik.* Berlin-Leipzig: Teubner Verlag.

Weissenbek E., Bohm, H.J., Rammerstorfer F.G. (1994). Micromechanical investigation of arrangement effects in particle reinforced metal matrix heterogeneous. *Comput Mater Sci., 3* , 263-278.

Yilmaz, S. (2010). An approach for predicting the elastic modulus of heterogeneous materials, Materials and Design. *Materials and Design, 30* , 2938-2945.

Yilmaz, S., Aran A. (1998). Finite element analysis of deformation behavior in ductile matrix containing hard particles. *Mate. Sci. Tech., 14* , 1154-1162.

APPENDIX

The Gf value of a simple cubic (SC) arrangement: Due to the shape and symmetric distribution of inhomogenity, the boundary conditions are defined so that the angles between the surfaces of the RVE are preserved; thus, deformed unit cell surfaces remain parallel. Therefore, the outermost layer of the RVE is under a parallel loading condition. The Gf value for the Voronoi cell of an SC unit cell becomes zero (0.00) since it has parallelepiped walls and the angles between walls non-deform as if they are under parallel loading. Therefore, the Gf values were initially set to the value of the inhomogenity and then reduced linearly down to 0 during the numerical iteration carried out for an SC arrangement loaded in an 001 orientation.

Similarly, with respect to orientation, Voronoi tessellations of BC, FCC and CPH arrangements has some parallelepiped surfaces kept during deformation such as in the SC arrangement mentioned above. For example, the Gf value of 0.23 can be used in the 001 orientation for RVE belonging to a CPH arrangement, since 44 % of the total RVE surfaces remain parallelepiped during deformation in the 001 direction (i.e. 0.44x0.00+0.56x0.405=0.23). Therefore, the elastic modulus calculated with PAA is going to be higher calculated as 5.51 GPa which is closer to the FEM prediction value of 5.81 GPa. Accordingly, a Gf value of 0.33 can be used in the 011 orientation for a RVE belonging to the FCC arrangement, since 1/3 of the total RVE surfaces remain parallelepiped during deformation in the 011 direction (i.e. 0.33x0.00+0.66x0.5=0.33). Therefore, the elastic modulus calculated with PAA is going to be higher calculated as 91.4 GPa which is very close to the FEM prediction value of 91.6 GPa.

Previous Publications

Proceedings of the 1st Risø International Symposium on
"Recrystallization and Grain Growth of Multi-Phase and Particle Containing Materials"
Editors: N. Hansen, A.R. Jones, T. Leffers
Risø National Laboratory 1980

Proceedings of the 2nd Risø International Symposium on
"Deformation of Polycrystals: Mechanisms and Microstructures"
Editors: N. Hansen, A. Horsewell, T. Leffers, H. Lilholt
Risø National Laboratory 1981

Proceedings of the 3rd Risø International Symposium on
"Fatigue and Creep of Composites Materials"
Editors: H. Lilholt, R. Talreja
Risø National Laboratory 1982

Proceedings of the 4th Risø International Symposium on
"Deformation of Multi-Phase and Particle containing Materials"
Editors: J.B. Bilde-Sørensen, N. Hansen, A. Horsewell, T. Leffers, H. Lilholt
Risø National Laboratory 1983

Proceedings of the 5th Risø International Symposium on
"Microstructural Characterization of Materials by non-Microscopical Techniques"
Editors: N. Hessel Andersen, M. Eldrup, N. Hansen, D. Juul Jensen, T. Leffers, H. Lilholt, O.B. Pedersen, B.N. Singh
Risø National Laboratory 1984

Proceedings of the 6th Risø International Symposium on
"Transport-Structure Relations in Fast Ion and Mixed Conductors"
Editors: F.W. Poulsen, N. Hessel Andersen, K. Clausen, S. Skaarup, O. Toft Sørensen
Risø National Laboratory 1985

Proceedings of the 7th Risø International Symposium on
"Annealing Processes – Recovery, Recrystallization and Grain Growth"'
Editors: N. Hansen, D. Juul Jensen, T. Leffers, B. Ralph
Risø National Laboratory 1986

Proceedings of the 8th Risø International Symposium on
"Constitutive Relations and Their Physical Basis"
Editor: S.I. Andersen, J.B. Bilde-Sørensen, N. Hansen, T. Leffers, H. Lilholt, O.B. Pedersen, B. Ralph
Risø National Laboratory 1987

Proceedings of the 9th Risø International Symposium on
"Mechanical and Physical Behaviour of Metallic and Ceramic Composites"
Editors: S.I. Andersen, H. Lilholt, O.B. Pedersen
Risø National Laboratory 1988

Proceedings of the 10th Risø International Symposium on
"Materials Architecture"
Editors: J.B. Bilde-Sørensen, N. Hansen, D. Juul Jensen, T. Leffers, H. Lilholt, O.B. Pedersen
Risø National Laboratory 1989

Proceedings of the 11th Risø International Symposium on
"Structural Ceramics – Processing, Microstructure and Properties"
Editors: J.J. Bentzen, J.B. Bilde-Sørensen, N. Christansen, A. Horsewell, B. Ralph
Risø National Laboratory 1990

Proceedings of the 12th Risø International Symposium on
"Metal Matrix Composites – Processing, Microstructure and Properties"
Editors: N. Hansen, D. Juul Jensen, T. Leffers, H. Lilholt, T. Lorentzen, A.S. Pedersen, O.B. Pedersen
Risø National Laboratory 1991

Proceedings of the 13th Risø International Symposium on
"Modelling of Plastic Deformation and Its Engineering Applications"
Editors: S.I. Andersen, J.B. Bilde-Sørensen, N. Hansen, D. Juul Jensen, T. Leffers, H. Lilholt, T. Lorentzen, O.B. Pedersen, B. Ralph
Risø National Laboratory 1992

Proceedings of the 14th Risø International Symposium on
"High Temperature Electrochemical Behaviour of Fast Ion and Mixed Conductors"
Editors: F.W. Poulsen, J.J. Bentzen, T. Jacobsen, E. Skov, M.J.L. Østergård,
Risø National Laboratory 1993

Proceedings of the 15th Risø International Symposium on
"Numerical Predictions of Deformation Processes and the Behaviour of Real Materials"
Editors: S.I. Andersen, J.B. Bilde-Sørensen, T. Lorentzen, O.B. Pedersen, N.J. Sørensen
Risø National Laboratory 1994

Proceedings of the 16th Risø International Symposium on
"Microstructural and Crystallographic Aspects of Recrystallization"
Editors: N. Hansen, D. Juul Jensen, Y.-L. Liu, B. Ralph
Risø National Laboratory 1995

Proceedings of the 17th Risø International Symposium on
"High Temperature electrochemistry: Ceramics and Metals"
Editors: F.W. Poulsen, N. Bonanos, S. Linderoth, M. Mogensen, B. Zachau-Christensen
Risø National Laboratory 1996

Proceedings of the 18th Risø International Symposium on
"Polymeric Composites – Expanding the Limits"
Editors: S.I. Andersen, P. Brønsted, H. Lilholt, Aa. Lystrup, J.T. Rheinländer, B.F. Sørensen, H. Toftegaard
Risø National Laboratory 1997

Proceedings of the 19th Risø International Symposium on
"Modelling of Structure and Mechanics of Materials from Microscale to Product"
Editors: J.V. Carstensen, T. Leffers, T. Lorentzen, O.B. Pedersen, B.F. Sørensen, G. Winther
Risø National Laboratory 1998

Proceedings of the 20th Risø International Symposium on
"Deformation-Induced Microstructures: Analysis and Relation to Properties"
Editors: J.B. Bilde-Sørensen, J.V. Carstensen, N. Hansen, D. Juul Jensen, T. Leffers, W. Pantleon, O.B. Pedersen, G. Winther
Risø National Laboratory 1999

Proceedings of the 21st Risø International Symposium on
"Recrystallization – Fundamental Aspects and Relations to Deformation Microstructure"
Editors: N. Hansen, X. Huang, D. Juul Jensen, E.M. Lauridsen, T. Leffers,
W. Pantleon, T.J. Sabin, J.A. Wert
Risø National Laboratory 2000

Proceedings of the 22nd Risø International Symposium on
"Science of Metastable and Nanocrystalline Alloys – Structure, Properties and Modelling"
Editors: A.R. Dinesen, M. Eldrup, D. Juul Jensen, S. Linderoth,
T.B. Pedersen, N.H. Pryds, A. Schrøder Pedersen, J.A. Wert
Risø National Laboratory 2001

Proceedings of the 23rd Risø International Symposium on
"Sustainable Natural and Polymeric Composites – Science and Technology"
Editors: H. Lilholt, B. Madsen, H.L. Toftegaard, E. Cendre,
M. Megnis, L.P. Mikkelsen, B.S. Sørensen
Risø National Laboratory 2002

Proceedings of the 24th Risø International Symposium on
"Superconductivity and Magnetism: Materials Properties and Developments"
Editors: N.H. Andersen, N. Bay, J.-C. Grivel, P. Hedegård, D. McMorrow, S. Mørup, L.T. Kuhn,
A. Larsen, B. Lebech, K. Lefmann, P.-E. Lindelof, S. Linderoth, N.F. Pedersen
Risø National Laboratory 2003

Proceedings of the 25th Risø International Symposium on
"Evolution on Deformation Microstructures in 3D"
Editors: C. Gundlach, K. Haldrup, N. Hansen, X. Huang, D. Juul Jensen, T. Leffers, Z.J. Li, S.F. Nielsen, W. Pantleon, J.A. Wert, G. Winther.
Risø National Laboratory 2004

Proceedings of the 26th Risø International Symposium on
"Solid State Electrochemistry"
Editors: S. Linderoth. A. Smith, N. Bonanos, A. Hagen, L. Mikkelsen, K. Kammer, D. Lybye, P.V. Hendriksen, F.W. Poulsen, M. Mogensen, W.G. Wang.
Risø National Laboratory 2005

Proceedings of the 27th Risø International Symposium on
"Polymer Composite Materials for Wind Power Turbines"
Editors: H. Lilholt, B. Madsen, T.L. Andersen, L.P. Mikkelsen, A. Thygesen
Risø National Laboratory 2006

Proceedings of the 28th Risø International Symposium on
"Interface Design of Polymer Matrix Composites – Mechanics, Chemistry, Modelling and Manufacturing"
Editors: B.F. Sørensen, L.P. Mikkelsen, H. Lilholt, S. Goutianos, F.S. Abdul-Mahdi
Risø National Laboratory 2007

Proceedings of the 29th Risø International Symposium on
"Energy Materials – Advances in Characterization, Modelling and Application"
Editors: N.H. Andersen, M. Eldrup, N. Hansen, D. Juul Jensen, E.M. Nielsen, S.F. Nielsen, B.F. Sørensen, A.S. Pedersen, T. Vegge, S.S. West.
Risø National Laboratory 2008

Proceedings of the 30th Risø International Symposium on
"Nanostructured metals. Fundamentals to applications"
Editors: J.-C. Grivel, N. Hansen, X. Huang, D. Juul Jensen, O.V. Mishin, S.F. Nielsen, W. Pantleon, H. Toftegaard, G. Winther, T. Yu
Risø National Laboratory 2009

Proceedings of the 31st Risø International Symposium on
"Challenges in materials science and possibilities in 3D and 4D characterization techniques"
Editors: N. Hansen, D. Juul Jensen, S.F. Nielsen, H.F. Poulsen and B. Ralph
Risø National Laboratory 2010

AUTHOR INDEX